UNIVERSITÀ
DEGLI STUDI
FIRENZE

DOTTORATO DI RICERCA IN

SCIENZE CHIMICHE

CICLO XXXV

COORDINATORE Prof. Anna Maria Papini

Ruthenium(II) polypyridyl complexes: versatile tools in the design of light-responsive therapeutic agents

Settore Scientifico Disciplinare CHIM/03

Dottorando

Dott. Gina Elena Giacomazzo

Tutore

Prof. Claudia Giorgi

Coordinatore

Prof. Anna Maria Papini

Anni 2019/2022

Premise

The widely known side effects associated with the use of commonly employed antitumoral drugs, along with the growing multidrug resistance of bacterial pathogens, make it urgent to develop new and effective antitumoral as well as antimicrobial agents, which should be based on a new class of compounds, rather than analogues of known scaffolds. In this scenario, ruthenium(II) polypyridyl complexes (RPCs) are an appealing family of compounds due to their unique chemical-physical repertoires, structural diversity, chemical, and redox properties, which provide a unique opportunity for designing photostable sensitizers for photodynamic therapy (PDT) or photoactivable complexes capable to release biologically active compounds for photoactivated chemotherapy (PACT). In both cases, the main advantage is the spatial and temporal control of the drug activation using a light source, allowing for improved discrimination between malignant and healthy tissues.

Therefore, the main purpose of this PhD Thesis was devoted to take advantage of the versatile chemistry of RPCs in the design and development of effective light-responsive therapeutic agents both for anticancer and antibacterial applications. The findings here discussed are the result of the work of the author as well as of many collaborators.

Even though the use of RPCs as light-responsive tools in biomedical applications is well known to the inorganic chemistry community, we chose to structure this Thesis starting with an *Introduction* that may help any reader understand the key concepts that constitute the basis for RPCs' application in the biomedical field.

The Thesis is then organized into four chapters, each of which introduces a different class of RPCs that were synthesized and studied in this research work.

Chapter 1 discusses the properties and applications of a class RPCs featuring peculiar polyamine frameworks that confer them high water solubility as well as the ability to form heteronuclear Ru(II)/Cu(II) complexes capable of catalysing intracellular ROS

production via Fenton-like reactions. The findings revealed that this class of *highly charged RPCs* can induce a specific photoactivation-dependent cell death, both in antitumoral and antibacterial phototherapy, due to their capacity to produce $^1O_2$ and/or ROS directly in aqueous matrices.

Taking advantage of RPCs' versatile chemistry, *Chapter 2* and *Chapter 3* highlight the efforts to develop RPCs with a *'boosted'* capacity to produce singlet oxygen upon photoactivation via the incorporation of π-extensive aromatic ligands. The latter allow the existence of quasi-isoenergetic ^{3}MLCT and ^{3}ILCT states, providing the formation of an excited-state energy reservoir that prolongs the ^{3}MLCT emission and results in the reaching of high $^1O_2$ quantum yield values.

In particular, *Chapter 2* provides a straightforward synthetic approach for preparing *bis-heteroleptic RPCs containing two π-extensive benzo[i]dipyrido[3,2-a:2',3'-c]phenazine (dppn) ligands*. This class of complexes induces a potent photoactivation-dependent cell death on squamous epithelial carcinoma cells (A431), demonstrating a high specificity. Furthermore, in order to facilitate their administration and accumulation in tumour tissues, further studies were conducted on their encapsulation in cubosome nanoparticles. These findings are part of a pending patent: n 102022000023862. In addition, this chapter also discusses an intriguing application of RPCs photosensitization, in which we investigated the effect of photoinduced $^1O_2$ generation on the transport activity of sarco(endo)plasmic reticulum Ca^{2+}-ATPase (SERCA).

Chapter 3 describes Ru(II)-PSs featuring a pendant perylenemonoimide (PMI) derivative. The resulting complexes are dyads, consisting of a Ru(II) diimine complex covalently linked to an organic chromophore (PMI), with high quantum yield of $^1O_2$ production ($\phi_{(470\ nm)}$ $^1O_2$ between 0.60 and 0.70) and a marked ability to intercalate the DNA.

Finally, *Chapter 4* is dedicated to the description of a novel class of RPCs for "*photorelease antimicrobial therapy"*. In this regard, Nitroimidazole-based drugs, which are well-known antibiotics active against anaerobic bacteria, were incorporated on a ruthenium scaffold capable of releasing them upon light activation. The antibacterial activity assays in hypoxic conditions (<1% O_2) highlighted that the released nitroimidazole-based compounds reproduce the effectiveness of the free drugs, but with the key advantage arising from the spatial and temporal control over the drug activation ensured by light.

Each chapter includes the corresponding experimental section, which contains details of the synthetic procedures and adopted method.

Index

Introduction

1. Ruthenium coordination compounds: versatile tools for biological applications

Ruthenium is the 44th element in the periodic table and belongs to the platinum-group of transition metals. It possesses an electronic configuration [Kr] $4d^7\,5s^1$ and an average atomic mass of 101.07 g mol^{-1}. With an electronegativity of 2.2, ruthenium has seven naturally isotopes: ^{96}Ru (5.54 %), ^{98}Ru (1.87%), ^{99}Ru (12.76%), ^{100}Ru (12.60%), ^{101}Ru (17.06%), ^{102}Ru (31.55%) and ^{104}Ru (18.62%), of which only ^{99}Ru and ^{101}Ru are active NMR nuclei with a nuclear spin of 5/2. Karl Ernest isolated this rare element in 1844 and named it ruthenium, which comes from Ruthenia, the Latin word for Russia. Concerning its coordination chemistry, known compounds exist in at least eight oxidation states, but the most common are the +2, +3 and +4 states. Its great variety and well-studied coordination and organometallic chemistry results in wide variety of compounds with peculiar features that are utilized in a very broad field. Due to its Lewis acidic and oxophilic nature, ruthenium organometallic compounds display a wide range of properties useful both in industrial and scientific research fields such as electronics, alloys, solar cells,[1] catalysts,[2,3] and diagnostic and therapeutic agents.[4–6]

Among the various fields of applications, the efforts in the present work have been dedicated to the rational design of ruthenium(II) compounds with peculiar features for their use as therapeutic agents, including anticancer and antimicrobial.

The increasing interest in the medical application of ruthenium coordination compounds dates to the 1978 Food and Drug Administration (FDA) approval of *cisplatin* as a chemotherapeutic drug. Notwithstanding the known side effects of *cisplatin* and the other related platinum drugs, they still represent one of the most effective

chemotherapeutic drugs for the treatment of a wide variety of cancers.[7] In contrast, ruthenium compounds reveal anti-cancer activity comparable to that of *cisplatin* but with significantly less collateral toxicity and side effects.[8,9] Despite this, none of them are currently in clinical use as anti-cancer drugs. However, four complexes have successfully entered clinical trials: NAMI-A,[10,11] KP1019,[12] NK1339 as chemotherapeutics and TLD1443 as photosensitizer (PS) in photodynamic therapy (PDT) (Figure 1a).[6] And, more recently, half-sandwich Ru-arene complexes, containing 1,3,5-triaza-7-phosphaticyclo-[3.3.1.1]decane (PTA) ligand, called RAPTAs have received renewed interest as chemotherapeutics. Among these, RAPTA-C has recently progressed in clinical trials (Figure 1b). [6,13–15]

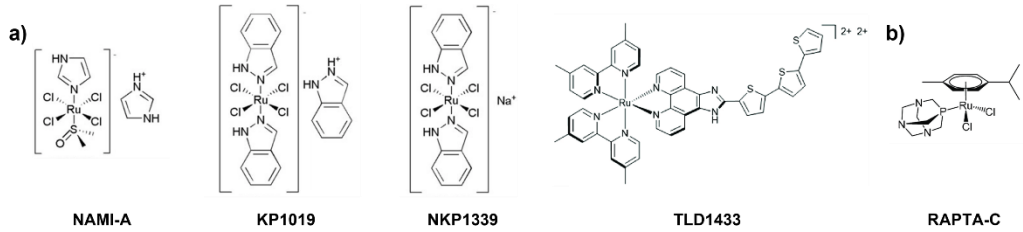

Figure 1: Anticancer ruthenium complexes (a) currently in clinical trials and (b) recently progressing in clinical trials.

Among the Ru(II)-coordination compounds' properties, the fascinating photoreactive feature of ruthenium(II) polypyridyl complexes (RPCs) is unquestionably the most intriguing feature and is the main focus of our research work. The inorganic chemistry community is widely aware of the usage of the latter family of ruthenium coordination compounds as light-responsive elements in biomedical applications. Over the past few decades, synthesis and investigation on RPCs have grown significantly. The advantages of utilizing this class of complexes include:

i) Established synthetic protocols.

ii) Reliable preparation of stable complexes with predictable structures.

iii) The ease to tune electronic properties by varying the ancillary ligands.

Polypyridyl ligands include the polypyridine backbone, in which the lone pair of pyridine nitrogen provides electrons as a σ-donor to the metal centre. The pyridine-Ru coordination bond is effective and leads to large ligand field stabilization energy. As a result, Ru(II) polypyridyl complexes prefer a d^6 low-spin electronic configuration with an octahedral geometry that can be easily exploited to access complicated three-dimensional molecular structures.[16] Furthermore, the ease with which polypyridyl ligands can be varied in nature, number, and specific functionalization allows for modulation of the final complexes' photophysical and photochemical properties: they frequently exhibit a good luminescence emission at room temperature but also provide high triplet-triplet energy and electron transfer reactions, opening up oxygen and oxygen-independent mediated photochemical reactions.[17,18] Because of the latter property, RPCs can be thought of as prodrugs that benefit from their precise temporal and spatial photoinduced activation. Light activation can be categorized into Photodynamic Therapy (PDT) and Photoactivated Chemotherapy (PACT). The former entails the generation of reactive oxygen species (ROS), such as singlet oxygen ($^1O_2$), whereas the latter involves an irreversible photochemical reaction that leads to cell death via the generation of cytotoxic photoproducts (photoreleased ligands and/or Ru(II)-based frameworks).[4]

2. Ruthenium complexes as Photosensitizers (PSs) in Photodynamic Therapy (PDT)

Photodynamic Therapy (PDT) is a non-invasive treatment used clinically to treat a wide range of pathological (*e.g.* skin, head and neck, gastrointestinal, gynecological cancers, and psoriasis) and non-pathological (*e.g.* age related macular degradation) medical conditions. The mechanism of action is as simple as it is fascinating: it is based on the synergic action of oxygen, light, and a photosensitizer (PS) agent, which trigger an oxidative process in the surrounding biological environment capable of leading to cell death (Figure 2).

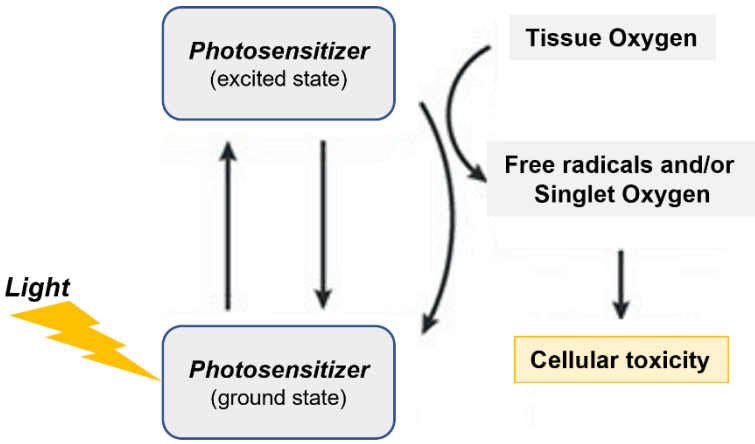

Figure 2: Simplified scheme of PDT mechanism of action.

PDT includes a sequence of energy transfers: the PS in its singlet ground state (^{0}PS) rises to its first singlet excited state ^{1}PS* with the absorption of a photon with adequate energy. The singlet excited state ^{1}PS* has lifetime ranging between nanoseconds and microseconds, afterwards, different deactivation pathways can follow: i) nonradiative relaxation to the ground state ^{0}PS, ii) fluorescence emission into its ground state ^{0}PS, iii) intersystem crossing into the triplet excited state ^{3}PS*. The latter can decay to ^{0}PS

through vibronic relaxation, radiative phosphorescence, or elicit an oxidative process which is designed into two distinct oxidation mechanisms named *Type I* and *Type II* (Figure 3).[19]

The *Type I* mechanism involves hydrogen or electron transfer between the excited PS and the surrounding biomolecules or dioxygen to produce radical oxygen species (ROS). When an electron or a proton is transferred from or to the PS, a radical anion and the corresponding cation, $PS^{\bullet -}$ and $PS^{\bullet +}$, are formed. Radical anion $PS^{\bullet -}$ reactions with biological substrate can generate a superoxide anion radical ($O_2^{\bullet -}$) via oxidative quenching. The latter can further react to form hydrogen peroxide, which can lead to hydroxyl radical by means of Fenton Reaction. A cascade of other free radicals can be initiated and can lead to diverse oxidation processes for the biological substrates (Figure 3b).[19]

The *Type II* mechanism, instead, involves energy transfer from the triplet excited state ($^3PS^*$) of the PS to the ground state of molecular oxygen ($^3O_2$) to generate singlet oxygen ($^1O_2$) (Figure 3a-b). This highly reactive species has a lifetime ranging from 30 ns to 100 ns [20,21] depending on the surroundings. Considering this, the diffusion distance of $^1O_2$ in a biological environment is less than a cell diameter, and the subcellular localization of the drug becomes an important parameter for the efficacy of PSs. In the *Type II* mechanism, the PS is not consumed and can undergo numerous $^1O_2$-producing cycles. This prerogative makes PSs capable to produce singlet oxygen those of choice in PDT.[22] Accordingly, the PDT approach allows for temporal selectivity, *in situ*, and spatial control of the pro-drug activation, which are the foundations for ensuring the success of this therapeutical method to influence medicine in the coming decade.

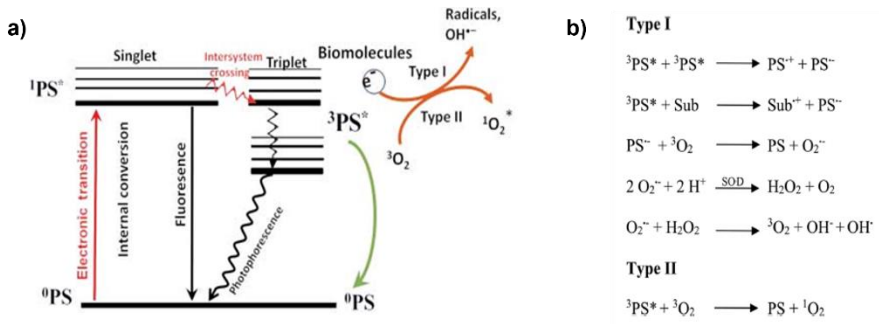

Figure 3: a) The photosensitization process in PDT; b) reactions involved in Type I and Type II oxidative mechanisms.

The clinical application of PDT has been documented for at least a century. The first scientific publication demonstrating the need for light at wavelengths capable of being absorbed by a sensitizing dye is dated 1900 by Rabb. It was Von Tappeiner, a few years later, in 1907, who coined the term "*photodynamic*" to refer to the photosensitization of a dye, eosin, applied topically to basal cell carcinomas. Following the application of localized visible light, Von Tappeiner demonstrated that tissue destruction was achieved by the dynamic interaction of light, oxygen, and the photosensitizing agent.[23] However, it wasn't until 1995, thanks to Dougherty's efforts, that Photofrin® (the commercial name for hematoporphyrin derivative (HpD)) was approved by the Food and Drug Administration (FDA) for clinical use as photosensitizers in PDT.[24]

Since then, scientific research has rekindled considerable interest in PDT. In the last two decades, a wide variety of examples have followed one another concerning the development of successive generations of photosensitizers designed to overcome the limitations of HpD, such as its scarce absorption in the near-infrared (NIR) region. PSs of the second generation, such as the chlorin-based Foscan® and NPe6, must be recognized and cited; [25] as well as PSs of the third generation, which integrate strategies for the active and passive targeting using high affinity ligands (*e.g.* proteins/peptides, nucleic acids, carbohydrates or vitamins)[26–28] or delivery methods such as nanoparticles (NPs), liposomes, and biocompatible vesicles.[29,30]

Taking this into account, in the present thesis work, a particular emphasis has been placed on the design of structural modifications that could be exploited to optimize the characteristics of RPCs as PSs in anti-cancer and anti-bacterial PDT.

For instance, the design of new RPCs for PDT applications must consider the importance of having long excited-state lifetimes, which is reflected in an increased ability to produce $^1O_2$ upon photoexcitation. Considerable efforts have been expended toward prolonging the excited-state lifetimes of RPCs. Generally, it is necessary to start from the premise that the ^{3}MLCT (metal-to-ligand charge transfer state) lifetimes depend on the interaction between the lowest energy ^{3}MLCT state and the higher-lying ^{3}MC (metal centred) state.[31] Considering this, the ^{3}MLCT lifetimes can be extended by either lowering its own energy or raising the energy of the ^{3}MC state (Figure 4).[32]

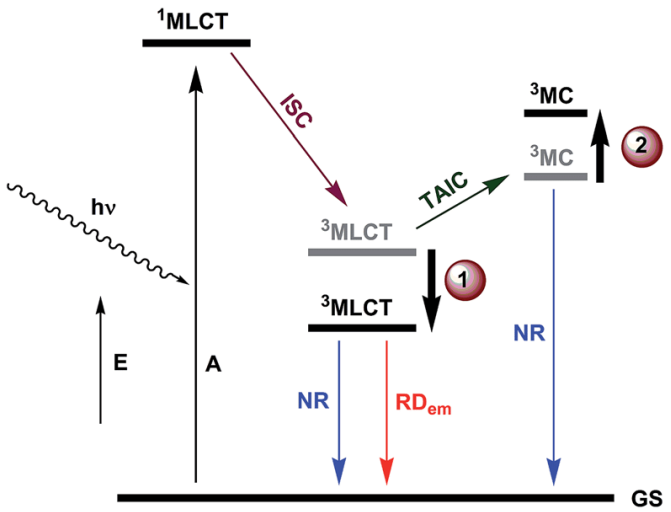

Figure 4: Two strategies for increasing the emissive ^{3}MLCT lifetime of RPCs: (1) stabilizing the ^{3}MLCT state and/or (2) destabilizing the ^{3}MC state. (E: energy, A: absorption of photon, ISC: intersystem crossing, TAIC: thermally activated internal conversion, NR: non-radiative decay, RD_{em}: radiative decay).

Stabilization of ^{3}MLCT can be achieved introducing coplanar aromatic moieties with extended π-conjugated systems or conjugating spatially separated organic chromophore.[31,33–35] These ligands provide low-lying $^3\pi\pi^*$ states in close energetic

proximity to the ^{3}MLCT state. The result is a lower energetic ^{3}ILCT (intraligand charge transfer) level than the ^{3}MLCT and the existence of quasi-isoenergetic ^{3}MLCT and ^{3}ILCT states allows for prolonging the ^{3}MLCT lifetimes.[31] Furthermore, ^{3}ILCT state may be compatible with the energy required to convert $^3O_2$ in $^1O_2$, and it may be able to contribute to the increase in $^1O_2$ production (Figure 5).[36] As opposed, increasing the energy of the ^{3}MC state is an alternative method for increasing the ^{3}MLCT-^{3}MC energy-gap (Figure 4). The ^{3}MC state can be destabilized by increasing the ligand field strength by widening the ligand bite angle, thus making the coordination geometry around the metal-ion more octahedral, or by using strong σ-donor ligands. [32]

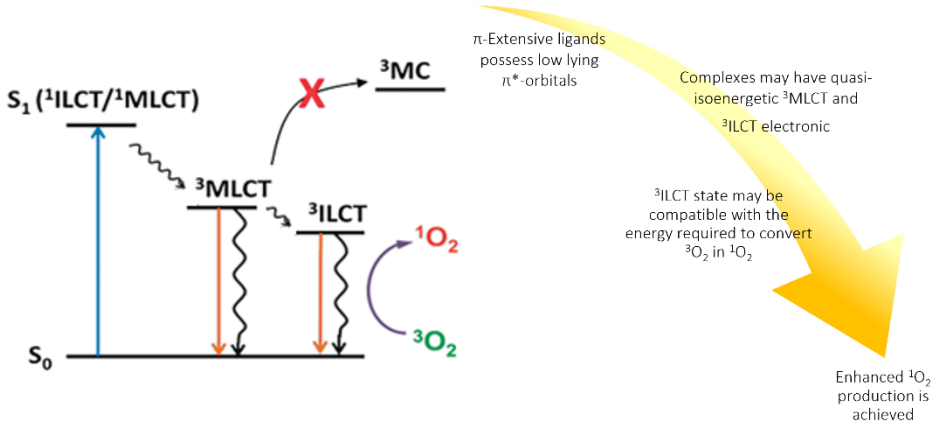

Figure 5: The introduction of π-extensive aromatic ligands provides a strategy to enhance the efficiency of $^1O_2$ production.

Another important consideration in the design of a RPC for PDT applications is the properties of the light that is used for its excitation. The penetration of light in tissues depends on the wavelength and on the optical properties of the tissues: the high percentage of water affects long wavelength light penetration in depth, instead, endogenous dyes, such as melanin and hemoglobin, absorb light at short wavelengths.

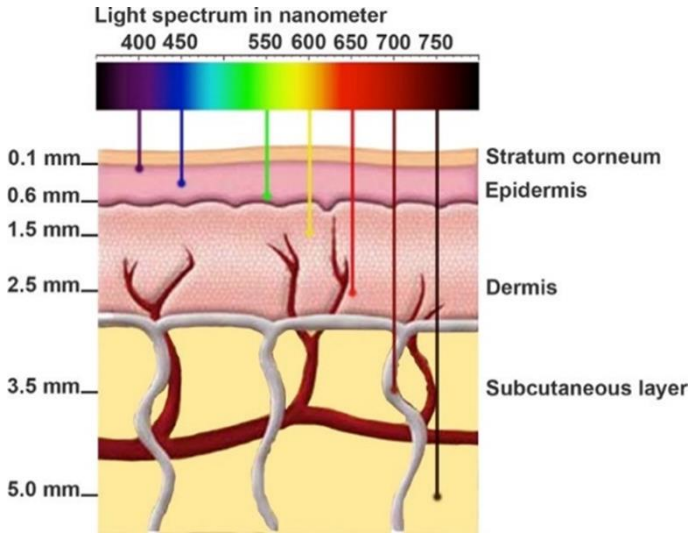

Figure 6: Schematic representation of approximate depths of light penetration into the skin based on wavelength.[37]

Furthermore, heterogeneity sites, like membranes, nuclei, and so on can cause light scattering, absorption, or reflection of light. These factors make it clear why using light in the so-called *"phototherapeutic window"* (600-1300 nm) is crucial for PDT applications (Figure 6).[37] More specifically, light over 850 nm typically does not provide enough energy to activate a PS, thus, the range of wavelengths between 620 nm and 850 nm frequently finds a fair compromise between tissue penetration and PS activation.

Exploited approaches in coordination chemistry of RPCs to achieve NIR electronic transitions are:

i) The stabilization of the ^{1}MLCT state by using large π-extensive aromatic ligands with narrowed HOMO-LUMO gaps. As a result of the low-energy π-π* transitions, the ligand may exhibit intense long-wavelength absorption.[38–41]

ii) The coordination of radical-containing ligands which makes possible to have low-energy shifted ^{1}MLCT or ^{1}ILCT transitions.[42]

iii) The preparation of mixed-valent oligo-metal or oligo-ligand complexes. Oligo-metal complexes may possess a low energy metal-to-metal charge transfer state (MMCT), instead oligo-ligands complexes possess low ligand-to ligand energy inter-valence charge transfer state (LLIVCT).[42]

Recently, another approach has come to the rescue. The advent of multiphoton lasers makes possible the application of two-photon activation in PDT. The latter is due to the fact that the absorption of two photons of NIR light leads to an increase in the population of the same excited state rises with one photon having around twice energy (Figure 7). The requirements of PSs in two-photon excitation (TPE) are a great photostability and a high two-photon absorption cross-section (TPA). [19,43]

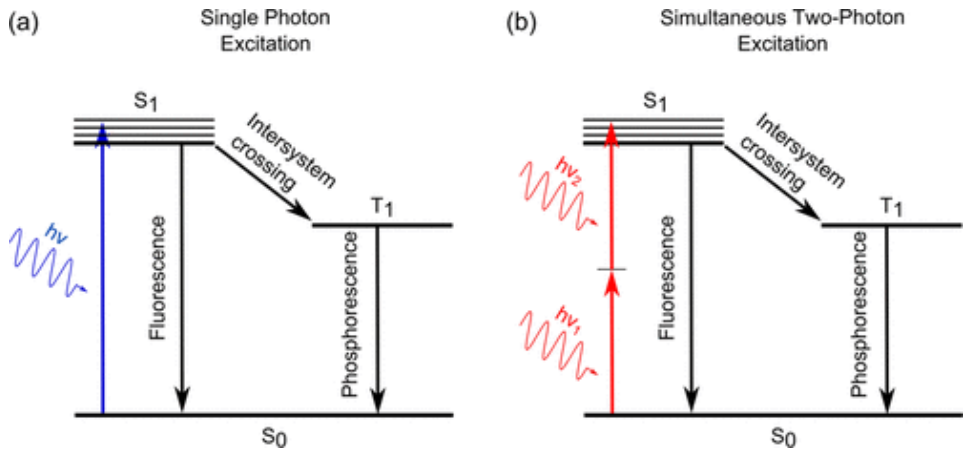

Figure 7: Comparison of a single photon excitation (a) and a simultaneous two photon-excitation.[19]

The great potential for using TPE in PDT has sparked numerous efforts to develop new metal-based PSs with high TPA. A high TPA is frequently associated with the presence of extended conjugated π system around the metal centre, and a number of Ru(II) polypyridyl complexes with such peculiarities have been studied under TPE condition (Figure 8). [44–46]

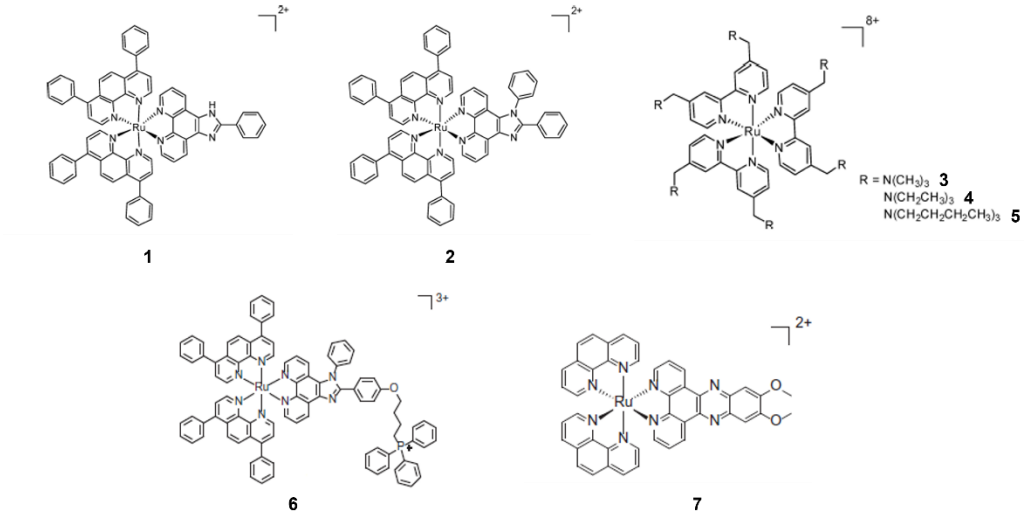

*Figure 8: Chemical structure of RPCs investigated as PSs in two-photon excitation condition. Complexes **1**, **2** and **6** [44]; complexes **3**, **4** and **5** [45]; complex **7** [46]*

3. Mechanism of action of Ruthenium(II)-containing drugs involving direct interaction with DNA

The discovery of anticancer properties of Pt(II) drugs, *cisplatin* and their analogues *carboplatin* and *oxaliplatin*, triggered the request of novel metal drugs with potential anticancer activity (Figure 9). [47–49]

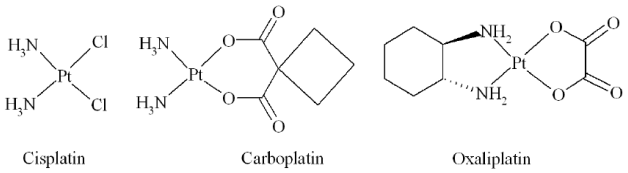

Figure 9: Chemical structures of platin-based chemotherapeutics.

Knowing the resistance of various carcinoma cells to platinum drugs, the design and development of non-platinum metallodrugs has become a research field of great interest. Among numerous metal complexes, ruthenium compounds offer new perspectives.[50,51] Pharmacological targets of antitumoral ruthenium complexes are not yet completely and univocally identified, but it is well known that their cytotoxic activity is derived from their interaction with both classical targets, such as DNA [52] and non-classical targets, such as RNA and proteins.[53,54] DNA binding studies are so far the most investigated, and it has been long demonstrated that RPCs interact strongly with DNA through covalent and/or non-covalent interactions (Figure 10).[55]

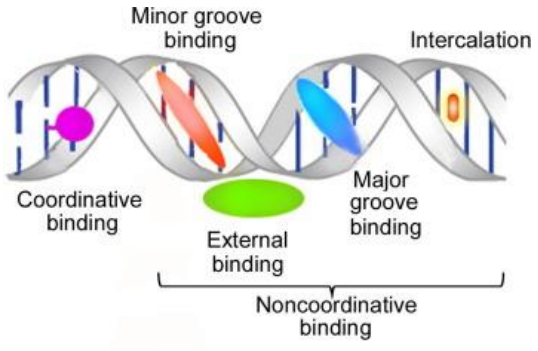

Figure 10: Schematic representation of DNA binding modes of ruthenium complexes.

In a *cisplatin* fashion-like mode of action,[56] ruthenium complexes that undergo ligand exchange reactions could covalently bind DNA. The coordinative binding is common in literature and is demonstrated to be due to the ruthenium-aqua species that can form in physiological media both spontaneously and upon photoactivation.[55] In the case of aquation reactions initiated by photoactivation, the greatest advantage as compared to *cisplatin,* is the spatial and temporal activation of DNA binding ability.[57–59]

Covalent binding is not the only possible mode of interaction. Ruthenium complexes are also extensively studied as metallointercalators; their octahedral geometry allows the targeting of specific DNA sites by tuning the symmetry, the shape, and the functionalities on the metal center. Moreover, their peculiar photophysical and photochemical properties can be exploited to design effective DNA probes.[60]

Early studies on the DNA interaction mechanisms of $[Ru(phen)_3]^{2+}$ (phen: 1,10-phenantroline) elucidated three noncovalent interaction modes: i) electrostatic, ii) hydrophobic binding against the minor groove, and iii) partial intercalation of one of the phenanthroline ligands into the DNA base stack from the major groove side.[61] These finding provide the basis for the development of novel Ru-intercalators, demonstrating how intercalative binding affinity can be significantly increased. In this regard, the choice of extended and flat aromatic heterocyclic ligands can provide a powerful tool to probe the DNA. Their insertion and staking between base pairs provide stable anchors in the major groove with the consequence of placing the metal centre in proximity to the bases, facilitating direct photo-induced cleavage of DNA provoked by $^1O_2$ and/or ROS.[62,63]

The diverse DNA damages carried by a ruthenium-containing drug can be evaluated using different analytical techniques, including spectrophotometric and spectrofluorimetric measurements, mass spectrometry, and electrophoresis. These techniques can be utilized either to quantify the strength of the interaction or the nature of drug-DNA complexation.[64] In the present work, we mainly used UV-Visible

and fluorescence spectroscopies to investigate the effective interaction of our RPCs with DNA. Both techniques are commonly employed and allow for the study of the drug-DNA interaction by comparing the electronic absorption and emission spectra of the free drug and the drug-DNA complex.

For instance, by examining the variation in absorbance intensity and the shifting position of the absorbance maxima, it is possible to rationalize whether there is an interaction and the type of the interaction. Intercalation usually results in hypocromism and bathochromism. Since the intercalative mode involves a stacking interaction between the π electrons of an aromatic chromophore and those of the base pair of DNA, the energy level of π-π* electron transitions decreases. As a result, both a hypochromic effect and a red shift can be observed.[65] Moreover, the extent of the hypocromism and the magnitude of the shift are normally consistent with the interaction strength.[66] On the other side, when charged cations bind to the phosphate group of the DNA backbone via electrostatic attraction, secondary structure damage can occur. The latter results in a hyperchromic effect due to the remarkable increase in DNA absorbance caused by the disruption of the double helix structure, which results in the absence of hydrogen bonding between complementary bases.[67]

The strength of the binding between drugs and DNA can be quantified using absorbance variations by determining the intrinsic binding constant (Kb). The latter can be calculated by applying Benesi-Hidebrand equation (Eq. 1) where [DNA] is the molar concentration of DNA in base pairs, ε_a is the molar absorptivity at the given DNA concentration, ε_f is the molar absorptivity of the free drug, and ε_b is the molar absorptivity of the drug in the fully bound form.[64]

$$\frac{[DNA]}{(\varepsilon_a - \varepsilon_f)} = \frac{[DNA]}{(\varepsilon_b - \varepsilon_f)} + \frac{1}{K_b(\varepsilon_b - \varepsilon_f)} \qquad (Eq. 1)$$

Parallelly, fluorescence spectroscopy can also be used. The main advantages of molecular fluorescence are its high sensitivity, large linear concentration range, and

selectivity. Analytical techniques based on fluorescence emission can provide particularly useful information about the orientation of the fluorophore and its closeness to the DNA base pairs. The effects of drug-DNA interaction on fluorescence emission of the drug can be rationalized considering that covalent, electrostatic, hydrophobic interactions, and hydrogen bonding bring the drug molecule close to the sugar-phosphate backbone, resulting in a decrease in fluorescence intensity. Instead, when an intercalative mode is involved, drug molecules insert into the bases stack of the helix, and the free rotation of the drug is reduced. As a result, the radiationless deactivation of the excited states is decreased and an increment in luminescence emission is observed.[64]

4. Ruthenium(II) polypyridyl complexes (RPCs) in Photoactivated Chemotherapy (PACT)

The rich photochemistry of ruthenium compounds has been exploited for decades in supramolecular chemistry and makes ruthenium-based dyes appealing for PDT applications. Although many other transition metal complexes can be successfully exploited in PDT applications, there is one type of reactivity that ennobles ruthenium compounds compared to analogues of other metal-containing compounds: their ability to photo-substitute ligands.[22] This reactivity was discovered initially while researching the decomposition pathway of $[Ru(bpy)_3]^{2+}$.[68] The electronic structure and excited-state dynamics of $[Ru(bpy)_3]^{2+}$ are showed in Figure 11.[69] A simplified scheme of $[Ru(bpy)_3]^{2+}$ frontier molecular orbitals (MOs) is depicted in Figure 11b. Its lowest energy ^{1}MLCT transition is centered at 452 nm and the bpy ππ* transition is observed at 285 nm in water. $[Ru(bpy)_3]^{2+}$ undergoes an ultrafast (40 fs) [70] intersystem crossing (ISC) between the ^{1}MLCT state and the ^{3}MLCT state. This ultrafast ISC time is usually observed for most of RPCs and allows to say that the excited-state chemistry of these compounds takes place from the triplet manifold. In $[Ru(bpy)_3]^{2+}$, the ^{3}MLCT state is emissive; instead, in complexes where the ligand-centred ^{3}LC excited state, which involves promoting an electron from ligands(π) MOs to ligands(π*) MOs, has lower energy than the ^{3}MLCT state, the ^{3}MLCT lifetime is comparable to that found for the ^{3}ππ* state of the free ligands, and the complexes are typically not emissive, exhibit long lifetimes, and effectively sensitize $^1O_2$. On the contrary, the stabilization of the metal-centred triplet ligand field ^{3}LF states, involving transitions from t_{2g} orbitals to e_g antibonding orbitals, results in photoinduced ligand exchange. This goal can be achieved by introducing distortion around the metal centre, in this way, the orbitals overlap and the energy of e_g orbitals is reduced; the result is a ^{3}LF state with lower energy than the ^{3}MLCT state (Figure 11c).[69]

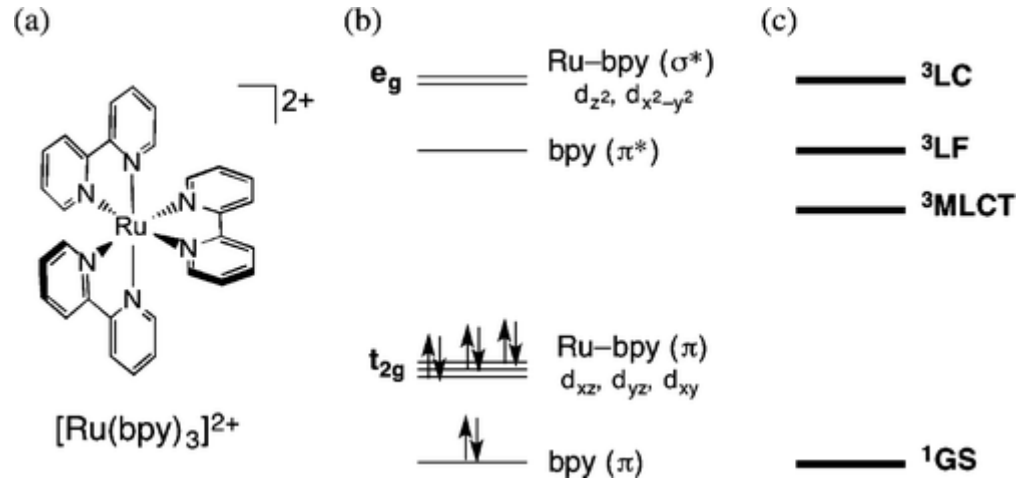

Figure 11: Molecular structure (a) and simplified (b) MO and (c) state diagrams of $[Ru(bpy)_3]^{2+}$.[69]

In other words, an efficient population of the dissociative ^{3}LF state is required to maximize photoinduced ligand exchange, which can be accomplished by introducing a distortion of the pseudo-octahedral geometry around the metal centre. To do this, one of the most commonly used methods is the introduction of sterically bulky ligands. In fact, it has been widely demonstrated that the energy of ^{3}LF state decreases as steric bulk increases.[71]

A common example of photoinduced ligand exchange is the photosubstitution of pyridine from pseudo-octahedral ruthenium(II) complexes Figure 12.[72] To increase the photodissociation quantum yield of pyridine, steric hindrance is gradually increased in the series $[Ru(tpy)(NN)(py)]^{2+}$ (tpy = 2,2':6',2''-terpyridine; NN = 2,2'-bipyridine, 6,6'-dimethyl-2,2'-bipyridine, 2,2'-biquinoline biq; py = pyridine) (Figure 12). Complex a) in figure 12 is not capable to release pyridine upon light-activation, instead irradiation of complexes b) and c) in acetonitrile generates the corresponding ruthenium photoproducts $[Ru(tpy)(NN)(CH_3CN)]^{2+}$ with a photodissociation yield of 0.16(1) and 0.033(1) respectively.[72] As expected, the crystal structures of these complexes revel a marked structural distortion of the octahedral geometry due to the presence of Me_2bpy (b) and biq (c) with a reduction of the angle between the plane defined by the

bidentate ligand and that of tridentate tpy ligand from 83.34° (a) to 67.87 and 61.89 respectively for (b) and (c) (Figure 12).[72]

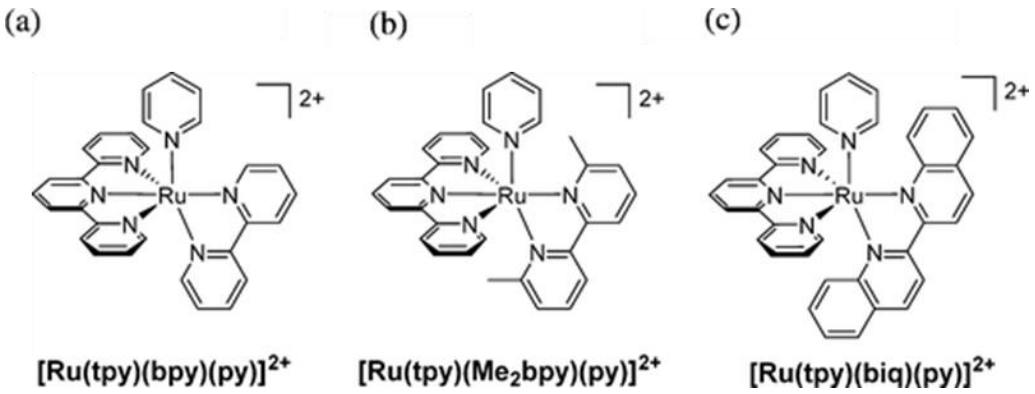

Figure 12: Molecular structurs of $[Ru(tpy)(NN)(py)]^{2+}$ (NN=bpy, Me_2bpy, biq)

This remarkable property was immediately applied in supramolecular applications, such as light-controlled molecular machines,[73,74] and it has recently been applied in biological setting as well. Ligand photosubstitution reactions can be exploited to control the spatial and temporal release of a biologically active compound, allowing the development of ruthenium-containing pro-drugs useful in the so called photoactivated chemotherapy (PACT) approach.[22] In PACT, the light-induced cleavage of a chemical bond results in a Ru-aqua species (in physiological media), capable of interacting with lipids, proteins, or DNA in a *cisplatin*-like fashion, and in the uncaging of a ligand, which can then explain its biological function (Figure 13).[22] It should be also noted that the application of photosubstitutionally labile RPCs in PACT may result in the synthesis of new photoresponsive inorganic compounds that operate via O_2-independent mechanism and are useful in both normoxic (21 % O_2) and hypoxic conditions (1 % O_2).[4]

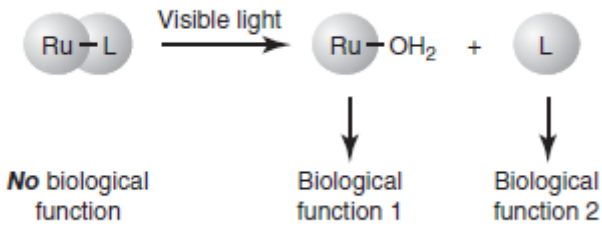

Figure 13: Schematic representation of the PACT mechanism: light-triggered photo-substitution of ligand L yields a ruthenium photoproduct and/or a free-ligan capable of explaining biological functions.

Besides the independence of PACT mechanism from molecular oxygen, which is the most significant advantage of PACT over PDT, other relevant differences between these two approaches can be highlighted. A crucial point is that the PDT approach involves a catalytic process, whereas in PACT, photochemical activation can only occur once. Indeed, high photoproducts toxicity is commonly required for Ru(II)-based PACT complexes to achieve high efficiency. On the other side, contrary to PDT, which has already been approved in clinics, none of the RPCs investigated as PACT agents have advanced to clinical trials yet. This enables PACT research to potentially benefit from the knowledge gained through the clinical advancement of PDT, such as the application of fiber-optic technology for delivering light to regions of the body that are hardly accessible.[4]

Chapter 1

Highly charged RPCs as photosensitizers in PDT

The first class of complexes discussed in the present work can be mentioned as highly charged ruthenium(II) polypyridyl complexes and are depicted in Figure 14. The peculiarity of this class of complexes is their strategic functionalization with polyazamacrocyclic units **L'** and **L''** (**L'** = 4,4'-(2,5,8,11,14-pentaaza[15])-2,2'-bipyridilophane, **L''** = 4,4'-bis-[methylen-(1,4,7,10-tetraazacyclododecane)]-2,2' bipyridine) which confers on them desirable features to be employed as PSs in PDT.

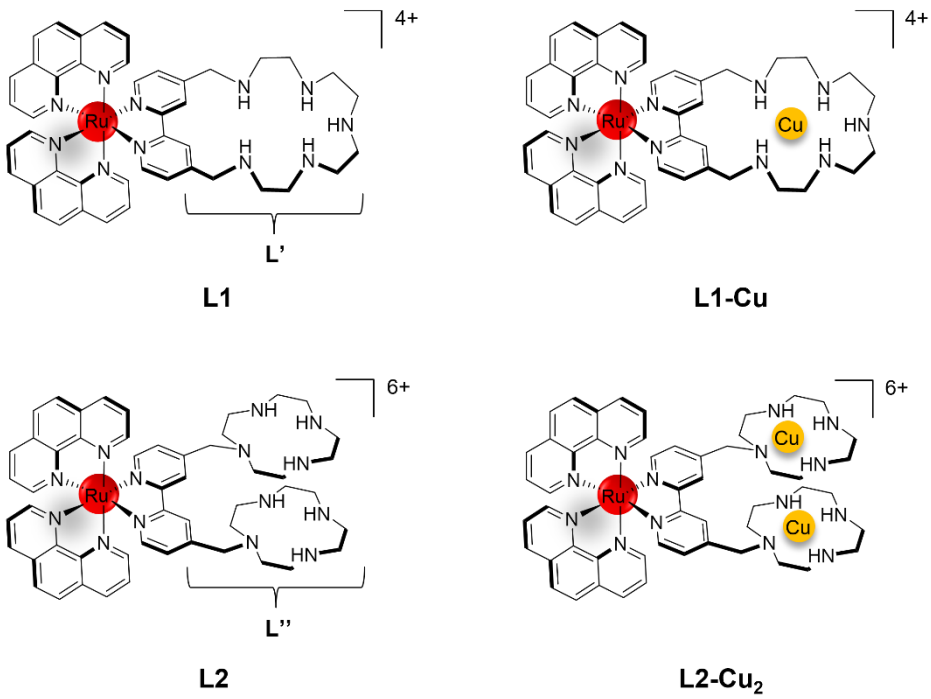

Figure 14: Molecular structure of the highly charged RPCs studied in this work.

The high number of easily protonable amine groups allows the formation of highly charged species in aqueous media, ensuring to complexes **L1** and **L2** an excellent water solubility and a strengthened capacity to interact with potential biological targets, such as the DNA (distribution coefficients $logD_{7.4}$ and intrinsic binding constants K_b with *ct*-DNA are listed in Table 2) (see EXPERIMENTAL SECTION).[75]

We point out that, since the protonation state of each ruthenium compound depends on the pH, these complexes can be present in solution in differently charged forms at different pH values. Since herein is discussed their application in biomedical field, the experimental conditions always required to work at physiological pH. The predominant species of each complex at pH 7.2 were potentiometrically determined and are listed in Table 1. According to Table 1, for clarity of discussion, we will refer to the most abundant species and merely name them **L1** and **L1-Cu** and **L2** and **L2-Cu_2**.[75]

Complex	*Species*	*pH = 7.2* *[Ru] = 0.78 – 50 μM*
L1	$[H_2Ru(phen)_2L']^{4+}$	85.0 – 85.9 %
L1-Cu	$[CuRu(phen)_2L']^{4+}$	71.6 – 72.2 %
L2	$[H_4Ru(phen)_2L'']^{6+}$	75.3 – 78.2 %
L2-Cu_2	$[Cu_2Ru(phen)_2L'']^{6+}$	99.6 – 99.9 %

Table 1: The potentiometrically determined percentage of formation of the most abundant species of ruthenium complexes present in solution in the experimental condition used in biological experiments.

Importantly, both the polyazamacrocyclic ligand, **L'** in complex **L1** and the two distinct cyclen (1,4,7,10-tetraazacyclododecane) moieties of ligand **L''** in complex **L2**, do not alter the good $^1O_2$ sensitizing property, making them appealing PS agents for the generation of $^1O_2$ directly in aqueous matrices (Table 2).[75,76]

In addition to the singlet oxygen sensitization, the versatility of the polyamine moieties of **L1** and **L2** can also be exploited to explore different pathways to exert cellular damages. Indeed, **L'** and **L''** units confer the ability to stably bind up to two Fenton-

active copper(II) ion/s, leading to the formation of mixed Ru(II)/Cu(II) complexes, namely **L1-Cu** and **L2-Cu$_2$** (Figure 14). These heteronuclear complexes are in principle able to favour the generation of other types of ROS, such as hydroxyl radicals, and thus may represent versatile tools in the research of alternative and potential mechanisms of action, even under hypoxic conditions (see EXPERIMENTAL SECTION).[75,77]

Complex	$\lambda_{abs}/\lambda_{em}$ *(nm)*	$logD_{7.4}$	K_b *(x10^4 M^{-1})*	φ_Δ *($^1O_2$)*
L1	452/611	-1.8 ± 0.1	2.77 ± 0.09	0.29 ± 0.06
L1-Cu	452/611	-1.5 ± 0.3	1.47 ± 0.01	-
L2	454/615	-1.4 ± 0.2	2.41 ± 0.09	0.38 ± 0.08
L2-Cu$_2$	454/615	-1.2 ± 0.1	1.28 ± 0.08	-

Table 2: Absorption and emission maxima ($\lambda_{abs}/\lambda_{em}$), distribution coefficients ($logD_{7.4}$), intrinsic binding constants (K_b) with ct-DNA obtained via UV-vis titrations, and $^1O_2$ quantum yields φ_Δ($^1O_2$) determined in air saturated CH_3CN solution of ruthenium compounds.

The synthetic strategy for the preparation of **L'** and **L''** polyazamacrocyclic ligands was previously reported [78,79] and is not explained in this thesis work.

Complexes **L1** and **L2** were obtained following the synthetic pathway shown in Scheme 1. [75,76]

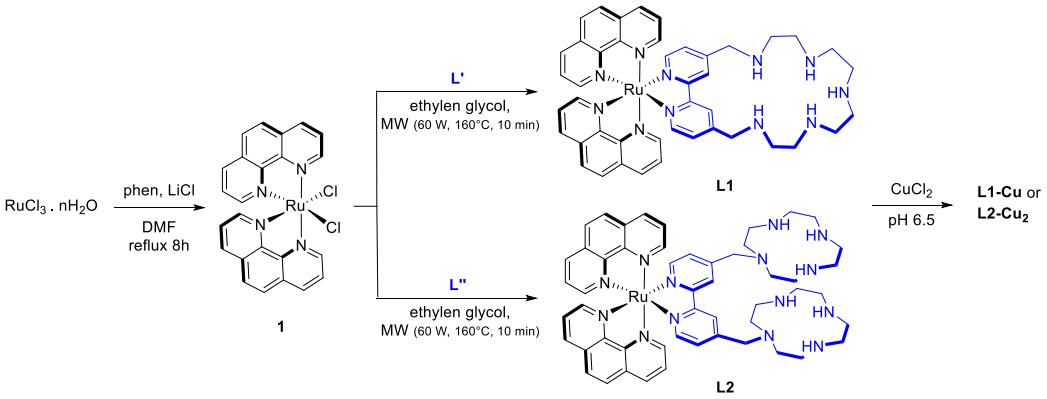

*Scheme 1: Synthetic route followed for the preparation of complexes **L1** and **L2**.*

Ruthenium intermediate **1** was prepared, according to method described in literature,[57,80] by reacting $RuCl_3 \cdot nH_2O$ with two equivalents of 1,10-phenantroline (phen) in refluxed DMF in the presence of an excess of LiCl. In this step, the volatile dimethylamine generated in situ from the decomposition of DMF at its boiling temperature reduces Ru(III) to Ru(II). The following step consists in the direct reaction of **1** with polyazamacrocyclic bidentate ligands, **L'** or **L''**, in ethylene glycol conducted with the support of microwave irradiation. The use of microwave assisted technology permits to improve the yield and effectively reduces the reaction time. Finally, treatment of **L1** or **L2** at pH 6.5 with an equimolar amount or two equivalents of $CuCl_2$ respectively affords the correspondent **L1-Cu** and **L2-Cu$_2$**.

An exhaustive research work was completed on the application of **L1** and **L2** and their mixed ruthenium(II)/copper(II) complexes, **L1-Cu** and **L2-Cu$_2$**, as photoresponsive anticancer and antibacterial agents.[75–77,81]

1.1 Antimicrobial photodynamic therapy (aPDT)

A case of study on complexes **L1** and **L2**, as well as their heteronuclear Ru(II)/Cu(II) complexes, **L1-Cu** and **L2-Cu$_2$**, was conducted in collaboration with Prof. Alessio Mengoni of the Department of Biology at the University of Florence, and concerns their use as antimicrobial agents (Figure 15).[75]

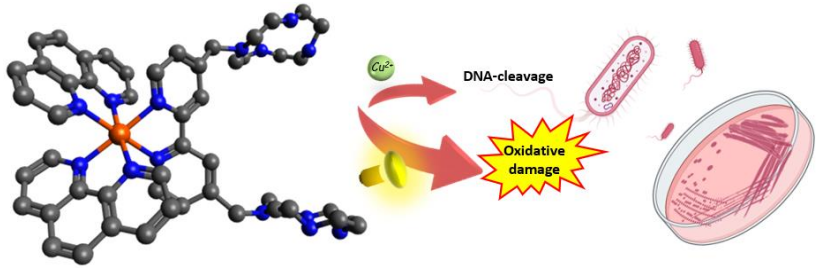

Figure 15: To fine-tune their antibacterial activity, Ru(II)-polypyridyl complexes can be designed with peculiar polyamine macrocyclic moieties that allow for effective photo-inactivation of B. subtilis while also providing mixed heteronuclear Ru^{2+}/Cu^{2+} species with DNA-cleavage properties.

Having been motivated by a recent study by Feng et al.,[82] which demonstrated that strong electrostatic interactions between highly charged ruthenium complexes and the negative charges of Gram-positive bacteria's cell walls may be essential for the efficient and selective photoinactivation of *Staphylococcus aureus,* we decided to investigate the antibacterial activity of all four ruthenium compounds. In this regard, the Gram-positive bacterium *Bacillus subtilis* strain 168 was selected as non-pathogenic model, and its inactivation was tested both in dark conditions and upon light-activation.

The obtained results, expressed in terms of cell viability (OD_{600nm}) as a function of the drug concentration, are reported in Figure 16. Data collected in dark conditions highlight that inhibition of *B. subtilis* growth starts at 6.25 μM for complex **L1** (ca. 60% of growth of the untreated control), and 3.12 μM for complex **L1-Cu** (ca. 50% of growth of the untreated control) (Figure 16a). At 3.12 μM, the difference between **L1** and **L1-Cu** is significant ($p < 0.05$, *t-test*), suggesting that the mixed Ru(II)/Cu(II) complex has a higher antibacterial efficacy than the Cu(II)-unbonded species. Similarly, both the antibacterial activities of **L2** and **L2-Cu$_2$** start at 6.25 μM, revealing no significant differences in the activities of the two systems under dark conditions (Figure 16b).

When the data collected after irradiation with LED light (λ > 430 nm, 30 W, 15 min) are analysed, no significant differences between **L1** and **L1-Cu** are detected, and neither complex improved antibacterial efficacy over those found in dark conditions (Figure 16a). A different behaviour is instead observed for complexes **L2** and **L2-Cu$_2$** that exhibit an improved concentration-dependent bactericidal effect in comparison to those found in dark conditions (Figure 16b). The minimal inhibitory concentrations (MIC) of both **L2** and **L2-Cu$_2$** upon-light activation is found to be 3.12 μM, 8-folds lower than that obtained in dark conditions (25 μM). This result denotes a marked and comparable photodynamic inactivation (aPDI) by the two compounds. With this respect, we can speculate that the aPDI of **L2** and **L2-Cu$_2$** may reflect, in the former case, the good

singlet oxygen sensitization and, in the second case, the synergistic contribution of lethal ROS species produced by Fenton-active copper centres.

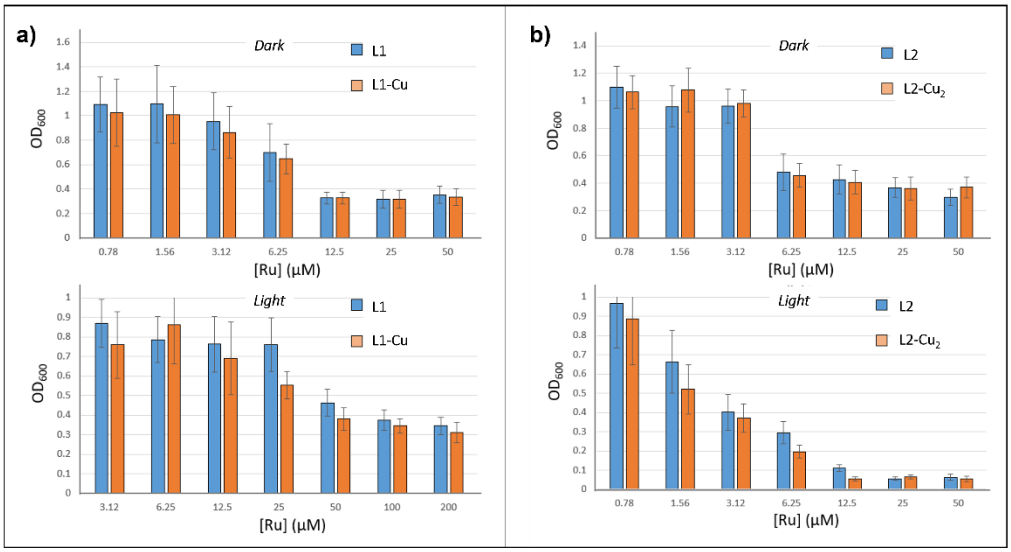

*Figure 16: Determination of the antibacterial effect of a) **L1** and **L1-Cu** and b) **L2** and **L2-Cu₂** evaluated under dark conditions and upon light-activation. The proportion of $OD_{600\,nm}$ values with respect to blank control is reported (Y-axis) for the different concentrations of the ruthenium complexes ([Ru]).*

On the other hand, the lack of phototoxicity of **L1** and **L1-Cu** compared to **L2** and **L2-Cu₂** appears harder to explain. To address this issue, the cellular uptake by *B. subtilis* was investigated. Bacteria suspensions were incubated in the dark in the presence of fixed concentration of each ruthenium compounds (25 µM) at pH 7.2 from 30 min to 24 h. After centrifugation to remove the supernatant, the Ru-content internalized by cells was determined by ICP-AES (Figure 17). It can be noted that for incubation times up to 5 h, **L2** and **L2-Cu₂** display a marked tendency to be internalized into bacterial cells, exhibiting a Ru-content up to twice-folds higher with respect to those found for **L1** and **L1-Cu.** On the other side, following 24h of incubation, an inversion on tendency is observed, with **L2** and **L2-Cu₂** appearing to be released by cells (probably partially lysed by the toxicity of the compounds), while the cellular up -take of **L1** and **L1-Cu** increases. This result suggests that the lack of phototoxicity of complexes **L1** and **L1-Cu**

after 30 min of incubation might be related, or partially related, to a difference in the kinetics of cellular internalization of such compounds.

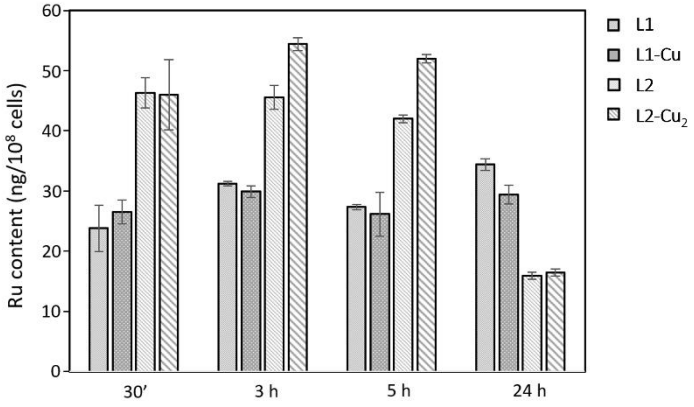

Figure 17: Cellular uptake of ruthenium compounds after 30 minutes, 3 h, 5 h and 24 h of incubation with B. subtilis obtained by means of ICP-AES analysis.

Although further research is needed to better understand the mechanisms underlying the biological effects of the compounds here investigated, these finding unequivocally show that the structural features of the polyamine frameworks appended to the 4, 4' positions of the Ru-coordinated bipyridyl ligands markedly affect cellular uptake by bacteria cells in ways that cannot be predicted simply based on lipophilicity of the compounds. These findings demonstrate the attractiveness of polyamino frameworks as design tools for Ru(II)- polypyridyl complexes, allowing for the precise modification of their chemical-physical repertoire and hence influencing their potential as powerful antibacterial candidates.

1.2 Photodynamic therapy of Epithelial Ovarian Cancer Cells

Ovarian cancer is one of the most common among gynaecologic cancers and is the major cause of tumour-associated death in reproductive women.[83,84] Surgery and chemotherapy are the major therapeutic choices, but they have limited benefits, due to the development of therapeutic resistance in response to platinum-based chemotherapy.[85] Therefore, innovative therapeutic strategies to overcome drug resistance are urgently needed, and minimally invasive and spatially/temporally precise photodynamic therapy is a technique of choice.

This scenario prompted us to conduct an in-depth investigation concerning the efficacy of photoresponsive **L1**, **L2** and their mixed Ru(II)/Cu(II) complexes, on A2780 human ovarian cancer cells. This study was conducted with the collaboration of Prof. Francesca Cencetti and Prof. Paola Bruni of the department of Experimental and Clinical Biomedical Sciences at the University of Florence. A particular emphasis was placed on the biological behaviours of Ru-containing compounds by investigating the occurrence of apoptotic cell death, ROS production, and mitochondrial function.[77]

1.2.1 Internalization and effect of Ru(II) complexes on A2780 cells

Firstly, the kinetic of Ru(II) complexes internalization and distribution into A2780 cells was studied using laser scanning confocal microscopy, which took advantage of the intrinsic fluorescence properties of Ru(II) compounds, to determine the time of incubation prior to photoactivation (Figure 18a). A similar kinetic profile emerged for all four complexes: a barely detectable green fluorescence is observed after 15 minutes, whereas the internalization increases at 6 hours of incubation and reached a plateau at 24 h. Due to the lesser emissive properties of Ru(II)/Cu(II) mixed complexes compared to **L1** and **L2**, a quantitative evaluation of internalized ruthenium compounds was performed, measuring the content of ruthenium in cell lysates by ICP analysis, after

24h incubation with a 10µM dose of each compound (Figure 18b). It should be noted that **L1** and **L2** have greater capacity to be internalized by A2780 cells than **L1-Cu** and **L2-Cu$_2$**. Based on these results, the photoactivation experiments were performed after a prior 24h incubation.

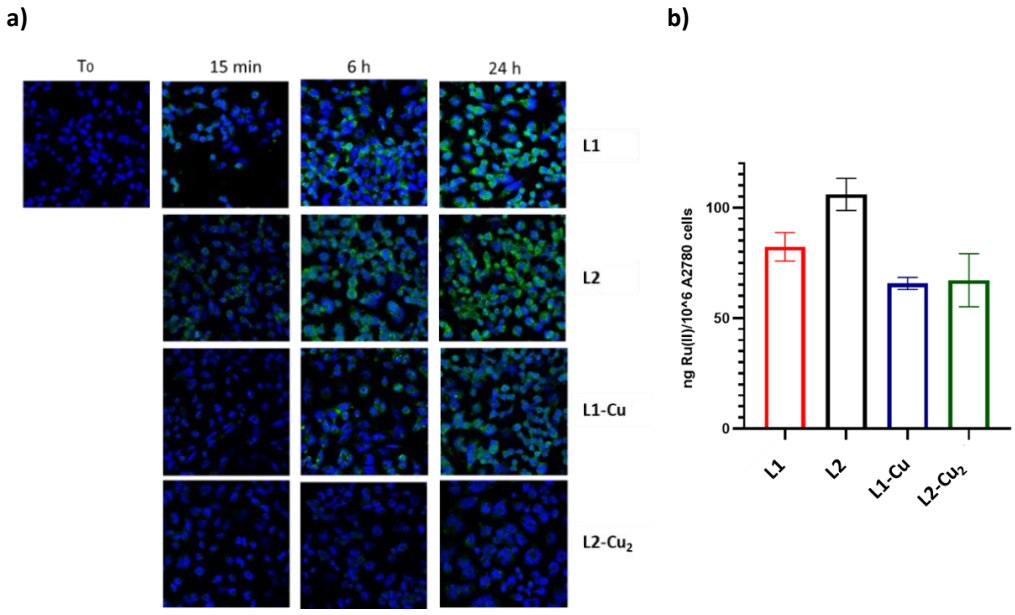

Figure 18: Internalization of Ru(II) complexes in A2780 cells. a) Laser scanning confocal microscopy was performed in A2780 cells incubated with each Ru(II) complex ([Ru] = 10 µM), for the indicated time. DAPI (λ_{exc} = 405 nm, λ_{em} = 461 nm) was used to stain nuclei (blue spots) while the fluorescence emission in green represents Ru(II) complexes (λ_{exc} = 405 nm, λ_{em} = 600-640 nm). b) Amount of internalized ruthenium obtained by IVP analysis, after 24 h of incubation of 10^6 A2780 cells with 10 µM of each ruthenium compound. Data represent the mean ± SD of 3 independent experiments.

Dose-dependent effect on dark cytotoxicity and photoactivity was evaluated by MTT assays on A2780 cells incubated for 24 hours with different concentration of Ru(II) complexes. As shown in Figure 19, under dark conditions, cell survival is only slightly affected by **L1** and **L2** at least up to a 1 µM dose of compounds; an even lower cytotoxicity is displayed by **L1-Cu** and **L2-Cu$_2$** which are almost ineffective within 0-10 µM range of concentration tested. On the contrary, irradiation of complexes (LED light, λ > 430 nm, 30 W) triggers a significant anti-cancer effect. The good singlet oxygen sensitizers **L1** and **L2** exhibit marked differences between activities in darkness and

after irradiation beginning at 100 nM; mixed heteronuclear complexes, instead, exhibit a sharper increase in phototoxicity when dosed at 10 µM, implying that, beyond the singlet oxygen sensitization, alternative oxidative pathways must be accessible to heteronuclear compounds, leading to similar photoinduced effectiveness compared to the one of copper-unbonded complexes. However, further efforts will be needed to obtain further insights into these processes, which likely occur under biological conditions and appear to be hard to mimic in cell-free experiments.

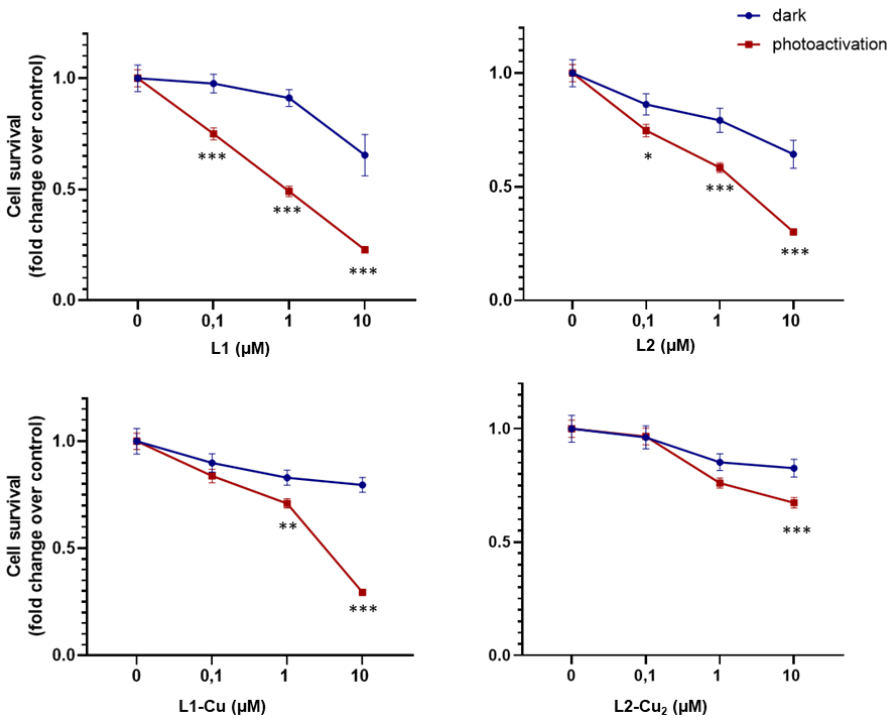

*Figure 19: Dose dependent effect of Ru(II) complexes on cell survival of ovarian cancer cells after photosensitization. A2780 were incubated for 24 h in the presence of **L1**, **L2**, **L1-Cu** and **L2-Cu$_2$** at 0, 0.1 µM, 1 µM, 10 µM in serum-deprived culture media (RPMI with BSA 0.1%). Photoactivation was carried out using a 30W LED lamp with 430-470 nm blue emission for 20 minutes, at a distance of 5 cm from the cell plate. Data reported are mean ± SD of three independent experiments. The effect of photoactivation of Ru(II) complexes on the inhibition of cell survival is statistically significant by two-way ANOVA followed by Bonferroni post-hoc test. *P<0.05, **P<0.01, ***P<0.001.*

With the purpose of dissecting the possible involvement of ROS species production in the biological effect induced by these PSs, confocal analysis was performed in A2780

cells employing the CM-H_2DCFDA (DCF) probe to detect cytosolic ROS after 10 µM PSs incubation for 24 hours followed by photoactivation for 20 minutes.

As shown in Figure 20, cytosolic ROS are almost completely undetectable in A2780 after Ru(II) administration in darkness, even when complexes are efficiently internalized (red fluorescence). Instead, as early as 2 hours after photoactivation, cytosolic ROS are detected in the majority of cell populations, suggesting a critical role for ROS in the cytotoxic effect of the PSs.

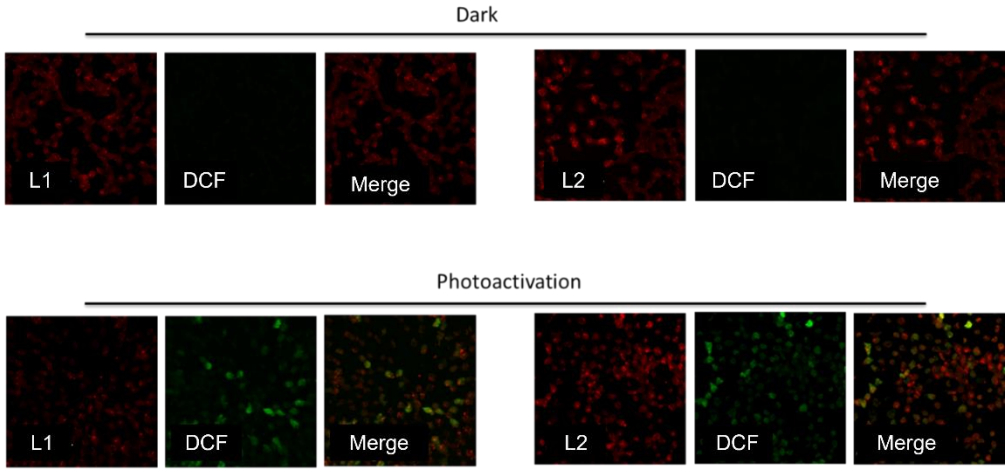

*Figure 20: Effect of **L1** and **L2** on ROS production after photoactivation. Confocal analysis was performed using 63X oil immersion objective. The fluorescence of Ru(II) complexes is shown in red ($\lambda_{exc}/\lambda_{em}$: 405/600-640 nm), while DCF in green ($\lambda_{exc}/\lambda_{em}$: ~492-495/517-527 nm). Images are representative of six fields of each condition in three independent experiments with analogous results.*

1.2.2 Effect of Ru(II) complexes on apoptosis in A2780 cells

Apoptotic programmed cell death is clearly advantageous for the organism compared to necrosis because during apoptosis the cell membrane remains intact, preventing the release of intracellular content. Hence, the elucidation of the mechanisms that triggered cell death after the light activation of Ru(II) complexes appears to be crucial. To this aim, the involvement of apoptosis was studied analysing the effect of photosensitization on caspase 3 protein which is an effector for apoptosis execution.

Caspase 3 activity assay was performed on 30 µg of total cell lysate of A2780 cells that had previously been incubated 24 hours with 10 µM of PSs, photoactivated or not, and incubated again for 24 hours. A specific fluorogenic substrate Ac-DEVD-ACF (ex/em: 400/505nm) and CHO specific inhibitor of caspase 3 were incubated in reaction mixture to quantify the unspecific emission of the probe.

As shown in Figure 21a the treatment with all the photosensitizers is completely ineffective on caspase 3 activity under dark conditions, whereas the light activation of each complex after 24 hour-incubation caused a significant and potent activation of the pro-apoptotic enzyme. Contemporary, apoptosis involvement in the photoactivity of Ru(II) complexes was confirmed by measuring the cleavage of poly ADP-ribose polymerase (PARP), which is one of the major hallmarks of apoptosis (Figure 21b). The specific inactivation of PARP by proteolytic cleavage results undetectable under dark conditions, while it is significantly appreciable after photoactivation of each Ru(II) complexes. These results point to a crucial role for programmed cell death in the anti-tumour activity of the systems here investigated.

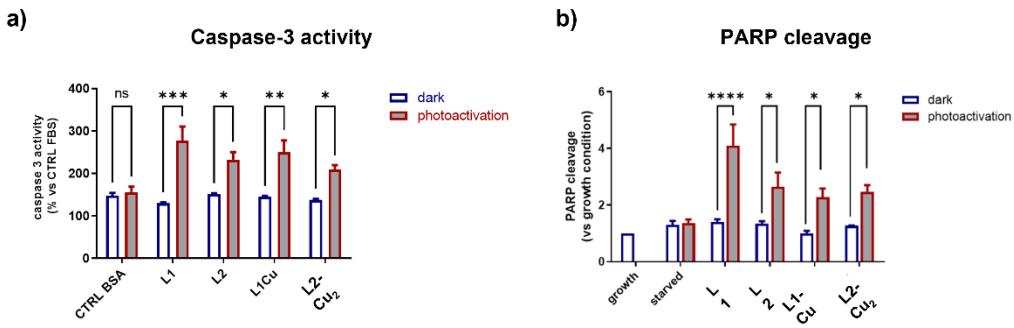

*Figure 21: a) Effect of Ru(II) complexes on caspase 3 activation in A2780 cells after photosensitization. Data are reported as mean±SD of fluorescence compared to control cells under growth (10% FBS RPMI) condition, set as 100. The effect of photoactivation was statistically significant for each Ru(II) complexes tested by two-way ANOVA analysis followed by Bonferroni post-hoc test: *P<0.05, **P<0.01. b) Effect of Ru(II) complexes on PARP cleavage in ovarian cancer cells after photosensitization. Data are the mean ± SEM and are reported as cleaved protein levels normalized to β-actin, -fold change over FBS control. Results are statistically significant by two-way ANOVA followed by Bonferroni's post hoc test: *P<0.05, ****P<0.0001.*

Lastly, the apoptotic involvement in A2780 cells death was investigated even considering the effect of Ru(II) complexes, in dark and upon photoactivation, on mitochondria. Mitochondria might be seen as a gatekeeper to entrap pro-apoptotic proteins. A lost in the mitochondrial membrane potential (Δϕm) is considered an early event of the apoptotic process.

For this reason, Δϕm was analysed by laser-scanning confocal microscopy imaging using the cationic fluorescent probe Mito-Tracker Red CMXRos, which accumulates in the negatively charged mitochondrial matrix. A2780 cells were plated in microscope slides and either challenged or not (CTRL) with 10 µM of each Ru(II)-complex. After 24 h of incubation, A2780 were subjected to photoactivation or not (dark) for 20 min. As shown in Figure 22, the administration of PSs under dark conditions does not affect the Δϕm or cell morphology. However, irradiation provokes a different behaviour between **L1** and **L2** and the Ru(II)/Cu(II) heteronuclear complexes: a dramatic loss of Δϕm is observed for **L1** and **L2**, wheras **L1-Cu** and **L2-Cu$_2$** do not provoke any mitochondrial change or decrease in Δϕm, thus ruling out the possible involvement of early mitochondrial membrane potential in the pro-apoptotic effect of mixed Ru(II)/Cu(II) complexes.

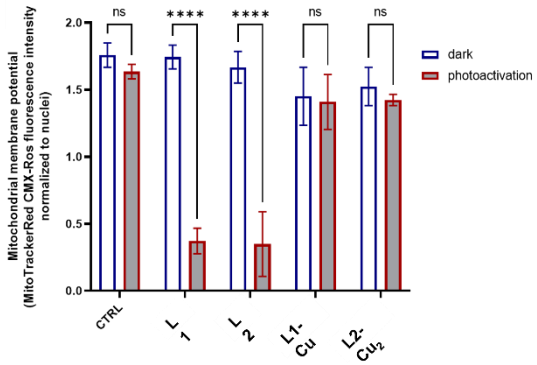

*Figure 22: Effect of Ru(II) complexes on mitochondrial membrane potential after photoactivation. Data are reported as mean ± SD of MitoTracker Red CMXRos fluorescence intensity normalized to the number of nuclei in six fields for each condition in three independent experiments by using Leica Application Software. Results are statistically significant according to two-way ANOVA followed by Bonferroni post hoc test: **** p < 0.0001, not significant (ns).*

In summary, the current study demonstrates that all four synthesized Ru(II) complexes are effectively internalized into the ovarian cancer A2780 cells, and their administration, regardless of the low-level dark cytotoxicity, induces a specific photoactivation-dependent cell death, with the extent of cytotoxicity that varies slightly depending on the chemical structures of the PSs. Apoptosis emerged as the main mechanism of light-mediated cellular death. In particular, among the four compounds, **L1** and **L2** profoundly altered mitochondrial activity after photoactivation, accompanied by cytosolic ROS production.

1.3 Ferritin nanocomposites for the selective delivery of Ru-PSs

Despite the great PDT potential of **L1** and **L2**, among the main disadvantages of PDT approach is the limited selectivity of the PS agents, which can lead to several side effects. To address this issue, in collaboration with Prof. Paola Turano of the Magnetic Resonance Center (CERM) of the University of Florence, the employment of an innovative delivery method using human ferritin as nanocarrier for the selective delivery of Ru-PSs to cancer cells was studied.

Endogenous human ferritin is a heteropolymeric nanocage of 24 subunits involved in iron storage and release.[86] While *in vivo t*he *heavy*- and *light*- chins self-assemble to form a nanosphere structure with an internal hole cavity of 8 nm, recombinant ferritins are generally expressed as homopolymeric (pure *heavy*- and pure *light- chains*) cages. The potential of recombinant homopolymeric human H-ferritin (HuHf) as a nanocarrier relies on its possibility to be loaded with low-molecular weight compounds, on its low immunogenicity due to its human origin and on its selective recognition and internalization in cells through endocytosis mediated by Trasferin Receptror 1 (TfR1).[87] The latter feature is of particular interest if it is considered that TfR1 results

overexpressed in a wide variety of cancer cells, making HuHf a promising platform for selective target drug delivery.[88]

With this in mind, complexes **L1** and **L2** were successfully encapsulated into HuHf using a pH assisted disassembly and reassembly method harnessing the ability of ferritin to partially dissociate at pH 12, followed by reconstitution at neutral pH (Figure 23).

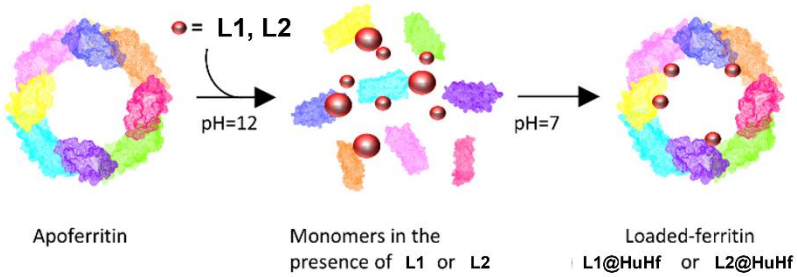

Figure 23: PSs encapsulation into HuHf by exploiting the pH-assisted disassembly/reassembly method.

Following purification of the nanocomposites by ultrafiltration and size exclusion chromatography, the successful encapsulation was assessed by means of UV-visible spectroscopy and ICP-AES analysis and revealed a ligand to protein cage ratio of 5 and 4 for **L1@HuHf** and **L2@HuHf** respectively. Table 3 summarizes the nanocomposites' chemical-physical and structural properties. The main optical and chemical-physical features of ruthenium complexes remain unchanged after encapsulation: the absorption spectra of **L1@HuHf** and **L2@HuHf** are almost identical to the reference spectra of the free ligands (Figure 24a) and the fluorescence emission is maintained (Figure 24b). Furthermore, following an in-depth investigation into the preservation of structural integrity of HuHf after the encapsulation process, it was demonstrated that loaded ferritin retains its spherical nanocage structure, as evaluated by single particle cryo-TEM micrographs acquired on **L1@HuHf** and **L2@HuHf** (Figure 24e-f). Contemporary, SAXS patterns for the apo HuHf before and after Ru(II) complexes internalization show that protein's hollow shell structure is preserved (Figure 24c).

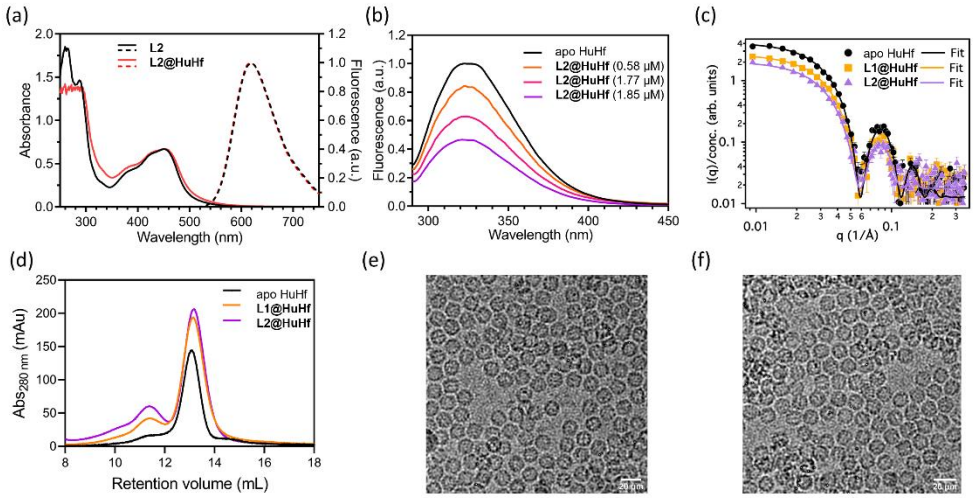

*Figure 24: Characterization of Ru(II)-HuHf nanocomposites. (a) Combined UV-visible and fluorescence spectra (λ_{exc} 411 nm) of free **L2** and of **L2@HuHf** (Ru(II) concentration: 50 μM and 6 μM for UV-visible and fluorescence measurements, respectively). (b) Intrinsic fluorescence emission of apo HuHf and of **L2@HuHf** (HuHf 0.32 μM, λ_{exc} 280 nm) with increasing amounts of encapsulated **L2**. (c) SAXS intensity distribution of apo HuHf, **L1@HuHf** and **L2@HuHf** (markers represent experimental data while continuous lines refer to the core–shell modelling. (d) Size exclusion chromatography analysis of **L1@HuHf** and **L2@HuHf**, in 50 mM sodium phosphate pH 7 buffer, superimposed with the reference chromatogram of apo-HuHf not subjected to the disassembly process. (e) and (f) Cryo-EM representative micrographs of **L1@HuHf** and **L2@HuHf**, respectively.*

To notice, the overall size of the cavity slightly decreases with the insertion of the Ru(II) complexes (from 8.32 nm to 8.13 nm and 8.02 nm for **L1@HuHf** and **L2@HuHf**, respectively) (Table 3). This shrinkage is directly associated with the increase in the thickness of the protein shell from about 2.2 nm to 2.5 nm and a good fit of these data could only be achieved considering the hollow shell topology. The increment in shell thickness and the simultaneous reduction in the diameter of the cavity confirmed that **L1** and **L2** are likely localized in proximity to the internal protein surface. Indeed, even the ^{1}H NMR signals corresponding to **L1** and **L2** in the encapsulated formulation are broad due to the interaction with protein (data not shown). Taken together, SAXS and NMR data lead us to hypothesize that the interaction of **L1** and **L2** with HuHf would be driven by electrostatic contributions between the metal compounds, namely through

the positively charged polyammonium groups on their **L'** and **L"** units and the negatively charged residues facing the inner cavity of the protein.[89]

Additional evidence that the interaction of the Ru compounds with the protein does not occur on the external surface arose by the similar ζ-potential of **L1@HuHf** and **L2@HuHf** (-5.0 ± 1.1 mV and -3.1 ± 0.4 mV respectively) compared to those found for apo HuHf (-4.2 ± 0.6 mV).

Importantly, **L1@HuHf** and **L2@HuHf** formulations demonstrate the ability to preserve the capacity to produce singlet oxygen upon light activation. To address this issue, two different indirect chemical trapping methods using water-soluble substrates as scavengers for $^1O_2$ were employed (Figure 25). Firstly, 1,5-dihydroxynaphthalen (DHN) (λ_{max} 297 nm) was used as probe exploiting its prompt and quantitative oxidation in presence of $^1O_2$ to give 1,4-naphtalendione (Juglone) (λ_{max} 427 nm) (Figure 25a). Experiments were carried out by irradiating (LED light, λ > 430 nm, 30 W) aqueous solutions, pre-saturated with air, and containing sensitizers (**L1**, **L2**, **L1@HuHf**, **L2@HuHf** or $[Ru(phen)_3]_{2+}$ as standard reference) in the presence of DHN. Light activation of ferritin nanocomposites determines the progressive decrease of the DHN absorption band, along with the simultaneous increase of the Juglone band, clearly demonstrating its capacity to efficiently sensitize $^1O_2$ production (Figure 25a). As better shown by the inset in Figure 25a, which reports the semilogarithmic plots of $\ln(A_t/A_0)$ obtained for all the Ru(II)-based formulations over the investigated irradiation time frame, Ru(II)-ferritin nanocomposites produce a similar amount of $^1O_2$ in about 45 minutes as 'free' molecules did in 6–7 min. A semi-quantitative estimation of the relative rate constants for the DHN photooxidation processes (k_{obs}) was accomplished, and values are listed in Table 3.

The effectiveness of Ru-nanocomposites in producing $^1O_2$ was confirmed by employing an independent experiment based on the monitoring of the green fluorescence emission (at 525 nm) of the commercially available Singlet Oxygen Sensor Green®

reagent (SOSGR) as selective probe.[90,91] As demonstrated in Figure 25b, the irradiation of a water neutral solution containing the probe in presence of **L1@HuHf** or **L2@HuHf** determines a progressive increase of the SOSGR fluorescence emission, revealing a similar, but inferior, ability of Ru-nanocomposites to effectively produce $^1O_2$ compared to the 'free' complexes.

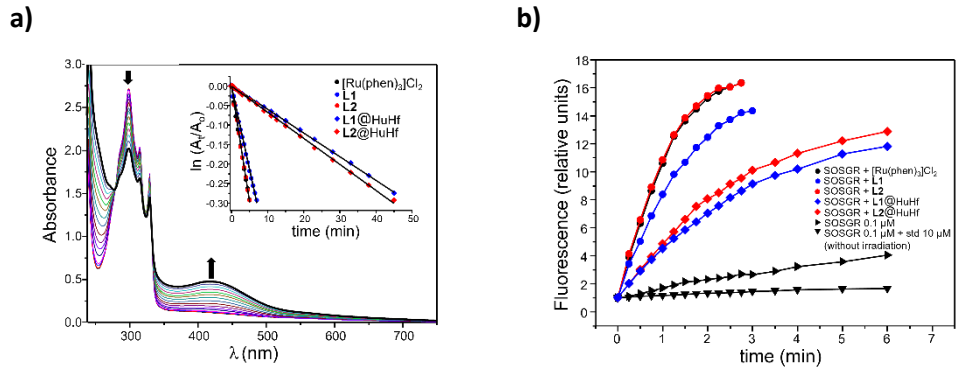

*Figure 25: (a) Absorption spectra of an aqueous solution at pH 7 containing DHN and **L2@HuHf** at different irradiation times (up to 45 minutes). In the inset the semilogarithmic plots of $ln(A_t/A_0)$ as a function of the irradiation time obtained for all the investigated systems ([DHN] = 3.3 × 10^{-4} M, [Ru] =10 μM, 50 mM NaPi buffer) are compared. (b) Singlet oxygen production from free and HuHf-loaded Ru(II) PSs as monitored by the Singlet Oxygen Sensor Green reagent (SOSGR) in 50 mM NaPi buffer, (pH 7), ([SOSGR] = 0.5 μM, [Ru] = 5 μM, λexc/λem 488/525 nm).*

	Ru atoms/cage					SAXS Modeling[c]	
Sample name	UV vis-based	ICP OES-based	$\lambda_{Abs}/\lambda_{em}$ (nm)	k_{obs}(min^{-1})[a]	Φ_Δ[b]	Core diameter (nm)	Shell thickness (nm)
$[Ru(phen)_3]^{2+}$	-	-	447/605[d]	0.0595 (±5)	0.38 ± 0.08	-	-
L1	-	-	452/615	0.0434 (±3)	0.29 ± 0.06	-	-
L2	-	-	452/615	0.0594 (±4)	0.36 ± 0.08	-	-
Apo HuHf	-	-	-	-	-	8.32 ± 0.08	2.17 ± 0.06
L1@HuHf	5.2 ± 0.8[e]	4.1 ± 0.5[e]	452/615	0.0061 (±5)	-	8.14 ± 0.08	2.34 ± 0.09
L2@HuHf	4.3 ± 0.5[e]	3.4 ± 0.4[e]	452/615	0.0067 (±4)	-	8.02 ± 0.08	2.48 ± 0.10

*Table 3: Characterization of **L1@HuHf** and **L2@HuHf**: [a] Photo-oxidation rate constants (k_{obs}) spectrometrically determined by the photo-oxidation of DHN in aqueous media at neutral pH. [b] Quantum yields (φΔ) of singlet oxygen production determined by measurements of $^1O_2$ phosphorescence at 1270 nm in air saturated CH_3CN solutions. [c] Parameters obtained using a core–shell model. [d] Values determined in water at 298 K. [e] Mean values with SEM of three independent experiments.*

1.3.1 *In vitro* cytotoxicity of ruthenium-ferritin assemblies upon photoactivation

The targeting ability of TfR1-expressing cell models, as well as the delivery of **L1@HuHf** and **L2@HuHf** into the cytosol, were assessed using cell lines with varying levels of TfR1 expression. For this purpose, were selected cervical carcinoma (HeLa) and ovarian carcinoma (A2780) cells, both human cancer cell lines with high levels of TfR1 expression, and C2C12 myoblasts, a non-tumoral cell line with negligible levels of TfR1 expression. Levels of TfR1 expression were confirmed by western blot analysis and confocal immunofluorescence analysis (data not shown).

When the uptake of Ru-ferritin composites was assessed by measuring the content of ruthenium in cell lysate by ICP analysis and immunofluorescence analysis, it effectively demonstrated that only HeLa and A2780 cells are able to internalize the nanocomposites (Figure 26).

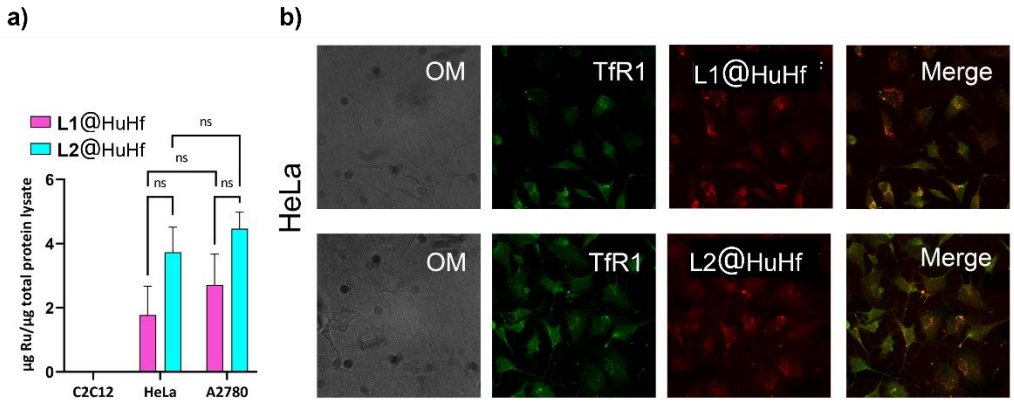

*Figure 26: Cells internalization of **L1@HuHf** and **L2@HuHf**. (a) The amount of internalized ruthenium after 24 h incubation of Ru-ferritin nanocomposites (10 µM of encapsulated ruthenium) for each cell line found by ICP measurements. b) Laser scanning confocal microscopy on HeLa cells incubated with **L1@HuHf** and **L2@HuHf**. Immunofluorescence analysis was performed by using specific anti-TfR1 primary antibody and secondary anti-mouse antibody conjugated with fluorescein (green). Ru(II) nanocomposites display fluorescent properties, λ_{exc} = 440–480 nm and λ_{em} = 600–640 nm (red). Representative confocal microscope images show the colocalization of TfR1 with Ru(II) nanocomposites on the right (Merge) and the corresponding optical microscope images on the left (OM).*

As expected from the selective targeting ability of Ru-ferritin assemblies, their photosensitization markedly affects the cell survival of HeLa and A2780 cancer cells, leaving unchanged the viability of C2C12 myoblasts (Figure 27). The MTT reduction assay was carried out by incubating the cells for 24 h with different concentrations of **L1@HuHf** and **L2@HuHf**, afterwards cell plates were photoactivated with a blue emitting LED lamp for 20 minutes (30 W, 430-470 nm) and after 24 hours cell viability was analysed. The obtained results demonstrate that both the Ru-ferritin assemblies provoke a 50% decrease in cell viability at a drug dose of 40 µM, which corresponds to approximately 10 µM of the encapsulated Ru(II) complex.

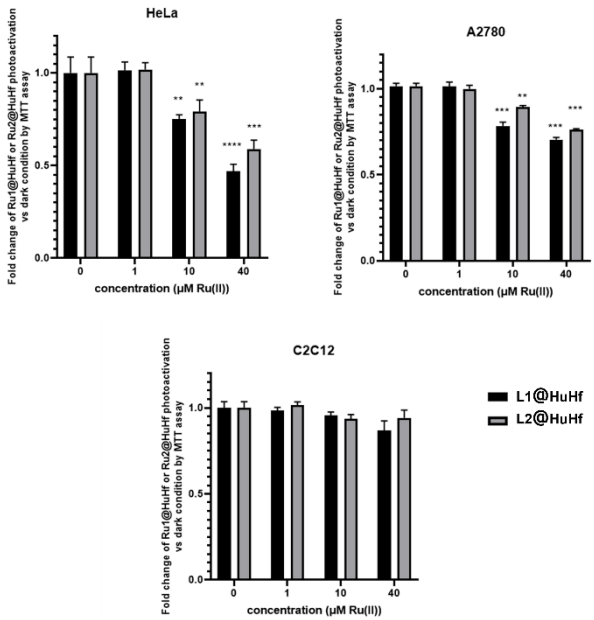

*Figure 27: Dose dependent cytotoxic effect of **L1@HuHf** and **L2@HuHf** after photoactivation. Cellular viability of different cancer (HeLa and A2780) and non-cancer (C2C12) cell lines was assessed by MTT reduction analysis. Cells were incubated for 24 h in the presence of **L1@HuHf** and **L2@HuHf** at 0 µm, 1 µM, 10 µM and 40 µM in serum-deprived culture media (supplemented with BSA 0.1%). Photoactivation was carried out using a 30 W three-arm LED lamp with 470-430 nm blue emission for 20 minutes, at a distance of 5 cm from the cell plate. Twenty-four hours after photoactivation MTT analysis was performed to assess anti-tumor effect of Ru(II) nanocages. Experiments were performed in triplicate, representative of three independent ones with similar results. Data reported are mean ± SEM of fold change absorbance at 570 nm in photoactivated compared to dark condition normalized to apoferritin treatment. The effect of photoactivation of Ru(II) nanocages on the inhibition of cell survival was statistically significant by 1-way ANOVA followed by Bonferroni post-hoc test. **P<0.01, ***P<0.001, ****P<0,0001.*

Acknowledgments

The findings presented in this chapter are the result of a multidisciplinary effort that benefited from the valuable contribution of several collaborations to which special thanks are due. These results have already been published as follow:

Conti L., Mengoni A., Giacomazzo G. E., Mari L., Perfetti M., Fagorzi C., Sorace L., Valtancoli B., Giorgi C.; Exploring the potential of highly charged Ru(II)- and heteronuclear Ru(II)/Cu(II)-polypyridyl complexes as antimicrobial agents; *J. Inorg. Biochem.*, ***2021***, 220, 111467 DOI: 10.1016/j.jinorgbio.2021.111467

Conti L., Giacomazzo G. E., Valtancoli B., Perfetti M., Privitera A.,Giorgi C., Sfragano P., S., Palchetti I., Pecchioli S., Bruni P., Cencetti F.; Highly charged Ru(II) polypyridyl complexes as photosensitizer agents in photodynamic therapy of epithelial ovarian cancer cells; *Int. J. Mol. Sci.*, ***2022***, 23(21), 13302 DOI: 10.3390/ijms232113302

Conti L., Ciambellotti S., Giacomazzo G. E., Ghini V., Casottini L., Puliti E., Severi M., Fratini E., Cencetti F., Bruni P., Valtancoli B., Giorgi C., Turano P.; Ferritin nanocomposites for selective delivery of photosensitizing ruthenium-polypyridyl compounds to cancer cell; *Inorg. Chem. Front*., ***2022,*** 9, 1070-1081 DOI: 10.1039/D1QI01268A

EXPERIMENTAL SECTION

Synthesis

Materials and methods

Reagents and solvents were purchased from Sigma Aldrich and Alfa Aesar and were used without further purification. Anion-exchange resin Dowex 1 x 4 50 mesh-chloride form was purchased from Sigma Aldrich. Compounds 4,4'-(2,5,8,11,14-pentaaza[15])-2,2'-bipyridilophane (**L'**) and 4,4'-bis-[46ethylene-(1,4,7,10-tetraazacyclododecane)]-2,2' bipyridine (**L''**) were prepared in accordance with the methods already described in literature.[78,79] The common ruthenium intermediate **1** was synthesized according to literature.[57,80] NMR spectra were recorded on a Bruker 400 MHz instrument. ESI-MS spectra were collected on a TSQ 700 Finnigan Mat or ABSciex triple TOF 5600+ equipments.

Synthesis of L1

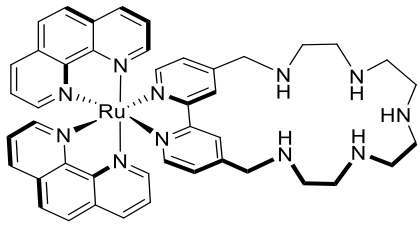

Following the treatment of **L'**·7HBr (0.13 mmol) with Dowex 1 X 4 chloride form anion-exchange resin to obtain the macrocycle in its deprotonated amine form (**L'**), compound **1** (72 mg, 0.13 mmol) was added and the solid mixture was suspended in 4 mL of ethylene glycol. Reaction was conducted in a microwave reactor (60 W) at 160°C for 10 minutes. The dark-violet suspension became a clear orange solution. After cooling at r.t., the solvent was removed by distillation under reduced pressure. The resulting red-orange solid residue was dissolved in a minimum amount of HCl 6 M (1 mL) and the coevaporation with ethanol (5 x 6 mL) and 2-propanol (3 x 6 mL) led to the precipitation of complex **L1** which was collect by filtration and washed with 2-propanol and ethyl ether. The final product is obtained as penta-protonated hepta-chloride salt [**L1**]Cl_2·5HCl with a yield of 60%. ^{1}H-NMR (400 MHz, D_2O + DCl, pD <2): δ 8.70 (d, J = 8.0 Hz, 2H), 8.61 (d, J = 8.0 Hz, 2H), 8.28 (m, 6H), 7.96 (d, J = 4.8 Hz, 2H), 7.86 (d, J = 12.8, 2H), 7.83 (dd, J_1 = 8.4 J_2 = 5.2 Hz, 2H) 7.58 (dd, J_1 = 8.4 Hz, J_2 = 5.6 Hz, 2H) 7.35 (d, J = 5.2, 2H), 4.59 (m, 4H); 3.71-3.29 (m, 16H) ppm. ^{13}C-NMR (400 MHz, D2O, pD <2): δ 152.5, 152.3, 151.8, 148.3, 147.6, 146.9, 137.0, 136.8, 133.7, 130.9, 127.8, 127.49, 127.1, 126.7, 125.9, 125.3, 123.1, 53.7, 47.9, 45.3, 44.9, 44.6 ppm. ESI-MS: m/z found for $C_{44}H_{47}N_{11}Ru$ $[M]^{2+}$ 415.65.

Synthesis of L2

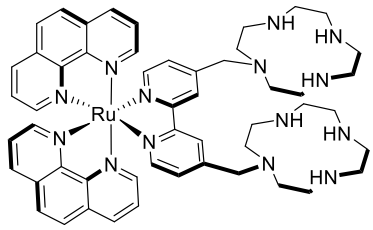

Following the treatment of **L''**·7HBr (0.22 mmol) with Dowex 1 X 4 chloride form anion-exchange resin to obtain the macrocycle in its deprotonated amine form (**L''**), compound **1** (117 mg, 0.22 mmol) was added and the solid mixture was suspended in 4 mL of ethylene glycol. Reaction was conducted in a microwave reactor (60 W) at 160°C for 10 minutes. The dark-violet suspension became a clear orange solution. After cooling at r.t., the solvent was removed by distillation under reduced pressure. The resulting red-orange solid residue was dissolved in a minimum amount of HCl 6 M (1 mL) and the coevaporation with ethanol (5 x 6 mL) and 2-propanol (3 x 6 mL) led to the precipitation of complex **L2** which was collect by filtration and washed 2-propanol and ethyl ether. The final product is obtained as hexa-protonated octa-chloride salt [**L2**]Cl_2·6HCl·H_2O with a yield of 59%. ^{1}H-NMR (400 MHz, D_2O + DCl, pD < 2): δ 8.67 (d, J = 8.3 Hz, 2H), 8.61–8.53 (m, 4H), 8.33–8.20 (m, 6H), 7.93 (d, J = 4.5 Hz, 2H), 7.84–7.75 (m, 4H), 7.58–7.52 (m, 2H); 7.29 (d, J = 4.5 Hz, 2H), 4.5 (s, 4H, -CH_2), 3.37–3.19 (m, 8H), 3.19–3.09 (m, 8H), 3.04–2.94 (m, 8H), 2.94–2.76 (m, 8H) ppm. ^{13}C-NMR (100 MHz, D2O + DCl, pD < 2): δ 158.3, 153.2, 152.7, 148.4, 148.2, 146.8, 141.3, 137.7, 137.5, 137.4, 131.5, 128.6, 126.5, 126.2, 125.5, 56.0, 53.0, 51.0, 49.9, 49.7, 49.6, 48.2, 48.1, 47.3, 46.8, 45.1, 44.5, 43.7, 43.4, 42.6, 42.2, 41.7 ppm. ESI-MS: m/z found for $C_{52}H_{64}N_{14}Ru$ $[M]^{2+}$ 493.236 $[M + CH_3CN]^{2+}$ 513.743.

Synthesis of L1-Cu and L2-Cu_2

The treatment of **L1** or **L2** at pH 6.5 with an equimolar amount or two equivalents of $CuCl_2$ respectively affords the correspondent **L1-Cu** and **L2-Cu_2**.

Complexes Characterization

Absorption spectra were collected by using a PerkinElmer Lambda 6 spectrophotometer while fluorescence measurements were performed on a Horiba FluoroMax Plus spectrofluorometer.

Determination of singlet oxygen quantum yields

Singlet oxygen quantum yields were determined by monitoring the phosphorescence signal of $^1O_2$ at 1270 nm, generated from air-saturated acetonitrile solutions of **L1** and **L2** upon laser excitation (Ti-Sapphire ultrafast laser delivering 100 fs long pulses at 82 MHz repetition rate and 800 nm wavelength; the laser pulse was frequency doubled at 400 nm to excite the samples). Phosphorescence signal was recorded with N_2 cooled InGaAs photodiode. Experiments were carried out by employing different concentrations of ruthenium compounds, with absorbance values at 400 nm in the range 0.08–0.2 and the ϕ_Δ values were calculated by applying the formula:

$$\Phi_\Delta = \Phi_\Delta^{ST} \frac{m}{m^{ST}}$$

Where ϕ_Δ^{ST} represents the $^1O_2$ quantum yield of tetraphenylporphyrin (TPP) used as standard reference (ϕ_Δ^{ST}=0.60 in acetonitrile),[92] m and m^{ST} are the slopes of the linear plots of absorptivity at 400 nm as a function of the $^1O_2$ intensity signal for the ruthenium complex and TPP respectively.

Reactive oxygen species (ROS) production by Ru(II)/Cu(II) heteronuclear complexes

The effective ROS production by **L1-Cu** and **L2-Cu₂** was assessed by using Electron Paramagnetic Resonance (EPR) spin trapping technique, involving the reaction of an initially generated short-living radical with an added organic spin trap (5,5-dimethyl-1-pyrroline-N-oxide (DMPO)), to generate longer-living radical adducts with clear EPR fingerprints. DMPO efficiently captures the free radicals generated by an unstable species (H_2O_2) due to the catalyzing action of a supposedly active molecule. X-band EPR (Electron Paramagnetic Resonance) spectra were recorded on a Bruker Elexsys E500

spectrometer. All the spectra were acquired at room temperature by using the same modulation frequency (100 kHz), modulation amplitude (1 G), microwave power (~0.2 mW, 30 dB) and receiver gain (60 dB). The magnetic field was calibrated with a crystal of DPPH. The spectra collected for a solution containing only H_2O_2 (100 mM) and DMPO (750 mM), as reference sample, are reported, together with those obtained by adding **L1-Cu** or **L2-Cu$_2$** (5 mM) to this mixture, in Figure 28. When **L1-Cu** or **L2-Cu$_2$** were added to the mixture, an EPR signal appeared (green and red traces for **L1-Cu** and **L2-Cu$_2$**), clearly indicating ROS production. The acquired EPR spectra were also simulated by using the core function *pepper* of the open-source MATLAB toolbox EasySpin.[93] As shown by the black trace in Figure 28, the best simulation of the experimental spectra was obtained by considering the production of a 50:50 mixture of hydroxide (OH·) and perhydroxyl (HOO·) radicals.

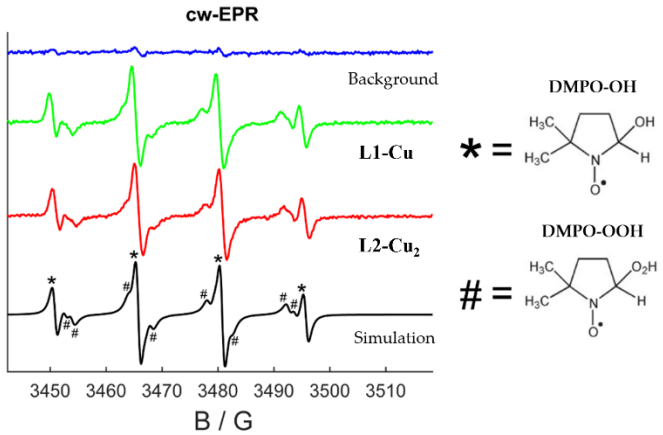

*Figure 28: EPR spectra registered at 298 K on solutions containing DMPO and H_2O_2 (blue line), together with **L1-Cu** (red line) or **L2-Cu$_2$** (green line). On the bottom, the black trace is the best simulation obtained as a 50:50 mixture of hydroxide and peroxide radicals (molecular structures of the corresponding adducts formed with DMPO are shown in the right part of the figure); the EPR lines referring to hydroxide and peroxide radicals are respectively labelled with symbols * and #. ([DMPO] = 750 mM, [H_2O_2] = 100 mM, [**L1-Cu**] = [**L2-Cu$_2$**] = 5 mM).*

Determination of octanol-water distribution coefficient

The determination of octanol-water distribution coefficients ($logD_{7.4}$) was assessed by employing the shake-flask procedure.[94] Briefly, aqueous solutions of the tested

compounds (16 µM) buffered with phosphate buffer at pH 7.4 were mixed in a flask with n-octanol. Both solvents were mutually pre-saturated at room temperature. The compounds were then allowed to equilibrate between the organic and the aqueous media by flask handshaking and then were left resting for at least 24 h to ensure the complete separation of the two phases. Afterwards, the concentrations of ruthenium compounds in the aqueous phase were spectrophotometrically determined while those in the organic phase were obtained by difference. The $logD_{7.4}$ values were calculated by using the formula:

$$logD_{7.4} = log\ \frac{[Ru]_{oct}}{[Ru]_{water}}$$

Where $[Ru]_{oct}$ and $[Ru]_{wat}$ represent the total concentration of the ruthenium compound in the organic and in aqueous phase respectively. Each determination was performed in triplicate.

Interaction with ct-DNA

The intrinsic binding constant (K_b) of ruthenium compounds with *calf thymus*-DNA were determined by monitoring the changes at ^{1}MLCT absorption band of ruthenium complexes, centred at ca. 454 nm, induced by addition of increasing amounts of the biopolymer (0–400 µM) to buffered solutions (Tris-HCl buffer, 10 mM, NaCl 50 mM, pH 7.2) containing the metal compounds at fixed concentration (10 µM). To eliminate the contribute to the absorbance of the DNA itself, equal amounts of concentrated solutions of DNA were added both to the sample and to the reference solution. After each DNA addition, samples were incubated for 10 min at 298.1 ± 0.1 K before collecting the absorption spectra. Values of K_b were calculated applying Benesi-Hidebrand equation as explain in paragraph 3 of the introduction.

Antimicrobial photodynamic therapy (aPDT)

Microbiological methods

The model bacterium *Bacillus subtilis* 168 strain was used for determination of inhibitory concentrations. Bacterial strains were grown in Luria Bertani (Lysogeny broth) medium (NaCl 10 g/L, Tryptone 10 g/L, Yeast Extract 5 g/L) at 37 ◦C.

Determination of inhibitory concentrations

Overnight grown liquid cultures were prepared in LB medium (10 mL) from single colonies freshly grown on LB agar Petri plates. Cultures were incubated at 37 ◦C, 225 rpm shaking. From overnight cultures, cells were diluted to $OD_{600\ nm}$ = 0.1 in fresh LB medium, then solutions of ruthenium compounds were added to the diluted cultures. The mixtures (150 µL total volume) were then splitted in a 96-well microtiter plate (Sarstedt, Germany). Irradiation for photoactivation was performed on the surface of the microtiter plate after 30 min incubation by employing LED light (λ > 430 nm, 30 W, 15 min). Microtiter plates were then incubated on an Infinite Pro 200 plate reader (Tecan, Switzerland). $OD_{600\ nm}$ was read every hour for up to 20 h, until growth reached the stationary phase. The MIC values (minimal inhibitory concentrations) were expressed in µM and calculated as the drug concentration inducting at least 60% growth reduction or 40% residual growth.

Cell permeation

To investigate the kinetics of cell permeation of ruthenium compounds, *B. subtilis* bacterial cultures were added to 1.5 mL polyproprilene tubes (7.5 × 108 cells/tube) and treated with a fixed concentration of ruthenium compounds (25 µM) at pH 7.2. Cells were incubated for 30 min, 3 h, 5 h, 24 h, centrifuged and pellets were washed three times with 1 mL 0.9% NaCl solution to remove extracellular ruthenium compounds present in the medium. In the washed bacterial cell pellets the ruthenium-content was assumed as indicator for drug permeation and was determined by Inductively Coupled

Plasma Atomic Emission Spectroscopy (ICP-AES); results were expressed as ng of Ru/108 cells. Experiments were performed in triplicate.

Photodynamic therapy of Epithelial ovarian cancer cells

Cell Culture

All cell culture reagents were purchased from Merck Life Science. Human A2780 ovarian cancer cell culture (ECACC 93112519) was maintained in RPMI-1640 medium containing 10% fetal bovine serum (FBS), 100 µg/mL streptomycin, 100 U/mL penicillin and 2mM L-glutamine, at 37°C in 5% CO_2. A2780 cells were shifted to RPMI without serum supplemented with 1 mg/mL Bovine Serum Albumin (BSA) and treated with each Ru(II) complex (0.1, 1 and 10 µM) for 24 h. After incubation, cells were photoactivated with a three-arm LED light lamp (430–470 nm emission, 30 W) for 20 min at the distance of 5 cm from the cell culture plate and then kept in the incubator at 37°C, 5% CO_2. Cells were washed twice with PBS and then collected after photoactivation at different times, which depended on each kind of experiment.

ICP-AES Measurements

The Ru contents in A2780 cells was determined through Inductively Coupled Plasma Atomic Emission Spectrometer (ICP-AES) utilizing a Varian 720-ES. Measurements were performed in triplicate, and each sample was spiked with 1.0 ppm of Ge, used as an internal standard. The calibration standards were prepared by gravimetric serial dilution from commercial stock standard solutions of Ru at 1000 mg/L (Honeywell Fluka). For Ru determination, the 267.876 and 245.657 nm wavelengths were used, whereas the line at 209.426 nm was considered for Ge. The operating conditions were optimized to obtain maximum signal intensity, and between each sample, a rinse solution containing 2% v/v of HNO_3 was used.

MTT Reduction Assay for Cell Survival

Cell viability of A2780 cells was evaluated by the reduction of the yellow tetrazolium salt 3-(4,5-dimethylthiazol- 2-yl)-2,5-diphenyltetrazolium bromide (MTT) to purple formazan crystals performed by metabolically active cells. MTT colorimetric analysis was performed after the treatment with the ruthenium(II) complexes at different concentrations (0.1, 1 and 10 μM) for 24 h, followed by photoactivation (three-arm LED light lamp 30 W with 470 nm–430 nm emission for 20 minutes at a distance of 5 cm) or not and then incubation for further 24 h. Cell viability was assayed in the presence of 0.5 mg/mL of MTT salt for 1 h at 37 °C; DMSO was used to dissolve insoluble formazan crystals produced by viable cells. The absorbance was measured at 595 nm using a microplate reader (iMark Microplate Absorbance Reader, Bio-Rad, CA, USA).

Caspase-3 activity assay

A2780 cells were seeded in 6-well plates (100.000 cells/well) and after 24 h were incubated with 10 μM of each Ru(II) complex in serum-deprived culture media, then light-irradiated for 20 min. After 24 h, cells were washed twice with PBS, collected, and analyzed, as previously described.[95]

Laser-scanning confocal microscopy

A2780 cells were seeded on microscope slides and treated with each Ru(II) complex (10 μM). The internalization of Ru(II) complexes was evaluated by incubating cells at three different times (15 min, 6 h and 24 h). Afterward, cells were washed with PBS and fixed in 2% paraformaldehyde in PBS for 20 min. Complexes were excited using a 405 nm laser diode and the emission signal was recorded in the range of 600/620 nm.

To evaluate the mitochondrial membrane potential and ROS production were used MitoTracker Red CMXRos (#M7512; $\lambda_{Ex/Em}$: 579 / 599 nm) and CM-H2DCFDA (#C6827; $\lambda_{Ex/Em}$: 492–495/517–527 nm) as probes, respectively. Cells were incubated with Ru(II) complexes for 24 h at 37°C and cell slides were photoactivated or not for 20 min and

incubated for 2 h at 37°C, 5% CO_2 in humidified atmosphere. Probes were diluted in RPMI medium without phenol red, incubated for 30 min at 37°C in dark and then fixed in 2% paraformaldehyde, as suggested by the manufacturer's instruction. After 30 min at r.t., slides were incubated with a permeabilization and quenching solution, obtained by adding Triton 0.1% X-100 and ethanolamine (1:165) in PBS. The DAPI solution was administered to cell slides to detect the nuclei. Slides were mounted by using the Fluoromount Aqueous Mounting Medium (Sigma-Aldrich, Saint Louis, MA, USA), and images were obtained using a Leica SP8 laser-scanning confocal microscope (Leica Microsystems GmbH) using a 63x oil immersion objective.

Ferritin nanocomposites for the selective delivery of Ru-PSs

Preparation of L1@HuHf and L2@HuHf

Encapsulation of **L1** and **L2** was assessed by pH-assisted disassembly/reassembly method of ferritin cage (HuHf). A buffered solution of HuHf (in 50 mM sodium phosphate buffer pH 7) was diluted with Universal buffer at pH 12 up to a final concentration of HuHf of 1.25 µM in a final volume of 5 mL. The pH was adjusted to 12 adding NaOH 1M. Different concentrations of **L1** and **L2** (25, 125 and 250 µM) were incubated with disassembled ferritin solution for 15 min. Then, the pH was brought at 7 with HCl 1M to let the protein reassemble, trapping **L1** and **L2** inside the cavity in 2 h. The entire process was run under stirring at 30 °C. The protein samples were purified by centrifugation at 7000 rpm for 10 min to discard precipitates and filtration in centrifugal devices (Amicon® Ultra 15 mL with cutoff 50 kDa, Merck LifeScience) to remove excess of **L1** and **L2**. To recoup the portion of protein with the correct folding, size exclusion chromatography (Superdex 200 10/300 GL column, GE Healthcare) was applied. The encapsulated products were eluted in 50 mM sodium phosphate pH 7 buffer and the fractions with a retention volume corresponding to 24-mer HuHf were recovered. Protein concentration was determined by Bradford assay.

Characterization of L1@HuHf and L2@HuHf

The estimation of ruthenium content into HuHf cages was performed by UV-Visible/fluorescence spectroscopy and ICP-AES.

Absorption spectra were recorded on a PerkinElmer Lambda 6 spectrophotometer. The electronic absorption profiles of **L1@HuHf** and **L2@HuHf** were compared with the spectra of references compounds **L1** and **L2**. All the spectra were registered in 50 mM sodium phosphate pH 7 buffer. The quantity of the compounds internalized into HuHf was initially calculated with the absorbance at 450 nm of Ru(II)-centres given the extinction molar coefficients of **L1** and **L2**.

Luminescence properties of encapsulated **L1@HuHf** and **L2@HuHf** was evaluated recording the emission spectra of 6 µM solutions of the free and the encapsulated Ru(II) complexes (λ_{Ex} = 411 nm, λ_{Em} = 615 nm). Fluorescence measurements were collected on a PerkinElmer LS55 spectrofluorometer.

ICP-AES measurements for the determination of the content of Ru(II) complexes in **L1@HuHf** and **L2@HuHf** samples was performed in triplicate by a Varian 720-ES axial inductively coupled plasma atomic emission spectrometer (ICP-AES). Samples were treated with 100 µL of suprapure HNO_3 (obtained by sub-boiling distillation) and 100 µL of suprapure HCl (30%) and, then diluted to a final volume of 5.0 mL with ultrapure water. Each sample was spiked with 1.0 ppm of Ge used as an internal standard prior to the analysis. Calibration standards were prepared by gravimetric serial dilution from commercial stock standard solutions of Ru at 1000 mg/L (Honeywell Fluka). Wavelengths used for Ru determination were 267.876 and 245.657 nm, whereas for Ge the line at 209.426 nm was used. ICP-AES analysis revels a ligand to protein cage ratio of 5 and 4 for **L1@HuHf** and **L2@HuHf** respectively.

The structural integrity of HuHf upon the encapsulation process was analysed employing SAXS and Cryo-EM analysis.

Small-angle scattering (SAXS) measurements were performed using a HECUS S3-Micro apparatus. The Kratky-type camera is equipped with a position sensitive, 50 M OED detector comprising of 1024 channels (width = 54 μm). Cu Kα radiation with a wavelength, λ, of 1.542 Å at a power of 50 W is provided by an ultra-brilliant point microfocus X-ray generator (GENIX-Fox 3D, Xenocs, Grenoble). A sample-to-detector distance of 281 mm (calibrated using the well-known silver behenate lamellar lattice, d = 58.34 Å16 provided a measurable q-range between 0.009 and 0.54 Å−1 (where q, the scattering vector, is given by $q = 4\pi/\lambda \sin\theta$, and 2θ is the scattering angle). Protein samples were placed into borosilicate glass capillaries with a diameter of 1 mm. Measurements were performed under vacuum to reduce scattering from air and at a temperature of 25 °C. Raw scattering data were corrected for the empty capillary/buffer contribution. The acquisition time was from 30 min to 1 h depending on the sample. Short measurements (1 min) were performed on each sample to confirm that the radiation damage was negligible under these experimental conditions.

Cryo-EM screening analysis of apo HuHf, **L1@HuHf** and **L2@HuHf** were acquired using a ThermoFisher Glacios at 200 kV instrument, equipped with a Falcon III direction electron detector. Holey-carbon R1.2/1.3 grids (Quantifoil Micro Tools GmbH) covered by a 2 nm film of carbon were prepared. Grid surfaces were treated with plasma cleaning using O2 for 45 s before applying 3 μL of the sample (1 mg/mL of **L1@HuHf** and **L2@HuHf** in PBS buffer pH 7.4). Grids were blotted in 100% humidity and 10°C with filter paper and vitrified by rapidly plunging into liquid ethane at −180 °C using a Vitrobot Mark IV (FEI, Hillsboro).

The interaction of the Ru compounds with protein internal surface was analysed by means of ^{1}H-NMR and Zeta potential measurements.

^{1}H-NMR analysis of free **L1** and **L2** (100 μM), apo HuHf (25 μM in cage) and **L1@HuHf** and **L2@HuHf** (100 μM of encapsulated **L1**/**L2**) in phosphate NMR buffer (pH 7.4) were

recorded and compared to further investigate the interaction of the encapsulated Ru-compounds with HuHf. NMR spectra were acquired using a Bruker 900 MHz spectrometer (Bruker BioSpin) at 298 K. One-dimensional ^{1}H-NMR spectra with water peak suppression and a standard CPMG pulse sequence were recorded (3k scans, 102 400 data points, a spectral width of 19 167 Hz, acquisition time of 2.97 s, and a relaxation delay of 4 s). This type of sequence has been used to selectively observe the sharp signals arising from the low molecular weight Ru-compounds free in solution and to suppress the broad resonances coming from ferritin. Before applying Fourier transform, free induction decays were multiplied by an exponential function equivalent to a 2.0 Hz line-broadening factor. Transformed spectra were automatically corrected for phase and baseline distortions using TopSpin 3.5 (Bruker BioSpin).

Zeta potential measurements were performed with a ZetaPALS system coupled with a Brookhaven 90Plus particle sizer (Brookhaven Instruments).

Singlet oxygen determination using 1,5-dihydroxynaphtalene (DHN) and the singlet oxygen sensor green reagent (SOSGR)

UV-Vis titrations employing 1,5-dihydroxynaphthalene (DHN) as an indirect $^{1}O_2$ reporter were performed in phosphate buffer (50 mM, pH 7, with 10% v/v MeOH) in the presence of a selected free Ru(II)-based photosensitizer or Ru(II)-HuHf formulation. Following the preparation of a 3.3×10^{-3} M solution of DHN in methanol, this solution was diluted 1 : 10 with an aqueous buffered solution at pH 7 containing the Ru(II)-based PS, obtaining a final buffer/MeOH (9 : 1) solution of DHN 3.3×10^{-4} M with a Ru(II)-content of 1×10^{-5} M. Samples were irradiated (LED Lamp, 30 W, $\lambda > 430$ nm) in a quartz cuvette with 1 cm optical path for a total time varying between 6 and 50 minutes. All spectra were acquired using as blank reference a solution containing the selected PS at the same concentration and pH of those of the measuring cuvette.

Fluorescence measurements by employing the Singlet Oxygen Sensor Green reagent (SOSGR) were assessed by preparing aqueous buffered solutions at pH 7 (50 mM sodium phosphate) containing SOSGR (0.5 μM) in the presence of **L1** or **L2** at 5 μM concentration or **L1@HuHf** and **L2@HuHf** in an amount in order to have a final Ru(II) equivalent concentration. The solutions were irradiated in a quartz cuvette with 0.1 cm optical path. Fluorescence spectra were collected using $\lambda_{Ex}/\lambda_{Em}$ of 488/525 nm.

In vitro- phototoxicity studies

Cell culture

All culture media and reagents were purchased from Merck KGaA (Darmstadt, Germany). Human ovarian cancer cell line A2780 and human epithelioid cervix carcinoma cell line HeLa (ATCC, VA, USA) were cultured in RPMI-1640 medium supplemented with 10% fetal bovine serum (FBS), 100 μg mL−1 streptomycin, 100 U mL^{-1} penicillin and 2 mM l-glutamine. C2C12 myoblasts (ATCC, VA, USA) were cultured in Dulbecco's Modified Eagle's Medium (DMEM) supplemented with 10% FBS, 100 μg mL^{-1} streptomycin, 100 U mL^{-1} penicillin and 2 mM l-glutamine. These cell lines were maintained in a humidified atmosphere at 95% air/55% CO_2 and constant temperature of 37 °C. All cell treatments were performed in serum-deprived RPMI or DMEM medium, supplemented with 1 mg mL^{-1} bovine serum albumin (0.1% BSA).

Laser scanning confocal microscopy

Cell internalization of **L1@HuHf** and **L2@HuHf** and colocalization analysis with transferrin receptor-1 was performed using a Leica SP8 laser scanning confocal microscope (Leica Microsystems GmbH). Cells (HeLa, A2780 and C2C12) were seeded on microscope slides and treated for 24 h with 10 μM of **L1@HuHf** or **L2@HuHf**, followed by washing with PBS and fixed with 2% paraformaldehyde in PBS for 20 minutes at room temperature.

Colocalization of **L1@HuHf** or **L2@HuHf** with anti-CD71 (transferrin receptor-1) was performed by immunofluorescence analysis: after 24 h of incubation with 10 μM of **L1@HuHf** or **L2@HuHf**, microscope slides were incubated with anti-CD71 (TfR1) monoclonal antibody (OKT-9; 1 : 100 dilution) for 2 h at room temperature followed by treatment with Texas Red-conjugate secondary anti-rabbit antibody (1 : 200 dilution) purchased from Vector Laboratories Inc. (Burlingame, CA, USA). Microscope slides were incubated with DAPI solution (1 mg ml−1, Thermo Fisher Scientific Inc., MA, USA) to probe the cell nucleus and then were mounted using Fluoromount aqueous mounting medium (Merck KGaA, Darmstadt, Germany).

MTT reduction assay

Cell viability of HeLa, A2780 and C2C12 cells was evaluated by the reduction of the yellow tetrazolium salt 3-(4,5-dimethylthiazol-2-yl)-2,5-diphenyltetrazolium bromide (MTT) to purple formazan crystals performed by metabolically active cells. MTT colorimetric analysis was performed after the treatment with increasing concentrations of Ru(II) in **L1@HuHf** or **L2@HuHf** (0, 1, 10 and 40 μM obtained by ICP measurement), and in parallel with the same corresponding concentration of HuHf (determined by Bradford assay) in serum deprived culture media for 24 h. Afterwards, cells were irradiated with 30 W three-arm LED light lamp with 470 nm–430 nm emission for 20 minutes at 5 cm from cell monolayers and then incubated for 24 h at 37 °C in 5% CO2 atmosphere. Cell viability was assayed in the presence of 0.5 mg mL^{-1} of MTT salt (Merck KGaA, Darmstadt, Germany) for 1 h at 37 °C; DMSO (Dimethyl Sulfoxide, Merck KGaA, Darmstadt, Germany) was used to dissolve insoluble formazan crystals produced by viable cells. The absorbance was measured at 595 nm using a microplate reader (iMark Microplate Absorbance Reader, Bio-Rad, CA, USA).

Chapter 2

Bis-heteroleptic RPCs with π-expansive benzo[i]di-pyrido[3,2-a:2′,3′-c]phenazine ligands

As discussed in the introduction, the design of new performant Ru(II)-PSs for application in PDT requires an accurate choice of the ligands around the metal center. A key feature is to maximize the sensitization of singlet oxygen ($^1O_2$) upon excitation with low energy light. To this aim, extended π-conjugation of the ancillary ligands provide complexes with prolonged ^{3}MLCT lifetimes reaching high values of singlet oxygen quantum yields. Furthermore, planar aromatic units also increase the ease of the interaction with important biological targets, such as DNA and/or proteins. These latter features are crucial for the effectiveness of the potential PSs.[4]

In this chapter, a reliable synthetic pathway for the preparation of a series of RPCs featuring two benzo[*i*]dipyrido[3,2-*a*:2′,3′-*c*]phenazine (dppn) moieties and a symmetrically bipyridine ligand functionalized with various R groups is provided. Of particular importance is the simultaneous presence of two dppn ligands, which represents a key feature to maximize the properties of ruthenium compounds as PSs in PDT (Figure 29).

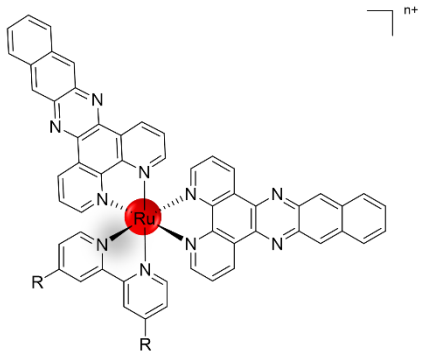

Figure 29: Chemical structure of RPCs discussed in this chapter. (n = 0 or 2 depending on R group).

Notwithstanding several studies previously reported on the positive effects induced by the insertion of a single dppn unit into the resulting Ru(II)-based PSs, [96–98] the use of metal complexes containing two dppn ligands remains almost unexplored. We can assume that this is likely associated with the synthetic difficulties encountered in using the most common synthetic approach to prepare bisheteroleptic RPCs which provides: i) refluxing of commercially available $RuCl_3 \cdot nH_2O$ in dimethylformamide with a thermally insensitive bidentate ligand (NN) to obtain the intermediate *cis*-$Ru(NN)_2Cl_2$, ii) the introduction of the third chelate (N'N') to give the bisheteroleptic complex with formula $[Ru(NN)_2(N'N')]^{2+}$ (Scheme 2). [99] In the case where NN-ligand is a dppn unit, the intermediate *cis*-$Ru(NN)_2Cl_2$ (NN = dppn) has a very low solubility in most organic media, preventing the obtainment of the final product.

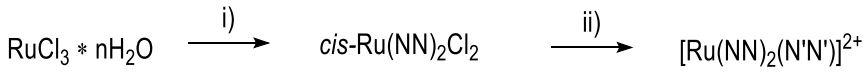

Scheme 2: Common synthetic procedure for the synthesis of bis-heteroleptic RPCs. i) refluxed DMF in the presence of LiCl; ii) ethylene glycol or alcoholic solution at reflux.

To the best of our knowledge, to date only three compounds were reported in literature in which the Ru(II) centers are simultaneously coordinated to two dppn ligands.[100,101] Among them, only two complexes, $[Ru(bpy)(dppn)_2]^{2+}$ and $[Ru(phpy)(dppn)_2]^{2+}$ (with bpy = bipyridine, phpy = 2-phenyl pyridine), were successfully synthesized and appropriately characterized by Turro et al. [100] These complexes were obtained in relatively low overall reaction yields (28%), with long reaction times (in the order of days). Moreover, their properties as potential PSs for PDT were not evaluated. Sun and co-workers, instead, reported the synthesis of $[RuL(dppn)_2]^{2+}$ (L = 3,8-di(benzothiazolylfluorenyl)-1,10-phenanthroline) performed by the reaction of the L ligand with the intermediate $[Ru(dppn)_2Cl_2]$ in ethylene glycol but synthetic details on the preparation of the Ru(II) intermediate were missing. Furthemore, no adequate characterization of $[RuL(dppn)_2]^{2+}$ was provided. [101]

This scenario prompted us to provide a straightforward synthetic alternative route for obtaining RPCs with the general formula $[Ru(RR\text{-}bpy)(dppn)_2]^{n+}$ (n = 0, 2) (Figure 29). The simultaneous presence of two dppn ligands in $[Ru(RR\text{-}bpy)(dppn)_2]^{n+}$ complexes ensures the high photosensitization of singlet oxygen and the interaction with key biological targets, whereas the optimal choice of the R functional groups in 4 and 4' positions of the bipyridine permits to finely modulate their chemical-physical properties as well as providing a potential synthetic platform for the obtaining of differently functionalized $(dppn)_2$-RPCs.

2.1 Synthesis of $[Ru(RR\text{-}bpy)(dppn)_2]^{n+}$ complexes

To overcome the above-mentioned difficulties in following the common synthetic approach for bisheteropleptic ruthenium(II) polypyridyl complexes (Scheme 2), a *"reverse"* procedure was purposefully developed and optimized (Scheme 3).

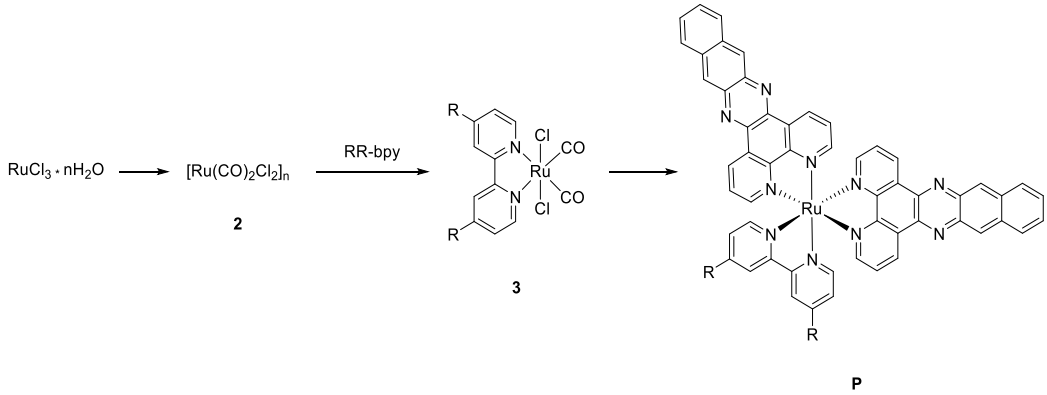

*Scheme 3:General synthetic route for the preparation of complexes with formula **P.***

This approach begins with the synthesis of the reactive polymeric compound $[Ru(CO)_2Cl_2]_n$ (**2**), which is then allow to react with the appropriately designed RR-bpy ligand to produce the *trans*-Cl$[Ru(RR\text{-}bpy)Cl_2(CO)_2]$ complex of formula **3**. The final

complexes, with formula $[Ru(RR\text{-}bpy)(dppn)_2]^{n+}$ (**P**), are then obtained due to the contemporary addition of two equivalents of dppn to the metal centre. The whole synthetic process leads to the final products with yields ranging between 22 % and 47 % depending on the different R substituents on the bipyridyl ligand.

On following are presented the synthetic details of three suitable examples of the series $[Ru(RR\text{-}bpy)(dppn)_2]^{n+}$ named as **P1-3** (Figure 30). All the three complexes can be obtained starting from the same precursors and differ for the R symmetrical groups on the bipyridyl ligand.

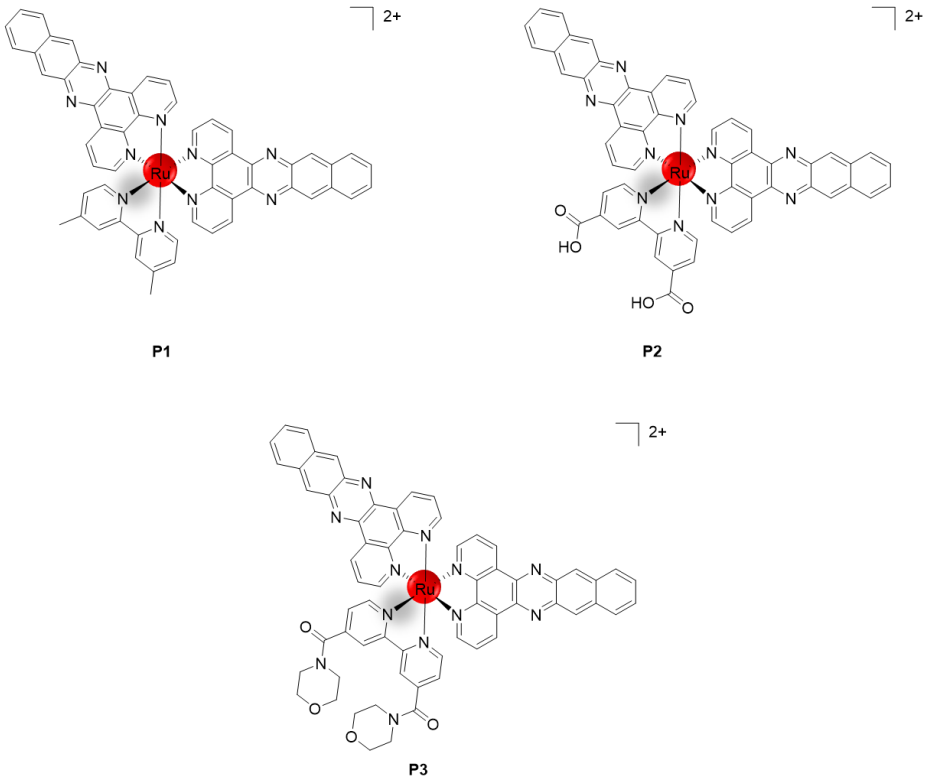

*Figure 30: Chemical structures of **P1**, **P2** and **P3**.*

For each complex, the dppn ligand **7** is synthetized according to literature procedure through Schiff-base condensation reaction of 1,10-phenantroline-5,6-dione **6** with commercially available 2,3-diaminonaphtalene (Scheme 4).[102]

Different symmetrical substitutions in the 4 and 4’ positions of bipyridyl ligand are obtained using commercially available 4,4’-dimethyl-2,2’-bipyridine **8** as starting material (for complexes **P2-3**) or directly (for complex **P1**) (Scheme 5). The oxidation of **8** to yield compound **9** (2,2’-bipyridine-4,4’-carboxylic acid) provides both a suitable ligand for complex **P2** as well as a precursor for the easy preparation of ester or amide derivatives, such as the newly synthesized 2,2'-bipyridine-4,4'-diylbis(morpholinomethanone) **11** (Scheme 5). The derivatization with morpholine in **11** leads to a strongly increased water solubility of the final complex **P3** as compared to **P2** where ligand **9** is in its dianionic form at neutral pH.

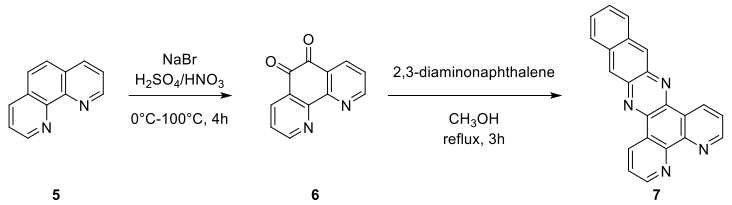

Scheme 4: Synthetic route followed for the preparation of the dppn ligand.

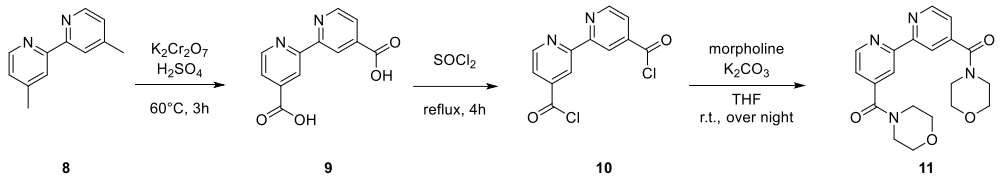

*Scheme 5: Synthetic route followed for the preparation of RR-bpy ligands (2,2’-bipyridine-4,4’-carboxylic acid **9** and 2,2’-bipyridine-4,4’-diylbis(morpholinomethanone) **11**).*

Using the general synthetic approach in Scheme 3, complexes **P1-3** are synthesized via stepwise ligand addition, with the reactive polymeric compound $[Ru(CO)_2Cl_2]_n$ **2** as starting material. The latter, is obtained by refluxing the commercial $RuCl_3 \cdot nH_2O$ in grams scale and paraformaldehyde in 1.4 : 1 w/w ratio in formic acid at 90% for 6 hours (Schema 6).[103] The resulting polymer **2** is isolated as pale-yellow powder through trituration from hexane with a yield of 80%. The selected RR-bpy ligand (**8**, **9** or **11**) is

then coordinated to the metal centre using slight modifications to previously described procedures.[103,104] In the case of intermediates **3a** and **3c**, the precursor **2** is allowed to react with **8** and **11** in refluxed methanol at a molar ratio of 1 : 1.1. For intermediate **3b**, instead, the use of dimethylformamide is necessary due to the scarce solubility of ligand **9** in most of organic solvent (Schema 6). The solubility of the ligands also influences the yields for compounds **3a-c** lowering them from 75% and 74% respectively for **3a** and **3c**, to 55% for compound **3b**. Importantly, all three intermediates (**3a-c)** are collected by hot filtration of the reaction mixture with a high grade of purity suitable for moving on to the final step without further purification. In the final synthetic step, complexes **3a-c** react with two equivalents of dppn ligand (**7**) in refluxed 2-methoxyethanol. Trimethylamine N-oxide (TMAO) is used to break the strong coordination bond between the ruthenium and the carbon monoxide molecules.[105] The addition of a 0.1 M aqueous solution of KPF_6 promotes the precipitation of **P1-3** that are collected by filtration in vacuum with adequate grade of purity. When necessary, a successive purification by flash chromatography on silica gel is employed to obtain the desired products as the hexafluorophosphate salts $[Ru(RR\text{-}bpy)(dppn)_2](PF_6)_2$ with yields ranging between 50% and 78% depending on the R substituents (Schema 6).

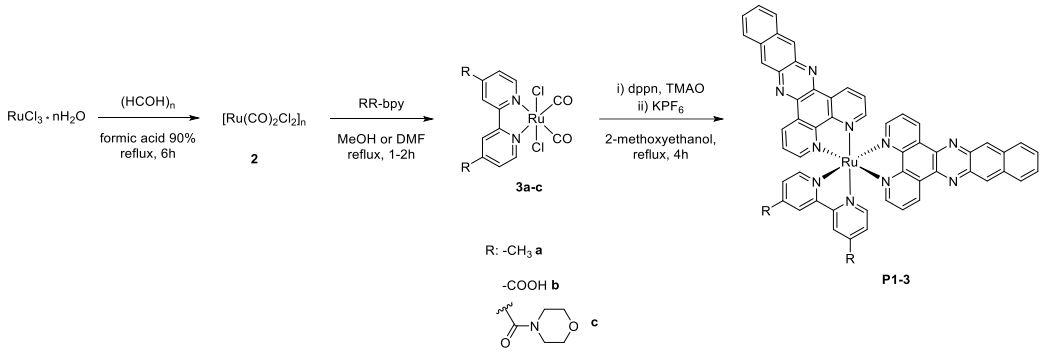

*Scheme 6: Synthetic route followed for the preparation of complexes **P1-3**.*

2.2 Characterization of $[Ru(RR\text{-}bpy)(dppn)_2]^{n+}$ complexes

The electronic absorption spectra of complexes **P1-3** in acetonitrile are reported in Figure 31, whereas their molar extinction coefficients (ε) at different absorption maxima λ_{max} are listed in Table 4. As shown in Figure 31 the absorption profiles exhibit an intense intraligand π→π* transitions at 280-330 nm, a double humped absorption at about 385 nm and 410 nm and the typical broad ^{1}MLCT absorption band centred between 440 and 455 nm.

On the other side, **P1-3** result to be weakly luminescent. Fluorescence spectra recorded in different solvents (Figure 32) reveal an increase of luminescence for complexes **P2** and **P3** in comparison to complex **P1**, with the highest emission being displayed in acetonitrile and ethanol; a very weak emission is instead observed for all the complexes in aqueous solution.

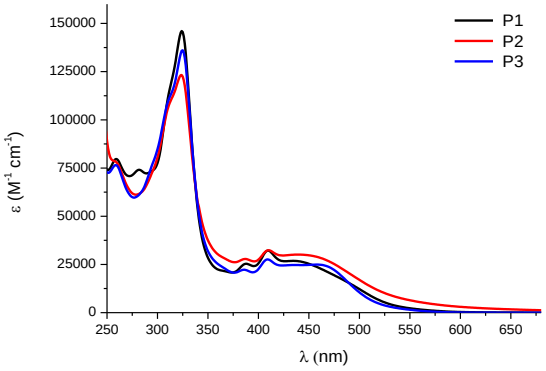

Figure 31: Absorption spectra of complexes P1-3 in CH_3CN.

Complex	*λ_{abs}/nm ($\varepsilon \times 10^3$ M^{-1} cm^{-1})*
P1	440 (26.6) 409 (32.2) 387 (25.3) 324 (146.1)
P2	445 (30.0) 410 (32.4) 387 (27.8) 323 (123.2)
P3	455 (24.9) 408 (27.5) 384 (22.1) 325 (136.1)

Table 4: Electronic absorption maxima measured in acetonitrile.

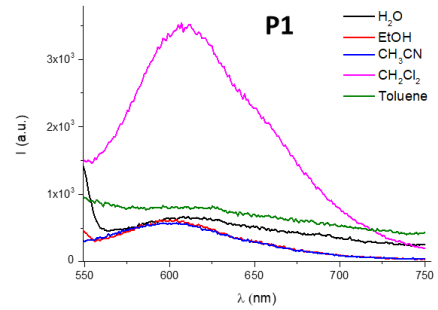

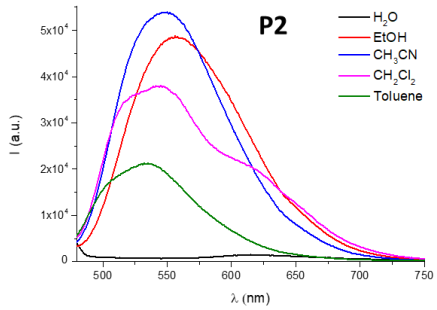

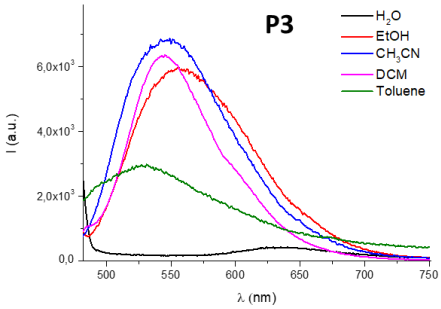

	λ_{max} (nm)				
	H_2O	EtOH	CH_3CN	CH_2Cl_2	Toluene
P1	610	-	-	610	-
P2	615	557	547	545	535
P3	640	557	574	540	530

*Figure 32: Fluorescence emission of **P1-3** and maximum emission wavelengths (λ_{em}) registered in different solvents. ([RPCs] = 5 μM, λ_{exc} (**P1**) = 460 nm, λ_{exc} (**P2**) = 410 nm), λ_{exc} (**P3**) = 410 nm).*

Lastly, given the presence of the ionizable 2,2'-bipyridine-4,4'-carboxylic acid (**7**) ligand in **P2**, the acid-base behaviour of this complex was investigated by monitoring the UV-Vis absorption and fluorescence spectra of aqueous solutions of the complex at different pH values. As observed in Figure 33, the increase in pH of aqueous solutions of **P2** determined a progressive hypochromism in the absorption spectra. On the other side, a significant enhancement of emission is observed with increasing the pH, accompanied by the presence of two inflection points, at *ca.* 2.5 and 4.5, suggesting a two-step acid-base equilibrium of the carboxylic moieties of the 2,2'-bipyridine-4,4'-carboxylic acid ligand. Analogously to what was previously reported for parental RPCs,[106] only the second pKa value was determined. In particular, the pK_{a2} in the ground state (pK_{a2}°) was obtained from the UV-Vis absorption titration by fitting the data to the Henderson-Hasselbach equation:[107,108]

$$pH = pK_a^\circ - log\frac{(A_{max} - A)}{(A - A_{min})}$$

where A_{max} and A_{min} are respectively the maximum and minimum absorbance values at 454 nm registered of **P2**. The pK_{a2} in the excited state (pK_{a2}^*) was obtained from the fluorescence titration by using the following the equation:

$$pK_a^* = pH - log\frac{\tau}{\tau'}$$

where τ and τ' are respectively the excited state lifetimes of the protonated and deprotonated form of **P2**.[109] From these measurements, values of 3.6 ± 0.3 and 4.6 ± 0.4 were respectively obtained for pK_{a2}° and pK_{a2}^*. The higher value found for pK_{a2}^* relative to pK_{a2} would be in line with the higher basicity of the complex in the excited state. Based on these findings, the carboxylic functions of **P2** are likely to be fully deprotonated at neutral pH, conferring to the complex an overall total neutral charge. Therefore, along with the different nature of their ancillary ligands, it can be envisaged that the different charges of metal complexes in physiological media (+2 for **P1** and **P3** and 0 for **P2**) might have an influence on their biological behaviour.

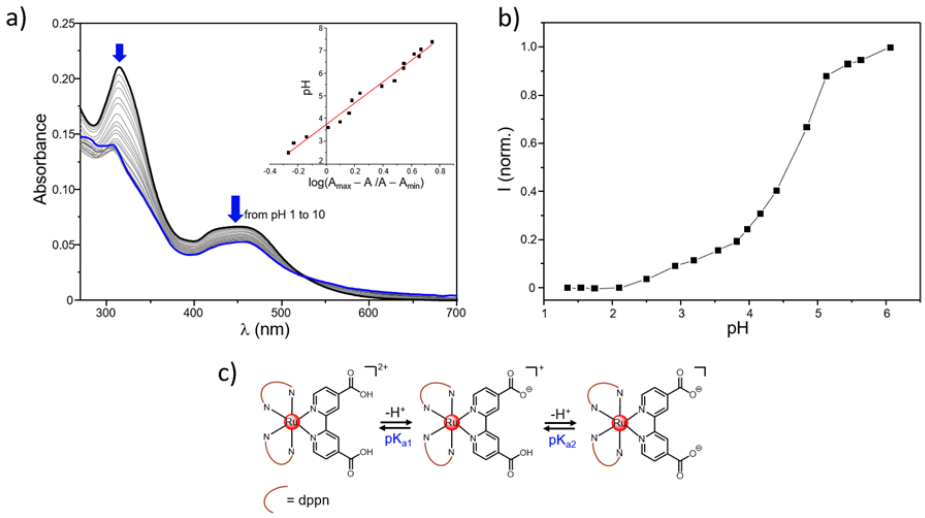

*Figure 33: a) Absorption spectra of **P2** (2 µM) in water collected at different pH and, in the inset, determination of the pk_{a2}° through the Henderson-Hasselbach-type equation. b) Fluorescence emission at 620 nm of **P2** (2 µM) in aqueous solution reported as a function of pH (λ_{exc} = 410 nm). c) Two-step acid-base equilibrium involving the carboxylic moieties of the 2,2'-bipyridine-4,4'-carboxylic acid ligand of **P2**.*

2.3 Determination of singlet oxygen quantum yields

As discussed above, a key requisite for a candidate PS for PDT relies on its capacity to effectively promote $^1O_2$ production upon light-irradiation according to *type II*-based process. In this regard, the singlet oxygen sensitizing properties of complexes **P1-3** were firstly assessed spectrophotometrically, by employing 1,5-dihydroxynaphthalene (DHN) as indirect reporter for singlet oxygen, and then further probed by direct measurements of the $^1O_2$ phosphorescence signal at 1270 nm. In both case, dichlorotris(1,10-phenantroline)ruthenium(II) chloride ($[Ru(phen)_3Cl_2]$) was used as standard reference ($\phi_{\Delta s} = 0.38$).[76]

The obtained rate constants k_{obs} for the photooxidation process of DHN and the quantum yields values (ϕ_Δ $^1O_2$) obtained by means of direct phosphorescence measurements are listed in Table 5.

In the indirect DHN assay, the probe is selectively and quantitively oxidized in the presence of $^1O_2$ to give its corresponding photooxidation product 5-hydroxy-1,4-naphthalendione (Juglone) (Figure 34, Equation 2). The effective sensitization of $^1O_2$, due to the irradiation of 10 μM solutions of **P1-3,** can be monitored by the decrease of DHN absorption band at λ = 297 nm and the corresponding increase of Juglone band at λ = 427 nm. Considering instantaneous the reaction between DHN and $^1O_2$ can be apply the steady-state approximation. The disappearance rate of $^1O_2$ coincides with the DHN consumption, and the rate of the photo-oxidation can be assumed to be first order, as shown in Equation 3. The rate constant (k_{obs}) can be thus obtained as semilogarithmic plot of $\ln(A_{297})_t/(A_{297})_0$ as a function of irradiation time by using Equation 4, where $[DHN]_0$ and $[DHN]_t$ are the molar concentration of DHN at time 'zero' and at a generic time '*t*', while $A(_{297})_0$ and $A(_{297})_t$ are the correspondent absorbance values measured at 297 nm.

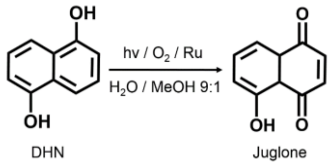

Figure 34: Photochemical conversion of DHN to Juglone.

$$\mathrm{DHN} + {}^{1}\mathrm{O}_2 \rightarrow \mathrm{Juglone} + \frac{1}{2}\,{}^{3}\mathrm{O}_2 \qquad (\mathrm{Eq.\ 2})$$

$$\upsilon = -\frac{d[{}^{1}\mathrm{O}_2]}{dt} = -\frac{d[\mathrm{DHN}]}{dt} = \mathrm{k}_{obs}[\mathrm{DHN}] \qquad (\mathrm{Eq.\ 3})$$

$$\ln \frac{[\mathrm{DHN}]_t}{[\mathrm{DHN}]_0} = \ln \frac{(A_{297})_t}{(A_{297})_0} = -\mathrm{k}_{obs}\,\mathrm{t} \qquad (\mathrm{Eq.\ 4})$$

In Figure 35 are reported the UV-Vis titration obtained for complex **P1-3**. Experiments were carried out by irradiating (LED Lamp: λ_{max} 434 nm, 160 mW) a 10 μM air pre-saturated acetonitrile solution containing the photosensitizer in presence of 3.3×10^{-4} M of DHN. All spectra were acquired using as blank reference a solution containing the selected PS in acetonitrile at the same concentration of those used in the measuring cuvette. Photosensitization of **P1-3** determines a strong decrease of DHN absorption, along with the simultaneous increase of Juglone absorption band (Figure 35). The rate constants of the photooxidation process (k_{obs}) for complexes **P1-3** are shown in Figure 35d in comparison with those found for $[Ru(phen)_3]Cl_2$ under the same experimental conditions. It can be noted that **P1-3** exhibit remarkably higher photosensitizing features with a similar amount of $^1O_2$ produced within 65-75s by **P1-3** and in more than 200s by $[Ru(phen)_3]Cl_2$.

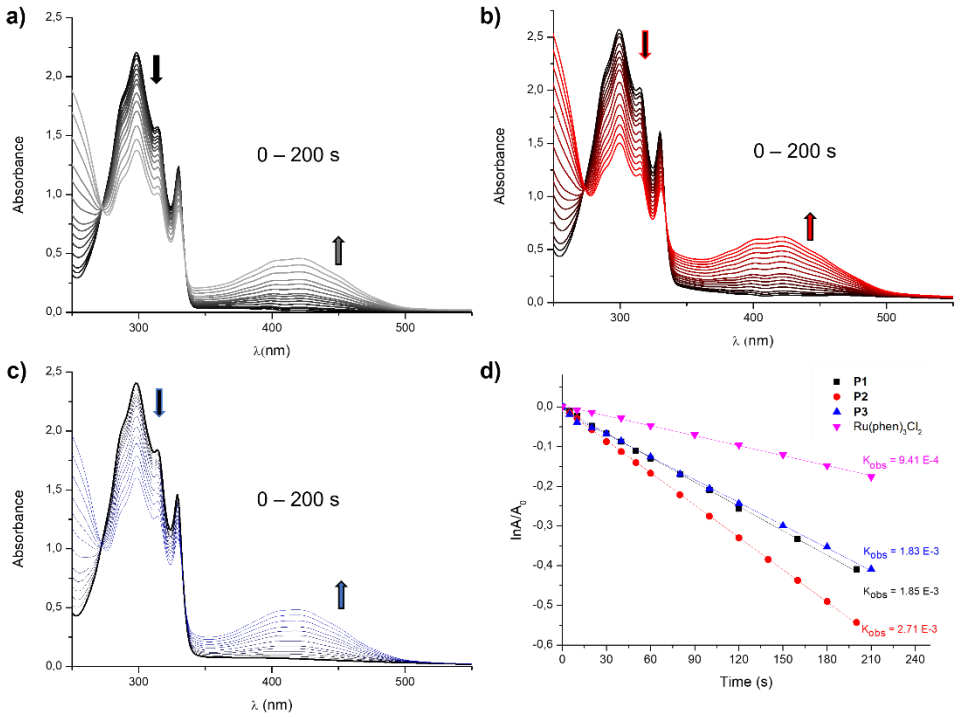

*Figure 35: a) Absorption spectra of solutions containing DHN (3.3×10^{-4} M) and complex a) **P1**, b) **P2** and c) **P3** (10 μM) in acetonitrile at different irradiation times (up to 200 seconds); b) Linear regression of the semilogarithmic plots of $\ln(A_t/A_o)$ as a function of the irradiation time: black square **P1**, red points **P2** , blue triangles **P3** and pink triangles $[Ru(phen)_3]Cl_2$.*

In addition to the indirect DHN method, the $^1O_2$ quantum yield of complexes **P1-3** were further probed through direct measurement of the phosphorescence signal of $^1O_2$ at 1270 nm, induced by irradiation of air-saturated solutions of the PSs at 440 nm. The correspondent $^1O_2$ quantum yields (ϕ_Δ) were evaluated by comparison with $[Ru(phen)_3Cl_2]$ taken as standard reference.[76] Briefly, the direct method is based on the fact that singlet oxygen in solution can decay through two different pathways:

i) Quenching by the solvent molecules: $O_2^*(S_1) + S \overset{k_d}{\rightarrow} O_2 + S^*$

ii) Phosphorescence emission: $O_2^*(S_1) \overset{k_f}{\rightarrow} O_2 + h\nu$

Accordingly, the kinetic equation for $^1O_2$ production can be derive as:

$$\frac{d[O_2^*(S_1)]}{dt} = \Phi_\Delta I_{abs} - \{k_f + k_d[S]\}[O_2^*(S_1)]$$

where ϕ_Δ is the singlet oxygen quantum yield and I_{abs} is the absorbed irradiance that can be expressed as $I_0(1\text{-}10^{-A})$ in which I_0 is the irradiance and A is the absorbance at irradiation wavelength. Considering constant the solvent concentration and applying the steady-state approximation, the above equation can be simplified as:

$$[O_2^*(S_1)] = \frac{\Phi_\Delta I_0(1 - 10^{-A})}{k}$$

Being $^1O_2$ concentration proportional to the integrated area of phosphorescence signal at 1270 nm, the linear fitting of $(1\text{-}10^{-A})$ plotted values in function of the phosphorescence integrated area is a line passing through the origin with angular coefficient:

$$m = \frac{\Phi_\Delta I_0}{k}$$

Considering the ratio between *m* values find for complexes **P1-3** and the m_s value find for the standard the final equation is:

$$\Phi_\Delta = \frac{m}{m_s} \Phi_{\Delta s}$$

Below are shown data collected for complex **P2** (Figure 36).

The quantum yields found for complexes **P1-3** are listed in Table 5.

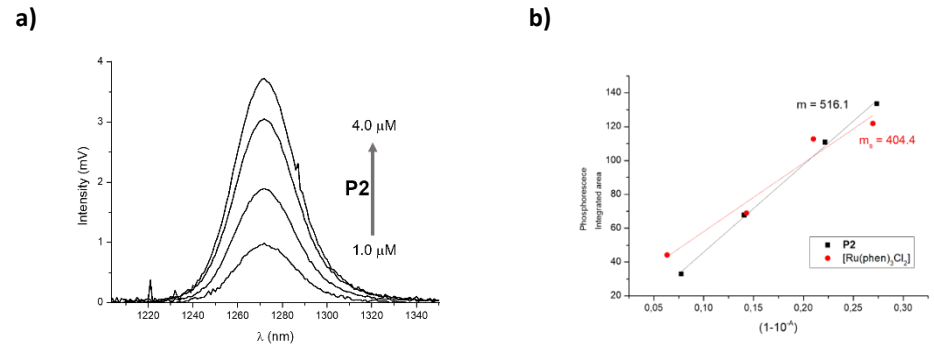

*Figure 36: a) Phosphorescence signals of $^1O_2$ produced by excitation at 440 nm of acetonitrile solutions of complex **P2** with concentrations between 1.0 μM and 4.0 μM. b) Linear fittings of plotted $(1\text{-}10^{-A})$ values in function of the integrated area of phosphorescence signals for complex **P2** and the reference standard $[Ru(phen)_3Cl_2]$.*

Complex	K_{obs} (s^{-1})	φ_Δ ($^1O_2$)
$[Ru(phen)_3]Cl_2$	9.41 (± 0.03) ×10^{-4}	0.38 ± 0.06[76]
P1	1.85 (± 0.01) ×10^{-3}	0.54 ± 0.06
P2	2.71 (± 0.03) ×10^{-3}	0.50 ± 0.07
P3	1.83 (± 0.02) ×10^{-3}	0.53 ± 0.06

*Table 5: Values of rate constants (K_{obs}) determined by DHN assay and single oxygen quantum yield determined by direct measurement of $^1O_2$ phosphorescence signal at 1270 nm for complexes [Ru(phen)3]Cl2 and **P1-3**.*

2.4 Interaction with *calf thymus*-DNA

Since it is known that $^1O_2$ rapidly reacts with the surrounding biological substrates (estimated half-life < 40 ns, range of action in the order of 20 nm), leading to extremely localized oxidative damage, the ability of a PS to effectively interact with a desired biological target may be important for its potential application in PDT, as it would ensure the drug localization in the close proximity of the target to be treated.[64]

These considerations prompted us to consider the DNA-binding properties of **P1-3** prior to testing their activity as anti-cancer agents. For this purpose, the DNA-binding ability of **P1-3** was evaluated on *calf thymus* DNA (ct-DNA) monitoring the changes in UV-Vis spectra profile upon titration with increasing amounts of the biopolymer (see paragraph 3 of the introduction for details).

The UV-Vis titrations with increasing amounts of *ct*-DNA in buffered solution (Tris-HCl 10 mM, NaCl 50 mM, pH 7.4) of the complexes **P1-3** at fixed concentration (10 µM) are shown in Figure 37a-c. At each addition, samples were incubated at room temperature for 10 minutes and the UV-Vis spectra were recorded using as blank a Tris-HCl buffered solution containing equal amounts of *ct*-DNA. As it is possible to note in Figure 37a-c the consecutive addition of *ct*-DNA (up to a maximum of 3.4 µM) results in hypochromism of the whole absorption spectrum of all complexes. Instead, no blue or

red shift are observed. The binding constants (K_b) are obtained as the ratio of slope and intercept for the linear regression of [DNA]/| $\varepsilon_a - \varepsilon_f$ | *vs.* [DNA] as shown in Figure 37d and are listed in Table 6. These results demonstrate that complexes **P1-3** effectively interact with *ct*-DNA, even in sub-stoichiometric quantities, presumably via a predominant intercalation mode since the main effect on their absorption spectra is hypochromism.[110] The K_b values, in the order of 10^6 M^{-1}, are in accordance with those reported in literature for intercalators [111] [110] [60] and can be related to those found for the famous ruthenium molecular *"Light Switch"* for DNA $[Ru(bpy)_2(dppz)]^{2+}$ (dppz: dipyrido[3,2-a:2',3'-c]phenazine).[112] The highest binding constant value was found for complex **P2** ($Kb = 2.34 \times 10^6$) for which the percentage of hypocorism (H %)[110] was found to be 21% in the ^{1}MLCT (450 nm) and 43% in ligand-based $^1\pi\pi^*$ band at 322 nm and eventually reached saturation at [DNA]/[**P2**]=5.

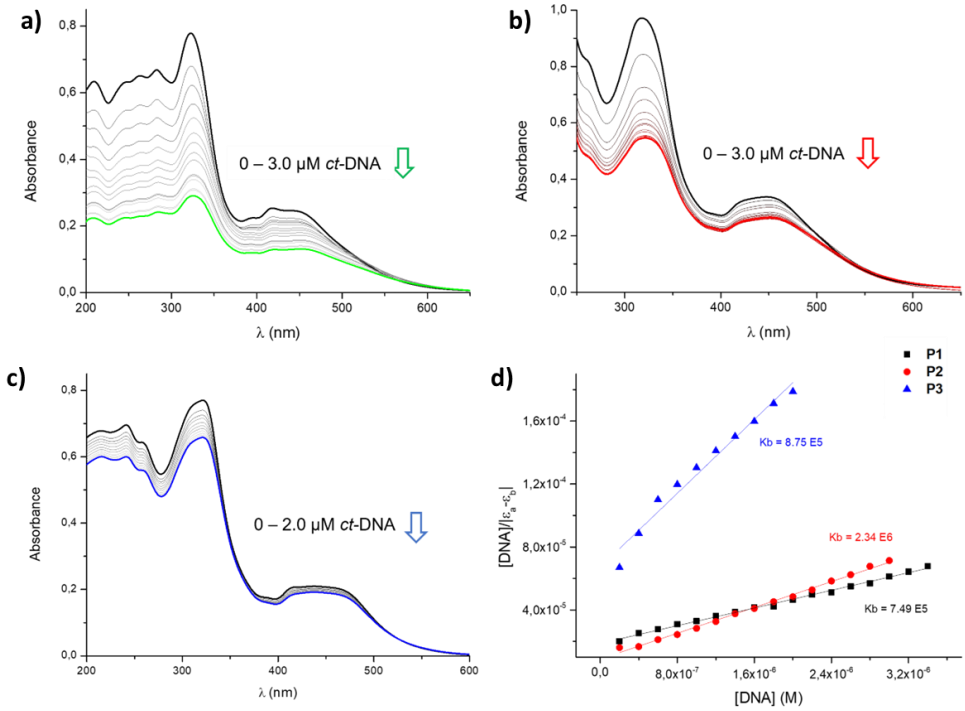

*Figure 37: Absorption spectra a) **P1**, b) **P2** and c) **P3** recorded in the presence of increasing concentrations of ct-DNA; d) linear fittings of plotted [DNA]/|ε_a-ε_b| values in function of the ct-DNA molar concentration for complexes **P1** (black), **P2** (red) and **P3** (blue). (Ru=10 μM, Tris-HCl buffer 10 mM, NaCl 50 mM, pH 7.4).*

Complex	*Kb (ct-DNA)*
P1	7.49 (± 0.05) × 10^5
P2	2.34 (± 0.09) × 10^6
P3	8.75 (± 0.2) × 10^5

*Table 6: Binding constants (Kb) found by means of UV-Vis titration of complexes **P1-3** with increased concentration of ct-DNA ([Ru]=10 µM in Tris buffer 10 mM, pH=7.4).*

To thoroughly investigate the DNA binding ability of complex **P2**, ct-DNA interaction was also studied by means of fluorescence emission spectroscopy. Since no appreciable luminescence was observed upon excitation in the MLCT bands of **P2** following the addition of ct-DNA, a competitive binding experiment utilizing ethidium bromide (EB) as intercalator was employed. The EB competitive binding assay is a well-established procedure based on the displacement of the intercalating drug (EB) from ct-DNA. EB emits intense fluorescence in presence of DNA, due to its strong intercalation between the base pairs. If a second compound can replace EB, the fluorescence of the solutions would be efficiently quenched. The extent of the binding between the second molecule and the DNA can be indirectly evaluated from fluorescence quenching extent of EB.

The fluorescence emission spectra of fixed concentration solutions of ct-DNA (10 µM) and EB (10 µM) in Tris buffer (pH 7.4) were recorded following the addition of increasing concentrations (up to 50 µM) of **P2**. After 5 minutes of incubation at room temperature, the DNA-EB complex was excited at 527 nm and the emission intensity was monitored at 610 nm. The experiment shows a significant quenching in the fluorescence intensity (up to 90 %) of the DNA-EB complex with increased concentrations of complex **P2** (Figure 38a). This result suggests that **P2** can strongly interact with ct-DNA displacing EB from the DNA-EB complex. The DNA-EB fluorescence quenching study for **P2** was performed applying the Stern-Volmer equation (Equation 5):

$$\frac{F_0}{F} = K_{SV}[Q] + 1 \quad (Eq.5)$$

where F_0 and F are the emission intensities of DNA-EB complex in the absence and in the presence of compound **P2**, [Q] is the concentration of **P2** and Ksv is the quenching constant. As suggested by the curvature of Stern-Volmer plot (Figure 38b), the nature of the quenching is not only static but also dynamic. To verify this, data were also plotted using modified Stern-Volmer or Scatchard equation (Equation 6) where K_a is the association constant and *n* is the number of binding sites:

$$\log\left(\frac{F_0 - F}{F}\right) = logK_a + n\ log[Q] \quad (Eq.6)$$

Furthermore, the apparent DNA binding constants (K_{app}) was calculated using equation 7 where K_{EB} is the binding constant of ethidium bromide with DNA that is 10^7, [EB] is molar concentration of ethidium bromide in the experimental set up, [Q] is the concentration of complex **P2** at which the fluorescence intensity of DNA-EB is reduced of 50% which corresponds to 13 µM.

$$K_{EB}[EB] = K_{app}[Q] \quad (Eq.7)$$

All the mentioned values, K_{SV}, K_a, *n* and K_{app}, are listed in table 7. The values of the calculated parameters confirm that complex **P2** strongly interact with DNA via intercalation mode. The binding affinities quantified by K_B, trough UV-Visible absorption studies, and K_{app}, found by means of ethidium bromide displacement assay, are in great accordance.

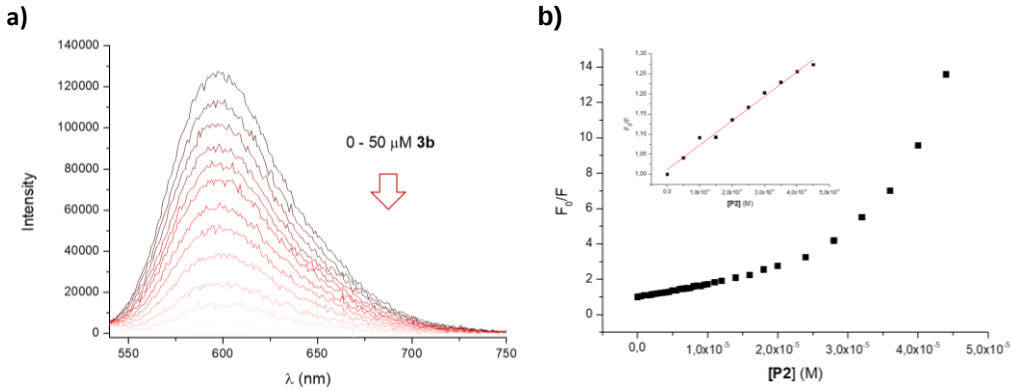

*Figure 38: a) Molecular fluorescence emission spectra associated to the titration of DNA-EB (10 µM, Tris buffer pH 7.4, λ_{ex} 527 nm, λ_{em} 610 nm) with increased concentrations of complex **P2*** recorded at 298 K. b) Stern-Volmer plot for the calculation of quenching constant (K_{SV}) for the interaction of DNA-EB and ***P2***.

Quenching constant (K_{SV}) (M^{-1})	*Association constant (K_a) (M^{-1})*	*No. of binding site (n)*	*Apparent DNA binding constant (K_{app}) (M^{-1})*
$6.46 \pm 0.04 \times 10^4$	$1.00 \pm 0.26 \times 10^4$	0,85 ± 0,04	$7.69 \pm 0.006 \times 10^6$

*Table 7: Values of quenching constant (K_{SV}), association constant (K_a), number of binding site (n) and apparent DNA binding constant (K_{app}) for complex **P2** obtained from ethidium bromide (EB) competitive assay.*

2.5 Cytotoxicity and photoactivity of $[Ru(RR\text{-}bpy)(dppn)_2]^{n+}$ complexes

To verify the potentiality of $[Ru(RR\text{-}bpy)(dppn)_2]^{n+}$ complexes as photosensitizing agents, *in vitro* studies were conducted with the collaboration of Prof. Chiara Sinico and Prof. Sergio Murgia of the department of Life and Environmental Sciences at the University of Cagliari.

On following are reported the preliminary data obtained for complexes **P1** and **P2** on A431 cells, an *in vitro* model of squamous epithelial carcinoma cells.

In both cases, cells cultured on 96-well plates were treated with increasing concentrations of complexes **P1-2** dispersed in the culture medium for 1 hour. At the end of the incubation, the medium was replaced, and the cells were exposed to LED light (λ_{max} 462 nm) for 30 minutes or left in the dark for the same time. At the end of the thirty minutes, the cells were placed in the incubator for 24 hours before measuring the metabolic activity by MTT assay. For each concentration were used 6 replicates, and cell viability of 100% was calculated from the response of untreated and unexposed cells to LED light.

As shown in Figure 39, both the compounds show high power and specificity on A431 cells. Indeed, when no light is provided to the culture dishes, a minimal or no toxic effect is detected. A slight difference between their *in dark* toxicity is observed: cell viability is reduced to 75.1 ± 4.1 % and 82.4 ± 2.0 % upon exposure to the highest dose of **P1** and **P2** (25 µM), thus indicating that seemingly small modifications on the bpy

ligand of complexes (methyl or carboxylic functions) may influence their toxicity. Conversely, a 30 minutes irradiation with a LED Lamp emitting at 462 nm induces an extensive cells death (viability < 10%) at concentration of 0.25 µM of **P1** (Figure 39a) and 5 µM of **P2** (Figure 39b).

IC_{50} values for both complexes on tested cell lines are listed in Table 8 along with the photoindex values (PI) defined as IC_{50}(dark) / IC_{50}(light). These results highlighted the high specificity (defined as toxicity only when exposed to light) and the great potential of **P1-2** as photosensitizing agent in the photodynamic therapy of different A431 cells. Albeit the comparison of cytotoxic activity with already published results for analogue RPCs is difficult to define, it should be noted that PI values are higher to those reported for complexes with only one dppn as auxiliary ligand on different cancer cells model.[97,98] Furthermore, both complexes possess PI values higher than TLD1344, the only ruthenium complex in clinical trial in photodynamic treatment of cancer, on epithelial squamous carcinoma cells (A431).[113]

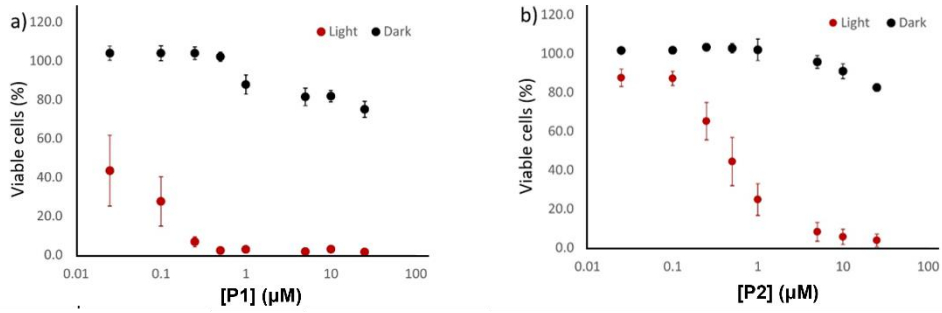

*Figure 39: Cells viability assays of squamous epithelial carcinoma cells (A431) treated with increased concentration of complex a) **P1** and b) **P2** measured before (black) and upon (red) LED light irradiation for 30 minutes (λ_{max} 462 nm). Tests were carried out in six replicates. All data were normalized with respect to control tests.*

Complex	*Cell Culture*	*IC_{50} Light (30' LED)*	*IC_{50} Dark*	Photoindex (PI)
P1	A431	0.0253 ± 0.0107 µM	> 40 µM	> 988
P2		0.191 ± 0.023 µM	> 40 µM	> 130

*Table 8: Average values of IC50 obtained by cells viability assays for complex **P1** and **P2** on squamous epithelial carcinoma cells (A431).*

2.6 $[Ru(RR\text{-}bpy)(dppn)_2]^{n+}$-Cubosome nanocomposites

The main goal in medicine is probably the improvement in the selectivity of therapeutic tools available in clinics. In the last two decades, considerable efforts have been made to develop delivery systems able to improve selective drug accumulation in malignant cells. Considering the possibility of using $[Ru(RR\text{-}bpy)(dppn)_2]^{n+}$ complexes as PS agents *in vivo,* encapsulating them in nanoparticles is a strategic choice to overcome their poor water solubility and increase their translational potential. For this purpose, among the various engineered nanocarriers, monoolein-based cubosomes were selected. The latter were proposed only recently for imaging and theragnostic application.[114] Basically, cubosomes are nanosized carriers formulated by exploiting the self-assembling properties of lipids in water. They differ from other lipidic nanoparticles due to their unique honeycomb-like internal structure, which consists of a lipid bilayer arranged in three dimensions to form two disjoined water channels and to describe an Infinite Periodic Minimal Surface belonging to a cubic space group (*Pn3m*, *Ia3d* or *Im3m*).[115] The loaded-cubosome formulation should allow the facile administration of poorly-water soluble drugs in the blood stream. Moreover, the accumulation of nanocomposites in tumour tissues passively occurs as a result of aberrant tumour angiogenesis that forms nonmature capillaries, facilitating the permeability to nanoparticles in comparison to physiological vessels. This phenomenon is called enhanced permeation and retention effect. [116]

On these bases, with the collaboration of Prof. Chiara Sinico and Prof. Sergio Murgia of the Department of Life and Environmental Sciences at the University of Cagliari, cubosomes-loaded formulations, **P1-cubo** and **P2-cubo,** were prepared by dispersing the selected PS in melted monoolein (MO) at 40°C and the lipidic phase was stabilized with Pluronic F108. The obtained samples were fluid aqueous dispersions with a milky macroscopic appearance. After drug loading, cubosomes were purified from non-encapsulated PS by dialysis. A percentage value of 9 % for **P1** and 60 % for **P2** were

determined as drug-loading efficiency (E %), expressed as percentage of the initially used amount of drug. The different percentages of loading efficiency can be reasonably ascribed to the different overall charges of the two complexes at neutral pH (**P1** features a double positive charge, whereas **P2** is likely to be present in its neutral form) that affect the encapsulation efficiency into cubosomes.

Loaded cubosomes were characterized by means of Dynamic Light Scattering (DLS) analysis, Cryogenic Transmission Electron Microscopy (cryo-TEM), Small-Angle X-ray Sacttering (SAXS) experiments and UV-visible analysis, and all the relevant parameters are summarized in Table 9.

DLS analysis reveal the presence of nanoparticles with an average diameter (D_{av}) of 138 ± 2 and 142 ± 1 nm, for **P1**-**cubo** and **P2**-**cubo** respectively. Both formulations have a narrow size distribution with a polydispersity (PDI) value below 0.2 and a ζ-potential of -13 ± 3 mV for **P1**-**cubo** and -30 ± 2 mV **P2**-**cubo**, indicating that the latter is more stable. Monitoring the average diameter, the polydispersity index, and the ζ potential for up to 30 days provided information on formulation stability over time at 25 °C. Furthermore, the chemical stability of encapsulated complexes **P1** and **P2** was analysed during this time via UV-Vis spectroscopy. Measurements reveal a great deal of stability for **P2-cubo** formulation: the diameter of loaded nanoparticles was maintained at about 140 nm for the entire observation time. The dimensional distribution is maintained constant, as demonstrated by the maintenance of polydispersity index under 0.15. Similarly, the ζ-potential is evermore around -30 mV and the concentration of **P2** inside the nanoparticles decreases gradually until day 7, after which it stabilizes for up to 30 days (Figure 40). Conversely, **P1-cubo** formulation results not stable already in the first seven days (Figure 40).

Given the unsatisfactory preliminary results obtained for **P1-cubo**, **P2-cubo** was chosen for additional characterization and *in vitro* bioactivity studies.

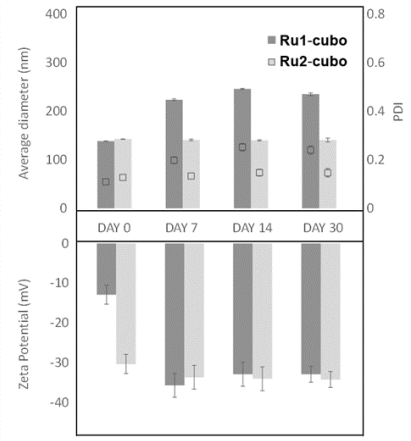

*Figure 40: Average diameter (nm), polydispersion index (PDI), zeta potential (mV) of **P1-cubo** and **P2-cubo** over 30 days of storage at 25°C.*

Figure 41a shows the Cryo-TEM image of the **P2-cubo** formulation, in which cubosomes appear as spherical nanoparticles with a peculiar inner vesicular structure. The internal nanostructure was further analysed by means of SAXS experiments. The SAXS pattern (Figure 41b), unequivocally suggests the contemporary presence of two different cubic space, Pn3m and Im3m, that are respectively characterized by a lattice parameter (a) of 92 ± 1 Å and 117 ± 1 Å and a water channel radius (r_w) of 38 ± 1 Å e 37 ± 1 Å.

a) **b)**

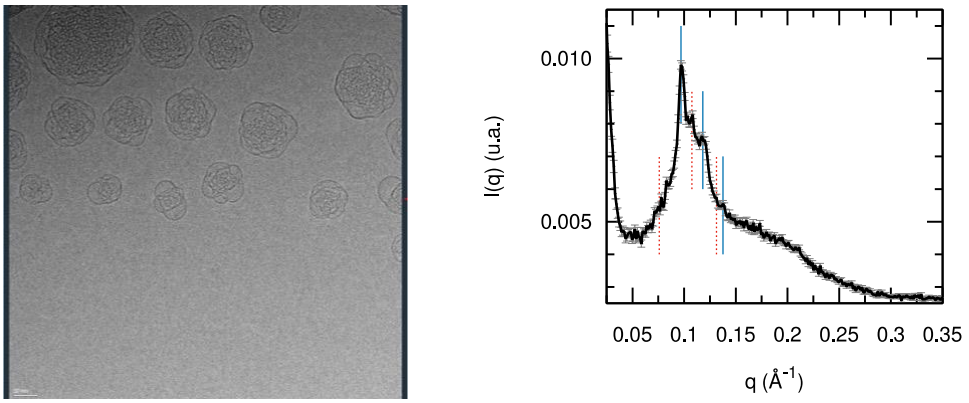

*Figure 41: a) Cryo-TEM image of MO-based cubosomes containing complex **P2** and stabilized with F108; b) SAXS patterns of **P2-cubo** with indication of the relevant Bragg peaks corresponding to the Im3m phase (red dashed line) and Pn3m (blue line) cubic continuous phases.*

	Composition (% w/w)					Characterization			
	MO	**PF108**	**P1**	**P2**	**H_2O**	**D_{av} [a](nm)**	**PDI[b]**	**ζ[b] (mV)**	**EE %**
P1-cubo	3.3	0.03	0.02	-	96.65	138 ± 2	0.11 ± 0.01	-13 ± 3	9 ± 3
P2-cubo	3.3	0.03	-	0.02	96.64	142 ± 1	0.13 ± 0.01	-30 ± 2	60 ± 5

*Table 9: Summary of composition and relevant characterization parameters for **P1-cubo** and **P2-cubo**. [a]Values found by means of SAXS analysis; [b] values found by means of DLS analysis.*

The cytotoxicity of **P2-cubo** nanocomposite in dark conditions and upon light activation were tested on the previously described epidermoid carcinoma model (A431) and compared to that of empty cubosomes (E-cubo). As expected, **P2-cubo** shows negligible toxicity in dark condition; instead, photoactivation for 30 minutes with LED visible light promotes an extensive decrease in cell viability with more than 50 % reduction of cell viability at the dose of 0.25 µM (Figure 42a). The risk of unspecific toxicity of other components of the nanoformulation was ruled out by exposing cells to E-cubo in the same conditions (Figure 42b). The average IC_{50} value found for **P2-cubo** is compared in Table 10 with the ones found for free **P2**. As expected, the cytotoxicity is reduced to about half, but specificity against A431 cells upon irradiation is maintained.

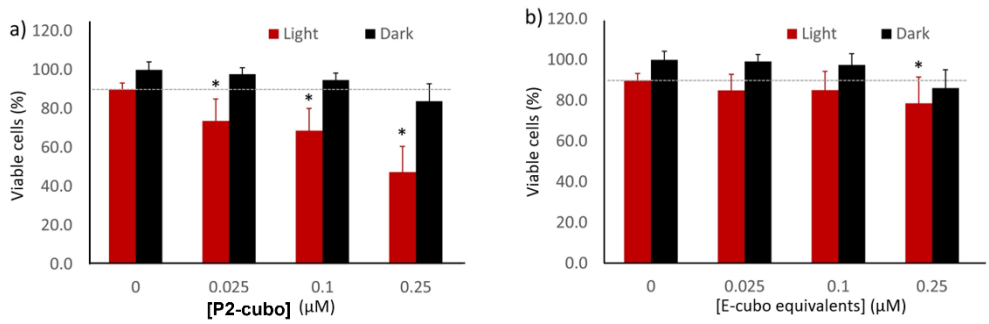

*Figure 42: Cells viability assays of squamous epithelial carcinoma cells (A431) treated with increased concentration of a) **[P2-cubo]** and b) **E-cubo** measured before (black) and upon (red) LED light irradiation for 30 minutes (λ_{max} 462 nm). Tests were carried out in six replicates. All data were normalized with respect to control tests.*

Cell cultures: A431

	IC_{50} Light (30' LED)	IC_{50}Dark
P2-cubo	0.268 ± 0.079 µM	ND
P2	0.191 ± 0.023 µM	> 40 µM

*Table 10: Comparison of average IC_{50} values obtained by cells viability assays for **P2-cubo** and free-**P2** on squamous epithelial carcinoma cells (A431).*

Finally, to gain preliminary information on the mechanism of the observed phototoxicity, the production of intracellular ROS upon irradiation was investigated using the 2',7'-dichlorodihydrofluorescein diacetate (DCFH-DA) assay. DCFH-DA, into cells, is deacetylated by cytosolic esterases to a non-fluorescent metabolite (DCFH) that is then oxidized in the presence of intracellular ROS to produce the highly fluorescent 2',7'-dichlorofluorescein (DCF). The amount of ROS produced by cells in response to the illumination of **P2-cubo** can be estimated by measuring the green fluorescent intensity of DCF localized within the cells. Following treatment of A431 cells with DCFH-DA probe and 100 µM of **P2-cubo** and illumination, confocal laser scanning microscopy measurements reveal a diffuse green fluorescence within the majority of the cells (Figure 43c). Conversely, a widely lower green fluorescence is observed for untreated (Figure 43a) and treated in dark conditions (Figure 43b) cell culture. Overall, these results confirm that the cytotoxic effect observed for the irradiation of **P2-cubo** would be related to the capacity of the formulation to effectively trigger the production of intracellular ROS/$^1O_2$ species.

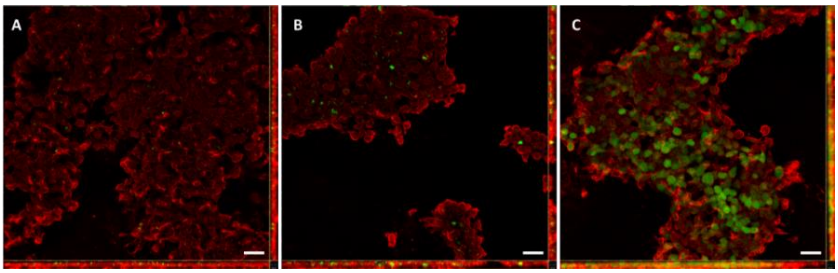

*Figure 43: Production of ROS by A431 epidermoid carcinoma cells estimated by the oxidation of DCF-DA sensor and visualized by confocal laser scanning microscopy. Cells were either not treated (**A**) or treated with **P2-cubo** (100 µM) and incubated in the dark (**B**) or exposed for 10 minutes to blue light (**C**). The green fluorescence corresponds to oxidized probe (DCF) by intracellularly produced ROS. Red signal shows the cell membranes, stained with WGA after fixation with PFA 4%. Scalebar = 50 µm.*

Acknowledgement

Some of the data presented in this chapter are part of a pending patent: n 102022000023862

I would like to express my sincere gratitude to Prof. Sergio Murgia, Prof. Chiara Sinico, Dr. Michele Schlich and Dr. Luca Casula from the University of Cagliari for their invaluable assistance in the investigation of the biological activity of the ruthenium complexes described here, as well as in the preparation of cubosome-based formulations and related studies.

Some of the results reported here have already been published as follows:

Giacomazzo G. E., Schlich M., Casula L., Galantini L., Del Giudice A., Pietraperzia G., Sinico C., Cencetti F., Pecchioli S., Valtancoli B., Conti L., Murgia S., Giorgi C.; Ruthenium(ii) polypyridyl complexes with π-expansive ligands: synthesis and cubosome encapsulation for photodynamic therapy of non-melanoma skin cancer; *Inorg. Chem. Front.* **2023** DOI: 10.1039/D2QI02678C

EXPERIMENTAL SECTION

Numbering example

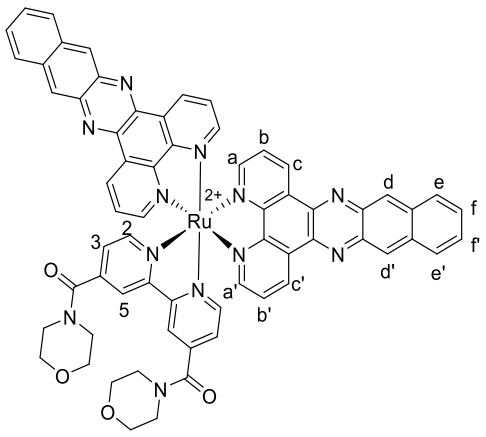

Synthesis

Materials and methods

Reagents and solvents were purchased from Sigma Aldrich and Alfa Aesar and were used without further purification. The NMR spectra were collected with a Bruker 400 MHz spectrometer.

Synthesis of 2

$[Ru(CO)_2Cl_2]n$

Compound **2** was synthesized according to the previously reported procedure.[103] Ruthenium (III) chloride trihydrate (395 mg, 1.90 mmol) was dissolved in 13 mL of an aqueous solution of formic acid 90%. The reaction mixture was heated by reflux while maintaining a constant nitrogen flow and sheltering from light. Over the next 6 hours, it was observed to undergo a characteristic colour change from green to blue and then to yellow. The acidic solution was then evaporated under reduced pressure, and the residue was triturated and filtered by hexane. The polymeric precursor **2** was obtained as a yellow powder with a yield of 68%.

Synthesis of 6

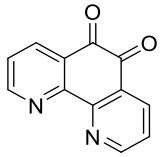

Compound **6** was synthesized according to previously reported procedure.[117] A solid mixture of 1,10-phenantroline (1.12 g, 6.21 mmol) and NaBr (6.4 g, 62.2 mmol) was dissolved at 0°C in 35 mL of an acidic mixture of H_2SO_4:HNO_3 (2:1). The reaction mixture was vigorously stirred for 10 min at 0°C and then heated to 100°C for 4 h. Then, it was quenched with 100 mL of ice-cold water and neutralized with a solution of NaOH 6 M. The aqueous phase was then extracted three times with chloroform, and the organic

phases were collected, dried on Na_2SO_4 and evaporated to dryness. The yellow crude product was purified by crystallization from hot ethanol to obtain **6** as crystalline yellow needles (689 mg, 3.28 mmol). Yield 53%. ^{1}H-NMR (400 MHz, CD_3Cl): δ 9.16 (d, $J_{a\text{-}b}$ = 3.6 Hz, 2H, $\mathbf{H_a}$) 8.54 (d, $J_{c\text{-}b}$ = 7.6 Hz, J2=1.8 Hz 2H, $\mathbf{H_c}$) 7.63 (dd, $J_{b\text{-}c}$ = 8.0 Hz, $J_{b\text{-}a}$ = 4.8, 2H, $\mathbf{H_b}$) ppm.

Synthesis of 7

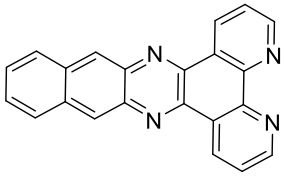

Compound **7** was synthesized according to previously reported procedure.[117] To a hot solution of **6** (256 mg, 1.22 mmol) in 52 mL of dry methanol at 40°C, was added 2,3-diaminonaphtalene (212 mg, 1.34 mmol). The reaction mixture was heated to reflux and stirred for 3 h under N_2 atmosphere. The bright orange precipitate was collected by filtration and washed with water, methanol, and diethyl ether to obtain **7** as an orange solid (375 mg, 1.13 mmol) with a yield of 93%. ^{1}H-NMR (400 MHz, $(CD_3)_2SO$): δ 9,59 (d, J= 7.5Hz, 2H), 9.25-9.21 (m, 2H), 9.14 (s, 2H), 8.45-8.37 (m, 2H), 7.98 (dd, J= 7.6 Hz, J= 4.2 Hz, 2H); 7.79-7.71 (m, 2H) ppm.

Synthesis of 9

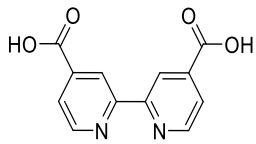

Compound **9** was synthesized according to literature procedure.[118] 4,4'-dimethyl-2,2'-biprydine (2.0 g, 10.8 mmol) was dissolved in 27 mL of concentrated sulfuric acid at -10°C. Potassium dichromate (9.6 g, 32.3 mmol) was then added slowly over 30 minutes and the mixture was stirred and heated to 60°C. After 4 hours, the reaction mixture

was poured in 500 mL of ice-cold water, allowing the precipitation of a white solid that was filtered and washed abundantly with water. Yield 86%. ^{1}H-NMR (400 MHz, $(CD_3)_2SO$): δ 8.93 (d, $J_{2\text{-}3}$=4.8 Hz, 2H, **H_2**), 8.86 (s, 2H, **H_5**), 7.93 (d, $J_{3\text{-}2}$=4.4, 2H, H_3).

Synthesis of 10

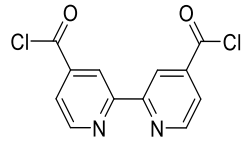

Compound **10** was synthesized according to literature procedure.[119] A catalytic amount of DMF (a drop) was added to a suspension of **9** (500 mg, 2.04 mmol) in 6 mL of thionyl chloride. The reaction mixture was stirred at reflux for 2 h under N_2 atmosphere. After cooling at r.t., thionyl chloride was coevaporated with toluene, and product **10** was obtained as a red powder and was immediately used in following reactions without further purification. Quantitative yield.

Synthesis of 11

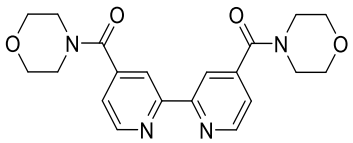

To a suspension of compound **10** (576 mg, 2.05 mmol) in 10 mL of dry THF, were added potassium carbonate (860 mg, 6.15 mmol) and morpholine (179 mg, 4.10 mmol). The reaction mixture was stirred at room temperature overnight under N_2 atmosphere and then filtered on a Celite pad washing with chloroform. The solution was washed three times with water and once with brine. The organic phase was dried on Na_2SO_4 and evaporated to dryness. Compound **11** was obtained as a pale-yellow powder (294 mg, 0.77 mmol) with a yield of 38% over two reaction steps. ^{1}H-NMR (400 MHz, $CDCl_3$): δ 8.80 (d, J = 4.8 Hz, 2H, **H2**), 8.49 (s, 2H, **H5**), 7.41 (d, J=4.8, 2H, **H3**), 3.86 (s, 8H, -CH_2

morpholine), 3.70 (s, 4H, -CH_2 morpholine), 3.49 (s, 4H, -CH_2 morpholine) ppm. ^{13}C-NMR (100 MHz, $CDCl_3$): δ 168.3, 156.1, 150.4, 145.0, 122.5, 119.5, 67.4, 48.5, 43.0 ppm.

Synthesis of 3a

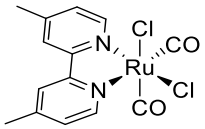

Complex **3a** was synthesized with slight modification of previously reported procedure.[103] 4,4'-dimethyl-2,2'-biprydine (184 mg, 0.58 mmol) was added to a solution of **2** (150 mg, 0.64 mmol) in 11 mL of dry methanol. The reaction mixture was hated to reflux and stirred under N_2 atmosphere for 2 h excluding light. The precipitate was then filtered hot and washed with methanol to obtain complex **3a** as a creamy white solid with a yield of 75 %. ^{1}H-NMR (400 MHz, $(CD_3)_2SO$): δ 9.04 (d, J=6 Hz, 2H, **H2**) 8.65 (s, 2H, **H5**) 8.21 (d, J=6, 2H, **H3**) ppm. ^{13}C-NMR (100 MHz, $(CD_3)_2SO$): δ 197.2, 155.2, 153.6, 153.4, 129.5, 125.7, 21.9 ppm.

Synthesis of 3b

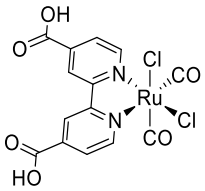

Complex **3b** was synthesized with slight modification of previously reported procedure.[104]

2,2'-bipyridine-4,4'-carboxylic acid (76 mg, 0.31 mmol) was dissolved in 5 mL of dry DMF hated at 80°C. Then, polymeric precursor **2** (80 mg, 0.34 mmol) was added and the reaction mixture was hated to reflux for 3 hours under N_2 atmosphere excluding light. After cooling at r.t., solvent was removed in vacuum and complex **3b** was

obtained thought hot crystallization from methanol with a yield of 55 %. ^{1}H-NMR (400 MHz, $(CD_3)_2SO$): δ 9.41 (d, J=5.9 Hz, 2H, **H2**) 9.16 (s, 2H, **H5**) 8.21 (d, J=5.9, 2H, **H3**) ppm.

Synthesis of 3c

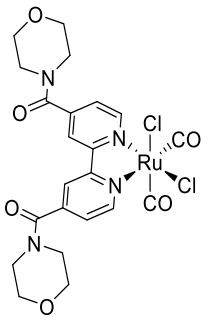

To a solution of **2** (150 mg, 0.64 mmol) in 11 mL of dry methanol was added compound **11** (221 mg, 0.58 mmol) and the reaction mixture was hated to reflux and stirred under N_2 atmosphere for 2 h excluding light. The precipitate was filtered hot and washed with methanol to obtain complex **3c** as yellow solid with a yield of 74%. ^{1}H-NMR (400 MHz, $(CD_3)_2SO$): δ 9.34 (d, J=5.6, 2H, **H2**), 8.93 (s, 2H, **H5**), 7.90 (d, J=5.2, 2H, **H3**), 3.73 (s, 8H, -CH_2 morpholine), 3.62 (s, 4H, -CH_2 morpholine), 3.36 (s, 4H, -CH_2 morpholine) ppm. ^{13}C-NMR (100 MHz, $(CD_3)_2SO$): δ 196.4, 163.3, 154.9, 154.3, 147.6, 126.1, 122.9, 66.5, 66.2, 47.7, 42.3 ppm.

Synthesis of P1

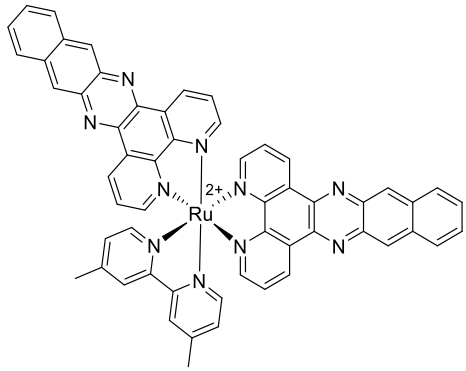

To a solution of **3a** (80 mg, 0.19 mmol) in 8 mL of degassed 2-methoxyethanol, compound **7** (129 mg, 0.39 mmol) and trimethylamine N-oxide (106 mg, 0.95 mmol) were added. The reaction mixture was stirred for 4 hours at reflux under N_2 atmosphere. After cooling at r.t., the addition of 3 mL solution 0.1 M of KPF_6 allows the complete precipitation of **P1**. The precipitate was filtered and washed with water and chloroform. The crude product was purified by flash chromatography on silica gel (eluent: starting from DCM:MeOH 50:1 with 10% Acetone to DCM:MeOH 30:1 with 10% Acetone) to obtain **P1** as red powder with a yield of 78%. ^{1}H-NMR (400 MHz, $(CD_3)_2CO$): δ 9.83 (d, $J_{c\text{-}b}$=8.0 Hz, 2H, **Hc**), 9.73 (d, $J_{c'\text{-}b'}$=8.0 Hz, 2H, **Hc'**), 9.23 (s, 2H, **Hd**), 9.20 (s, 2H, **Hd'**), 8.81 (s, 2H, **H5**), 8.67 (d, J=4.0 Hz, 2H, **Ha**), 8.62 (d, $J_{a\text{-}b}$=4.0, 2H, **Ha'**), 8.49-8.44 (m, 4H, **He/He'**), 8.18 (dd, $J_{b\text{-}c}$=8.0 Hz $J_{b\text{-}a}$ =4.0 Hz, 2H, **Hb**), 8.12 (d, $J_{H2\text{-}H3}$=4.0 Hz, 2H, **H2**), 7.95 (dd, $J_{b'\text{-}c'}$=8.0 Hz $J_{b'\text{-}a'}$=4.0 Hz, 2H, **Hb'**), 7.87-7.80 (m, 4H, **Hf/Hf'**), 7.38 (d, $J_{H3\text{-}H2}$=4.0 Hz, 2H, **H3**), 2.61 (s, 6H, -CH_3) ppm. ^{13}C-NMR (100 MHz, $(CD_3)_2CO$): δ 157.59, 155.08, 154.71, 152.34, 152.26, 152.13, 151.45, 141.51, 139.11, 135.80, 134.31, 134.23, 131.85, 131.77, 129.27, 129.19, 128.85, 128.80, 128.67, 128.45, 128.27, 125.89, 20.91 ppm. HR-MS (ESI+) m/z: calcd. for $C_{56}H_{36}N_{10}Ru$ $[M\text{-}2PF_6^-]^{2+}$ 475.10791 found: 475.10791. Anal. calcd for $C_{56}H_{36}F_{12}N_{10}P_2Ru$: C 54.24, N 11.30, H 2.93; found C 54.00, N 10.53, H 3.24

Synthesis of P2

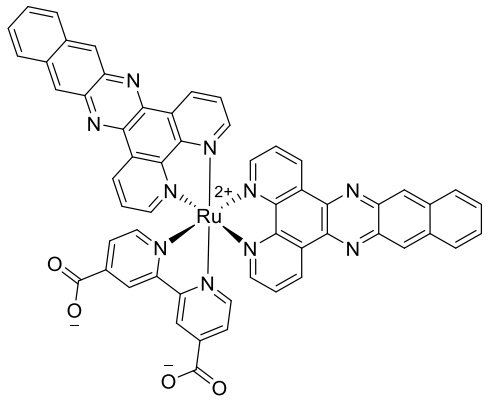

To a solution of **3b** (80 mg, 0.17 mmol) in 8 mL of degassed 2-methoxyethanol compound **7** (113 mg, 0.34 mmol) and trimethylamine N-oxide (95 mg, 0.85 mmol) were added. The reaction mixture was stirred for 6 hours at reflux under N_2 atmosphere. After cooling at r.t., the addition of 3 mL solution 0.1 M of KPF_6 allows the complete precipitation of complex **P2** that was filtered, washed with water and then triturated with $CHCl_3$ to obtain **P2** as red powder with a yield of 50%. ^{1}H-NMR (400 MHz, DMSO): δ 9.62 (d, $J_{c\text{-}b}$=8.0 Hz Hz, 2H, **Hc**), 9.56 (d, $J_{c'\text{-}b'}$=8.0 Hz, 2H, **Hc'**), 9.27 (s, 2H, **Hd**), 9.22 (s, 2H, **Hd'**), 8.87 (s, 2H, **H5**), 8.50-8.40 (m, 2H, **Hf** and **Hf'**), 8.35 (d, $J_{a\text{-}b}$=8.0 $J_{a\text{-}b}$=4.8 Hz, 2H, **Ha**), 8.31 (d, $J_{a'\text{-}b'}$=4.8 2H, **Ha'**) 8.08 (dd, 2H, **Hb**), 7.93-7.84 (m, 4H, **Hb'** and **H2**), 7.82-7.75 (m, 4H, **He** and **He'**), 7.68 (d, J=5.2 Hz, 2H, **H3**) ppm. Low solubility (0.5 mM in DMSO) prevents ^{13}C-NMR experiment registration. HR-MS (ESI+) m/z: calcd. for $C_{56}H_{32}N_{10}O_4Ru$ $[M\text{-}2PF_6^-]^{2+}$ 505.08188, found: 505.08177. Anal. calcd for $C_{56}H_{30}N_{10}O_4Ru$: C 66.73, N 13.90, H 3.00; found C 62.56, N 12.62, H 3.89.

Synthesis of P3

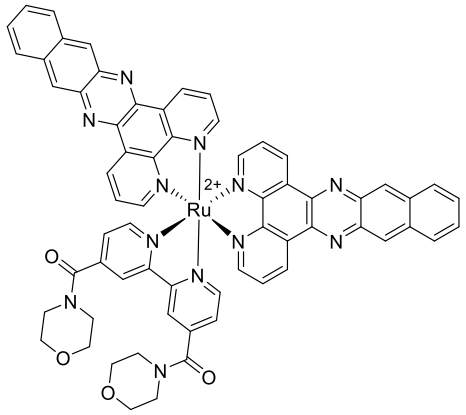

To a solution of **3c** (100 mg, 0.16 mmol) in 8 mL of degassed 2-methoxyethanol compound **7** (106 mg, 0.32 mmol) and trimethylamine N-oxide (116 mg, 1.04 mmol) were added. Reaction mixture was stirred for 4 hours at reflux under N_2 atmosphere. After cooling at r.t., addition of 2 mL of 0.1 M of KPF_6 aqueous solution allows the complete precipitation of complex **P3**. The crude product was filtered and washed with water, methanol, and diethyl ether. Successively, was purified trough flash chromatography on silica gel (eluent: starting from DCM:MeOH 30:1 with 10% Acetone) to obtain complex **P3** as red solid with a yield of 62%. ^{1}H-NMR (400 MHz, $(CD_3)_2CO$): δ 9.83 (d, $J_{c\text{-}b}$ = 8Hz, 2H, **Hc**), 9.74 (d, $J_{c'\text{-}b'}$= 8Hz, 2H, **Hc'**), 9,22 (s, 2H, **Hd**), 9.18 (s, 2H, **Hd'**), 8.98 (s, 2H, **H5**), 8.76 (d, $J_{a\text{-}b}$=4 Hz, 2H, **Ha**), 8.62 (d, $J_{a'\text{-}b'}$= 4 Hz, 2H, **Ha'**), 8.48-8.40 (m, 6H, **H2**, **He/He'**), 8.15 (dd, $J_{b\text{-}c}$ = 4 Hz, $J_{b\text{-}a}$ = 8 Hz, 2H, **Hb**), 7,97 (dd, $J^1_{b'\text{-}c'}$ = 4 29 Hz, $J^2_{b'\text{-}a'}$ = 8 Hz, 2H, **Hb'**), 7.85-7.79 (m, 4H, **Hf/Hf'**), 7.53 (d, $J_{H3\text{-}H2}$= 4Hz, 2H, **H3**), 3.71 (bs, 8H, -CH_2 morpholine), 3.60 (bs, 4H, -CH_2 morpholine), 3.50 (bs, 4H, -CH_2 morpholine) ppm. ^{13}C-NMR (100 MHz, $(CD_3)_2CO$): δ165,4; 157,9; 154,8; 154,4; 153,1; 151,4; 145,4; 140,9; 140,9; 138,6; 135,3; 134,1; 134,1; 131,4; 131,3; 128,7; 128,3; 128,2; 128,1; 128,1; 127,7; 125,4; 122,9 ppm. HR-MS (ESI+) m/z: calcd. for $C_{64}H_{46}N_{12}O_4Ru$ $[M\text{-}2PF_6^-]^{2+}$ 574.13987, found: 574.13897. Anal. calcd for $C_{64}H_{46}N_{12}F_{12}O_4P_2Ru$: C 53.45, N 11.69, H 3.22; found C 53.28, N 11.04, H 3.42.

UV-Vis spectroscopy and fluorescence measurements

UV-Vis absorption spectra were acquired on a Perkin-Elmer Lambda 6 spectrophotometer. Fluorescence spectra and measurements of the phosphorescence signal of $^1O_2$ were carried out on a spectrofluorometer Horiba FluoroMax Plus.

Acid-base properties of P2

The acid-base properties of **P2** were investigated by monitoring the variation of UV-Vis absorption and fluorescence spectra of aqueous solutions of **P2** at 2 x 10^{-6} M at different pH values. The pK_{a2}° in the ground state was determined from UV-Vis absorption titration by fitting the data to the Henderson-Hasselbach equation as explained in details in paragraph 2.2. The pK_{a2}* in the excited state was obtained from the fluorescence titration as described in paragraph 2.2.

Singlet oxygen determination

The singlet oxygen sensitizing properties of $[Ru(RR\text{-}bpy)(dppn)_2]^{n+}$ complexes were first investigated spectrophotometrically using 1,5-dihydroxynaphthalene (DHN) as indirect $^1O_2$ reporter, accordingly to literature.[120] Air-saturated acetonitrile solutions containing DHN 3.3 x 10^{-4} M and RPCs 1 x 10^{-5} M were irradiated (LED emitting at 434 nm, 160 mW) in a quartz cuvette with a 1 cm optical path over a total time of 200 s. Each spectrum was registered by using as blank reference a solution containing the selected RPC at the same concentration of that of the measuring cuvette. The estimation of the relative rate constants for the DHN photooxidation processes (k_{obs}) was performed by applying the steady-state approximation to the $^1O_2$ intermediate, according to procedures previously described.[81]

The quantum yields of $^1O_2$ generation (ϕ_Δ) by $[Ru(RR\text{-}bpy)(dppn)_2]^{n+}$ complexes were determined by measuring the phosphorescence of $O_2(^1\Delta_g) \rightarrow {}^3O_2$ at 1270 nm after irradiating compounds at 440 nm in air-saturated acetonitrile solutions. Experiments

were run on solutions of $[Ru(RR\text{-}bpy)(dppn)_2]^{n+}$ complexes at different concentrations, with the ^{1}MLCT absorbance values within the range 0.08-0.2 and signals were collected by a N_2 cooled InGaAs photodiode. ϕ_Δ values were obtained by comparing them to $[Ru(phen)_3]^{2+}$, which was chosen as reference compound for $^1O_2$ production (ϕ_Δ = 0.38 ± 0.06).[76] Measurements were performed on a spectrophotofluorimeter Horiba FluoroMax Plus.

Evaluation of the interaction with *ct*-DNA

Calf thymus DNA (*ct*-DNA) was purchased from Sigma Aldrich and dissolved in Tris-HCl buffer (10 mM Tris-HCl, 50 mM NaCl, pH 7.4). An absorbance ratio between 260 and 280 nm within 1.8-1.9:1 indicated that the biopolymer was sufficiently free of proteins. A molar absorption coefficient at 260 nm of 6600 M^{-1} cm^{-1} was used to determine the *ct*-DNA concentration per nucleotide.

The binding properties of ruthenium complexes towards *calf thymus* DNA (ct-DNA) were first investigated spectrophotometrically by analysing the variations in the absorption bands of the $[Ru(RR\text{-}bpy)(dppn)_2]^{n+}$ complexes by adding increasing amounts of concentrated solutions of the biopolymer to aqueous solutions (TRIS buffer, pH 7.4) containing the tested RPC at a fixed concentration (10 μM). The contribution arising from the absorbance of the DNA itself was eliminated by adding equal amounts of DNA both to the sample and to the reference solution. After each addition, samples were incubated for 10 minutes at 298.1 ± 0.1 K before collecting the absorption spectra. The intrinsic binding constants (K_b) with *ct*-DNA were determined accordingly to the literature, from the intercept-to-slope ratios of the plot of [*ct*-DNA]/Iε_a-ε_fI *vs*. [*ct*-DNA], where ε_a and ε_f correspond to $A_{obs.}$/[RPC] and to the molar extinction coefficient for the DNA-free metal compound. Linearity within the 0-3 μM range of [*ct*-DNA] was observed.

The DNA-EB fluorescence quenching study for **P2** was performed by adding increasing amounts of a concentrated solution of **P2** solubilized in DMSO (up to 50 µM) to aqueous solutions (TRIS buffer, 10 mM Tris-HCl, 50 mM NaCl, pH 7.4) containing fixed concentrations of ct-DNA (10 µM) and EB (10 µM). Each sample was incubated for 5 minutes at room temperature, afterward the DNA-EB complex was excited at 527 nm and the emission intensity was monitored at 610 nm. The data obtained from the fluorescence titration were processed as described in detail in Paragraph 2.4.

Cytotoxicity and photoactivity of $[Ru(RR\text{-}bpy)(dppn)_2]^{n+}$ complexes

Cell culture

The human epidermoid carcinoma cell line A431 was purchased by ATCC and grown in DMEM (High Glucose) medium, supplemented with 10% fetal bovine serum, Penicillin/Streptomycin (50 units/mL each) and L-glutamine. Cells were cultured in 95% humidified atmosphere with 5% CO_2 at 37 °C.

Cytotoxicity and phototoxicity **P1-2**

A431 cells were seeded onto 96 well plates at a density of 10^4 cells/well. After 24h of incubation, cells were treated with ruthenium complexes (**P1** or **P2**) solubilized in DMSO and diluted in complete medium (0.025-25 µM). After 1 hour, the medium was replaced, and cells were either exposed to light (LED emitting at 462 nm, 18 mW/cm^2) for 30 minutes employing a customized cell illumination device or incubated in the dark for the same time. The cell illumination device (Figure 44) was built using an array of 6 x 12 commercially available 5050 blue LED. The standoff distance between the LED tops and the bottom of the culture plates was 1 cm. The emission spectrum of the device was measured using a USB4000 spectrometer (Ocean Optics). Both groups were moved back to the incubator for a further 24 hours before replacing the medium with 3-(4,5-dimethylthiazolyl)-2,5-diphenyltetrazolium bromide (MTT) (0.25 mg/ml) and incubating for 3 hours. The formazan crystals were dissolved in ethanol, and optical

density (OD) of wells was recorded on a plate reader (Infinite® 200 PRO, Tecan) at 570 nm. The optical density values were used to calculate the percentage of viable cells in each well, setting the OD of untreated cells (without PS and not exposed to light) at 100%. Each condition was tested in 5 replicates.

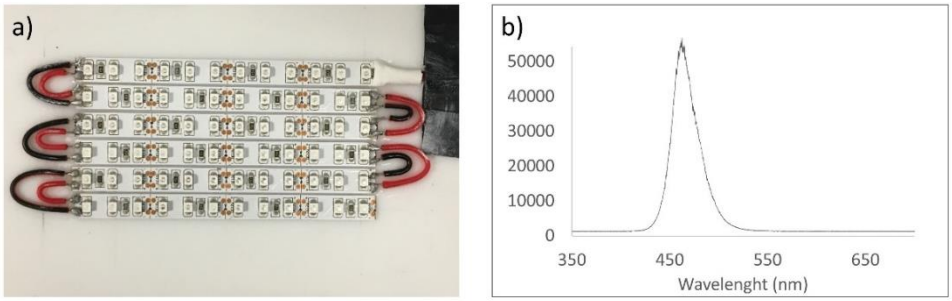

Figure 44: Picture of the customized cell illumination device, fabricated with an array of 12 x 6 5050 blue LED (a). Emission spectrum of the cell illumination device used for PDT experiments (λ_{max} = 462 nm) (b).

Cubosomes preparation and characterization

Glycerol monooleate (MO, 1-monooleoylglycerol, RYLO MG 19 PHARMA, 98.1 wt%), for cubosomes preparation, was kindly provided by Danisco A/S (Denmark). Pluronic F108 (PF108, PEO132-PPO50-PEO132) was purchased from Sigma Aldrich. Fresh distilled water purified using a MilliQ system (Millipore) was used to prepare each sample, and it was filtered with a 0.22 µm pore size hydrophilic filter prior to any use.

Cubosomes were prepared by melting MO at 40 °C and dispersing ruthenium complexes (**P1** or **P2**) in the melted MO with the help of an ultrasonic bath. An appropriate amount of an aqueous solution of the stabilizers (PF108) was then added to the lipid phase, and the mixture was ultrasonicated using a UP100H ultrasonic processor developed by Hiescher (amplitude 90%; 1 s ON, 1 s OFF) for 5, 4, 3, 2, and 1 min cycles. The cubosome formulation investigated (**P1**-**cubo** and **P2**-**cubo**) had a composition of MO/PF108/ **P1** or **P2** = 3.3/0.3/0.02 % (w/w).

Average hydrodynamic diameter (D) and polydispersity index (PDI, as a measure of the size distribution width) of the samples were determined by Dynamic Light Scattering (DLS) using a Zetasizer nano (Malvern Instrument, Worcestershire, United Kingdom). Samples were backscattered by a helium–neon laser (633 nm) at an angle of 173◦ and a constant temperature of 25 °C.

Zeta potential was estimated using the Zetasizer nano by means of the M3-PALS (Phase Analysis Light Scattering) technique.

To evaluate the drug entrapment efficiency, the complexes-loaded cubosomes were separated from the free complex by dialyzing the formulation using a tubing cellulose membrane (14 kDa molecular weight cutoff, Sigma Aldrich) against 2 L of water for 2 h (water was changed after 1 h) at room temperature.

Drug quantitative determination was performed by UV-vis spectroscopy at 325 nm after cubosomes disruption in methanol, using a Synergy 4 multiplate reader (BioTek, Winooski, USA). The encapsulation/entrapment efficiency (EE%) was calculated exploiting the following expression:

$$EE\% = \frac{mass\ of\ drug\ after\ dialysis}{mass\ of\ weighted\ drug}\ x\ 100\%$$

Stability of the cubosomes dispersion

A medium-term stability study of the formulation stored at 25 °C was performed by monitoring mean hydrodynamic diameter, polydispersity index, and zeta potential for 30 days. The samples were visually inspected before every DLS measurement to check for the absence of large aggregates or phase separation.

Small angle X-ray scattering (SAXS)

SAXS measurements were performed at SAXSLab Sapienza with a Xeuss 2.0 Q-Xoom system (Xenocs SAS, Grenoble, France), equipped with a micro-focus Genix 3D X-ray

source with Cu anode (λ = 1.542 Å) and a two-dimensional Pilatus3 R 300K detector which can be placed at variable distance from the sample (Dectris Ltd., Baden, Switzerland). The beam size was defined to be 0.5 mm × 0.5 mm through the two-pinhole collimation system equipped with "*scatterless*" slits. Calibration of the scattering vector q range ($q = 4\pi\sin\theta/\lambda$ with 2θ the scattering angle and λ the photon wavelength), was performed using silver behenate. Measurements with two sample-to-detector distances were performed so that the overall explored q region was 0.004 Å $^{-1} < q < 0.6$ Å $^{-1}$. The sample was loaded into a vacuum-tight quartz capillary cell and measured in the instrument sample chamber at reduced pressure (~0.2 mbar) within a thermalized holder (21°C). The two-dimensional scattering patterns collected with a total acquisition time of 3.5 hours were subtracted for the "*dark*" counts, and then masked, azimuthally averaged, and normalized for transmitted beam intensity, exposure time and subtended solid angle per pixel, using the FOXTROT software developed at SOLEIL. The one-dimensional intensity *vs.* q profiles were then subtracted for the data of water measured in the same cell and divided by the capillary thickness (0.135 cm) calibrated using water scattering to obtain intensity in absolute scale units (cm^{-1}). The two angular ranges were merged using the SAXS utilities tool.

Electron microscopy at cryogenic temperature (cryo-TEM)

Cryo-EM micrographs of RPCs embedded into cubosomes were acquired by a ThermoFisher Glacios at 200-keV instrument, equipped with a Falcon III direction electron detector. Holey-carbon R2/2 grids (Quantifoil Micro Tools GmbH) covered by 2 nm film of carbon were prepared. Grid surfaces were treated with plasma cleaning using O_2 for 45 s before applying 3 µL of sample (1 mg/mL in PBS buffer pH 7.4). Grids were blotted in 100% humidity and 10 °C with filter paper and vitrified by rapidly plunging into liquid ethane at -180 °C using a Vitrobot Mark IV (FEI, Hillsboro).

Cytotoxicity and phototoxicity of Ru(II)-cubosome formulations

A431 cells were seeded onto 96 well plates at a density of 10^4 cells/well. After 24h incubation, cells were treated with **P2**-**cubo** or E-cubo diluted in complete medium (0.025-0.25 µM **P2**, or the corresponding volume for E-Cubo). The experiment and data analysis were carried out as described for the free PS. Each condition was tested in 8 replicates.

Intracellular ROS production

A431 cells were seeded onto µ-Slide 8 well plates (ibiTreat, Ibidi) at a density of $4x10^4$ cells/well. After 24 h incubation with complete medium, the cells were treated with **P2**-**cubo** (100 nM) for 1 hour. After the treatment, cells were washed with PBS and incubated with the intracellular ROS sensor 2,7-dichlorodihydrofluorescein diacetate (DCFH-DA) (2.5 µM in PBS) for 30 minutes. The sensor was removed, and wells were rinsed with PBS before exposure to blue light for 10 minutes or incubation in the dark for the same time. Finally, cells were washed again with PBS, fixed with PFA 4% and stained with Wheat Germ Agglutinin (WGA)-AlexaFluor™ 647-conjugate (ThermoFisher). Cells were observed under a Nikon A1plus confocal laser scanning microscope using a 20x objective. As control, cells without PS were included in the experiment.

2.7 A case of study: Inhibition of Ca^{2+}-ATPase transport activity mediated by complex P3

The following section discusses an intriguing and novel application of the photosensitization of complex **P3**. Inspired by ROS and $^1O_2$ interaction studies on Ca^{2+}-ATPase transport proteins,[121,122] we investigated the effect of photoinduced $^1O_2$ generation by complex **P3** on the transport activity of sarco(endo)plasmic reticulum Ca^{2+}-ATPase (SERCA).

The SERCA enzyme is a well-characterized membrane transport protein belongs to the P-type ATPases superfamily of membrane transporters (Figure 45).[123]

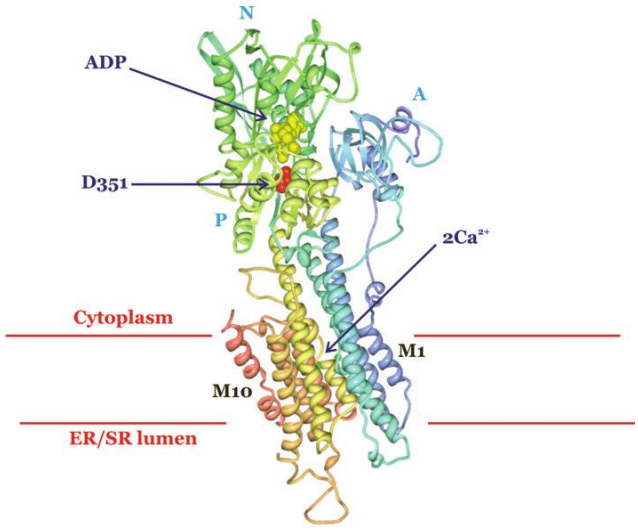

Figure 45: Crystal structure of sarco/endoplasmic reticulum Ca^{2+}-ATPase (SERCA) in the ADP (shown in yellow) and Ca^{2+} (shown in green) bound state. D351 (in red) is the residue phosphorylated during the movement of Ca^{2+} ions into the ER or SR.

It is localized in the sarcoplasmic reticulum (SR) of muscle cells,[124,125] where couples the hydrolysis of one ATP molecule to the transport of two Ca^{2+} ions against their electrochemical gradient from the cytoplasm into the lumen of the sarcoplasmic reticulum (SR) (Figure 46a). Activation of SERCA requires the binding of two Ca^{2+} ions

per enzyme molecule ($E_1 \cdot Ca_2$), followed by ATP phosphorylation and the formation of a phosphoenzyme intermediate (E_1~P·Ca_2). The conformational transition from E_1~P to E_2~P favors the translocation and release of the bound Ca^{2+} against the concentration gradient. Calcium ions are delivered to the intravescicular lumen in antiport with luminal protons, which are translocated to the cytosol during the following enzyme dephosphorylation (Figure 46b).

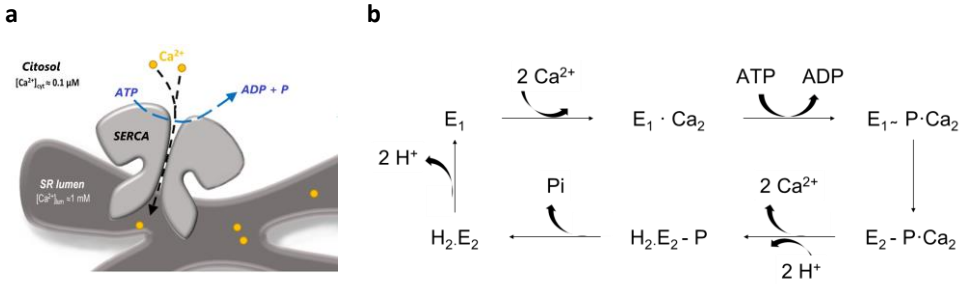

Figure 46: a) Simplified scheme of the transport activity mediated by SERCA: SERCA transports two Ca^{2+} ions against their electrochemical potential gradient from the cytoplasm [Ca^{2+}] = 0.1 µM into the SR lumen [Ca^{2+}] = 1 mM using the free energy provided by ATP hydrolysis; b) Schematic diagram of sequential reactions in the transport cycle of SERCA.

Thus, SERCA maintains a low cytoplasmic Ca^{2+} concentration, contributing to the maintenance of intracellular calcium homeostasis, which is essential for cell signaling and survival. Dysfunctions of SERCA enzyme are associated with several diseases, such as cardiovascular diseases, diabetes and cancer.[124,126,127] It is therefore evident that SERCA represents an important target for the development of novel therapeutic compounds.

In the present study, the effect of **P3** photoactivation on SERCA transport activity was investigated. Compound **P3** was selected between [Ru(RR-bpy)(dppn)]$^{n+}$ class of complexes due to its appropriate water solubility conferred by the two morpholinomethanone units on bipyridine ligand.

To characterize the interaction between SERCA and **P3**, we adapted a biosensing approach, developed in the BioElectroLab at the University of Florence with the

support of Dr. Francesco Tadini-Buoninsegni, based on a solid supported membrane (SSM) that had already been successfully employed to evaluate the effects of pharmacologically relevant compounds on P-type ATPases.[128–130]

The SSM consists of a hybrid alkanethiol/phospholipid bilayer supported by a gold electrode. In particular, the gold electrode is covered by an octadecanethiol monolayer covalently bound via the sulfur atom and a diphytanoylphosphatidylcholine monolayer is laid down on top of it. The SSM is mounted in a Plexiglas flow-through cuvette and acts as the working electrode. The cuvette also contains a reference electrode, e. g. Ag/AgCl electrode, which is separated from the main fluid pathway by a salt bridge. The cuvette and the entire fluid pathway are enclosed in a Faraday cage. A commercially available semi-automated device for SSM-based electrophysiological measurements was employed. This instrument is based on the SURFE^{2}R (Surface Electrogenic Event Reader) technology (Figure 47).

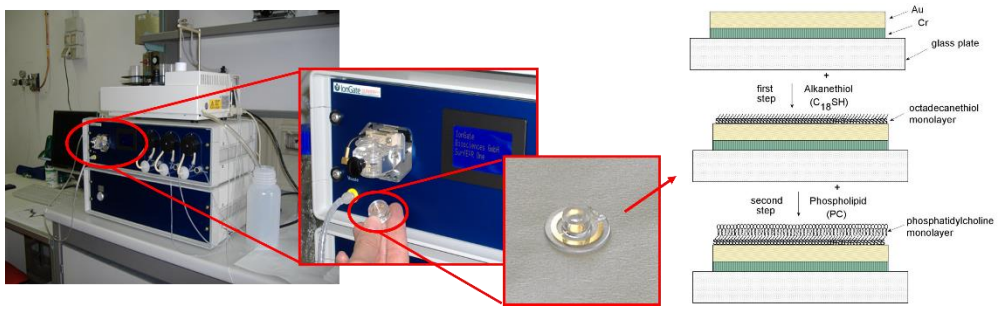

Figure 47: Instrumental set-up: instrument SURFE^{2}R^{One} (IonGate Biosciences) with a zoom on analytical unit which contains the cuvette with the work electrode constitutes by the SSM covered by alkanethiol/phospholipid bilayer.

The SSM work electrode is then covered by rabbit skeletal muscle (SR) vesicles containing SERCA. Once adsorbed on the SSM, SERCA can be activated by ATP concentration jumps via fast solution exchange technique and a SERCA-related current signals are measured.

Using this experimental set up, we can demonstrate that incubating SSM-adsorbed SR vesicles with complex **P3** in dark conditions has no effect on SERCA activity; instead, illumination with visible LED light induces the synthesis of $^1O_2$, which remarkably affects SERCA transport activity with an inhibitory effect dependent on light exposure duration (Figure 48).

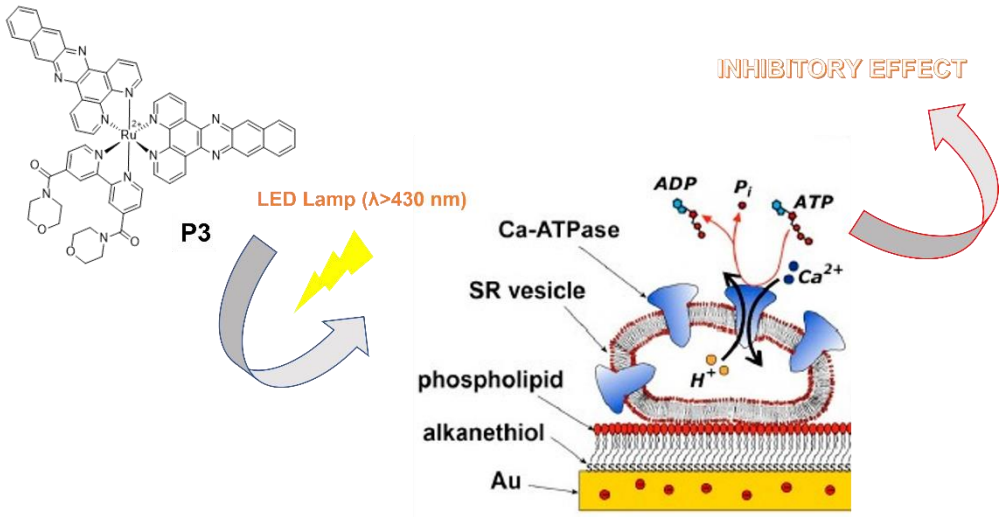

*Figure 48: Schematic diagram of experimental set-up: a **P3** buffered solution is irradiated on SSM with adsorbed SR vesicles containing SERCA.*

2.7.1 Electrical measurements

Electrical current measurements were performed on rabbit skeletal muscle SR vesicles containing a high amount of SERCA 1a isoform. Following the preparation of the biosensor with absorbed SR vesicles, a fast solution exchange was performed on it to activate SERCA transport activity. The electrical response can be monitored in potentiostatic conditions. In this case, a rapid exchange between a non-activating solution (without ATP) to an activating one (which contains ATP) produces a current signal. The latter is attributed to an electrogenic event in the SERCA transport cycle corresponding to ATP-dependent translocation and release of calcium ions into the SR

vesicle interior. To keep the potential difference applied across the whole circuit constant, the accumulation of positive charges (Ca^{2+} ions) in vesicles is counterbalanced by an electrons flow in the external circuit. The transient nature of the observed electrical currents is a consequence of the capacitively coupled system formed by the SSM and the vesicles absorbed (Figure 49). Useful information can be gained from current transients: the numerical integration of each transient is related to a net charge movement that depends upon the electrogenic calcium translocation by SERCA.[131] Eventually, due to the continuous pumping, the flow of Ca^{2+} ions out of the vesicles (favored by a Ca^{2+} ionophore A23187 Calcimycin) becomes equal to their flow into the vesicles, and steady-state conditions are gained. Under these conditions, the potential difference across the vesicular membrane becomes constant, and no further signal is detected.[131]

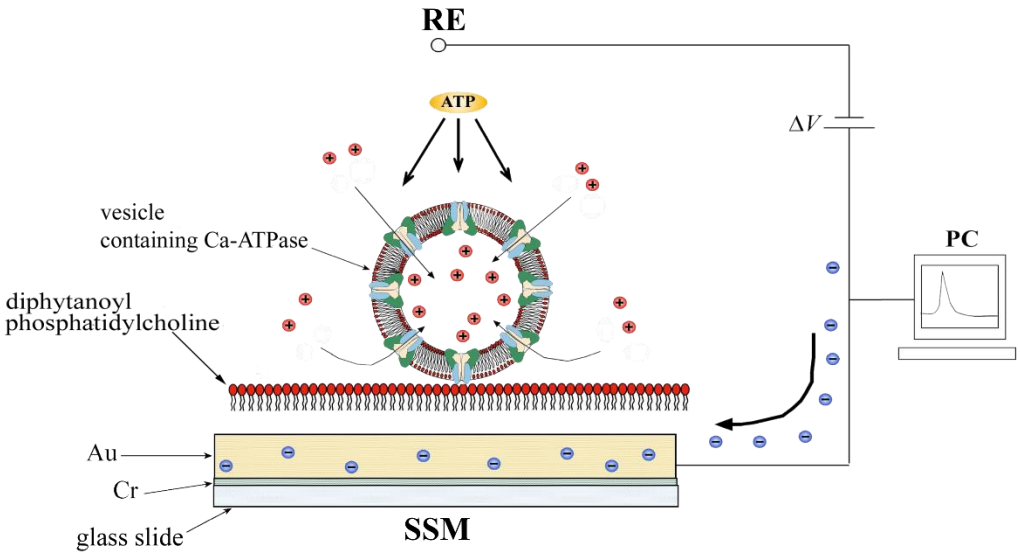

Figure 49: Schematic representation of employed electrical circuit: when SR vesicle adsorbed on a SSM are subjected to an ATP concentration jump, is induced a net charge displacement due to the translocation of Ca^{2+} ions inside the vesicles (red spheres). A compensating current flow along the external circuit (blue spheres represent electrons) is induced to keep constant the applied potential difference (1V) across the whole system. RE is the reference electrode.

On this basis, preliminary experiments were carried out to evaluate the effect of **P3** without illumination on Ca^{2+} translocation by SERCA. Incubation of SR vesicles with a buffered solution containing 10 µM of complex **P3** in dark conditions does not affect the ATP-dependent current signal associated with Ca^{2+} translocation mediated by SERCA (Figure 50). Similarly, no changes in the current signal are observed upon illumination (λ > 430 nm, 5 min) of SR vesicles in the absence of the photosensitizer **P3** (Figure 50 inset).

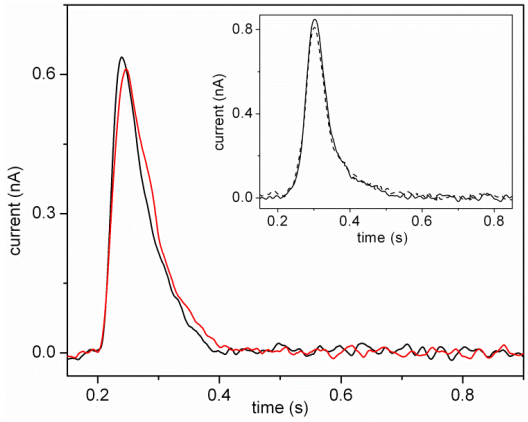

Figure 50: Current signals induced by ATP concentration jumps on SR vesicles adsorbed on the SSM in the absence (black line) and after 10 min of incubation with Ru-PS (red line) in dark condition. Insert: current signals induced by ATP jumps before (solid line) and after illumination (dashed line) with blue light for 5 min in the absence of Ru-PS. [ATP] = 100 µM, Ru-PS [10 µM]

Instead, to analyze the impact of **P3** photoactivation on SERCA transport activity, the SR vesicles were incubated with a buffered solution of 10 µM of **P3** and exposed to visible blue light for 5 min. Afterwards, a 100 µM ATP jump was carried out, and the SERCA-generated current signal was compared to that obtained in the absence of **P3** (initial control measurement) (Figure 51). As a result, a remarkable decrease in current amplitude (red line in Figure 51) and translocated charge (red column in Figure 51) was observed. Thus, photoactivation of **P3** when incubated with SR vesicles results in a significant inhibition of ATP-dependent Ca^{2+} translocation by SERCA.

To further understand if the inhibitory effect is dependent on the irradiation time, SR vesicles incubated with 10 µM of **P3** were irradiated for increasing times, at intervals of 5 minute. The ATP-induced current signal is almost completely suppressed after a total irradiation time of 15 min (Figure 51). These results suggest that $^1O_2$ generated form the photosensitization of **P3** provokes a strong inhibitory effect on SERCA transport activity. These findings are consistent with previous reported studies on the inhibition of Ca^{2+} uptake and Ca^{2+}-ATPase activity in cardiac and skeletal SR mediated by that singlet oxygen $^1O_2$ produce by Rose Bengal irradiation.[121,122]

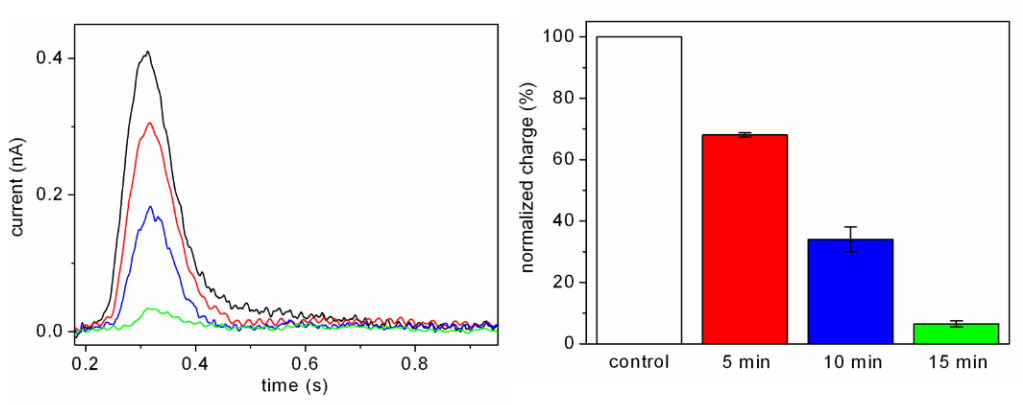

Figure 51: Current signals (left panel) and average translocated charges (right panel) induced by ATP concentration jumps (100 µM) on SR vesicles in the absence (initial control, black line and white column) and in the presence of Ru-PS (10 µM) after incubation and photoactivation for 5 min (red line and column), 10 min (blue line and column) and 15 min (green line and column). The translocated charges were normalized with reference to the charge obtained in the absence of Ru-PS. The error bars represent standard deviation of two independent measurements.

Afterwards, in subsequent experiments, the dependence of the inhibitory effect on **P3** concentration was also considered. Thus, under the same experimental conditions, an analogous experiment to the ones above was carried out using a concentration of **P3** of 1 µM. Remarkably, the same progressive decrease in current amplitude and translocated charge upon increased time of irradiation is observed (Figure 52).

Although, as expected, such a decrease in current amplitude is less pronounced than that obtained for 10 µM concentration of **P3**.

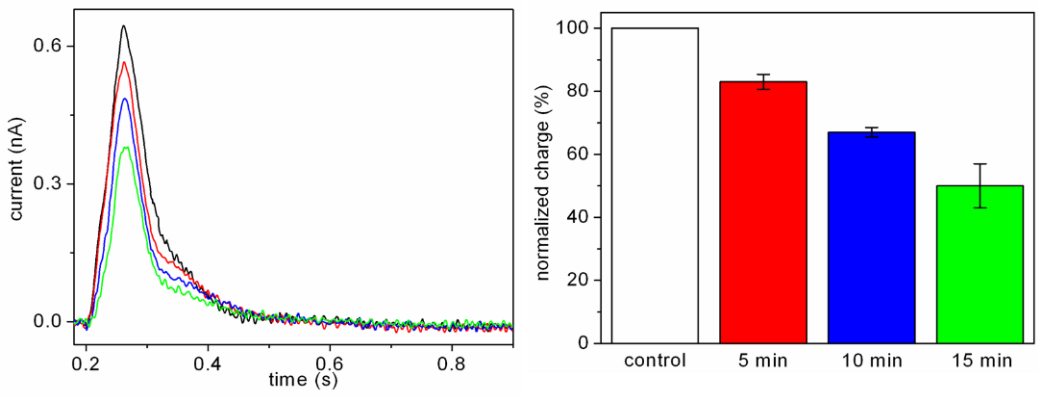

Figure 52: Current signals (left panel) and average translocated charges (right panel) induced by ATP concentration jumps (100 µM) on SR vesicles in the absence (initial control, black line and white column) and in the presence of Ru-PS (1 µM) after incubation and photoactivation for 5 min (red line and column), 10 min (blue line and column) and 15 min (green line and column). The translocated charges were normalized with reference to the charge obtained in the absence of Ru-PS. The error bars represent standard deviation of two independent measurements.

Acknowledgments

A dutiful thanks to Dr Francesco Tadini Buoninsegni who perfected the entire experimental set up used in this work. A special thanks also to Alessia Diddi (Master thesis student) for her valuable contribution to this work.

EXPERIMENTAL SECTION

Material and methods

Calcium and magnesium chlorides and MOPS were obtained from Merck at analytical grade. ATP (97 %) and 1,4-dithiothreitol (DTT) (99%) were purchased by Fluka. EGTA, calcimycin (calcium ionophore A23187) and octadecanethiol were purchased from Sigma Aldrich. The lipid solution containing diphytanoylphosphatidylcholine (Avanti Polar Lipids) was prepared at a concentration of 1.5% (w/v) in *n*-decane.

Buffer solution composition:

MOPS (3-(N-morpholino)propanesulfonic acid) 25 mM

KCl 100 mM (supporting electrolyte for the maintenance of ionic strength)

$CaCl_2$ 0.25 mM

$MgCl_2$ 1 mM

EGTA **(**ethylene glycol-bis (β-aminoethyl ether)-*N*,*N*,*N*′,*N*′-tetraacetic acid) 0.25 mM

DTT (1,4-dithiothreitol) 0.2 mM prevents the oxidation of disulfuric bridge

pH is adjusted to 7.

Preparation of SR vesicles containing Ca^{2+}-ATPase

SR vesicles were obtained by isolation from the fast twitch hind leg muscle of New Zealand white rabbit utilizing an extraction protocol developed by Eletr and Inesi.[132]

Protein concentration was determined by the Lowry method using bovine serum albumin as a standard.[133] The total protein content of SR vesicles was calculated to be 8.4 mg/mL. SERCA (isoform 1a) accounts for approximately 50% of the microsomal protein.

Preparation of Solid Supported Membrane (SSM)

The experimental steps employed in the preparation of the hybrid octadecanethiol/diphytanoylphosphatidylcholine bilayer supported by gold electrode can be summarized as follow:

i) A solution of octadecanethiol 1 mM in 2-propanol (50 µL) is incubated on the nude gold electrode for 45 minutes. The electrode is washed with ultrapure water and dried in nitrogen flux.

ii) A solution of 1,2-Diphytanoil-sn-Glycero-3-[phosphor-L-choline] (3.5 µL) is added to evenly cover the entire surface of the gold electrode. Immediately after, 50 µL of buffer solution is added.

iii) Incubation at room temperature overnight allows the self-assembled formation of the octadecanethiol/phospholipidic bilayer.

iv) After forming the SSM the capacitance and resistance of the SSM attained constant values of the order of 0.2-0.4 μFcm^{-2} and 10-20 $M\Omega cm^2$.

Vesicles containing SERCA are then absorbed on SSM surface:

v) 20 µL of buffer diluted protein suspension (0.5 mg/mL) containing 1µM calcimycin (calcium ionophore A23187) is prepared and sonicated for 1 min to eliminate any vesicles aggregates. Afterward, the solution is added to evenly cover the entire surface of the gold electrode and incubated at room temperature for 1 hour.

The SSM capacitance and resistance remained practically constant after vesicle adsorption.

ATP concentration jump experiments

SERCA is activated by an ATP concentration jump which is realized by rapidly switching from a *non-activating solution* (buffer) to an *activating solution* at the SSM surface.

-*non-activating solution* contains 100 mM KCl, 25 mM MOPS (pH 7.0), 0.25 mM EGTA, 1 mM $MgCl_2$, 0.25 mM $CaCl_2$ (10 µM free Ca^{2+}, as calculated by the WinMAXC program), and 0.2 mM DTT.

-*activating solution* is identical except for addition of 100 µM ATP. To prevent Ca^{2+} accumulation into the vesicles 1 µM calcium ionophore A23187 (calcimycin) is added.

Jump ATP method can be described as follow:

i) *Non-activating solution* flows on SSM surface for 1 second.

ii) A fast exchange with *activating solution* follows and it flows on SSM surface for 2 seconds.

iii) *Non-activating solution* flows again for 2 seconds.

If the ATP jump induced charge displacement across the membrane by the ATPase, a current transient was measured due to capacitive coupling between the SSM and the vesicles. The numerically integrated current transient is related to a net charge movement within the protein, which depends upon the electrogenic calcium translocation by SERCA. In particular, the current signal of the transport protein was detected under potentiostatic conditions. In this case, movement of a net charge across the activated protein was compensated by a flow of electrons along the external circuit toward the gold electrode to keep the applied voltage constant across the whole metal/solution interphase. Normally, experiments were carried out under short-circuit conditions, i.e. at zero applied voltage relative to the reference electrode.

The ATP concentration jump experiments were carried out by employing the $SURFE^2R^{One}$ instrument (Nanion Technologies, Munich, Germany). The temperature was maintained at 20-22 °C for all the experiments.

Each single measurement was repeated 5 times and then averaged to improve the signal to noise ratio. Standard deviations did not exceed 5%. Moreover, each set of measurements were usually reproduced using two different SSM sensors.

Chapter 3

RPCs featuring Perylenemonoimide (PMI) derivative

According to the assumptions stated in the introduction, a ruthenium(II)-based PS for PDT applications may be considered much more successful if it is effectively able to produce $^1O_2$ via *type-II* catalytic photoreaction using long wavelength light. Aside from using π-extensive aromatic polypyridyl ligands, as described in Chapter 2, another strategy to consider is conjugating a pendant organic chromophore on commonly used bipyridyl or phenanthroline ligands. This strategy was firstly reported by Ford and Rodgers in 1992.[134] The resulting bichromophores, consisting of a Ru(II) diamine complex covalently linked to an organic chromophore, place the Ru(II)-based ^{3}MLCT excited state in equilibrium with the lowest-lying long-lived triplet state (^{3}IL) contributed by the organic unit. The consequence of this bichromophoric arrangement and the existence of quasi-isoenergetic ^{3}MLCT and ^{3}IL states is the creation of an excited-state energy reservoir that prolongs the ^{3}MLCT emission.[31] Furthermore, bichromophoric systems could take advantage in the increased light absorption, even in the NIR region of the spectrum (see paragraph 2 of the introduction).[4]

On this basis, RPCs featuring bpy or phen-based ligands covalently linked to organic chromophores are widely studied.[4] Among them, complexes containing bpy-pyrene-conjugated ligands are particularly effective at stabilizing the ^{3}MLCT excited state [135] [31] and providing a high yield of $^1O_2$ sensitization. Consequently, chromophores with similar structure but significantly more extensive π-conjugation and diverse electronic features were considered. Between them, a great deal of interest has been reserved for perylene and perylene-imides. The latter belong to a class of polyaromatic hydrocarbons that gained popularity for almost a century because of their multifaceted

properties suitable for a variety of uses. Perylene dyes can be classified into two major classes: perylene diimide (PDI), featuring two electron-withdrawing symmetrical imide moieties on the top and bottom of the electron-rich perylene core, and asymmetric perylene monoimide (PMI) possessing only one imide group (Figure 53). Both type of compounds have extreme thermal and photochemical stability, chemical robustness, high molar-absorptivity, remarkable photoluminescence, and impressive electron-accepting properties.[136]

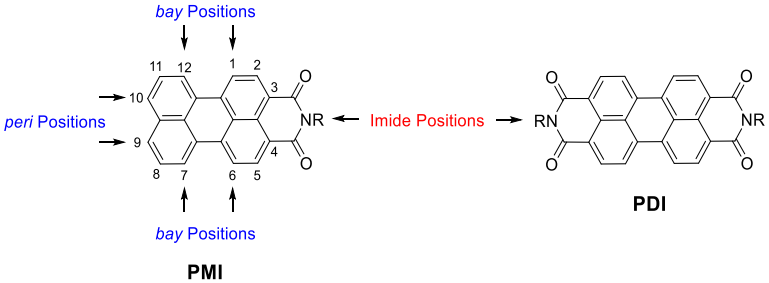

Figure 53: Numbering and general structure of perylene monoamide (PMI) and perylene diimide (PDI) dyes.

These interesting features could be successfully exploited in the preparation of perylene-metal complexes. In particular, RPCs containing perylene imides generally show high absorption coefficient in the visible/NIR region and enhanced $^1O_2$ production.[137–140]

It is noteworthy that most RPCs containing perylene imide derivatives have pendant PDI chromophores conjugated in the *bay* or *imide* positions, and they are mostly studied in photoinduced energy and electron transfer processes [137,139,141,142] with a few examples in PDT.[139,143] On the other hand, there are far fewer systems containing PMI chromophores described in the literature.[144]

In light of this, in collaboration with Prof. Tomàs Torroba of the University of Burgos and leveraging his expertise in the synthesis and application of perylenemonoimide (PMI) compounds as sensors, we developed a new class of RPCs featuring PMI pendant derivatives (Figure 54).

In complexes **Ru-5PMI** and **Ru-3PMI**, the PMI derivative has the imide nitrogen functionalized with a bulky aliphatic group (1-adamantyl-ethylamine) to increase its own solubility.[144] Furthermore, unlike the most previously reported perylene-RPCs in which PDI chromophores are bonded through the imido nitrogen, effectively decoupling the PDI unit from the ruthenium core, [139,140,142] in complexes **Ru-5PMI** and **Ru-3PMI**, the PMI is directly conjugated to the phenanthroline ligand via a C-C bond at positions 5 or 3, respectively. This bichromophoric arrangement allows a high electronic coupling between the metal core and the PMI. The choice to functionalize positions 5 or 3 of the 1,10-phenanthroline serves to investigate possible differences in the chemical-physical properties of the two complexes. Due to the asymmetric functionalization of only one phenanthroline ligand, both complexes were obtained as racemic mixture, Δ and Λ enantiomers, of two not separable constitutional isomers. The synthetic process was improved by applying Suzuki-Miyaura coupling directly on the ruthenium complex, which effectively increased the yields of the final products.

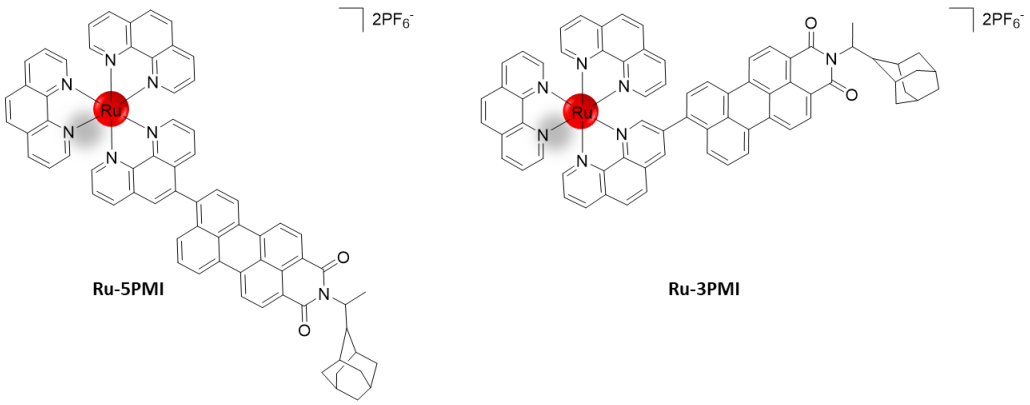

Figure 54: Chemical structures of RPCs containing PMI chromophore studied in this thesis.

3.1 Synthesis of Ru-Perylenemonoimide complexes

The optimization of the synthetic process for the preparation of complexes **Ru-5PMI** and **Ru-3PMI** was part of this thesis work and I carried out personally in Prof. Tomás Torroba's research laboratories at the University of Burgos.

The synthesis of the PMI derivative **15** was previously optimized by Torroba et al.[144,145] In brief, commercially available perylene tetracarboxylic dianhydride **12** is subjected to a one-pot process of imidization-decarboxylation using 1-(1-adamantyl)ethylamine hydrochloride as amine to insert a bulky-aliphatic group and avoid π-stacking phenomena that complicate purification procedures.[144] Mono-bromination in *peri* position of compound **13** is then carried out using bromine and iron powder as catalyst, yielding compound **14** which is then converted in the PMI-pinacol boronic ester **15** through Miyaura borylation reaction with the bis(pinacolato)diboron (Scheme 7)**.**

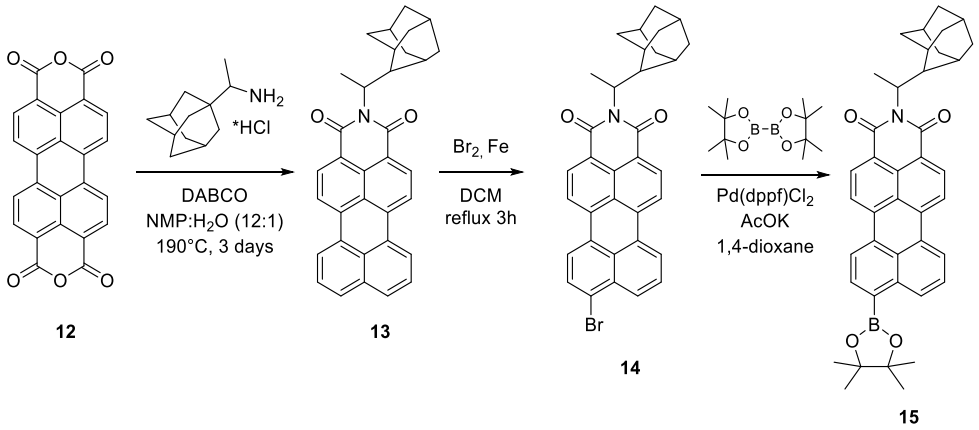

*Scheme 7: Synthetic route follewe for the preparation of PMI-pinacol boronic ester derivative **15**.*

Following the synthesis of the PMI-pinacol boronic ester **15**, the first synthetic strategy designed to prepare the complexes **Ru-5PMI** and **Ru-3PMI** involved the synthesis of the phenanthroline ligands, N-(2-adamantyl-ethylamine)-9-(5-phenanthroline)-3,4-perylenemonoimide (**5PMI**) and N-(2-adamantyl-ethylamine)-9-(3-phenanthroline)-

3,4-perylenemonoimide (**3PMI**), via Suzuki-Miyaura coupling reaction between compound **15** and commercially available 5-bromo-1,10-phenanthroline or 3-bromo-1,10-phenanthroline respectively, followed by reactions with $Ru(Phen)_2Cl_2$ (**1**)(Scheme 8).

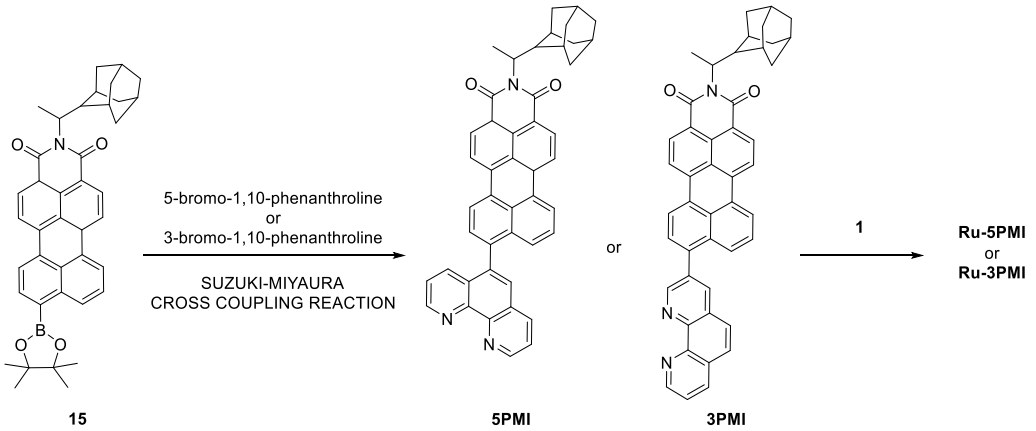

*Scheme 8: First synthetic strategy designed to prepare the complexes **Ru-5PMI** and **Ru-3PMI.***

Unfortunately, the synthetic route in scheme 8 prevents the obtainment of complexes **Ru-5PMI** and **Ru-3PMI** due to the synthetic issues encountered in the Suzuki-Miyaura coupling reaction for the preparation of ligands **5PMI** and **3PMI**. The Suzuki-Miyaura coupling was conducted using $Pd(PPh_3)_4$ as catalyst and K_2CO_3 as a base in a deaerated dimethylformamide/water mixture. The catalytic cycle starts with the o*xidative addition* of the bromo-phenanthroline to Pd(0), resulting in a Pd(II) species that reacts in *trasmetalation* with the PMI-pinacol boronic ester **15**. The *reductive elimination* leads to products **5PMI** or **3PMI**, and regenerates the Pd(0) catalyst (Schema 9). Adopting this strategy, the compounds **5PMI** and **3PMI** were obtained in very low yields (5% and 10%, respectively). We can speculate that these results partly depend on the electron-poor character of both the bromo-phenanthrolines and the PMI-pinacol boronic ester **15** that hinder both the *oxidative addition* step and the *transmetalation* step, permitting the coordination of palladium at the free-phenanthroline and causing

the interruption of the catalytic cycle.[146] Additionally, difficult purification processes due to limited solubility and the formation of π-stacking aggregates reduce yields further.

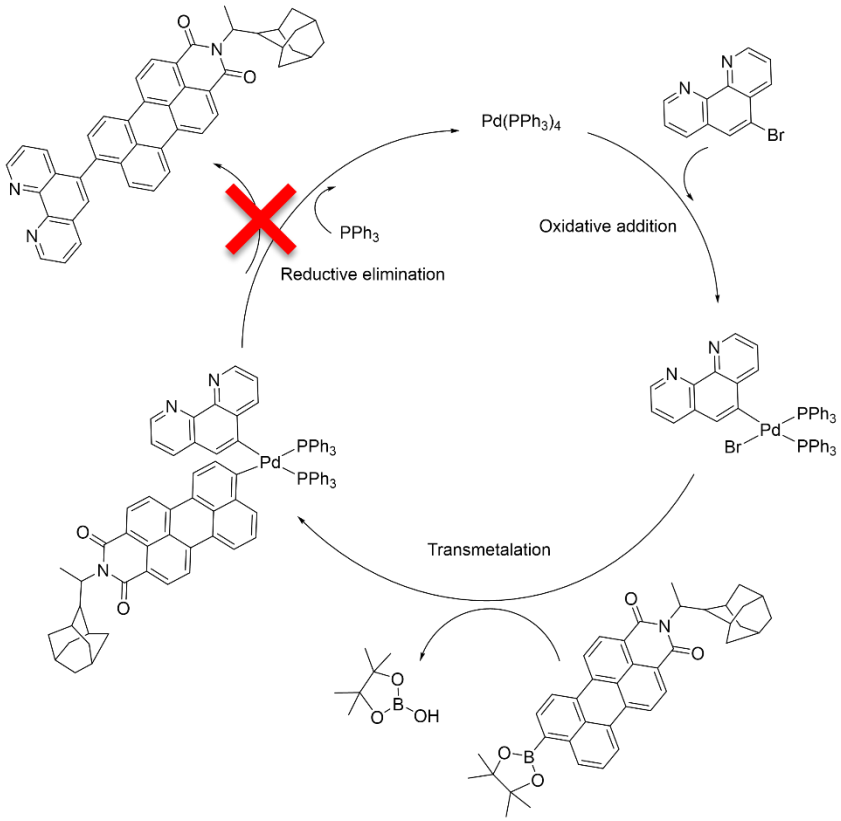

Scheme 9

The synthetic strategy was therefore reconsidered using the so called "chemistry-on-the-complex".[147] In the synthetic approach reported in Scheme 10 the PMI-pinacol boronic ester **15** is inserted in the last step via a Suzuki-Miyaura coupling reaction directly conducted on a stable mono-brominated ruthenium complex (**18** or **19**).

Briefly, complexes **Ru-5PMI** and **Ru-3PMI** were prepared by reacting the polymeric precursor $[Ru(CO)_2Cl_2]_n$ **2** with 5-bromo-1,10-phenanthroline or 3-bromo-1,10-phenanthroline at a molar ratio of 1 : 1.1 in refluxed methanol for 2h to obtain *trans*-

Cl[Ru(Br-Phen)Cl_2($CO)_2$] complexes with formula **16** and **17**. The latter are obtained pure by simple hot filtration of the reaction mixture with a yield of 46% and 53% respectively. Afterward, reaction with two equimolar amounts of 1,10-phenanthroline (**5**) and TMAO in 2-methoxyethanol affords complexes **18** and **19**, which are isolated with high purity from the reaction mixture after precipitation with an aqueous solution of KPF_6 yielding 82% and 75%, respectively. Of noting that, depending on the coordination of the asymmetric bromo-phenanthroline, a mixture of not-separable isomers is formed in this step. This feature complicates the assignment of ^{1}H NMR signals that are split into two sets of signals, one for each of the two isomers. The last reaction step, as mentioned before, is the Suzuki-Miyaura coupling between PMI-pinacol boronic ester **15** and the bromo-phenanthroline already coordinated on the ruthenium metal centre. The reaction is carried out using an equimolar amount of complexes **18** or **19** and compound **15** dissolved in a mixture of deaerated dimethylformamide/water 2:1. After adding $Pd(PPh_3)_4$ (1 % w/w) as catalyst and K_2CO_3 as a base, the reaction mixture is heated to 100°C and stirred for 3h. Appling Suzuki-Miyaura coupling directly on the pre-formed ruthenium complexes **18** and **19** reveals itself to be an efficient and straightforward method to avoid the issues found in the first synthetic approach (Scheme 2) obtaining the complexes **Ru-5PMI** and **Ru-3PMI** in high yields (64 % and 88%, respectively) and easily purified through flash chromatography.

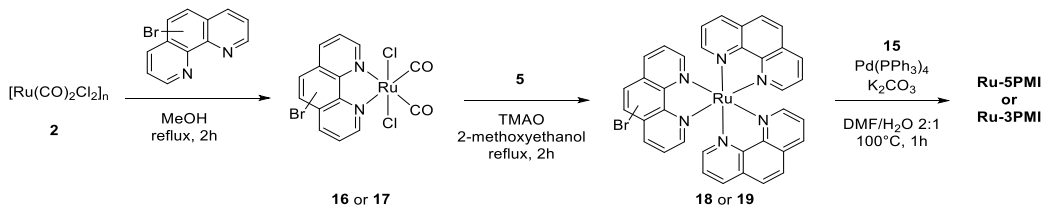

*Scheme 10: Synthetic route followed for the preparation of complexes **Ru-5PMI** and **Ru-3PMI**.*

3.2 Characterization of Ru-Perylenemonoimide complexes

For comparison, the chemical-physical properties of complexes **Ru-5PMI** and **Ru-3PMI** were investigated using the PMI chromophore **(13)** and $[Ru(phen)_3]Cl_2$ as reference. The electronic absorption spectra of each of the four compounds in acetonitrile and water are reported in Figure 55, whereas their molar extinction coefficients (ε) at different absorption maxima λ_{max} are listed in Table 11. As it is possible to note, the absorption profiles of the two complexes exhibit both in acetonitrile and water two intense intraligand π→π* electronic transitions between 250-280 nm, which is also observed in the absorption profile of $[Ru(phen)_3]Cl_2$. On the other side, the broad bands between 400-600 nm in both the solvents is not the sum of those of the individual components ($[Ru(phen)_3]Cl_2$ and PMI **13**), indicating that the moieties interact at the ground state.

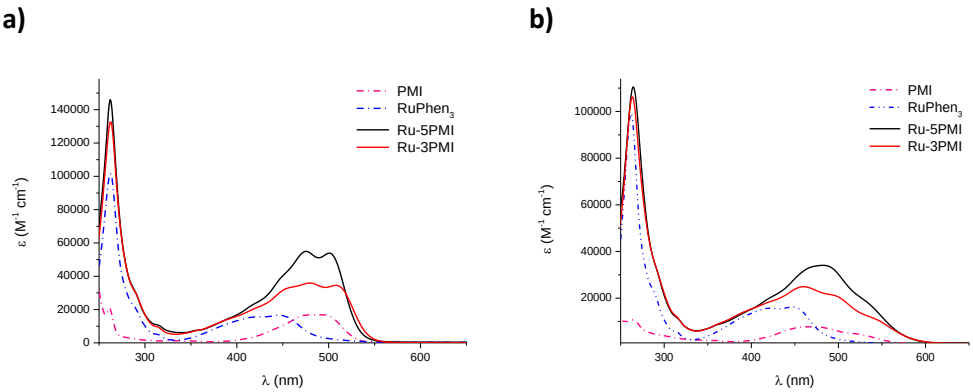

Figure 55: Absorption spectra of 5 μM solutions of compounds PMI (pink dash line), $[Ru(Phen)_3]^{2+}$ (blue dash line), ***Ru-5PMI*** *(black solid line) and* ***Ru-3PMI*** *(red solid line) in acetonitrile a) and water b).*

Compound	*CH_3CN* λ_{abs}/nm ($\varepsilon \times 10^3\ M^{-1}\ cm^{-1}$)	*H_2O* λ_{abs}/nm ($\varepsilon \times 10^3\ M^{-1}\ cm^{-1}$)
Ru-5PMI	500 (53.8) 475 (54.9) 262 (146.1)	480 (34.0) 265 (110.4)
Ru-3PMI	510 (34.9) 480 (35.9) 262 (132.1)	500 (20.5) 460 (25.0) 265 (106.2)
PMI	485 (16.8)	470 (7.70)
RuPhen3	440 (16.2) 262 (101.7)	440 (15.8) 265 (98.3)

Table 11: Electronic absorption maxima measured in acetonitrile and water.

The emission spectra of the four compounds in acetonitrile recorded at different excitation wavelengths are reported in Figure 56. Figure 56a and Figure56b show the emission spectra of 5 μM solutions of PMI and $[Ru(phen)_3]Cl_2$ in acetonitrile, respectively. The PMI has a broad emission band centred at 540 nm with a shoulder at 580nm, whereas $[Ru(phen)_3]Cl_2$ exhibit an emission band with maximum at 590 nm. When the emission spectra of **Ru-5PMI** (Figure 56c) and **Ru-3PMI** (Figure 56d) are considered, it can be observed that the emission spectrum of **Ru-5PMI** remains almost unchanged even if the excitation wavelength is shifted between 500 nm (excitation wavelength centring on the PMI component) and 400 nm (excitation wavelength centring on the ruthenium metal centre). The emission profile is almost identical to that observed for the free-PMI chromophore, with a maximum at 540 nm and a shoulder at 580 nm. In contrast, the emission spectrum of complex **Ru-3PMI** upon excitation at 500 nm (excitation wavelength centring on the PMI component) shows a broad emission with a maximum around 500 nm and a broad shoulder at 580 nm, whereas upon excitation at 400 nm (excitation wavelength centring on the ruthenium metal centre) exhibits an emission spectrum identical to that of $[Ru(phen)_3Cl_2]$ with a maximum at 590 nm. Taken together, the absorption and emission spectra seem to indicate that the position of PMI functionalization determines a different behaviour of the two complexes: **Ru-5PMI** behaves similar to a supermolecule, with the PMI almost completely coupled to the metal centre, whereas **Ru-3PMI** behaves as a dyad, with the metal centre decoupled from the PMI.

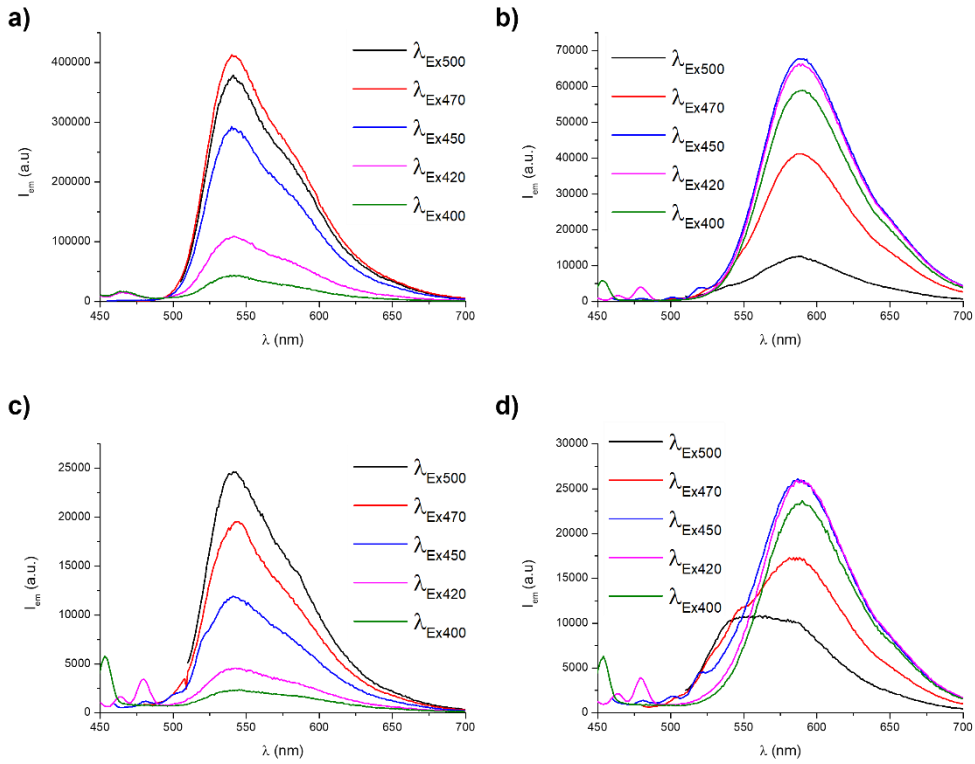

Figure 56: Luminescence spectra of 5 µM solutions a) PMI, b) $[RuPhen_3]^{2+}$, c) Ru-5PMI and d) Ru-3PMI in acetonitrile recorded by excitation at different λ_{Ex} (500, 470, 450, 420 and 400 nm)

Secondly, the DHN assay was preliminarily used (see chapter 2 paragraph 2.2 for deteils) to compare the efficiencies of **Ru-5PMI** and **Ru-3PMI** to generate $^1O_2$ with those of the two components, PMI chromophore **(13)** and $[Ru(phen)_3]Cl_2$, as reference. In Figure 57, the UV-Vis titration obtained for complex **Ru-5PMI** is reported, along with the semilogarithmic plots of (A/A_0) as a function of the irradiation time for each of the four compounds. The rate constants (kobs) of the photo-oxidation process paid by DHN are listed in Table 12. Experiments were carried out by irradiating (LED Lamp: λ_{max} 434 nm, 160 mW) 10 µM air pre-saturated acetonitrile solution containing **Ru-5PMI**, **Ru-3PMI**, $[Ru(phen)_3]^{2+}$ or PMI **(13)** in the presence of 3.3×10^{-4} M of DHN. As can be observed from the insert in Figure 57, **Ru-5PMI** and **Ru-3PMI** exhibit remarkably higher

photosensitizing features with a similar amount of $^1O_2$ produced within 70 and 110 s by **Ru-5PMI** and **Ru-3PMI** respectively, and in more than 300 s by $[Ru(phen)_3]^{2+}$. To note, also, that PMI **(13)** alone can produce $^1O_2$ upon photoexcitation with blue light in an amount that is about half that found for $[Ru(phen)_3]Cl_2$.

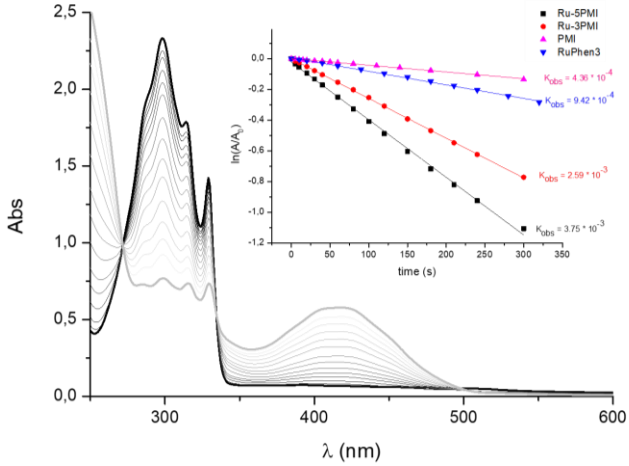

*Figure 57: Absorption spectra of a solution containing DHN (3.3 × 10^{-4} M) and complex **Ru-5PMI** (10 μM) in acetonitrile at different irradiation times (up to 300 seconds) along with the linear regressions of the semilogarithmic plots of ln(A_t/A_o) as a function of the irradiation time (insert) for **Ru-5PMI** (black square), **Ru-3PMI** (red points), PMI (pink triangles) and [Ru(phen)$_3$]2+ (blue triangles).*

Parallelly, the $^1O_2$ quantum yields for complexes **Ru-5PMI** and **Ru-3PMI** in acetonitrile were further assessed by measuring the phosphorescence signal of $^1O_2$ at 1270 nm induced by irradiation of air-saturated solutions of the PSs at 470nm using $[Ru(phen)_3]Cl_2$ as standard reference (see chapter 2 paragraph 2.2 for deteils). The $^1O_2$ quantum yields for **Ru-5PMI** and **Ru-3PMI,** along with the rate constants for the DHN oxidation process are listed in Table 12. Both Ru-Perylenemonoimide complexes are more efficient singlet oxygen sensitizers than $[Ru(phen)_3]Cl_2$, as demostrated by results (Table 12), demonstrating that the extension of π-conjugation improves singlet oxygen sensitization capacity. On the other hand, no appreciable differences are found between **Ru-5PMI** and **Ru-3PMI,** proving that the position of the PMI functionalization does not influence the $^1O_2$ sensitization capacity.

Complex	K_{obs} (s^{-1})	φ_{Δ} ($^1O_2$)
$[Ru(phen)_3]Cl_2$	9.41 (± 0.03) × 10^{-4}	0.38 ± 0.06[76]
PMI (13)	4.36 (± 0.05) × 10^{-4}	-
Ru-5PMI	3.75 (± 0.04) × 10^{-3}	0.69 ± 0.06
Ru-3PMI	2.59 (± 0.01) × 10^{-3}	0.66 ± 0.06

Table 12: Values of rate constants (K_{obs}) for the photo-oxidation process of DHN in air saturated acetonitrile solutions ([PS]=10 μM, [DHN]=3×10^{-4} M) and single oxygen quantum yield determined by direct measurement of $^1O_2$ phosphorescence signal at 1270 nm.

3.2 DNA-binding studies

The ability of complexes **Ru-5PMI** and **Ru-3PMI** to interact with DNA, a key target for anticancer drugs as well as for antibacterial compounds, was assessed using electronic absorption spectroscopy and fluorescence spectroscopy. Both techniques provide important information on the metal-complex's affinity for DNA and help to understand the mode of interaction (see paragraph 3 of the Introduction).

Firstly, the DNA-binding capacity of complexes **Ru-5PMI** and **Ru-3PMI** was evaluated on *calf thymus* DNA (*ct*-DNA) by monitoring the changes at the ^{1}MLCT band in their UV-Vis spectra upon addition of increasing amounts of the biopolymer to solutions of ruthenium compounds at fixed concentrations at pH 7.2. As shown in the UV-Vis titrations in Figure 58a and Figure 59a, the progressive addition of *ct*-DNA determines a hypochromic effect on the whole absorption profile of both complexes. In particular, the extent of hypochromism is found to be greater for **Ru-3PMI**, which undergoes a reduction of about 34% of the absorbance in the ^{1}MLCT band in the presence of 0.3 equimolar amounts of the biopolymer. On the other side, the absorbance of **Ru-5PMI** is diminished of about 15% in the ^{1}MLCT absorption band when a 0.3 equimolar amount of *ct*-DNA is added. However, when evaluating the strength by determining the intrinsic

binding constants as the ratio of the slope and intercept for the linear regression of [DNA]/| $\varepsilon_a - \varepsilon_f$ \ *vs.* [DNA] using the Benesi-Hidebrand equation (see paragraph 3 of the Introduction), a linear trend is found for complex **Ru-3PMI** (Figure 59b) from which it is possible to define that the value of K_b is 3.75 x 10^6. Conversely, the trend is not linear for **Ru-5PMI** (Figure 58b), for which two different slopes appear. Discomposing the titration in two parts, until adding a 0.1 equimolar amount of *ct*-DNA the slope is steeper, and the K_{b1} for the first six points is determined to be 6.41 x 10^6. In the second part of the titration, between 0.2 and 0.3 equimolar amounts of ct-DNA added the slope of the linear fit is diminished and the K_{b2} is determined to be 4.14 x 10^5. Besides the lack of linearity of **Ru-5PMI**, is evident that both the complexes strongly interact with *ct*-DNA, presumably via a predominant intercalation mode since the main effect on their absorption spectra is hypochromism.

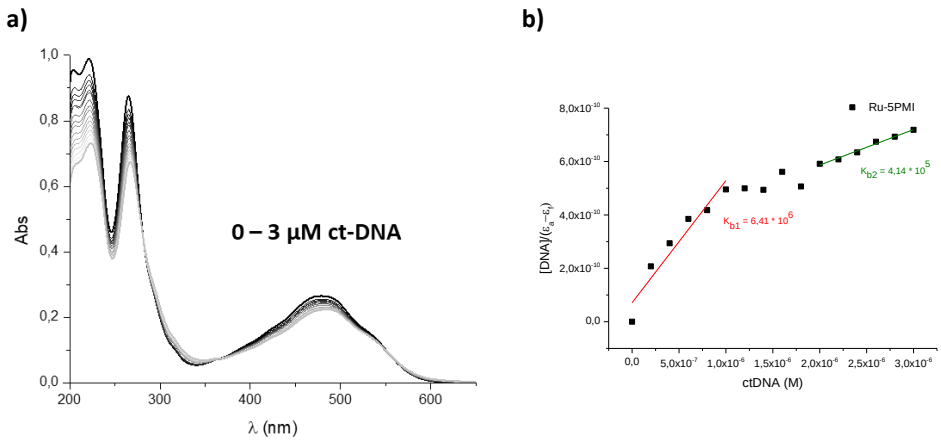

*Figure 58: a) Absorption spectra of **Ru-5PMI** recorded in the presence of increasing concentrations of ct-DNA; b) linear regression of plotted [DNA]/|εa-εb| values in function of the ct-DNA molar concentration (Ru=10 µM, Tris-HCl buffer 10 mM, NaCl 50 mM, pH 7.4).*

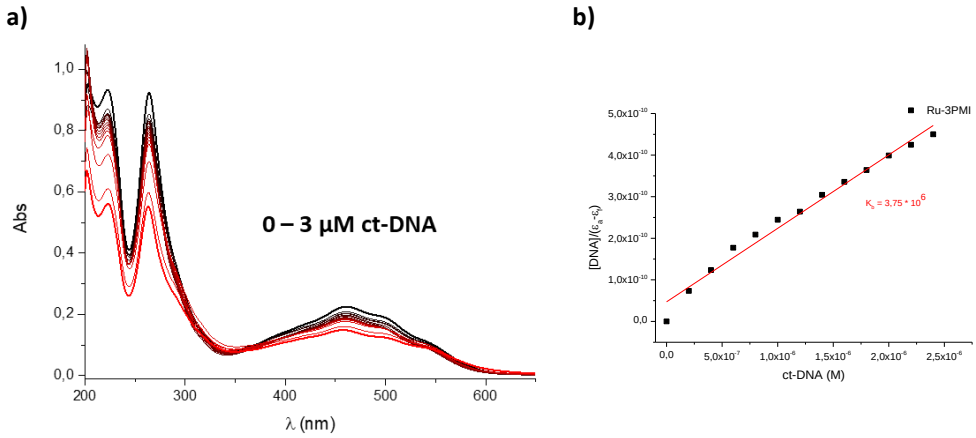

*Figure 59: a) Absorption spectra of **Ru-3PMI** recorded in the presence of increasing concentrations of ct-DNA; b) linear regression of plotted [DNA]/|εa-εb| values in function of the ct-DNA molar concentration (Ru=10 µM, Tris-HCl buffer 10 mM, NaCl 50 mM, pH 7.4).*

Considering the difficulties found in the determination of the binding constant (K_b) for complex **Ru-5PMI** through UV-Vis titration, a direct fluorescence titration were also performed by exciting 2 µM buffered solutions of the complex in the presence of increasing concentrations of *ct*-DNA (Figure 60). As shown in the insert in Figure 60, the emission intensity decreased progressively with increasing *ct*-DNA concentration (decrease percentage: 72%) until a plateau was reached when two equimolar amounts of *ct*-DNA were added. This behaviour denotes a strong and effective interaction between **Ru-5PMI** and the biopolymer, in accordance with what is observed in the UV-Vis titration.

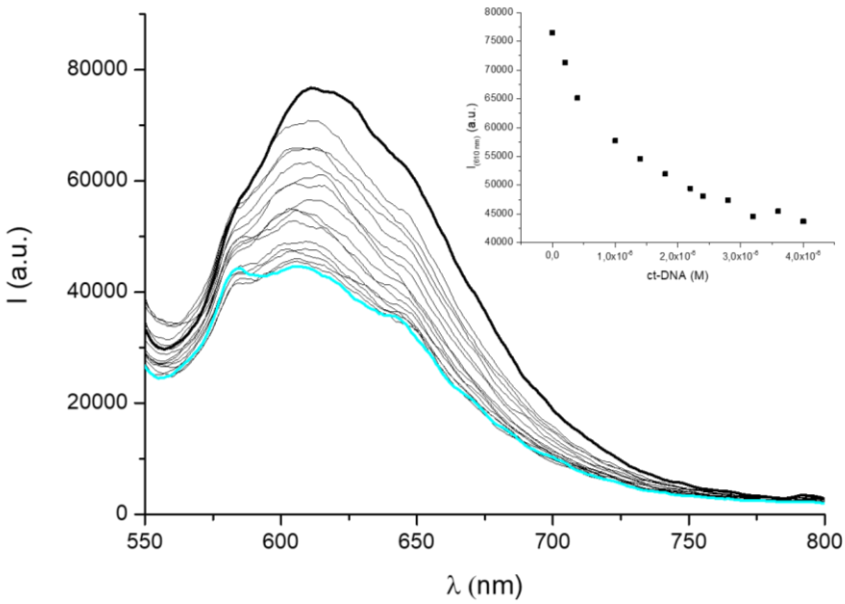

*Figure 60: Fluorescence spectra (λ_{Ex} 530 nm) of **Ru-5PMI** recorded in the presence of increasing concentrations of ct-DNA. Insert: trend of fluorescence intensity (λ_{Em} 610 nm) as a function of ct-DNA concentration. ([Ru-5PMI] = 2 µM, TRIS buffer pH=7.2)*

The DNA-binding ability of the two Ru-Perylenemonoimide complexes was lastly assessed by fluorescence competitive binding tests using ethidium bromide (EB) as an intercalator, their respective graphs are shown in Figure 51. Following the addition of increasing concentrations of **Ru-5PMI** and **Ru-3PMI**, the fluorescence emission spectra of fixed concentration solutions of ct-DNA (10 µM) and EB (10 µM) in Tris buffer (pH 7.4) were recorded. Experiments reveal that as Ru-PSs concentrations are raised, the fluorescence intensity of the DNA-EB complex significantly decreases (79% and 75% respectively for **Ru-5PMI** and **Ru-3PMI**). These findings confirm that both complexes have substantial intercalating abilities that can effectively displace EB from the DNA-EB complex. The Stern-Volmer and Scatchard equations were used in the DNA-EB fluorescence quenching studies (as reported in chapter 2, pharagraph 2.4), and the results allowed for the determination of values for the quenching constants (K_{SV}), association constants (K_a), number of binding sites (n) and apparent DNA binding

constants (K_{app}) which are listed in Table 13. The calculated parameters confirm that both complexes have a similar and strong ability to interact with the DNA in a preferentially intercalative mode of action.

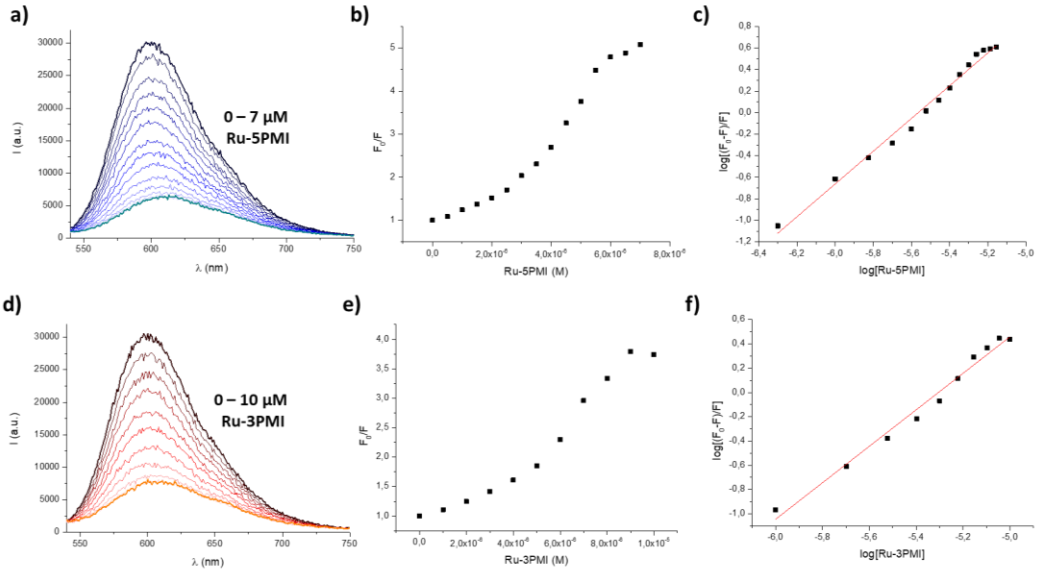

Figure 61: Molecular fluorescence emission spectra associated to the titrations of DNA-EB (10 µM, Tris buffer pH 7.4, λ_{ex} 527 nm, λ_{em} 610 nm) with increased concentrations of complexes a) Ru-5PMI and d) Ru-3PMI recorded at 298 K; b) and e) show the Stern-Volmer plot for the calculation of quenching constant (K_{SV}) respectively for Ru-5PMI and Ru-3PMI; c) and f) show the Scatchard plots for the determination of apparent DNA binding constants (Kapp) and the number of binding sites (n) respectively for Ru-5PMI and Ru-3PMI.

	Ru-5PMI	*Ru-3PMI*
K_{SV} (M^{-1})	5.4 ± 0.01 x 10^5	2.6 ± 0.01 x 10^5
K_a (M^{-1})	2.8 ± 0.004 x 10^8	2.9 ± 0.002 x 10^8
n	1.52	1.50
K_{app} (M^{-1})	3.3 ± 0.006 x 10^7	2.0 ± 0.006 x 10^7

Table 13: Values of quenching constants (K_{SV}), association constants (K_a), number of binding sites (n) and apparent DNA binding constant (K_{app}) for complexes Ru-5PMI and Ru-3PMI obtained from ethidium bromide (EB) competitive assay.

Acknowledgments

We are grateful to Prof. Tomás Torroba Pérez of the University of Burgos for allowing me to work in his research labs to improve the method used to prepare the ruthenium complexes described in this chapter. A special thanks to master's thesis students Nicola De Monte and Lorenzo Chellini for their contribution to the development of this project.

EXPERIMENTAL SECTION

Synthesis

Materials and methods

Reagents and solvents were purchased from Sigma Aldrich and Alfa Aesar and were used without further purification. The NMR spectra were collected with a Bruker 400 MHz spectrometer. The synthesis of PMI derivative **14** was previously optimized by Torroba et al.[144] utilizing as starting material the commercialy available compound **12.**

Synthesis of 15

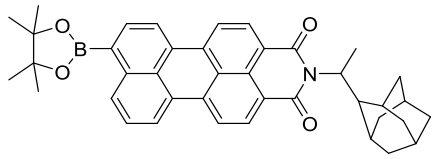

Previously synthesized compound **14** (580 mg, 1.02 mmol),[144] was dissolved in 40 mL of dry 1,4-dioxane under N_2 atmosphere. Bis(pinacolato)diboron (380 mg, 1.5 mmol) and potassium acetate (200 mg, 2.04 mmol) were added, the mixture was stirred at r.t. and 7 mg (0.01 mmol) of Pd(dppf)Cl_2 ([1,1'-Bis(diphenylphosphino) ferrocene] dichloropalladium (II)) catalyst was added. The reaction mixture was heated ad 75°C

and stirred overnight under N_2 atmosphere. The solvent was removed at reduced pressure and the solid residue was dissolved in dichloromethane and washed three times with water and once with BRINE. The organic phase was dried with Na_2SO_4 and evaporated to dryness. The crude product was then purified via flash chromatography on silica gel by using a mixture of dichloromethane and hexane as eluent (from 1:1 to 5:1 DCM:Hex). Yield 60%. ^{1}H-NMR (300 MHz, $CDCl_3$): δ 8.18 (dd, J_1 = 8.4 J_2 = 1.8, 1H), 8.54-8.45 (m, 2H), 8.36-8.25 (m, 4H), 8.14 (d, J_1 = 7.8, 1H), 7.60 (td, J_1 = 9.3, J_2 = 8.1, J_3 = 1.8, 1H), 5.10 (dd, J_1 = 14.7, J_2 = 7.2, 1H), 1.98 (bs, 3H), 1.89-1.77 (m, 3H), 1.73-1.63 (m, 13H), 1.48 (12H).

Synthesis 16

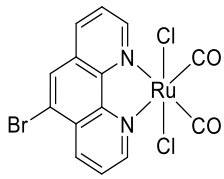

Polymeric precursor **2** (59 mg, 0.25 mmol) was dissolved in dry methanol under N_2 atmosphere. Then, 5-bromo-1,10-phenantroline (60 mg, 0.23 mmol) was added and the reaction mixture was stirred at reflux for 1 h. The white precipitate formed was then filtered and washed with hot methanol to obtain complex **16** as a white solid. Yield 46 %. ^{1}H-NMR (400 MHz, $(CD_3)_2SO$): δ 9.77 (d, J = 5.2 Hz, 1H), 9.70 (d, J = 4.0 Hz, 1H), 9.10 (d, J=8.0 Hz, 1H), 8.98 (d, J=8.0 Hz, 1H), 8.91 (s, 1H), 8.33 (dd, J_1=4.0 Hz, J_2= 8.0 Hz, 1H), 8.24 (dd, J_1=4.0 Hz, J_2= 8.0 Hz, 1H) ppm. ^{13}C-NMR (100 MHz, $(CD_3)_2SO$): δ 155.0, 154.7, 144.8, 139.5, 131.5, 130.7, 129.8, 128.2, 127.8, 121.3 ppm.

Synthesis 17

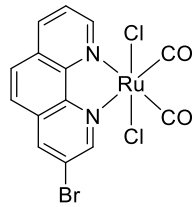

Polymeric precursor **2** (117 mg, 0.50 mmol) was dissolved in dry methanol under N_2 atmosphere. Then, 3-bromo-1,10-phenantroline (118 mg, 0.45 mmol) was added and the reaction mixture was stirred at reflux for 2 h. The white precipitate formed was then filtered and washed with hot methanol to obtain complex **17** as a yellow/orange solid. Yield 80 %.

^{1}H-NMR (400 MHz, $(CD_3)_2SO$): δ 9.78 (d, J = 4.0 Hz, 1H), 9.69 (d, J=4.0 Hz, 1H), 9.42 (d, J = 4.0 Hz, 1H), 9.04 (d, J=8.0 Hz, 1H), 8.45 (d, J=8.0 Hz, 1H), 8.32 (d, J = 8.0 Hz, 1H), 8.23 (dd, J_1=8.0 Hz, J_2= 4.0 Hz, 1H) ppm.

^{13}C-NMR (100 MHz, $(CD_3)_2SO$): δ 199.8, 195.8, 154.2, 144.9, 144.0, 142.0, 140.1, 131.3, 130.8, 129.7, 127.3, 120.9 ppm.

Synthesis 18

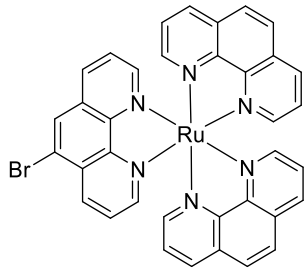

To a solution of **16** (50 mg, 0.10 mmol) in 5 mL of degassed 2-methoxyethanol were added 1,10-phenantroline (56 mg, 0.20 mmol) and trimethylamine N-oxide (38 mg, 0.50 mmol). The reaction mixture was stirred 1 hours at reflux under N_2 atmosphere. After cooling at r.t., the addition of 0.1 M aqueous solution of KPF_6 (2 mL) allowed the

precipitation of complex **18** as dihexafluorophosphate salt, that was collected by filtration under vacuum and the solid was washed with water and diethyl ether. The crude product was obtained with a high grade of purity to proceed with the next synthetic step. Yield 82%. Noting that product **18** is obtained as a mixture of not separable isomers. This feature complicates the assignment of ^{1}H NMR signals that are split into two sets of signals, one for each of the two isomers. Recording ^{1}H-NMR spectra at low concentration (~5 mM) (Figure 62a) allows to increase the resolution compared to spectra recorded at higher concentrations (~14 mM) (Figure 62b). ^{1}H-NMR (400 MHz, $(CD_3)_2CO$): δ 8.91 (d, J = 8.0 Hz, 1H), 8.88-8.75 (m, 5H), 8.52 (d, J = 8Hz, 1H), 8.50-8.38 (m, 8H), 7.94 (dd, J_1=8.0 Hz, J_2 = 12.0 Hz, 1H), 7.88-7.79 (m, 5H) ppm. ^{13}C-NMR (100 MHz, $(CD_3)_2CO$): δ 154.0, 153.7, 153.4, 153.1, 148.0, 137.1, 136.3, 136.2, 134.2, 131.1, 128.3, 127.0, 126.7, 126.3 ppm. HR-MS: calcd for $C_{36}H_{23}N_{6Br}Ru$ $[M]^{2+}$ 361.00997, found $[M]^{2+}$ 361.00901.

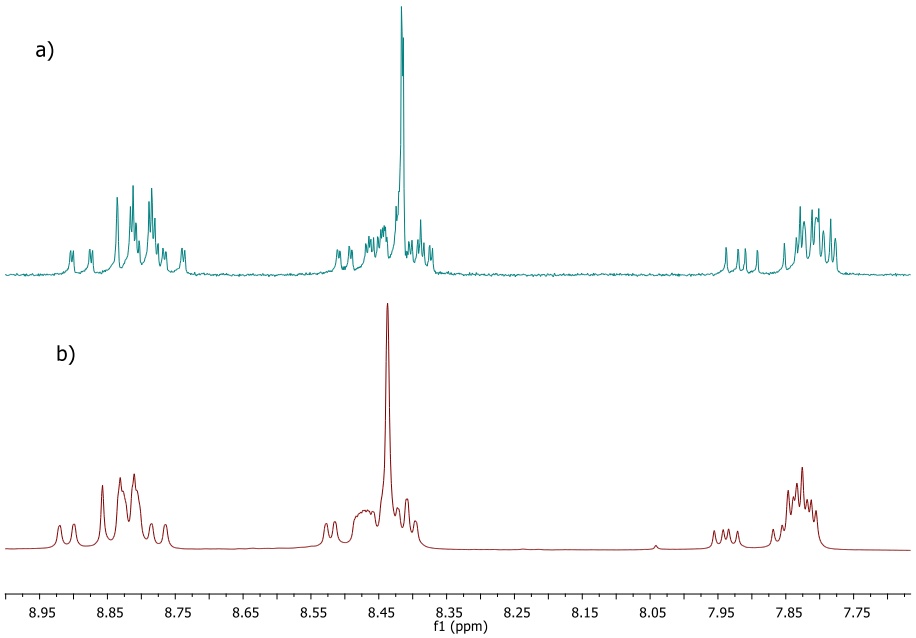

*Figure 62: ^{1}H-NMR (400 MHz) spectra of compound **18** in acetone-D6 recorded at a) 5 mM and b) 14 mM.*

Synthesis 19

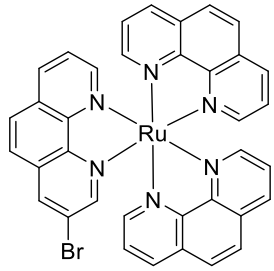

To a solution of **17** (65 mg, 0.13 mmol) in 7 mL of degassed 2-methoxyethanol were added 1,10-phenantroline (48 mg, 0.26 mmol) and trimethylamine N-oxide (74 mg, 0.67 mmol). The reaction mixture was stirred 2 hours at reflux under N_2 atmosphere. After cooling at r.t., the addition of 0.1 M aqueous solution of KPF_6 (2 mL) allowed the precipitation of complex **19** as dihexafluorophosphate salt, that was collected by filtration under vacuum and the solid was washed with water and diethyl ether. The crude product was obtained with a high grade of purity to proceed with the next synthetic step. Yield 75%. Noting that product **19** is obtained as a mixture of not separable isomers. This feature complicates the assignment of ^{1}H NMR signals that are split into two sets of signals, one for each of the two isomers. ^{1}H-NMR (400 MHz, $(CD_3)_2CO$): δ 9.07 (d, J = 2.0 Hz, 1H), 8.85-8.79 (m, 5H), 8.61 (d, J = 4.0 Hz, 1H), 8.54-8.37 (m, 8H), 8.33 (d, J = 4.0Hz, 1H), 7.87-7.79 (m, 5H) ppm. HR-MS: calcd for $C_{36}H_{23}N_6BrRu$ $[M]^{2+}$ 361.00997, found $[M]^{2+}$ 361.00896.

Synthesis Ru-5PMI

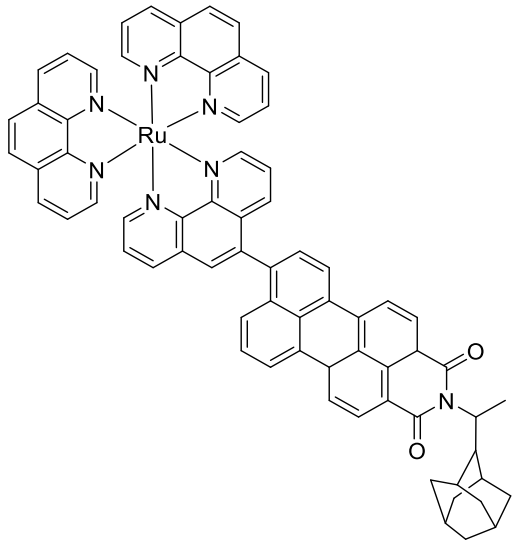

In a Schlenk apparatus, a solid mixture of complex **18** (80 mg, 0.08 mmol) and compound **15** (53 mg, 0.09 mmol) was solubilized in 4 mL of deaerated mixture of dimethylformamide and water 2:1. Potassium carbonate (55 mg, 0.40 mmol) was added, and three vacuum/nitrogen cycles were performed. Then, a catalytic amount (1 % w/w) of Tetrakis(triphenylphosphine)palladium(0) as catalyst was added and three vacuum/nitrogen cycles were performed again. The reaction mixture was stirred at 100°C for 3 hours, then cooled at r.t. and filtered on a Celite pad with methanol to remove the catalyst. Filtered solution was evaporated to dryness and the resulting red solid was solubilized in dichloromethane (60 mL) ad washed three times with 10 mL of water and once with 10 mL of BRINE. The organic phase was dried with Na_2SO_4, filtered, and evaporated to dryness. The red crude product was purified via flash chromatography on silica gel (dichloromethane : methanol 60:1) to obtain complex **Ru-5PMI** as a red/orange solid with a yield of 64%. Noting that product **Ru-5PMI** is obtained as a mixture of not separable isomers. This feature complicates the assignment of ^{1}H NMR signals that are split into two sets of signals, one for each of the

two isomers. ^{1}H-NMR (400 MHz, $(CD_3)_2CO$): δ 9.10-8.78 (m, 5H), 8.72-8.15 (m, 18H), 8.73-8.14 (m, 5H), 7.79-7.35 (m, 4H), 5,04 (q, 1H), 1.94-1.74 (m, 6H), 1.72-1.45 (m, 12H) ppm. ^{13}C-NMR (100 MHz, $(CD_3)_2CO$) δ 165.34, 165.20, 164.63, 156.08, 154.04, 153.91, 153.77, 153.67, 151.46, 149.08, 148.96, 148.73, 148.70, 148.65, 147.86, 138.86, 138.73, 137.70, 137.06, 136.38, 136.22, 134.88, 133.82, 133.45, 131.78, 131.41, 131.28, 131.04, 130.48, 130.25, 130.06, 129.84, 129.43, 128.87, 128.51, 128.14, 127.83, 127.20, 126.89, 126.64, 126.52, 126.20, 124.62, 124.24, 123.84, 123.57, 122.62, 122.48, 121.71, 121.48, 119.82, 58.08, 40.73, 38.16, 38.14, 37.34, 37.26, 30.32, 30.15, 29.96, 29.76, 29.57, 29.38, 29.29, 29.27, 29.19, 28.99, 12.95, 12.90 ppm. HR-MS: calcd for $C_{70}H_{51}N_7O_2Ru$ $[M]^{2+}$ 561.66779, found $[M]^{2+}$ 561.65710.

Synthesis Ru-3PMI

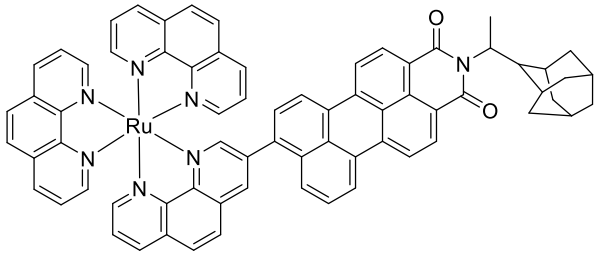

In a Schlenk apparatus, a solid mixture of complex **19** (80 mg, 0.08 mmol) and compound **15** (53 mg, 0.09 mmol) was solubilized in 4 mL of deaerated mixture of dimethylformamide and water 2:1. Potassium carbonate (55 mg, 0.40 mmol) was added, and three vacuum/nitrogen cycles were performed. Then, a catalytic amount (1 % w/w) of Tetrakis(triphenylphosphine)palladium(0) as catalyst was added and three vacuum/nitrogen cycles were performed again. The reaction mixture was stirred at 100°C for 3 hours, then cooled at r.t. and filtered on a Celite pad with methanol to remove the catalyst. Filtered solution was evaporated to dryness and the resulting red solid was solubilized in dichloromethane (60 mL) ad washed three times with 10 mL of water and once with 10 mL of BRINE. The organic phase was dried with Na_2SO_4, filtered,

and evaporated to dryness. The red crude product was purified via flash chromatography on silica gel (dichloromethane → dichloromethane : methanol 20:1) to obtain complex **Ru-3PMI** as a red/orange solid with a yield of 88%. Noting that product **Ru-3PMI** is obtained as a mixture of not separable isomers. This feature complicates the assignment of ^{1}H NMR signals that are split into two sets of signals, one for each of the two isomers. ^{1}H-NMR (400 MHz, $(CD_3)2CO$): δ 8.96-8.76 (m, 6H), 8.59-8.40 (m, 10H), 8.00-7.81 (m, 10H), 7.74-7.56 (m, 6H), 4.79 (m, 1H), 1.87 (sb, 3H), 1.77-1.62 (m, 6H), 1.58-1.50 (m, 6H), 1.47-1.41 (m, 3H) ppm. ^{13}C-NMR (100 MHz, $(CD_3)2CO$) δ 165.08, 164.63, 164.41, 158.57, 154.09, 153.77, 152.55, 148.75, 148.69, 148.32, 147.94, 146.36, 138.23, 138.06, 137.82, 137.68, 137.57, 137.35, 136.47, 136.26, 134.80, 133.93, 133.78, 132.90, 132.42, 132.38, 132.32, 131.96, 131.78, 131.71, 131.62, 131.14, 130.29, 129.67, 129.42, 129.19, 129.08, 128.99, 128.82, 128.62, 127.97, 127.85, 127.03, 126.88, 126.82, 126.38, 126.04, 125.58, 124.56, 122.40, 121.32, 57.96, 40.67, 38.19, 37.31 ppm. HR-MS: calcd for $C_{70}H_{51}N_7O_2Ru$ $[M]^{2+}$ 561.66779, found $[M]^{2+}$ 561.65689.

UV-Vis spectroscopy and fluorescence measurements

UV-Vis absorption spectra were acquired on a Perkin-Elmer Lambda 6 spectrophotometer. Fluorescence spectra and measurements of the phosphorescence signal of $^{1}O_2$ were carried out on a spectrofluorometer Horiba FluoroMax Plus.

Singlet oxygen determination

The singlet oxygen sensitizing properties of **Ru-5PMI** and **Ru-3PMI** were firstly analyzed spectrophotometrically by using 1,5-dihydroxynaphthalene (DHN) as indirect $^{1}O_2$ reporter and were compared with those of $[Ru(Phen)_3]^{2+}$ and PMI derivative **13**. To do this, air-saturated acetonitrile solutions containing DHN 3.3 x 10^{-4} M and the selected

compound at 1 x 10^{-5} M were irradiated (LED emitting at 434 nm, 160 mW) in a quartz cuvette with 1 cm optical path over a total time of 300s. Each spectrum was registered by using as blank reference a solution containing the selected PS at the same concentration of that of the measuring cuvette. The estimation of the relative rate constants for the DHN photooxidation processes (k_{obs}) was performed by applying the steady-state approximation to the $^1O_2$ intermediate, according to procedures previously described.[81]

Direct determination of singlet oxygen quantum yields for **Ru-5PMI** and **Ru-3PMI** was determined through the direct measurement of $O_2(^1\Delta_g) \rightarrow {}^3O_2$ phosphorescence at 1270 nm, upon irradiation of compounds at 470 nm in air-saturated acetonitrile solutions. Experiments were run on solutions of $[Ru(RR\text{-}bpy)(dppn)_2]^{n+}$ complexes at different concentrations, with the ^{1}MLCT absorbance values within the range 0.08-0.2 and signals were collected by a N_2 cooled InGaAs photodiode. ϕ_Δ values were obtained as previously reported by comparison with $[Ru(phen)_3]^{2+}$, which was chosen as reference compound for $^1O_2$ production (ϕ_Δ = 0.38 ± 0.06).[76] Measurements were performed on a spectrophotofluorimeter Horiba FluoroMax Plus.

Evaluation of the interaction with *ct*-DNA

Calf thymus DNA (*ct*-DNA) was purchased from Sigma Aldrich and dissolved in Tris-HCl buffer (10 mM Tris-HCl, 50 mM NaCl, pH 7.4). An absorbance ratio between 260 and 280 nm within 1.8-1.9:1 indicated that the biopolymer was sufficiently free of proteins. A molar absorption coefficient at 260 nm of 6600 M^{-1} cm^{-1} was used to determine the *ct*-DNA concentration per nucleotide.

The binding properties of ruthenium complexes towards *calf thymus* DNA (ct-DNA) were first investigated spectrophotometrically analysing the variations in the absorption bands of **Ru-5PMI** and **Ru-3PMI** by adding increasing amounts of concentrated solutions of the biopolymer to aqueous solutions (TRIS buffer, pH 7.4)

containing the tested RPC at fixed concentration (10 μM). The contribution arising from the absorbance of the DNA itself was eliminated by adding equal amounts of DNA both to the sample and to the reference solution. After each addition, samples were incubated for 10 minutes at 298.1 ± 0.1 K before collecting the absorption spectra. The intrinsic binding constants (K_b) with *ct*-DNA were determined accordingly to literature, from the intercept-to-slope ratios of the plot of [*ct*-DNA]/Iε_a-ε_fI *vs*. [*ct*-DNA] (see Figure 58 and Figure 59), where ε_a and ε_f correspond to $A_{obs.}$/[RPC] and to the molar extinction coefficient for the DNA-free metal compound. Linearity within the 0-3 μM range of [*ct*-DNA] was observed.

The capacity of **Ru-5PMI** to interact with *ct*-DNA was further investigated via direct fluorescence titration by exciting 2 μM buffered solutions (TRIS buffer, pH 7.4) of the complex in the presence of increasing concentrations of *ct*-DNA (up to 4 μM of the biopolymer). Each sample was incubated for 5 minutes at r.t. and then excited at 530 nm. The variation in the emission intensity was monitored at 610 nm.

The DNA-EB fluorescence quenching studies for **Ru-5PMI** and **Ru-3PMI** were performed by adding increasing amounts of a concentrated solution of the selected Ru-PS (up to 7 μM or 10 μM for **Ru-5PMI** and **Ru-3PMI** respectively) to aqueous solutions (TRIS buffer, 10 mM Tris-HCl, 50 mM NaCl, pH 7.4) containing fixed concentration of ct-DNA (10 μM) and EB (10 μM). Each sample was incubated for 5 minutes at room temperature, afterward the DNA-EB complex was excited at 527 nm and the emission intensity was monitored at 610 nm. The data obtained from the fluorescence titration were processed applying Stern-Volmer and Scatchard equations as described in detail in Chapter 2, Paragraph 2.4.

Chapter 4

RPCs in "photorelease antibacterial therapy"

Bacterial pathogens multidrug resistance represents a major challenge for the global public health community. The introduction of antibiotics in the 1940s revolutionized medicine; however, their widespread use in the last decades has determined the emergence and spread of drug-resistant populations of microorganisms, which causes treatment failures, severe and longer-lasting diseases, more deaths, and higher costs to society. Antibiotic resistance has become an important international public health problem that urgently requires attention.[148] Therefore, there is an urgent need for the development of new antimicrobial agents, which should be based on new classes of compounds, rather than on analogues of known scaffolds.[149]

In this scenario, considerable attention has been focused on the biological potential of RPCs, that represent an attractive class of compounds due to their unique chemical-physical repertoires, structural diversity, and thermodynamic/kinetic stability making them an appealing and versatile choice in the rational design of effective antibacterial agents.[150] [149] [151] [152]According to the suggested categorization for metal-anticancer compounds, antimicrobial ruthenium(II) complexes can also be classified into five classes, based on their mechanism of action: [153]

1) Functional role: the antimicrobial activity depends on the coordination of the ruthenium metal center with biological targets. In a *cis*-platin fashion like mode, these complexes could bind labile ligands, which can be dissociated, leaving coordinatively unsaturated intermediates.
2) Structural role: kinetically and biologically stable complexes that interacting with biological targets through non-covalent interactions.

3) Carrier: the ruthenium metal center acts as a carrier for active ligands to enhance their pharmaceutical activity via temporary coordination.
4) Catalyst: the ruthenium complex can catalyze a redox cycle for the oxidation of glutathione (GSH) to glutathione disulfide (GSSG), which will lead to an increase in reactive oxygen species (ROS) with an obvious cytotoxic effect against some cells lines.
5) Photosensitizer: the ruthenium complex is a photoactive compound capable of producing singlet oxygen ($^1O_2$) due to its low-energy triplet excited state.

Up to now, hundreds of RPCs have been reported in antimicrobial studies.[149] Dwyer and coworkers published the first pioneering work demonstrating the antibacterial potential of this class of complexes around 1970s.[154] Notwithstanding, RPCs have sparked renewed interest in their antimicrobial properties only in the last ten years. Besides the difficulties in the complete elucidation of their antibacterial mechanism of action, a promising approach is represented by the use of ruthenium complexes in combination with light in the so-called anti-bacterial photodynamic therapy (aPDT). The aPDT approach exploits the presence of molecular oxygen to generate ROS and $^1O_2$ upon photoactivation of the ruthenium PS and takes advantage of complete spatial and temporal control over the drug activation. However, despite the high efficacy of aPDT against multidrug-resistant bacteria,[155] the need of oxygen still represents a limit in the treatment of anaerobic bacterial disease. This led to the development of light-responsive complexes able to release biologically active compounds via O_2-indepentent mode of action, an interesting approach called Photoactivated Chemoterapy (PACT).[69,72]

4.1 Nitroimidazole-based RPCs

Starting from our previous expertise in the exploration of the antibacterial efficacy of photostable ruthenium(II) polypyridyl complexes in aPDT approach [75] (Chapter 1, paragraph 1.1) we decided to explore this area further designing new RPCs adaptable in hypoxic conditions. In this respect, a new series of light-responsive complexes, able to release biologically active compounds via O_2-independent mechanism, were synthesized and studied. Such process typically requires the population of dissociative ^{3}LF state. It is generally accepted that photoinduced ligand exchange of ruthenium(II) complexes proceeds trough thermal population of the dissociative ^{3}LF states from vibrationally cooled emissive $^3MLCT_{v=0}$ state.[69] To overcome this issue, strain-inducing substituents are inserted in the ruthenium scaffolds, lowering the energy of the ^{3}LF states and allowing their thermal population upon excitation to the ^{3}MLCT state (see Introduction, paragraph 4 for details) (Figure 63).[69]

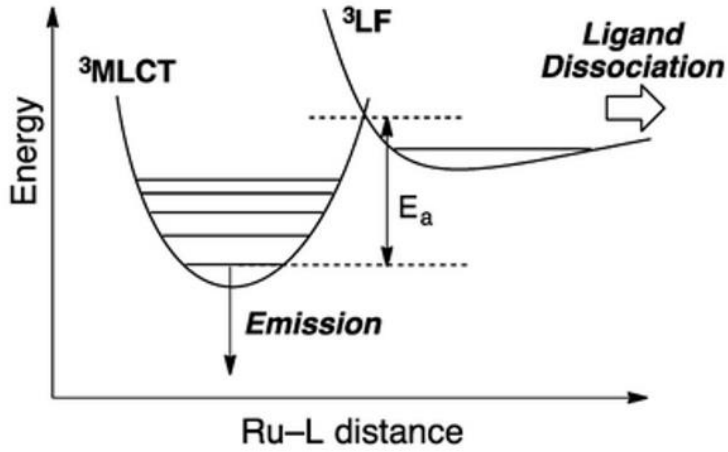

Figure 63: Schematic representation of activation energy E_a required for going from ^{3}MLCTv=0 to ^{3}LF state.

Given the versatile chemistry of RPCs, as well as being inspired by the work of Sasahara at al., who designed two kinetically inert compounds, $[Ru(NO_2)(bpy)(5NIMH)]PF_6$ and cis-$[RuCl(bpy)_2(MTZ)]PF_6$ (bpy = 2,2'-bipyridine, MTZ = metronidazole, NIMH = 5-nitoimidazole), effective toward *Helicobacter pylori* strain,[156] nitroimidazole-based drugs were selected as bioactive compounds to be incorporated on ruthenium complexes for the development of new challenging photoresponsive antimicrobials.[157] Nitroimidazoles are a class of antimicrobial drugs with remarkable broad-spectrum activity against mycobacteria, parasites, and anaerobic Gram-negative and Gram-positive bacteria.[158] The discovery of nitroimidazole antibiotics dates back to the early 1950s, and their versatility is further demonstrated by considering that infection from these pathogens occurs in many different sites of the body (Figure 64a).[158] The broad-spectrum activity of nitroimidazole drugs can be explained by their relatively "nonspecific" mode of action and is attributable to the presence of nitro groups that require bioactivation to initiate their antimicrobial activity. The mechanism is generally understood to involve the following steps (Figure 64b):

i) Entry of the molecule by passive diffusion.

ii) Reduction of the nitro group to reactive radical species.

iii) Reactions of formed radicals with cellular components such as DNA or proteins.

Under anaerobic conditions, the redox potential of the electron-transport system (generally pyruvate:ferrodoxine oxidoreductase complex in anaerobes)[159] in microbes is sufficiently negative to reduce the nitro group; instead, the presence of oxygen in aerobic microbes, gives rise to a futile cycle in which cytotoxic nitro radical anion is rapidly reoxidized and the bactericidal effect is diminished.[158]

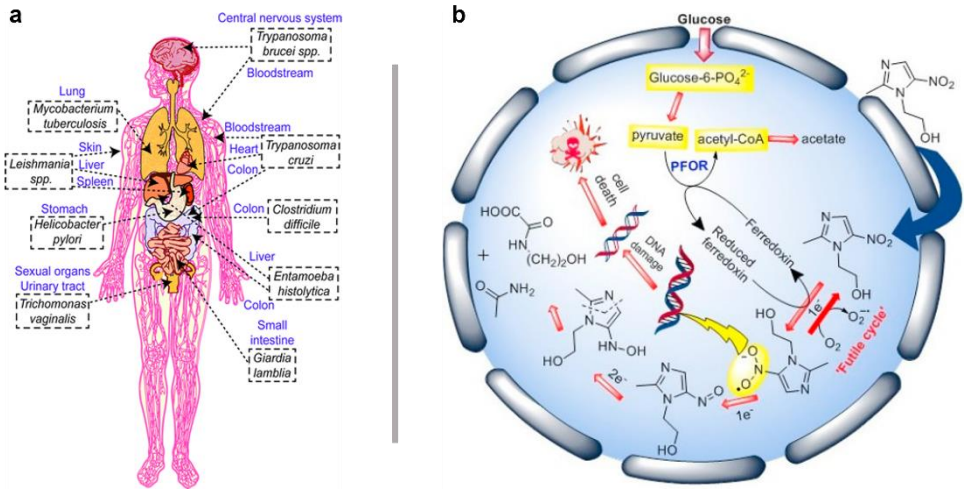

Figure 64: a) Sites within the human body that can be infected by nitroimidazoles sensitive pathogen, b) mechanism of action of metronidazole, a clinically utilized antibiotic.

Based on these assumptions, 5-nitroimidazole (**5NIMH**) was preliminary chosen as the simplest molecular model of nitroimidazole-based drugs to explore its ruthenium(II) coordination chemistry and the effect of increased steric hindrance on the electronic properties and photoreactivity of the designed complexes. For this purpose, **5NIMH** was incorporated into the ruthenium complexes [Ru(tpy)(phen)(5NIM)]PF_6 (**N1**) and [Ru(tpy)(dmphen)(5NIM)]PF_6 (**N2**) (tpy = 2,2':6',2''-terpyridine; phen = 1,10-phenantroline; dmphen = 2,9-dimrthyl-1,10-phenantroline) (Figure 65)[157] Following the demonstration that the presence of the two bulky methyl groups in the 2 and 9 positions of the dmphen bidentate ligand of **N2** favours the selective photoejection of **5NIMH** upon light exposure, we selected the N2-ruthenium scaffold to obtain more effective light-responsive antibacterial agents binding two new metronidazole derivatives (**N3-4**) (Figure 65). Although some anaerobic bacteria and protozoa have been reported to acquire resistance to Metronidazole (2-nitro-5-methyl-1*H*-imidazolyl = **MTZ**), it is still one of the mainstay drugs among 5-nitroimidazoles for the treatment of anaerobic infections, making it crucial to look into acceptable substitutes.[160] For this

reason, we synthesized and characterized two novel derivatives of metronidazole (**MTZ-1** and **MTZ-2**), in which MTZ is esterified with 1H-imidazole-5-carboxylic acid and 5-imidazoleacryl acid (Urocanic acid), both imidazole-containing carboxylic acid whose imidazole moieties is exploited as linking units for the Ru(II) centre.

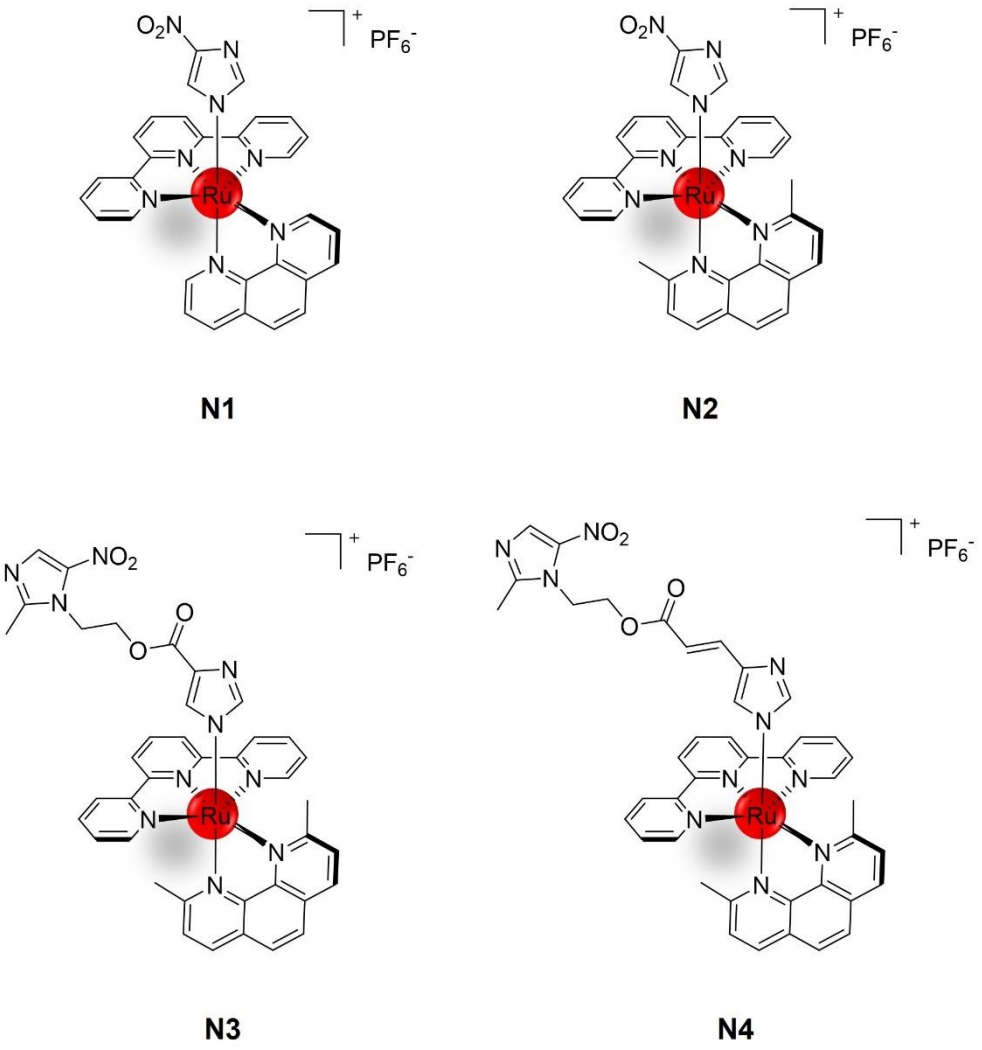

Figure 65: Molecular structures of Nitroimidazole-based ruthenium complexes synthetized in this work.

4.2 Synthesis and characterization of Nitroimidazole-based RPCs

Complexes from this series (**N1-4**) were prepared through stepwise ligand addition (Scheme 11).

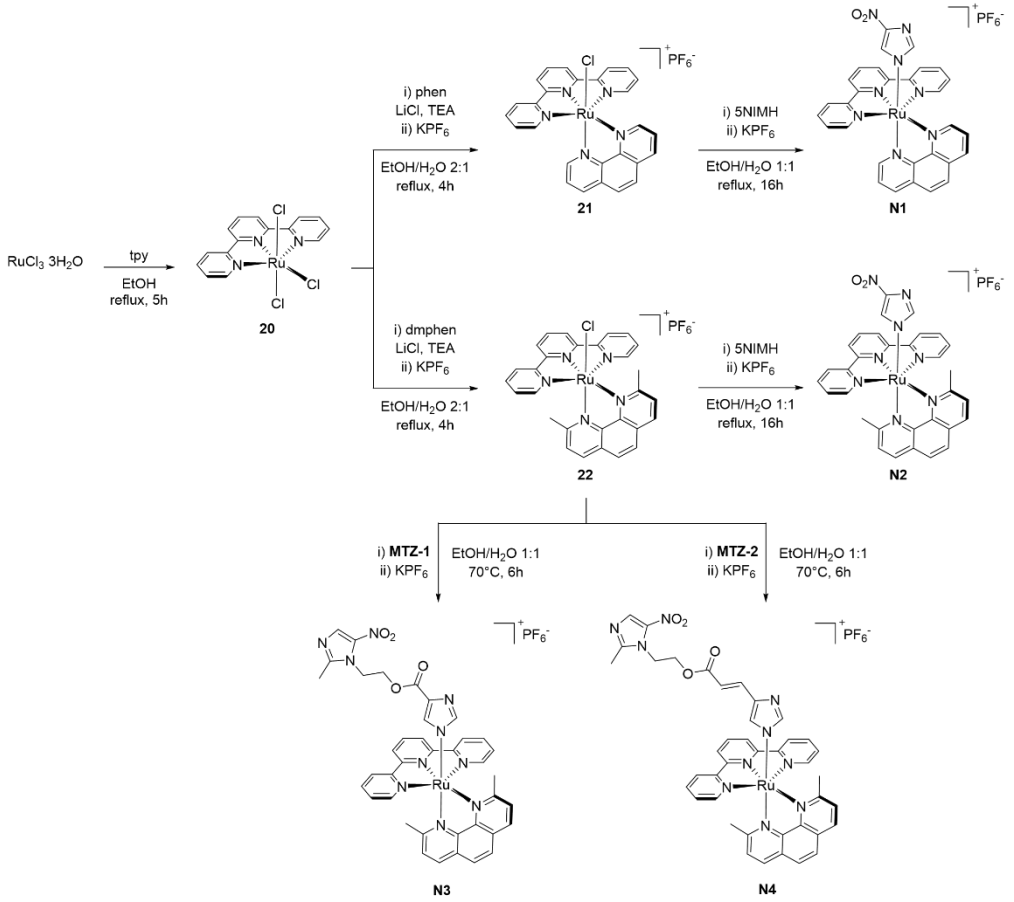

Scheme 11

The first synthetic step involves treating ruthenium chloride trihydrate ($RuCl_3 \cdot 3H_2O$) with an equimolar amount of 2,2':6',2''-terpyridine (tpy) in ethanol heated to reflux for 4 hours to produce the common precursor **20**.[161] The resulting paramagnetic intermediate was isolated by filtration and used directly in the second step, which involves the treatment with the appropriate bidentate ligand (phen or dmphen) in the

presence of triethylamine as reducing agent and lithium chloride.[161] Complexes **21** and **22** were isolated through precipitation with potassium hexafluorophosphate and collected by filtration, obtaining adequate purity to proceed to the next reaction without further purification. In the final step of the synthesis, the selected nitroimidazole-containing monodentate ligand is added to complex **21** for the preparation of **N1** and to complex **22** for the preparation of **N2-4**. In each case, the reaction proceeds in ethanol-water mixture using an excess of the nitroimidazole compund. In the case of complexes **N1** and **N2**, commercially available **5NIMH** was used as reagent; instead metronidazole derivatives **MTZ-1** and **MTZ-2** were prepared here for the first time via Steglich esterification from 1H-imidazole-5-carboxylic acid or 5-imidazoleacryl acid (Urocanic acid) and metronidazole (MTZ) using N,N'-dicycloexylcarbodiimide (EDC) as coupling reagent and 4-dimethylaminopyridine (DMAP) as catalyst in dimethylformamide (DMF) (Scheme 12).

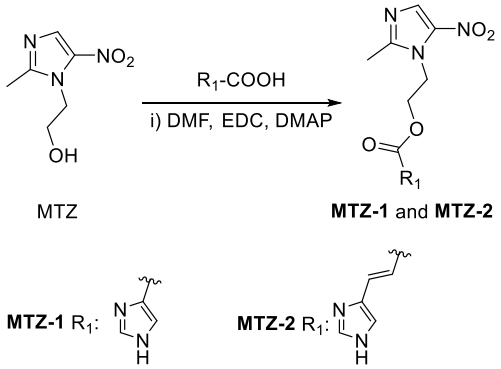

Scheme 12

Despite the use of standard synthetic procedures for the coordination of nitroimidazole compounds,[162] it is should be noted and discussed in depth that high resolution mass spectrometry (HR-MS) and X-ray diffraction spectroscopy reveal a *"nonstandard"* coordination of the imidazole ring to the ruthenium centres of this series of complexes. The aza nitrogen (-N=) atom of imidazole (Him) can be employed as a donor for Lewis

acidic metal ions. Imidazole is more basic than pyridine due to the delocalization of six electrons on five atoms, resulting in higher electron density and stronger coordination ability as a neutral ligand. However, the imidazolate anion (Im-), obtained by deprotonation of amine (-NH-) nitrogen of Him in basic condition, can act as a bidentate bridging ligand (Figure 66).[163]

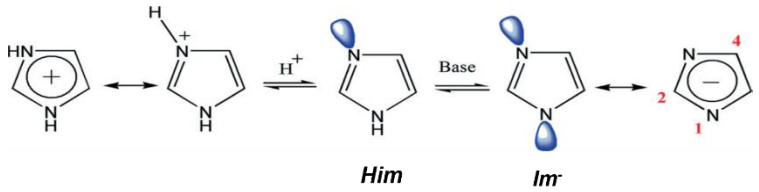

Figure 66: Scheme of protonation and deprotonation of imidazole.

According to these considerations, it is normally reported that imidazole-containing ligands act as neutral ligands unless deprotonated in basic condition.[163,164] Several examples in the literature report the ruthenium-coordination of various substituted imidazoles as neutral ligands via the aza (-N=) nitrogen under similar experimental conditions to ours.[52,165,166] Conversely, the coordination to ruthenium in complexes **N1-4** involves the deprotonated amine (-NH-) nitrogen atom of the imidazole moiety in 5-nitroimidazole (5NIM in Figure 67) and in compounds **MTZ-1** and **MTZ-2**, as demonstrated by X-Ray structures of complexes **N1** and **N2** (5NIM in Figure 68) and confirmed by the presence of the isotopic patterns of the mono positively charged species [**N1-4**]$^+$ in the HR-MS spectra of each complex (Table 14). This occurs without using strong bases to preliminary generate the imidazolate species. In this regard, we can speculate that the marked electron withdrawing character of the nitro group and the Ru(II)-coordination may work synergically to lower the pKa of the imidazole ring, favouring its metal coordination as imidazolate anion, contrary to the structure proposed by Sasahara et al.[156]

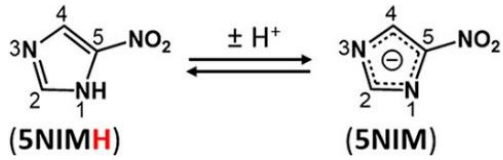

Figure 67: Proton transfer reaction between 5NIMH and 5NIM and the standard numbering for imidazole ring.

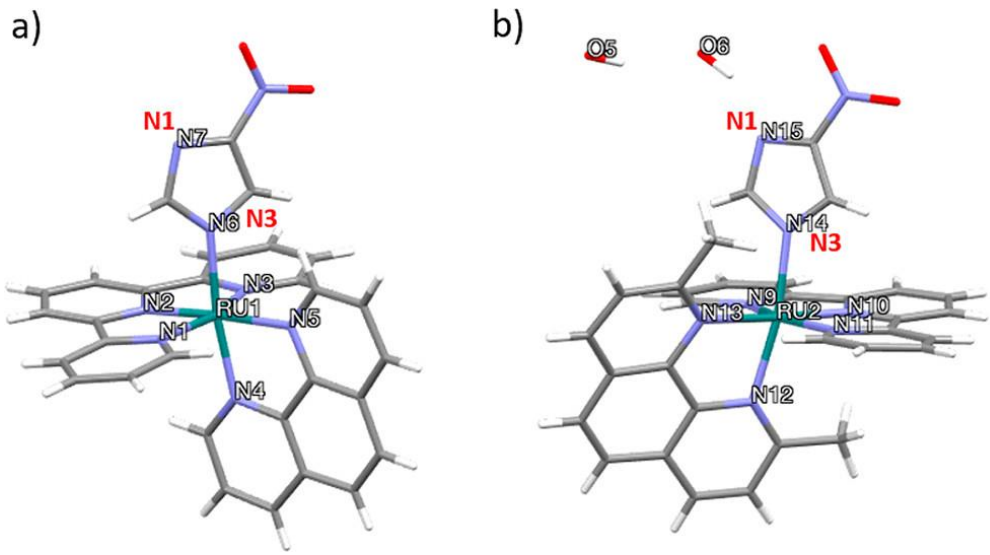

Figure 68: X-Ray structures of a) N1 and b) N2. In red is highlighted the adopted nitrogen numbering for imidazole ring.

Complex	*formula*	*m/z calcd $[M]^+$*	*m/z found $[M]^+$*
N1	$C_{30}H_{21}N_8O_2Ru$	627.0833	627.0872
N2	$C_{32}H_{25}N_8O_2Ru$	655.1147	655.1186
N3	$C_{39}H_{33}N_{10}O_4Ru$	807.17243	807.17124
N4	$C_{41}H_{35}N_{10}O_4Ru$	833.18808	833.18796

*Table 14: Comparison between theoretical and found m/z peaks for the mono positively charged species $[$**N1-4**$]^+$ in HR-MS spectra.*

The electronic absorption spectra of **N1-4** in acetonitrile and in aqueous solution (PBS buffer, pH 7.4) are reported in Figure 69. These complexes display the typical $^1\pi\pi^*$ transitions relative to tpy and phen/dmphen ligands in the UV region along with a broad metal-to-ligand Ru(dπ) → tpy/dmphen(π^*) charge transfer band (^{1}MLCT) in the visible range. In acetonitrile, the lowest energy absorption bands of **N3** and **N4** are slightly blue shifted compared to those of **N2** and **N1** (Table 15). A residual absorption tail within the 550-650 nm range of the spectra can also be evidenced for all the complexes, thus providing a promising feature for their activation by using low energy light, with enhanced depth penetration into tissues.

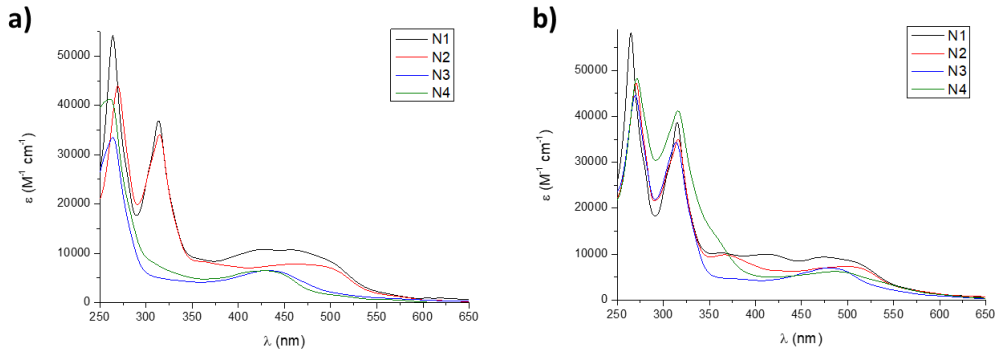

*Figure 69: Electronic absorption spectra of **N1-N4** in acetonitrile (a) and in PBS buffer solution pH 7.4 (b).*

Complex	λ_{abs} (nm) (ε (M^{-1} cm^{-1}))
N1	473 (9616)
N2	500 (7912)
N3	480 (7000)
N4	485 (6190)

Table 15: Absorption maxima of ^{1}MLCT band for complexes N1-4.

4.3 Photoreactivity of Nitroimidazole-based RPCs

The structures of **N1** and **N2** were assessed by means of X-ray scattering analysis.

The asymmetric unit of **N1** contains one metal complex with one PF_6^- anion as a counterion plus an acetonitrile molecule (Figure 70a), while the one of **N2** features two molecules of the metal complex (**N2A** and **N2B**) counterbalanced by two PF_6^- anions, along with one acetonitrile and two water molecules (Figure 70b).

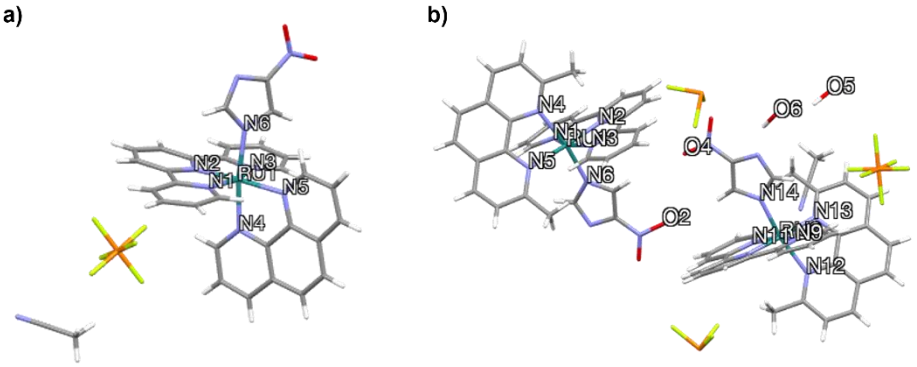

Figure 70: a) Asymmetric unit of ruthenium compound N1; b) asymmetric unit of ruthenium compound N2.

Importantly, the structural analysis demonstrates that the insertion of two bulky methyl groups in the 2 and 9 positions of the dmphen unit causes a distortion of the pseudo-octahedral geometry of **N2** relative to **N1**. These effects can be summarized as follows:

1) significant lengthening of the Ru-dmphen bonds;

2) displacing (tilting) of the dmphen ligand, as indicated by the angles between the mean planes containing the tpy and dmphen, of 62.97° (**N2A**) and 67.36° (**N2B**), compared to 88.78° in **N1**;

3) tilting of the 5NIM toward the N(1) and N(2) atoms of tpy as denoted, for instance, by the N(1)[9]−Ru(1) [2]−N(6)[14] and N(2)[10]−Ru(1)[2]−N(6)[14] angles (numbers in

square brackets refer to **N2B**) which range from 82.93° to 87.51° and thus are smaller than the corresponding ones in **N1**;

4) significative rotation of 5NIM about its Ru−N bond relative to **N1** (Table 16-18). Although they stem from a solid-state analysis, these structural differences may affect, along with the different electronic properties imparted by phen or dmphen, the photoinduced ligand dissociation of complexes.

(a)	**N1**	**N2**A	**N2**B
Ru(1)[2]−N(1)[9]	2.068(3)	2.094(8)	2.07(1)
Ru(1)[2]−N(2)[10]	1.972(3)	1.982(8)	1.94(1)
Ru(1)[2]−N(3)[11]	2.068(3)	2.07(1)	2.06(1)
Ru(1)[2]−N(4)[12]	2.064(3)	2.12(1)	2.12(1)
Ru(1)[2]−N(5)[13]	2.107(3)	2.130(9)	2.11(1)
Ru(1)[2]−N(6)[14]	2.079(3)	2.07(1)	2.08(1)
N(1)[9]−Ru(1)[2]−N(2)[10]	79.86(13)	79.49(37)	80.39(49)
N(1)[9]−Ru(1)[2]−N(3)(11)	158.74(13)	159.00(37)	159.43(43)
N(1)[9]−Ru(1)[2]−N(4)(12)	90.87(12)	86.66(35)	83.58(41)
N(1)[9]−Ru(1)[2]−N(5)(13)	96.77(12)	97.83(35)	100.96(42)
N(1)[9]−Ru(1)[2]−N(6)(14)	93.87(13)	86.20(36)	87.39(39)
N(2)[10]−Ru(1)[2]−N(3)(11)	78.89(13)	79.65(37)	79.11(45)
N(2)[10]−Ru(1)[2]−N(4)(12)	98.27(13)	99.51(35)	102.72(42)
N(2)[10]−Ru(1)[2]−N(5)(13)	175.76(13)	176.73(35)	177.65(45)
N(2)[10]−Ru(1)[2]−N(6)(14)	88.94(13)	87.51(35)	82.93(42)
N(3)[11]−Ru(1)[2]−N(4)(12)	91.51(12)	99.13(36)	99.26(39)
N(3)[11]−Ru(1)[2]−N(5)(13)	104.42(13)	103.10(35)	99.58(38)
N(3)[11]−Ru(1)[2]−N(6)(14)	86.41(12)	90.53(38)	91.78(37)
N(4)[12]−Ru(1)[2]−N(5)(13)	79.12(13)	78.40(34)	79.39(36)
N(4)[12]−Ru(1)[2]−N(6)(14)	171.98(12)	168.91(35)	168.35(37)
N(5)[13]−Ru(1)[2]−N(6)(14)	93.88(13)	94.19(34)	95.18(36)

Table 16: Bond lengths (Å) and angles for complexes N1 and N2.

	N1	**N2**A	**N2**B
N(2)-Ru(1)-N(6)-C(29)	-129.7(3)		
N(2)-Ru(2)-N(6)-C(31)		53(1)	
N(10)-Ru(2)-C(63)			-54(1)
N(10)-Ru(2)-C(64)			125(1)

*Table 17: Dihedral angles (°) for complex **N1** and **N2**.*

Mean Planes			
Terpyridine (a)			
Phenanthrene (b)			
5NIMH (c)			
	N1	**N2**A	**N2**B
a-b	88.78(14)	62.97(16)	67.36(20)
a-c	87.33(11)	87.61(29)	82.40(32)
b-c	54.03(13)	33.60(29)	47.53(35)

*Table 18: Mean planes and angles between ruthenium compounds **N1** and **N2**.*

The effective capacity of complexes **N2-4** to undergo photosubstitution reactions, as opposed to **N1,** were explored by coupling UV-vis and HPLC analysis. In the dark, UV-Vis measurements reveal a remarkable stability of each complex both in acetonitrile and phosphate buffer saline at pH 7.4 (Figure 71), likely due to the deprotonated nature of the coordinated nitroimidazole ligand.[157]

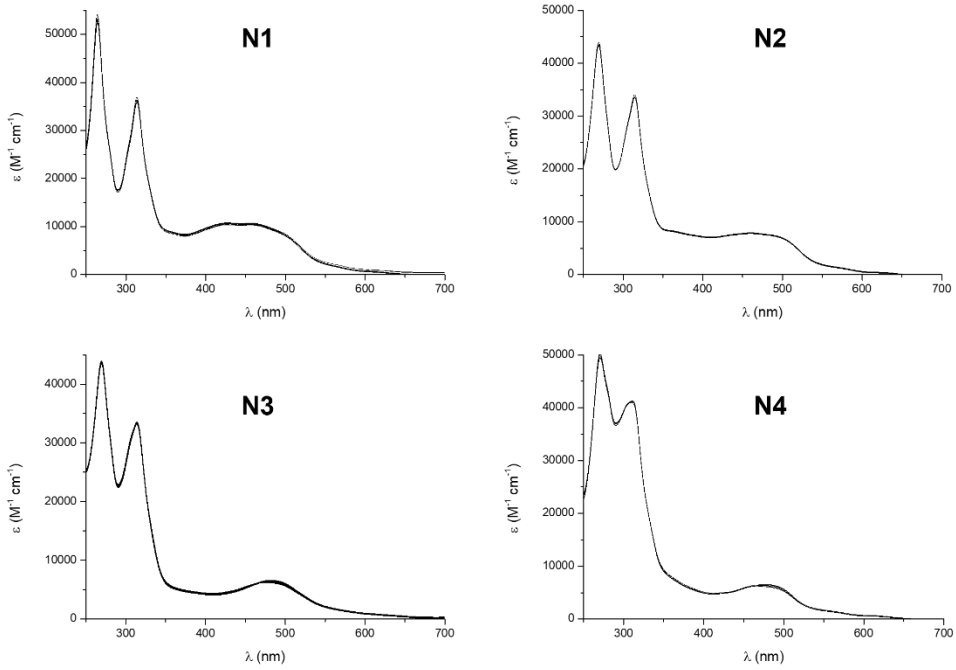

*Figure 71: Electronic absorption spectra of **N1-4** in phosphate buffer saline (PBS, pH 7.4) collected under dark condition over a total period of 72 h. ([**N1-4**] = 10 μM).*

Conversely, light irradiation (LED emitting at 434 nm, 160 mW) of both acetonitrile and aqueous solutions provokes a sharp blue shift in the MLCT absorption maximum of compounds **N2-4** (Figure 73b-c), indicating the replacement of nitroimidazole-containing ligand by acetonitrile to give $[Ru(tpy)(dmphen)(CH_3CN)]^{2+}$ (Figure 72); a similar behaviour is also found for aqueous solution of **N2-4** at neutral pH.[157] No changes are instead observed for complex **N1** (Figure 73a), thus confirming that the different stereoelectronic properties imparted by phen and dmphen are crucial for the photoreactivity of the resulting complexes.

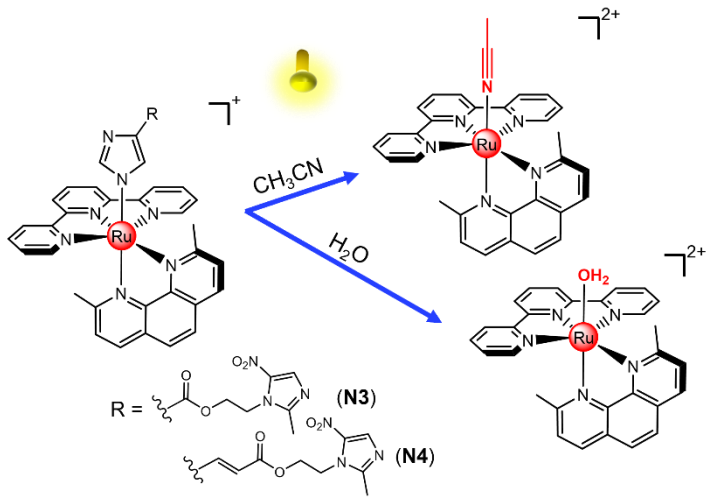

*Figure 72: Sketch of the ligand photoejection processes proposed for **N2-4** in acetonitrile and aqueous solution.*

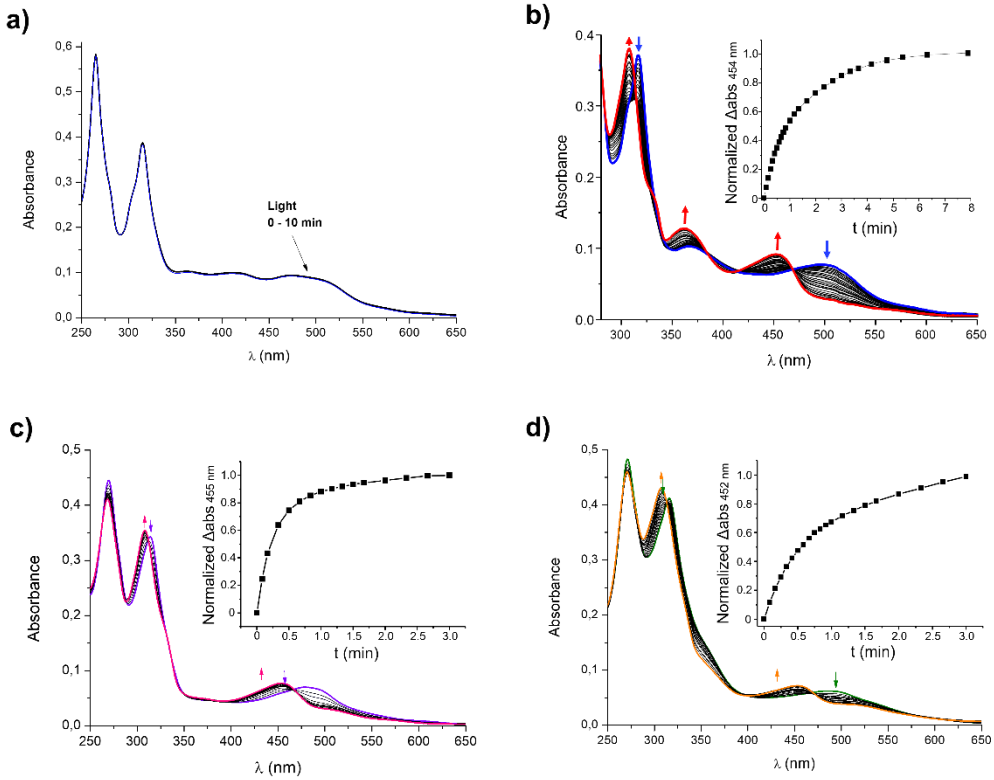

*Figure 73: Electronic absorption spectra of **N1-4** in acetonitrile collected at different irradiation times with a LED lamp (λ_{max} 434 nm, 160 mW) of complexes a) **N1**, b) **N2**, c) **N3** and d) **N4**. ([**N1-4**] = 10 μM).*

Parallel HPLC experiments evidence the selectivity of the photoejection process both in acetonitrile and aqueous neutral solution.[157] As shown by chromatograms in Figure 74, which report HPLC titrations for complexes **N2-4** in water at neutral pH subjected to progressive irradiation times, in each case the peaks attributed to nitroimidazole-ligands (**5NIMH**, **MTZ-1** and **MTZ-2**) and to the ruthenium photoproduct $[Ru(tpy)(dmphen)H_2O]^{2+}$ increase and the ones attributed to **N2-4** decrease, while no evidence of free dmphen and/or tpy is observed (retention times in Table 19).

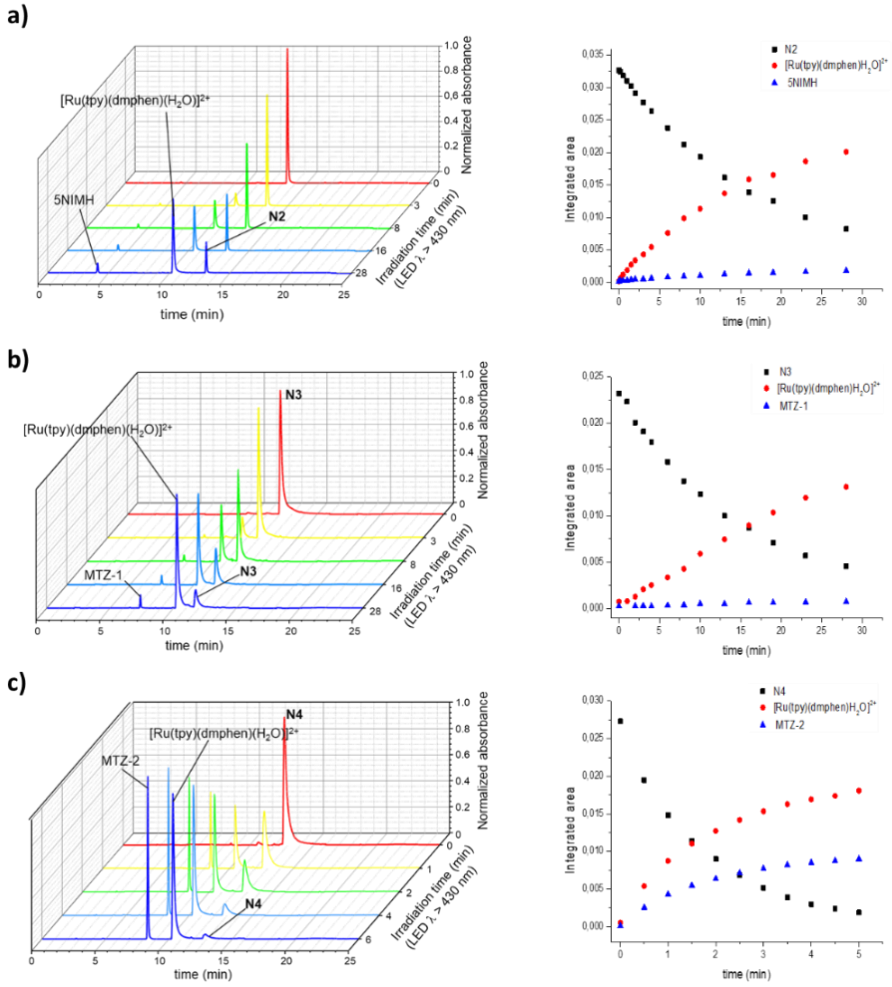

*Figure 74: HPLC chromatograms along with the time trends of integrals underlying by chromatographic peaks in aqueous solution with 10% of dimethyl sulfoxide at neutral pH subjected to progressive irradiation time for complex a) **N2**, b) **N3** and c) **N4**.*

Compound	*Retention time (min)*
N2	13.33
N3	11.77
N4	12.78
[Ru(tpy)(dmphen)H_2O]$^{2+}$	10.35
5NIMH	4.91
MTZ-1	7.42
MTZ-2	8.53

Table 19: Table of the retention times in the experimental set up utilized for HPLC titrations.

Following the determination of photon flux of the LED light source used by the potassium ferrioxalate actinometry (see Experimental for details), UV-Vis and HPLC titrations were used to determine the quantum yields of ligands photodissociation ($\phi_{434\ nm}$) for complexes **N2-4** in acetonitrile and water at neutral pH according to methods reported in literature (see Experimental for details).[167] The resulting values are summarized in Table 20.

In acetonitrile, the uncaging of metronidazole derivatives **MTZ-1** and **MTZ-2** is slightly more efficient (*ca*. 2-fold) if compared to the photorelease of **5NIMH** from the same ruthenium scaffold (ϕ_{434} values of 0.0079(9) for **N3**, 0.0059(4) for **N4**, and 0.0039(3) for **N2** respectively). Lower quantum yields are instead registered in aqueous solutions, according to the higher efficiency of photolysis in the former medium, with **N4** being the most efficient (ϕ_{434} = 0.0015(2)). Additionally, it should be noted that the **N2-4** values for ϕ_{434} are at least one order of magnitude lower if compared to the parental compound [Ru(tpy)(dmphen)(py)]$^{2+}$ (py = pyridine), whose light-induced release of a py unit in acetonitrile is reported to take place with a ϕ_{436} of 0.059.[168] Contrarily, the lower photoreactivity of **N2-4** is counterbalanced by their remarkable stabilities in dark conditions (Figure 71), in accordance with the inverse relationship between ϕ_{PS} and thermal stability mentioned most recently by Glazer and coworkers in their description of other ruthenium polypyridyl based photocages.[168]

These data point out that the photoinduced ejection of potentially bioactive compounds can be conveniently controlled by employing imidazole-based moieties as linking units to Ru(II) centers. Besides the most popular class of molecules studied for this purpose, such as pyridine,[169] pyrazine,[167] thiols,[170] and nitriles,[171] the use of imidazolate ligands as caging groups in PACT has never been investigated so far and it holds great promise for the design of challenging Ru(II) photocages with an appropriate quantum yield of photo-ejection (Φ_{PS}) without a concomitant loss in thermal stability.

Complex	*Φ_{434} in CH_3CN* [a]	*Φ_{434} in H_2O* [a]
N2	0.0039(3)	0.0011(3)
N3	0.0079(9)	0.00027(2)
N4	0.0059(4)	0.0015(2)

Table 20: Photoinduced ligand substitution quantum yields (Φ_{434}) for N2-4. [a]Determined through UV-vis measurements and [b] Determined by HPLC analysis.

4.4 Antibacterial activity

The antibacterial activities of ruthenium complexes **N2-4**, in comparison with their corresponding imidazole-based ligands (**5NIMH**, **MTZ-1**, **MTZ-2**), were investigated both in aerobiosis and anaerobiosis on *Bacillus subtilis* strain 168, chosen as a model of Gram-positive bacteria. **MTZ** was also tested for comparison. Experiments were carried out both in dark and following blue light irradiation (λ_{max} = 434 nm, t = 40 min) using a anaerobiosis jar specifically designed engineered with a LED illumination device, whose photon flux were determined by potassium ferrioxalate actinometry (see Experimental for details).[167] Reproducing the experimental setup of the antibacterial activity tests, the photon flux in each plate well was determined to be 4.72×10^{-9} E/s (Power 1.25 mW) (Figure 75).

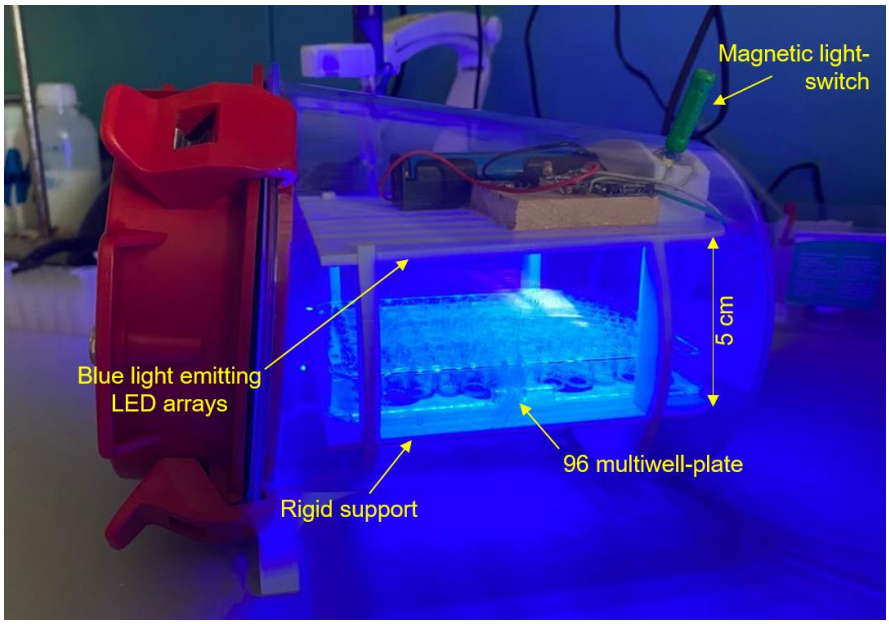

Figure 75: Engineered anaerobiosis jar with LED illumination (λ_{max} = 434 nm) used to perform antibacterial activity assays. The photograph illustrates the experimental set up adopted in the measurements.

Figure 76 and Figure 77 show the results obtained in aerobic and anerobic conditions, respectively. In aerobiosis, all the tested compounds display negligible toxicity in the dark, except for **MTZ** and **MTZ-2**, which show a significant inhibition of bacterial growth starting at relatively high drug doses (200 µM) and lead to a more marked effect (*ca.* 75% reduction of cell growth) at 300 µM. Parallelly, irradiation does not significantly improve the toxicity of tested compounds in aerobiosis. Only modest phototoxicity is observed for ruthenium compounds at high concentrations, with **N4** being the most effective, leading to a *ca*. 40% reduction of cell growth at the highest dose tested of 300 µM (Figure 76). A completely different scenario is instead observed in the experiments performed under anaerobic conditions. Indeed, as shown in Figure 77, both the newly synthesized metronidazole derivatives, **MTZ-1** and **MTZ-2**, exhibit a sharp dose-dependent activity in dark conditions. Of particular relevance, **MTZ-2** displays the highest potency, being comparable to Metronidazole. For instance, at a concentration

of 100 µM **MTZ** and **MTZ-2** induce a reduction of cell growth equal to or superior to 75%, whereas a lower, but remarkable effect (*ca*. 50%), is found for **MTZ-1** at the same dose. Worth of noting, even the less potent **5NIMH** exhibits a net dose-dependent activity, in contrast to the low efficacy seen in aerobic conditions (Figure 77).

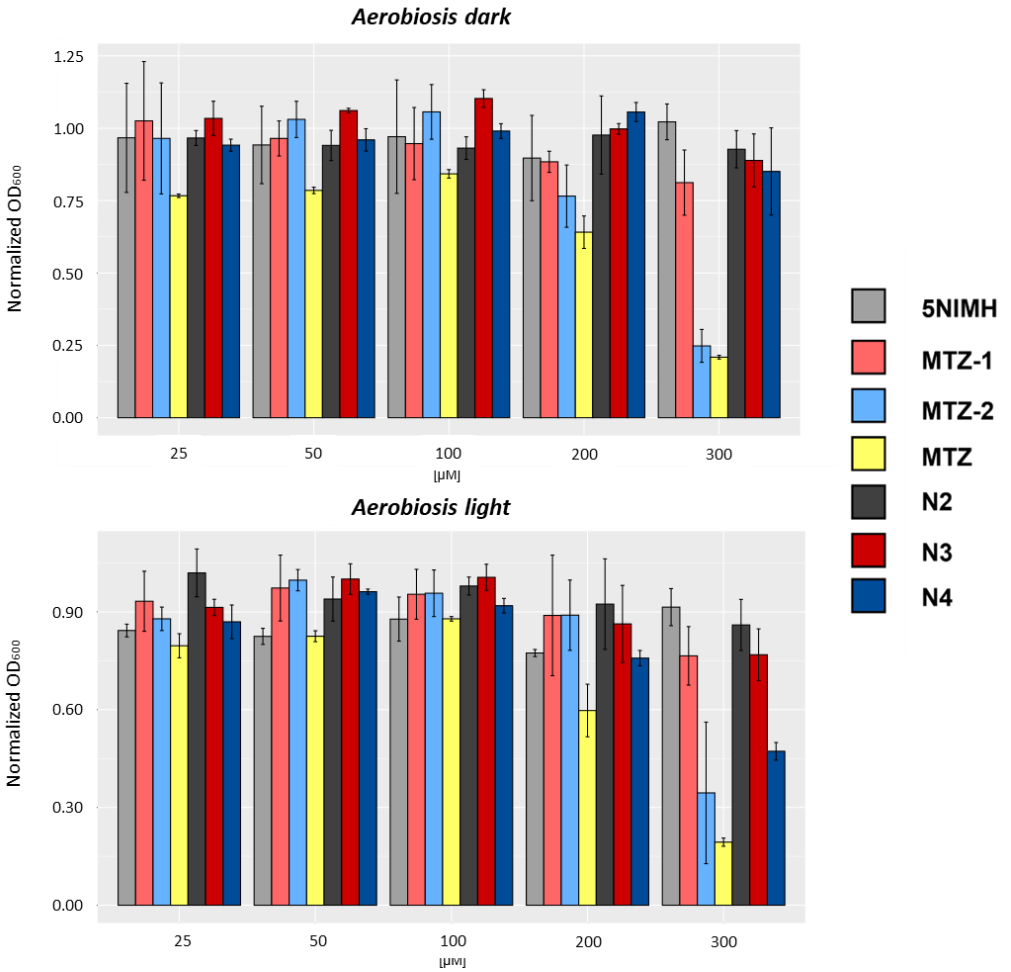

*Figure 76: Antibacterial effect of **N2-4**, their corresponding imidazole-based ligands **5NIMH**, **MTZ-1** and **MTZ-2**, and **MTZ** evaluated in dark and following light-activation under aerobic conditions. Ratios of the normalized OD_{600} values are reported with respect to blank control (Y-axis) as a function of different drug concentrations ([µM], X-axis).*

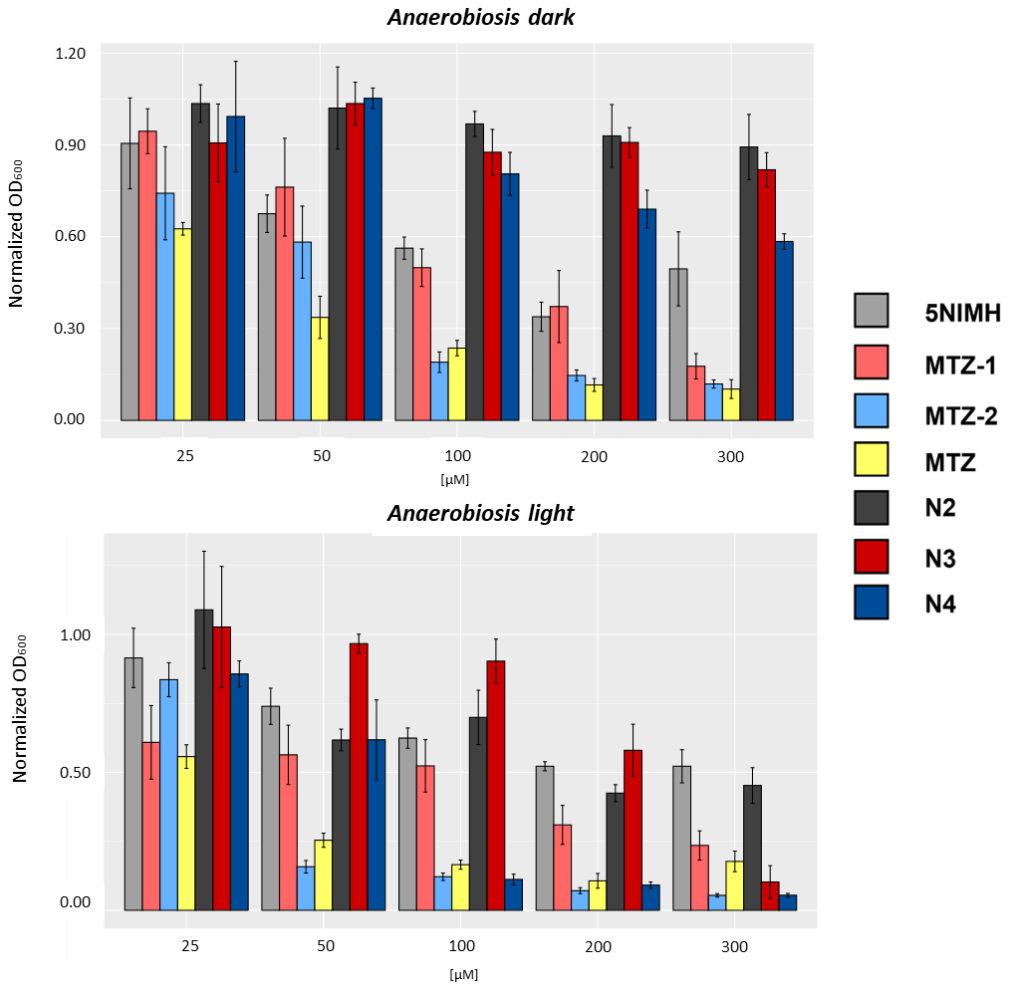

*Figure 77: Antibacterial effect of **N2-4**, their corresponding imidazole-based ligands **5NIMH**, **MTZ-1** and **MTZ-2**, and **MTZ** evaluated in dark and following light-activation under anaerobic conditions. Ratios of the normalized OD_{600} values are reported with respect to blank control (Y-axis) as a function of different drug concentrations ([µM], X-axis).*

It is possible to explain the greater activity of nitroimidazole compounds reported in anaerobic conditions by taking into account the well acknowledged mechanism of action of these classes of antibiotics.[158]

When considering complexes **N2-4,** is found that in dark, they are well tolerated by cells, with **N4** possessing the highest toxicity that does not exceed a *ca*. 48% reduction of cell

viability at the maximum dose tested (300 µM). Conversely, light irradiation unleashes the bactericidal potential of **N2-4**, which feature a sharp light-triggered dose-dependent effect, with **N4** being the most potent compound across the series with a growth reduction of *ca*. 88% at 100 µM. Lower, despite being remarkable, phototoxicities are displayed by **N2** and **N3**, with **N3** that is the most effective in the 0-200 µM range. These results highlight that **N2-4** allow to reproduce the effectiveness of **5NIMH**, **MTZ-1** and **MTZ-2** compounds but with the key advantage arising from the spatio-temporal control over the drug activation ensured by light.

Lastly, it is generally accepted that bactericidal resistance to nitroimidazole-based antibiotics is related to decreased drug uptake and/or altered/deficient reduction efficiency of the nitro group. Regarding the latter, it has been discovered that various types of resistant bacterial strains possess Nim genes, which encode for reductase enzyme capable of converting the nitro group into a non-bactericidal amine and thus preventing the accumulation of the toxic nitro radical. More in detail, a previous study reporting on the crystal structure of NimA from *Deinococcus radiodurans* (drNimA) complexed with MTZ,[172] proposed that the inactivation of this antibiotic would be the result of a 2-electron reduction process occurring in the active site of the protein and being mediated by the covalent binding of the cofactor pyruvate with His-71. Therefore, being inspired by these findings, we further considered the interaction of the newly synthesized MTZ-derivatives with the active site of NimA, which was selected as a representative model for this family of reductases. To this aim, the molecular structure of **MTZ**, **MTZH-1**, and **MTZH-2** were optimized with DFT calculations at B3LYP/6-31+G(d) level of theory. The obtained results, shown in Figure 78a, evidenced an intramolecular hydrogen bond between the -NO_2 group and the nearest hydrogen atom of a -CH_2 residue (in agreement with experimental structure of MTZ available in the PDB file 1W3R), in good agreement with the X-Ray data for **MTZH-2** (data not

shown). The intramolecular hydrogen bond reduces the mobility of the MTZ ring moiety with respect to the substituents. When the ring of each compound was superimposed on the MTZ in 1W3R in NimA (Figure 78b) it was observed that the rigidity imparted by the intramolecular interactions combined with the more extended chains gathered on the ester functions of **MTZH-1** and **MTZH-2** made these compounds clash to NimA protein structure, whereas **MTZ** is nicely accommodated within the active site of the protein. Therefore, these preliminary data suggest that the different chemical structures of the two MTZ-derivatives would impart lower susceptibility to drug inactivation by NimA and hint at their possible use as potential options for clinicians to manage resistance to nitroimidazole-based antibiotics.

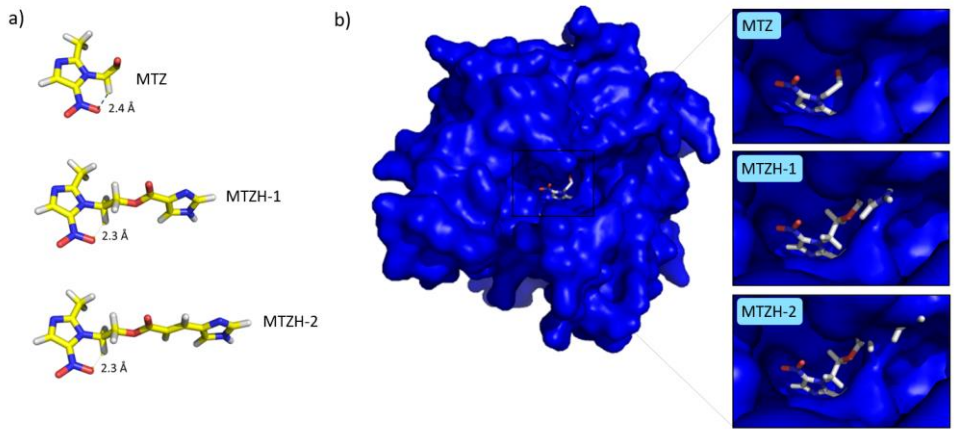

*Figure 78: Experimental **MTZ** structure in 1W3R PDB file and optimized **MTZH-1** and **MTZH-2** structures computed through DFT calculations (a) and **MTZ**, **MTZ-1** and **MTZ-2** ligands interacting with NimA protein (in blue the surface of the protein) (b)*

Acknowledgments

A special thanks goes to all the collaborators who contributed to the results reported in this chapter. In particular, to Prof. Alessio Mengoni and Dr. Camilla Fragozi for having optimized the antibacterial activity assays in aerobiotic/anaerobiotic condition. A heartfelt thank you to Ing. Matteo Giacomazzo for the design and realization of the illumination device for antibacterial tests in anaerobic condition. Some of the results reported here have already been published as follows:

Giacomazzo G. E., Conti L., Guerri A., Pagliai M., Fagorzi C., Severin Sfragano P., Palchetti I., Pietraperzia G., Mengoni A., Valtancoli B., Giorgi C.; Nitroimidazole-based ruthenium(II) complexes: playing with structural parameters to design photostable and light-responsive antibacterial agents; *Inorg. Chem.*, ***2021***, 61, 18, 6689-6694 DOI: 10.1021/acs.inorgchem.1c03032

Giacomazzo G. E., Conti L., Fagorzi C., Pagliai M., Andreini C., Guerri A. Perito B., Mengoni A., Valtancoli B., Giorgi C.; Ruthenium(II) Polypyridyl Complexes and Metronidazole Derivatives: A Powerful Combination in the Design of Photoresponsive Antibacterial Agents Effective under Hypoxic; Conditions *Inorg. Chem.* ***2023*** DOI: 10.1021/acs.inorgchem.3c00214

EXPERIMENTAL SECTION

Numbering example

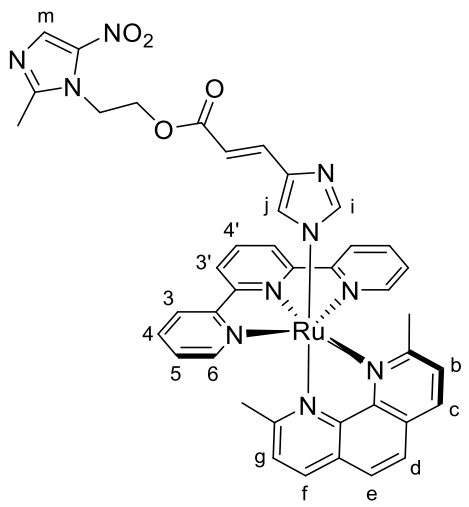

Synthesis of 20

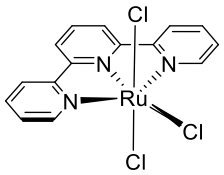

Complex **20** was synthesized according to previously reported procedure.[161] To a solution of ruthenium chloride trihydrate (179 mg, 0.86 mmol) in 43 mL of ethanol was added 2,2':6',2''-terpyridine (200 mg, 0.86 mmol). The reaction mixture was heated to reflux and stirred for 5 h. After cooling at r.t., the formed precipitate was collected by filtration washing with ethanol, water and diethyl ether. Compound **20** was obtained as brown solid and used in following synthetic steps without further purification. Yield 67%.

Synthesis of 21

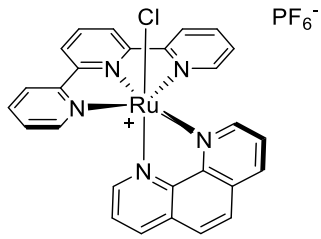

Complex **21** was synthesized according to previously reported procedure.[161] To a solution of **20** (130 mg, 0.29 mmol) in 72 mL of a mixture of ethanol-water (2:1) were added 1,10-phenantroline (58.5 mg, 0.29 mmol), TEA (0.41 mL, 2.9 mmol) and LiCl (55.3 mg, 1.3 mmol). The reaction mixture was stirred at reflux for 4 h. After cooling to r.t., a saturated solution of KPF_6 was added. The precipitate was collected by filtration washing with water, ethanol, and diethyl ether to obtain complex **21** as black-reddish solid with a yield of 94%. ^{1}H-NMR (400 MHz, (CD3)2CO): δ 10.57 (d, J=4.6 Hz, 1H, **Ha**), 9.01 (d, J=8.0 Hz, 1H, **He** o **Hd**), 8.80 (d, J=8.1 Hz, 2H, **H3'**), 8.65 (d, J=8.0 Hz, 2H, **H3**), 8.50-8.46 (m, 2H, **Hb**, **He** o **Hd**), 8.42 (d, J=8.0 Hz, 1H, **Hh**), 8.29-8.23 (m, 2H, **Hc** e **H4'**),

8.00 (m, 3H, **H4** e **Hf**), 7.72 (d, J=5.2 Hz, 2H, **H6**), 7.49 (dd, J1= 8.1 J2=5.4, 1H, **Hg**), 7.31-7.25 (m, 2H, **H5**) ppm. ^{13}C-NMR (100 MHz, (CD3)2CO): δ158.9, 158.3, 153.3, 152.7, 152.5, 149.2, 147.4, 136.9, 135.5, 134.4, 133.6, 130.8, 130.4, 128.1, 127.5, 127.1, 125.9, 125.1, 123.4, 122.4 ppm.

Synthesis of 22

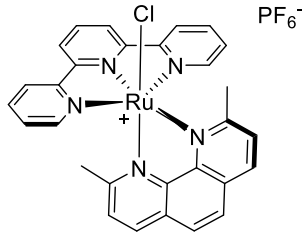

Compound **22** was synthesized according to previously reported procedure.[161] To a solution of **20** (197 mg, 0.45 mmol) in 75 mL of a mixture of ethanol-water (2:1) were added 2,9-methyl-1,10-phenantroline (94 mg, 0.45 mmol), TEA (0.62 mL, 4.5 mmol) and LiCl (86 mg, 2.03 mmol). The reaction mixture was stirred at reflux for 4 h protecting by light. After cooling to r.t., a saturated solution of KPF_6 was added. The precipitate was collected by filtration washing with water, ethanol and diethyl. The crude product was solubilized in dichloromethane (150 mL), filtered on cotton and washed with HCl 0.1 M (30 mL × 5). The organic phase was dried with Na_2SO_4 and concentrated to dryness to obtain **22** as black-violet solid with a yield of 78%. ^{1}H-NMR (400 MHz, (CD3)2CO): δ 8.83 (d, J=8.3 Hz, 1H, **He** o **Hd**), 8.72 (d, J=8.1 Hz, 2H, **H3'**), 8.62 (d, J=8.0 Hz, 2H, **H3**), 8.31 (d, J=8.7 Hz, 1H, **Hb** o **Hc**), 8.27 (d, J=8.2 Hz, 1H, **Hg** o **Hf**), 8.20-8.16 (m, 2H, **H4'** , **He** o **Hd**), 8.09 (d, J=8.7 Hz, **1H, Hb** o **Hc**), 8.00 (dd, J1=8.0 J2=1.2 Hz, 2H, **H4**), 7.91 (d, J=5.4 Hz, 2H, **H6**), 7.36 (m, 2H, **H5**), 7.32 (d, J=8.2 Hz, 1H, **Hg** o **Hf**), 3.63 (s, 3H, -CH_3 dmphen), 1.88 (s, 3H, -CH_3 dmphen) ppm. ^{13}C-NMR (100 MHz, (CD3)2CO): δ 168.8, 166.5, 160.2, 159.9, 153.1, 149.6, 148.3, 136.9, 136.4, 135.4, 133.8, 129.0, 129.0, 128.9, 127.1, 127.0, 126.9, 126.4, 125.8, 123.4, 122.3, 23.4 ppm.

Synthesis of MTZ-1

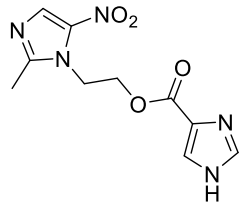

To a solution of 1*H*-imidazole-5-carboxylic acid (300 mg, 2.68 mmol) in 4 mL of anhydrous DMF were added N,N'-dicycloexylcarbodiimide (458 mg, 2.95 mmol) and DMAP (66 mg, 0.54 mmol). After stirring for 20 min at 45°C, 2-nitro-5-methyl-1*H*-imidazolyl (metronidazole) (493 mg, 2.68 mmol) was added and the reaction mixture was stirred at 45°C over 2 days. The solvent was removed in vacuum and the oily residue was dissolved in 200 mL of CH_2Cl_2 and washed twice with 30 mL of H_2O and once with 20 mL of a saturated solution of NaCl. Organic phase was dried over Na_2SO_4 and evaporated under reduced pressure. The crude product was purified on silica gel using CH_2Cl_2 : MeOH (from 15:1 to 10:1) as eluent. Yield 18 %. ^{1}H-NMR (400 MHz, CD_3OD): 7.95 (s, 1H, Hm), 7.80(s, 1H, Hi) 7.73 (s, 1H, Hj), 4.78 (t, 2H, J=5.2 Hz, -CH_2), 4.71 (t, 2H, J=4.8 Hz, -CH_2), 2.51 (s, 3H, CH_3) ppm. ^{13}C-NMR (100 MHz, CD_3OD): 151.8, 139.5, 137.9, 131.9, 62.3, 45.8, 13.2 ppm. ESI-MS: m/z calcd for $C_{10}H_{11}N_5O_4$ $[M]^+$: 265.08; found: 288.08 [M + Na^+] and 552.83 [2M + Na^+].

Synthesis of MTZ-2

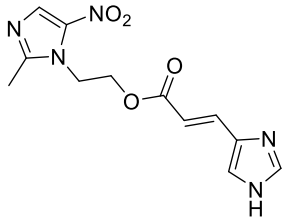

To 5-imidazoleacryl acid (Urocanic acid) (300 mg, 2.17 mmol) dissolved in 5 mL of anhydrous DMF were added N,N'-dicycloexylcarbodiimide (370 mg, 2.39 mmol) and

DMAP (54 mg, 0.44 mmol). After stirring for 15 min at r.t., 2-nitro-5-methyl-1*H*-imidazolyl (metronidazole) (399 mg, 2.17 mmol) was added and the reaction mixture was stirred at 45°C over 4 days. The solvent was removed in vacuum and the oily residue was dissolved in 200 mL of CH_2Cl_2 and washed twice with 30 mL of H_2O and once with 20 mL of a saturated solution of NaCl. Organic phase was dried over Na_2SO_4 and evaporated under reduced pressure. The crude product was purified on silica gel using CH_2Cl_2 : MeOH (from 20:1 to 10:1) as eluent. Yield 26 %. ^{1}H-NMR (400 MHz, $(CD_3)_2SO$): 8.05 (s, 1H, Hm), 7.80 (s, 1H, Hi), 7.56 (s, 1H, Hj) 7.49 (d, J = 15.6 Hz, 1H, -CH), 6.27 (d, J=15.6, 1H, -CH), 4.65 (t, J=4.8 Hz, 2H, -CH_2), 4.49 (t, J=4.8 Hz, 2H, -CH_2), 2.48 (s, 3H, -CH_3). ^{13}C-NMR (100 MHz, $(CD_3)_2SO$): 167.2, 152.5, 139.6, 139.0, 134.1, 113.4, 62.9, 46.0, 15.0 ppm. ESI-MS: m/z calcd for $C_{12}H_{13}N_5O_4$ $[M]^+$: 291.09; found: 314.17 $[M + Na^+]$.

Synthesis of N1

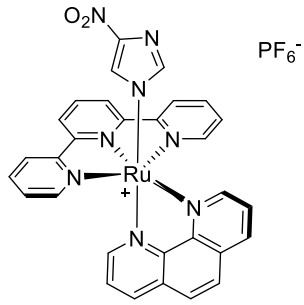

A solution of 5-nitroimidazole (158 mg, 1.40 mmol) in 20 mL of ethanol-water mixture (50% v/v) was added dropwise to a solution of **21** (100 mg, 0.14 mmol) in 30 mL of the same solvent mixture. The reaction mixture was stirred at reflux for 16 hours under N_2 atmosphere covering from light. After cooling at r.t., the ruthenium compound was precipitated by the addition of 7 mL of 0.1 M aqueous solution of KPF_6 and the solvent was reduced up to 1/3. The precipitate was solubilized and extracted in dichloromethane (2 x 50 mL). The organic phases were collected and washed with water (6 x 20 mL) and once with BRINE (20 mL). The organic phase was dried over

Na_2SO_4 and concentrated to drynessto afford **N1**. The crude product was purified by flash chromatography on silica gel (DCM:MeOH 40:1 with 10% of Acetone) to obtain 63 mg (0.082 mmol) of complex **N1** as a red solid. Yield 58%. ^{1}H-NMR (400 MHz, $(CD_3)_2CO$): δ 9.14 (d, J_{a-b}=4.8 Hz, 1H, **Ha**), 9.03 (d, J_{c-b}=8.0 Hz, 1H, **Hc**), 8.85 (d, $J_{3'-4'}$=8.0 Hz, 2H, **H3'**), 8.76 (d, J_{3-4}=8.0 Hz, 2H, **H3**), 8.57 (d, J_{h-g}=8.0 Hz, 1H, **Hh**), 8.51 (d, J=8.8 Hz, 1H, **Hd** o **He**), 8.39 (dd, J_{b-c}=8.0 J_{b-a}=5.6 Hz, 1H, **Hb**), 8.36-8.28 (m, 2H, **H4'**, **Hd** o **He**) 8.17-8.10 (m, 2H, **H4**), 8.08 (d, J=4.8 Hz, 1H, **Hf**), 7.97 (d, J_{6-5}=5.2 Hz, 2H, **H6**), 7.61 (dd, J_{g-h}=8.0 J2=5.2 Hz, 1H, **Hg**), 7.47-7.41 (m, 2H, **H5**), 6.81 (s, 1H, **Hi** o **Hj**), 6.35 (s, 1H, **Hi** o **Hj**) ppm. ^{13}C-NMR (100 MHz, $(CD_3)_2CO$): δ 159.2, 158.4, 153.6, 153.1, 152.8, 148.6, 147.7, 143.8, 138.6, 136.7, 136.4, 135.3, 131.8, 131.1, 128.8, 128.7, 128.4, 127.1, 125.9, 124.9, 123.8 ppm. HR-MS (ESI+): m/z calcd for $C_{30}H_{21}N_8O_2Ru$ $[M]^+$ 627.0831 found: 627.0872.

Synthesis of N2

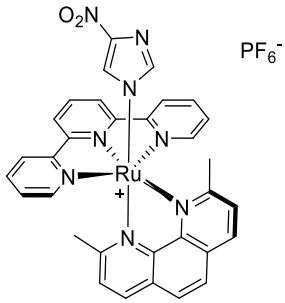

A solution of 5-nitroimidazole (320 mg, 2.83 mmol) in 40 mL of ethanol-water mixture (50% v/v) was added dropwise to a solution of **22** (205 mg, 0.28 mmol) in 60 mL of the same solvent mixture. The reaction mixture was stirred at reflux for 16 hours under N_2 atmosphere protecting by light. After cooling at r.t., the ruthenium compound was precipitated with 11 mL of aqueous solution of KPF_6 0.1 M and the solvent was reduced up to 1/3. The precipitate was solubilized and extracted in dichloromethane (2 x 70 mL) and the organic phases were collected and washed with water (6 x 30 mL) and BRINE (30 mL). The organic phase was dried on Na_2SO_4 and concentrated to dryness to afford

N2 as a red solid. The crude was purified by flash chromatography on silica gel (DCM:MeOH 40:1 with 10% of acetone) to obtain 78 mg (0.097 mmol) of complex **N2** as a red solid. Yield 35%. ^{1}H-NMR (400 MHz, $(CD_3)_2CO$): δ 8.87 (d, J=8.4 Hz, 1H, **He** o **Hd**), 8.81-8.71 (br, 4H, **H3** e **H3'**), 8.42 (d, J=8.3 Hz, 1H, **Hf** o **Hg**), 8.38 (d, J=8.7 Hz, 1H, **Hb** o **Hc**), 8.26-8.11 (m, 7H, **H4**, **H4'**, **H6, Hd/e, Hb/c**), 7.57-7.49 (br, 2H, **H5**), 7.44 (d, J=8.3 Hz, 1H, **Hf** o **Hg**), 6.57 (s, 1H, **Hi** o **Hj**), 6.14 (s, 1H, **Hi** o **Hj**), 2.42 (s, 3H, -CH_3 dmphen), 1.94 (s, 3H, -CH_3 dmphen) ppm. ^{13}C-NMR (100 MHz, $(CD_3)_2CO$): δ 167.8, 166.6, 159.8, 159.6, 149.0, 148.8, 143.2, 138.7, 137.5, 137.3, 135.4, 130.0, 129.7, 128.9, 128.2, 127.6, 127.4, 127.0, 126.9, 124.9, 124.0, 25.0, 24.0 ppm. HR-MS (ESI+): m/z calcd for $C_{32}H_{25}N_8O_2Ru$ $[M]^+$ 655.1144 found: 655.1186.

Synthesis of N3

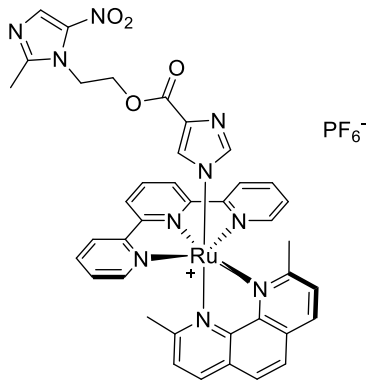

To a solution of **22** (180 mg, 0.25 mmol) in 60 mL of degassed H_2O-EtOH (50:50 % v/v) was added compound **MTZ-1** (80 mg, 0.30 mmol). The reaction mixture was stirred at 70°C for 6 hours under N_2 atmosphere and protecting by light. After cooling at r.t., addition of a saturated KPF_6 aqueous solution and evaporation of EtOH determined the precipitation of the complex that is collected by filtration at reduced pressure and washed with water. The crude product was purified by flash chromatography on silica gel (DCM:MeOH 20:1 with 10% Acetone) to obtain 130 mg of complex **N3** as a red solid. Yield 64%. ^{1}H-NMR (400 MHz, $(CD_3)_2CO$): δ 8.90 (d, J = 8.4 Hz, 1H, Hd or He), 8.86-8.70

(m, 4H, H3' and H3), 8.43 (d, J = 8.0 Hz, 1H, Hf or Hg), 8.40 (d, J = 8.8 Hz, 1H, Hb or Hc), 8.30 (t, J = 8.0 Hz , 1H, H4'), 8.26-8.04 (m, 6H, Hd or He, Hb or Hc, H6, H5), 7.90 (s, 1H, Hm), 7.56 (br, 2H, H4), 7.44 (d, J = 8.0 Hz, 1H, Hf or Hg), 7.24 (s, 1H, Hi), 6.51 (s, 1H, Hj), 4.68 (t, J = 5.2 Hz, 2H, -CH_2 MTZ-1), 4.51 (t, J = 5.2 Hz, 2H, -CH_2 MTZ-1), 2.45 (s, 3H, -CH_3 MTZ-1), 2.32 (s, 3H, CH_3 dmphen), 1.94 (s, 3H, CH_3 dmphen) ppm. ^{13}C-NMR (100 MHz, $(CD_3)_2CO$): δ 167.5, 166.9, 159.7, 159.6, 159.0, 154.3, 151.8, 149.1, 148.7, 142.6, 139.2, 137.7, 137.6, 136.2, 133.3, 132.6, 130.1, 129.7, 129.3, 128.3, 127.7, 127.5, 127.1, 126.6, 125.3, 124.4, 63.2, 55.1, 45.2, 25.5, 23.9, 14.1 ppm. HR-MS (ESI+): m/z calcd for $C_{39}H_{33}N_{10}O_4Ru$ $[M]^+$: 807.17243; found: 807.17124 $[M]^+$, 404.09067 $[M^+ + H^+]$.

Synthesis of N4

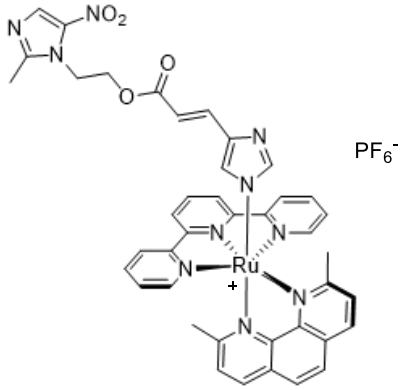

To a solution of **22** (150 mg, 0.21 mmol) in 60 mL of degassed H_2O-EtOH (50:50 % v/v) was added compound **MTZ-2** (73 mg, 0.25 mmol). The reaction mixture was stirred at 70°C for 7 hours under N_2 atmosphere and protecting by light. After cooling at r.t., addition of a saturated KPF_6 aqueous solution and evaporation of EtOH determined the precipitation of the complex that is collected by filtration at reduced pressure and washed with water. The crude product was purified by flash chromatography on silica gel (DCM:MeOH 15:1 with 10% Acetone) to obtain 112 mg of complex **N4** as a red solid. Yield 62%.

^{1}H-NMR (400 MHz, $(CD_3)_2CO$): δ 8.90 (d, J = 8.8 Hz, 1H, Hd or He), 8.81 (d, J = 8.8 Hz, 2H, H3'),8.75 (d, J = 7.2 Hz, 2H, H3), 8.43 (d, J = 8.8 Hz, 1H, Hf or Hg), 8.38 (d, J = 8.8 Hz, 1H, Hb or Hc), 8.32 (t, J = 8.4 Hz, 1H, H4'), 8.25-8.03 (m, 6H, Hd or He, Hb or Hc, H4, H6), 7.88 (s, 1H, Hm), 7.54 (br, 2H, H5), 7.45 (d, J = 8.4 Hz, 1H, Hf or Hg), 7.39 (s, 1H, Hi), 7.23 (d, J = 17.2 Hz, 1H, -CH MTZ-2), 6.73 (s, 1H, Hj), 6.15 (d, J = 16.4 Hz, 1H, -CH MTZ-2), 4.71 (t, J = 5.2, 2H, $-CH_2$ MTZ-2), 4.52 (t, J = 4.8 Hz, 2H, $-CH_2$ MTZ-2), 2.56 (s, 3H, $-CH_3$ MTZ-2), 2.44 (s, 3H, $-CH_3$ dmphen), 1.95 (s, 3H, $-CH_3$ dmphen) ppm.

^{13}C-NMR (100 MHz, $(CD_3)_2CO$): δ 167.4, 167.0, 165.7, 159.7, 154.4, 151.8, 149.1, 148.7, 139.2, 137.7, 137.6, 136.4, 129.2, 128.3, 127.6, 127.5, 127.1, 125.3, 124.4, 117.3, 63.0, 45.5, 25.6, 24.0, 14.0 ppm.

HR-MS (ESI+): m/z calcd for $C_{41}H_{35}N_{10}O_4Ru$ $[M]^+$: 833.18808; found: 833.18796 $[M^+]$, 417.09812 $[M^+ + H^+]$.

Instrumentation

NMR spectra were collected with a Bruker 400 MHz spectrometer. Electronic absorption spectroscopy was performed by using a PerkinElmer Lambda 6 spectrophotometer in a 1×1 cm quart cuvette. HPLC analysis were performed on a Water Alliance 2690 HPLC equipped with a Waters 2487 Abs UV-Vis detector set at 270 nm and a KROMASIL 100 Å C-18 150 × 4.6 column. In the determination of inhibitory concentration, the OD 600 values were registered by using an Infinite Pro 200 plate reader (Tecan, Switzerland); the experiments performed under anaerobic conditions were conducted in an anaerobiosis jar (Oxoid jar with Anaerogen 2.5 L), with the system described in paragraph 4.4.

X Ray crystallography

X-ray data collections for compounds **N1** and **N2** were both performed with a Bruker D8 Venture equipped with IμS 3.0 Microfocus Incoatec Source and a Photon III

Detector. The Cu Kα radiation was used for the two data collections, performed at a temperature of 100 K (CryoStream 700 by Oxford Cryosystems). The APEX II suite was employed to collect the datasets and then they were reduced and refined with the program SAINT by Bruker (APEX3 v2018.7-0, Copyright 2003, 2004 Bruker Nonius; Copyright 2005-2018 Bruker AXS). Absorption correction was achieved through the SADABS program5 included in the Bruker Package of data treatment.

The structures were solved with the Shelxt 2014/5 Program and refined with Shelxl6 by full-matrix least-squares techniques with anisotropic displacement parameters for all non-hydrogen atoms. The hydrogen atoms in both complexes were introduced in calculated positions and refined considering a riding model with isotropic thermal parameters.

All calculations were performed by using the program PARST7 and molecular plots were produced with Mercury.8 For compound **N2** several crystals were screened and finally the one suitable for the data collection was found. Albeit the dataset for this complex was not of excellent quality (i.e., the completeness is not excellent), the crystal structure was determined with good confidence. Crystal data and refinement parameters for **N1** and **N2** are reported in Table 21.

The checkcif report shows alerts A and B for compound **N2** for which several crystals were screened and finally the one suitable for the data collection was found. Albeit the dataset for this complex was not of excellent quality (i.e., the completeness is not excellent), the crystal structure was determined with good confidence.

CCDC 2087305 and 2087306 contain the supplementary crystallographic data for compounds **N1** and **N2**, respectively. These data can be obtained free of charge from the Cambridge Crystallographic Data Centre via http://www.ccdc.cam.ac.uk/Community/Requestastructure.

	N1·(CH_3CN)	**N2·[2(H_2O)]·(CH_3CN)**
Empirical formula	C_{32} H_{24} F_6 N_9 O_2 P Ru	C_{66} H_{55} F_{12} N_{17} O_6 P_2 Ru_2
Formula weight	812.64	1674.35
Temperature (K)	100(2)	100(2)
Wavelength (Å)	1.54178	1.54178
Crystal system, space group	Triclinic, P-1	Triclinic, P-1
Unit cell dimensions (Å)	*a*=8.7832(2) *α*=87.2750(10) *b*=10.8061(3) *β*=78.4700(10) *c*=16.6952(4) *γ*=88.5950(10)	*a*=10.1169(7) *α*=75.078(5) *b*=13.9421(10) *β*=82.737(5) *c*=26.9554(19) *γ*=71.206(4)
Volume (Å^3)	1550.66(7)	3474.06(67)
Z, D_c (mg/cm^3)	2, 1.740	2, 1.60
μ (mm^{-1})	5.343	4.805
F(000)	816	1688
Crystal size (mm)	0.1x0.04x0.04	0.1x0.04x0.03
θ range (°)	2.704<θ<72.452	3.397<θ<69.273
Reflections collected / unique	38664/6062	48237/11879
Data / restraints / parameters	5800/0/461	7656/0/990
Goodness-of-fit on F^2	1.044	1.041
Final R indices [I>2σ(I)]	R1=0.052 wR2=0.142	R1=0.099 wR1=0.273
R indices (all data)	R1= 0.054 wR2=0.144	R1= 0.143 wR2=0.315

Table 21: Crystal data and structure refinement parameters for complexes N1 and N2

Stability under dark condition and photorectivity of N1-4

Prior to study the photoreactivity of ruthenium complexes **N1-4**, their stability under dark conditions was evaluated. This was performed by monitoring the electronic absorption spectra of 10 μM solutions of metal complexes in acetonitrile, as well as in water at pH 7.4 and at 37 °C, with increasing incubation times under dark. The electronic absorption spectra of all the complexes did not undergo appreciable variations over a total period of 72 h under dark conditions as demonstrated in Figure 70. Irradiation of ruthenium complexes was performed by employing as light source a low energy blue light-emitting diode (LED, l_{max} = 434 nm, 160 mW). Photolysis experiments were performed in acetonitrile and in aqueous solution (PBS buffer, pH 7.4) and were followed by UV-Vis spectroscopy and HPLC analysis.

In the UV-vis measurements, solutions of **N2-4** (10 μM) in acetonitrile or aqueous media (total volume of 2 mL) were subjected to increasing irradiation times and the resulting absorption spectra were collected (Figure 72).

In the HPLC measurements, solutions of ruthenium complexes ([**N2-4**] = 100 μM) in aqueous media with 10% of DMSO (total volume of 1 mL) were irradiated for increasing time frames and, at each irradiation point, a 10 μL aliquot of the irradiated solution was injected in the HPLC system. Chromatographic conditions were optimized by using as eluent a gradient mixture of H_2O/CH_3CN acidified with 0.1% of formic acid, as specified in Table 22.

Time (min)	*% H_2O (0.1 % HCOOH)*	*% CH_3CN (0.1 % HCOOH)*
0	98	2
2	95	5
5	85	15
10	70	30
15	40	60
20	5	95
25	98	2

Table 22: HPLC gradient used for photoejection studies.

Determination of ligands photoejection quantum yields

The quantum yields for the photodissociation of **5NIMH**, **MTZ-1** and **MTZ-2** from **N2, N3** and **N4** (Φ_{434} values) in acetonitrile and water were respectively determined through UV-Vis spectroscopy and HPLC analysis.

The Φ_{434} values in acetonitrile were determined via UV-Vis spectroscopy. Experiments were performed using solutions of complexes **N2-4** in acetonitrile (10 μM) (total volume of 2 mL) which were irradiated for increasing intervals of time with a LED lamp (λ_{max} 434 nm, 160 mW). The quantum yields of photosubstitution reactions were determined as the slope of the linear regression of moles of reactant as a function of the moles of absorbed photons for the first 5 points of the titration as reported previously.[167] [157]

The close proximity between the ^{1}MLCT absorption maximum values of the starting ruthenium compounds and that of the aqua-photoproduct $[Ru(tpy)(dmp)(H_2O)]^{2+}$ (centered at around 480-490 nm)[168] in water made difficult an equally accurate determination of the Φ_{434} values by means of UV-Vis measurements. Therefore, the Φ_{434} values in water were determined by HPLC titrations. The Φ_{434} values in aqueous solution were determined as the slope of the linear regression of moles of reactant as a function of the moles of absorbed photons for the first 4 points of the titration.[167]

The determination of the Φ_{434} values were assessed following the determination of the photon flux of the light source by the potassium ferrioxalate actinometry procedure according to methods reported in literature,[173] and explained in details below.

Determination of the photon-flux of light irradiation devices with Ferrioxalate actinometer procedure

i) Light irradiation device for UV-Vis and HPLC measurements

Light irradiation of ruthenium compounds was performed by using a blue light-emitting diode (LED) light source with a maximum at 434 nm (160 mW).

The photon flux of the lamp was determined to be ***5.76 x 10^{-7} E/s (Power 160 mW)***, by using the ferrioxalate actinometer procedure. This method is briefly summarized as follows:

1) Solution 1: A solution of potassium ferrioxalate 0.15 M in 0.05 M sulfuric acid was used as an actinometer.
2) Solution 2: A solution of 1% 1,10-phenanthroline was prepared in buffer 1.65 M sodium acetate trihydrate, in H2SO4 0.5M.
3) Solution 1 (**V1**-2 ml) was added into a cuvette and irradiated for increasing set times. At each time point, 10 µl aliquots (**V2**) of solution 1, 30 µl of solution 2, and 1.96 ml of H_2O were combined (**V3**-2 ml) and the absorbance of Fe^{2+} complex at 510 nm was collected.
4) The photon flux of light source was determined, as shown below, by performing the experiments in triplicate.

The absorbance values of $[Fe(phen)_3]^{2+}$ at 510 nm were plotted against the irradiation time, obtaining the graph shown in Figure 78. The slope in the figure corresponds to dA/dt in the following equation:

$$q = \frac{dA}{dt}\frac{V_1}{\varepsilon \times l}\frac{V_3}{V_2 \times \phi \times F}$$

where *q* is photon flux (einstein/s), dA/dt is slope of the linear fitting, **V1** is the volume of the irradiated actinometer (2 mL), **V2** is the aliquot of actinometer taken to determine the concentration of $[Fe(phen)_3]^{2+}$ (10 µl), **V3** is the volume of the solution measured after complexation (2 ml), ε is the extinction coefficient of $[Fe(phen)_3]^{2+}$ (11.000 M cm-1)[174], *l* is the path length (1 cm), φ is the quantum yield of actinometer at the considered wavelength (1.11)[175] and F = 1-(1/$10^{Abs(434\ nm)}$) is the photon absorption probability for the actinometer (which was calculated to be 0.13 at 434 nm).

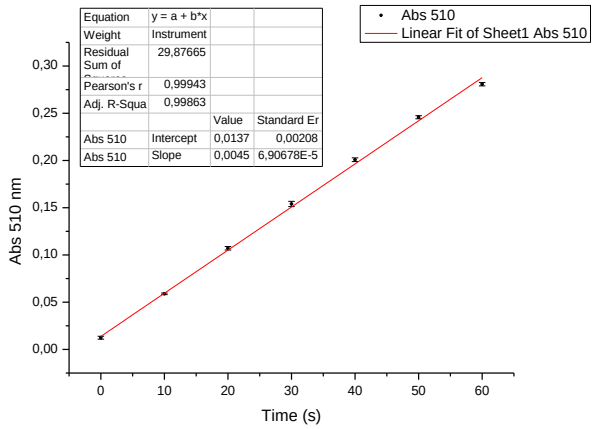

Figure 79: Linear regression of absorbance versus time (s) for $[Fe(phen)_3]^{2+}$ complex formation.

ii) Light irradiation device for antibacterial activity test

To allow the determination of antibacterial activity of complexes **N1-4** in anaerobic condition was used an anaerobiosis jar specially engineered with a LED illumination device (Figure 74), whose photon flux was determined by potassium ferrioxalate actinometer.

To reproduce the experimental setup of the antibacterial activity tests, 200 µL of solution 1 (**V1**) were irradiated directly in a plate well for increasing set times. Afterward, at each time point, 1 µL aliquots (**V2**) of solution 1, 3 µL of solution 2, and 200 µL of H_2O were combined (**V3**-200 µL) and the absorbance of Fe^{2+} complex at 510 nm was collected by using an Infinite Pro 200 plate reader (Tecan, Switzerland). Figure 79 shows the linear regression of the absorbance values of $[Fe(phen)_3]^{2+}$ at 510 nm against the irradiation time. The photon absorption probability for the actinometer ($F = 1-1/(10^{Abs(434nm)})$) was determined to be 0.21 at 434 nm. The photon flux in each plate well was determined to be ***4.72 × 10^{-9} E/s (Power 1.25 mW)***.

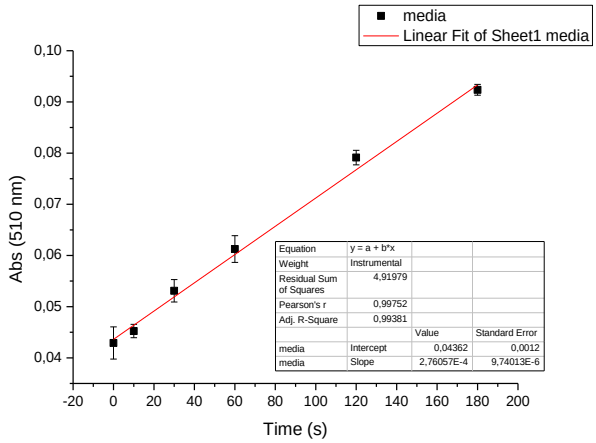

Figure 80: Linear regression of absorbance versus time (s) for $[Fe(phen)_3]^{2+}$ complex formation.

Determination of inhibitory concentrations

Overnight grown liquid cultures of the facultative anaerobic bacterium *B. subtilis* 168 were prepared in 10 ml LB medium from single colonies freshly grown on LB agar Petri plates. Cultures were incubated at 37 °C in a rotatory shaker, at 225 rpm for 24 hours and diluted cultures of *B. subtilis* (OD_{600} = 0.05) were dosed with different concentrations of nitroimidazole-based compounds and ruthenium complexes. The activity of each compound was tested under dark and following light irradiation, both in normoxia (21% O_2) and under hypoxic conditions (< 1% O_2). In the photoirradiation experiments cells were exposed to a LED emitting at 434 nm for 40 min; under these conditions no statistical differences in the blank absorbance between the light- and dark-treated groups of cells were observed. The photon flux in each plate resulted to be 4.72 x 10^{-9} E/s, as determined by the ferrioxalate actinometer method. Cell growth was carried out statically, by incubating microtiter plates at 37°C, and it was evaluated by registering the OD_{600} values after 24h for aerobiosis cultures and after 7 days for anaerobiosis test. Each test was performed in triplicate, using as culture media LB with

0.25% glucose and 0.1% potassium nitrate to sustain the growth of *B. subtilis* both in aerobiotic and anaerobiotic conditions.[176]

In Figure 75 and Figure 76, where are reported the observed antibacterial activities displayed by the tested compounds, the OD_{600} values are normalized and indicate the ratio of cell growth compared to the (untreated) control cells. Differences in the growth were statistically evaluated by one-way ANOVA test and Tukey post-hoc test.

Computational Details

Density Functional Theory calculations have been carried out with the Gaussian 09 suite of programs[177] at B3LYP/6-31+G(d) level of theory. The molecular structure of all studied molecules was optimized with very tight criterium, and it was verified that a minimum was located by computing the vibrational frequencies, which are all real. Mulliken, Lowdin, and Natural population analysis were performed to determine the atomic charges and to provide further insights on the ligand/ruthenium complex interactions.

Concluding remarks

The increasing interest in the medical application of ruthenium polypyridyl complexes (RPCs) dates to the 1978 Food and Drug Administration (FDA) approval of *cisplatin* as a chemotherapeutic drug. Since then, considering new metal-based drugs for medical purposes has become a successful strategy. Among the newly investigated coordination compounds, RPCs revealed anti-cancer activity comparable to that of *cisplatin* but with lower collateral toxicity and side effects. Furthermore, the well-known photoreactive properties of RPCs are unquestionably the most intriguing feature of these complexes that can be exploited in medicine in a variety of ways. For instance, RPCs can be successfully designed to be applied in the Photodynamic Therapy (PDT) by taking advantage of their efficient population of the triplet excited metal-to-ligand charge transfer state (^{3}MLCT), from which an energy transfer process to molecular oxygen can catalyze the production of singlet oxygen ($^1O_2$), a highly reactive oxidizing species. Alternatively, varying the molecular structure and the ligands around the metal center, can be obtained photo-labile complexes capable of releasing biologically active compounds for Photoactivated Chemotherapy (PACT). In both cases, the main advantage is the spatial and temporal control of the drug activation using a light source and allowing for improved discrimination between malignant and healthy tissues.

On these bases, the primary goal of this PhD thesis was to address the development of effective light-responsive therapeutic agents, with a particular emphasis on the rational design of adaptable molecular structure, taking advantage of the versatile chemistry of RPCs.

For this purpose, we started with the synthesis of water-soluble RPCs featuring polyaminomacrocyclic frameworks (**L1** and **L2**). We were able to prove that such

decorated RPCs have unique chemical-physical properties, resulting in highly charged species in physiological media that can, on the one hand, generate singlet oxygen upon illumination and, on the other side, allow the coordination of copper(II) ions capable of catalysing intracellular ROS production by Fenton-like processes, providing an alternative mechanism for drug-activation. We conducted an extensive research work on their photodynamic potential: first, we demonstrated that the structural features provided by the polyamine frameworks can be successfully exploited to allow Ru-drugs penetration through the peptidoglycan layers of Gram-positive bacteria cell walls, using *Bacillus subtilis* as a bacteria model. Photoactivation experiments on bacteria cultures revealed that the presence of copper(II) ions within polyamine macrocycles has not effect on cytotoxicity, with nearly identical MIC values for the heteronuclear Ru(II)/Cu(II) compounds and Cu(II)-free compounds. However, due to the inability of Ru(II)/Cu(II) species to generate $^1O_2$, a different mechanisms of action, such as the formation of cytotoxic ROS species produced by the synergistic action of Fenton-active copper centres and light, may be responsible for equally harmful cytotoxic effects.[75]
Parallelly, an in-depth study on the photoinduced toxicity of these complexes was conducted on epithelial ovarian cancer cells, identifying a marked enhancement of the toxicity after exposure to light. Further insights on the biological behaviour of these complexes demonstrate that $^1O_2$ and/or ROS production alter mitochondrial function and trigger pro-apoptotic effects. These findings point out a crucial role for programmed cell death in the anti-tumour activity of herein investigated systems.[77]
Lastly, the encapsulation of complexes **L1** and **L2** into human H-ferritin was exploited for their selective delivery to cancer cells. We showed that all the main chemical-physical properties of the PSs, including their capacity to produce $^1O_2$, are retained in the nanocomposite. Equally, the protein maintains its quaternary structure, ensuring its selective recognition and internalization in cells through endocytosis mediated by Transferrin Receptor 1 (TfR1). The biological potential of the nanocomposites was

tested against two human cancer cell lines, HeLa and A2780 cells that overexpress TfR1, as well as in non-tumoral C2C12 myoblasts. Results indicate that only cancer cells can internalize the nanocomposites, and their photosensitization markedly affects cell survival.[81]

In the second part of the Thesis, we focused on the effort to "*boost"* the $^1O_2$ production. To that end, a first class of bis-heteroleptic RPCs with the formula $[Ru(RR\text{-}bpy)(dppn)_2]^{n+}$ was developed. These complexes are characterized by the simultaneous presence of two extensive benzo[i]di-pyrido[3,2-a:2',3'-c]phenazine (dppn) ligands, which makes their synthesis a challenge that was solved by optimizing a new *reverse synthetic route* that represents a valid alternative to commonly employed methods. $[Ru(RR\text{-}bpy)(dppn)_2]^{n+}$ complexes exhibit excellent singlet oxygen sensitizing features and DNA-interaction properties, as well as a potent light-triggered toxicity on squamous epithelial carcinoma cells. Further studies on PS-cubosome-based formulation were carried out in order to facilitate the administration and accumulation of the newly synthesized PSs in tumour tissues. Our results probed the potent photoactivity of the resultant nanocomposites at very low drug concentrations, whereas mechanistic studies confirmed that intracellular ROS generation was likely responsible for the nanocomposites' PDT efficacy.

In addition, we discussed an intriguing application of $[Ru(2,2'\text{-bipyridine-}4,4'\text{-diylbis(morpholinomethanone)})(dppn)_2]^{2+}$ (**P3**), chosen for its appropriate water solubility, in which we investigated the effect of photoinduced $^1O_2$ generation on the transport activity of sarco(endo)plasmic reticulum Ca^{2+}-ATPase (SERCA). Our findings demonstrate that illumination with visible LED light induces an inhibitory effect on SERCA due to the photosensitization of $^1O_2$ dependent on the concentration of the PS and the duration of the light exposure.

Taking advantage of the versatile chemistry of RPCs, we designed another class of high-performance PSs decorated with a pendant perylenemonoimide (PMI) chromophore

conjugated through a C-C bond to a phenanthroline directly coordinated to the metal centre. To verify how the chemical-physical properties of these complexes can change by changing the position of the phenanthroline decoration with PMI, two different complexes were synthesized: one with the PMI dye in position 5 of the phenanthroline (**Ru-5PMI**), and another with the PMI conjugated in position 3 (**Ru-3PMI**). The behaviour of the two complexes is effectively different, with **Ru-5PMI** behaving similarly to a supermolecule, with the PMI almost completely coupled to the metal centre, whereas **Ru-3PMI** behaves as a dyad, with the metal centre decoupled from the PMI. Nevertheless, both complexes have great $^1O_2$ quantum yields approaching 0.70 and a strong capacity to intercalate the DNA.

Finally, a class of RPCs designed for the '*photorelease antimicrobial therapy*' was presented in the final section of the Thesis. In this project, Nitroimidazole-based antibiotics, which are well-known broad-spectrum drugs used clinically for fighting anaerobic bacterial infections, were incorporated on a ruthenium(II) scaffold capable of photoreleasing them upon visible light activation. The "unusual" coordination of 5-nitroimidazole[157] and the two newly synthesized Metronidazole derivatives, MTZ-1 and MTZ-2, as anionic imidazolates confers to the resulting Ru(II) complexes promising features as photocages, as denoted by the good stability shown *in dark* and by the possibility to easily cause the detachment of nitroimidazole-based ligands upon exposure to visible light. The biological potential of *Ru-free* nitroimidazole-based ligands and of metal complexes was tested on *B. subtilis*, chosen as Gram-positive bacteria model, in both normoxic (21% O_2) and hypoxic (< 1% O_2) conditions. Our results highlighted two main findings: *i*) the activity of nitroimidazole-based ligands was remarkably enhanced by switching from aerobic to anaerobic conditions, as expected in consideration of the peculiar mode of action of nitroimidazole-based antimicrobials; *ii*) the insertion of ligands into ruthenium complexes masked their activity when kept *in the dark* whereas light-irradiation under hypoxia provoked a strong dose-dependent

activity. Lastly, preliminary studies on the interaction of the newly synthesized Metronidazole-derivatives with NimA, a model of reductases responsible for bacterial resistance to 5-nitroimidazole-based antibiotics, revealed that the different chemical architectures of these bioactive ligands made protein sequestration unfavourable when compared to Metronidazole, implying their potential use in the treatment of bacteria resistant to common nitroimidazole-based antimicrobials.

Abbreviations and acronyms

$[Ru(bpy)_3]^{2+}$	tris(2,2'-bipyridyl)ruthenium(II)
$[Ru(phen)_3]^{2+}$	Tris(1,10-phenanthroline)ruthenium(II)
5NIMH	5-nitroimidazole
ATP	Adenosine 5'-(tetrahydrogen triphosphate)
bpy	2,2'-bipyridine
Cryo-TEM	Cryogenic Transmission Electron Microscopy
ct-DNA	*calf thymus* DNA
DLS	Dynamic Light Scattering
dmphen	2,9-methyl-1,10-phenanthroline
dppn	benzo[*i*]dipyrido[3,2-*a*:2',3'-*c*]phenazine
DTT	1,4-dithiothreitol
EGTA	ethylene glycol-bis (β-aminoethyl ether)-*N*,*N*,*N*',*N*'-tetraacetic acid
FDA	Food and Drug Administration
HpD	Hematoporphyrin derivatives
ILCT	intraligand charge transfer state
ISC	intersystem crossing
LC	ligand centred
LF	ligand field
LLIVCT	ligand low-energy inter-valence charge transfer state
MC	metal-centred state
MIC	minimal inhibitory concentrations
MLCT	metal-to-ligand charge transfer state
MMCT	metal-to-metal charge transfer state
MO	molecular orbital
MOPS	3-(N-morpholino)propanesulfonic acid
MTZ	metronidazole
NIR	Near-Infrared
NPs	Nanoparticles
PACT	Photoactivated Chemotherapy
PDI	photodynamic inactivation
PDT	Photodynamic Therapy
phen	1,10-phenanthroline
PMI	Perylene monoimide
PSs	Photosensitizers
PTA	1,3,5-triaza-7-phosphaticyclo-[3.3.1.1]decane
ROS	radical oxygen species
RPCs	ruthenium(II) polypyridyl complexes
SAXS	Small-Angle X-ray Sacttering
TEA	Triethylamine
TMAO	Trimethylamine N-oxide
TPA	two-photon absorption cross-section
TPE	two-photon excitation
tpy	2,2':6',2'-terpyridine
ϕ_Δ	singlet oxygen quantum yield

Bibliography

1. Pashaei B., Shahroosvand H., Graetzel M., Nazeeruddin M. K., Influence of Ancillary Ligands in Dye-Sensitized Solar Cells, *Chem. Rev.*, *116*, 9485–9564, **2016**.
2. Wang C.-S., Dixneuf P. H., Soulé J.-F., Photoredox Catalysis for Building C–C Bonds from C(sp 2)–H Bonds, *Chem. Rev.*, *118*, 7532–7585, **2018**.
3. Gramage-Doria R., Bruneau C., Ruthenium-catalyzed C–H bond functionalization in cascade and one-pot transformations, *Coord. Chem. Rev.*, *428*, 213602, **2021**.
4. Conti L., Macedi E., Giorgi C., Valtancoli B., Fusi V., Combination of light and Ru(II) polypyridyl complexes: Recent advances in the development of new anticancer drugs, *Coord. Chem. Rev.*, *469*, 214656, **2022**.
5. Wang X., Wang X., Jin S., Muhammad N., Guo Z., Stimuli-Responsive Therapeutic Metallodrugs, *Chem. Rev.*, *119*, 1138–1192, **2019**.
6. Lee S. Y., Kim C. Y., Nam T. G., Ruthenium complexes as anticancer agents: A brief history and perspectives, *Drug Des. Devel. Ther.*, *14*, 5375–5392, **2020**.
7. Muggia F., Platinum compounds 30 years after the introduction of cisplatin: Implications for the treatment of ovarian cancer, *Gynecol. Oncol.*, *112*, 275–281, **2009**.
8. Meng X. *et al.,* A Ruthenium-Containing Organometallic Compound Reduces Tumor Growth through Induction of the Endoplasmic Reticulum Stress Gene CHOP, *Cancer Res.*, *69*, 5458–5466, **2009**.
9. Wang J.-Q., Zhang P.-Y., Ji L.-N., Chao H., A ruthenium(II) complex inhibits tumor growth in vivo with fewer side-effects compared with cisplatin, *J. Inorg. Biochem.*, *146*, 89–96, **2015**.
10. Sava G. *et al.,* Dual action of NAMI-A in inhibition of solid tumor metastasis: Selective targeting of metastatic cells and binding to collagen, *Clin. Cancer Res.*, *9*, 1898–1905, **2003**.
11. Rademaker-Lakhai J. M., van den Bongard D., Pluim D., Beijnen J. H., Schellens J. H. M., A Phase I and Pharmacological Study with Imidazolium- trans- DMSO-imidazole-tetrachlororuthenate, a Novel Ruthenium Anticancer Agent, *Clin. Cancer Res.*, *10*, 3717–3727, **2004**.
12. Hartinger C. G. *et al.,* From bench to bedside – preclinical and early clinical development of the anticancer agent indazolium trans-[tetrachlorobis(1H-indazole)ruthenate(III)] (KP1019 or FFC14A), *J. Inorg. Biochem.*, *100*, 891–904, **2006**.
13. Hartinger C. G. *et al.,* KP1019, A New Redox-Active Anticancer Agent – Preclinical Development and Results of a Clinical Phase I Study in Tumor Patients, *Chem. Biodivers.*, *5*, 2140–2155, **2008**.
14. Trondl R. *et al.,* NKP-1339, the first ruthenium-based anticancer drug on the edge to clinical application, *Chem. Sci.*, *5*, 2925–2932, **2014**.
15. Weiss A. *et al.,* In vivo anti-tumor activity of the organometallic ruthenium(ii)-arene complex [Ru(η^6-p-cymene)Cl_2(pta)] (RAPTA-C) in human ovarian and colorectal carcinomas, *Chem. Sci.*, *5*, 4742–4748, **2014**.
16. Tong L., Thummel R. P., Mononuclear ruthenium polypyridine complexes that catalyze water oxidation, *Chem. Sci.*, *7*, 6591–6603, **2016**.

17. Clarke M. J., Ruthenium metallopharmaceuticals, *Coord. Chem. Rev.*, *232*, 69–93, **2002**.
18. Garner R. N., Joyce L. E., Turro C., Effect of electronic structure on the photoinduced ligand exchange of Ru(II) polypyridine complexes, *Inorg. Chem.*, *50*, 4384–4391, **2011**.
19. Heinemann F., Karges J., Gasser G., Critical Overview of the Use of Ru(II) Polypyridyl Complexes as Photosensitizers in One-Photon and Two-Photon Photodynamic Therapy, *Acc. Chem. Res.*, *50*, 2727–2736, **2017**.
20. Niedre M., Patterson M. S., Wilson B. C., Direct Near-infrared Luminescence Detection of Singlet Oxygen Generated by Photodynamic Therapy in Cells In Vitro and Tissues In Vivo, *Photochem. Photobiol.*, *75*, 382–391, **2002**.
21. Skovsen E., Snyder J. W., Lambert J. D. C., Ogilby P. R., Lifetime and Diffusion of Singlet Oxygen in a Cell, *J. Phys. Chem. B*, *109*, 8570–8573, **2005**.
22. Holder A. A., Lilge L., Browne W. R., A.W. Lawrence M., Bullock Jr. J. L., Ruthenium Complexes, **2010**
23. Loeb L. Über den Einfluß des Lichtes auf die Färbung und die Entwicklung von Eiern von Asterias in Lösungen verschiedener Farbstoffe, *Arch Entwicklmech Org*, *23*, 359–378, **1907**.
24. Dougherty T. J. *et al.,* Photodynamic Therapy., *J. Natl. Cancer Inst.*, *90*, 889–905, **1998**.
25. O'Connor A. E., Gallagher W. M., Byrne A. T., Porphyrin and Nonporphyrin Photosensitizers in Oncology: Preclinical and Clinical Advances in Photodynamic Therapy, *Photochem. Photobiol.*, *85*, 1053–1074, **2009**.
26. Garanger E., Boturyn D., Dumy P. Tumor Targeting with RGD Peptide Ligands-Design of New Molecular Conjugates for Imaging and Therapy of Cancers, *Anticancer Agents Med Chem*, *7*, 552–558, **2007**.
27. Adamson K., Dolan C., Moran N., Forster R. J., Keyes T. E., RGD labeled Ru(II) polypyridyl conjugates for platelet integrin αIIb3 recognition and as reporters of integrin conformation, *Bioconjug. Chem.*, *25*, 928–944, **2014**.
28. Wilson W. R., Hay M. P., Targeting hypoxia in cancer therapy, *Nat. Rev. Cancer*, *11*, 393–410, **2011**.
29. Soliman N., Gasser G., Thomas C. M., Incorporation of Ru(II) Polypyridyl Complexes into Nanomaterials for Cancer Therapy and Diagnosis, *Adv. Mat.*, *32*, 2003294, **2020**.
30. Villemin E., Ong Y. C., Thomas C. M., Gasser G., Polymer encapsulation of ruthenium complexes for biological and medicinal applications, *Nat. Rev. Chem.*, *3*, 261–282, **2019**.
31. Lincoln R. *et al.,* Exploitation of Long-Lived 3 IL Excited States for Metal − Organic Photodynamic Therapy: Verification in a Metastatic Melanoma Model, *J. Am. Chem. Soc.*, *135*(45), 17161-17175, **2013**.
32. Pal A. K., Serroni S., Zaccheroni N., Campagna S., Hanan G. S., Near infra-red emitting Ru(ii) complexes of tridentate ligands: Electrochemical and photophysical consequences of a strong donor ligand with large bite angles., *Chem. Sci.*, *5*, 4800–4811, **2014**.
33. Pen B., Leed N. A., Dunbar K. R., Turro C., Excited State Dynamics of Two New Ru(II) Cyclometallated Dyes: Relation to Cells for Solar Energy Conversion and Comparison to Conventional Systems, *J. Phys. Chem. C*, *116(42)*, 22186-22195, **2012**.
34. Simon J. A. *et al.,* Intramolecular Electronic Energy Transfer in Ruthenium (II) Diimine Donor / Pyrene Acceptor Complexes Linked by a Single C - C Bond, *J. Am. Chem. Soc., 7863*, 11012–11022, **1997**.

35. Kozlov D. v, Tyson D. S., Goze C., Ziessel R., Castellano F. N., Room Temperature Phosphorescence from Ruthenium (II) Complexes Bearing Conjugated Pyrenylethynylene Subunits, *Inorg. Chem.*, *43*, 4063–4071, **2004**.
36. Kanti S., Purkayastha P., Unusually Large Singlet Oxygen ($^1O_2$) Production by Very Weakly Emissive Pyrene-Functionalized Iridium (III) Complex: Interplay between Excited ^{3}ILCT / ^{3}IL and ^{3}MLCT States, *Eur. J. Inorg. Chem.,* 31, 2990–2997, **2020**
37. Gunaydin G., Gedik M. E., Ayan S., Photodynamic Therapy—Current Limitations and Novel Approaches, *Front. Chem.*, *9*, 1–25, **2021**.
38. Thorley K. J., Hales J. M., Anderson H. L., Perry J. W., Porphyrin Dimer Carbocations with Strong Near Infrared Absorption and Third-Order Optical Nonlinearity, *Angewandte Chemie*, *47*, 7095–7098, **2008**.
39. Zhao W., Carreira E. M., Conformationally Restricted Aza-Bodipy: A Highly Fluorescent, Stable, Near-Infrared-Absorbing Dye, *Angewandte Chemie*, *117*, 1705–1707, **2005**.
40. Muranaka A., Yonehara M., Uchiyama M., Azulenocyanine: A New Family of Phthalocyanines with Intense Near-IR Absorption, *J. Am. Chem. Soc.*, *132*, 7844–7845, **2010**.
41. Kohlmann S., Ernst S., Kaim W., Extremely Long-Wavelength Charge-Transfer Absorptions of Binuclear Complexes with Azo-Modified 2,2?-Bipyridyl Ligands, *Angewandte Chemie*, *24*, 684–685, **1985**.
42. Kaim W., Concepts for metal complex chromophores absorbing in the near infrared, *Coord. Chem. Rev.*, *255*, 2503–2513, **2011**.
43. McKenzie L. K., Bryant H. E., Weinstein J. A., Transition metal complexes as photosensitisers in one- and two-photon photodynamic therapy, *Coord. Chem. Rev.*, *379*, 2–29, **2019**.
44. Liu J. *et al.,* Ruthenium(II) polypyridyl complexes as mitochondria-targeted two-photon photodynamic anticancer agents, *Biomaterials*, *56*, 140–153, **2015**.
45. Huang H. *et al.,* Highly Charged Ruthenium(II) Polypyridyl Complexes as Lysosome-Localized Photosensitizers for Two-Photon Photodynamic Therapy, *Angewandte Chemie*, *54*, 14049–14052, **2015**.
46. Hess J. *et al.,* Evaluation of the Medicinal Potential of Two Ruthenium(II) Polypyridine Complexes as One- and Two-Photon Photodynamic Therapy Photosensitizers, *Chem. Eur. J.*, *23*, 9888–9896, **2017**.
47. Lazarević T., Rilak A., Bugarčić Ž. D., Platinum, palladium, gold and ruthenium complexes as anticancer agents: Current clinical uses, cytotoxicity studies and future perspectives, *Eur. J. Med. Chem.*, *142*, 8–31, **2017**.
48. Ragab M. S., Shehata M. R., Shoukry M. M., Haukka M., Ragheb M. A., Oxidative DNA cleavage mediated by a new unexpected [Pd(BAPP)][PdCl $_4$] complex (BAPP = 1,4-bis(3-aminopropyl)piperazine): crystal structure, DNA binding and cytotoxic behavior, *RSC Adv.*, *12*, 1871–1884, **2022**.
49. Bergamo A., Sava G., Linking the future of anticancer metal-complexes to the therapy of tumour metastases, *Chem. Soc. Re.v*, *44*, 8818–8835, **2015**.
50. Mital M., Ziora Z., Biological applications of Ru(II) polypyridyl complexes, *Coord. Chem. Rev.*, *375*, 434–458, **2018**.
51. Levina A., Mitra A., Lay P. A., Recent developments in ruthenium anticancer drugs, *Metallomics*, *1*, 458, **2009**.

52. Yan Y. K., Melchart M., Habtemariam A., Sadler P. J., Organometallic chemistry, biology and medicine: ruthenium arene anticancer complexes, *Chem. Comm.*, 4764, **2005**.
53. Wee H. A., Dyson P. J., Classical and Non-Classical Ruthenium-Based Anticancer Drugs: Towards Targeted Chemotherapy, *Eur. J. Inorg. Chem.*, *2006*, 4003–4018, **2006**.
54. Bergamo A., Gaiddon C., Schellens J. H. M., Beijnen J. H., Sava G., Approaching tumour therapy beyond platinum drugs, *J. Inorg. Biochem.*, *106*, 90–99, **2012**.
55. Brabec V., Kasparkova J., Ruthenium coordination compounds of biological and biomedical significance. DNA binding agents, *Coord. Chem. Rev.*, *376*, 75–94, **2018**.
56. Siddik Z. H., Cisplatin: mode of cytotoxic action and molecular basis of resistance, *Oncogene*, *22*, 7265–7279, **2003**.
57. Wachter E., Heidary D. K., Howerton B. S., Parkin S., Glazer E. C., Light-activated ruthenium complexes photobind DNA and are cytotoxic in the photodynamic therapy window, *Chem. Comm.*, *48*, 9649–9651, **2012**.
58. Hidayatullah A. N., Wachter E., Heidary D. K., Parkin S., Glazer E. C., Photoactive Ru(II) complexes with dioxinophenanthroline ligands are potent cytotoxic agents, *Inorg. Chem.*, *53*, 10030–10032, **2014**.
59. Howerton B. S., Heidary D. K., Glazer E. C., Strained Ruthenium Complexes Are Potent Light-Activated Anticancer Agents, *J. Am. Chem. Soc.*, *134*, 8324–8327, **2012**.
60. Erkkila K. E., Odom D. T., Barton J. K., Recognition and Reaction of Metallointercalators with DNA, *Chem. Rev.*, *99*, 2777–2796, **1999**.
61. Barton J. K., Danishefsky A. T., Goldberg J. M., Tris(phenanthroline)ruthenium(II): Stereoselectivity in Binding to DNA, *J. Am. Chem. Soc.*, *106*, 2172–2176, **1984**.
62. Vanderlinden W. *et al.,* Mesoscale DNA structural changes on binding and photoreaction with $Ru[(TAP)_2PHEHAT]^{2+}$, *J. Am. Chem. Soc.*, *134*, 10214–10221, **2012**.
63. Chen Y. *et al.,* Fusion of photodynamic therapy and photoactivated chemotherapy: A novel Ru(ii) arene complex with dual activities of photobinding and photocleavage toward DNA, *Dalton Trans.*, *43*, 15375–15384, **2014**.
64. Sirajuddin M., Ali S., Badshah A., Drug–DNA interactions and their study by UV–Visible, fluorescence spectroscopies and cyclic voltammetry, *J. Photochem. Photobiol. B*, *124*, 1–19, **2013**.
65. Sirajuddin M., Ali S., Shah N. A., Khan M. R., Tahir M. N., Synthesis, characterization, biological screenings and interaction with calf thymus DNA of a novel azomethine 3-((3,5-dimethylphenylimino)methyl)benzene-1,2-diol, *Spectrochim. Acta A Mol. Biomol. Spectrosc.*, *94*, 134–142, **2012**.
66. Liu J. *et al.,* DNA-binding and cleavage studies of macrocyclic copper(II) complexes, *J. Inorg. Biochem.*, *91*, 269–276, **2002**.
67. Shahabadi N., Kashanian S., Khosravi M., Mahdavi M., Multispectroscopic DNA interaction studies of a water-soluble nickel(II) complex containing different dinitrogen aromatic ligands, *Trans. Metal Chem.*, *35*, 699–705, **2010**.
68. van Houten J., Watts R. J., Temperature dependence of the photophysical and photochemical properties of the tris(2,2'-bipyridyl)ruthenium(II) ion in aqueous solution, *J. Am. Chem. Soc.*, *98*, 4853–4858, **1976**.
69. Knoll J. D., Albani B. A., Turro C., New Ru(II) Complexes for Dual Photoreactivity: Ligand Exchange and $^1O_2$ Generation, *Acc. Chem. Res.*, *48*, 2280–2287, **2015**.

70. Mccusker J. K., Femtosecond Absorption Spectroscopy of Transition Metal Charge-Transfer Complexes, *36*, 876–887, **2003**.
71. Sun Q. *et al.,* Experimental Evidence of Ultrafast Quenching of the ^{3} MLCT Luminescence in Ruthenium(II) Tris-bipyridyl Complexes via a ^{3} dd State, *J. Am. Chem. Soc.*, *135*, 13660–13663, **2013**.
72. Knoll J. D., Albani B. A., Durr C. B., Turro C., Unusually Efficient Pyridine Photodissociation from Ru(II) Complexes with Sterically Bulky Bidentate Ancillary Ligands, *J. Phys. Chem. A, 118, 45, 10603-10610,* **2014**.
73. Bonnet S., Collin J. P., Koizumi M., Mobian P., Sauvage J. P., Transition-metal-complexed molecular machine prototypes, *Adv. Mat.*, *18*, 1239–1250, **2006**.
74. Bonnet S., Collin J.-P., Ruthenium-based light-driven molecular machine prototypes: synthesis and properties, *Chem. Soc. Rev.*, *37*, 1207, **2008**.
75. Conti L. *et al.,* Exploring the potential of highly charged Ru(II)- and heteronuclear Ru(II)/Cu(II)-polypyridyl complexes as antimicrobial agents, *J. Inorg. Biochem.*, *220*, 111467, **2021**.
76. Conti L. *et al.,* Highly Charged Ruthenium(II) Polypyridyl Complexes as Effective Photosensitizer in Photodynamic Therapy, *Chem. Eur. J.*, *25*, 10606–10615, **2019**.
77. Conti L. *et al.,* Highly Charged Ru(II) Polypyridyl Complexes as Photosensitizer Agents in Photodynamic Therapy of Epithelial Ovarian Cancer Cells, *Int. J. Mol. Sci.*, *23*, 13302, **2022**.
78. Lodeiro C. *et al.,* Protonation and Zn(II) coordination by dipyridine-containing macrocycles with different molecular architecture. A case of pH-controlled metal jumping outside - Inside the macrocyclic cavity, *Inorg. Chem.*, *40*, 2968–2975, **2001**.
79. Conti L. *et al.,* Exploring the Ability of Luminescent Metal Assemblies to Bind and Sense Anionic or Ionizable Analytes A Ru(phen)2bipy-Based Dizinc Complex for Bisphenol A (BPA) Recognition, *Molecules*, *26*, 527, **2021**.
80. Keyes T. E. *et al.,* Tuning of the photostability of bis(2,2′-biquinoline)ruthenium(II) complexes containing pyridyltriazole ligands by variation of pH, *Inorg. Chim. Acta*, *245*, 237–242, **1996**.
81. Conti L. *et al.,* Ferritin nanocomposites for the selective delivery of photosensitizing ruthenium-polypyridyl compounds to cancer cells, *Inorg. Chem. Front.*, *9*, 1070–1081, **2022**.
82. Feng Y., Sun W. Z., Wang X. S., Zhou Q. X., Selective Photoinactivation of Methicillin-Resistant Staphylococcus aureus by Highly Positively Charged RuII Complexes, *Chem. Eur. J.*, *25*, 13879–13884, **2019**.
83. Siegel R. L., Miller K. D., Fuchs H. E., Jemal A., Cancer Statistics, 2021. *CA Cancer J Clin*, *71*, 7–33, **2021**.
84. Coburn S. B., Bray F., Sherman M. E., Trabert B., International patterns and trends in ovarian cancer incidence, overall and by histologic subtype, *Int. J. Cancer*, *140*, 2451–2460, **2017**.
85. Mikuła-Pietrasik J. *et al.,* Comprehensive review on how platinum- and taxane-based chemotherapy of ovarian cancer affects biology of normal cells, *Cell. Mol. Life Sci. 76(4),* 681–697, **2019**.
86. Crichton R. R. Structure and Function of Ferritin, *Angewandte Chemie*, *12*, 57–65, **1973**.

87. Jutz G., van Rijn P., Santos Miranda B., Böker A., Ferritin: A Versatile Building Block for Bionanotechnology, *Chem. Rev.*, *115*, 1653–1701, **2015**.
88. Li L. *et al.,* Binding and uptake of H-ferritin are mediated by human transferrin receptor-1, *PNAS*, *107*, 3505–3510, **2010**.
89. Pozzi C. *et al.,* Iron binding to human heavy-chain ferritin, *Acta Crystallogr. D Biol. Crystallogr.*, *71*, 1909–1920, **2015**.
90. Entradas T., Waldron S., Volk M., The detection sensitivity of commonly used singlet oxygen probes in aqueous environments, *J. Photochem. Photobiol. B*, *204*, 111787, **2020**.
91. Gollmer A. *et al.,* Singlet Oxygen Sensor Green®: Photochemical Behavior in Solution and in a Mammalian Cell., *Photochem. Photobiol.*, *87*, 671–679, **2011**.
92. Schmidt R., Afshari E., Comment on 'Effect of solvent on the phosphorescence rate constant of singlet molecular oxygen (1.DELTA.g)', *J Phys. Chem., 94*, 4377–4378, **1990**.
93. Stoll S., Schweiger A., EasySpin, a comprehensive software package for spectral simulation and analysis in EPR, *J. Magn. Reason.*, *178*, 42–55, **2006**.
94. Andrés A. *et al.,* Setup and validation of shake-flask procedures for the determination of partition coefficients (logD) from low drug amounts, *Eur. J. Pharm. Sci. 76*, 181–191, **2015**.
95. Donati C. *et al.,* TGFβ protects mesoangioblasts from apoptosis via sphingosine kinase-1 regulation, *Cell Signal*, *21*, 228–236, **2009**.
96. Albani B. A. *et al.,* Marked improvement in photoinduced cell death by a new tris-heteroleptic complex with dual action: Singlet oxygen sensitization and ligand dissociation, *J. Am. Chem. Soc.*, *136*, 17095–17101, **2014**.
97. Yin H. *et al.,* In vitro multiwavelength PDT with 3IL States: Teaching old molecules new tricks, *Inorg. Chem.*, *53*, 4548–4559, **2014**.
98. Reichardt C. *et al.,* Predictive Strength of Photophysical Measurements for in Vitro Photobiological Activity in a Series of Ru(II) Polypyridyl Complexes Derived from π-Extended Ligands, *Inorg. Chem.*, *58*, 3156–3166, **2019**.
99. Ware D. C., Lay P. A., Taube H., Chou M. H., Creutz C., (2,2'-Bipyridine- *N,N* ')(2,2':6',2"-Terpyridine- *N,N',N* ") Complexes of Ruthenium(III)/(II) and Osmium(III)/(II). *Inorganic Syntheses,* Vol 24, **1986.**
100. Peña B., Leed N. A., Dunbar K. R., Turro C., Excited state dynamics of two new Ru(II) cyclometallated dyes: Relation to cells for solar energy conversion and comparison to conventional systems, *J. Phys. Chem. C*, *116*, 22186–22195, **2012**.
101. Wang L. *et al.,* π-Expansive Heteroleptic Ruthenium(II) Complexes as Reverse Saturable Absorbers and Photosensitizers for Photodynamic Therapy, *Inorg. Chem.*, *56*, 3245–3259, **2017**.
102. Molphy Z. *et al.,* Copper Phenanthrene Oxidative Chemical Nucleases, *Inorg. Chem.*, *53*, 5392–5404, **2014**.
103. Anderson P. A. *et al.,* Designed Synthesis of Mononuclear Tris(heteroleptic) Ruthenium Complexes Containing Bidentate Polypyridyl Ligands, *Inorg. Chem.*, *34*, 6145–6157, **1995**.
104. Kubeil M. *et al.,* Studies of Carbon Monoxide Release from Ruthenium(II) Bipyridine Carbonyl Complexes upon UV-Light Exposure, *Inorg. Chem.*, *56*, 5941–5952, **2017**.

105. Nickita *et al.,* Synthesis, Structure, Spectroscopic Properties, and Electrochemical Oxidation of Ruthenium(II) Complexes Incorporating Monocarboxylate Bipyridine Ligands, *Inorg. Chem.*, *46*, 8638–8651, **2007**.
106. Shimidzu T., Iyoda T., Izaki K., Photoelectrochemical properties of bis(2,2'-bipyridine)(4,4'-dicarboxy-2,2'-bipyridine)ruthenium(II) chloride, *J. Phys. Chem.*, *89*, 642–645, **1985**.
107. Kalyanasundaram K., Nazeeruddin M. K., Protonation behavior in the ground and excited states of some Os(II) Polypyridyl complexes, *Inorganica Chim. Acta*, 171(2), 213-216, **1990**.
108. Jing B., Wu T., Tian C., Zhang M., Shen T., pH-Dependent Luminescence of Ruthenium(II) Polypyridine Complexes, *Bull Chem. Soc. Jpn.*, *73*, 1749–1755, **2000**.
109. Shimidzu T., Iyoda T., Izaki K., Photoelectrochemical properties of bis(2,2'-bipyridine)(4,4'-dicarboxy-2,2'-bipyridine) ruthenium(II) chloride, *J. Phys. Chem.*, *89*(4), 642-645, **1985.**
110. Perdisatt L. *et al.,* Synthesis, characterisation and DNA intercalation studies of regioisomers of ruthenium (II) polypyridyl complexes, *J. Inorg. Biochem.*, *182*, 71–82, **2018**.
111. Liu X.-W., Chen Y.-D., Li L., Lu J.-L., Zhang D.-S., DNA-binding and photocleavage studies of ruthenium(II) complexes containing asymmetric intercalative ligand, *Spectrochim. Acta A Mol. Biomol. Spectrosc.*, *86*, 554–561, **2012**.
112. Friedman A. E., Chambron J. C., Sauvage J. P., Turro N. J., Barton J. K., A molecular light switch for DNA: $Ru(bpy)_2(dppz)^{2+}$, *J. Am. Chem. Soc.*, *112*, 4960–4962, **1990**.
113. Chen Q. *et al.,* TLD1433 Photosensitizer Inhibits Conjunctival Melanoma Cells in Zebrafish Ectopic and Orthotopic Tumour Models, *Cancers (Basel)*, *12*, 587, **2020**.
114. Murgia S. *et al.,* Drug-loaded fluorescent cubosomes: Versatile nanoparticles for potential theranostic applications, *Langmuir*, *29*, 6673–6679, **2013**.
115. Mulet X., Boyd B. J., Drummond C. J., Advances in drug delivery and medical imaging using colloidal lyotropic liquid crystalline dispersions, *J. Colloid. Interface Sci.*, *393*, 1–20, **2013**.
116. Barreto J. A. *et al.,* Nanomaterials: Applications in Cancer Imaging and Therapy, *Adv. Mater.*, *23*, H18–H40, **2011**.
117. Molphy Z. *et al.,* Copper Phenanthrene Oxidative Chemical Nucleases, *Inorg. Chem.*, *53*, 5392–5404, **2014**.
118. Huang T. *et al.,* Rational Design of Phosphorescent Iridium(III) Complexes for Selective Glutathione Sensing and Amplified Photodynamic Therapy, *ChemBioChem*, *20*, 576–586, **2019**.
119. Roy R., Kim J. M., Cu(II)-Self-assembling bipyridyl-glycoclusters and dendrimers bearing the Tn-antigen cancer marker: syntheses and lectin binding properties, *Tetrahedron*, *59*, 3881–3893, **2003**.
120. Maggioni D. *et al.,* A Luminescent Poly(amidoamine)–Iridium Complex as a New Singlet-Oxygen Sensitizer for Photodynamic Therapy, *Inorg. Chem.*, *54*, 544–553, **2015**.
121. Ishibashi T., Lee C. il, Okabe E., Skeletal sarcoplasmic reticulum dysfunction induced by reactive oxygen intermediates derived from photoactivated rose Bengal, *J. Pharmacol. Exp. Ther.*, *277*, 350–358, **1996**.

122. Kukreja R. C., Kearns A. A., Zweier J. L., Kuppusamy P., Hess M. L., Singlet oxygen interaction with Ca2+-ATPase of cardiac sarcoplasmic reticulum, *Circ. Res.*, *69*, 1003–1014, **1991**.
123. Toyoshima C., Nakasako M., Nomura H., Ogawa H., Structure determination of the calcium pump of sarcoplasmic reticulum at 2.6 Å resolution, *Nat.*, *405*, 647–55, **2001**.
124. Chen J., Sitsel A., Benoy V., Sepúlveda M. R., Vangheluwe P., Primary active Ca2+ transport systems in health and disease, *Cold Spring Harb. Perspect. Biol.*, *12*, 1–27, **2020**.
125. Møller J. v., Olesen C., Winther A.-M. L., Nissen P., The sarcoplasmic Ca $^{2+}$ -ATPase: design of a perfect chemi-osmotic pump, *Q. Rev. Biophys.*, *43*, 501–566, **2010**.
126. Hovananian A., Serca pumps and human diseases, *Calcium Signalling and Disease Vol.45*, 337–363, **2007**.
127. Brini M., Carafoli E, Calcium pumps in health and disease, *Physiol. Rev.*, *89*, 1341–1378, **2009**.
128. Tadini-Buoninsegni F., Smeazzetto S., Gualdani R., Moncelli M. R., Drug interactions with the Ca^{2+}-ATPase from Sarco(Endo)plasmic reticulum (SERCA), *Front. Mol. Biosci.*, *5*, 1–8, **2018**.
129. Sordi G., Goti A., Young H. S., Palchetti I., Tadini-Buoninsegni F., Stimulation of Ca2+-ATPase Transport Activity by a Small-Molecule Drug, *ChemMedChem*, *16*, 3293–3299, **2021**.
130. Tadini-Buoninsegni F., Palchetti I., Label-free bioelectrochemical methods for evaluation of anticancer drug effects at a molecular level, *Sensors*, *20*, **2020**.
131. Tadini-Buoninsegni F., Bartolommei G., Moncelli M. R., Guidelli R., Inesi G., Pre-steady state electrogenic events of Ca^{2+}/H^{+} exchange and transport by the Ca2+-ATPase, J. *Biol. Chem., 281*, 37720–37727, **2006**.
132. Eletr S., Inesi G., Phospholipid orientation in sacroplasmic membranes: Spin-label ESR and proton NMR studies, *BBA - Biomembranes*, *282*, 174–179, **1972**.
133. Lowry O. H., Rosebrough N. J., Farr A. L., Randall R. J., Protein measurement with the Folin phenol reagent, *J. Biol. Chem.*, *193*, 265–275, **1951**.
134. Ford W. E., Rodgers M. A. J., Reversible triplet-triplet energy transfer within a covalently linked bichromophoric molecule, *J. Phys. Chem.*, *96*, 2917–2920, **1992**.
135. Tyson D. S., Henbest K. B., Bialecki J., Castellano F. N., Excited state processes in ruthenium(II)/pyrenyl complexes displaying extended lifetimes, *J. Phys. Chem. A*, *105*, 8154–8161, **2001**.
136. Roy R., Khan A., Chatterjee O., Bhunia S., Koner A. L., Perylene Monoimide as a Versatile Fluoroprobe: The Past, Present, and Future, *Org. Mat.*, *3*, 417–454, **2021**.
137. Dubey R. K. *et al.,* Excited-state interaction of red and green perylene diimides with luminescent Ru(II) polypyridine complex, *Inorg. Chem.*, *52*, 9761–9773, **2013**.
138. Mari C., Pierroz V., Ferrari S., Gasser G., Combination of Ru(ii) complexes and light: new frontiers in cancer therapy, *Chem. Sci.*, *6*, 2660–2686, **2015**.
139. Maia P. J. S. *et al.,* Singlet oxygen production by a polypyridine ruthenium (II) complex with a perylene monoimide derivative: A strategy for photodynamic inactivation of Candida albicans, *J. Photochem. Photobiol. A Chem.*, *353*, 536–545, **2018**.

140. Kodama K., Kobayashi A., Hirose T., Synthesis and spectral properties of ruthenium(II) complexes based on 2,2'-bipyridines modified by a perylene chromophore, *Tetrahedron Lett.*, *54*, 5514–5517, **2013**.
141. Jiménez A. J. *et al.,* Synthesis, Characterization, and Photoinduced Energy and Electron Transfer in a Supramolecular Tetrakis (Ruthenium(II) Phthalocyanine) Perylenediimide Pentad, *Chem. Eur. J.*, *17*, 5024–5032, **2011**.
142. Prodi A. *et al.,* Wavelength-dependent electron and energy transfer pathways in a side-to-face ruthenium porphyrin/perylene bisimide assembly, *J. Am. Chem. Soc.*, *127*, 1454–1462, **2005**.
143. Mari C. *et al.,* Evaluation of Perylene Bisimide-Based Ru II and Ir III Complexes as Photosensitizers for Photodynamic Therapy, *Eur. J. Inorg. Chem.*, *2017*, 1745–1752, **2017**.
144. García-Calvo J., Robson J. A., Torroba T., Wilton-Ely J. D. E. T., Synthesis and Application of Ruthenium(II) Alkenyl Complexes with Perylene Fluorophores for the Detection of Toxic Vapours and Gases, *Chem. Eur. J.*, *25*, 14214–14222, **2019**.
145. García-Calvo J. *et al.,* Surface functionalized silica nanoparticles for the off-on fluorogenic detection of an improvised explosive, TATP, in a vapour flow, *J. Mater. Chem. A Mater.*, *6*, 4416–4423, **2018**.
146. Li B., Qin X., You J., Cong X., Lan J., Direct arylation of phenanthroline derivatives via oxidative C-H/C-H cross-coupling: Synthesis and discovery of excellent ligands, *Org Biomol. Chem.*, *11*, 1290–1293, **2013**.
147. Mede T., Jäger M., Schubert U. S., 'Chemistry-on-the-complex': Functional RuII polypyridyl-type sensitizers as divergent building blocks, *Chem. Soc. Rev.*, *47*, 7577–7627, **2018**.
148. Sugawara E., Nikaido H., Properties of AdeABC and AdeIJK efflux systems of Acinetobacter baumannii compared with those of the AcrAB-TolC system of Escherichia coli, *Antimicrob. Agents Chemother.*, *58*, 7250–7, **2014**.
149. Li F., Collins J. G., Keene F. R. Ruthenium complexes as antimicrobial agents, *Chem. Soc. Rev.*, *44*, 2529–2542, **2015**.
150. Frei A. *et al.,* Metal complexes as a promising source for new antibiotics, *Chem. Sci.*, *11*, 2627–2639, **2020**.
151. Smitten K. L. *et al.,* Ruthenium based antimicrobial theranostics-using nanoscopy to identify therapeutic targets and resistance mechanisms in Staphylococcus aureus, *Chem. Sci.*, 11, 70-79, **2020.**
152. Liao X. *et al.,* Two ruthenium polypyridyl complexes functionalized with thiophen: synthesis and antibacterial activity against Staphylococcus aureus, *New J. Chem.*, *44*, 17215, **2020**.
153. Yang Y., Liao G., Fu C. Recent Advances on Octahedral Polypyridyl Ruthenium(II) Complexes as Antimicrobial Agents, *Polymers (Basel)*, *10*, 650, **2018**.
154. Dwyer F. P., Reid I. K., Shulman A., Laycock G. M., Dixson S., The biological actions of 1,10-phenanthroline and 2,2'-bipyridine hydrochlorides, quaternary salts and metal chelates and related compounds. 1. Bacteriostatic action on selected gram-positive, gram-negative and acid-fast bacteria, *Aust. J. Exp. Biol. Med. Sci.*, *47*, 203–218, **1969**.
155. Jain A., Garrett N. T., Malone Z. P. Ruthenium-based Photoactive Metalloantibiotics, *Photochem. Photobiol.*, *98*, 6–16, **2022**.

156. Sasahara G. L. *et al.,* Nitro-imidazole-based ruthenium complexes with antioxidant and anti-inflammatory activities, *J. Inorg. Biochem.*, *206*, 111048, **2020**.
157. Giacomazzo G. E. *et al.,* Nitroimidazole-Based Ruthenium(II) Complexes: Playing with Structural Parameters to Design Photostable and Light-Responsive Antibacterial Agents, *Inorg. Chem.*, *61*, 6689–6694, **2022**.
158. Ang C. W., Jarrad A. M., Cooper M. A., Blaskovich M. A. T., Nitroimidazoles: Molecular Fireworks That Combat a Broad Spectrum of Infectious Diseases, *J. Med. Chem.*, *60*, 7636–7657, **2017**.
159. Edwards D. I., Nitroimidazole drugs-action and resistance mechanisms I. Mechanism of action, *J. Antimicrob. Chemother., 31*, 9–20, **1993**.
160. Dingsdag S. A., Hunter N., Metronidazole: an update on metabolism, structure–cytotoxicity and resistance mechanisms, *J. Antimicrob. Chemother.*, *73*, 265–279, **2018**.
161. Bonnet S., Collin J.-P., Gruber N., Sauvage J.-P., Schofield E. R., Photochemical and thermal synthesis and characterization of polypyridine ruthenium(ii) complexes containing different monodentate ligands, *Dalton Trans.*, 4654-4662, **2003**
162. Yang X.-J. *et al.,* From model compounds to protein binding: syntheses, characterizations and fluorescence studies of $[Ru^{II}(bipy)(terpy)L]^{2+}$ complexes (bipy = 2,2′-bipyridine; terpy = 2,2′:6′,2″-terpyridine; L = imidazole, pyrazole and derivatives, cytochrome c), *Dalton Trans.*, 256–267, **2005**
163. Chen S. S., The roles of imidazole ligands in coordination supramolecular systems, *CrystEngComm*, *18*, 6543–6565, **2016**.
164. Zhang J. P., Zhang Y. B., Lin J. bin, Chen X. M., Metal azolate frameworks: From crystal engineering to functional materials, *Chem. Rev.*, *112*, 1001–1033, **2012**.
165. Djukić M. *et al.,* Further insights into ruthenium(II) piano-stool complexes with N-alkyl imidazoles, *Inorganica Chim. Acta*, *483*, 359–370, **2018**.
166. Wang L. *et al.,* Toward controlling water oxidation catalysis: Tunable activity of ruthenium complexes with axial imidazole/DMSO ligands, *J. Am. Chem. Soc.*, *134*, 18868–18880, **2012**.
167. Havrylyuk D., Deshpande M., Parkin S., Glazer E. C., Ru(ii) complexes with diazine ligands: electronic modulation of the coordinating group is key to the design of “dual action” photoactivated agents, *Chem. Comm.*, *54*, 12487–12490, **2018**.
168. Havrylyuk D., Stevens K., Parkin S., Glazer E. C., Toward Optimal Ru(II) Photocages: Balancing Photochemistry, Stability, and Biocompatibility Through Fine Tuning of Steric, Electronic, and Physiochemical Features, *Inorg. Chem.*, *59*, 1006–1013, **2020**.
169. Havrylyuk D., Hachey A. C., Fenton A., Heidary D. K., Glazer E. C., Ru(II) photocages enable precise control over enzyme activity with red light, *Nat. Commun.*, *13*, 3636, **2022**.
170. Zayat L., Filevich O., Baraldo L. M., Etchenique R., Ruthenium polypyridyl phototriggers: from beginnings to perspectives, *Philos. Trans. Royal Soc.*, *371*, 20120330, **2013**.
171. Li A., Turro C., Kodanko J. J., Ru(ii) polypyridyl complexes as photocages for bioactive compounds containing nitriles and aromatic heterocycles, *Chem. Comm.*, *54*, 1280–1290, **2018**.
172. Leiros H.-K. S. *et al.,* Structural Basis of 5-Nitroimidazole Antibiotic Resistance, *J. Biol. Chem., 279*, 55840–55849, **2004**.

173. Havrylyuk D., Deshpande M., Parkin S., Glazer E. C., Ru(ii) complexes with diazine ligands: electronic modulation of the coordinating group is key to the design of “dual action” photoactivated agents, *Chem. Comm.*, *54*, 12487–12490, **2018**.
174. Oktavia B., Lim L. W., Takeuchi T., Simultaneous Determination of Fe(III) and Fe(II) Ions via Complexation with Salicylic Acid and 1,10-Phenanthroline in Microcolumn Ion Chromatography, *Anal. Sci.*, *24*, 1487–1492, **2008**.
175. Heath H., A new sensitive chemical actinometer - II. Potassium ferrioxalate as a standard chemical actinometer, *Proc. R. Soc. Lond. A Math Phys. Sci.*, *235*, 518–536, **1956**.
176. Nicholson W. L., Park R., Anaerobic growth of Bacillus subtilis alters the spectrum of spontaneous mutations in the rpoB gene leading to rifampicin resistance, *FEMS Microbiol. Lett.*, *362*, fnv213, **2015**.
177. Frisch M. J. *et al.* Gaussian 09, Gaussian, Inc. Wallingford CT. *Gaussian, Inc. Wallingford CT* Preprint at (2009).

Appendix

Publications

Journal of Inorganic Biochemistry 220 (2021) 111467

Contents lists available at ScienceDirect

Journal of Inorganic Biochemistry

journal homepage: www.elsevier.com/locate/jinorgbio

Exploring the potential of highly charged Ru(II)- and heteronuclear Ru(II)/Cu(II)-polypyridyl complexes as antimicrobial agents

Luca Conti [a,*], Alessio Mengoni [b,*], Gina Elena Giacomazzo [a], Lorenzo Mari [a], Mauro Perfetti [a], Camilla Fagorzi [b], Lorenzo Sorace [a], Barbara Valtancoli [a], Claudia Giorgi [a,*]

[a] Department of Chemistry "Ugo Schiff", University of Florence, via della Lastruccia 3, 50019 Sesto Fiorentino, Italy
[b] Department of Biology, University of Florence, via Madonna del Piano 6, 50019 Sesto Fiorentino (FI), Italy

ARTICLE INFO

Keywords:
Ru(II)-polypyridyl complexes
aPDT
Singlet oxygen
ROS
Supramolecular chemistry
B. subtilis

ABSTRACT

The antimicrobial potential of two ruthenium(II) polypyridyl complexes, $[Ru(phen)_2\mathbf{L1}]^{2+}$ and $[Ru(phen)_2\mathbf{L2}]^{2+}$ (phen = 1,10-phenanthroline) containing the 4,4′-(2,5,8,11,14-pentaaza[15])-2,2'-bipyridilophane (**L1**) and the 4,4′-bis-[methylen-(1,4,7,10-tetraazacyclododecane)]-2,2′ bipyridine (**L2**) units, is herein investigated. These peculiar polyamine frameworks afford the formation of highly charged species in solution, influence the DNA-binding and cleavage properties of compounds, but they do not undermine their singlet oxygen sensitizing capacities, thus making these complexes attractive $^1O_2$ generators in aqueous solution. **L1** and **L2** also permit to stably host *Fenton* -active Cu^{2+} ion/s, leading to the formation of mixed Ru^{2+}/Cu^{2+} forms capable to further strengthen the oxidative damages to biological targets. Herein, following a characterization of the Cu^{2+} binding ability by $[Ru(phen)_2\mathbf{L2}]^{2+}$, the water-octanol distribution coefficients, the DNA binding, cleavage and $^1O_2$ sensitizing properties of $[Ru(phen)_2\mathbf{L2}]^{2+}$ and $[Cu_2Ru(phen)_2\mathbf{L2}]^{6+}$ were analysed and compared with those of $[Ru(phen)_2\mathbf{L1}]^{2+}$ and $[CuRu(phen)_2\mathbf{L1}]^{4+}$. The antimicrobial activity of all compounds was evaluated against *B. subtilis,* chosen as a model for gram-positive bacteria, both under dark and upon light-activation. Our results unveil a notable phototoxicity of $[Ru(phen)_2\mathbf{L2}]^{2+}$ and $[Cu_2Ru(phen)_2\mathbf{L2}]^{6+}$, with MIC (minimal inhibitory concentrations) values of 3.12 μM. This study highlights that the structural characteristics of polyamine ligands gathered on highly charged Ru(II)-polypyridyl complexes are versatile tools that can be exploited to achieve enhanced antibacterial strategies.

1. Introduction

The fight against bacterial infections represents a major challenge for the global public health community. The widespread use of antibiotics over the last decades has determined the emergence of drug-resistant populations of microorganisms, which have become an important cause of death worldwide. Only in Europe, the WHO reports that each year over 25,000 people die from infections caused by antibiotic-resistant bacteria [1] while the cost for the management of hospital-acquired infections in the USA was estimated to be 4.4 billion USD per year [2]. Therefore, there is an urgent need for the development of new antimicrobial agents, which should be based on a new class of compounds, rather than on analogues of known scaffolds.

To this aim, following the successful application of *cis*-diamminedichlorido-platinum(II) (*cis*-platin) and its derivatives as chemotherapeutics [3,4] a considerable attention have been focused on the biological properties of compounds based upon other transition metals [5–7]. In particular, Ru(II) polypyridyl complexes constitutes attracting molecules due to their high thermodynamic/kinetic stabilities, the capacity to reversibly interact with key biological substrates (DNA, RNA and proteins), and their versatile chemical-physical repertoire. Moreover, some of their fundamental physicochemical properties, such as water/lipid solubility, charge, absorption and targeting features, can be easily modified by tuning the nature of the metal-coordinated ligands, thus making this class of compounds an appealing and versatile choice not only as chemotherapeutics, but even in the rational design of effective antibacterial agents.

Dwyer and coworkers [8,9] were the first who shown the antibacterial potential of this typology of compounds, as demonstrated by their pioneering work on $[Ru(phen)_3]^{2+}$, $[Ru(Me_4phen)_2(acac)]^+$ and $[Ru(Me_4phen)_3]^{2+}$, (phen = 1,10-phenanthroline, acac = acetylacetonato), where the latter two complexes were found to be particularly effective,

* Corresponding authors.
E-mail address: luca.conti@unifi.it (L. Conti).

https://doi.org/10.1016/j.jinorgbio.2021.111467
Received 15 February 2021; Received in revised form 29 March 2021; Accepted 18 April 2021
Available online 22 April 2021

especially against gram-positive bacteria. However, notwithstanding the promising results, it has only been over the last ten years that Ru(II)-polypyridyl complexes have attracted a renewed interest in their antimicrobial features, probably due to the increasing incidence of drug-resistance bacterial strains nowadays; this has greatly expanded the range of ruthenium complexes investigated for this purpose [10–16]. The mechanisms underlying the antimicrobial effect of such compounds are still to be completely elucidated: nucleic acids and/or proteins are generally proposed as the most important intracellular targets [17,18] but alternative mechanisms of action involving different targets, such as the membrane depolarization [19], are also possible.

In this scenario, a promising approach is represented by the use of ruthenium complexes in combination with light in the so-called antibacterial photodynamic therapy (aPDT) [20,21]. This technique relies on the use of a molecule, called photosensitizer (PS), that can be activated with low-energy light to produce highly reactive oxygen species (ROS), namely free radicals (*type I* reactions) and/or the potent singlet oxygen ($^1O_2$) (*type II* reactions), which can in turn seriously damage biological substrates leading to cell death [22–24]. The main advantages of this technique thus consist not only in the possibility to achieve a complete spatial and temporal control over the drug-activation but even in the multi-target character of the light-induced ROS, which makes bacteria extremely difficult to develop any resistance against these multiple attacks [25,26]. The rich physicochemical repertoire of Ru(II)-polypyridyl complexes, which also include long luminescence lifetimes and good singlet oxygen sensitizing capacities, makes such compounds natural candidates as PS agents in aPDT. Indeed, since Donnelly et al. in 2007 reported that the antimicrobial activity of $[Ru(dmob)_3]Cl_2$ (dmob = 4,4′-dimethoxy-2,2′-bipyridine) was significantly enhanced upon white light irradiation, with MIC values of 12.5, 50 and 12.5 μg/ml against *S. aureus*, *P. aeruginosa* and *C. albicans*, respectively [27], the number of Ru(II)-polypyridyl complexes studied in aPDT has considerably increased [28–32].

An interesting case has been recently reported by Feng et al. [33], who demonstrated that highly charged ruthenium complexes featuring quaternary ammonium-modified bipyridine ligands selectively inactivate *S. aureus* and methicillin-resistant *Staphylococcus aureus* (MRSA) strains upon light-activation, over mammalian cells. Since the highest activity was observed for the most charged compound (bearing eight positive charges, 6–7 log reduction in bacterial viability when irradiated with 470 nm light), the hydrophilic character of the ruthenium complexes, along with their spherical octahedron coordination structures, were proposed to play a central role in both the efficacy and the selectivity of these compounds. In particular, the authors linked the great antimicrobial activity to the possibility to establish strong electrostatic interactions between the complexes and the negative charges of the bacterial cell wall (i.e. the teichoic acids of Gram-positive bacteria as *Bacillus subtilis*) [34].

Being inspired by this panorama, we decided to investigate the antimicrobial properties of two highly charged ruthenium(II)-polypyridyl complexes which have been recently synthesized by our group; $[Ru(phen)_2\mathbf{L1}]^{2+}$ [35] and $[Ru(phen)_2\mathbf{L2}]^{2+}$ [36], featuring the peculiar 4,4′-(2,5,8,11,14-pentaaza [15])-2,2′-bipyridilophane (**L1**) and the 4,4′-bis-[methylen-(1,4,7,10-tetraazacyclododecane)]-2,2′ bipyridine (**L2**) units, respectively (Chart 1). The presence of a high number of easily protonable nitrogen groups on the polyazamacrocyclic moieties appended to the 4,4′ position of the metal-coordinated bipyridyl units affords the formation in solution of highly charged species and confers to

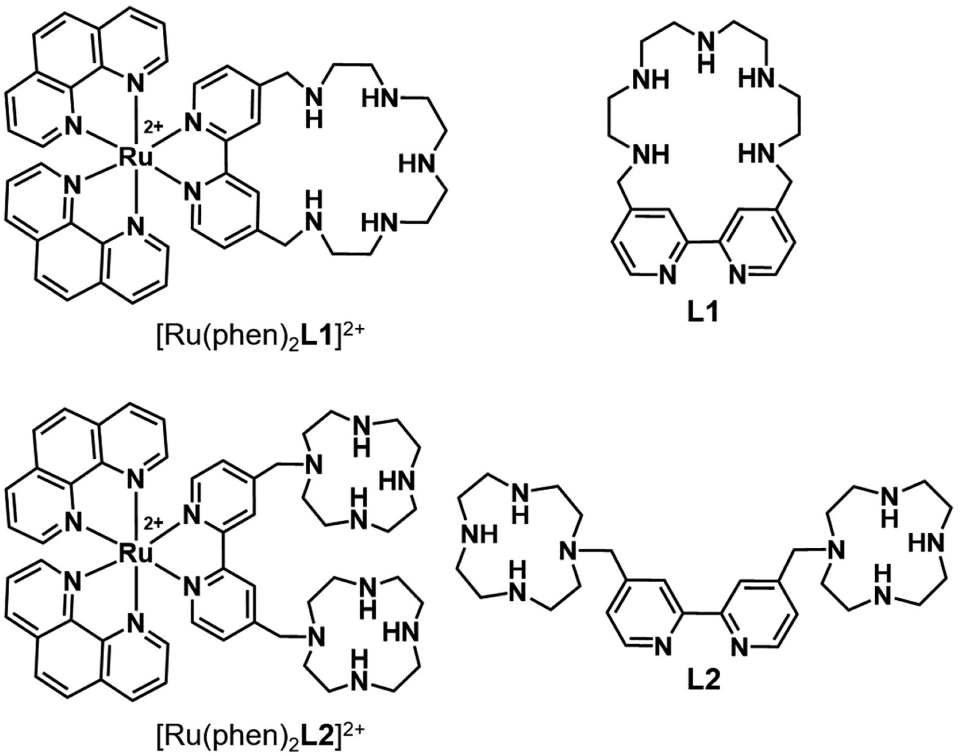

Chart 1. Sketch of $[Ru(phen)_2\mathbf{L1}]^{2+}$ and of $[Ru(phen)_2\mathbf{L2}]^{2+}$ along with their correspondent polyaminomacrocyclic frameworks **L1** and **L2**. Ligands are shown in their neutral (not-protonated amino groups) form for clarity.

the resulting compounds not only an excellent water-solubility, a necessary prerequisite for their biological application, but also influences their DNA-binding and -cleavage properties. On the other side, the $^1O_2$ sensitizing capabilities of Ru-centers are not significantly affected by the modified bipyridyl residue, thus making [Ru(phen)$_2$**L1**]$^{2+}$ and [Ru(phen)$_2$**L2**]$^{2+}$ attractive PS agents for the light-activated $^1O_2$ generation directly in aqueous media. Moreover, the polyamine moieties **L1** and **L2** can stably bind one or two metal ions, such as the *Fenton*-active Cu^{2+} ion, resulting in the formation of the heteronuclear [CuRu(phen)$_2$**L1**]$^{4+}$ and [Cu$_2$Ru(phen)$_2$**L2**]$^{6+}$ complexes. These mixed Ru^{2+}/Cu^{2+} species may lead, in principle, to the production of ROS species via *Fenton* or *Fenton*-like processes involving the Cu^{2+} centers, thus providing an alternative/additional mechanism of action capable to further strengthen the oxidative damage of selected targets. In the case of [Ru(phen)$_2$**L1**]$^{2+}$ and [CuRu(phen)$_2$**L1**]$^{4+}$, their biological potential was previously evaluated on an A375 human melanoma cell line, chosen as a model for cancer cell; our study [35] revealed good cellular-uptake and phototoxicities for both compounds, with the mixed Ru^{2+}/Cu^{2+} complex exhibiting the greatest photo-induced dose-dependent cytotoxicity.

Based on these results, we decided to extend the investigation of [Ru(phen)$_2$**L1**]$^{2+}$ and [Ru(phen)$_2$**L2**]$^{2+}$, along with their corresponding mixed Ru^{2+}/Cu^{2+} complexes [CuRu(phen)$_2$**L1**]$^{4+}$ and [Cu$_2$Ru(phen)$_2$**L2**]$^{6+}$, to their possible use as antimicrobial agents. In particular, the replacement by the unique macrocyclic framework of [Ru(phen)$_2$**L1**]$^{2+}$ with the two distinct polyamine units of [Ru(phen)$_2$**L2**]$^{2+}$, would allow us to establish whether different structural features of the modified bipyridyl moiety of ruthenium compounds may affect their chemical-physical properties and/or their biological behaviour.

In the present work, we report on the Cu^{2+} binding ability by [Ru(phen)$_2$**L2**]$^{2+}$ in aqueous media, studied by means of potentiometric, UV–vis and fluorescence measurements. Afterwards, the distribution coefficients (log$D_{7.4}$), the DNA binding, cleavage and $^1O_2$ sensitizing properties of [Ru(phen)$_2$**L2**]$^{2+}$ and [Cu$_2$Ru(phen)$_2$**L2**]$^{6+}$ were determined. The obtained results are herein compared to those of [Ru(phen)$_2$**L1**]$^{2+}$ and [CuRu(phen)$_2$**L1**]$^{4+}$ and discussed. Finally, the antimicrobial activities of [Ru(phen)$_2$**L1**]$^{2+}$, [Ru(phen)$_2$**L2**]$^{2+}$, [CuRu(phen)$_2$**L1**]$^{4+}$ and [Cu$_2$Ru(phen)$_2$**L2**]$^{6+}$ were evaluated against *Bacillus subtilis* (strain 168), chosen as a model for gram positive bacteria, both under dark conditions and upon irradiation with low-energy light.

The results herein reported may constitute an important knowledge about the relation between the different structural characteristics of polyamino ligands gathered on Ru(II)-polypyridyl complexes and their potential antibacterial activities.

2. Materials and methods

2.1. Synthesis and materials

The ruthenium compounds [Ru(phen)$_2$**L1**]$^{2+}$, and [Ru(phen)$_2$**L2**]$^{2+}$ were obtained as their respective hydrochloride salts [Ru(phen)$_2$**L1**]Cl$_2$·5HCl·2H$_2$O and [Ru(phen)$_2$**L2**]Cl$_2$·6HCl·2H$_2$O while [CuRu(phen)$_2$**L1**]$^{4+}$ was obtained as [CuRu(phen)$_2$**L1**](ClO$_4$)$_4$·4H$_2$O, as described in our previous reports [35,36], All materials were of reagent grade and used without further purification. *Calf thymus* DNA (ct-DNA) was purchased from Sigma Aldrich in the form of sodium salt. Its solutions were obtained by dissolving ct-DNA in Tris-HCl buffer (10 mM Tris-HCl, 50 mM NaCl, pH 7.2), while its purity was controlled by UV–vis absorption measurements; an absorbance ratio between 260 and 280 nm within 1.8–1.9:1 indicates that DNA is sufficiently free of protein [37]. The DNA concentration per nucleotide was obtained by using the molar absorption coefficient at 260 nm of 6600 M^{-1} cm^{-1} [38].

We point out that, since the protonation state of each ruthenium compound depends on the pH (*vide infra*), these complexes can be present in solution in differently charged forms at different pH values.

In the experimental conditions (range of ruthenium concentration and pH) of the experiments discussed in paragraphs 3.3–3.6, the predominant species of [Ru(phen)$_2$**L1**]$^{2+}$ and [Ru(phen)$_2$**L2**]$^{2+}$ present in solution are their corresponding di- and tetra-protonated forms [H$_2$Ru(phen)$_2$**L1**]$^{4+}$ and [H$_4$Ru(phen)$_2$**L2**]$^{6+}$, while their respective copper complexes are effectively present as [CuRu(phen)$_2$**L1**]$^{4+}$ and [Cu$_2$Ru(phen)$_2$**L2**]$^{6+}$. The relative abundances of such species (expressed in terms of ligand percentage) in each condition tested have been potentiometrically determined and are listed in Table S2 of Supplementary Material).

For the clarity of discussion, we will keep on referring to ruthenium compounds simply as [Ru(phen)$_2$**L1**]$^{2+}$, [Ru(phen)$_2$**L2**]$^{2+}$, [CuRu(phen)$_2$**L1**]$^{4+}$ and [Cu$_2$Ru(phen)$_2$**L2**]$^{6+}$ while specifying in each case their prevalent forms in solution in the experiments herein reported.

2.1.1. Synthesis of [Cu$_2$Ru(phen)$_2$**L2**](ClO$_4$)$_6$·3H$_2$O

The copper(II)-complex [Cu$_2$Ru(phen)$_2$**L2**]$^{6+}$ was synthesized by following a similar procedure to that reported for preparation of the analogues [CuRu(phen)$_2$**L1**]$^{4+}$ [35]. Briefly, 5.56 mg of Cu(ClO$_4$)$_2$·6H$_2$O (0.015 mmol) were added to an aqueous solution (20 ml) containing an equimolar amount (19.68 mg) of [Ru(phen)$_2$**L2**]Cl$_2$·6HCl·2H$_2$O and the pH was adjusted to 6.5 with NaOH 0.1 M. Following addition of NaClO$_4$ (100 mg), the solution was stirred at room temperature for 3 h. The slow evaporation of the solvent led to the precipitation of the hexaperchlorate threehydrated salt of [Cu$_2$Ru(phen)$_2$**L2**]$^{6+}$, which was collected by filtration and washed with cold diethyl ether.

Yield: 19 mg (72%). Elem. Anal. calcd for $C_{52}H_{70}N_{14}RuCu_2Cl_6O_{27}$: C, 35.40; H, 3.99; N, 11.12. Found: C, 35.51; H, 4.03; N, 11.11%.

2.2. Potentiometric measurements

The ability of [Ru(phen)$_2$**L2**]$^{2+}$ to coordinate Cu^{2+} ions in aqueous media was investigated by means of potentiometric titrations in NaCl 0.1 M at 298 ± 0.1 K, by using equipment and procedures that have been previously described [39–41].

As hydrogen concentration probe, we used a combined glass electrode, which was calibrated by titrating with CO_2-free NaOH solutions known amounts of HCl solutions while using an Ag/AgCl electrode in saturated aqueous KCl as reference electrode. The NaOH solution was standardized against carbonate-free potassium hydrogen phthalate (standard reference material for pH measurement, Sigma Aldrich) and stored under nitrogen atmosphere. Measurements were carried out in a range of pH within 2–12 by using a total concentration of ruthenium compound of generally 1×10^{-3} mol/dm^3; the Cu^{2+} concentration was varied from 0.2[Ru(phen)$_2$**L2**]$^{2+}$ to 1.8[Ru(phen)$_2$**L2**]$^{2+}$ to ascertain the stoichiometries of the complexed species formed in solution. The Gran's method [42] was employed to determine the equivalent point, the ionic product (pK_w = 13.73 ± 0.01 in the present experimental conditions) and the value of the standard potential E_o. For each system at least three titration experiments, consisting of ca. 100 data points each, were performed. From the resulting *e.m.f.* data the equilibrium constants for Cu^{2+} complexation by [Ru(phen)$_2$**L2**]$^{2+}$ were determined by employing the computer program HYPERQUAD [43]. The corresponding distribution diagrams of the species present in solution were then calculated by using the Hyss program [44]. All the reagent solutions were prepared by using freshly boiled, doubly deionized water, saturated with anhydrous nitrogen prior to use.

The obtained LogK values for metal complexation of [Ru(phen)$_2$**L2**]$^{2+}$ are compared with those previously determined for [Ru(phen)$_2$**L1**]$^{2+}$ in Table 1, while the protonation constants of both the ruthenium compounds are listed in Table S1 (ESI).

2.3. Electronic absorption, fluorescence and EPR measurements

Absorption spectra were collected by using a PerkinElmer Lambda 6 spectrophotometer while fluorescence measurements were performed on a LS55 spectrofluorimeter. All experiments were performed at 298.1

± 0.1 K. X-band EPR (Electron Paramagnetic Resonance) spectra were recorded on a Bruker Elexsys E500 spectrometer equipped with an ESR900 (Oxford Instruments) continuous-flow ^{4}He cryostat to work at low temperature and a SHQ resonator.

2.4. Singlet oxygen detection

The singlet oxygen sensitizing properties of $[Ru(phen)_2\mathbf{L2}]^{2+}$ and of $[Cu_2Ru(phen)_2\mathbf{L2}]^{6+}$ were analysed by monitoring the phosphorescence signal of $^1O_2$ at 1270 nm, generated from air-saturated CH_3CN solutions of Ru(II)-compounds upon laser excitation. The obtained results expressed as $^1O_2$ quantum yields $\varphi_\Delta(^1O_2)$ are compared with those previously obtained by the same method for $[Ru(phen)_2\mathbf{L1}]^{2+}$ and $[CuRu(phen)_2\mathbf{L1}]^{4+}$ in Table 2.

As laser source we used a Ti-Sapphire ultrafast laser delivering 100 fs long pulses at 82 MHz repetition rate and 800 nm wavelength; the laser pulse was frequency doubled at 400 nm to excite the samples. Following saturation with air of acetonitrile solutions of Ru(II)-compounds directly in 1 cm path quartz cuvettes, the samples were laser irradiated and the $^1O_2$ emission was collected by a lens set at 90° with respect to the 400 nm exciting laser beam and focused on a N_2 cooled InGaAs photodiode. An interference filter centered at 1270 ± 20 nm was placed in front of the photodiodie to select the $^1O_2$ emission while a chopper working at 90 Hz, placed on the exciting beam and used to trigger a lock-in amplifier, singled out and averaged the signal from the photodiode.

To ascertain that only singlet oxygen emission was measured by our experimental set-up, the solutions of samples were degassed through pump-freeze-thow cycles in quartz tubes sealed under vacuum; no signal from these samples was detected. Experiments were carried out by employing different concentrations of ruthenium compounds, with absorbance values at 400 nm in the range 0.08–0.2, and by increasing the power of laser applied. Linearity with respect to applied laser power was observed. The $^1O_2$ quantum yields (φ_Δ) of samples were calculated by applying the formula:

$$\varphi_\Delta(S) = \varphi_\Delta(R)\frac{s(S)x\left[1-10^{-A(R)}\right]}{s(R)x\left[1-10^{-A(S)}\right]} \quad (1)$$

where φ_Δ (S) and φ_Δ (R) represent the $^1O_2$ quantum yields of samples (S) and of the reference (R) respectively, s is the slope of the linear plot of the intensity of $^1O_2$ luminescence signal as a function of the intensity of the exciting laser, while $A(R/S)$ represents the absorbance values at 400 nm of the R/S solutions.

As reference compound (R) we used tetraphenylporphyrin (TPP), for which a φ_Δ value of 0.60 was reported by R. Schmidt and E. Afshari by chemical methods in acetonitrile [45]. The resulting φ_Δ values obtained for ruthenium compounds were also compared with that of $[Ru(phen)_3]^{2+}$, given the analogues chemical makeup of the ruthenium center of the latter compound.

2.5. Determination of distribution coefficients ($logD_{7.4}$)

The octanol–water distribution coefficients of all the ruthenium compounds were determined at pH 7.4 by employing the shake-flask procedure [46]. The obtained results, expressed as logarithm values $logD_{7.4}$, are shown in Table 2. Briefly, aqueous solutions of the tested compounds (16 μM) buffered with phosphate buffer at pH 7.4 were mixed in a flask with n-octanol. Both solvents were mutually pre-saturated at room temperature. The compounds were then allowed to equilibrate between the organic and the aqueous media by flask hand-shaking and then were left resting for at least 24 h to ensure the complete separation of the two phases. Afterwards, the concentrations of ruthenium compounds in the aqueous phase were spectrophotometrically determined while those in the organic phase were obtained by difference. The $logD_{7.4}$ values were calculated by using the Eq. 2:

$$\log D_{7.4}(S) = log\frac{C_{Octanol}}{C_{Water}} = log\left(\frac{m_O \text{ x } V_W}{m_W \text{ x } V_O}\right) \quad (2)$$

where S stands for the sample (ruthenium compounds) analysed, $C_{Octanol}$ and C_{Water} represent the total concentration of the compound in the organic and in the aqueous phase, m stands for the mass of compound in the aqueous (w) or in the organic phase (o) and V was the volume of each phase. A ligand concentration of 15 μM was used while different V_w/V_o ratios were employed, varying from 0.5:1 to 2:1. Each determination was performed in triplicate.

Because of the ionizable nature of compounds herein analysed, we referred to distribution coefficients (D) instead of partition coefficients (P). In fact, differently from logP, which can be used to characterize the octanol-water partition of a compound in its neutral/uncharged form, $logD_{7.4}$ more adequately describes the distribution of a compound that can be partially ionized at a given pH value.

2.6. UV titrations of Ru compounds with ct-DNA

The binding ability of the **L2**-bearing ruthenium systems towards *calf thymus* DNA (ct-DNA) was explored by monitoring the changes at the $d\pi$–π^* metal to ligand charge transfer (MLCT) band of ruthenium complexes, centered at ca. 454 nm, induced by addition of increasing amounts of the biopolymer (0–400 μM) to buffered solutions (Tris-HCl buffer, 10 mM, NaCl 50 mM, pH 7.2) containing the metal compounds at fixed concentration. To eliminate the contribute to the absorbance of the DNA itself, equal amounts of concentrated solutions of DNA were added both to the sample and to the reference solution, the latter consisting of only Tris-HCl buffer. After each DNA addition, samples were incubated for 10 min at 298.1 ± 0.1 K before collecting the absorption spectra. From the absorption data, the intrinsic binding constants K_b of ruthenium compounds with ct-DNA were determined by using Eq. 3: [47–49].

$$\frac{[DNA]}{(\varepsilon_a-\varepsilon_f)} = \frac{[DNA]}{(\varepsilon_b-\varepsilon_f)} + \frac{1}{K_b(\varepsilon_b-\varepsilon_f)} \quad (3)$$

where [DNA] is the concentration of ct-DNA in base pairs, and the apparent absorption coefficients ε_a, ε_f and ε_b correspond to $A_{obs.}/[Ru]$ (Ru = Ru compounds), to the molar extinction coefficient for the free (DNA-unbounded) Ru complex and to the molar extinction coefficient for the Ru complex in its totally DNA-bound form. The binding constants (K_b) are obtained by the ratio of slope to the intercept in the linear plots of $[DNA]/|\varepsilon_a-\varepsilon_f|$ vs. [DNA]. The obtained results are listed, along with those of **L1**-containing compounds, in Table 2.

2.7. DNA-cleavage activity

Plasmid (pUC18) DNA was extracted from overnight grown cultures of *E. coli* DH5alpha strain in Luria-Bertani medium supplemented with 50 mg/mL Ampicillin. Extracted plasmid DNA was checked for integrity by 1% agarose gel electrophoresis in Tris-Acetate EDTA buffer (TAE, 40 mM Tris, 20 mM acetic acid, 1 mM EDTA) run at 7 V/cm for 40′ and stained with 10 μg/mL ethidium bromide and quantified by spectrophotometric reading at 260 nm and 280 nm (NanoQuantPlate, Infinite Pro 200 plate reader Tecan, Switzerland). DNA cleavage by ruthenium compounds was performed by incubating them with plasmid DNA (50 μg/mL) in Tris-HCl buffer (Tris-HCl 10 mM, NaCl 50 mM, pH 7.2), then checking supercoiled plasmid disappearance by 1% agarose gel electrophoresis in TAE run at 7 V/cm for 60′ and stained with 10 μg/mL ethidium bromide, as previously reported [35]. Photoactivation experiments were performed by irradiating the samples with visible light (LED, λ > 430 nm, 30 W, 15 min).

2.8. Microbiological methods

Bacterial strains were grown in Luria Bertani (Lysogeny broth [50])

medium (NaCl 10 g/L, Tryptone 10 g/L, Yeast Extract 5 g/L) at 37 °C. The model bacterium *Bacillus subtilis* 168 strain [51] was used for determination of inhibitory concentrations.

2.8.1. Determination of inhibitory concentrations

Overnight grown liquid cultures were prepared in LB medium (10 mL) from single colonies freshly grown on LB agar Petri plates. Cultures were incubated at 37 °C, 225 rpm shaking. From overnight cultures, cells were diluted to OD $_{600\ nm}$ = 0.1 in fresh LB medium, then solutions of ruthenium compounds were added to the diluted cultures. The mixtures (150 μL total volume) were then splitted in a 96-well microtiter plate (Sarstedt, Germany). Irradiation for photoactivation was performed on the surface of the microtiter plate after 30 min incubation by employing LED light (λ > 430 nm, 30 W, 15 min). Microtiter plates were then incubated on an Infinite Pro 200 plate reader (Tecan, Switzerland). OD $_{600\ nm}$ was read every hour for up to 20 h, until growth reached the stationary phase. The MIC values (minimal inhibitory concentrations) were expressed in μM and calculated as the drug concentration inducting at least 60% growth reduction or 40% residual growth.

2.9. Cell permeation

To investigate the kinetics of cell permeation of ruthenium compounds, *B. subtilis* bacterial cultures were added to 1.5 mL polyproprilene tubes (7.5 × 10^8 cells/tube) and treated with a fixed concentration of ruthenium compounds (25 μM) at pH 7.2. Cells were incubated for 30 min, 3 h, 5 h, 24 h, centrifuged and pellets were washed three times with 1 mL 0.9% NaCl solution to remove extracellular ruthenium compounds present in the medium. In the washed bacterial cell pellets the ruthenium-content was assumed as indicator for drug permeation and was determined by Inductively Coupled Plasma Atomic Emission Spectroscopy (ICP-AES) [52]; results were expressed as ng of Ru/10^8 cells. Experiments were performed in triplicate.

3. Results and discussion

3.1. Cu^{2+} binding by $[Ru(phen)_2L2]^{2+}$

The coordination ability of $[Ru(phen)_2\mathbf{L2}]^{2+}$ towards Cu^{2+} was studied by means of potentiometric measurements in NaCl 0.1 M at 298.1 ± 0.1 K. Since the process of metal complexation generally competes with that of ligand protonation, the acid-base properties of the compound need be taken into account. For that reason, in Table S1 of the Supplementary Material the protonation constants of $[Ru(phen)_2\mathbf{L2}]^{2+}$ are summarized along with those of $[Ru(phen)_2\mathbf{L1}]^{2+}$. Briefly, the two compounds possess up to three ($[Ru(phen)_2\mathbf{L1}]^{2+}$) or four ($[Ru(phen)_2\mathbf{L2}]^{2+}$) nitrogen atoms which behave as strong to moderate bases (with LogK values ranging from 5.32 to 11.02 log. units) and two nitrogen groups which behave as weak bases (LogK < 4 log. units). In the case of $[Ru(phen)_2\mathbf{L2}]^{2+}$, the constants for the addition of the last two protons in the $[H_4Ru(phen)_2\mathbf{L2}]^{6+}$ species appear as a unique value, because of the occurrence of these protonation equilibria in very close pH regions.

Potentiometric measurements afforded us to obtain the binding constants for the Cu^{2+}-complexation by $[Ru(phen)_2\mathbf{L2}]^{2+}$; these values are compared with those previously found for $[Ru(phen)_2\mathbf{L1}]^{2+}$ [35] in Table 1, while the distribution diagrams of the species present in solution for the systems $[Ru(phen)_2\mathbf{L2}]^{2+}$:$Cu^{2+}$ in 1:2 and 1:1 molar ratios are respectively reported in Fig. 1 and Fig. S1 (ESI). A first analysis of these data reveals that $[Ru(phen)_2\mathbf{L2}]^{2+}$ roughly parallels the binding behaviour of $[Ru(phen)_2\mathbf{L1}]^{2+}$, but it also shows significative differences likely accounting for the possibility to host protons, as well as cationic guests, into two separate binding units instead of into a single polyamino macrocyclic framework (*vide infra*).

In particular, $[Ru(phen)_2\mathbf{L2}]^{2+}$ displays a high tendency to form both stable mono- and dinuclear complexes with Cu^{2+} in aqueous media,

Table 1
Equilibrium constants (LogK values) for the Cu^{2+} complexation by $[Ru(phen)_2\mathbf{L1}]^{2+}$ and $[Ru(phen)_2\mathbf{L2}]^{2+}$ determined by means of potentiometric measurements in 0.1 M NaCl at 298.1 ± 0.1 K ($[L^{2+}] = 1 \times 10^{-3}$ M).

Equilibria	$Log_{10}K^*$	
L^{2+} =	$[Ru(phen)_2\mathbf{L1}]^{2+}$[a]	$[Ru(phen)_2\mathbf{L2}]^{2+}$[b]
$L^{2+} + Cu^{2+} = [CuL]^{4+}$	15.12 (6)	16.50 (5)
$[CuL]^{4+} + H^+ = [HCuL]^{5+}$	5.63 (7)	7.61 (6)
$[HCuL]^{5+} + H^+ = [H_2CuL]^{6+}$	3.94 (7)	6.01 (5)
$[CuL]^{4+} + OH^- = [CuL(OH)]^{3+}$	6.12 (9)	–
$[CuL]^{4+} + Cu^{2+} = [Cu_2L]^{6+}$	–	10.89 (3)
$L^{2+} + 2Cu^{2+} + OH^- = [Cu_2L(OH)]^{5+}$	12.71 (8)	–
$[Cu_2L]^{6+} + 2OH^- = [Cu_2L(OH)_2]^{4+}$	–	11.30 (7)

[*] Values in parenthesis are standard deviations on the last significative figures.
[a] L. Conti et al., Chem. Eur. J., 25, (2019), 10,606–10,615.
[b] This work.

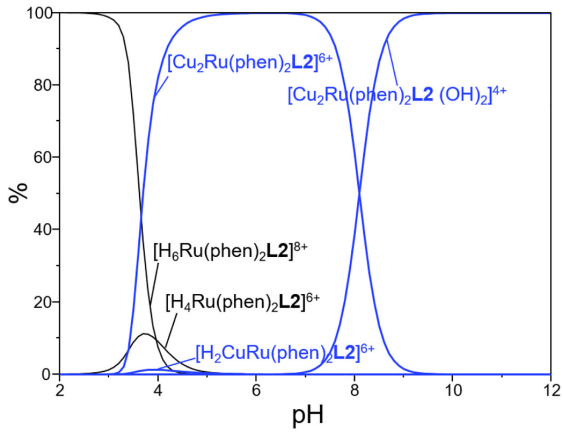

Fig. 1. Distribution diagram of the species present in solution for the system $[Ru(phen)_2\mathbf{L2}]^{2+}/Cu^{2+}$ in 1:2 molar ratio. [Ru] = 1 × 10^{-3} M, [Cu^{2+}] = 2 × 10^{-3} M, NaCl 0.1 M, 298.1 ± 0.1 K (Ru = $[Ru(phen)_2\mathbf{L2}]^{2+}$).

with LogK values of 16.50 and 10.59 for the addition of the first and the second metal ion, respectively. The decrease of the binding constant relative to the addition of the second Cu^{2+} can be mainly explained in terms of increased electrostatic repulsion between the positive charged metal centers, as reported, for example, in the coordination of Cu^{2+} by polyamine receptors containing up to three distinct cyclen moieties. [53] Another point that can be evidenced is that the stability of the Cu^{2+}-mononuclear complex of $[Ru(phen)_2\mathbf{L2}]^{2+}$ is somewhat comparable to that formed by $[Ru(phen)_2\mathbf{L1}]^{2+}$ (LogK of 16.50 and 15.12 log. units respectively for $[CuRu(phen)_2\mathbf{L2}]^{4+}$ and $[CuRu(phen)_2\mathbf{L1}]^{4+}$) and, analogously to $[Ru(phen)_2\mathbf{L1}]^{2+}$, [54] this value is considerably diminished with respect to that one corresponding to the metal complex formed by the free (Ru-unbounded) polyamine unit. Indeed, the LogK value for the addition of Cu^{2+} to $[Ru(phen)_2\mathbf{L2}]^{2+}$ is c.ca. 6.9 log. units lower than that reported for the addition of the cation directly to the 'Ru-free' cyclen moiety. [55] This is a commonly observed effect that arises from the reduced metal-ion coordination ability of the polyamine units when linked, through a bipyridyl unit, to the ruthenium center, because of to the increased electrostatic repulsion between the two metals in the mixed Ru^{2+}/Cu^{2+} species. Moreover, in the case of $[Ru(phen)_2\mathbf{L2}]^{2+}$, the tertiary amine groups of the **L2** cyclen units possess a lower coordination ability with respect to the secondary ones of a pure cyclen moiety.

A significative difference between $[Ru(phen)_2\mathbf{L2}]^{2+}$ and $[Ru(phen)_2\mathbf{L1}]^{2+}$ consists in the more pronounced tendency of the Cu^{2+}-

mononuclear complex of the former to coordinate two extra protons, as revealed by the high LogK values (> 6 log. units) found for the addition of H^+ to $[CuRu(phen)_2\mathbf{L2}]^{4+}$ and to $[HCuRu(phen)_2\mathbf{L2}]^{5+}$; the relative protonation constants for $[Ru(phen)_2\mathbf{L1}]^{2+}$ are 5.63 and 3.94 log. units, respectively (Table 1). Such remarkably high values are compatible with the protonation constants of a '*Cu^{2+}-free*' cyclen moiety, and thus suggest that in the $[HCuRu(phen)_2\mathbf{L2}]^{5+}$ and in the $[H_2CuRu(phen)_2\mathbf{L2}]^{6+}$ species the Cu^{2+} ion is coordinated within one cyclen unit while the addition of protons interests the other, metal-unbounded, macrocyclic residue. On this basis, the minor stability of the protonated forms of $[CuRu(phen)_2\mathbf{L1}]^{4+}$ can be ascribed to the close proximity of protons to the metal ion hosted within the same macrocyclic cavity (**L1**). As a result, in a system containing equimolar amounts of $[Ru(phen)_2\mathbf{L2}]^{2+}$ and Cu^{2+} (Fig. S1, ESI), $[HCuRu(phen)_2\mathbf{L2}]^{5+}$ and $[H_2CuRu(phen)_2\mathbf{L2}]^{6+}$ are easily formed in solution, from slightly acidic to slightly alkaline pH values. Differently, in a system containing two equivalents of Cu^{2+} (Fig. 1), the predominant species at neutral pH values is the dinuclear $[Cu_2Ru(phen)_2\mathbf{L2}]^{6+}$ one, which prevails in solution in a wide range of pH, from pH 3.5 to pH 8.2. At higher pH values, $[Cu_2Ru(phen)_2\mathbf{L2}(OH)_2]^{4+}$ becomes predominant in solution, evidencing a marked tendency of $[Cu_2Ru(phen)_2\mathbf{L2}]^{6+}$ to form dihydroxylated species, likely arising from the deprotonation of water molecules bound to the Cu^{2+} ions. In these conditions, the formation of mononuclear complexes is almost negligible in the overall range of pH, with only the $[H_2CuRu(phen)_2\mathbf{L2}]^{6+}$ species being formed in very low percentage at pH of *c.ca* 4 (< 5% relative to ligand percentage). Finally, we highlight that in a wide range of pH both the **L1**- and **L2**-containing mixed Ru^{2+}/Cu^{2+} complexes are not affected by copper decomplexation, which is expected only in very strong acidic conditions (pH < 3.5).

3.1.1. *Cu^{2+}binding by $[Ru(phen)_2\mathbf{L2}]^{2+}$ by means of UV–visible and fluorescence measurements*

Besides the potentiometric data, the ability of $[Ru(phen)_2\mathbf{L2}]^{2+}$ to bind Cu^{2+} in aqueous media has been also studied by means of spectrophotometric and spectrofluorimetric measurements.

The coordination of Cu^{2+} does not significantly alter the absorption properties of this typology of Ru-compounds. In fact, the UV-absorption spectrum of $[Ru(phen)_2\mathbf{L2}]^{2+}$ presents a typical broad metal-to-ligand dπ–π* charge transfer (MLCT) band centered at about 454 nm and a structured band at lower wavelengths (around c.ca. 270 nm) relative to the ligand centered π–π* transitions of phen moieties. As in the case of $[Ru(phen)_2\mathbf{L1}]^{2+}$, the absorption profile of $[Ru(phen)_2\mathbf{L2}]^{2+}$ appears to be almost fully superimposable to the absorption spectra registered in the presence of one or two equivalents of Cu^{2+} (Fig. S2, ESI). On the contrary, the luminescence properties of these ruthenium compounds are markedly influenced by metal coordination. This is particularly evident in Fig. 2, where are reported the emission spectra of aqueous solutions of $[Ru(phen)_2\mathbf{L2}]^{2+}$ at neutral pH registered upon addition of increasing amounts of Cu^{2+}. The addition of the metal strongly quenches the luminescence of the compound, leading to an almost total loss of signal in the presence of 2 equivalents of Cu^{2+} (inset in Fig. 2). This effect can be naturally ascribed to the paramagnetic nature of Cu^{2+}.

3.2. *Singlet oxygen production*

The capacity to effectively generate the highly oxidant singlet oxygen $^1O_2$ species upon light-irradiation (*type II* reactions), stands for a key factor in evaluating the biological potential of a candidate photosensitizer for possible application in aPDT. However, other types of reactive radical species, issued from suitable substrates for instance by *type I* photochemical processes, are able to elicit severe damages to biological targets as well [56].

With this regard, the singlet oxygen sensitizing properties of $[Ru(phen)_2\mathbf{L2}]^{2+}$ and $[Cu_2Ru(phen)_2\mathbf{L2}]^{6+}$ were investigated by directly monitoring the phosphorescence signal of $^1O_2$ at 1270 nm generated by

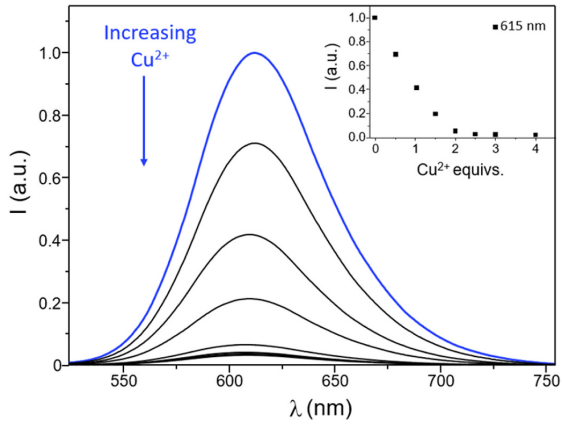

Fig. 2. Fluorescence spectra of aqueous solutions of $[Ru(phen)_2\mathbf{L2}]^{2+}$ buffered at pH 7, registered by adding increasing amounts of Cu^{2+}. In the inset of the figure is shown the quenching of the fluorescence emission monitored at 615 nm determined by the presence of increasing equivalents of the metal ion ([Ru] = 3 μM, $[Cu^{2+}]$ = 0–12 μM, λ_{exc} = 411 nm, Ru = $[Ru(phen)_2\mathbf{L2}]^{2+}$).

irradiation of air-saturated CH_3CN solutions of compounds. Tetraphenylporphyrin (TPP) was taken as a reference for $^1O_2$ production, as described in the experimental section. The results obtained, expressed in terms of $^1O_2$ quantum yields (φ_Δ), are compared with those of $[Ru(phen)_2\mathbf{L1}]^{2+}$ and $[CuRu(phen)_2\mathbf{L1}]^{4+}$ in Table 2.

As shown, the φ_Δ of $[Ru(phen)_2\mathbf{L2}]^{2+}$ was found to be 0.38 ± 0.08. It can be noted that this value emerges to be almost identical to that measured in the same experimental conditions for the parental compound $[Ru(phen)_3]^{2+}$ and only slightly higher with respect to that one obtained for $[Ru(phen)_2\mathbf{L1}]^{2+}$ (0.29 ± 0.06). This clearly indicates that the replacement of a phen unit with a 2,2′-bipyridyl moiety with two cyclen units appended to its 4 and 4′ positions does not affect the capacity of the ruthenium compound to produce $^1O_2$ upon light-activation.

Intriguingly, no $^1O_2$ emission was detected from the corresponding copper complex $[Cu_2Ru(phen)_2\mathbf{L2}]^{6+}$. As in the case of $[CuRu(phen)_2\mathbf{L1}]^{4+}$, the lack of evidence for $^1O_2$ production, together with the quenching of the fluorescence emission by the mixed Ru^{2+}/Cu^{2+} complex, can be rationalized by considering that the deactivation of the MLCT excited states in presence of Cu^{2+} ion/s may occur predominantly through internal conversion and likely on a faster timescale if compared to the Cu^{2+}-free forms of ruthenium compounds.

Table 2
Distribution coefficients ($logD_{7.4}$), $^1O_2$ quantum yields determined in air-saturated CH_3CN solutions $\varphi_\Delta(^1O_2)$ and intrinsic binding constants (K_b values) with ct-DNA obtained via UV–vis titrations of ruthenium compounds herein investigated.

Compound[a]	$\lambda_{abs}/\lambda_{em}$ (nm) †	$logD_{7.4}$	$\varphi_\Delta(^1O_2)$	K_b † (x10^4 M^{-1})
$[H_2(phen)_2Ru\mathbf{L1}]^{4+}$	452/611[b]	−1.8 ± 0.1	0.29 ± 0.06[b]	2.77 ± 0.09[b]
$[Cu(phen)_2Ru\mathbf{L1}]^{4+}$	452/611[b]	−1.5 ± 0.3	–[b]	1.47 ± 0.01[b]
$[H_4(phen)_2Ru\mathbf{L2}]^{6+}$	454/615	−1.4 ± 0.2	0.38 ± 0.08	2.41 ± 0.09
$[Cu_2(phen)_2Ru\mathbf{L2}]^{6+}$	454/615	−1.2 ± 0.1	–	1.28 ± 0.08

[a] Most abundant species of ruthenium complexes present in solution at physiological pH; † Values determined at pH 7.2 (Tris-HCl buffer 10 mM, NaCl 50 mM).
[b] ref [35].

3.3. Distribution coefficients of ruthenium compounds

The polyamino frameworks **L1** and **L2** confer to the resulting ruthenium complexes a marked hydrophilic nature. This influences their lipophilicity, a physicochemical descriptor of central interest in the pharmaceutical industry, as it describes the affinity of a drug for a lipid environment, affording useful clues on its biological, pharmacokinetic, and metabolic properties [57,58]. However, despite lipophilicity is an important determinant of activity, it usually refers to the level that allows the drug to easily diffuse across the cell membrane. As a result, the cytotoxicity of a drug not always goes hand in hand with its lipophilicity, and highly charged compounds, namely positively charged ruthenium (II) polypyridyl complexes, may exhibit remarkable antimicrobial activities as well [33,59,60].

To gain insight on the lipophilicity of our systems, the water-octanol distribution coefficients (D) of ruthenium complexes were quantitatively determined by employing the shake-flash method. Given the well-established dependence on pH of the species formed in solution by all the tested compounds, the analysis was performed at pH 7.4 because of its close resemblance to real biological partitions. As mentioned in the experimental section (see paragraph 2.1), at physiological pH the predominant species present in solution for each system are the di- and tetra-protonated forms of the 'Cu^{2+}-free' compounds $[H_2Ru(phen)_2\mathbf{L1}]^{4+}$ and $[H_4Ru(phen)_2\mathbf{L2}]^{6+}$ and the $[CuRu(phen)_2\mathbf{L1}]^{4+}$ and $[Cu_2Ru(phen)_2\mathbf{L2}]^{6+}$ complexes. For this reason, hereinafter we will refer to such species when discussing the results obtained under these conditions. The obtained results, expressed as logarithmic values ($logD_{7.4}$), are listed in Table 2. As shown, all systems are characterized by markedly negative $logD_{7.4}$, exhibiting overall values ranging between −1.2 and −1.8, accordingly with the pronounced hydrophilic character of the polyamine moieties introduced in the structure of ruthenium compounds.

3.4. Interaction of $[Ru(phen)_2\mathbf{L2}]^{2+}$ and $[Cu_2Ru(phen)_2\mathbf{L2}]^{6+}$ with calf-thymus DNA

The ability of a metal complex to interact with DNA, a key target for anticancer drugs as well as for antibacterial compounds, constitutes a relevant sign about its biological potential. In fact, the possibility to effectively interact with DNA would ensure the localization of a drug in close proximity of such important biological target, permitting to considerably strengthen the oxidative damage determined by the therapeutic production of singlet oxygen and/or ROS species. These considerations prompted us to consider the DNA-binding properties of Ru compounds prior to test their activity as anti-bacterial agents.

In general, Ru polypyridyl complexes mainly interact with double-stranded DNA by means of non-covalent binding modes, such as intercalation, groove binding and electrostatic interactions [61,62]. In this view, electronic absorption spectroscopy represents a useful technique to probe the affinity of metal-complexes with DNA, affording important insights on their mode of interaction. For example, covalent base-binding usually leads to a perturbation of the ligand field transition of the metal compound resulting in hyperchromism at its Metal to Ligand Charge Transfer (MLCT) band [63]. Classical Ru(II)-based intercalators on the other hand generally undergo hypochromism, along with a bathochromic shift, at their MLCT band, with the extent of hypochromism being directly correlated to the strength of the intercalation [64]. However, hyperchromism or hypochromism have also been associated to other typology of interaction, such as partial intercalative/non intercalative and electrostatic binding modes [65–67].

The DNA-binding capacities of $[Ru(phen)_2\mathbf{L2}]^{2+}$ and $[Cu_2Ru(phen)_2\mathbf{L2}]^{6+}$ were evaluated on *calf thymus* DNA (ct-DNA), by monitoring the changes at the MLCT band in their UV–vis spectra upon addition of increasing amounts of the biopolymer to solutions of ruthenium compounds at fixed concentrations at pH 7.2. As shown in Figs. 3a-b, both $[H_4Ru(phen)_2\mathbf{L2}]^{6+}$ and $[Cu_2Ru(phen)_2\mathbf{L2}]^{6+}$ (the predominant species of compounds in these conditions) result in hypochromism at their MLCT band with no blue or red shift on addition of the biopolymer. The extent of hypochromism was found to be greater for $[H_4Ru(phen)_2\mathbf{L2}]^{6+}$, which undergoes a reduction of about 32% of the absorbance at 454 nm in the presence of c.ca 200 μM of the biopolymer (Fig. 3a). On the other side, when two Cu^{2+} ions are bound within the polyamino pockets of the ruthenium compound such effect accounts for only a 15% reduction (Fig. 3b).

The intrinsic binding constants (K_b values) of ruthenium complexes were calculated from titration data as described in the experimental section and result to be $(2.41 \pm 0.09) \times 10^4\ M^{-1}$ and $(1.28 \pm 0.08) \times 10^4\ M^{-1}$, respectively for $[H_4Ru(phen)_2\mathbf{L2}]^{6+}$ and $[Cu_2Ru(phen)_2\mathbf{L2}]^{6+}$; these values are compared with those previously found for the **L1**-containing ruthenium complexes in the same conditions in Table 2. A first analysis of these data confirms that the K_b constants of all the investigated Ru-compounds are significantly higher than that one reported in literature for the interaction of the parental compound $[Ru(phen)_3]^{2+}$ with ct-DNA in the same buffer media ($<10^3\ M^{-1}$) [68,69]. For this compound, non-classical intercalation processes including semi-intercalation and quasi-intercalation modes, along with external electrostatic binding within the major groove of DNA, were reported to underlie its interaction with the biopolymer [70,71]. On the other hand, these values are almost two order of magnitude lower relative to those associated to classical Ru(II)-based intercalators, such as $[Ru(bpy)_2(dppz)]^{2+}$ (dppz = dipyrido[3,2-*a*:2′,3′-*c*]phenazine) for example, which more strongly binds DNA featuring a Kb in the order of $10^6\ M^{-1}$ [72,73].

As a consequence, for all the ruthenium complexes herein analysed a pure intercalative mode of interaction with DNA should be ruled out. This finding was also confirmed by analogues fluorescence titration experiments conducted on $[Ru(phen)_2\mathbf{L2}]^{2+}$, shown in Fig. S3, that evidenced only a weak increase of the ligand fluorescence emission in the presence of a large excess of the biopolymer (c.ca 12% for [DNA]/[Ru] > 20). Unfortunately, the poor luminescence of the mixed Ru^{2+}/Cu^{2+} systems precluded their study by this technique.

Interestingly, a comparison of the absorption data obtained for Ru (II)-complexes with those of mixed Ru^{2+}/Cu^{2+} compounds, indicates a significative decrease (almost two-folds) of the K_b values when one ($[CuRu(phen)_2\mathbf{L1}]^{4+}$) or two ($[Cu_2Ru(phen)_2\mathbf{L2}]^{6+}$) copper ions are bound within the macrocyclic cavities of complexes. Indeed, the mixed Ru^{2+}/Cu^{2+} complexes display a higher intercept value of the plot of $[DNA]/|\varepsilon_a - \varepsilon_f|$ versus [DNA], which is inversely proportional to K_b, as shown in Fig. 3c for $[H_4Ru(phen)_2\mathbf{L2}]^{6+}$ and $[Cu_2Ru(phen)_2\mathbf{L2}]^{6+}$.

Taken together these finding highlight that the polyamine frameworks contained in $[Ru(phen)_2\mathbf{L1}]^{2+}$ and $[Ru(phen)_2\mathbf{L2}]^{2+}$ play a central role in their interaction with DNA. In fact, we can reasonably assume that the phosphate groups of the biopolymer interact with the positively charged polyammonium groups gathered on the polyamine moieties mainly via electrostatic and hydrogen-bonding interactions. This agrees with the higher binding constants obtained for Ru-compounds, relative to that of the reference compound $[Ru(phen)_3]^{2+}$, where **L1** or **L2** are replaced by a phen unit. On the other hand, the coordination of Cu^{2+} would determine a charge-redistribution within the macrocyclic residues of ligands, leading to a diminished availability of the polyamine nitrogen donors to establish electrostatic/hydrogen-bonding interactions with the DNA backbone, and thus justifying the lower K_b values.

3.5. DNA cleavage activity

The abilities of $[Ru(phen)_2\mathbf{L2}]^{2+}$ and $[Cu_2Ru(phen)_2\mathbf{L2}]^{6+}$ to induce a DNA damage (as nick of the phosphodiester bond) were investigated by means of gel electrophoresis experiments on plasmid DNA, in analogy to previous studies conducted on $[Ru(phen)_2\mathbf{L1}]^{2+}$ and $[CuRu(phen)_2\mathbf{L1}]^{4+}$ [35].

The size resolution of the biopolymer by this technique allows in fact

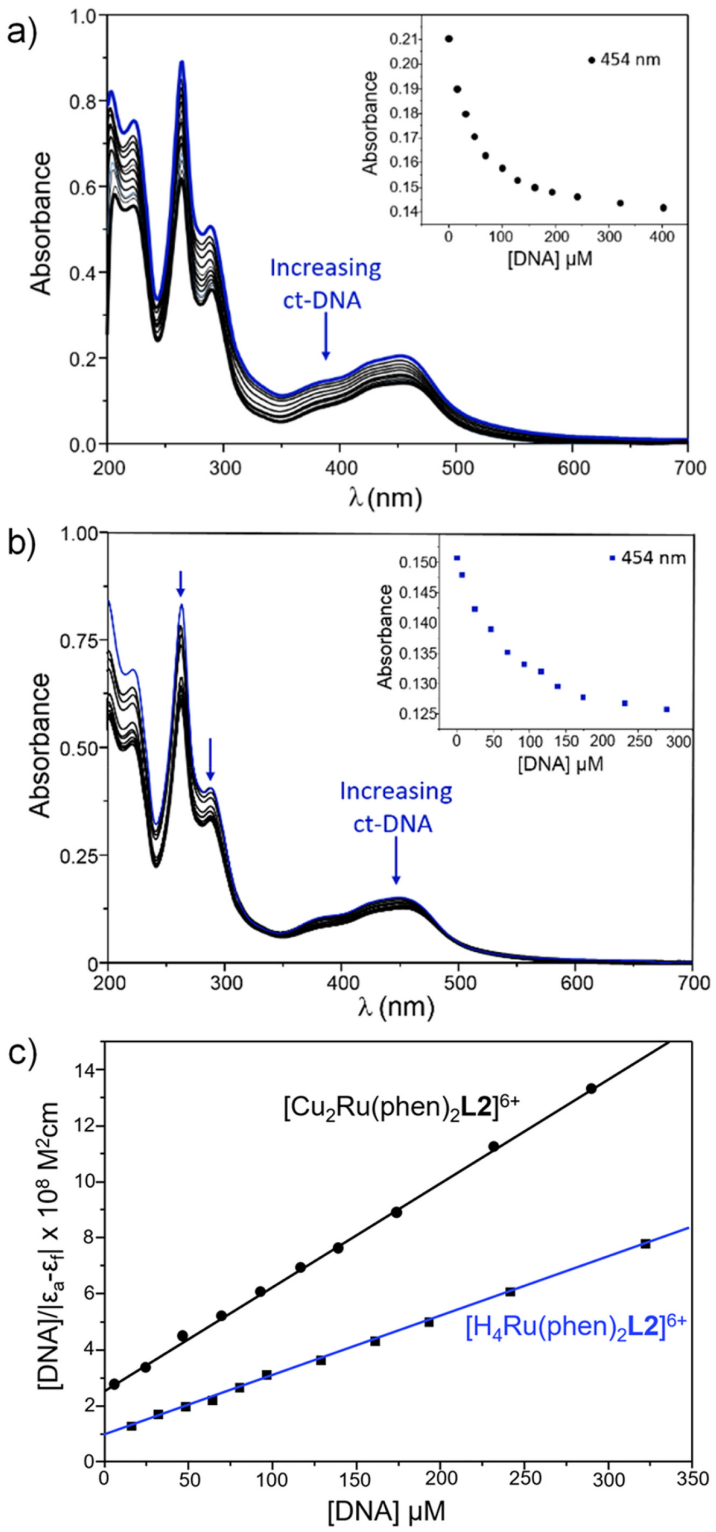

Fig. 3. Absorption spectra of aqueous solutions of [Ru(phen)$_2$**L2**]$^{2+}$ (a) and of [Cu$_2$Ru(phen)$_2$**L2**]$^{6+}$(b) at pH 7.2 registered in the presence of increasing concentrations of *calf-thymus* DNA (ct-DNA). In the insets of top right of the figures are shown the absorbance values measured at 454 nm as a function of increasing concentrations of the biopolymer. In panel (c) are reported the relative plots of the [DNA]/|ε_a-ε_f| values versus the DNA molar concentration. ([Ru] = 18 μM, [Cu$_2$Ru] = 14 μM, Tris-HCl buffer 10 mM, NaCl 50 mM, pH 7.2, [H$_4$Ru(phen)$_2$**L2**]$^{6+}$ and [Cu$_2$Ru(phen)$_2$**L2**]$^{6+}$: major species of compounds present in solution, Ru = [Ru(phen)$_2$**L2**]$^{2+}$, Cu$_2$Ru = [Cu$_2$Ru(phen)$_2$**L2**]$^{6+}$).

to distinguish the different conformational states of the plasmid, obtained as a result of its interaction with a drug, on the basis of their relative mobility on the gel. In particular, plasmid DNA naturally appears as a covalently closed circular or "supercoiled" form, which migrates faster (as an apparently lighter molecule, ~ 2000 bp) than the open circular form (~ 4000 bp) or the linear form (~ 3000 bp), being the latter forms arising from single or double strand breaks of the biopolymer, respectively. Consequently, cleavage on one or both strands leads to the decrease in the intensity of the supercoiled form (the lightest band) and to an increase in the intensity of the higher bands. Given its singlet oxygen sensitizing properties, we firstly investigated the DNA-cleavage activity of $[Ru(phen)_2\mathbf{L2}]^{2+}$ upon light-activation. To this aim, plasmid pUC18 was incubated with increasing concentrations of the ruthenium compound (0–12.5 μM) at pH 7.2, and then we analysed the resulting gels collected both under dark conditions and following irradiation with LED light (λ > 450 nm, 30 W, 15 min); the corresponding gels are respectively reported in Fig. 4a and b. As shown in Fig. 4a, no significant cleavage of the plasmid occurs under dark within the overall range of ruthenium concentrations tested. Only a slight increase of the plasmid retention is observed with increasing drug concentrations indicating a progressive interaction of the ruthenium compound with DNA. Higher doses of compound ([Ru] ≥ 25 μM, data not shown), caused the precipitation of "heavier" Ru-DNA aggregates which precluded their analysis through this technique.

On the other side, the photo-activation of $[Ru(phen)_2\mathbf{L2}]^{2+}$ triggered the progressive conversion of the supercoiled form of DNA to the relaxed-nicked conformation with increasing drug concentrations, evidencing a marked dose-dependent DNA-cleavage activity. Such behaviour parallels the effect previously found for $[Ru(phen)_2\mathbf{L1}]^{2+}$ [35] and would be consistent with the capacity of $[Ru(phen)_2\mathbf{L2}]^{2+}$ to sensitize the production of $^1O_2$, whose damages to DNA are typically associated to the occurrence of single strand breaks on plasmid [74,75].

We then inspected the DNA-cleavage activity of $[Cu_2Ru(phen)_2\mathbf{L2}]^{2+}$. It is known that the Fenton-active Cu^{2+} ion/s can produce ROS under suitable conditions, e.g. in the presence of H_2O_2, thus leading to oxidative damages on plasmid that can be easily monitored through gel-electrophoresis. In this respect, solutions of plasmid containing increasing concentration of $[Cu_2Ru(phen)_2\mathbf{L2}]^{2+}$ (0–12.5 μM), were analysed in the absence (Fig. 5a) and in the presence (Fig. 5b) of a fixed concentration of hydrogen peroxide as co-reactant.

As shown in Fig. 5a, in the absence of H_2O_2 no cleavage activity was observed within the overall range of ruthenium concentrations tested. It can be also pointed out that, on contrary to what observed for $[Ru(phen)_2\mathbf{L2}]^{2+}$, the DNA mobility results to be almost unaffected by the metal compound. This denotes a diminished capability of $[Cu_2Ru(phen)_2\mathbf{L2}]^{2+}$ to interact with the biopolymer with respect to the Cu^{2+}-*free* ruthenium complex, in good agreement with the UV–Vis titration data.

In the presence of H_2O_2 (Fig. 5b) a marked and progressive conversion of the lightest form of DNA to the relaxed-nicked conformation is observed with increasing concentrations of compound. This effect closely resembles that one provoked on the plasmid by the simultaneous presence of Cu^{2+} and H_2O_2, thus suggesting the generation of ROS species by means of Fenton and/or Fenton-like reactions. On the contrary, no DNA-cleavage was observed when Cu^{2+} and H_2O_2 were added separately into the DNA solutions (see the control experiments shown in Fig. S4, ESI).

The effective ROS production was confirmed by coupling EPR and further gel-electrophoresis measurements. As shown in Fig. 6 (green line), the EPR spectrum of a solution containing $[Cu_2Ru(phen)_2\mathbf{L2}]^{6+}$ in the presence of H_2O_2 and 5,5-dimethyl-1-pyrroline-N-oxide (DMPO) as a spin trapping agent for free radicals [76], exhibits the four peaks corresponding to the typical hyperfine split transition of a radical species. These signals were not observed in the control experiments for solutions containing DMPO and H_2O_2 (blue line) or DMPO and the ruthenium compound (red line). The EPR signals detected for the simultaneous presence of the ruthenium compound, H_2O_2 and DMPO (green line) emerge to be the result of the generation of hydroxyl radicals ($OH^{\bullet}$), as revealed by the good agreement with the simulated EPR spectrum of the DMPO/$OH^{\bullet}$ adduct (black line in Fig. 6, see ESI for further details). In addition, parallel gel-electrophoresis experiments also evidenced that the DNA-cleavage by $[Cu_2Ru(phen)_2\mathbf{L2}]^{6+}$ is strongly inhibited by the presence of common hydroxyl radical quenchers, such as sodium formate and D-mannitol (Fig. S7, ESI) [77].

Therefore, taken together these results point out that the simultaneous presence of $[Cu_2Ru(phen)_2\mathbf{L2}]^{6+}$ and H_2O_2 leads to the production of ROS species, e.g. the hydroxyl radical ($OH^{\bullet}$). In this respect, we can reasonably speculate that these radicals are the result of Fenton/Fenton-like processes involving the Cu^{2+} centers positioned in the polyamine residues of the ruthenium complex, in strictly analogy to what previously reasoned for $[CuRu(phen)_2\mathbf{L1}]^{4+}$ and other Cu^{2+}-containing compounds [35,78].

In summary, these experiments show that the polyamino frameworks appended to the Ru-coordinated bipyridyl units of ruthenium complexes can be successfully exploited to switch among different mechanisms of action depending on whether Cu^{2+} ion/s are bound, or not, within such binding pockets. In fact, while $[Ru(phen)_2\mathbf{L2}]^{2+}$ is an effective singlet oxygen sensitizer that can lead to photo-induced cleavage on DNA, its mixed heteronuclear Cu^{2+}/Ru^{2+} complex may provide an alternative mechanism of action which does not require the use of light to cause the production of cytotoxic ROS species.

3.6. Antibacterial effect of ruthenium complexes

The antibacterial activity of all the four ruthenium compounds $[Ru(phen)_2\mathbf{L1}]^{2+}$, $[Ru(phen)_2\mathbf{L2}]^{2+}$, $[CuRu(phen)_2\mathbf{L1}]^{4+}$, and $[Cu_2Ru(phen)_2\mathbf{L2}]^{6+}$ was evaluated against the gram-positive bacterium *B. subtilis* strain 168, by testing the activity of compounds both under dark conditions and upon light-activation. The obtained results, expressed in terms of cell viability (OD_{600nm}) as a function of the drug

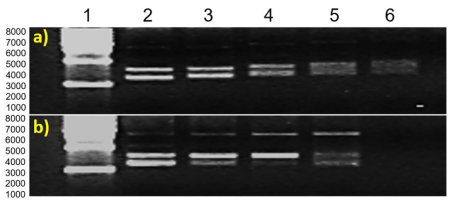

Fig. 4. Agarose gels showing the dose response of $[Ru(phen)_2\mathbf{L2}]^{2+}$ incubated with 25 μg/ml plasmid puC18 at pH 7.2, before (a) and after (b) 15 min of irradiation with visible light (λ > 450 nm, 30 W, 15 min). Lane 1: DNA molecular weight standard; lanes 2–6: 0, 1.56, 3.12, 6.25, 12.5 μM of ruthenium compound ($[H_4Ru(phen)_2\mathbf{L2}]^{6+}$ major ligand species).

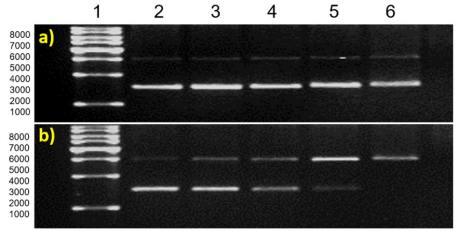

Fig. 5. Agarose gels showing the dose response of $[Cu_2Ru(phen)_2\mathbf{L2}]^{6+}$ incubated with 25 μg/ml plasmid puC18 at pH 7.2, in the absence (a) and in the presence of a fixed concentration of H_2O_2 (25 μM) (b). Lane 1: DNA molecular weight standard; lanes 2–6: 0, 1.56, 3.12, 6.25, 12.5 μM of ruthenium compound.

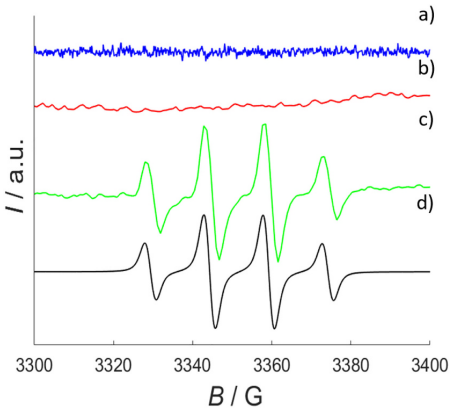

Fig. 6. EPR spectra registered at 298 K on solutions containing DMPO (250 mM) in the presence of 5 mM of H_2O_2 (a), or 5 mM of the ruthenium compound $[Cu_2Ru(phen)_2\mathbf{L2}]^{6+}$(b). In c) and d) are respectively shown the spectra obtained for a solution containing DMPO (250 mM), H_2O_2 (5 mM) and the ruthenium compound (5 mM) and its relative simulated spectrum constructed by considering the formation of the DMPO/$OH^{\bullet}$ radical adduct.

concentration, for the **L2**-containing ruthenium compounds are shown in Fig. 7, while those corresponding to the **L1**-containing complexes are reported in Fig. S8 (ESI).

Data collected under dark conditions evidenced that both $[Ru(phen)_2\mathbf{L1}]^{2+}$ and $[CuRu(phen)_2\mathbf{L1}]^{4+}$ possess an antibacterial effect, with inhibition of *B. subtilis* growth starting at 6.25 μM for $[Ru(phen)_2\mathbf{L1}]^{2+}$ (ca. 60% of growth of the untreated control), and 3.12 μM for $[CuRu(phen)_2\mathbf{L1}]^{4+}$ (ca. 50% of growth of the untreated control) (Fig. S8-a). Differences between $[Ru(phen)_2\mathbf{L1}]^{2+}$ and $[CuRu(phen)_2\mathbf{L1}]^{4+}$ are significant at 3.12 μM ($p < 0.05$, *t*-test), suggesting a higher antibacterial efficacy of the mixed Ru^{2+}/Cu^{2+} complex with respect to the Cu^{2+}-unbound species. However, at higher concentrations $[Ru(phen)_2\mathbf{L1}]^{2+}$ and $[CuRu(phen)_2\mathbf{L1}]^{4+}$ determine a similar antibacterial effect, as evidenced by a comparable residual growth of cells, around 30% with respect to the control. Similarly, both the antibacterial activities of $[Ru(phen)_2\mathbf{L2}]^{2+}$ and $[Cu_2Ru(phen)_2\mathbf{L2}]^{6+}$ start at 6.25 μM, revealing no significant differences in the activity of the two systems under dark (Fig. 7-a).

We then analysed the antibacterial potential of ruthenium compounds upon irradiation with LED light ($\lambda > 430$ nm, 30 W, 15 min) (Fig. 7-b and S8-b). Analogously to data collected in dark, no significative differences in activity among $[Ru(phen)_2\mathbf{L1}]^{2+}$ and $[CuRu(phen)_2\mathbf{L1}]^{4+}$ were detected and none of these two complexes led to improved antibacterial efficacy relative to measurements performed under dark (Fig.S8-b). A different behaviour was instead observed for $[Ru(phen)_2\mathbf{L2}]^{2+}$ and $[Cu_2Ru(phen)_2\mathbf{L2}]^{6+}$. In fact, as shown in Fig. 7-b, upon light-activation these compounds showed an enhanced concentration-dependent bactericidal effect against *B. subtilis* with respect to dark conditions. The MIC value (minimal inhibitory concentrations) of both $[Ru(phen)_2\mathbf{L2}]^{2+}$ and $[Cu_2Ru(phen)_2\mathbf{L2}]^{6+}$ upon light-activation was found to be 3.12 μM, c.ca 8-folds lower than that obtained in dark conditions (25 μM), thus denoting a marked and comparable photodynamic inactivation (aPDI) by the two compounds. As an example, the irradiation in the presence of 3.12 μM of ruthenium compounds determines a 40% of residual growth (Fig. 7-b) while at the same drug dose an almost 100% of growth was preserved in dark (Fig. 7-a). With this respect we can speculate that the aPDI of $[Ru(phen)_2\mathbf{L2}]^{2+}$ and $[Cu_2Ru(phen)_2\mathbf{L2}]^{6+}$ may reflect the good singlet oxygen properties of the former compound while, in the case of $[Cu_2Ru(phen)_2\mathbf{L2}]^{6+}$, the Fenton-active copper centers may play a synergistic role with light activation in the development of cytotoxic ROS species.

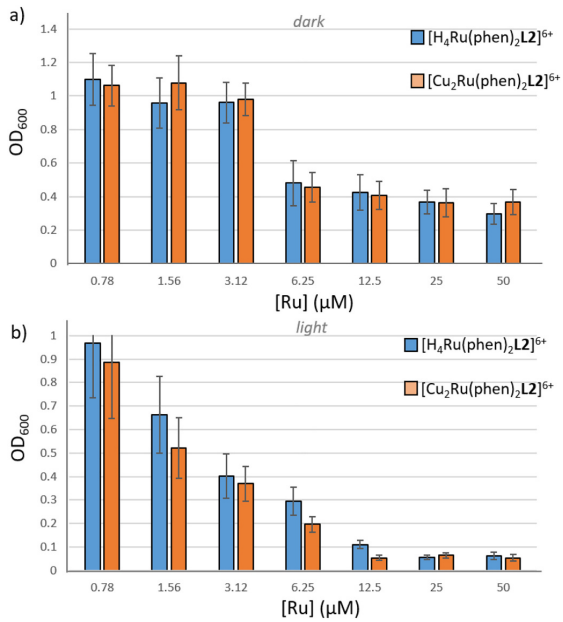

Fig. 7. Determination of the antibacterial effect of $[Ru(phen)_2\mathbf{L2}]^{2+}$ and $[Cu_2Ru(phen)_2\mathbf{L2}]^{6+}$ evaluated (a) under dark conditions and (b) upon light-activation. The proportion of $OD_{600\ nm}$ values with respect to blank control in is reported (Y-axis) for the different concentrations of the ruthenium complexes ([Ru], X-axis). ($[H_2Ru(phen)_2\mathbf{L1}]^{4+}$, $[H_4Ru(phen)_2\mathbf{L2}]^{6+}$, $[CuRu(phen)_2\mathbf{L1}]^{4+}$ and $[Cu_2Ru(phen)_2\mathbf{L2}]^{6+}$: major species present in solution).

On the other hand, the lack of phototoxicity of $[Ru(phen)_2\mathbf{L1}]^{2+}$ and $[CuRu(phen)_2\mathbf{L1}]^{4+}$ appear much harder to explain. To address this issue, we decided to investigate the cellular uptake of $[Ru(phen)_2\mathbf{L1}]^{2+}$, $[Ru(phen)_2\mathbf{L2}]^{2+}$, $[CuRu(phen)_2\mathbf{L1}]^{4+}$ and $[Cu_2Ru(phen)_2\mathbf{L2}]^{6+}$ by *B. subtilis*. Bacteria suspensions were incubated in the dark in the presence of a fixed concentration of each ruthenium compound (25 μM) at pH 7.2 and by employing different incubation times, from 30 min to 24 h. After centrifugation to remove the supernatant, the Ru-content internalized by cells was determined by ICP-AES.

As shown in Fig. 8, for incubation times up to 5 h, $[Ru(phen)_2\mathbf{L2}]^{2+}$ and $[Cu_2Ru(phen)_2\mathbf{L2}]^{6+}$ displayed a marked tendency to be internalized into bacterial cells, exhibiting Ru-contents up to twice-folds higher with respect to those found for $[Ru(phen)_2\mathbf{L1}]^{2+}$ and $[CuRu(phen)_2\mathbf{L1}]^{4+}$. On the other side, following 24 h incubation an inversion of such tendency is observed, with $[Ru(phen)_2\mathbf{L2}]^{2+}$ and $[Cu_2Ru(phen)_2\mathbf{L2}]^{6+}$ that appear to be released by cells (probably partially lysed by the toxicity of the compounds), while the cellular uptake of $[Ru(phen)_2\mathbf{L1}]^{2+}$ and $[CuRu(phen)_2\mathbf{L1}]^{4+}$ increases. This led us to assume that the higher phototoxicity of the **L2**-containing ruthenium complexes relative to the **L1**-containing ones might be related, or partially related, to the different kinetics of cellular internalization of such compounds. In fact, the preferential internalization of $[Ru(phen)_2\mathbf{L2}]^{2+}$ and $[Cu_2Ru(phen)_2\mathbf{L2}]^{6+}$ at the incubation time employed in the in vitro studies (30 min, see paragraph 2.8.1) would bring to increased intra-cellular damages induced by light-activation, leading to a greater antibacterial effect.

Although these findings may not completely account for the different antibacterial activities observed, and further studies need to be undertaken to better elucidate this topic, they clearly probe that slightly different structural characteristics of the polyamino moieties linked to the Ru-coordinated bipyridyl ligands may deeply affect some key features of this class of compounds, including their cellular uptake and, consequently, may affect their antibacterial potential.

4. Conclusion

In this work we compared some key chemical-physical features of a series of ruthenium(II) polypyridyl complexes featuring peculiar polyaminomacrocyclic frameworks linked, via methylene bridges, to the 4,4′ positions of a metal-coordinated bipyridyl unit, for their possible biological application. **L1** and **L2** markedly influence the overall chemical-physical properties of the respective ruthenium complexes leading to highly water-soluble singlet oxygen generators, but even affording the formation of stable Ru^{2+}/Cu^{2+} heteronuclear complexes in aqueous solution.

The Cu^{2+} binding ability of $[Ru(phen)_2\mathbf{L2}]^{2+}$ was investigated by performing potentiometric, UV–vis and fluorescence measurements. Our studies indicate that the two distinct cyclen moieties gathered on the Ru-coordinated bipyridyl ligand can bind up to two cations, affording the formation of the mixed heteronuclear compound $[Cu_2Ru(phen)_2\mathbf{L2}]^{6+}$, the predominant species in a wide interval of pH around neutrality. While the presence of Cu^{2+} ion/s does not significantly alter the absorption properties of the ruthenium complex, it strongly quenches its fluorescence emission. On the other hand, it also affects the singlet oxygen sensitizing properties of the ruthenium compound. In fact, $[Ru(phen)_2\mathbf{L2}]^{2+}$ displays a good ability to produce $^1O_2$ upon light-activation ($\varphi_\Delta = 0.38 \pm 0.08$), whereas it almost completely loses this property when present in its dinuclear Cu^{2+}-complexed species.

The capacity of $[Ru(phen)_2\mathbf{L2}]^{2+}$ and $[Cu_2Ru(phen)_2\mathbf{L2}]^{6+}$ to interact and induce a damage on DNA was assessed by means of UV–vis titrations and gel electrophoresis experiments, respectively. Our data suggest that the polyamino residues play a central role in favouring the interaction of $[Ru(phen)_2\mathbf{L1}]^{2+}$ and $[Ru(phen)_2\mathbf{L2}]^{2+}$ with ct-DNA, being probably stabilized by electrostatic interactions between the negatively charged phosphate backbone of the biopolymer and the high number of positively charged ammonium groups of the compound at neutral pH. On the contrary, when these polyamine nitrogen donors are involved into the Cu^{2+} coordination the affinity for DNA decreases of a factor of c.ca two folds. The gel-electrophoresis experiments confirm the capability of $[Ru(phen)_2\mathbf{L2}]^{2+}$ to effectively sensitize the singlet oxygen production upon light-activation, leading to a progressive dose-dependent conversion of the fast migration bands of the plasmid to its relaxed nicked conformations. On the other hand, $[Cu_2Ru(phen)_2\mathbf{L2}]^{6+}$ damages the plasmid in the presence of a co-reactant showing a dose dependent cleavage activity as well. This highlights that the polyamino frameworks can be exploited to achieve different mechanisms of action. In their metal-unbounded forms they facilitate the interaction with DNA without altering the effective singlet oxygen production of the ruthenium center whereas in their Cu^{2+}-bound forms they lead to oxidative damages to DNA, likely due to the ROS production mediated by Fenton or Fenton-like processes, and thus providing an alternative mechanism for drug-activation.

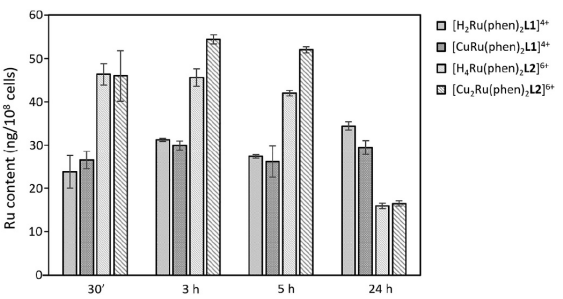

Fig. 8. Cellular uptake of ruthenium compounds after 30 min, 3 h, 5 h and 24 h of incubation with *B. subtilis* obtained by means of ICP-AES analysis. ($[H_2Ru(phen)_2\mathbf{L1}]^{4+}$, $[H_4Ru(phen)_2\mathbf{L2}]^{6+}$, $[CuRu(phen)_2\mathbf{L1}]^{4+}$ and $[Cu_2Ru(phen)_2\mathbf{L2}]^{6+}$: predominant species present in solution).

Following the comparison of the results obtained for $[Ru(phen)_2\mathbf{L2}]^{2+}$ and $[Cu_2Ru(phen)_2\mathbf{L2}]^{6+}$ with previous studies on $[Ru(phen)_2\mathbf{L1}]^{2+}$ and $[CuRu(phen)_2\mathbf{L1}]^{4+}$, which highlighted similarities between these systems, we then focused on the antibacterial potential of the four ruthenium compounds, which was evaluated both under dark and upon light-activation against *Bacillus subtilis*, chosen as a model for gram-positive bacteria.

Obtained results allow to speculate about relationships between chemical structure, mode of action and the antibacterial effect. The presence of Cu^{2+} ion/s within the polyamino macrocyclic units of ruthenium compounds does not significantly alter the cytotoxicity of these compounds, both in dark and upon irradiation, resulting in almost identical MIC values of the mixed Ru^{2+}/Cu^{2+} complexes compared to the Cu^{2+}-free compounds. However, we do not exclude that the heteronuclear complexes may lead to different results on different types of bacterial cells.

Among the four compounds tested, irradiation with low-energy light effectively enhances the antibacterial activity of $[Ru(phen)_2\mathbf{L2}]^{2+}$ and $[Cu_2Ru(phen)_2\mathbf{L2}]^{6+}$, leading to MIC values of 8-folds lower than those obtained under dark conditions. The good phototoxicities of these two compounds reflect the singlet oxygen sensitizing capabilities of $[Ru(phen)_2\mathbf{L2}]^{2+}$, while in the case of $[Cu_2Ru(phen)_2\mathbf{L2}]^{6+}$ we speculate that, due to its inability to generate $^1O_2$, different mechanisms of action, namely the development of cytotoxic ROS species produced by the synergistic action of Fenton-active copper centers and light, may be responsible of equally harmful cytotoxic effects. On the other side, the lack in photoactivity found for $[Ru(phen)_2\mathbf{L1}]^{2+}$ and $[CuRu(phen)_2\mathbf{L1}]^{4+}$ may be linked or partially linked to their inferior cellular uptake in the experimental conditions adopted. In fact, despite the similar LogD values calculated for the four ruthenium systems, $[Ru(phen)_2\mathbf{L2}]^{2+}$ and $[Cu_2Ru(phen)_2\mathbf{L2}]^{6+}$ exhibit a faster kinetic of cellular internalization if compared to $[Ru(phen)_2\mathbf{L1}]^{2+}$ and $[CuRu(phen)_2\mathbf{L1}]^{4+}$, permitting to strengthen the intra-cellular damages induced by light-activation. Although further studies will be requested to better elucidate the mechanisms that underlie the biological effects of the compounds herein investigated, these data clearly demonstrate that the structural features of the polyamine frameworks appended to the 4, 4′ positions of the Ru-coordinated bipyridyl ligands markedly affect the cellular uptake by bacteria cells, in a way that could not be simple predicted on the basis of the lipophilicity of compounds.

In conclusion, these data show that polyamino frameworks are appealing tools that can be successfully exploited in the design of Ru(II)-polypyridyl complexes to finely modify their chemical-physical repertoire and thus to affect their potential as effective candidates for the treatment of bacterial infections.

Declaration of Competing Interest

The authors declare that they have no known competing financial interests or personal relationships that could have appeared to influence the work reported in this paper.

The authors declare the following financial interests/personal relationships which may be considered as potential competing interests.

Acknowledgements

‘Fondazione Cassa di Risparmio di Firenze’ and MIUR, for the economic contribution within the “Progetto Dipartimenti di Eccellenza 2018-2022” allocated to Department of Chemistry “Ugo Schiff”, are gratefully acknowledged for financial support. The authors also thank Mirko Severi and Camilla Ferrante for the ICP-AES analysis and the determination of the singlet oxygen quantum yields.

Appendix A. Supplementary data

Supplementary data to this article can be found online at https://doi.

org/10.1016/j.jinorgbio.2021.111467.

References

[1] World Health Organisation, Tackling Antibiotic Resistance from a Food Safety Perspective in Europe, World Heal. Organ., 2011.

[2] C.I. Michaelidis, M.J. Fine, C.J. Lin, J.A. Linder, M.P. Nowalk, R.K. Shields, R. K. Zimmerman, K.J. Smith, The hidden societal cost of antibiotic resistance per antibiotic prescribed in the United States: an exploratory analysis, BMC Infect. Dis. 655 (2016), https://doi.org/10.1186/s12879-016-1990-4.

[3] A.M. Florea, D. Büsselberg, Cisplatin as an anti-tumor drug: cellular mechanisms of activity, drug resistance and induced side effects, Cancers (Basel). 3 (2011) 1351–1371, https://doi.org/10.3390/cancers3011351.

[4] A. Khoury, K.M. Deo, J.R. Aldrich-Wright, Recent advances in platinum-based chemotherapeutics that exhibit inhibitory and targeted mechanisms of action, J. Inorg. Biochem. 207 (2020) 11070, https://doi.org/10.1016/j.jinorgbio.2020.111070.

[5] X. Li, A.K. Gorle, M.K. Sundaraneedi, F.R. Keene, J.G. Collins, Kinetically-inert polypyridylruthenium(II) complexes as therapeutic agents, Coord. Chem. Rev. 375 (2018) 134–147, https://doi.org/10.1016/j.ccr.2017.11.011.

[6] P. Jia, R. Ouyang, P. Cao, X. Tong, X. Zhou, T. Lei, Y. Zhao, N. Guo, H. Chang, Y. Miao, S. Zhou, Review: recent advances and future development of metal complexes as anticancer agents, J. Coord. Chem. 70 (2017) 2175–2201, https://doi.org/10.1080/00958972.2017.1349313.

[7] R.S. Correa, L.M. Bomfim, K.M. Oliveira, D.R.M. Moreira, M.B.P. Soares, J. Ellena, D.P. Bezerra, A.A. Batista, Ru(II) complexes containing uracil nucleobase analogs with cytotoxicity against tumor cells, J. Inorg. Biochem. 198 (2019) 110751, https://doi.org/10.1016/j.jinorgbio.2019.110751.

[8] F.P. Dwyer, E.C. Gyarfas, W.P. Rogers, J.H. Koch, Biological activity of complex ions, Nature. 170 (1952) 190–191, https://doi.org/10.1038/170190a0.

[9] F.P. Dwyer, I.K. Reid, A. Shulman, G.M. Laycock, S. Dixson, The biological actions of 1,10-phenanthroline and 2,2′-bipyridine hydrochlorides, quaternary salts and metal chelates and related compounds. Bacteriostatic action on selected gram-positive, gram-negative and acid-fast bacteria, Aust. J. Exp. Biol. Med. Sci. 47 (1969) 203–218, https://doi.org/10.1038/icb.1969.21.

[10] F. Li, M. Feterl, Y. Mulyana, J.M. Warner, J.G. Collins, F.R. Keene, In vitro susceptibility and cellular uptake for a new class of antimicrobial agents: Dinuclear ruthenium(II) complexes, J. Antimicrob. Chemother. 67 (2012) 2686–2695, https://doi.org/10.1093/jac/dks291.

[11] F. Li, J.G. Collins, F.R. Keene, Ruthenium complexes as antimicrobial agents, Chem. Soc. Rev. 44 (2015) 2529–2542, https://doi.org/10.1039/c4cs00343h.

[12] K.A. Kumar, K.L. Reddy, S. Vidhisha, S. Satyanarayana, Synthesis, characterization and DNA binding and photocleavage studies of $[Ru(bpy)_2BDPPZ]^{2+}$, $[Ru(dmb)_2BDPPZ]^{2+}$ and $[Ru(phen)_2BDPPZ]^{2+}$ complexes and their antimicrobial activity, Appl. Organomet. Chem. 23 (2009) 409–420, https://doi.org/10.1002/aoc.1534.

[13] M. Mital, Z. Ziora, Biological applications of Ru(II) polypyridyl complexes, Coord. Chem. Rev. 375 (2018) 434–458, https://doi.org/10.1016/j.ccr.2018.02.013.

[14] N.L. Kilah, E. Meggers, Sixty years young: the diverse biological activities of metal polypyridyl complexes pioneered by Francis P. Dwyer, Aust. J. Chem. 65 (2012) 1325–1332, https://doi.org/10.1071/CH12275.

[15] Y. Yang, G. Liao, C. Fu, Recent advances on octahedral polypyridyl ruthenium(II) complexes as antimicrobial agents, Polymers (Basel) 10 (2018) 650, https://doi.org/10.3390/polym10060650.

[16] Z. Ude, I. Romero-Canelón, B. Twamley, D. Fitzgerald Hughes, P.J. Sadler, C. J. Marmion, A novel dual-functioning ruthenium(II)-arene complex of an anti-microbial ciprofloxacin derivative - anti-proliferative and anti-microbial activity, J. Inorg. Biochem. 160 (2016) 210–217, https://doi.org/10.1016/j.jinorgbio.2016.02.018.

[17] H.M. Southam, J.A. Butler, J.A. Chapman, R.K. Poole, The microbiology of ruthenium complexes, Adv. Microb. Physiol. 71 (2017) 1–96, https://doi.org/10.1016/bs.ampbs.2017.03.001.

[18] D. Sun, W. Zhang, M. Lv, E. Yang, Q. Zhao, W. Wang, Antibacterial activity of ruthenium(II) polypyridyl complex manipulated by membrane permeability and cell morphology, Bioorg. Med. Chem. Lett. 25 (2015) 2068–2073, https://doi.org/10.1016/j.bmcl.2015.03.090.

[19] F. Li, M. Feterl, J.M. Warner, F.R. Keene, J. Grant Collins, Dinuclear polypyridylruthenium(II) complexes: flow cytometry studies of their accumulation in bacteria and the effect on the bacterial membrane, J. Antimicrob. Chemother. 68 (2013) 2825–2833, https://doi.org/10.1093/jac/dkt279.

[20] S. Monro, K.L. Colón, H. Yin, J. Roque, P. Konda, S. Gujar, R.P. Thummel, L. Lilge, C.G. Cameron, S.A. McFarland, Transition metal complexes and photodynamic therapy from a tumor-centered approach: challenges, opportunities, and highlights from the development of TLD1433, Chem. Rev. 119 (2019) 797–828, https://doi.org/10.1021/acs.chemrev.8b00211.

[21] M. Klausen, M. Ucuncu, M. Bradley, Design of photosensitizing agents for targeted antimicrobial photodynamic therapy, Molecules. 25 (2020) 5239, https://doi.org/10.3390/molecules25225239.

[22] F. Cieplik, D. Deng, W. Crielaard, W. Buchalla, E. Hellwig, A. Al-Ahmad, T. Maisch, Antimicrobial photodynamic therapy-what we know and what we don't, Crit. Rev. Microbiol. 44 (2018) 571–589, https://doi.org/10.1080/1040841X.2018.1467876.

[23] J. Ghorbani, D. Rahban, S. Aghamiri, A. Teymouri, A. Bahador, Photosensitizers in antibacterial photodynamic therapy: an overview, Laser Ther. 27 (2018) 293–302, https://doi.org/10.5978/islsm.27_18-RA-01.

[24] G. Boccalini, L. Conti, C. Montis, D. Bani, A. Bencini, D. Berti, C. Giorgi, A. Mengoni, B. Valtancoli, Methylene blue-containing liposomes as new photodynamic anti-bacterial agents, J. Mater. Chem. B 5 (2017) 2788–2797, https://doi.org/10.1039/c6tb03367a.

[25] J.F. Lin, J. Li, A. Gopal, T. Munshi, Y.W. Chu, J.X. Wang, T.T. Liu, B. Shi, X. Chen, L. Yan, Synthesis of photo-excited Chlorin e6 conjugated silica nanoparticles for enhanced anti-bacterial efficiency to overcome methicillin-resistant: Staphylococcus aureus, Chem. Commun. 55 (2019) 2656–2659, https://doi.org/10.1039/c9cc00166b.

[26] M.H. Staegemann, B. Gitter, J. Dernedde, C. Kuehne, R. Haag, A. Wiehe, Mannose-functionalized Hyperbranched Polyglycerol loaded with zinc Porphyrin: investigation of the Multivalency effect in antibacterial photodynamic therapy, Chem. Eur. J. 23 (2017) 3918–3930, https://doi.org/10.1002/chem.201605236.

[27] R. Donnelly, N. Fletcher, P. McCague, J. Donnelly, P. McCarron, M. Tunney, Design, synthesis and photodynamic antimicrobial activity of ruthenium Trischelate Diimine complexes, Lett. Drug Des. Discov. 4 (2007) 175–179, https://doi.org/10.2174/157018007780077390.

[28] K.L. Smitten, E.J. Thick, H.M. Southam, J. Bernardino De La Serna, S.J. Foster, J. A. Thomas, Mononuclear ruthenium(II) theranostic complexes that function as broad-spectrum antimicrobials in therapeutically resistant pathogens through interaction with DNA, Chem. Sci. 11 (2020) 8828–8838, https://doi.org/10.1039/d0sc03410j.

[29] F. Heinemann, J. Karges, G. Gasser, Critical overview of the use of Ru(II) Polypyridyl complexes as photosensitizers in one-photon and two-photon photodynamic therapy, Acc. Chem. Res. 50 (2017) 2727–2736, https://doi.org/10.1021/acs.accounts.7b00180.

[30] T. Le Gall, G. Lemercier, S. Chevreux, K.S. Tücking, J. Ravel, F. Thétiot, U. Jonas, H. Schönherr, T. Montier, Ruthenium(II) Polypyridyl complexes as photosensitizers for antibacterial photodynamic therapy: a structure-activity study on clinical bacterial strains, ChemMedChem. 13 (2018) 2229, https://doi.org/10.1002/cmdc.201800392.

[31] A. Frei, R. Rubbiani, S. Tubafard, O. Blacque, P. Anstaett, A. Felgenträger, T. Maisch, L. Spiccia, G. Gasser, Synthesis, characterization, and biological evaluation of new Ru(II) polypyridyl photosensitizers for photodynamic therapy, J. Med. Chem. 57 (2014) 7280–7292, https://doi.org/10.1021/jm500566f.

[32] N. Deepika, Y.P. Kumar, C. Shobha Devi, P.V. Reddy, A. Srishailam, S. Satyanarayana, Synthesis, characterization, and DNA binding, photocleavage, cytotoxicity, cellular uptake, apoptosis, and on-off light switching studies of Ru(II) mixed-ligand complexes containing 7-fluorodipyrido[3,2-a:2′,3′-c] phenazine, J. Biol. Inorg. Chem. 18 (2013) 751–766, https://doi.org/10.1007/s00775-013-1018-0.

[33] Y. Feng, W.Z. Sun, X.S. Wang, Q.X. Zhou, Selective photoinactivation of methicillin-resistant *Staphylococcus aureus* by highly positively charged Ru(II) complexes, Chem. Eur. J. 25 (2019) 13879, https://doi.org/10.1002/chem.201903923.

[34] S. Brown, J.P. Santa Maria, S. Walker, Wall teichoic acids of gram-positive bacteria, Annu. Rev. Microbiol. 67 (2013) 313–336, https://doi.org/10.1146/annurev-micro-092412-155620.

[35] L. Conti, A. Bencini, C. Ferrante, C. Gellini, P. Paoli, M. Parri, G. Pietraperzia, B. Valtancoli, C. Giorgi, Highly charged ruthenium(II) Polypyridyl complexes as effective photosensitizer in photodynamic therapy, Chem. Eur. J. 25 (2019) 10606–10615, https://doi.org/10.1002/chem.201901570.

[36] L. Conti, L. Mummolo, G.M. Romano, C. Giorgi, G.E. Giacomazzo, L. Prodi, A. Bencini, Exploring the ability of luminescent metal assemblies to bind and sense anionic or ionizable analytes A $Ru(phen)_2$bipy-Based dizinc complex for Bisphenol A (BPA) recognition, Molecules 36 (26) (2021) 527, https://doi.org/10.3390/molecules26030527.

[37] J. Marmur, A procedure for the isolation of deoxyribonucleic acid from micro-organisms, J. Mol. Biol. 3 (3) (1961) 208–218, https://doi.org/10.1016/S0022-2836(61)80047-8.

[38] M.E. Reichmann, S.A. Rice, C.A. Thomas, P. Doty, A further examination of the molecular weight and size of Desoxypentose nucleic acid, J. Am. Chem. Soc. 76 (1954) 3047–3053, https://doi.org/10.1021/ja01640a067.

[39] M.C. Aragoni, M. Arca, A. Bencini, C. Caltagirone, L. Conti, A. Garau, B. Valtancoli, F. Isaia, V. Lippolis, F. Palomba, L. Prodi, N. Zaccheroni, Zn^{2+}/Cd^{2+} optical discrimination by fluorescent acridine-based bis-macrocylic receptors, Supramol. Chem. 29 (2017) 912–921, https://doi.org/10.1080/10610278.2017.1387262.

[40] F. Bartoli, A. Bencini, L. Conti, C. Giorgi, B. Valtancoli, P. Paoli, P. Rossi, N. Le Bris, R. Tripier, Catching anions with coloured assemblies: binding of pH indicators by a giant-size polyammonium macrocycle for anion naked-eye recognition, Org. Biomol. Chem. 14 (2016) 8309–8321, https://doi.org/10.1039/c6ob01474g.

[41] A. Garau, A. Bencini, A.J. Blake, C. Caltagirone, L. Conti, F. Isaia, V. Lippolis, R. Montis, P. Mariani, M.A. Scorciapino, AneN3-based fluorescent receptors for metal ion sensing, featuring urea and amide functional groups, Dalton Trans. 48 (2019) 4949–4960, https://doi.org/10.1039/c9dt00288j.

[42] G. Gran, Determination of the equivalence point in potentiometric titrations. Part II, Analyst. 77 (1952) 661–671, https://doi.org/10.1039/AN9527700661.

[43] P. Gans, A. Sabatini, A. Vacca, Investigation of equilibria in solution. Determination of equilibrium constants with the HYPERQUAD suite of programs, Talanta. 43 (1996) 1739–1753, https://doi.org/10.1016/0039-9140(96)01958-3.

[44] L. Alderighi, P. Gans, A. Ienco, D. Peters, A. Sabatini, A. Vacca, Hyperquad simulation and speciation (HySS): a utility program for the investigation of equilibria involving soluble and partially soluble species, Coord. Chem. Rev. 184 (1999) 311–318, https://doi.org/10.1016/S0010-8545(98)00260-4.

[45] R. Schmidt, E. Afshari, Effect of solvent on the phosphorescence rate constant of singlet molecular oxygen (1.DELTA.G), J. Phys. Chem. 94 (1990) 4377–4378, https://doi.org/10.1021/j100373a096.

[46] A. Andrés, M. Rosés, C. Ràfols, E. Bosch, S. Espinosa, V. Segarra, J.M. Huerta, Setup and validation of shake-flask procedures for the determination of partition coefficients (log D) from low drug amounts, Eur. J. Pharm. Sci. 76 (2015) 181–191, https://doi.org/10.1016/j.ejps.2015.05.008.

[47] A. Wolfe, G.H. Shimer, T. Meehan, Polycyclic aromatic hydrocarbons physically intercalate into duplex regions of denatured DNA, Biochemistry. 26 (1987) 6392–6396, https://doi.org/10.1021/bi00394a013.

[48] H. Chao, W.J. Mei, Q.W. Huang, L.N. Ji, DNA binding studies of ruthenium(II) complexes containing asymmetric tridentate ligands, J. Inorg. Biochem. 92 (2002) 165–170, https://doi.org/10.1016/S0162-0134(02)00543-3.

[49] Y.J. Liu, H. Chao, L.F. Tan, Y.X. Yuan, W. Wei, L.N. Ji, Interaction of polypyridyl ruthenium (II) complex containing asymmetric ligand with DNA, J. Inorg. Biochem. 99 (2005) 530–537, https://doi.org/10.1016/j.jinorgbio.2004.10.030.

[50] J. Sambrook, E.F. Fritsch, T. Maniatis, Molecular Cloning: A Laboratory Manual, Cold Spring Harbor Laboratory Press, 1989.

[51] D.R. Zeigler, Z. Prágai, S. Rodriguez, B. Chevreux, A. Muffler, T. Albert, R. Bai, M. Wyss, J.B. Perkins, The origins of 168, W23, and other Bacillus subtilis legacy strains, J. Bacteriol. 190 (2008) 6983–6995, https://doi.org/10.1128/JB.00722-08.

[52] M. Becatti, A. Bencini, S. Nistri, L. Conti, M.G. Fabbrini, L. Lucarini, V. Ghini, M. Severi, C. Fiorillo, C. Giorgi, L. Sorace, B. Valtancoli, D. Bani, Different antioxidant efficacy of two Mn^{II}-containing superoxide anion scavengers on hypoxia/Reoxygenation-exposed cardiac muscle cells, Sci. Rep. 9 (2019) 10320, https://doi.org/10.1038/s41598-019-46476-2.

[53] A. Bencini, E. Berni, A. Biancini, C. Giorgi, B. Valtancoli, D.K. Chand, H. J. Schneider, Proton and Cu(II) binding to tren-based tris-macrocycles. Affinity towards nucleic acids and nuclease activity, Dalton Trans. 5 (2003) 793–800, https://doi.org/10.1039/b211001f.

[54] C. Lodeiro, A.J. Parola, F. Pina, C. Bazzicalupi, A. Bencini, A. Bianchi, C. Giorgi, A. Masotti, B. Valtancoli, Protonation and Zn(II) coordination by dipyridine-containing macrocycles with different molecular architecture. A case of pH-controlled metal jumping outside - Inside the macrocyclic cavity, Inorg. Chem. 40 (2001) 2968–2975, https://doi.org/10.1021/ic001381k.

[55] R.D. Hancock, M. Salim Shaikjee, S.M. Dobson, J.C.A. Boeyens, The Stereochemical activity or non-activity of the "Inert" pair of electrons on lead(II) in relation to its complex stability and structural properties. Some considerations in ligand design, Inorg. Chim. Acta 154 (1988) 229–238, https://doi.org/10.1016/S0020-1693(00)90141-5.

[56] A.P. Castano, T.N. Demidova, M.R. Hamblin, Mechanisms in photodynamic therapy: part one - photosensitizers, photochemistry and cellular localization, Photodiagn. Photodyn. Ther. 1 (2004) 279–293, https://doi.org/10.1016/S1572-1000(05)00007-4.

[57] B. Testa, P. Crivori, M. Reist, P.A. Carrupt, The influence of lipophilicity on the pharmacokinetic behavior of drugs: concepts and examples, Perspect. Drug Discov. Des. 19 (2000) 179–211, https://doi.org/10.1023/A:1008741731244.

[58] S. Movassaghi, M. Hanif, H.U. Holtkamp, T. Söhnel, S.M.F. Jamieson, C. G. Hartinger, Making organoruthenium complexes of 8-hydroxyquinolines more hydrophilic: impact of a novel l-phenylalanine-derived arene ligand on the biological activity, Dalton Trans. 47 (2018) 2192–2201, https://doi.org/10.1039/c7dt04451h.

[59] A.K. Gorle, M. Feterl, J.M. Warner, L. Wallace, F.R. Keene, J.G. Collins, Tri- and tetra-nuclear polypyridyl ruthenium(II) complexes as antimicrobial agents, Dalton Trans. 43 (2014) 16713–16725, https://doi.org/10.1039/c4dt02139h.

[60] F. Li, Y. Mulyana, M. Feterl, J.M. Warner, J.G. Collins, F.R. Keene, The antimicrobial activity of inert oligonuclear polypyridylruthenium(II) complexes against pathogenic bacteria, including MRSA, Dalton Trans. 40 (2011) 5032–5038, https://doi.org/10.1039/c1dt10250h.

[61] B.M. Zeglis, V.C. Pierre, J.K. Barton, Metallo-intercalators and metallo-insertors, Chem. Commun. 44 (2007) 4565–4579, https://doi.org/10.1039/b710949k.

[62] M.R. Gill, J.A. Thomas, Ruthenium(II) polypyridyl complexes and DNA - from structural probes to cellular imaging and therapeutics, Chem. Soc. Rev. 41 (2012) 3179–3192, https://doi.org/10.1039/c2cs15299a.

[63] M. Sirajuddin, S. Ali, A. Badshah, Drug-DNA interactions and their study by UV-visible, fluorescence spectroscopies and cyclic voltametry, J. Photochem. Photobiol. B Biol. 124 (2013) 1–19, https://doi.org/10.1016/j.jphotobiol.2013.03.013.

[64] T. Nandhini, K.R. Anju, V.M. Manikandamathavan, V.G. Vaidyanathan, B.U. Nair, Interactions of Ru(II) polypyridyl complexes with DNA mismatches and abasic sites, Dalton Trans. 44 (2015) 9044–9051, https://doi.org/10.1039/c5dt00807g.

[65] Y.J. Liu, H. Chao, L.F. Tan, Y.X. Yuan, W. Wei, L.N. Ji, Interaction of polypyridyl ruthenium (II) complex containing asymmetric ligand with DNA, J. Inorg. Biochem. 99 (2005) 530–537, https://doi.org/10.1016/j.jinorgbio.2004.10.030.

[66] A. Łęczkowska, J. Gonzalez-Garcia, C. Perez-Arnaiz, B. Garcia, A.J.P. White, R. Vilar, Binding studies of metal-salphen and metal-bipyridine complexes towards G-Quadruplex DNA, Chem. - A Eur. J. 24 (2018) 11785–11794, https://doi.org/10.1002/chem.201802248.

[67] R. Indumathy, M. Kanthimathi, T. Weyhermuller, B.U. Nair, Cobalt complexes of terpyridine ligands: crystal structure and nuclease activity, Polyhedron. 27 (2008) 3443–3450, https://doi.org/10.1016/j.poly.2008.08.003.

[68] A.M. Pyle, J.P. Rehmann, R. Meshoyrer, C.V. Kumar, N.J. Turro, J.K. Barton, Mixed-ligand complexes of ruthenium(II): factors governing binding to DNA, J. Am. Chem. Soc. 111 (1989) 3051–3058, https://doi.org/10.1021/ja00190a046.

[69] P. Lincoln, B. Norden, DNA binding geometries of ruthenium(II) complexes with 1,10-phenanthroline and 2,2′-bipyridine ligands studied with linear dichroism spectroscopy. Borderline cases of intercalation, Doktorsavhandlingar Vid Chalmers Tek. Hogsk 102 (1998) 9583–9594, https://doi.org/10.1021/jp9824914.

[70] S. Satyanarayana, J.C. Dabrowiak, J.B. Chaires, Tris(phenanthroline)ruthenium(II) enantiomer interactions with DNA: mode and specificity of binding, Biochemistry. 32 (1993) 2573–2584, https://doi.org/10.1021/bi00061a015.

[71] M. Eriksson, M. Leijon, C. Hiort, B. Norden, A. Graeslund, Minor groove binding of $[Ru(phen)_3]^{2+}$ to $[d(CGCGATCGCG)]_2$ evidenced by two-dimensional NMR, J. Am. Chem. Soc. 114 (1992) 4933–4934, https://doi.org/10.1021/ja00038a085.

[72] C. Mari, V. Pierroz, R. Rubbiani, M. Patra, J. Hess, B. Spingler, L. Oehninger, J. Schur, I. Ott, L. Salassa, S. Ferrari, G. Gasser, DNA intercalating Ru(II) polypyridyl complexes as effective photosensitizers in photodynamic therapy, Chem. Eur. J. 20 (2014) 14421–14436, https://doi.org/10.1002/chem.201402796.

[73] S.R. Dalton, S. Glazier, B. Leung, S. Win, C. Megatulski, S.J.N. Burgmayer, DNA binding by Ru(II)-bis(bipyridine)-pteridinyl complexes, J. Biol. Inorg. Chem. 13 (2008) 1133, https://doi.org/10.1007/s00775-008-0399-y.

[74] A. Hergueta-Bravo, M.E. Jiménez-Hernández, F. Montero, E. Oliveros, G. Orellana, Singlet oxygen-mediated DNA photocleavage with Ru(II) polypyridyl complexes, J. Phys. Chem. B 106 (2002) 4010–4017, https://doi.org/10.1021/jp013542r.

[75] A. Ratanaphan, T. Nhukeaw, P. Temboot, K. Hansongnern, DNA-binding properties of ruthenium(II) complexes with the bidentate ligand 5-chloro-2-(phenylazo) pyridine, Transit. Met. Chem. 37 (2012) 207–214, https://doi.org/10.1007/s11243-012-9576-5.

[76] Y. Zhang, Q. Zhou, N. Tian, C. Li, X. Wang, Ru(II)-complex-based DNA Photocleaver having intense absorption in the phototherapeutic window, Inorg. Chem. 56 (2017) 1865–1873, https://doi.org/10.1021/acs.inorgchem.6b02459.

[77] H. Yu, J. Liu, Z. Hao, J. He, M. Sun, S. Hu, L. Yu, H. Chao, Synthesis, characterization and biological evaluation of ruthenium(II) Complexes $[Ru(dtzp)(dppz)Cl]^+$ and $[Ru(dtzp)(dppz)CH_3CN]^{2+}$ for photodynamic therapy, Dyes Pigments 136 (2017) 416–426, https://doi.org/10.1016/j.dyepig.2016.08.059.

[78] L. Kucková, K. Jomová, A. Švorcová, M. Valko, P. Segľa, J. Moncol', J. Kožíšek, Synthesis, crystal structure, spectroscopic properties and potential biological activities of salicylate-neocuproine ternary copper(II) complexes, Molecules. 20 (2015) 2115–2137, https://doi.org/10.3390/molecules20022115.

International Journal of
Molecular Sciences

MDPI

Article

Highly Charged Ru(II) Polypyridyl Complexes as Photosensitizer Agents in Photodynamic Therapy of Epithelial Ovarian Cancer Cells

Luca Conti [1], Gina Elena Giacomazzo [1], Barbara Valtancoli [1], Mauro Perfetti [1], Alberto Privitera [1], Claudia Giorgi [1,*], Patrick Severin Sfragano [1], Ilaria Palchetti [1], Sara Pecchioli [2], Paola Bruni [2] and Francesca Cencetti [2,*]

[1] Department of Chemistry "Ugo Schiff", University of Florence, 50019 Sesto Fiorentino, Italy
[2] Department of Experimental and Clinical Biomedical Sciences "Mario Serio", University of Florence, 50134 Florence, Italy
* Correspondence: claudia.giorgi@unifi.it (C.G.); francesca.cencetti@unifi.it (F.C.); Tel.: +39-0554573365 (C.G.); +39-0552751243 (F.C.)

Abstract: Ovarian cancer recurrence is frequent and associated with chemoresistance, leading to extremely poor prognosis. Herein, we explored the potential anti-cancer effect of a series of highly charged Ru(II)-polypyridyl complexes as photosensitizers in photodynamic therapy (PDT), which were able to efficiently sensitize the formation of singlet oxygen upon irradiation (**Ru1**$^{2+}$ and **Ru2**$^{2+}$) and to produce reactive oxygen species (ROS) in their corresponding dinuclear metal complexes with the Fenton active Cu(II) ion/s ([Cu**Ru1**]$^{4+}$ and [Cu_2**Ru2**]$^{6+}$). Their cytotoxic and anti-tumor effects were evaluated on human ovarian cancer A2780 cells both in the absence or presence of photoirradiation, respectively. All the compounds tested were well tolerated under dark conditions, whereas they switched to exert anti-tumor activity following photoirradiation. The specific effect was mediated by the onset of programed cell death, but only in the case of **Ru1**$^{2+}$ and **Ru2**$^{2+}$ was preceded by the loss of mitochondrial membrane potential soon after photoactivation and ROS production, thus supporting the occurrence of apoptosis via *type II* photochemical reactions. Thus, Ru(II)-polypyridyl-based photosensitizers represent challenging tools to be further investigated in the identification of new therapeutic approaches to overcome the innate chemoresistance to platinum derivatives of some ovarian epithelial cancers and to find innovative drugs for recurrent ovarian cancer.

Keywords: drug discovery; coordination complexes; phototoxicity; reactive oxygen species

Citation: Conti, L.; Giacomazzo, G.E.; Valtancoli, B.; Perfetti, M.; Privitera, A.; Giorgi, C.; Sfragano, P.S.; Palchetti, I.; Pecchioli, S.; Bruni, P.; et al. Highly Charged Ru(II) Polypyridyl Complexes as Photosensitizer Agents in Photodynamic Therapy of Epithelial Ovarian Cancer Cells. *Int. J. Mol. Sci.* **2022**, *23*, 13302. https://doi.org/10.3390/ijms232113302

Academic Editor: Young-Jin Kim

Received: 27 September 2022
Accepted: 27 October 2022
Published: 1 November 2022

1. Introduction

Ovarian cancer is one of the most common among gynecologic cancers and is the major cause of tumor-associated death in reproductive women [1,2]. Aggressive but asymptomatic progression frequently occurs followed by late diagnosis of advanced and metastatic stage in more than 70% of patients [3]. Surgery and chemotherapy are the major therapeutic choices, nevertheless with limited benefits, since the majority of ovarian cancer patients are initially sensitive to platinum- and taxane-based chemotherapies, which are the "golden standard" approach in ovarian cancer treatment, whereas almost half unfortunately suffer from recurrence, developing therapeutic resistance [4] in response to platinum-based chemotherapy. Therefore, innovative therapeutic strategies to overcome drug resistance are urgently needed.

Ruthenium polypyridyl complexes (RPCs) have been extensively studied and analyzed for their possibility of becoming alternative drugs in place of cisplatin [5–7]. Recently, their rich chemical–physical repertoire, which includes a wide range of photoluminescence characteristics, DNA binding abilities, tunable absorption properties and good singlet oxygen sensitizing features, made them ideal candidates as photosensitizer agents (PSs)

in the "so-called" photodynamic therapy (PDT). Their employment in this therapeutic approach continues to attract increasing attention due to the encouraging results obtained in the treatment of a wide variety of cancers, such as lung, bladder, skin tumors [8–11], and also bacterial infections [12–14].

In PDT, the PS is activated through irradiation with low-energy light to sensitize the generation of highly reactive species, namely reactive oxygen species (ROS), capable of ultimately leading to cytotoxic effects. This peculiar mechanism of action guarantees a complete spatial and temporal control over drug activation and thus offers the crucial advantage of potentially lowering the severe dose-limiting side effects normally occurring with standard therapeutics.

In general, ROS can be produced through distinct pathways. According to *Type I* reactions, the deactivation of the excited PS can occur via a direct electron or proton transfer to the surrounding biological substrates, leading to radical species that further interact with molecular oxygen to form ROS, such as superoxide, peroxides and hydroxyl radicals. *Type II* mechanisms are instead based on the direct interaction between the excited PS and ground-state molecular oxygen ($^3O_2$) to produce singlet oxygen ($^1O_2$), a highly cytotoxic species that is capable of rapidly reacting with biological targets (estimated half-life < 40 ns and radius of action of the order of 20 nm, in a biological environment) [15], leading to topical oxidative damages and, ultimately, to cellular death.

We have previously reported on the potential as PS agents of two highly charged Ru(II)-polypyridyl complexes $[Ru(phen)_2\mathbf{L'}]^{2+}$ (**Ru1**$^{2+}$) and $[Ru(phen)_2\mathbf{L''}]^{2+}$ (**Ru2**$^{2+}$), featuring the peculiar polyazamacrocyclic units **L′** and **L″** (**L′** = 4,4′-(2,5,8,11,14-pentaaza [15])-2,2′-bipyridilophane, **L″** = 4,4′-bis-[methylen-(1,4,7,10-tetraazacyclododecane)]-2,2′ bipyridine) and their corresponding copper(II) complexes [Cu**Ru1**]$^{4+}$ and [Cu_2**Ru2**]$^{6+}$ (see Scheme 1) [16,17]. Compared to the majority of RPCs used in PDT, the high number of easily protonable nitrogen groups gathered on the unique polyazamacrocyclic ligand of **Ru1**$^{2+}$, or on the two distinct cyclen (1,4,7,10-tetraazacyclododecane) moieties of **Ru2**$^{2+}$, confers to the resulting compounds the possibility to form highly charged species in aqueous media. This ensures excellent water solubility, a key requisite for biological application, but it also strengthens the capacity of ruthenium complexes to interact with possible biological targets, such as DNA. Importantly, the polyamine-based frameworks do not alter the good $^1O_2$ sensitizing properties of **Ru1**$^{2+}$ and **Ru2**$^{2+}$, making them appealing PSs for the generation of $^1O_2$ directly in aqueous matrices.

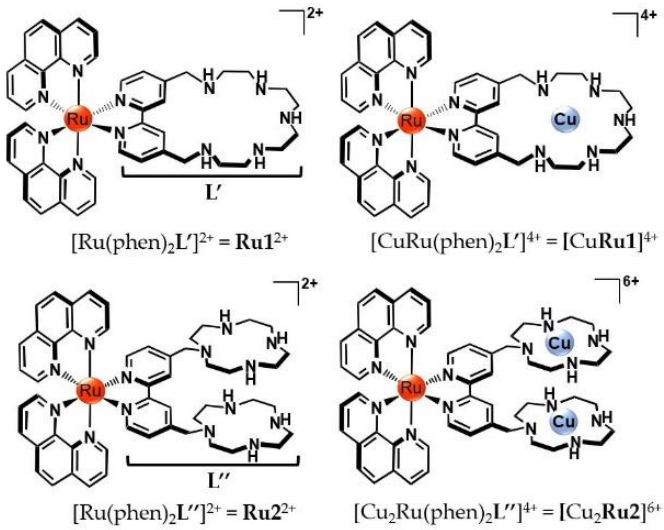

Scheme 1. Schematic representation of the ruthenium compounds studied in this work.

Furthermore, **L′** and **L″** allow stably binding up to two Fenton-active copper(II) ion/s, leading to the generation of mixed Ru(II)/Cu(II) complexed species, namely $[CuRu(phen)_2\mathbf{L'}]^{4+}$ ($[Cu\mathbf{Ru1}]^{4+}$) and $[Cu_2Ru(phen)_2\mathbf{L''}]^{6+}$ ($[Cu_2\mathbf{Ru2}]^{6+}$). These heteronuclear forms are able to generate other types of ROS, such as hydroxyl radicals, and thus may represent versatile tools in the research of alternative cytotoxic pathways to the singlet oxygen sensitization.

Prompted by the encouraging results previously displayed by $\mathbf{Ru1}^{2+}$ and $[Cu\mathbf{Ru1}]^{4+}$ in a human melanoma cell line [16], in this work, we explored the potential as photoresponsive anti-cancer compounds of all the $\mathbf{Ru1}^{2+}$, $[Cu\mathbf{Ru1}]^{4+}$, $\mathbf{Ru2}^{2+}$ and $[Cu_2\mathbf{Ru2}]^{6+}$ complexes in a unique and comparative study, where, in addition to the first comparison between the in-solution properties of these compounds, their in vitro anti-tumor efficacies were evaluated on A2780 human ovarian cancer cells. Moreover, a particular emphasis was placed on the study of the molecular mechanisms responsible for the observed anticancer effects by investigating the occurrence of apoptotic cell death, ROS production and mitochondrial function.

Our results show that ovarian cancer cells were capable of internalizing the ruthenium complexes at 6–24 h of incubation. Moreover, under dark conditions, these compounds exhibited extremely low cellular toxicity, which was particularly evident in non-cancer cells, whereas after photosensitization, they exerted a significant anti-tumor effect.

The results provided by this study can represent an important step forward in the research of alternative therapeutic approaches to platinum-based chemotherapy by employing ruthenium-based photoresponsive compounds.

2. Results

2.1. Protonation, Metal Binding of Ruthenium Compounds and Stability of the Mixed Ruthenium/Copper Complexed Species

The acid-base properties of $\mathbf{Ru1}^{2+}$ and $\mathbf{Ru2}^{2+}$ were investigated by means of potentiometric measurements in NMe_4Cl 0.1 M at 298 ± 0.1 K. The LogK values for the protonation constants and the corresponding distribution diagrams of the species present in solution are, respectively, reported in Table S1 and Figures S1 and S2 of SI. As shown, the presence of polyazamacrocycles **L′** and **L″** confers to the corresponding ruthenium compounds the ability to bind up to five ($[H_5\mathbf{Ru1}]^{7+}$) or six ($[H_6\mathbf{Ru2}]^{8+}$) protons in the overall range of pH investigated (between 2.5 and 10.5). Among the different protonated forms, the di- and tetra-protonated species $[H_2\mathbf{Ru1}]^{4+}$ and $[H_3\mathbf{Ru2}]^{5+}$ are the most abundant around neutral pH values (Figures S1 and S2, Supplementary Materials), including at the physiological pH value employed in biological experiments (vide infra). Nevertheless, for the sake of clarity, these species are simply referred to as $\mathbf{Ru1}^{2+}$ and $\mathbf{Ru2}^{2+}$ throughout the manuscript.

In addition to the ability to easily protonate in aqueous solution, the nitrogen donors gathered on the polyamine **L′** and **L″** frameworks can also act as suitable anchoring sites to host additional metal ions. Herein, we exploited this property to afford the formation of mixed heteronuclear Ru(II)/Cu(II) complexed species to evaluate whether the presence of Fenton-active Cu(II) center/s within the polyamine pockets of ruthenium compounds may have an influence on the biological potential of such hybrid, heteronuclear systems.

Analogously to the acid-base study, the formation of Ru(II)/Cu(II) complexes in solution was followed via potentiometric measurements; the LogK values for Cu(II) complexation by $\mathbf{Ru1}^{2+}$ and $\mathbf{Ru2}^{2+}$ and the corresponding distribution diagrams are, respectively, reported in Table 1 and Figures S3 and S4 of Supplementary Materials. As shown in Table 1, $\mathbf{Ru1}^{2+}$ and $\mathbf{Ru2}^{2+}$ form stable mono- and dinuclear complexes with Cu(II), with LogK values of 15.34 and 27.6 for the coordination of one ($\mathbf{Ru1}^{2+}$) and two ($\mathbf{Ru2}^{2+}$) Cu(II) ions. The coordination of copper is maintained in a wide range of pH, and, at the pH of the biological tests (7.4), these complexes are mainly present in their mononuclear $[Cu\mathbf{Ru}1]^{4+}$ and binuclear $[Cu_2\mathbf{Ru2}]^{6+}$ forms (Figures S3 and S4, Supplementary Materials).

Table 1. Stability constants of Cu(II), Zn(II), Ca(II) and Mg(II) complexes formed by **Ru1**$^{2+}$ and **Ru2**$^{2+}$ determined by means of potentiometric measurements in NMe_4Cl 0.1 M, at 298.1 ± 0.1 K.

Reaction	LogK	
	L = Ru1	**L = Ru2**
$\mathbf{L}^{2+} + Cu^{2+} = Cu\mathbf{L}^{4+}$	15.34 (6) [a]	16.72 (8)
$Cu\mathbf{L}^{4+} + H^{+} = CuH\mathbf{L}^{5+}$	5.60 (6)	7.58 (7)
$CuH\mathbf{L}^{5+} + H^{+} = CuH_2\mathbf{L}^{6+}$	3.91 (4)	5.89 (5)
$Cu\mathbf{L}^{4+} + OH^{-} = Cu\mathbf{L}(OH)^{3+}$	6.06 (4)	
$\mathbf{L}^{2+} + 2Cu^{2+} + OH^{-} = Cu_2\mathbf{L}(OH)^{5+}$	12.95 (5)	
$Cu\mathbf{L}^{4+} + Cu^{2+} = Cu_2\mathbf{L}^{6+}$		10.88 (7)
$Cu_2\mathbf{L}^{6+} + 2OH^{-} = Cu_2\mathbf{L}(OH)_2{}^{4+}$		9.48 (6)
$\mathbf{L}^{2+} + Zn^{2+} = Zn\mathbf{L}^{4+}$	8.90 (7)	14.91 (5)
$Zn\mathbf{L}^{4+} + H^{+} = ZnH\mathbf{L}^{5+}$	6.36 (7)	8.65 (4)
$ZnH\mathbf{L}^{5+} + H^{+} = ZnH_2\mathbf{L}^{6+}$	5.56 (6)	7.16 (5)
$ZnH_2\mathbf{L}^{6+} + H^{+} = ZnH_3\mathbf{L}^{7+}$	4.75 (8)	
$Zn\mathbf{L}^{4+} + 2OH^{-} = Zn\mathbf{L}(OH)_2{}^{2+}$	11.55 (4)	
$Zn\mathbf{L}^{4+} + Zn^{2+} = Zn_2\mathbf{L}^{6+}$		5.42 (7)
$Zn_2\mathbf{L}^{6+} + 3OH^{-} = Zn_2\mathbf{L}(OH)_3{}^{3+}$		15.48 (6)
$\mathbf{L}^{2+} + Ca^{2+} = Ca\mathbf{L}^{4+}$	2.62 (5)	2.55 (6)
$\mathbf{L}^{2+} + Mg^{2+} = Mg\mathbf{L}^{4+}$	2.23 (5)	2.06 (6)

[a] Values in parentheses are standard deviations in the standard deviations on the last significant figure.

Since different cations are naturally present in the biological environment, the metal-binding properties of ruthenium compounds toward other relevant metal ions were also considered. In particular, we focused on K^+, Na^+, Ca^{2+}, Mg^{2+} and Zn^{2+}, taken as the most abundant alkaline, alkaline-earth and transition cations in the cellular and extracellular matrices. As shown in Table 1, the most stable complexes among these cations were formed by Zn(II), with LogK values of 8.90 and 20.33, respectively, for the addition of one Zn(II) to **Ru1**$^{2+}$ and two Zn(II) ions to **Ru2**$^{2+}$. However, these values are considerably lower (up to ca. 1.7-fold) compared to Cu(II), thus highlighting the higher stability of the Ru(II)-Cu(II) complexed species compared to the ones formed by all the other cations tested. On the other hand, the affinity toward K^+ and Na^+ emerged to be too weak to permit an accurate determination of the relative LogK values via potentiometric analysis (LogK < 1.5).

The higher affinity of Ru(II) compounds for Cu(II) ion/s is further underlined by the selectivity diagrams reported in Figure S5 and determined as previously described [18]. As shown, the presence of Zn(II), Ca(II) and Mg(II), even in high concentrations, does not affect the formation of the Cu(II) complexes by both **Ru1**$^{2+}$ and **Ru2**$^{2+}$, and no Cu(II) release due to displacement by other metals takes place in the investigated range of pH. Metal decomplexation can only occur in low percentage (c.ca. 10%) at more acidic pH values, as expected, considering the protonation of polyamine residues of ruthenium compounds, which competes with metal binding in strong acidic conditions.

Therefore, taken together, these data underline the high stability of [Cu**Ru1**]$^{4+}$ and [Cu_2**Ru2**]$^{6+}$ in the adopted experimental conditions, suitable for the subsequent biological studies.

Lastly, it should also be mentioned that the coordination of Cu(II) markedly affects the fluorescence emission of the "metal-free" forms of ruthenium compounds. Indeed, **Ru1**$^{2+}$ and **Ru2**$^{2+}$ are highly luminescent and display an almost identical emission profile with a maximum centered at around 600 nm. Conversely, the presence of one ([Cu**Ru1**]$^{4+}$) or two ([Cu_2**Ru2**]$^{6+}$) Cu(II) ions within their polyamine pockets causes a tight decrease in the fluorescence emission (Figure S6, Supplementary Materials), an effect that can be naturally attributed to the paramagnetic nature of Cu(II) ion/s.

2.2. Reactive Oxygen Species (ROS) Production by Ruthenium Compounds

A key requisite for a candidate PS for PDT relies on its capacity to effectively produce ROS upon irradiation, such as the highly oxidant singlet oxygen $^1O_2$ species, which is produced according to *type-II*-based processes [19].

However, *type I* pathways can elicit severe damages as well [20]. Moreover, *type I* and *II* mechanisms can occur simultaneously, and recent studies underlined that radical species generated from *type I* processes can cooperate with $^1O_2$ to amplify the resulting PDT response, even under hypoxic conditions [21,22]. Therefore, the knowledge of the accessible pathways to PS agents is of paramount importance for their application in PDT.

As previously reported, **Ru1**$^{2+}$ and **Ru2**$^{2+}$ possess good singlet oxygen sensitizing properties, with comparable quantum yields (φ_Δ), respectively, of 0.29 ± 0.06 and 0.38 ± 0.08 (λ_{irr} = 400 nm, CH_3CN air-saturated solutions) [16,17]. On the contrary, the sensitization of $^1O_2$ becomes almost completely lost when Cu(II) is bound within the polyamine pockets of compounds. This effect can be easily rationalized with the fast deactivation of the excited states of [Cu**Ru1**]$^{4+}$ and [Cu_2**Ru2**]$^{6+}$ through internal conversion, which competes with the energy transfer to molecular oxygen.

For this reason, herein, we investigated the ability of [Cu**Ru1**]$^{4+}$ and [Cu_2**Ru2**]$^{6+}$ to elicit the formation of different typologies of ROS. This was performed through electron paramagnetic resonance (EPR), employing 5,5-dimethyl-1-pyrroline-N-oxide (DMPO) as the spin trap agent for free radicals (see Supplementary Materials for further details). Figure 1 reports a background experiment collected for a solution containing only H_2O_2 as co-reagent and DMPO, showing essentially no signal for ROS generation (blue trace in Figure 1). However, when [Cu**Ru1**]$^{4+}$ or [Cu_2**Ru2**]$^{6+}$ were added to the mixture, an EPR signal appeared (green and red traces for [Cu_2**Ru2**]$^{6+}$ and [Cu**Ru1**]$^{4+}$, respectively), clearly indicating ROS production by the mixed Ru(II)/Cu(II) complexes. The spectra recorded in the presence of [Cu**Ru1**]$^{4+}$ and [Cu_2**Ru2**]$^{6+}$ were strikingly similar, suggesting a comparable efficiency of the two systems in producing ROS.

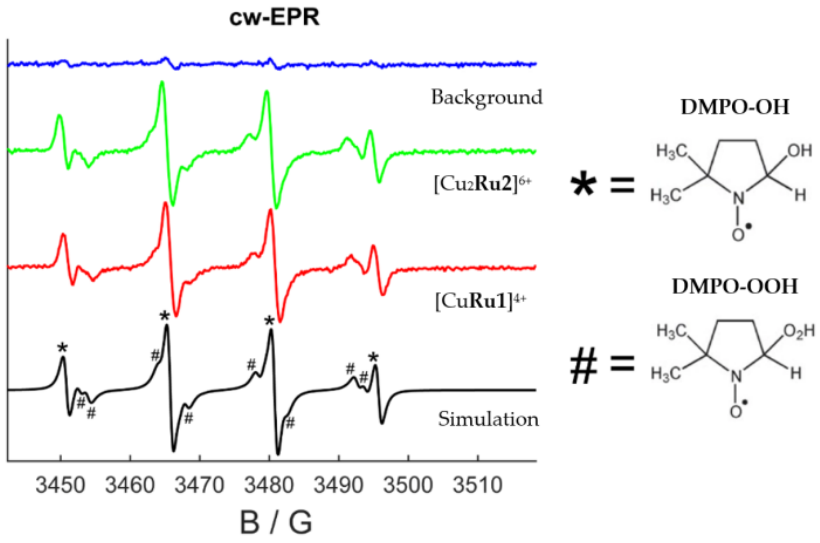

Figure 1. EPR spectra registered at 298 K of solutions containing DMPO and H_2O_2 (blue line), together with [Cu**Ru1**]$^{4+}$ (red line) or [Cu_2**Ru2**]$^{6+}$ (green line). The black trace is the best simulation (see text) obtained as a 50:50 mixture of hydroxide and peroxide radicals. Molecular structures of the corresponding adducts formed with DMPO are shown in the right part of the figure. The EPR lines referring to hydroxide and peroxide radicals are, respectively, labeled with symbols * and #. ([DMPO] = 750 mM, [H_2O_2] = 100 mM, [[Cu**Ru1**]$^{4+}$] = [[Cu_2**Ru2**]$^{6+}$] = 5 mM).

The analysis of the narrow EPR signals can also provide useful information regarding the nature of the produced radical species. As shown by the black trace in Figure 1, the best simulation of the experimental spectra was obtained by considering the production of a 50:50 mixture of hydroxide ($OH^{\bullet}$) and perhydroxyl ($HOO^{\bullet}$) radicals (EPR lines referring to the two radical species are labeled with symbols in Figure 1, and a simulation of the single contributions is reported in Figure S7, Supplementary Materials). In analogy to other studies [23,24], these species might be the result of Fenton/Fenton-like processes mediated by the presence of reducing agents and involving the Cu(II)/Cu(I) redox cycle/s. This would be of great relevance for the biological behavior of these compounds. In fact, the cellular environment typically contains high concentrations of common reducing agents, such as glutathione, ascorbic acid and NADH, just to cite a few, which can reduce the coordinated Cu(II) ions and therefore facilitate the occurrence of Fenton/Fenton-like pathways (e.g., $Cu(I) + H_2O_2 \rightarrow Cu(II) + OH^- + OH^{\bullet}$) [23]. On the other hand, oxidation-reduction potential (ORP) measurements and cyclic voltammetry (CV) analysis of aqueous solutions of $[Cu\mathbf{Ru1}]^{4+}$ and $[Cu_2\mathbf{Ru2}]^{6+}$ confirmed that the copper centers of the two heteronuclear compounds might be reduced under these conditions (see paragraph 5 of Supplementary Materials for further details).

2.3. Internalization of Ru(II) Complexes

The human ovarian cancer cell line A2780 has been established from an untreated patient bearing an ovarian adenocarcinoma, and it is commonly used as a model for ovarian cancer in particular to test the anti-cancer potency and delivery of various drugs [25]. Preliminarily, the analysis of Ru(II) complexes' uptake in cancer versus non-cancer cells showed that, after 24 h of incubation, $\mathbf{Ru1}^{2+}$, $\mathbf{Ru2}^{2+}$, $[Cu\mathbf{Ru1}]^{4+}$ and $[Cu_2\mathbf{Ru2}]^{6+}$ complexes were finely localized in discrete areas of A2780 cells, whereas they were undetectable in C2C12 myoblasts (Figure S10, Supplementary Materials), thus demonstrating that ovarian cancer cells, but not untransformed myoblasts, efficiently internalize Ru(II) complexes.

The kinetics of internalization of Ru(II) complexes in A2780 cells as well as their intracellular distribution was therefore checked, employing laser-scanning confocal microscopy, with the purpose to set the proper time of incubation before photoactivation by exploiting the intrinsic fluorescence properties of Ru(II) compounds. As shown in Figure 2A, a localized distribution of $\mathbf{Ru1}^{2+}$ and $\mathbf{Ru2}^{2+}$ complexes was barely detectable in cells after 15 min, whereas the internalization increased at 6 h of incubation, showing a plateau at 24 h. Notwithstanding, the Ru(II)-Cu(II) complexes featured a considerably less intense fluorescence emission than $\mathbf{Ru1}^{2+}$ and $\mathbf{Ru2}^{2+}$ (Figure S6, Supplementary Materials). Their residual emission was sufficient to monitor their cellular uptake over time, which occurs with a kinetic profile similar to the ones of $\mathbf{Ru1}^{2+}$ and $\mathbf{Ru2}^{2+}$.

In parallel with confocal microscopy, fluorometric analysis was used to evaluate the kinetics of internalization of Ru(II) compounds. A2780 cells were treated with Ru(II) complexes at 10 μM for the indicated time of incubation. The results, shown in Figure 2B, are comparable with those obtained by confocal microscopy; the fluorescence signal at 600 nm increased from 6 to 18 h, reaching a plateau at 24 h of incubation. Notwithstanding, $\mathbf{Ru1}^{2+}$ and $\mathbf{Ru2}^{2+}$, almost equally emissive when administered at the same concentration, differed with regard to the intensity of fluorescence, being higher in the latter, thus suggesting an enhanced cellular internalization of $\mathbf{Ru2}^{2+}$.

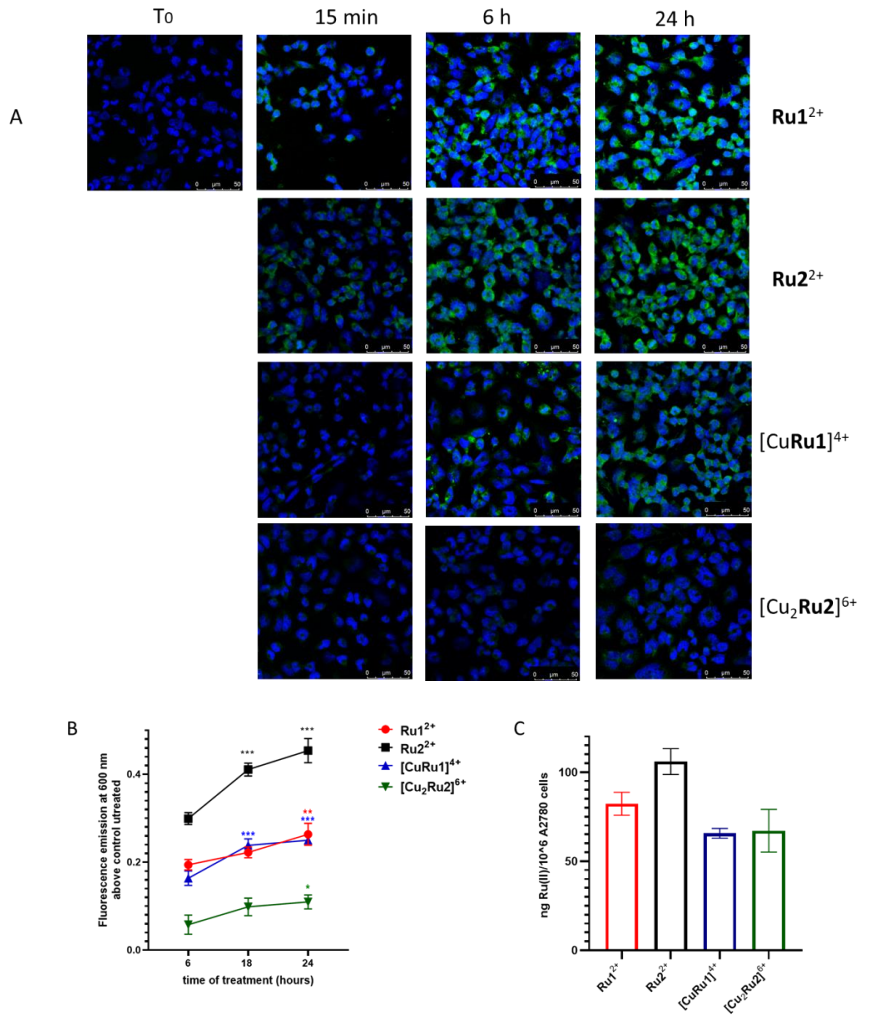

Figure 2. Internalization of Ru(II) complexes in A2780 cells. (**A**) Laser-scanning confocal microscopy was performed in A2780 cells incubated with each Ru(II) complex (10 μM) for the indicated time. DAPI (λ_{exc} = 405 nm, λ_{em} = 461 nm) was used to stain nuclei (blue spots), while the fluorescence emission in green represents that of Ru(II) complexes (λ_{exc} = 405 nm, λ_{em} = 600–640 nm). (**B**) Fluorometric analysis was performed in A2780 incubated with Ru(II) complexes (10 μM each) for 6–18–24 h. Data are reported as mean ± SD of fluorescence emission at 600 nm after subtraction of the background (untreated A2780 cells). The internalization of Ru(II) complexes was statistically significant according to one-way ANOVA followed by Bonferroni post hoc test. * $p < 0.05$, ** $p < 0.01$, *** $p < 0.001$. (**C**) Amount of internalized ruthenium after 24 h of incubation of 10^6 A2780 cells with each Ru(II) compound (10 μM). Data represent the mean ± SD of three independent experiments. The ruthenium content in the control sample, namely cells not treated with Ru(II) complexes, was not detectable.

Although the intrinsic fluorescence emission of compounds made it possible to follow their respective kinetics of internalization, it did not allow any quantitative estimation due to the different emissive properties, mainly between Cu(II)-free and Cu(II)-containing complexes. To this aim, the uptake of Ru(II) complexes in A2780 cells was also evaluated by measuring the content of ruthenium in cell lysates by ICP analysis, following 24 h incubation with a 10 μM dose of each compound (Figure 2C). As shown, **Ru1**$^{2+}$ and **Ru2**$^{2+}$

displayed higher internalization capacities compared to [Cu**Ru1**]$^{4+}$ and [Cu_2**Ru2**]$^{6+}$, the **Ru2**$^{2+}$ compound being one with the highest cellular uptake, in good agreement with confocal microscopy and fluorometric analysis.

Moreover, with the purpose of obtaining a hint on the possible internalization pathway of photosensitizers in A2780 cells, we performed immunofluorescence analysis using antibodies against Rab5, a crucial regulator of endocytosis, employed as a marker of early endosomes. Ru(II) complexes were differently localized compared to Rab5 (Figure S11A,B, Supplementary Materials), ruling out the possible involvement of a Rab5-dependent pathway in the internalization pathway of Ru(II) complexes.

Finally, based on these results, we chose to set the time of incubation with Ru(II) complexes before photoactivation at 24 h.

2.4. Effect of Ru(II) Complexes on A2780 Cell Survival after Photosensitization

The dose-dependent effect of **Ru1**$^{2+}$, **Ru2**$^{2+}$, [Cu**Ru1**]$^{4+}$ and [Cu_2**Ru2**]$^{6+}$ on dark cytotoxicity and photoactivity was evaluated through MTT assays in A2780 cells incubated for 24 h with different concentrations of Ru(II) complexes and exposed or not to photoirradiation 48 h before being analyzed. In the photoirradiation experiments, cells were irradiated with a light-emitting diode (LED, λ_{max} = 434 nm, 30 W) by employing the experimental set-up sketched in Figure S12 of Supplementary Materials.

As shown in Figure 3, under dark conditions, cell survival was only slightly affected by **Ru1**$^{2+}$ and **Ru2**$^{2+}$, at least up to a 1 μM dose of compounds. Then, beyond this value, cell viability underwent an approx. 35% decrease. An even lower cytotoxicity was displayed by the [Cu**Ru1**]$^{4+}$ and [Cu_2**Ru2**]$^{6+}$ complexes, being almost ineffective within the 0–10 μM range of concentration tested. In this respect, it can be tentatively speculated that the inferior activity of the mixed Ru(II)-Cu(II) complexed species would be associated with their lower capacity to be internalized by A2780 cells, as suggested by the internalization experiments described above.

Strikingly, the irradiation of complexes triggered a significant anti-cancer effect. Marked differences between the activities in dark and upon irradiation were indeed displayed by the good singlet oxygen sensitizers **Ru1**$^{2+}$ and **Ru2**$^{2+}$, starting from 100 nM.

Among the mixed heteronuclear complexes, [Cu**Ru1**]$^{4+}$ exhibited a sharper increase in phototoxicity when dosed at 10 μM, resulting in an approximatively 75% decrease of cell viability. Given the scarce ability of [Cu**Ru1**]$^{4+}$ and [Cu_2**Ru2**]$^{6+}$ to sensitize the formation of singlet oxygen, the anti-survival data suggest that alternative light-mediated pathways are made accessible by these systems in the cellular environment. Considering the redox activity of heteronuclear compounds (see Section 2.2), and in analogy to our previous study [16], a synergetic action between the Fenton-active copper center/s and light to generate harmful ROS species can be envisaged.

Interestingly, the effect of [Cu_2**Ru2**]$^{6+}$ was considerably less pronounced compared to the one of [Cu**Ru1**]$^{4+}$. This would suggest that, in addition to the similar cellular internalization and modes of activation of these latter two compounds, other less predictable features (such as differences in the chemical structures, chemical–physical properties, etc.) may play a role in the biological response of this typology of compounds.

Although PDT is a minimally invasive procedure, which effectively kills tumor cells, photosensitizers may have cytotoxic effects on normal cells. To study the effect of Ru(II) complexes on non-cancer cells, we performed MTT analysis in C2C12 myoblasts under dark and photoactivation conditions to assess Ru(II) complex cytotoxicity and photoactivity, respectively. As reported in Figure S13 of Supplementary Materials, Ru(II) complexes show negligible cytotoxicity and a minor photoactivity in myoblasts compared to A2780 cells, in agreement with the negligible internalization capacity of the PSs in this non-cancer cell model (Figure S10, Supplementary Materials).

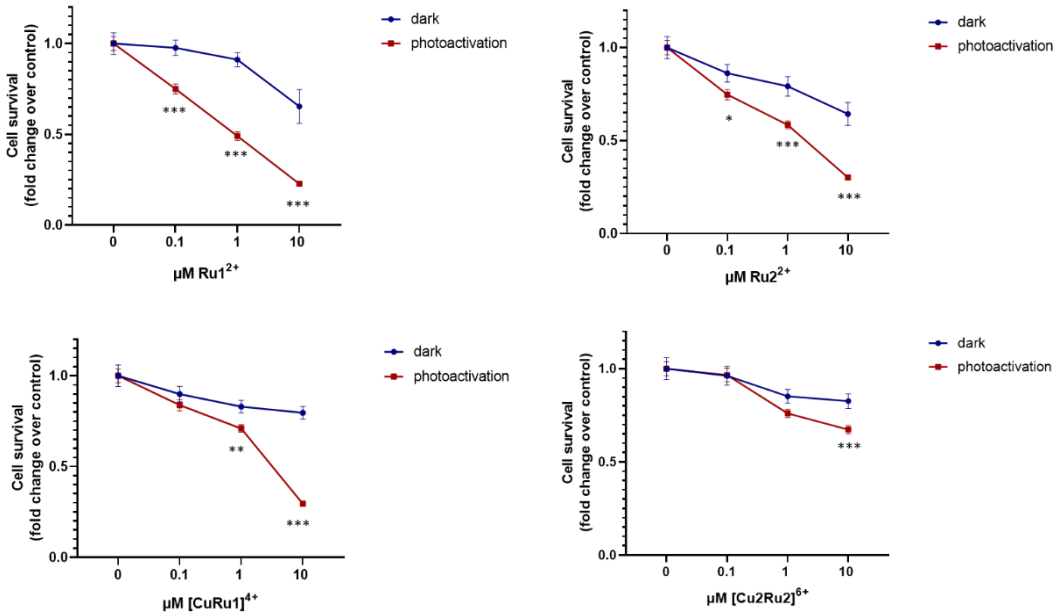

Figure 3. Dose-dependent effect of Ru(II) complexes on cell survival of ovarian cancer cells after photosensitization. A2780 were incubated for 24 h in the presence of Ru(II) complexes, **Ru1**$^{2+}$, **Ru2**$^{2+}$, [Cu**Ru1**]$^{4+}$ and [Cu_2**Ru2**]$^{6+}$ at the following concentrations (0, 0.1 μM, 1 μM, 10 μM) in serum-deprived culture media (RPMI with BSA 0.1%). Photoactivation for 20 min, as described in the Materials and Methods section. MTT reduction tests were performed in triplicate, representative of three independent experiments with similar results. Data reported are mean ± SD, fold change of absorbance at 570 nm over untreated control. The effect of photoactivation of Ru(II) complexes on the inhibition of cell survival was statistically significant according to two-way ANOVA followed by Bonferroni post hoc test. * $p < 0.05$, ** $p < 0.01$, *** $p < 0.001$.

2.5. Effect of Ru(II) Complexes on Apoptosis of A2780 Cells after Photoactivation

To dissect the molecular mechanism responsible for the selective anti-survival effect exerted by Ru(II) complexes, the involvement of apoptosis was studied by using different approaches in A2780 cells. As shown in Figure 4A, the treatment with each photosensitizer was completely ineffective on caspase 3 activity under dark conditions, whereas light irradiation of Ru(II) complexes after 24 h incubation caused a significant and potent activation of the pro-apoptotic enzyme.

Moreover, the involvement of caspase 3 in the mechanisms of action of Ru(II) photosensitizers was further investigated in dark conditions and after photoactivation employing Western blot analysis by measuring the proteolytic cleavage of the enzyme (Figure 4B). Although each Ru(II) complex was not able to induce caspase 3 cleavage under dark conditions, the cleaved form significantly increased after photoactivation, suggesting the involvement of caspase 3 in the anti-survival effect induced by photoactivation of Ru(II) complexes in A2780 cells.

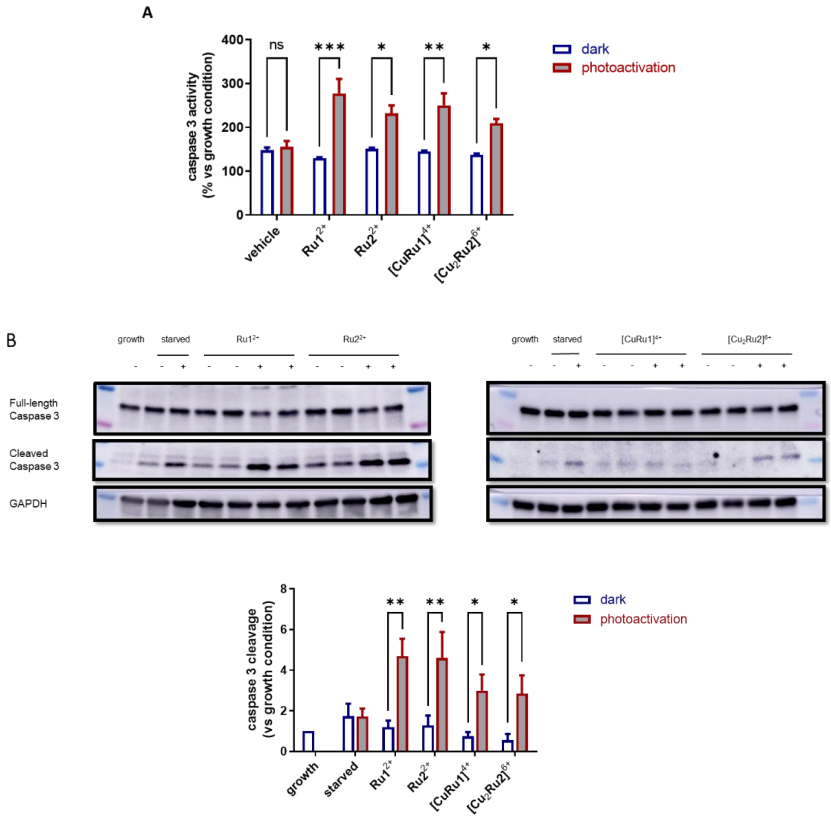

Figure 4. Effect of Ru(II) complexes on caspase 3 activation in ovarian cancer cells after photosensitization. A2780 cells were treated with each Ru(II) complex, **Ru1**$^{2+}$, **Ru2**$^{2+}$, [Cu**Ru1**]$^{4+}$ and [Cu_2**Ru2**]$^{6+}$, at 10 μM. After 24 h of incubation, cells were photoactivated (red) or not (blue), collected after 24 h of light irradiation, homogenized, and total protein concentration was analyzed in each lysate. (**A**) Caspase 3 activity assay was performed in 30 μg of total cell lysates by using a specific fluorogenic substrate Ac-DEVD-ACF (ex/em: 400/505 nm). Data are reported as mean ± SD of fluorescence compared to control cells under growth condition (10% FBS RPMI), set as 100. The effect of photoactivation was statistically significant for each Ru(II) complex tested according to two-way ANOVA analysis followed by Bonferroni post hoc test: * $p < 0.05$, ** $p < 0.01$, *** $p < 0.001$. (**B**) Western blot analysis was performed in 30 μg total cell lysates using specific anti-caspase 3 antibody. Densitometric analysis of cleaved caspase 3 was performed in three independent experiments performed in duplicate. Data are the mean ± SD and are reported as cleaved caspase 3 levels normalized to GAPDH, fold change over FBS control (growth), set as 1. Results are statistically significant according to two-way ANOVA followed by Bonferroni post hoc test: * $p < 0.05$, ** $p < 0.01$, not significant (ns).

Finally, programed cell death and its involvement in the photoactivity of Ru(II) complexes was confirmed by measuring the cleavage of poly ADP-ribose polymerase (PARP), which is one of the major hallmarks of apoptosis (Figure 5). The specific inactivation of PARP by proteolytic cleavage was undetectable under dark conditions, while it was significantly appreciable after photoactivation of each Ru(II) complex, although to a different extent.

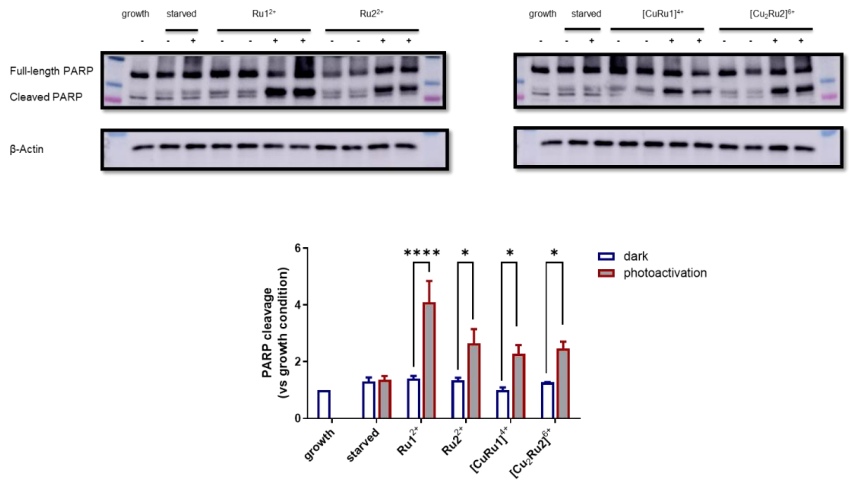

Figure 5. Effect of Ru(II) complexes on PARP cleavage in ovarian cancer cells after photosensitization. A2780 cells were treated for 24 h with each Ru(II) complex before being photoactivated and collected after 24 h of light irradiation. Western blot analysis was performed in 30 μg total cell lysates using specific anti-PARP (46D11) antibody. Densitometric analysis of cleaved form of PARP was performed in three independent experiments conducted in duplicate. Data are the mean ± SEM and are reported as cleaved protein levels normalized to β-actin, fold change over FBS control. Results are statistically significant according to two-way ANOVA followed by Bonferroni post hoc test: * $p < 0.05$, **** $p < 0.0001$.

2.6. Mitochondrial Membrane Potential Is Lost after Photosensitization of Ru(II) Complexes

Mitochondria play a key role in the intrinsic pathway of apoptosis in mammalian cells, and mitochondrial membrane potential (Δψm) loss is considered an early event of the apoptotic process in some cellular systems [26]. For this reason, Δψm was analyzed after photosensitizer administration in A2780 cells using a cationic fluorescent probe, which accumulates in the negatively charged mitochondrial matrix, by laser-scanning confocal microscopy imaging. Figure 6 illustrates the distribution of functional mitochondria in A2780 cells in the presence of Ru(II) complexes under dark conditions or after photoactivation. The administration of photosensitizers under dark conditions did not affect Δψm or cell morphology. However, photoactivation of **Ru1**$^{2+}$ and **Ru2**$^{2+}$ caused a dramatic loss of Δψm in almost all the cells. Remarkably, this was accompanied by the appearance of a pyknotic morphology of the nuclei, possibly representing an initial phase of chromatin condensation prior to DNA fragmentation [27]. Nonetheless, A2780 cells treated with [Cu**Ru1**]$^{4+}$ and [Cu_2**Ru2**]$^{6+}$ did not exhibit any mitochondrial change or decrease in Δψm in the presence or in the absence of photoactivation, thus ruling out the possible involvement of early loss of mitochondrial membrane potential in the pro-apoptotic effect of mixed Ru(II)-Cu(II) complexes. Given the cationic nature of Ru(II) complexes, mitochondrial localization subsequent to light-induced mitochondrial depolarization might occur. To analyze this possibility, we performed laser-scanning confocal microscopy employing a mitochondria-specific probe in A2780 cells incubated with **Ru1**$^{2+}$, **Ru2**$^{2+}$, [Cu**Ru1**]$^{4+}$ or [Cu_2**Ru2**]$^{6+}$, followed by a colocalization test, to assess the possible localization of Ru(II) complexes into mitochondria. Confocal microscopy images showed a random distribution of Ru(II) complexes compared to mitochondria (Figure S9, Supplementary Materials), thus ruling out the possibility that mitochondrial depolarization induced by photoactivation depends on Ru(II) complexes' localization in these organelles.

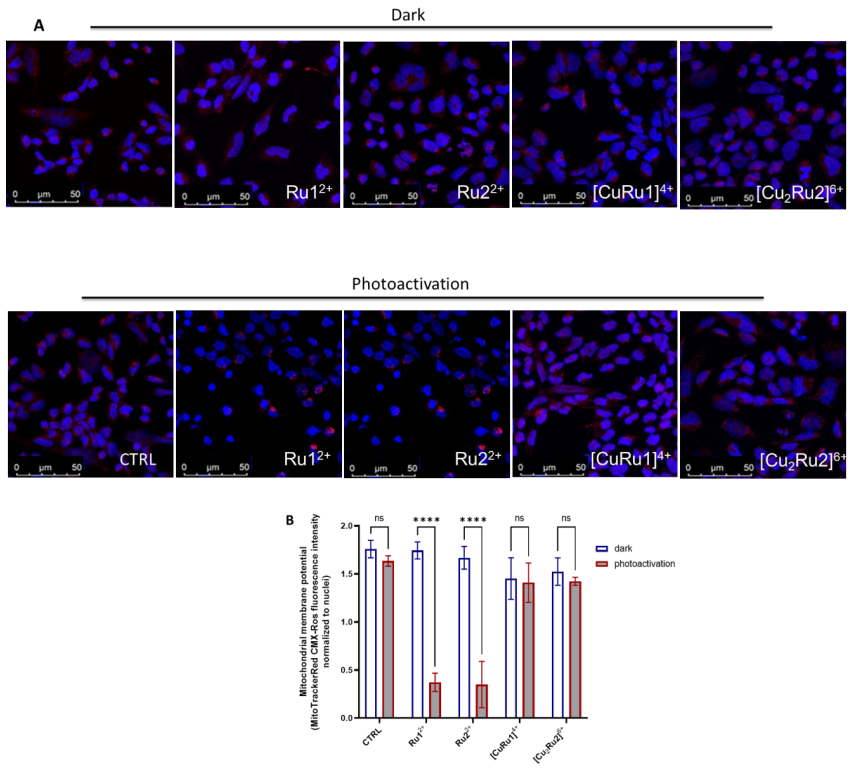

Figure 6. Effect of Ru(II) complexes on mitochondrial membrane potential after photoactivation. Mitochondrial membrane potential of A2780 cells was detected using cationic fluorescent dye MitoTracker Red CMXRos, which proportionally accumulates in the negatively charged mitochondrial matrix. (**A**) A2780 cells were plated in microscope slides and challenged or not (CTRL) with 10 µM of each Ru(II)-complex (**Ru1**$^{2+}$, **Ru2**$^{2+}$, [Cu**Ru1**]$^{4+}$ and [Cu$_2$**Ru2**]$^{6+}$). After 24 h of incubation, A2780 were subjected to photoactivation or not (dark) for 20 min, 2 h before being labeled with Mitotraker Red CMXRos and fixed in paraformaldehyde, as described in the Materials and Methods section. Confocal analysis was performed using 63X oil immersion objective. Images were representative of six fields of each condition in three independent experiments with analogous results. (**B**) Data are reported as mean ± SD of MitoTracker Red CMXRos fluorescence intensity normalized to the number of nuclei in six fields for each condition in three independent experiments by using Leica Application Software. Results are statistically significant according to two-way ANOVA followed by Bonferroni post hoc test: **** $p < 0.0001$, not significant (ns).

2.7. Cytosolic ROS Production after Photosensitization of Ru(II) Complexes Ru1^{2+} *and Ru2*$^{2+}$

With the purpose of dissecting the possible involvement of reactive oxygen species (ROS) production in the biological effect induced by **Ru1**$^{2+}$ and **Ru2**$^{2+}$ photosensitizers, confocal analysis was performed in A2780 cells employing the CM-H$_2$DCFDA probe to detect cytosolic ROS after **Ru1**$^{2+}$ and **Ru2**$^{2+}$ administration upon photoactivation compared to the dark conditions. As shown in Figure 7, cytosolic ROS were almost completely undetectable after each **Ru1**$^{2+}$ or **Ru2**$^{2+}$administration in A2780 under dark conditions, even if Ru(II) complexes were efficiently internalized (red fluorescence). However, as early as 2 h after photoactivation, cytosolic ROS were detected in the majority of cell populations, notwithstanding at different degrees of intensity, thus suggesting a critical role of ROS in the proapoptotic action exerted by **Ru1**$^{2+}$ and **Ru2**$^{2+}$ photosensitizers.

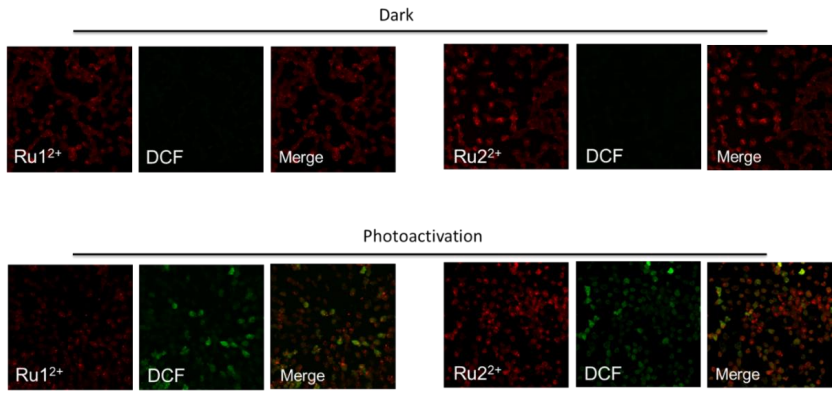

Figure 7. Effect of Ru(II) complexes, **Ru1**$^{2+}$ and **Ru2**$^{2+}$, on ROS production after photoactivation. ROS production in A2780 cells was detected using CM-H_2DCFDA. A2780 cells were plated on microscope slides and challenged with 10 μM of each Ru complex, **Ru1**$^{2+}$ and **Ru2**$^{2+}$. After 24 h of incubation, A2780 were exposed to photoactivation or not (dark) for 20 min, 2 h before being labeled with CM-H_2DCFDA (DCF) and fixed in paraformaldehyde, as described in the Materials and Methods section. Confocal analysis was performed using 63X oil immersion objective. The fluorescence of Ru(II) complexes is shown in red ($\lambda_{exc}/\lambda_{em}$: 405/600–640 nm) and DCF in green ($\lambda_{exc}/\lambda_{em}$: ~492–495/517–527 nm). Images were representative of six fields of each condition in three independent experiments with analogous results.

3. Discussion

Increasing evidence reports that platinum-based anti-cancer drugs have severe side effects, such as myelotoxicity and peripheral neuropathy [28]. Moreover, ovarian cancer recurrence less than six months after the completion of platinum-based therapy is frequent, and prognosis is extremely poor [29]. The main reason for the dramatic failure of ovarian cancer treatments [30,31] relies on the intrinsic and acquired resistance to platinum-based chemotherapy. Therefore, efforts are needed in this research field to develop other potential anti-cancer drugs. Ru(II) polypyridyl complexes have shown remarkable anti-tumor activity coupled with advantages over platinum drugs, such as higher potency, lower toxicity, minor drug resistance, and they are expected to become a new generation of clinical metal anti-cancer drugs [11,32,33].

In our study, a series of RPCs-based photosensitizers for PDT application were investigated for the capability of inducing anti-tumor effects following photoactivation with low-energy light. Their biological potential was evaluated in the A2780 ovarian cell line, which was taken as a model of ovarian cancer [25]. Since PDT activity may result from different pathways, such as the production of ROS through *type I* and *II* mechanisms, four different Ru(II) polypyridyl complexes, namely **Ru1**$^{2+}$, **Ru2**$^{2+}$, [Cu**Ru1**]$^{4+}$ and [Cu_2**Ru2**]$^{6+}$, featuring different modalities of activation, were evaluated in this study.

Among these metal complexes, **Ru1**$^{2+}$ and **Ru2**$^{2+}$ are highly luminescent and possess good (and comparable) abilities to sensitize the formation of singlet oxygen through *type II* reactions. On the other hand, the insertion of one or two Fenton-active Cu(II) ion/s in their corresponding heteronuclear Ru(II)-Cu(II) complexed species ([Cu**Ru1**]$^{4+}$ and [Cu_2**Ru2**]$^{6+}$) results in less luminescent compounds, which can mainly promote the generation of perhydroxyl and hydroxyl radicals via *type I* reactions. The coordination of Cu(II) ion/s in these latter two compounds is remarkably strong (LogK values between 15.34 and 27.6), making any transmetalation process unfavorable in conditions mimicking the cellular environment. Importantly, the peculiar polyamine frameworks confer to all these compounds excellent solubilities in water, a key requisite for their application in the biomedical field.

In a previous report, the Ru(II)-arene complex [Ru(η6-p-cymene)Cl_2] (RAPTA-C) was tested for efficacy in combination with the epidermal growth factor receptor inhibitor erlotinib, demonstrating an efficient anti-angiogenic and anti-tumor activity [34]. The therapeutic potential of these compounds and their combination was further confirmed in preclinical in vivo models of chicken chorioallantoic membrane grafted with A2780 tumors and in mice bearing A2780 tumors, highlighting the tumor growth inhibition and anti-angiogenic effect [34].

In line with the literature data, the RPCs investigated herein were found to possess negligible cytotoxicity without light irradiation in non-cancer and cancer cells, respectively, converted in turn in a tight dose-dependent and significant anti-tumor action upon photoactivation. In particular, a marked increase in the activity was observed upon light activation of **Ru1**$^{2+}$ and **Ru2**$^{2+}$, in agreement with the good singlet oxygen sensitizing properties of these compounds. Among the mixed heteronuclear complexes, [Cu**Ru1**]$^{4+}$ displayed the sharpest photoactivity. Interestingly, this suggests that, beyond the singlet oxygen sensitization, alternative oxidative pathways must be accessible to heteronuclear compounds, leading to similar photoinduced effectiveness compared to the one of copper-free complexes. However, further efforts will be needed to obtain further insights into these processes, which likely occur under biological conditions and appear to be hard to mimic in cell-free experiments. Moreover, the significant differences in activity observed between [Cu**Ru1**]$^{4+}$ and [Cu_2**Ru2**]$^{6+}$ suggest that other less predictable features, such as differences in the chemical structures, may play a critical role in the biological behavior of such compounds.

The investigated RPCs also displayed good capacities to be internalized by A2780 cancer compared to non-cancer cells, with **Ru1**$^{2+}$ and **Ru2**$^{2+}$ being the most effective. This result is of great interest, especially considering that similar RPCs-based PSs were shown to poorly penetrate the cell membrane, and additional expedients, such as ion pairing with suitable lipophilic counter-anions, were necessary to augment the cellular uptake [35]. In the present study, it is reasonable to assume that the significant cellular uptake by cancer cells is associated with the presence of the polyamino macrocyclic frameworks **L′** and **L″** of the Ru(II) compounds, which may impart optimal chemical–physical features for cellular internalization, such as hydrophilicity and total charge of the compounds. Even if the precise mechanism by which the Ru(II) compounds are internalized in A2780 cells was not investigated in detail, their uptake appears to be independent of the Rab5-dependent early endosome pathway. Nonetheless, taking into consideration the hydrophilic chemical nature of RPCs and their observed localized cellular distribution, the occurrence of an efficacious passive transport can be excluded, rather pointing at alternative endocytotic events accounting for RPC uptake. Indeed, this is in line with the literature data showing the occurrence of specific cellular transport of cytotoxic metallodrugs [36].

Apoptosis is clearly advantageous for the organism, since, during apoptosis, the cell membrane remains intact, thus preventing the release of intracellular content. Hence, the elucidation of the mechanisms that triggered cell death after the light activation of Ru(II) complexes appears to be crucial. In A2780 cells, the photoactivation of all the tested RPCs caused a potent caspase 3 activation, as well as both caspase 3 and PARP cleavage, while the RPCs were ineffective in the absence of photosensitization, pointing at a crucial role for programed cell death in the anti-tumor activity of these systems.

Mitochondria might be seen as a gatekeeper to entrap pro-apoptotic proteins and prevent the release and activation of these proteins in the cytosol [37]. In particular, the exit of pro-apoptotic proteins from the mitochondria activates caspase proteases. Of note, the opening of the mitochondrial permeability transition pore has been demonstrated to induce Δψm depolarization, loss of oxidative phosphorylation and release of apoptogenic factors. Thus, a distinctive feature of apoptosis can be represented by the disruption of the normal mitochondrial function, especially changes that affect the Δψm. In some apoptotic systems, the loss of Δψm may be an early event in the apoptotic process [38]. Here, using confocal microscopy, it was demonstrated that **Ru1**$^{2+}$ and **Ru2**$^{2+}$, but not [Cu**Ru1**]$^{4+}$ or [Cu_2**Ru2**]$^{6+}$,

caused a dramatic loss of Δψm depending on photoactivation and that this effect was accompanied by ROS production in the cytosol as soon as 2 h after light irradiation, thus upstream to the pro-apoptotic stimuli.

Lastly, although previous in vitro studies underlined the capacity of RPCs to effectively interact and damage plasmid DNA upon irradiation [16], in this work, we did not detect RPCs in the nucleus, at least within 24 h of incubation, since these compounds were found distributed into segregated areas of the cytosol. This finding suggests that the induced programed cell death is likely independent of the PSs–DNA interaction.

In summary, the present study demonstrates that all four synthesized Ru(II) complexes are effectively internalized into the ovarian cancer A2780 cells, and their administration, regardless of the low dark cytotoxicity, induces a specific photoactivation-dependent cell death, with the extent of cytotoxicity that varies slightly depending on the chemical structures of RPCs. Apoptosis emerged as the main mechanism of light-mediated cellular death. In particular, among the four compounds, **Ru1**$^{2+}$ and **Ru2**$^{2+}$ profoundly altered mitochondrial activity after photoactivation, accompanied by cytosolic ROS production.

4. Materials and Methods

4.1. Materials

All materials used for the preparation of ruthenium compounds were of reagent grade and used as received, unless otherwise specified.

4.2. Synthesis of Ru(II)-Complexes

Ruthenium compounds **Ru1**$^{2+}$, **Ru2**$^{2+}$, [Cu**Ru1**]$^{4+}$ and [Cu_2**Ru2**]$^{6+}$ were synthesized according to the procedures previously described [16,39]. Briefly, **Ru1**$^{2+}$ and **Ru2**$^{2+}$ were prepared by direct reaction of the intermediate $(phen)_2$**Ru**Cl_2 with the bidentate **L′** o **L″** ligands, in ethylene glycol and under microwave irradiation. The resulting complexes were then dissolved in concentrated HCl and precipitated as their respective hydrochloride salts [**Ru1**]$Cl_2 \cdot 5HCl \cdot 2H_2O$ and [**Ru2**]$Cl_2 \cdot 6HCl \cdot 2H_2O$, following the addition of ethanol.

The mixed Ru(II)/Cu(II) complexes were obtained as the perchlorate salts [Cu**Ru1**]$(ClO_4)_4 \cdot 4H_2O$ and [Cu_2**Ru2**]$(ClO_4)6 \cdot 3H_2O$, by adding equimolar amounts of $Cu(ClO_4)_2$ to aqueous solutions of **Ru1**$^{2+}$ or **Ru2**$^{2+}$ at pH 6.5 and following the slow evaporation of the solvent at r.t.

4.3. Potentiometric Measurements

The acid-base behavior and the binding ability toward Cu^{2+}, Zn^{2+}, Ca^{2+}, Na^+ and Mg^{2+} of ruthenium complexes were investigated by means of potentiometric measurements in NMe_4Cl 0.1 M at 298 ± 0.1 K by using the equipment and methods previously described [40–43].

4.4. EPR Measurements

X-band electron paramagnetic resonance (EPR) experiments were performed by using a Bruker Elexsys E500 spectrometer. All the spectra were acquired at room temperature by using the same modulation frequency (100 kHz), modulation amplitude (1 G), microwave power (~0.2 mW, 30 dB) and receiver gain (60 dB). The magnetic field was calibrated with a crystal of DPPH.

4.5. Cell Culture

Human A2780 ovarian cancer cell culture (ECACC 93112519) was maintained in RPMI-1640 medium containing 10% fetal bovine serum (FBS), 100 μg/mL streptomycin, 100 U/mL penicillin and 2 mM L-glutamine, at 37 °C in 5% CO_2, as previously reported [44]. All cell culture reagents were purchased from Merck Life Science (Darmstadt, Germany), including phosphate-buffered saline (PBS). A2780 cells were shifted to RPMI without serum supplemented with 1 mg/mL Bovine Serum Albumin (BSA) and treated with each Ru(II) complex (0.1, 1 and 10 μM) for 24 h. After incubation, cells were photoactivated with a 30 W three-arm LED light lamp (430–470 nm emission, 30 W) for 20 min at the distance of

5 cm from the cell culture plate and then kept in the incubator at 37 °C, 5% CO_2. Cells were washed twice with PBS and then collected after photoactivation at different times, which depended on each kind of experiment.

4.6. ICP-AES Measurements

A Varian 720-ES axial Inductively Coupled Plasma Atomic Emission Spectrometer (ICP-AES) was used to determine the Ru contents in the samples. Measurements were performed in triplicate, and each sample was spiked with 1.0 ppm of Ge, used as an internal standard. The calibration standards were prepared by gravimetric serial dilution from commercial stock standard solutions of Ru at 1000 mg L^{-1} (Honeywell Fluka). For Ru determination, the 267.876 and 245.657 nm wavelengths were used, whereas the line at 209.426 nm was considered for Ge. The operating conditions were optimized to obtain maximum signal intensity, and between each sample, a rinse solution containing 2% v/v of HNO_3 was used.

4.7. MTT Reduction Assay for Cell Survival

A2780 viability was evaluated by the MTT method, as previously described [45].

4.8. Caspase-3 Activity Assay

A2780 cells were seeded in 6-well plates (100.000 cells/well) and after 24 h were incubated with 10 μM of each Ru(II) complex in serum-deprived culture media, then light-irradiated for 20 min, as described above. After 24 h of photoactivation, cells were washed twice with PBS, collected and analyzed, as previously described [46].

4.9. Western Blot Analysis

A2780 lysates were quantified for total protein content by the Bradford Protein assay, resuspended in Leammli's sodium dodecyl sulphate (SDS) sample buffer, and subjected to SDS-PAGE and transferred to PVDF membranes, as previously described [46].

4.10. Laser-Scanning Confocal Microscopy

A2780 cells were seeded on microscope slides and treated with each Ru(II) complex (10 μM). To evaluate the internalization of Ru(II) complexes, cells were incubated at three different times, 15 min, 6 h and 24 h, washed with PBS and fixed in 2% paraformaldehyde in PBS for 20 min. Ru(II) complexes excitation was performed using 405 nm laser diode, acquiring emission in the range of 600/620 nm.

MitoTracker Red CMXRos (#M7512; Ex/Em: 579/599 nm) and CM-H_2DCFDA (#C6827; Ex/Em: ∼492–495/517–527 nm) probes (Invitrogen, Thermo Fisher Scientific INC, Waltham, MA, USA) were used to detect the mitochondrial membrane potential and ROS production, respectively. After 24 h incubation of Ru(II) complexes at 37 °C, cell slides were photoactivated or not for 20 min and incubated for 2 h at 37 °C, 5% CO_2 in humidified atmosphere. Probes were diluted in RPMI medium without phenol red, incubated for 30 min at 37 °C in dark and then fixed in 2% paraformaldehyde, as suggested by the manufacturer's instruction. After 30 min at room temperature, slides were incubated with a permeabilization and quenching solution, obtained by adding Triton 0.1% X-100 and ethanolamine (1:165) in PBS. The DAPI solution was administered to cell slides to detect the nuclei. Slides were mounted by using the Fluoromount Aqueous Mounting Medium (Sigma-Aldrich, Saint Louis, MA, USA), and images were obtained using a Leica SP8 laser-scanning confocal microscope (Leica Microsystems GmbH) using a 63x oil immersion objective.

4.11. Statistical Analysis

Densitometric analysis of Western blot bands was performed using the ImageJ software, and graphical representations were obtained by GraphPad Prism 5.0 (GraphPad Software, San Diego, CA, USA). Statistical analysis was performed using one-way or two-

way ANOVA analysis of variance followed by the Bonferroni post hoc test. Asterisks indicate statistical significance.

5. Conclusions

In conclusion, our study identifies Ru(II)-polypyridyl complexes as challenging tools to be further investigated in the research of new therapeutic strategies to overcome chemoresistance in epithelial ovarian cancers and provides further insights on the biological behavior of these complexes, which rely on ROS production and altered mitochondrial function to trigger pro-apoptotic effects.

Supplementary Materials: The following are available online at https://www.mdpi.com/article/10.3390/ijms232113302/s1. Refs. [47,48] are cited in Supplementary Materials.

Author Contributions: Conceptualization: C.G., L.C. and F.C.; Project administration: C.G., F.C. and L.C.; Supervision: C.G., F.C., P.B. and B.V.; Funding acquisition: L.C., C.G., P.B. and F.C.; Writing: C.G., L.C., F.C., P.B. and B.V.; Methodology: G.E.G., S.P., P.S.S., M.P. and A.P.; Investigation: G.E.G., S.P., P.S.S. and I.P., M.P. and A.P.; Data curation: L.C. and F.C. All authors have read and agreed to the published version of the manuscript.

Funding: A.P. acknowledges support from the Italian Ministry of Education and Research (MIUR) through PRIN project 2017 "Quantum detection of chiral-induced spin selectivity at the molecular level" (2017Z55KCW) The work was supported by University of Florence (Fondi Ateneo to P.B. and F.C.). The data presented in the current study were in part generated using the equipment of the Facility of Molecular Medicine and of the Department of Experimental and Clinical Biomedical Sciences "*Mario Serio*" and the Department of Chemistry "*Ugo Schiff*", funded by the Ministry of Education, University and Research of Italy–Dipartimenti di Eccellenza 2018–2022.

Institutional Review Board Statement: Not applicable.

Informed Consent Statement: Not applicable.

Data Availability Statement: All the data are reported in the manuscript.

Acknowledgments: The authors thank Mirko Severi for the ICP-AES analysis.

Conflicts of Interest: The authors declare no conflict of interest.

References

1. Siegel, R.L.; Miller, K.D.; Fuchs, H.E.; Jemal, A. Cancer Statistics, 2021. *CA Cancer J. Clin.* **2021**, *71*, 7–33. [CrossRef]
2. Coburn, S.B.; Bray, F.; Sherman, M.E.; Trabert, B. International patterns and trends in ovarian cancer incidence, overall and by histologic subtype. *Int. J. Cancer* **2017**, *140*, 2451–2460. [CrossRef]
3. Buys, S.S.; Partridge, E.; Black, A.; Johnson, C.C.; Lamerato, L.; Isaacs, C.; Reding, D.J.; Greenlee, R.T.; Yokochi, L.A.; Kessel, B.; et al. Effect of Screening on Ovarian Cancer Mortality. *JAMA* **2011**, *305*, 2295–2303. [CrossRef] [PubMed]
4. Mikuła-Pietrasik, J.; Witucka, A.; Pakuła, M.; Uruski, P.; Begier-Krasińska, B.; Niklas, A.; Tykarski, A.; Książek, K. Comprehensive review on how platinum- and taxane-based chemotherapy of ovarian cancer affects biology of normal cells. *Cell. Mol. Life Sci.* **2019**, *76*, 681–697. [CrossRef] [PubMed]
5. Simović, A.R.; Masnikosa, R.; Bratsos, I.; Alessio, E. Chemistry and reactivity of ruthenium(II) complexes: DNA/protein binding mode and anticancer activity are related to the complex structure. *Co-ord. Chem. Rev.* **2019**, *398*, 113011. [CrossRef]
6. Lee, S.Y.; Kim, C.Y.; Nam, T.-G. Ruthenium Complexes as Anticancer Agents: A Brief History and Perspectives. *Drug Des. Dev. Ther.* **2020**, *14*, 5375–5392. [CrossRef]
7. Kostova, I. Ruthenium Complexes as Anticancer Agents. *Curr. Med. Chem.* **2006**, *13*, 1085–1107. [CrossRef] [PubMed]
8. Liu, J.; Zhang, C.; Rees, T.W.; Ke, L.; Ji, L.; Chao, H. Harnessing ruthenium(II) as photodynamic agents: Encouraging advances in cancer therapy. *Co-ord. Chem. Rev.* **2018**, *363*, 17–28. [CrossRef]
9. Poynton, F.E.; Bright, S.A.; Blasco, S.; Williams, D.C.; Kelly, J.M.; Gunnlaugsson, T. The development of ruthenium(II) polypyridyl complexes and conjugates for *in vitro* cellular and *in vivo* applications. *Chem. Soc. Rev.* **2017**, *46*, 7706–7756. [CrossRef]
10. Monro, S.; Colón, K.L.; Yin, H.; Roque, J., III; Konda, P.; Gujar, S.; Thummel, R.P.; Lilge, L.; Cameron, C.G.; McFarland, S.A. Transition Metal Complexes and Photodynamic Therapy from a Tumor-Centered Approach: Challenges, Opportunities, and Highlights from the Development of TLD1433. *Chem. Rev.* **2019**, *119*, 797–828. [CrossRef]
11. Lin, K.; Zhao, Z.-Z.; Bo, H.-B.; Hao, X.-J.; Wang, J.-Q. Applications of Ruthenium Complex in Tumor Diagnosis and Therapy. *Front. Pharmacol.* **2018**, *9*, 1323. [CrossRef] [PubMed]

12. Mari, C.; Pierroz, V.; Ferrari, S.; Gasser, G. Combination of Ru(II) complexes and light: New frontiers in cancer therapy. *Chem. Sci.* **2015**, *6*, 2660–2686. [CrossRef] [PubMed]
13. Le Gall, T.; Lemercier, G.; Chevreux, S.; Tucking, K.-S.; Ravel, J.; Thetiot, F.; Jonas, U.; Schonherr, H.; Montier, T. Ruthenium(II) Polypyridyl Complexes as Photosensitizers for Antibacterial Photodynamic Therapy: A Structure-Activity Study on Clinical Bacterial Strains. *ChemMedChem* **2018**, *13*, 2229–2239. [CrossRef]
14. Giacomazzo, G.E.; Conti, L.; Guerri, A.; Pagliai, M.; Fagorzi, C.; Sfragano, P.S.; Palchetti, I.; Pietraperzia, G.; Mengoni, A.; Valtancoli, B.; et al. Nitroimidazole-Based Ruthenium(II) Complexes: Playing with Structural Parameters to Design Photostable and Light-Responsive Antibacterial Agents. *Inorg. Chem.* **2021**, *61*, 6689–6694. [CrossRef] [PubMed]
15. Castano, A.P.; Demidova, T.N.; Hamblin, M.R. Mechanisms in photodynamic therapy: Part one—Photosensitizers, photochemistry and cellular localization. *Photodiagn. Photodyn. Ther.* **2004**, *1*, 279–293. [CrossRef]
16. Conti, L.; Bencini, A.; Ferrante, C.; Gellini, C.; Paoli, P.; Parri, M.; Pietraperzia, G.; Valtancoli, B.; Giorgi, C. Highly Charged Ruthenium(II) Polypyridyl Complexes as Effective Photosensitizer in Photodynamic Therapy. *Chem.–A Eur. J.* **2019**, *25*, 10606–10615. [CrossRef] [PubMed]
17. Conti, L.; Mengoni, A.; Giacomazzo, G.E.; Mari, L.; Perfetti, M.; Fagorzi, C.; Sorace, L.; Valtancoli, B.; Giorgi, C. Exploring the potential of highly charged Ru(II)- and heteronuclear Ru(II)/Cu(II)-polypyridyl complexes as antimicrobial agents. *J. Inorg. Biochem.* **2021**, *220*, 111467. [CrossRef] [PubMed]
18. Conti, L.; Flore, N.; Formica, M.; Giorgi, L.; Pagliai, M.; Mancini, L.; Fusi, V.; Valtancoli, B.; Giorgi, C. Glyphosate and AMPA binding by two polyamino-phenolic ligands and their dinuclear Zn(II) complexes. *Inorg. Chim. Acta* **2021**, *519*, 120261. [CrossRef]
19. Juarranz, Á.; Jaén, P.; Sanz-Rodríguez, F.; Cuevas, J.; González, S. Photodynamic therapy of cancer. Basic principles and applications. *Clin. Transl. Oncol.* **2008**, *10*, 148–154. [CrossRef]
20. Ochsner, M. Photophysical and photobiological processes in the photodynamic therapy of tumours. *J. Photochem. Photobiol. B Biol.* **1997**, *39*, 1–18. [CrossRef]
21. Pineiro, M.; Pereira, M.M.; Gonsalves, A.M.D.R.; Arnaut, L.; Formosinho, S. Singlet oxygen quantum yields from halogenated chlorins: Potential new photodynamic therapy agents. *J. Photochem. Photobiol. A Chem.* **2001**, *138*, 147–157. [CrossRef]
22. Ding, H.; Yu, H.; Dong, Y.; Tian, R.; Huang, G.; Boothman, D.A.; Sumer, B.D.; Gao, J. Photoactivation switch from type II to type I reactions by electron-rich micelles for improved photodynamic therapy of cancer cells under hypoxia. *J. Control. Release* **2011**, *156*, 276–280. [CrossRef] [PubMed]
23. Kucková, L.; Jomová, K.; Švorcová, A.; Valko, M.; Segľa, P.; Moncoľ, J.; Kožíšek, J. Synthesis, Crystal Structure, Spectroscopic Properties and Potential Biological Activities of Salicylate–Neocuproine Ternary Copper(II) Complexes. *Molecules* **2015**, *20*, 2115–2137. [CrossRef] [PubMed]
24. Haas, K.L.; Franz, K.J. Application of Metal Coordination Chemistry To Explore and Manipulate Cell Biology. *Chem. Rev.* **2009**, *109*, 4921–4960. [CrossRef]
25. Kakar, S.S.; Jala, V.R.; Fong, M.Y. Synergistic cytotoxic action of cisplatin and withaferin A on ovarian cancer cell lines. *Biochem. Biophys. Res. Commun.* **2012**, *423*, 819–825. [CrossRef]
26. Ricci, J.E.; Waterhouse, N.; Green, D.R. Mitochondrial functions during cell death, a complex (I–V) dilemma. *Cell Death Differ.* **2003**, *10*, 488–492. [CrossRef]
27. Hu, X.-M.; Li, Z.-X.; Lin, R.-H.; Shan, J.-Q.; Yu, Q.-W.; Wang, R.-X.; Liao, L.-S.; Yan, W.-T.; Wang, Z.; Shang, L.; et al. Guidelines for Regulated Cell Death Assays: A Systematic Summary, A Categorical Comparison, A Prospective. *Front. Cell Dev. Biol.* **2021**, *9*, 634690. [CrossRef]
28. Oun, R.; Moussa, Y.E.; Wheate, N.J. The side effects of platinum-based chemotherapy drugs: A review for chemists. *Dalton Trans.* **2018**, *47*, 6645–6653. [CrossRef]
29. Rocconi, R.P.; Case, A.S.; Michael Straughn, J., Jr.; Estes, J.M.; Partridge, E.E. Role of chemotherapy for patients with recurrent platinum-resistant advanced epithelial ovarian cancer. *Cancer* **2006**, *107*, 536–543. [CrossRef]
30. Au, K.K.; Josahkian, J.A.; Francis, J.A.; Squire, J.A.; Koti, M. Current state of biomarkers in ovarian cancer prognosis. *Futur. Oncol.* **2015**, *11*, 3187–3195. [CrossRef]
31. Kurman, R.J.; Shih, I.-M. The Dualistic Model of Ovarian Carcinogenesis: Revisited, revised, and expanded. *Am. J. Pathol.* **2016**, *186*, 733–747. [CrossRef]
32. Thota, S.; Rodrigues, D.A.; Crans, D.; Barreiro, E.J. Ru(II) Compounds: Next-Generation Anticancer Metallotherapeutics? *J. Med. Chem.* **2018**, *61*, 5805–5821. [CrossRef] [PubMed]
33. Zeng, L.; Gupta, P.; Chen, Y.; Wang, E.; Ji, L.; Chao, H.; Chen, Z.-S. The development of anticancer ruthenium(II) complexes: From single molecule compounds to nanomaterials. *Chem. Soc. Rev.* **2017**, *46*, 5771–5804. [CrossRef]
34. Berndsen, R.H.; Weiss, A.; Abdul, U.K.; Wong, T.J.; Meraldi, P.; Griffioen, A.W.; Dyson, P.; Nowak-Sliwinska, P. Combination of ruthenium(II)-arene complex [Ru(η6-p-cymene)Cl2(pta)] (RAPTA-C) and the epidermal growth factor receptor inhibitor erlotinib results in efficient angiostatic and antitumor activity. *Sci. Rep.* **2017**, *7*, srep43005. [CrossRef] [PubMed]
35. Yan, Z.-Y.; Chen, J.; Shao, J.; Jiao, Z.-Q.; Tang, T.-S.; Tang, M.; Sheng, Z.-G.; Mao, L.; Huang, R.; Huang, C.-H.; et al. The cell-impermeable Ru(II) polypyridyl complex as a potent intracellular photosensitizer under visible light irradiation via ion-pairing with suitable lipophilic counter-anions. *Free Radic. Biol. Med.* **2021**, *171*, 69–79. [CrossRef]
36. Spreckelmeyer, S.; Orvig, C.; Casini, A. Cellular Transport Mechanisms of Cytotoxic Metallodrugs: An Overview beyond Cisplatin. *Molecules* **2014**, *19*, 15584–15610. [CrossRef]

37. Wang, C.; Youle, R.J. The Role of Mitochondria in Apoptosis. *Annu. Rev. Genet.* **2009**, *43*, 95–118. [CrossRef] [PubMed]
38. Ly, J.D.; Grubb, D.R.; Lawen, A. The mitochondrial membrane potential (deltapsi(m)) in apoptosis; an update. *Apoptosis Int. J. Program. Cell Death* **2003**, *8*, 115–128. [CrossRef] [PubMed]
39. Conti, L.; Mummolo, L.; Romano, G.; Giorgi, C.; Giacomazzo, G.; Prodi, L.; Bencini, A. Exploring the Ability of Luminescent Metal Assemblies to Bind and Sense Anionic or Ionizable Analytes A $Ru(phen)_2$bipy-Based Dizinc Complex for Bisphenol A (BPA) Recognition. *Molecules* **2021**, *26*, 527. [CrossRef]
40. Aragoni, M.C.; Arca, M.; Bencini, A.; Caltagirone, C.; Conti, L.; Garau, A.; Valtancoli, B.; Isaia, F.; Lippolis, V.; Palomba, F.; et al. Zn^{2+}/Cd^{2+} optical discrimination by fluorescent acridine-based *bis*-macrocylic receptors. *Supramol. Chem.* **2017**, *29*, 912–921. [CrossRef]
41. Conti, L.; Giorgi, C.; Valtancoli, B.; Paoli, P.; Rossi, P.; Marchionni, A.; Faggi, E.; Bencini, A. Switching on the Fluorescence Emission of Polypyridine Ligands by Simultaneous Zinc(II) Binding and Protonation. *ChemPlusChem* **2020**, *85*, 659–671. [CrossRef] [PubMed]
42. Garau, A.; Bencini, A.; Blake, A.J.; Caltagirone, C.; Conti, L.; Isaia, F.; Lippolis, V.; Montis, R.; Mariani, P.; Scorciapino, M.A. [9]aneN3-based fluorescent receptors for metal ion sensing, featuring urea and amide functional groups. *Dalton Trans.* **2019**, *48*, 4949–4960. [CrossRef] [PubMed]
43. Becatti, M.; Bencini, A.; Nistri, S.; Conti, L.; Fabbrini, M.G.; Lucarini, L.; Ghini, V.; Severi, M.; Fiorillo, C.; Giorgi, C.; et al. Different Antioxidant Efficacy of Two MnII-Containing Superoxide Anion Scavengers on Hypoxia/Reoxygenation-Exposed Cardiac Muscle Cells. *Sci. Rep.* **2019**, *9*, 10320. [CrossRef] [PubMed]
44. Bernacchioni, C.; Ghini, V.; Cencetti, F.; Japtok, L.; Donati, C.; Bruni, P.; Turano, P. NMR metabolomics highlights sphingosine kinase-1 as a new molecular switch in the orchestration of aberrant metabolic phenotype in cancer cells. *Mol. Oncol.* **2017**, *11*, 517–533. [CrossRef]
45. Conti, L.; Ciambellotti, S.; Giacomazzo, G.E.; Ghini, V.; Cosottini, L.; Puliti, E.; Severi, M.; Fratini, E.; Cencetti, F.; Bruni, P.; et al. Ferritin nanocomposites for the selective delivery of photosensitizing ruthenium-polypyridyl compounds to cancer cells. *Inorg. Chem. Front.* **2022**, *9*, 1070–1081. [CrossRef]
46. Donati, C.; Cencetti, F.; De Palma, C.; Rapizzi, E.; Brunelli, S.; Cossu, G.; Clementi, E.; Bruni, P. TGFβ protects mesoangioblasts from apoptosis via sphingosine kinase-1 regulation. *Cell. Signal.* **2009**, *21*, 228–236. [CrossRef]
47. Stoll, S.; Schweiger, A. EasySpin, a comprehensive software package for spectral simulation and analysis in EPR. *J. Magn. Reson.* **2006**, *178*, 42–55. [CrossRef]
48. Rosen, G.M.; Beselman, A.; Tsai, P.; Pou, S.; Mailer, C.; Ichikawa, K.; Robinson, B.H.; Nielsen, R.; Halpern, H.J.; MacKerell, A.D. Influence of Conformation on the EPR Spectrum of 5,5-Dimethyl-1-hydroperoxy-1-pyrrolidinyloxyl: A Spin Trapped Adduct of Superoxide. *J. Org. Chem.* **2004**, *69*, 1321–1330. [CrossRef]

INORGANIC CHEMISTRY
FRONTIERS

RESEARCH ARTICLE

View Article Online
View Journal

Cite this: DOI: 10.1039/d1qi01268a

Ferritin nanocomposites for the selective delivery of photosensitizing ruthenium-polypyridyl compounds to cancer cells†

Luca Conti, *‡[a] Silvia Ciambellotti, *‡[b,c] Gina Elena Giacomazzo,[a] Veronica Ghini,[a,c] Lucrezia Cosottini,[a,c] Elisa Puliti,[d] Mirko Severi,[a] Emiliano Fratini,[a,e] Francesca Cencetti,[d] Paola Bruni,[d] Barbara Valtancoli,[a] Claudia Giorgi[a] and Paola Turano[a,b,c]

Herein, we report on the successful encapsulation into human H-ferritin of two highly charged Ru(II) polypyridyl complexes, $[Ru(phen)_2\mathbf{L'}]^{2+}$ (**Ru1**, with **L'** = 4,4′-(2,5,8,11,14-pentaaza[15])-2,2′-bipyridilophane) and $[Ru(phen)_2\mathbf{L''}]^{2+}$ (**Ru2**, with **L''** = 4,4′-bis-[methylen-(1,4,7,10-tetraazacyclododecane)]-2,2′-bipyridine). The resulting Ru(II)-ferritin nanocomposites are highly luminescent, display great stability in physiological conditions and preserve the native shell–core structure of the protein. Moreover, the singlet oxygen sensitizing properties of metal complexes, established by independent spectrophotometric and spectrofluorimetric measurements, are largely maintained also in their encapsulated form. Ru(II)-ferritin nanocomposites are exclusively internalized by cancer cells expressing the transferrin receptor 1 (TfR1) (*i.e.* HeLa and A2780 with respect to non-cancerous C2C12 myoblasts). Immunofluorescence analysis also reveals the co-localization of **Ru1** and **Ru2** with the TfR1 in the internal cellular compartments of HeLa and A2780 cells, highlighting the crucial role played by the receptor-mediated endocytosis of H-type ferritins exerted by TfR1. Finally, an MTT assay probed that light-activation effectively leads to a marked dose-dependent cytotoxic effect uniquely against cancer cells. This study underlines the potential of human H-ferritin as a valuable tool for the tumor-targeted delivery of sensitizing agents for photodynamic therapy.

Received 7th October 2021,
Accepted 7th December 2021
DOI: 10.1039/d1qi01268a

rsc.li/frontiers-inorganic

Introduction

Human ferritin is a heteropolymeric nanocage of 24 subunits involved in iron storage and release, depending on cellular demand.[1] Iron accumulates into ferritin under the form of a ferric-oxo biomineral that starts to grow from iron clusters on the inner surface of the protein cage following iron(II) oxidation by diffusing O_2.[2–7] While *in vivo* the heavy- and light-chains (H- and L-respectively) self-assemble at variable ratios to form the characteristic hollow structure with an internal cavity of 8 nm, recombinant ferritins are generally expressed as homopolymeric pure-H and pure-L cages. The potential of recombinant homopolymeric human H-ferritin (HuHf) as a valuable nanocarrier relies mainly on its low immunogenicity upon administration due to its human origin,[8] the possibility to incorporate low-molecular weight compounds[8] and the well-known interaction with transferrin receptor 1 (TfR1) for endocytosis.[9,10] In addition, the overexpression of TfR1 in cancer cells and the possibility of decorating the external surface with different targeting moieties make HuHf a promising platform for targeted drug delivery in cancer therapy.[11] Among the variety of possible biomedical applications,[12–17] ferritin may be a safe vehicle for small molecules designed for photodynamic therapy (PDT).[18–20]

PDT is based on the use of a photosensitizer (PS) that can be light-activated to produce reactive oxygen species (ROS), such as the highly cytotoxic singlet oxygen ($^1O_2$), and takes advantage of a complete spatial and temporal control over drug activation.[18] Thus, the use of ferritin-based nanocarriers in PDT opens the way to novel PS candidates with enhanced

[a]Department of Chemistry "Ugo Schiff", University of Florence, Sesto Fiorentino 50019, Italy. E-mail: luca.conti@unifi.it
[b]Consorzio Interuniversitario Risonanze Magnetiche di Metallo Proteine (C.I.R.M.M.P.), Sesto Fiorentino 50019, Italy. E-mail: ciambellotti@cerm.unifi.it
[c]Magnetic Resonance Center (CERM), University of Florence, Sesto Fiorentino 50019, Italy
[d]Department of Experimental and Clinical Biomedical Sciences "Mario Serio", University of Florence, Florence 50134, Italy
[e]CSGI, University of Florence, Sesto Fiorentino 50019, Italy
†Electronic supplementary information (ESI) available. See DOI: 10.1039/d1qi01268a
‡These authors contributed equally.

selectivity and efficiency as has been found for a series of porphyrin derivatives, phthalocyanines and phenothiazine dyes.[21–25] In this scenario, Ru(II)-polypyridyl complexes are attracting PSs due to their high thermodynamic/kinetic stability, good singlet oxygen sensitizing capabilities and their vast photophysical and electrochemical repertoire, which can be tuned by a fine choice of ligands.[26–28]

Notwithstanding the enormous PDT potential, the employment of ferritin of human origin to modulate the drug delivery of Ru(II)-polypyridyl-based PSs remains an issue almost completely unexplored.[29] To date, only a few cases have been reported by Feng and coworkers,[30] with the encapsulation of the hydrophobic $[Ru(bpy)_3]^{2+}$, $[Ru(bpy)_2dppz]^{2+}$ and $[Ru(phen)_2dppz]^{2+}$ (bpy = bipyridine, phen = phenanthroline, dppz = dipyrido[3,2-*a*:2′,3′-*c*]phenazine) into horse spleen L-apoferritin. However, the $^1O_2$ sensitization by Ru(II)-ferritin systems was not evaluated.

We have previously reported on the potential of highly charged Ru(II)-polypyridyl complexes $[Ru(phen)_2\mathbf{L}']^{2+}$ (**Ru1**) and $[Ru(phen)_2\mathbf{L}'']^{2+}$ (**Ru2**) as PS agents, featuring the peculiar polyazamacrocyclic units **L′** and **L″** (**L′** = 4,4′-(2,5,8,11,14-pentaaza[15])-2,2′-bipyridilophane, **L″** = 4,4′-bis-[methylen-(1,4,7,10-tetraazacyclododecane)]-2,2′ bipyridine).[31,32] The presence of many easily protonatable nitrogen groups on the unique polyazamacrocyclic moiety of **Ru1**, or on the two distinct cyclen (1,4,7,10-tetraazacyclododecane) units of **Ru2**, appended to the 4,4′ position of a metal-coordinated bipyridyl ligand affords the formation of highly charged species in aqueous media.[31,33] This confers to the resulting Ru(II) complexes not only excellent water solubility, a necessary prerequisite for their biological applications, but also strengthens their interaction with important biological targets, such as DNA. On the other hand, the polyamino-modified bipyridyl frameworks do not affect the good $^1O_2$ sensitizing capabilities of **Ru1** and **Ru2** ($\Phi_{\Delta(\mathbf{Ru1})} = 0.29 \pm 0.06$ and $\Phi_{\Delta(\mathbf{Ru2})} = 0.38 \pm 0.08$ in air-saturated CH_3CN, $\lambda = 400$ nm), thus making them attractive PS agents for the light-promoted $^1O_2$ generation directly in aqueous media.

Herein, we report on the encapsulation of **Ru1** and **Ru2** within HuHf to obtain the respective nanocomposites, **Ru1**@HuHf and **Ru2**@HuHf. The two hybrid systems underwent an extensive chemical–physical characterization, which included the analysis of their structural, luminescence and photosensitizing properties. The TfR1-mediated internalization and the biological potential of Ru(II)-HuHf nanocomposites were comparatively tested on representative cancer and non-cancer cell lines. The crucial role played by TfR1-mediated recognition of **Ru1**@HuHf and **Ru2**@HuHf in their selective delivery, and the different cytotoxic activities found against the tested cellular models, are also described.

Results and discussion

Encapsulation of Ru-polypyridyl complexes into ferritin

The large dimension of the **Ru1** and **Ru2** metal complexes (Fig. 1a) hampers their inclusion into HuHf by means of passive diffusion through the limited pore size (about 0.3 nm) of the protein shell.[8] For this reason, loading of **Ru1** and **Ru2** into HuHf was accomplished by the pH assisted disassembly and reassembly method harnessing the ability of ferritin to partially dissociate at pH 12 followed by the reconstitution of the 24-mer cage at neutral pH (Fig. 1b; see the ESI for more details, Fig. S3 and S4†).[8,34,35] As **Ru1** and **Ru2** are highly hydrophilic and stable even at pH 12,[31,33] they were incubated in the presence of HuHf during the disassembly process at different molar ratios (20–200 fold with respect to the protein). In order to remove the excess of **Ru1** or **Ru2**, *i.e.* the compounds not entrapped into the ferritin cavity, protein samples were purified by ultrafiltration and then subjected to size exclusion chromatography to recover the fraction corresponding to the fully reconstituted 24-mer cage containing **Ru1** and **Ru2** (**Ru1**@HuHf and **Ru2**@HuHf, respectively) (Fig. 2d).

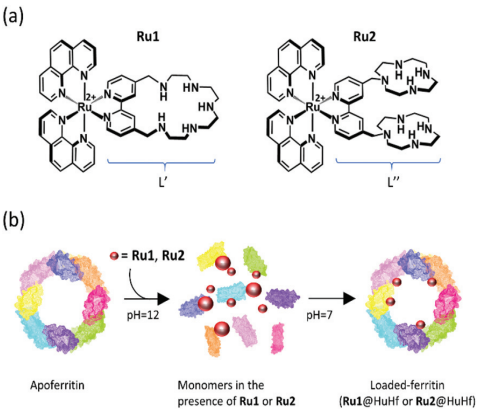

Fig. 1 (a) Ruthenium photosensitizers **Ru1** and **Ru2**; the respective macrocycle units **L′** and **L″** are indicated. (b) PSs encapsulation into HuHf by exploiting the pH-assisted disassembly/reassembly method.

Characterization of nanocomposites

The successful encapsulation of **Ru1** and **Ru2** was assessed by different means. A ligand to protein cage ratio of 5 and 4, for **Ru1**@HuHf and **Ru2**@HuHf respectively, was obtained as determined by UV-visible and ICP-AES analysis (Table 1). In this regard, only a few examples concerning the encapsulation of Ru(II) compounds into ferritin nanocages, accomplished by the pH assisted method, have been reported so far. Merlino and coworkers[37] encapsulated up to 36 molecules of $[(h^6\text{-}p\text{-}MeC_6H_4iPr)_2\mathbf{Ru_2}(m_2\text{-}S\text{-}p\text{-}C_6H_4tBu)_3]Cl$ per ferritin cage whereas the hydrophobic $[Ru(bpy)_3]^{2+}$, $[Ru(bpy)_2dppz]^{2+}$ and $[Ru(phen)_2dppz]^{2+}$ compounds reported by Feng *et al.*[30] were loaded in a ratio between 7–40 molecules per ferritin cage. However, all these studies referred to horse-spleen ferritin. ICP-AES measurements showed a negligible amount of ruthenium bound to the protein for the products obtained *via* direct incubation of Ru(II)-compounds in the presence of HuHf at pH 7 (without any disassembly process), thus confirming that the disassembly process is fundamental for **Ru1**/**Ru2** encapsula-

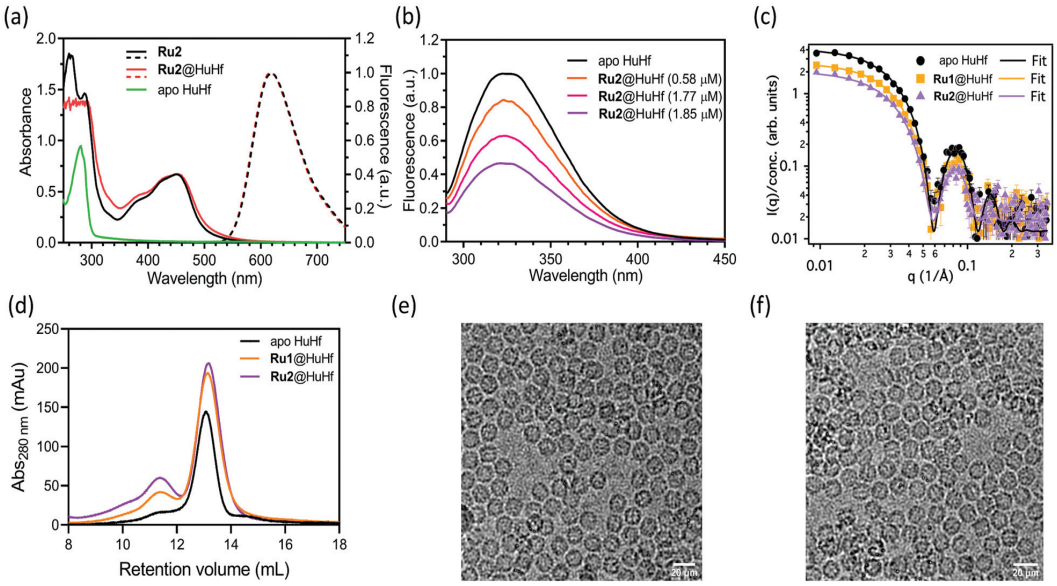

Fig. 2 Characterization of Ru(II)-HuHf nanocomposites. (a) Combined UV-visible and fluorescence spectra (λ_{exc} 411 nm) of free **Ru2** and of **Ru2**@HuHf (Ru(II) concentration of 50 μM and 6 μM for UV-visible and fluorescence measurements, respectively). UV-vis spectrum of apo HuHf is shown as reference. (b) Intrinsic fluorescence emission of apo HuHf and of **Ru2**@HuHf (HuHf 0.32 μM, λ_{exc} 280 nm) with increasing amounts of encapsulated **Ru2**. (c) SAXS intensity distribution of apo HuHf, **Ru1**@HuHf and **Ru2**@HuHf (markers represent experimental data while continuous lines refer to the core–shell modelling according to eqn (S1), ESI†). (d) Size exclusion chromatography analysis of ferritin nanocomposites upon encapsulation of **Ru1** and **Ru2** in 50 mM sodium phosphate pH 7 buffer. Chromatograms of encapsulated products were superimposed with the reference chromatogram of apo HuHf not subjected to the disassembly process. Eluted fractions related to peaks centered at about 13 mL of retention volume were taken for the subsequent experiments, thus corresponding to the reconstituted polymeric HuHf composed by 24 subunits. (e) and (f) Cryo-EM representative micrographs of **Ru1**@HuHf and **Ru2**@HuHf, respectively.

Table 1 Characterization of Ru(II)-loaded ferritin assemblies

	Ru atoms/cage					SAXS modeling[c]	
Sample name	UV vis-based	ICP AES-based	$\lambda_{Abs}/\lambda_{em}$ (nm)	k_{obs} [a] (min^{-1})	Φ_Δ [b]	Core diameter (nm)	Shell thickness (nm)
$[Ru(phen)_3]^{2+}$	—	—	447/605[d]	0.0595 (±5)	0.38 ± 0.08	—	—
Ru1	—	—	452/615	0.0434 (±3)	0.29 ± 0.06	—	—
Ru2	—	—	452/615	0.0594 (±4)	0.36 ± 0.08	—	—
Apo HuHf	—	—	—	—	—	8.32 ± 0.08	2.17 ± 0.06
Ru1@HuHf	5.2 ± 0.8[e]	4.1 ± 0.5[e]	452/615	0.0061 (±5)	—	8.14 ± 0.08	2.34 ± 0.09
Ru2@HuHf	4.3 ± 0.5[e]	3.4 ± 0.4[e]	452/615	0.0067 (±4)	—	8.02 ± 0.08	2.48 ± 0.10

[a] Photo-oxidation rate constants (k_{obs}) spectrometrically determined by the photo-oxidation of DHN in aqueous media at neutral pH. [b] Quantum yields (φ_Δ) of singlet oxygen production determined by measurements of $^1O_2$ phosphorescence at 1270 nm in air saturated CH_3CN solutions. [c] Parameters obtained using a core–shell model (see eqn (S1) in the ESI).† [d] Values determined in water at 298 K.[36] [e] Mean values with SEM of three independent experiments.

tion. The slight differences in the overall positive charge on compounds $[H_2\mathbf{Ru1}]^{4+}$ and $[H_4\mathbf{Ru2}]^{6+}$ at physiological pH only marginally affect the PS-loading content. The structural integrity of the nanocomposites was evaluated by single particle cryo-TEM micrographs acquired on **Ru1**@HuHf and **Ru2**@HuHf (Fig. 2e and f) showing the maintenance of the spherical nanocage structure characteristic of the apo HuHf, with an external diameter of 12 nm (ESI, Fig. S2 and S9†). CD spectra of apo HuHf, (**Ru1**/**Ru2**)@HuHf were acquired in the far UV region to control their stability looking at the signal intensities belonging to α-helix, which is the preeminent secondary structure element of ferritin. The results showed that the extraordinary structural stability of ferritin is preserved even after pH-guided encapsulation as observed in the temperature range of 25–85 °C (ESI, Fig. S8†).

The absorbance and fluorescence profiles of **Ru1**@HuHf and **Ru2**@HuHf were then analyzed. As shown in Fig. 2a and Fig. S5a (ESI),† the absorbance spectra of **Ru1**@HuHf and **Ru2**@HuHf are almost identical to the reference spectra of the free ligands; the typical MLCT band of ruthenium complexes

within the 400–500 nm range, well separated from the apoferritin background, indicates that no ligand-exchange occurred during the encapsulation process. (**Ru1**/**Ru2**)@HuHf nanocomposites feature marked fluorescence properties. In fact, **Ru1** and **Ru2** retain their native emission upon internalization into the protein (λ_{exc} 411 nm, λ_{em} 615 nm; Fig. 2a and ESI, Fig. S5a†). In addition, the intrinsic fluorescence emission of ferritin, generated from its tryptophan and tyrosine moieties (λ_{exc} 280 nm, λ_{em} 325 nm; ESI, Fig. S6†), was registered. A progressive quenching of the intrinsic fluorescence of the protein with increasing amounts of internalized ruthenium species evidenced the interaction between metal complexes and the protein, as shown for **Ru2**@HuHf and **Ru1**@HuHf in Fig. 2b and the ESI, Fig. S5b,† respectively and as reported for similar systems.[38,39] The interaction of the compounds with ferritin was further explored by ^{1}H NMR spectroscopy. CPMG experiments, which are designed to selectively observe the signals from low molecular weight compounds in mixtures containing large biomolecules by removing the broad unwanted resonances of the latter,[40,41] were performed. The ^{1}H NMR signals corresponding to **Ru1** and **Ru2** in the encapsulated formulations are broad beyond detection, most likely due to the interaction with the protein (ESI, Fig. S7a and b†). In contrast, if the same amount of Ru-compound is added to a solution of HuHf at neutral pH, the resonances belonging to the ligand are visible in the spectrum with line widths comparable to those of the individual metal compounds. These observations suggest that (**Ru1**/**Ru2**)@HuHf nanocomposites contain Ru complexes encapsulated inside the cage and that these complexes do not freely rotate inside the cavity but rather interact with the inner cage surface (ESI, Fig. S7a and b†). The SAXS patterns for the apo HuHf before and after Ru(II) complex internalization further show that the hollow shell structure of the protein is retained (Fig. 2c). In all cases, extracted density profiles are in agreement with a core–shell form factor characterized by the electron density of the core (cavity) being equal to that of the buffer solution (*i.e.* hollow shell system). The overall size of the cavity slightly decreases with the insertion of the Ru(II) complexes from 8.32 nm in the case of the apo form to 8.13 nm and 8.02 nm for **Ru1**@HuHf and **Ru2**@HuHf, respectively (Table 1). This shrinkage is directly associated with the increase of the thickness of the protein shell from about 2.2 nm to 2.5 nm and a good fit of these data could only be achieved considering the hollow shell topology. The increment in shell thickness and the simultaneous reduction in the diameter of the cavity confirmed that **Ru1** and **Ru2** are likely localized in proximity to the internal protein surface. Taken together, SAXS and NMR data lead us to hypothesize that the interaction of **Ru1** and **Ru2** with HuHf would be driven by electrostatic contributions between the metal compounds ($[H_2\mathbf{Ru1}]^{4+}$ and $[H_4\mathbf{Ru2}]^{6+}$), namely through the positively charged polyammonium groups on their **L**′ and **L**″ units, and the negatively charged residues facing the inner cavity of the protein.[42] On the other hand, an additional evidence that the interaction of the Ru compounds with the protein does not occur on the external surface arose by the comparison of zeta potential measurements of Ru-nanocomposites with respect to apo HuHf. The zeta potentials resulted to be similar under the experimental error, that are, – 5.0 ± 1.1 mV and – 3.1 ± 0.4 mV for **Ru1**@HuHf and **Ru2**@HuHf, respectively and – 4.2 ± 0.6 mV for apo ferritin, ruling out any external interaction of **Ru1** and **Ru2** with the protein.

Singlet oxygen production from ruthenium-ferritin assemblies

The capacity of Ru(II)-ferritin nanocomposites to generate singlet oxygen upon light-activation was assessed by employing two indirect chemical trapping methods (*vide infra*) and using water-soluble substrates as scavengers for $^1O_2$ (Fig. 3a and b). The results were then compared with those obtained for the 'non encapsulated'-PSs and for $[Ru(phen)_3]^{2+}$, the latter taken as reference for $^1O_2$ generation (Φ_Δ = 0.21 in air equilibrated D_2O).[43] Firstly, 1,5-dihydroxynaphthalene (DHN) was used as an indirect singlet oxygen reporter exploiting its prompt and quantitative oxidation in the presence of $^1O_2$ to give 5-hydroxy-1,4-naphthalenedione (Juglone), according to eqn (S2) and Scheme S1 (ESI).† This process can be easily followed *via* UV-vis spectroscopy by monitoring the decrease of the DHN absorption band at λ_{max} 297 nm and the simultaneous increase of the broad Juglone band centered at *ca.* 427 nm.[44,45]

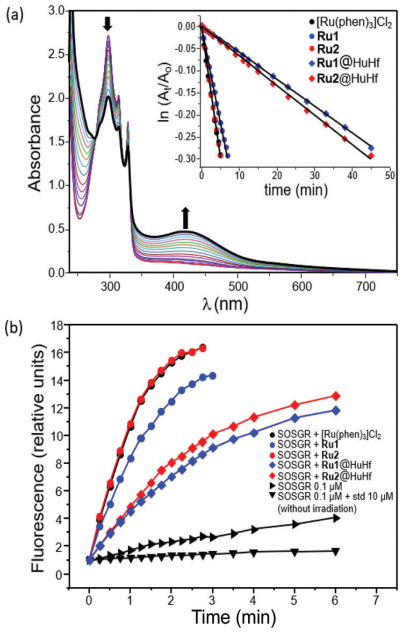

Fig. 3 (a) Absorption spectra of an aqueous solution at pH 7 containing DHN and **Ru2**@HuHf at different irradiation times (up to 7 minutes). As blank reference we used a solution containing the PS at the same concentration and pH of that of the measuring cuvette. In the inset the semilogarithmic plots of $\ln(A_t/A_0)$ as a function of the irradiation time obtained for all the investigated systems ([DHN] = 3.3 × 10^{-4} M, [Ru] = 10 μM, 50 mM NaPi buffer) are compared. (b) Singlet oxygen production from free and HuHf-loaded Ru(II) PSs as monitored by the Singlet Oxygen Sensor Green reagent (SOSGR) in 50 mM NaPi buffer, (pH 7), ([SOSGR] = 0.5 μM, [Ru] = 5 μM, $\lambda_{exc}/\lambda_{em}$ 488/525 nm).

Experiments were carried out by irradiating (LED light, λ > 430 nm, 30 W) aqueous solutions, pre-saturated with O_2, and containing sensitizers (**Ru1**, **Ru2**, **Ru1**@HuHf, **Ru2**@HuHf or $[Ru(phen)_3]^{2+}$) in the presence of DHN. Negligible Juglone formation was observed upon DHN irradiation in the absence of sensitizers under these experimental conditions (ESI, Fig. S11a†). As shown in Fig. S11e (ESI)† and Fig. 3a, which respectively report the UV-vis titrations obtained for **Ru1**@HuHf and for **Ru2**@HuHf (those obtained for the non-encapsulated PSs are shown in the ESI, Fig. S11b–d†), light-activation of Ru-ferritin nanocomposites determines the progressive decrease of the DHN absorption band, along with the simultaneous increase of the Juglone band, clearly demonstrating the capacity of Ru(II)-ferritin nanocomposites to efficiently sensitize $^1O_2$ production. Moreover, the appearance in these spectra of two clear isosbestic points around 280 and 330 nm ruled out the formation of long-lived intermediates or byproducts. In particular, as better shown by the inset in Fig. 3a, which reports the semilogarithmic plots of $\ln(A_t/A_0)$ obtained for all the Ru(II)-based formulations over the investigated irradiation time frame, Ru(II)-ferritin nanocomposites produce a similar amount of $^1O_2$ in about 45 minutes as 'free' molecules (**Ru1**, **Ru2** and $Ru(phen)_3Cl_2$) did in 6–7 min. A semi-quantitative estimation of the relative rate constants for the DHN photooxidation processes (k_{obs}) was accomplished by applying the steady-state approximation to the $^1O_2$ intermediate species, as described in detail in the ESI†; the obtained results are listed in Table 1. The slightly lower efficiency in the $^1O_2$ production found for protein-embedded ruthenium complexes if compared to ones of non-encapsulated molecules is a common feature that has been also observed for other PS agents confined into apoferritin[22] or linked to polymeric structures.[44]

We can rationalize this behavior by considering the fact that quenching of excited triplet states of sensitizers by $^3O_2$ requires the interaction of the PS and molecular oxygen. In this view, while $^3O_2$ can easily diffuse inside ferritin, the mobility of the PS molecules embedded into HuHf would be significantly reduced relative to non-encapsulated metal complexes, due to their interaction with the protein surface (Fig. 2b, c and ESI, Fig. S5b†).

The effectiveness of metal-protein composites in the $^1O_2$ production has been then confirmed from an independent experiment, by monitoring the green fluorescence emission (at 525 nm) of the commercially available Singlet Oxygen Sensor Green® reagent (SOSGR), a highly selective probe for $^1O_2$.[46,47] As shown in Fig. 3b, the irradiation over a period of time of solutions containing the probe in the presence of **Ru1**@HuHf or **Ru2**@HuHf determined a progressive increase of the SOSGR fluorescence emission, revealing a similar ability of Ru(II)-HuHf systems to sensitize $^1O_2$ generation, even though inferior to that of free molecules in agreement with the UV-visible analysis. Of note, the linear increase of the SOSGR luminescence observed for the first irradiation intervals suggests a prompt reaction between the encapsulated PSs and molecular oxygen, thus highlighting the facile diffusion of O_2 into ferritin, a key factor in the iron(II) oxidation reaction occurring in ferritin nanocages. During the same time frame, modest signal changes were observed upon irradiation of a control containing only the probe, or for a solution containing the probe and $[Ru(phen)_3]^{2+}$ held in dark conditions.

TfR1 targeting ability of ruthenium-ferritin assemblies

The targeting ability of cell models expressing TfR1 and the delivery of **Ru1**@HuHf and **Ru2**@HuHf into the cytosol were tested by different biological approaches.

Due to the binding of H-ferritin to TfR1,[9] we evaluated the cellular drug delivery of ruthenium-HuHf nanocomposites in cell lines featuring different expression levels of TfR1. The expression of TfR1 was first analyzed in cervical carcinoma (HeLa) and ovarian carcinoma (A2780) cells, both human cancer cell lines, and in C2C12 myoblasts, a non-tumoral cell line, by western blot analysis in different culture conditions. As shown in Fig. 4, the TfR1 protein level was appreciable in HeLa and A2780 cells, its expression being higher under growth compared to serum-deprivation conditions, whereas it was undetectable in non-cancer C2C12 myoblasts. The expression and localization of TfR1 in these cellular models were further confirmed by confocal immunofluorescence analysis (ESI, Fig. S12†). Subsequently, the uptake of Ru-ferritin nanocomposites in different cellular models was assessed by measuring the content of ruthenium in cell lysates by ICP analysis (Fig. 5a). As shown in Fig. 5a, HeLa and A2780 cells were found to be both able to internalize **Ru1**@HuHf and **Ru2**@HuHf, with no significant differences among the two PS-ferritin formulations. Conversely, lysates of C2C12 myoblasts did not contain detectable amounts of ruthenium, as expected due to the lack of TfR1 expression emerged from western blot (Fig. 4).

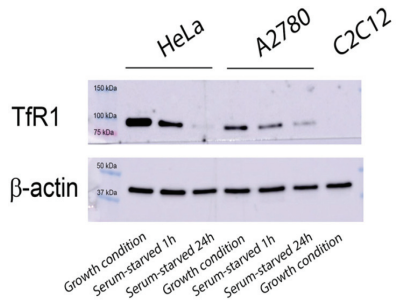

Fig. 4 Expression of TfR1 in cancer (HeLa and A2780) and non-cancer (C2C12) cell lines under different culture conditions. Western blot analysis was performed starting from 20 μg total protein lysates of cells incubated in 10% FBS supplemented growth medium (growth conditions), or serum-deprived medium supplemented with 0.1% BSA for 1 h and 24 h (serum-starved 1 h or 24 h) using specific mouse, monoclonal anti-TfR1 antibody CD71, OKT-9 (Thermo Fisher Scientific). Beta-actin (β-Actin) expression was evaluated as a loading control in each sample using specific antibodies. A blot representative of three independent experiments is shown.

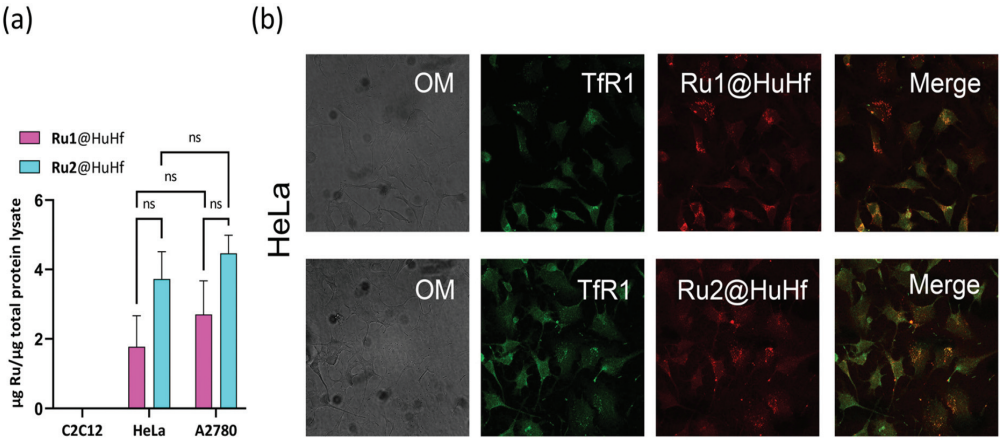

Fig. 5 Cell internalization of **Ru1**@HuHf and **Ru2**@HuHf. (a) The amount of internalized ruthenium after 24 h of incubation of Ru-ferritin nanocomposites (10 μM of encapsulated ruthenium) for each cell line is reported. The ruthenium content in C2C12 cells was not detectable indicating that ferritin is not endocytosed by this cell line. ICP data were normalized on the μg of total protein of each specimen. Statistical analysis was performed by 1-way and 2-way ANOVA followed by Bonferroni *post-hoc* test. (b) Laser scanning confocal microscopy on HeLa cells incubated with **Ru1**@HuHf and **Ru2**@HuHf. The concentration of encapsulated ruthenium and the time of incubation are the same as for the ICP analysis. Immunofluorescence analysis was performed using specific anti-TfR1 primary antibody and secondary anti-mouse antibody conjugated with fluorescein (green). Ru(II) nanocages display fluorescence properties, λ_{exc} 440–480 nm and λ_{em} 600–640 nm (red). Representative confocal microscope images show the colocalization of TfR1 with Ru(II) nanocomposites on the right (merge) and the corresponding optical microscope images on the left (OM).

Then, the uptake of Ru(II)-ferritin systems and the possible colocalization with TfR1 in HeLa cells were investigated by exploiting the luminescence properties of Ru(II)-polypyridyl complexes and by immunofluorescence analysis, using specific anti-TfR1 antibodies. Fig. 5b shows the distribution of **Ru1**@HuHf and **Ru2**@HuHf in the intracellular compartment together with TfR1 (merge). The same results were also obtained in A2780 cells (ESI, Fig. S13†).

In vitro cytotoxicity of ruthenium-loaded ferritin systems after photoactivation

To evaluate the light-induced dose-dependent effect of Ru(II)-ferritin assemblies on cancer cell viability, the MTT reduction assay was carried out in HeLa, A2780 and C2C12 cells incubated for 24 h with different concentrations of Ru(II)-HuHf formulations. Photoactivation was applied as described in Experimental section, 24 h before the cell viability was analyzed, while apo HuHf (*i.e.* not loaded with PSs) was used as negative control to subtract any toxicity due to the protein itself. In this regard, apo HuHf did not show significant cellular toxicity in the range of concentrations of 0–10 μM (corresponding to *ca.* 0–40 μM of Ru-PS loaded into ferritin). The obtained results are reported in Fig. 6. As shown in this figure, photosensitization of ferritin-ruthenium nanocomposites markedly affected cell survival of cancer cells, starting from 10 μM Ru(II) for both **Ru1**@HuHf and **Ru2**@HuHf, leading, as an example, to decreased cell viability of approximately 50% at a drug dose of 40 μM of **Ru1**@HuHf. Conversely, a different behavior was exhibited by C2C12 myoblasts, whose cell viability was negligibly influenced by light-activation, as expected due to the lack of **Ru1**@HuHf and **Ru2**@HuHf internalization in the absence of TfR1 expression in these cells. Thus, these results demonstrated the fundamental role played by TfR1 in the cellular uptake, as well as in the phototoxicity, of Ru(II)-HuHf formulations observed in the different cell lines. An analogous dose-dependent MTT analysis was repeated for free **Ru1** and **Ru2**, meaning not encapsulated into ferritin, (ESI, Fig. S14†). Ru-complexes are able to penetrate into the studied cancer cell lines, including the non-cancer C2C12 myoblasts and as expected, they are not completely inert molecules but rather, they are intrinsically toxic. For example, at the maximum dose investigated, **Ru1** and **Ru2** are found to decrease HeLa cell viability by 30 and 15%, respectively. In A2780 and C2C12 cell lines, the cytotoxic effects are even stronger. These data reinforced the importance of two aspects: (i) the targeted delivery to selectively accumulate the photosensitizers at the site of interest and at the same time (ii) the encapsulation into ferritin-based carrier prevents the toxicity exerted by free molecules before photoactivation.

Experimental

Synthesis and materials

All materials were of reagent grade and used without further purification unless otherwise specified.

The synthesis of the polyamino macrocycles **L′** and **L″** are reported in previous works[33,48] while the corresponding ruthenium(II) complexes were prepared according to our previous papers.[31,33]

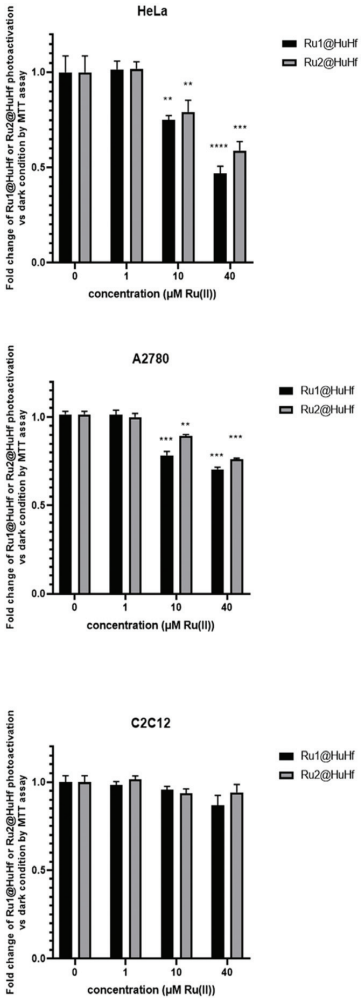

Fig. 6 Dose dependent cytotoxic effect of **Ru1**@HuHf and **Ru2**@HuHf after photoactivation. Cellular viability of different cancer (HeLa and A2780) and non-cancer (C2C12) cell lines was assessed by MTT reduction analysis. Cells were incubated for 24 h in the presence of Ru(II)-HuHf nanocomposites with **Ru1** and **Ru2** at the following concentrations, 0 μm, 1 μM, 10 μM and 40 μM in serum-deprived culture media (supplemented with BSA 0.1%). Photoactivation was carried out using a 30 W three-arm LED lamp with 470–430 nm blue emission for 20 minutes, at a distance of 5 cm from the cell plate. Twenty-four hours after photoactivation, MTT analysis was performed to assess the antitumor effect of Ru(II) nanocages. Experiments were performed in triplicate, representative of three independent ones with similar results. Data reported are mean ± SEM of fold change absorbance at 570 nm in photoactivated compared to dark conditions normalized to apoferritin treatment. The effect of photoactivation of Ru(II) nanocages on the inhibition of cell survival was statistically established by 1-way ANOVA followed by Bonferroni *post-hoc* test. $^{**}P < 0.01$, $^{***}P < 0.001$, $^{****}P < 0.0001$.

Ferritin expression and purification

Homopolymeric human heavy chain ferritin (HuHf) was produced in *E. coli* as previously reported.[42,49,50] The pET-9a plasmid carrying human heavy chain ferritin gene was transformed in BL21(DE3)-pLysS competent cells. Massive cultures were grown in rich Luria-Bertani medium at 37 °C adding kanamycin (50 μg mL^{-1}) and chloramphenicol (34 μg mL^{-1}) antibiotics. The overexpression of the protein was induced at $OD_{600\ nm}$ 0.6–0.8 with 1 mM of isopropyl β-D-1-thiogalactopyranoside (IPTG) for 4 h at 37 °C. At the end, the cells were harvested by centrifugation at 7500 rpm for 15 min and disrupted by sonication. Afterwards, the crude lysate was clarified with ultracentrifugation at 40 000 rpm for 40 min and the supernatant recovered and heated at 65 °C for 15 min to precipitate undesired proteins. The soluble fraction was subjected to anionic exchange chromatography with a linear sodium chloride gradient 0–1 M (Q-Sepharose Fast Flow resin, GE Healthcare) in 20 mM Tris pH 7.5 buffer. Ferritin-containing fractions were identified by SDS-PAGE and then pooled and loaded into a Superdex 200 HiLoad 16/600 column (GE Healthcare) for size exclusion chromatography in 20 mM Tris pH 7.5 buffer. To remove the metal ions taken up from the culture medium, four 5 L dialysis in the presence of chelating and reducing agents (20 mM Tris, 2.5 mM EDTA, 15 mL ammonium thioglycolate pH 7.5 buffer) followed by four dialysis against 5 L of 20 mM Tris pH 7.5 buffer were performed.

Encapsulation of Ru1 and Ru2

Encapsulation of **Ru1** and **Ru2** was promoted by the dissociation of ferritin cage (HuHf in 50 mM sodium phosphate pH 7 buffer) into its monomers at pH 12, diluting the protein solution (final concentration of 1.25 μM HuHf in a final volume of 5 mL) with Universal buffer at pH 12 (Britton Robinson buffer) and adjusting pH adding NaOH 1 M. Different concentrations of **Ru1** or **Ru2** (25, 125 and 250 μM) were incubated with ferritin for 15 min. Then, the pH was brought at 7 with HCl 1 M to let the protein reassemble in a 24-mer cage, trapping **Ru1** and **Ru2** inside the cavity in 2 h. The entire process was run under stirring at 30 °C. At this point, the protein samples were centrifuged at 7000 rpm for 10 min to discard precipitates and extensively filtered in centrifugal devices (Amicon® Ultra 15 mL with cutoff 50 kDa, Merck LifeScience) to remove excess photosensitizers. To recoup the portion of protein with the correct folding, size exclusion chromatography (Superdex 200 10/300 GL column, GE Healthcare) was applied. The encapsulated products were eluted in 50 mM sodium phosphate pH 7 buffer and the fractions with a retention volume corresponding to 24-mer HuHf were recovered. In order to exclude unspecific binding of Ru-based molecules on the external surface of the protein, control experiments with native HuHf were performed incubating **Ru1** and **Ru2** with HuHf in 50 mM sodium phosphate pH 7 buffer avoiding the opening of the protein cage. Protein concentration was determined by Bradford assay. The estimation of ruthenium content was performed by UV-visible and ICP-AES. For the following analysis in cell cultures, the encapsulates were further subjected to buffer exchange in PBS (phosphate buffer solution) at pH 7.4 and 0.2 μm filtered to obtain the sterility required for mammalian cells.

ICP-AES measurements

Samples were treated with 100 μL of suprapure HNO_3 (obtained by sub-boiling distillation) and 100 μL of suprapure HCl (30%) and, after dissolution, were diluted to a final volume of 5.0 mL with ultrapure water (UHQ – resistivity >18 MΩ cm – Milli-Q system by Millipore, Billerica, MA). The determination of Ru concentrations in the samples was performed in triplicate by a Varian 720-ES axial inductively coupled plasma atomic emission spectrometer (ICP-AES). Each sample was spiked with 1.0 ppm of Ge used as an internal standard prior to the analysis. The introduction system consisted of a concentric pneumatic nebulizer and a cyclonic spray chamber. Calibration standards were prepared by gravimetric serial dilution from commercial stock standard solutions of Ru at 1000 mg L^{-1} (Honeywell Fluka). Wavelengths used for Ru determination were 267.876 and 245.657 nm, whereas for Ge the line at 209.426 nm was used. The operating conditions were optimized to obtain maximum signal intensity, and between each sample, a rinsing solution constituted by 2% v/v of HNO_3 was used.

UV-visible, fluorescence and circular dichroism analysis

Absorption spectra were registered on a PerkinElmer Lambda 6 spectrophotometer. The electronic absorption profiles of **Ru1**@HuHf and **Ru2**@HuHf were compared with the spectra of the reference compounds **Ru1** and **Ru2**. All the spectra were registered in 50 mM sodium phosphate pH 7 buffer. The quantity of the compounds internalized into HuHf was initially calculated with the absorbance at 450 nm of Ru(II)-centers given the extinction molar coefficients of **Ru1** and **Ru2**. In order to evaluate the luminescence of **Ru1** and **Ru2** upon encapsulation, the fluorescence of 6 μM free and encapsulated **Ru1** and **Ru2** was read using excitation and emission wavelengths of 411 nm and 615 nm respectively. In addition, the intrinsic fluorescence of HuHf (0.3 μM in protein cage) was registered at 325 nm upon excitation of tryptophan and tyrosine aromatic residues at 280 nm for apo HuHf and for HuHf loaded with increasing amounts of **Ru1** (0.7 μM, 2.01 μM and 2.60 μM) and **Ru2** (0.58 μM, 1.77 μM and 1.85 μM). Fluorescence measurements were collected on a PerkinElmer LS55 spectrofluorometer. The slit width set for excitation and emission was 10 nm. All measurements were performed at 298.0 ± 0.1 K in 50 mM sodium phosphate buffer solution pH 7, while spectra at different pH values were collected by adding small amounts of concentrated HCl or NaOH to aqueous solutions of ligands.

Circular dichroism (CD) analysis was conducted with a Jasco spectropolarimeter J-810 in the far-UV region between 190–250 nm with a 0.1 cm path length quartz cuvette. Temperature-dependent CD spectra of 10 μM protein in subunits (50 mM sodium phosphate pH 7) were performed in the range 25–85 °C. The samples were incubated in the thermostatic cell (Jasco Peltier equipment) at the desired temperatures for 5 min before acquiring spectra at a scanning speed of 100 nm min^{-1}. The mean of 5 scans was calculated by subtracting the corresponding buffer spectrum and the molar ellipticity optical units were converted in mean residue weight ellipticity (θ_{MRW}).

SAXS measurements

All small-angle scattering measurements were performed using a HECUS S3-Micro apparatus. This Kratky-type camera is equipped with a position sensitive, 50 M OED detector comprising of 1024 channels (width = 54 μm). Cu Kα radiation with a wavelength, λ, of 1.542 Å at a power of 50 W is provided by an ultra-brilliant point microfocus X-ray generator (GENIX-Fox 3D, Xenocs, Grenoble). A sample-to-detector distance of 281 mm (calibrated using the well-known silver behenate lamellar lattice, d = 58.34 Å[16] provided a measurable q-range between 0.009 and 0.54 $Å^{-1}$ (where q, the scattering vector, is given by $q = 4\pi/\lambda \sin\theta$, and 2θ is the scattering angle). Protein samples were placed into borosilicate glass capillaries with a diameter of 1 mm. Measurements were performed under vacuum to reduce scattering from air and at a temperature of 25 °C. Raw scattering data were corrected for the empty capillary/buffer contribution. The acquisition time was from 30 min to 1 h depending on the sample. Short measurements (1 min) were performed on each sample to confirm that the radiation damage was negligible under these experimental conditions.

^{1}H NMR analysis

^{1}H NMR spectra of free **Ru1** and **Ru2** (100 μM), apo HuHf (25 μM in cage) and **Ru1**@HuHf and **Ru2**@HuHf (100 μM of encapsulated **Ru1**/**Ru2**) in phosphate NMR buffer (pH 7.4) were recorded and compared to further investigate the interaction of the encapsulated Ru-compounds with HuHf. NMR spectra were acquired using a Bruker 900 MHz spectrometer (Bruker BioSpin) at 298 K. One-dimensional ^{1}H-NMR spectra with water peak suppression and a standard CPMG pulse sequence were recorded (3k scans, 102 400 data points, a spectral width of 19 167 Hz, acquisition time of 2.97 s, and a relaxation delay of 4 s).[40,41] This type of sequence has been used to selectively observe the sharp signals arising from the low molecular weight Ru-compounds free in solution and to suppress the broad resonances coming from ferritin. Before applying Fourier transform, free induction decays were multiplied by an exponential function equivalent to a 2.0 Hz line-broadening factor. Transformed spectra were automatically corrected for phase and baseline distortions using TopSpin 3.5 (Bruker BioSpin). The spectra of free **Ru1** and **Ru2** were also recorded in plasma to prove their long-term stability in biological fluids (ESI, Fig. S1†).

Zeta potential measurements

Zeta potential measurements were performed with a ZetaPALS system coupled with a Brookhaven 90Plus particle sizer (Brookhaven Instruments). Measurements were performed on the very same dispersions and also after dilution up to 1 : 20 to reduce the overall ionic strength. Zeta potentials of the scattering objects were extracted by phase analysis light scattering according to standard procedures.

Cryo-EM screening analysis

Cryo-EM micrographs of apo HuHf, **Ru1**@HuHf and **Ru2**@HuHf were acquired using a ThermoFisher Glacios at 200 kV instrument, equipped with a Falcon III direction electron detector. Holey-carbon R1.2/1.3 grids (Quantifoil Micro Tools GmbH) covered by a 2 nm film of carbon were prepared. Grid surfaces were treated with plasma cleaning using O2 for 45 s before applying 3 μL of the sample (1 mg mL^{-1} of **Ru1**@HuHf and **Ru2**@HuHf in PBS buffer pH 7.4). Grids were blotted in 100% humidity and 10 °C with filter paper and vitrified by rapidly plunging into liquid ethane at −180 °C using a Vitrobot Mark IV (FEI, Hillsboro).

Singlet oxygen determination using 1,5-dihydroxynaphthalene (DHN) and the singlet oxygen sensor green reagent (SOSGR)

The ability of Ru-based formulations to effectively sensitize the singlet oxygen production was firstly assessed by means of UV visible titrations employing 1,5-dihydroxynaphthalene (DHN) as an indirect $^1O_2$ reporter. Experiments were performed in phosphate buffer (50 mM, pH 7, with 10% v/v MeOH and D_2O each)[44] in the absence and in the presence of a selected Ru(II)-based photosensitizer. In detail, following the preparation of a 3.3×10^{-3} M solution of DHN in methanol, this solution was diluted 1 : 10 with aqueous solutions of the Ru(II)-based PS at pH 7, obtaining a final water/MeOH (9 : 1) solution of DHN 3.3×10^{-4} M with a Ru(II)-content of 1×10^{-5} M. Samples were then transferred in a quartz cuvette with 1 cm optical path and irradiated (LED Lamp, 30 W, $\lambda > 430$ nm) for a total time varying between 6 and 50 minutes. All spectra were acquired using as blank reference a solution containing the selected PS at the same concentration and pH of those of the measuring cuvette. In close analogy with the UV-vis measurements, the $^1O_2$ sensitizing properties of the studied formulations were investigated by means of fluorescence measurements by employing the Singlet Oxygen Sensor Green reagent (SOSGR).[46] To this aim, we prepared aqueous solutions buffered at pH 7 (50 mM sodium phosphate) containing SOSGR in the presence of a selected photosensitizer. The probe concentration was fixed to 0.5 μM while the ruthenium concentrations of **Ru1** and **Ru2** were ten times higher (5 μM). Samples containing **Ru1**@HuHf or **Ru2**@HuHf were prepared in order to have a final Ru(II) equivalent concentration. The solutions were then transferred in a quartz cuvette with 0.1 cm optical path and irradiated. Fluorescence spectra were collected using excitation/emission wavelengths of 488/525 nm. Two additional controls were analyzed, one containing a mixture of SOSGR and $[Ru(phen)_3]^{2+}$ maintained under dark conditions, and the other consisting of only the probe exposed to different irradiation times.

Cell cultures

All culture media and reagents were purchased from Merck KGaA (Darmstadt, Germany), including phosphate buffer saline (PBS). Human ovarian cancer cell line A2780 and human epithelioid cervix carcinoma cell line HeLa (ATCC, VA, USA) were cultured in RPMI-1640 medium supplemented with 10% fetal bovine serum (FBS), 100 μg mL^{-1} streptomycin, 100 U mL^{-1} penicillin and 2 mM l-glutamine. C2C12 myoblasts (ATCC, VA, USA) were cultured in Dulbecco's Modified Eagle's Medium (DMEM) supplemented with 10% FBS, 100 μg mL^{-1} streptomycin, 100 U mL^{-1} penicillin and 2 mM l-glutamine. These cell lines were maintained in a humidified atmosphere at 95% air/55% CO_2 and constant temperature of 37 °C.

All cell treatments were performed in serum-deprived RPMI or DMEM medium, supplemented with 1 mg mL^{-1} bovine serum albumin (0.1% BSA).

Western blot analysis

Cells were collected in a lysis buffer containing 50 mM Tris, pH 7.5, 120 mM NaCl, 1 mM EDTA, 6 mM EGTA, 15 mM $Na_4P_2O_7$, 20 mM NaF, and 1% Nonidet supplemented with protease inhibitor cocktail and incubated 30 min at 4 °C. Cell lysates were centrifuged at $10^4 g$, 15 min 4 °C and 20 μg total protein amount was resuspended in sodium dodecyl sulphate (SDS) sample buffer and separated by SDS-polyacrylamide gel electrophoresis (SDS-PAGE) and finally transferred to polyvinylidene fluoride (PVDF) membranes by Trans-Blot® turbo transfer system (Bio-Rad Laboratories, CA, USA). PVDF membranes were incubated at 4 °C overnight with anti-CD71 (Transferrin receptor-1) monoclonal antibody (OKT-9; 1 : 1000 dilution) (eBioscience, Thermo Fisher Scientific Inc., MA, USA) and anti-β-actin (Santa Cruz Biotechnology, CA, USA). Horseradish peroxidase (HRP)-conjugated secondary antibodies (Santa Cruz Biotechnology, CA, USA) were incubated for 1 h at room temperature. Specific protein bands were detected by enhanced chemiluminescence using Clarity Western ECL substrate (Bio-Rad Laboratories, CA, USA), images were acquired with an Amersham Imager 600 (GE Healthcare, UK) and quantification performed by densitometric analysis using the ImageJ software (freely available at https://imagej.nih.gov/ij/).

MTT reduction assay

Cell viability of HeLa, A2780 and C2C12 cells was evaluated by the reduction of the yellow tetrazolium salt 3-(4,5-dimethylthiazol-2-yl)-2,5-diphenyltetrazolium bromide (MTT) to purple formazan crystals performed by metabolically active cells. MTT colorimetric analysis was performed after the treatment with **Ru1**@HuHf or **Ru2**@HuHf for 24 h, followed by photoactivation and then incubation for further 24 h. Briefly, for each cell line two 96-well plates were seeded: one was employed for light exposure (photoactivation conditions), and the other one was maintained in the dark (dark conditions). Cells were incubated with increasing concentrations of Ru(II) in **Ru1**@HuHf or **Ru2**@HuHf obtained by ICP measurement (0, 1, 10 and 40 μM), and in parallel with the same corresponding concentration of HuHf (determined by Bradford assay) in serum-deprived culture media. For the photoactivation conditions, after a 24 h-challenge with Ru(II) nanocages, cells were irradiated with 30 W three-arm LED light lamp with 470 nm–430 nm emission for 20 minutes at a distance of 5 cm from

cell monolayers and then incubated for 24 h at 37 °C in 5% CO_2 atmosphere. Cell viability was assayed in the presence of 0.5 mg mL^{-1} of MTT salt (Merck KGaA, Darmstadt, Germany) for 1 h at 37 °C; DMSO (Dimethyl Sulfoxide, Merck KGaA, Darmstadt, Germany) was used to dissolve insoluble formazan crystals produced by viable cells. The absorbance was measured at 595 nm using a microplate reader (iMark Microplate Absorbance Reader, Bio-Rad, CA, USA).

Laser scanning confocal microscopy

Cell internalization of ferritin-Ru(II) nanocages and colocalization analysis with transferrin receptor-1 was performed using a Leica SP8 laser scanning confocal microscope (Leica Microsystems GmbH). Cells (HeLa, A2780 and C2C12) were seeded on microscope slides and treated for 24 h with 10 μM Ru(II) of **Ru1**@HuHf or **Ru2**@HuHf, followed by washing with PBS and fixed with 2% paraformaldehyde in PBS for 20 minutes at room temperature. Colocalization of **Ru1**@HuHf or **Ru2**@HuHf with anti-CD71 (transferrin receptor-1) was performed by immunofluorescence analysis: after 24 h of incubation with 10 μM Ru(II) of **Ru1**@HuHf or **Ru2**@HuHf, microscope slides were incubated with anti-CD71 (TfR1) monoclonal antibody (OKT-9; 1 : 100 dilution) for 2 h at room temperature followed by treatment with Texas Red-conjugate secondary anti-rabbit antibody (1 : 200 dilution) purchased from Vector Laboratories Inc. (Burlingame, CA, USA). Microscope slides were incubated with DAPI solution (1 mg ml^{-1}, Thermo Fisher Scientific Inc., MA, USA) to probe the cell nucleus and then were mounted using Fluoromount aqueous mounting medium (Merck KGaA, Darmstadt, Germany).

Statistical analysis

Data obtained in the cell experiments are presented as means ± standard error of mean (SEM). Comparisons between the different groups were performed by one- or two-way ANOVA analysis of variances followed by Bonferroni's *post-hoc* test in the GraphPad Prism 9.0 software.

Conclusions

In summary, we herein report on the successful encapsulation into human H-ferritin of the photosensitizers **Ru1** and **Ru2**, affording the corresponding **Ru1**@HuHf and **Ru2**@HuHf nanocomposites.

A chemical–physical characterization of these fluorescent hybrid materials evidenced a retained protein quaternary structure (*i.e.* core–shell assembly and protein fold), with **Ru1** and **Ru2** giving rise to intermolecular contacts/interactions with the inner surface of the protein shell. Importantly, Ru(II)-ferritin assemblies featured high stability at physiological pH and demonstrated to effectively sensitize $^1O_2$ production upon light-activation.

The biological potential of **Ru1**@HuHf and **Ru2**@HuHf was tested against two human cancer cell lines, HeLa and A2780 cells, both expressing TfR1, and on the non-tumoral C2C12 myoblasts. ICP analysis indicated the selective internalization of Ru(II)-HuHf assemblies into tumoral cells. Confocal microscopy analysis also unveiled the co-localization of **Ru1** and **Ru2** with the TfR1 in the internal cellular compartments of HeLa and A2780 cells. Therefore, these results highlighted the crucial role played by TfR1-mediated endocytosis of H-type ferritin in the selective delivery of Ru-based PSs into tumoral cells.

Finally, **Ru1**@HuHf and **Ru2**@HuHf were found to be effectively able to elicit a significant dose-dependent cytotoxicity against HeLa and A2780 cells following irradiation.

In conclusion, this study underlines the suitability of H-ferritin platforms to selectively deliver Ru(II)-polypyridyl-based photosensitizers in cancer cells thus providing promising tools to be further exploited in photodynamic therapy.

Author contributions

L. Con. and G. E. G. synthesized the Ru(II) compounds. S. C. and L. Con. produced ferritin and its nanocomposites. L. Con. and S. C. carried out spectrophotometric characterization and measured singlet oxygen production. V. G., M. S. and E. F. performed ^1H NMR, ICP-AES and SAXS experiments, respectively. E. P., F. C. and P. B. conducted cell experiments. L. Con. and S. C. wrote the manuscript. P. B. and B. V. revised the manuscript. P. T. conceived the study and provided funding. C. G. and P. T. supervised the work.

Conflicts of interest

There are no conflicts to declare.

Acknowledgements

The authors thank Dr Giovanni Ferraro for zeta-potential measurements. Fondazione Cassa di Risparmio di Firenze funded the project "Development of ferritin-based nanodevices for the targeted delivery of drugs and imaging probes", which includes a research grant to L. Cos. The authors acknowledge MIUR for "Progetto Dipartimenti di Eccellenza 2018–2022" allocated to the Department of Chemistry "Ugo Schiff" and to the Department of Experimental and Clinical Biomedical Sciences "Mario Serio". E. F. acknowledges the financial support from CSGI. S. C. was supported by an AIRC fellowship for Italy. We acknowledge Instruct-ERIC, a Landmark ESFRI project, for the support and the use of resources and specifically the CERM/CIRMMP Italy Centre. The authors thank FloCEN, the Florence Centre for Electron Nanoscopy of the Department of Chemistry "Ugo Schiff", University of Florence, for Cryo-EM screening analysis.

Notes and references

1 R. R. Crichton, Structure and function of ferritin, *Angew. Chem., Int. Ed. Engl.*, 1973, **12**, 57–65.
2 S. Ciambellotti, C. Pozzi, S. Mangani and P. Turano, Iron Biomineral Growth from the Initial Nucleation Seed in L-Ferritin, *Chem. – Eur. J.*, 2020, **26**, 5770–5773.
3 C. Pozzi, S. Ciambellotti, C. Bernacchioni, F. Di Pisa, S. Mangani and P. Turano, Chemistry at the protein-mineral interface in L-ferritin assists the assembly of a functional (μ3-oxo)Tris[(μ2-peroxo)] triiron(III) cluster, *Proc. Natl. Acad. Sci. U. S. A.*, 2017, **114**, 2580–2585.
4 J. D. López-Castro, J. J. Delgado, J. A. Perez-Omil, N. Gálvez, R. Cuesta, R. K. Watt and J. M. Domínguez-Vera, A new approach to the ferritin iron core growth: influence of the H/L ratio on the core shape, *Dalton Trans.*, 2012, **41**, 1320–1324.
5 C. Quintana, J. M. Cowley and C. Marhic, Electron nanodiffraction and high-resolution electron microscopy studies of the structure and composition of physiological and pathological ferritin, *J. Struct. Biol.*, 2004, **147**, 166–178.
6 N. Gálvez, B. Fernández, P. Sánchez, R. Cuesta, M. Ceolín, M. Clemente-León, S. Trasobares, M. López-Haro, J. J. Calvino, O. Stéphan and J. M. Domínguez-Vera, Comparative Structural and Chemical Studies of Ferritin Cores with Gradual Removal of their Iron Contents, *J. Am. Chem. Soc.*, 2008, **130**, 8062–8068.
7 P. Arosio, F. Carmona, R. Gozzelino, F. Maccarinelli and M. Poli, The importance of eukaryotic ferritins in iron handling and cytoprotection, *Biochem. J.*, 2015, **472**, 1–15.
8 G. Jutz, P. van Rijn, B. Santos Miranda and A. Böker, Ferritin: a versatile building block for bionanotechnology, *Chem. Rev.*, 2015, **115**, 1653–1701.
9 L. Li, C. J. Fang, J. C. Ryan, E. C. Niemi, J. A. Lebrón, P. J. Björkman, H. Arase, F. M. Torti, S. V. Torti, M. C. Nakamura and W. E. Seaman, Binding and uptake of H-ferritin are mediated by human transferrin receptor-1, *Proc. Natl. Acad. Sci. U. S. A.*, 2010, **107**, 3505–3510.
10 L. C. Montemiglio, C. Testi, P. Ceci, E. Falvo, M. Pitea, C. Savino, A. Arcovito, G. Peruzzi, P. Baiocco, F. Mancia, A. Boffi, A. des Georges and B. Vallone, Cryo-EM structure of the human ferritin-transferrin receptor 1 complex, *Nat. Commun.*, 2019, **10**, 1121.
11 M. Truffi, L. Fiandra, L. Sorrentino, M. Monieri, F. Corsi and S. Mazzucchelli, Ferritin nanocages: A biological platform for drug delivery, imaging and theranostics in cancer, *Pharmacol. Res.*, 2016, **107**, 57–65.
12 G. Ferraro, S. Ciambellotti, L. Messori and A. Merlino, Cisplatin Binding Sites in Human H-Chain Ferritin, *Inorg. Chem.*, 2017, **56**, 9064–9070.
13 G. Fracasso, E. Falvo, G. Colotti, F. Fazi, T. Ingegnere, A. Amalfitano, G. B. Doglietto, S. Alfieri, A. Boffi, V. Morea, G. Conti, E. Tremante, P. Giacomini, A. Arcovito and P. Ceci, Selective delivery of doxorubicin by novel stimuli-sensitive nano-ferritins overcomes tumor refractoriness, *J. Controlled Release*, 2016, **239**, 10–18.
14 E. Falvo, E. Tremante, R. Fraioli, C. Leonetti, C. Zamparelli, A. Boffi, V. Morea, P. Ceci and P. Giacomini, Antibody-drug conjugates: targeting melanoma with cisplatin encapsulated in protein-cage nanoparticles based on human ferritin, *Nanoscale*, 2013, **5**, 12278–12285.
15 W. Liu, Q. Lin, Y. Fu, S. Huang, C. Guo, L. Li, L. Wang, Z. Zhang and L. Zhang, Target delivering paclitaxel by ferritin heavy chain nanocages for glioma treatment, *J. Controlled Release*, 2019, **323**, 191–202.
16 S. Ciambellotti, A. Pratesi, M. Severi, G. Ferraro, E. Alessio, A. Merlino and L. Messori, The NAMI A - human ferritin system: a biophysical characterization, *Dalton Trans.*, 2018, **47**, 11429–11437.
17 J. C. Cutrin, D. Alberti, C. Bernacchioni, S. Ciambellotti, P. Turano, C. Luchinat, S. G. Crich and S. Aime, Cancer cell death induced by ferritins and the peculiar role of their labile iron pool, *Oncotarget*, 2018, **9**, 27974–27984.
18 D. E. J. G. J. Dolmans, D. Fukumura and R. K. Jain, Photodynamic therapy for cancer, *Nat. Rev. Cancer*, 2003, **3**, 380–387.
19 P.-C. Lo, M. S. Rodríguez-Morgade, R. K. Pandey, D. K. P. Ng, T. Torres and F. Dumoulin, The unique features and promises of phthalocyanines as advanced photosensitisers for photodynamic therapy of cancer, *Chem. Soc. Rev.*, 2020, **49**, 1041–1056.
20 G. Boccalini, L. Conti, C. Montis, D. Bani, A. Bencini, D. Berti, C. Giorgi, A. Mengoni and B. Valtancoli, Methylene blue-containing liposomes as new photodynamic anti-bacterial agents, *J. Mater. Chem. B*, 2017, **5**, 2788–2797.
21 Z. Zhen, W. Tang, C. Guo, H. Chen, X. Lin, G. Liu, B. Fei, X. Chen, B. Xu and J. Xie, Ferritin nanocages to encapsulate and deliver photosensitizers for efficient photodynamic therapy against cancer, *ACS Nano*, 2013, **7**, 6988–6996.
22 F. Yan, Y. Zhang, H. Yuan, M. K. Gregas and T. Vo-Dinh, Apoferritin protein cages: a novel drug nanocarrier for photodynamic therapy, *Chem. Commun.*, 2008, 4579–4581.
23 L. Li, S. Zhou, N. Lv, Z. Zhen, T. Liu, S. Gao, J. Xie and Q. Ma, Photosensitizer-Encapsulated Ferritins Mediate Photodynamic Therapy against Cancer-Associated Fibroblasts and Improve Tumor Accumulation of Nanoparticles, *Mol. Pharm.*, 2018, **15**, 3595–3599.
24 Z. Zhen, W. Tang, W. Zhang and J. Xie, Folic acid conjugated ferritins as photosensitizer carriers for photodynamic therapy, *Nanoscale*, 2015, **7**, 10330–10333.
25 M. Liu, Y. Zhu, T. Wu, J. Cheng and Y. Liu, Nanobody-Ferritin Conjugate for Targeted Photodynamic Therapy, *Chemistry*, 2020, **26**, 7442–7450.
26 C. Mari, V. Pierroz, R. Rubbiani, M. Patra, J. Hess, B. Spingler, L. Oehninger, J. Schur, I. Ott, L. Salassa, S. Ferrari and G. Gasser, DNA intercalating Ru(II) polypyridyl complexes as effective photosensitizers in photodynamic therapy, *Chemistry*, 2014, **20**, 14421–14436.
27 S. Monro, K. L. Colón, H. Yin, J. Roque, P. Konda, S. Gujar, R. P. Thummel, L. Lilge, C. G. Cameron and S. A. McFarland, Transition Metal Complexes and

Photodynamic Therapy from a Tumor-Centered Approach: Challenges, Opportunities, and Highlights from the Development of TLD1433, *Chem. Rev.*, 2019, **119**, 797–828.

28 G. E. Giacomazzo, L. Conti, A. Guerri, M. Pagliai, C. Fagorzi, P. S. Sfragano, I. Palchetti, G. Pietraperzia, A. Mengoni, B. Valtancoli and C. Giorgi, Nitroimidazole-Based Ruthenium(II) Complexes: Playing with Structural Parameters to Design Photostable and Light-Responsive Antibacterial Agents, *Inorg. Chem.*, 2021, DOI: 10.1021/acs.inorgchem.1c03032.

29 D. M. Monti, G. Ferraro and A. Merlino, Ferritin-based anticancer metallodrug delivery: Crystallographic, analytical and cytotoxicity studies, *Nanomedicine*, 2019, **20**, 101997.

30 X. Li, Y. Zhang, H. Chen, J. Sun and F. Feng, Protein Nanocages for Delivery and Release of Luminescent Ruthenium(II) Polypyridyl Complexes, *ACS Appl. Mater. Interfaces*, 2016, **8**, 22756–22761.

31 L. Conti, A. Bencini, C. Ferrante, C. Gellini, P. Paoli, M. Parri, G. Pietraperzia, B. Valtancoli and C. Giorgi, Highly Charged Ruthenium(II) Polypyridyl Complexes as Effective Photosensitizer in Photodynamic Therapy, *Chemistry*, 2019, **25**, 10606–10615.

32 L. Conti, A. Mengoni, G. E. Giacomazzo, L. Mari, M. Perfetti, C. Fagorzi, L. Sorace, B. Valtancoli and C. Giorgi, Exploring the potential of highly charged Ru(II)- and heteronuclear Ru(II)/Cu(II)-polypyridyl complexes as antimicrobial agents, *J. Inorg. Biochem.*, 2021, **220**, 111467.

33 L. Conti, L. Mummolo, G. M. Romano, C. Giorgi, G. E. Giacomazzo, L. Prodi and A. Bencini, Exploring the Ability of Luminescent Metal Assemblies to Bind and Sense Anionic or Ionizable Analytes A Ru(phen)2bipy-Based Dizinc Complex for Bisphenol A (BPA) Recognition, *Molecules*, 2021, **26**, 527.

34 J. Zhang, D. Cheng, J. He, J. Hong, C. Yuan and M. Liang, Cargo loading within ferritin nanocages in preparation for tumor-targeted delivery, *Nat. Protoc.*, 2021, **16**, 4878–4896.

35 R. R. Crichton and C. F. A. Bryce, Subunit interactions in horse spleen apoferritin. Dissociation by extremes of pH, *Biochem. J.*, 1973, **133**, 289–299.

36 C. T. Lin, W. Boettcher, M. Chou, C. Creutz and N. Sutin, Mechanism of the quenching of the emission of substituted polypyridineruthenium(II) complexes by iron(III), chromium(III), and europium(III) ions, *J. Am. Chem. Soc.*, 1976, **98**, 6536–6544.

37 G. Petruk, D. M. Monti, G. Ferraro, A. Pica, L. D'Elia, F. Pane, A. Amoresano, J. Furrer, K. Kowalski and A. Merlino, Encapsulation of the Dinuclear Trithiolato-Bridged Arene Ruthenium Complex Diruthenium-1 in an Apoferritin Nanocage: Structure and Cytotoxicity, *ChemMedChem*, 2019, **14**, 594–602.

38 S. Stefanini, E. Chiancone and E. Antonini, Iron binding to apoferritin: a fluorescence spectroscopy study, *FEBS Lett.*, 1976, **69**, 90–94.

39 J. Michon, S. Frelon, C. Garnier and F. Coppin, Determinations of uranium(VI) binding properties with some metalloproteins (transferrin, albumin, metallothionein and ferritin) by fluorescence quenching, *J. Fluoresc.*, 2010, **20**, 581–590.

40 A. Vignoli, V. Ghini, G. Meoni, C. Licari, P. G. Takis, L. Tenori, P. Turano and C. Luchinat, High-Throughput Metabolomics by 1D NMR, *Angew. Chem., Int. Ed.*, 2019, **58**, 968–994.

41 P. G. Takis, V. Ghini, L. Tenori, P. Turano and C. Luchinat, Uniqueness of the NMR approach to metabolomics, *TrAC, Trends Anal. Chem.*, 2019, **120**, 115300.

42 C. Pozzi, F. Di Pisa, C. Bernacchioni, S. Ciambellotti, P. Turano and S. Mangani, Iron binding to human heavy-chain ferritin, *Acta Crystallogr., Sect. D: Biol. Crystallogr.*, 2015, **71**, 1909–1920.

43 A. A. Abdel-Shafi, M. D. Ward and R. Schmidt, Mechanism of quenching by oxygen of the excited states of ruthenium (II) complexes in aqueous media. Solvent isotope effect and photosensitized generation of singlet oxygen, O2(1Deltag), by [Ru(diimine)(CN)4]2- complex ions, *Dalton Trans.*, 2007, 2517–2527.

44 D. Maggioni, M. Galli, L. D'Alfonso, D. Inverso, M. V. Dozzi, L. Sironi, M. Iannacone, M. Collini, P. Ferruti, E. Ranucci and G. D'Alfonso, A luminescent poly(amido-amine)-iridium complex as a new singlet-oxygen sensitizer for photodynamic therapy, *Inorg. Chem.*, 2015, **54**, 544–553.

45 S. Takizawa, R. Aboshi and S. Murata, Photooxidation of 1,5-dihydroxynaphthalene with iridium complexes as singlet oxygen sensitizers, *Photochem. Photobiol. Sci.*, 2011, **10**, 895–903.

46 A. Gollmer, J. Arnbjerg, F. H. Blaikie, B. W. Pedersen, T. Breitenbach, K. Daasbjerg, M. Glasius and P. R. Ogilby, Singlet Oxygen Sensor Green®: photochemical behavior in solution and in a mammalian cell, *Photochem. Photobiol.*, 2011, **87**, 671–679.

47 T. Entradas, S. Waldron and M. Volk, The detection sensitivity of commonly used singlet oxygen probes in aqueous environments, *J. Photochem. Photobiol., B*, 2020, **204**, 111787.

48 C. Lodeiro, A. J. Parola, F. Pina, C. Bazzicalupi, A. Bencini, A. Bianchi, C. Giorgi, A. Masotti and B. Valtancoli, Protonation and Zn(II) coordination by dipyridine-containing macrocycles with different molecular architecture. A case of pH-controlled metal jumping outside-inside the macrocyclic cavity, *Inorg. Chem.*, 2001, **40**, 2968–2975.

49 E. Ravera, S. Ciambellotti, L. Cerofolini, T. Martelli, T. Kozyreva, C. Bernacchioni, S. Giuntini, M. Fragai, P. Turano and C. Luchinat, Solid-State NMR of PEGylated Proteins, *Angew. Chem., Int. Ed.*, 2016, **55**, 2446–2449.

50 S. Zanzoni, K. Pagano, M. D'Onofrio, M. Assfalg, S. Ciambellotti, C. Bernacchioni, P. Turano, S. Aime, L. Ragona and H. Molinari, Unsaturated Long-Chain Fatty Acids Are Preferred Ferritin Ligands That Enhance Iron Biomineralization, *Chemistry*, 2017, **23**, 9879–9887.

INORGANIC CHEMISTRY
FRONTIERS

RESEARCH ARTICLE

View Article Online
View Journal

Cite this: DOI: 10.1039/d2qi02678c

Ruthenium(II) polypyridyl complexes with π-expansive ligands: synthesis and cubosome encapsulation for photodynamic therapy of non-melanoma skin cancer†

Gina Elena Giacomazzo,‡[a] Michele Schlich, ‡[b] Luca Casula, ‡[b] Luciano Galantini, [c,d] Alessandra Del Giudice, [c,d] Giangaetano Pietraperzia,[a,e] Chiara Sinico,[b] Francesca Cencetti, [f] Sara Pecchioli, [f] Barbara Valtancoli,[a] Luca Conti, *[a] Sergio Murgia *[b,d] and Claudia Giorgi *[a]

In photodynamic therapy (PDT), Ru(II) polypyridyl complexes (RPCs) featuring the popular π-expansive benzo[*i*]dipyrido[3,2-*a*:2′,3′-*c*]phenazine (dppn) ligand have attracted much attention, mainly due to the good singlet oxygen sensitizing properties imparted by this peculiar ligand. However, notwithstanding the intriguing perspectives, much remains to be explored about the use of RPC-based photosensitizing agents (PSs) with more than a dppn ligand in their scaffolds. Herein, two bis-heteroleptic RPCs of the general formula $[Ru(dppn)_2L]^{n+}$ (L = 4,4′-dimethyl-2,2′-bipyridine, *n* = 2, **Ru1** or 2,2′-bipyridine-4,4′-dicarboxylate, *n* = 0, **Ru2**) were prepared in good yields by adopting an alternative synthetic approach to previously reported methods. The optimal singlet oxygen sensitizing properties and capabilities to interact with DNA displayed by **Ru1** and **Ru2** were paralleled by a potent light-triggered toxicity (λ_{max} = 462 nm) exerted on squamous epithelial carcinoma cells. To improve the biopharmaceutical properties of these compounds, **Ru1** and **Ru2** were encapsulated into cubosomes, soft nanoparticles with a lyotropic liquid crystalline core. *In vitro* studies probed the effectiveness of these formulations against light-irradiated cancer cells and confirmed intracellular ROS generation as the mechanism likely to be responsible for the observed PDT efficacy. This work highlights the potential of $[Ru(dppn)_2L]$-based PSs in PDT, beyond providing a general and straightforward synthetic route for the preparation of this class of compounds. To the best of our knowledge, this is also the first example of the encapsulation of a RPC into cubosome nanostructures, paving the way for the development of nano-formulations with augmented biopharmaceutical properties for PDT application.

Received 16th December 2022,
Accepted 6th April 2023

DOI: 10.1039/d2qi02678c

rsc.li/frontiers-inorganic

Introduction

Photodynamic therapy (PDT) continues to attract increasing attention thanks to the encouraging results that its application has led to the treatment of a variety of cancers, spanning from skin tumors to lung, bladder and prostate cancers,[1,2] as well as bacterial infections.[3,4] The main advantage of this therapeutic approach, which consists of the light activation of a prodrug, called a photosensitizer (PS), to produce harmful reactive oxygen species (ROS), is represented by the complete spatio-temporal control over drug activation, which provides a precious chance to limit the severe side effects normally occurring with standard chemotherapeutics.

Ruthenium(II) polypyridyl complexes (RPCs) have been largely employed in the research of suitable PSs in PDT, with the Mc Farland compound TLD1433 being the first Ru(II)-based PS to enter human clinical trials for bladder cancer.[5–8]

[a]*Department of Chemistry "Ugo Schiff", University of Florence, Via della Lastruccia 3, 50019 Sesto Fiorentino (FI), Italy. E-mail: luca.conti@unifi.it, claudia.giorgi@unifi.it*
[b]*Department of Life and Environmental Sciences, University of Cagliari, 09124 Cagliari (CA), Italy. E-mail: murgias@unica.it*
[c]*Department of Chemistry, University of Rome La Sapienza, P.le A. Moro 5, 00185 Rome, Italy*
[d]*CSGI, Consorzio Interuniversitario per lo Sviluppo dei Sistemi a Grande Interfase, 50019 Sesto Fiorentino (FI), Italy*
[e]*European Laboratory for Non-Linear Spectroscopy (LENS), Via Nello Carrara 1, 50019 Sesto Fiorentino (FI), Italy*
[f]*Department of Experimental and Clinical Biomedical Sciences "Mario Serio", 50134 Florence, Italy*

† Electronic supplementary information (ESI) available: Methods, supplementary figures and schemes, and the spectra of compounds. See DOI: https://doi.org/10.1039/d2qi02678c

‡ These authors contributed equally.

The interest towards this versatile class of compounds can be attributed to its rich chemical–physical repertoire, which includes a variety of excited-state electronic configurations accessible with light, good singlet oxygen sensitizing properties, and the capacity to interact with key biological targets (such as DNA or proteins).[9–11] Of relevance is that a fine choice of ligands in their octahedral geometries permits convenient modulation of the photophysical, photochemical, and photobiological properties of the resulting RPCs, in an effort to improve cellular uptake,[12,13] shift the absorption profiles towards red,[14] confer targeting ability,[15,16] and boost $^1O_2$ sensitization. With regard to the latter aim, as prolonged excited state lifetimes are important for efficient energy transfer to molecular oxygen to form $^1O_2$, changing the nature of the lowest-lying excited state from metal-to-ligand charge-transfer (^{3}MLCT) to long-lived intraligand ^{3}IL states represents a suitable way to endow the resulting RPCs with augmented cytotoxicity.[6,17] Following this strategy, over the past few years much interest has been devoted to the use of the π-expansive benzo[*i*]dipyrido[3,2-*a*:2′,3′-*c*]phenazine (dppn) ligand in the rational design of RPC-based PSs. Indeed, this peculiar ligand has been largely exploited not only to improve the photobiological activity of the resulting compounds, *via* the population of long-lived dppn-centered $^3\pi\pi^*$ excited states, but also to shift their ^{1}MLCT absorption towards longer wavelengths[18] and, given its known DNA-intercalating properties, to strengthen their interaction with the nucleic acid.[19–21] A recent example of this was reported by Zhao and coworkers, who showed the benefits derived from the substitution of a bpy (bipyridine) unit by a dppn ligand in their tris-heteroleptic RPC-based PSs.[22]

Notwithstanding the advantages derived from the use of dppn, it is surprising that PSs containing two dppn ligands simultaneously coordinated to a Ru(II) center have been only sparingly explored,[23,24] while numerous examples of dppn-containing RPCs for PDT are reported in the literature[25–31] (some of them have also been applied for compounds at the boundary between PDT and photoactivated chemotherapy PACT).[32,33] Such net discrepancy between RPCs containing one and two dppn units would be related to synthetic issues concerning the preparation of the latter compounds by the general procedures for bis-heteroleptic Ru(II) complexes,[34,35] involving the intermediate [$(dppn)_2RuCl_2$] which is scarcely soluble in most organic solvents.

In addition, the potential anticancer activity of these systems might be limited by their common hydrophobic nature, leading to poor bioavailability and compromised therapeutic outcomes. To overcome these limits, nanocarriers have been widely investigated as a formative approach to increase the water solubility of insoluble drug candidates, prevent drug degradation, and enhance their delivery.[36–38] In the midst of the innovative exploited nano-systems, great interest has arisen around cubosomes, also known as bicontinuous cubic liquid crystalline nanoparticles with a three-dimensional arrangement of the lipid bilayer forming a honeycomb-like inner structure. Compared to single-bilayer liposomes, cubosomes are characterized by an inner portion completely filled with the lipid matrix, providing a greater hydrophobic volume and thus a higher loading efficiency.[39] Despite the fact that some investigations illustrated a possible cubosome cytotoxicity,[40,41] appropriate formulation strategies and administration at lower concentrations can be used to achieve the desired therapeutic effects. In fact, recent studies have proven their useful biomedical applications for diagnostic purposes, anticancer activity, and PDT.[42–46]

Prompted by this scenario, herein we explored the potential as PSs of two Ru(II) compounds featuring two dppn ligands simultaneously coordinated to the Ru(II) centers; [Ru$(dppn)_2(dmbpy)]^{2+}$ (**Ru1**) and [$Ru(dppn)_2(dcbpy^{2-})$] (**Ru2**) (dmbpy = 4,4′-dimethyl-2,2′-bipyridine, $dcbpy^{2-}$ = 2,2′-bipyridine-4,4′-dicarboxylate) (Chart 1). Besides the $Ru(dppn)_2$-core, different dmbpy and $dcbpy^{2-}$ ancillary ligands were chosen to provide a potential synthetic platform for obtaining differently functionalized $(dppn)_2$-RPCs, to investigate their possible influence on the chemical–physical and biological properties of the resulting compounds.

Ru1 and **Ru2** were prepared by adopting a straightforward synthetic route where the dppn ligands were allowed to react with Ru(II)-intermediates in the last step of the reaction, thus avoiding the use of [$Ru(dppn)_2Cl_2$] and leading to the production of RPCs in good yields. These systems exhibited promising features as PSs, by virtue of optimal singlet oxygen sensitizing properties and capacity to interact with DNA, and for this reason their phototoxicity and biocompatibility were tested on non-melanoma skin cancer cells *in vitro*, a model tumor selected for the feasibility of its treatment by photodynamic therapy.[47] To further ascertain their potential as PSs, **Ru1** and **Ru2** were also encapsulated in monoolein-based cubosomes stabilized with Pluronic F108. Following a preliminary investigation of the obtained formulations, **Ru2-cubo** was then selected for further development including a thorough physicochemical characterization and the assessment of its phototoxic activity against epidermoid carcinoma cells.

The results herein discussed may provide fundamental knowledge for the design of novel and highly performant PSs

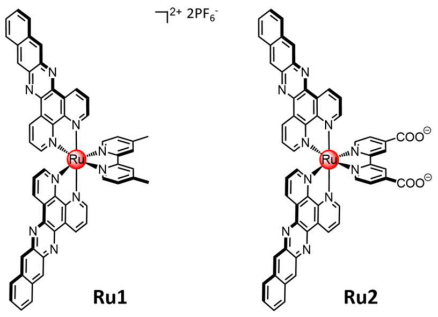

Chart 1 Chemical structures of ruthenium complexes **Ru1** and **Ru2** of this study.

based on $(dppn)_2$-containing RPCs. Moreover, to the best of our knowledge, this study reports the first example of the encapsulation of a RPC into cubosome nanostructures, thus paving the way for the development of pharmaceutically viable nano-formulations for PDT applications.

Results and discussion

Synthesis and characterization of ruthenium compounds

Ru(II) complexes **Ru1** and **Ru2** were obtained *via* stepwise ligand addition following the synthetic route shown in Scheme 1c. In this synthetic approach, the polymeric precursor $[Ru(CO)_2Cl_2]_n$ was first prepared by the reaction of the commercial $RuCl_3{\cdot}nH_2O$ with paraformaldehyde in formic acid. Then, this compound was allowed to react with the bidentate ligands in refluxing methanol (dmbpy) or DMF (dcbpy), affording the *trans*-Cl[Ru(dmbpy)$(CO)_2Cl_2$] and *trans*-Cl[Ru(dcbpy)$(CO)_2Cl_2$] intermediates, with yields of 75 and 55%, respectively. In the latter case, DMF was chosen as the solvent because of the limited solubility of dcbpy in methanol.[48] Finally, two equivalents of dppn ligands were added to solutions of the *trans*-Cl[RuL$(CO)_2Cl_2$] (L = 4,4′-dimethyl-2,2′-bipyridine or dmbpy, 2,2′-bipyridine-4,4′-dicarboxylic acid or dcbpy) intermediates in 2-methoxyethanol, and in the presence of trimethylamine *N*-oxide (TMAO), to favour the detachment of the strongly coordinated CO ligands[49] and allow their replacement by the bidentate dppn ligands. The addition of aqueous KPF_6 led to the precipitation of the hexafluorophosphate salt of **Ru1** whereas **Ru2** precipitated as a neutral product from the reaction mixture. **Ru1** and **Ru2** were obtained, after purification by flash chromatography, in 78% and 50% yields, respectively. The identity of the obtained compounds was confirmed by ^1H, ^{13}C, COSY and HSQC NMR and high-resolution mass spectrometry (HR-MS) analysis (see the ESI, Fig. S1–S10†). ^1H NMR signal assignment is reported in the ESI;† recording of ^{13}C and HSQC spectra of **Ru2** was prevented by its poor solubility in $(CD_3)_2SO$.

As shown in Scheme 1, it can be highlighted that, compared to the most employed synthetic approach used for the preparation of bis-heteroleptic complexes with the general formula $[Ru(NN)_2L]^{2+}$ (*N*,*N* = polypyridyl bidentate ligand)[50,51] (Scheme 1a), commonly obtained by the reaction of $[Ru(NN)_2Cl_2]$ with a third chelate ligand (L), in the method of this work the two dppn ligands are allowed to react with the Ru(II)-scaffolds only in the last step of the reaction. This would permit to overcome solubility issues arising from the use of the $[Ru(dppn)_2Cl_2]$ intermediate. A similar "*reverse*" concept was also previously applied by Turro and coworkers in the synthesis of a rare example of a $(dppn)_2$-containing RPC reported in the literature, namely $[Ru(bpy)(dppn)_2][PF_6]_2$,[24] which was indeed obtained by the reaction of dppn with $[Ru(bpy)(CH_3CN)_4]^{2+}$ in the last reaction step (Scheme 1b). However, long reaction times (in the order of 7–24 days) were required by this route to prepare the intermediate $[Ru(bpy)(CH_3CN)_4]^{2+}$ using $RuCl_3{\cdot}nH_2O$ as the starting material.[52,53]

In light of these considerations, the synthetic strategy employed in this work may provide an alternative and straightforward way for the preparation of RPCs featuring the general formula $[Ru(dppn)_2L]^{n+}$ (L = variously functionalized bidentate polypyridyl chelates), in good yields and reaction times.

The electronic absorption spectra of **Ru1** and **Ru2** in acetonitrile are shown in Fig. 1a, whereas their molar extinction coefficients (ε) at different absorption maxima (λ_{max}) are listed

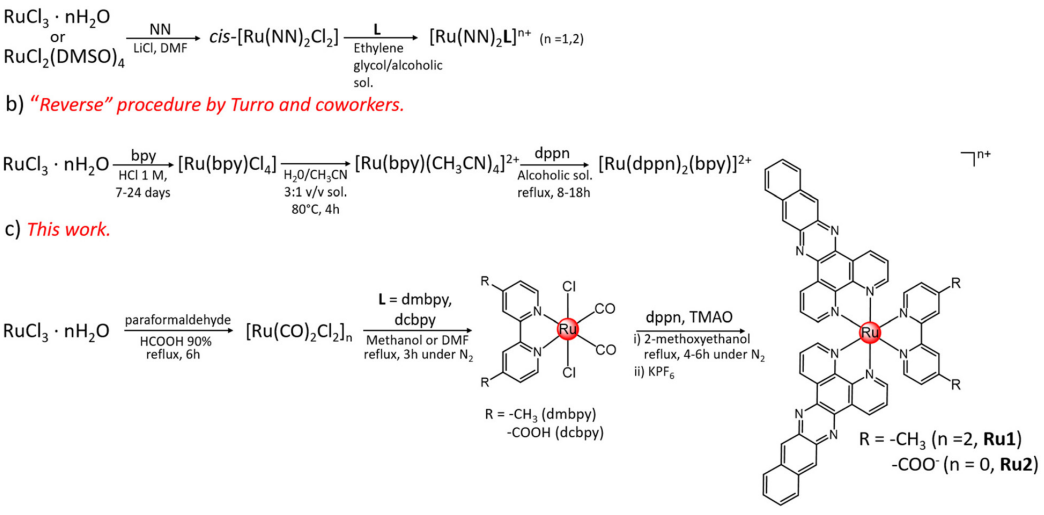

Scheme 1 Synthetic route followed for the preparation of complexes **Ru1** and **Ru2** of this work (3c), compared to the one generally employed for the preparation of bis-heteroleptic RPCs (3a) and to the one previously reported for the Turro's compounds $[Ru(bpy)(dppn)_2][PF_6]_2$ and $[Ru(phpy)(dppn)_2][PF_6]$ (3b).

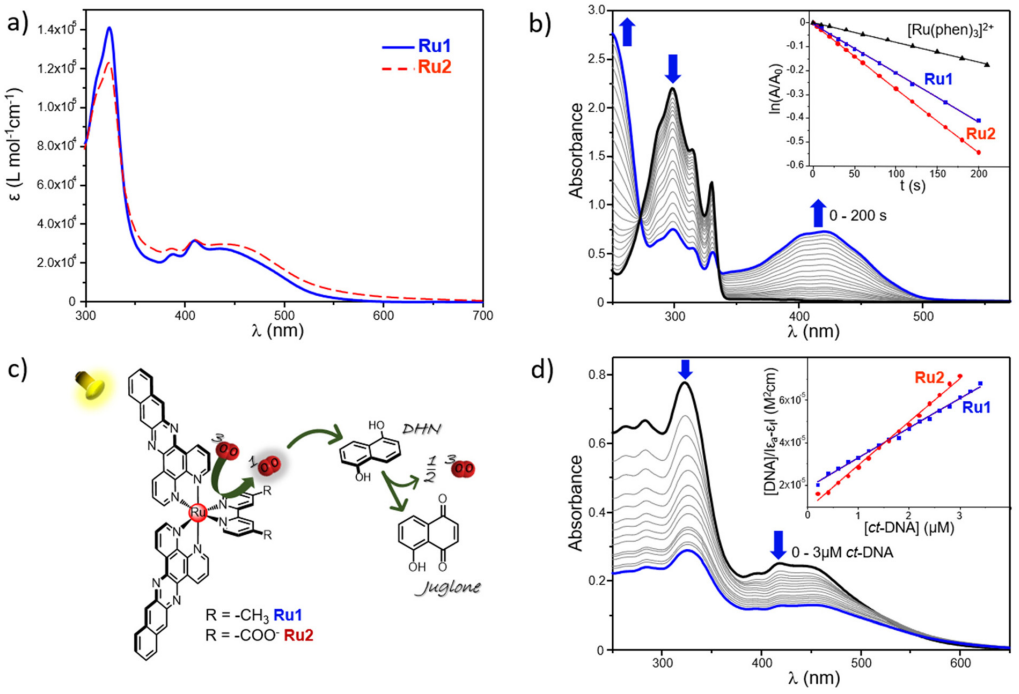

Fig. 1 Electronic absorption spectra of **Ru1** and **Ru2** in acetonitrile (a). Singlet oxygen determination as evaluated through UV-Vis analysis by using DHN as an indirect $^1O_2$ reporter; in the inset are compared the semilogarithmic plots of $\ln(A/A_0)$ as a function of the irradiation time registered for **Ru1** and **Ru2** and $[Ru(phen)_3]^{2+}$ as the reference control ([DHN] = 3.3 × 10^{-4} M, [**Ru1**] = [**Ru2**] = 10 μM) (b). Sketch of the $^1O_2$ determination by employing DHN as an indirect probe for $^1O_2$ (c). Absorption spectra of aqueous solutions of **Ru1** registered in the presence of increasing concentrations of *ct*-DNA; in the inset are reported the $[DNA]/|\varepsilon_a - \varepsilon_f|$ values obtained for **Ru1** and **Ru2** *versus* the molar concentration of DNA ([**Ru1**] = [**Ru2**] = 10 μM, TRIS buffer pH 7.4) (d).

Table 1 Electronic absorption maxima measured in acetonitrile, rate constants K_{obs}, quantum yields for $^1O_2$ generation (ϕ_Δ) and binding constants with *ct*-DNA (K_b) of ruthenium complexes of this study

Compound	λ_{abs} nm^{-1} ($\varepsilon \times 10^3$ M^{-1} cm^{-1})[a]	K_{obs}[a]	ϕ_Δ ($^1O_2$)[b]	K_b ($\times 10^6$ M^{-1})	pK_a
Ru1	324 (146.1), 387 (25.3), 409 (32.2), 440 (26.6)	1.85×10^{-3}	0.54 ± 0.06	7.49×10^5	—
Ru2	323 (123.2), 387 (27.8), 410 (32.4), 445 (30.0)	2.71×10^{-3}	0.50 ± 0.07	2.34×10^6	pK_{a1}; pK_{a2}° 3.6 ± 0.3, pK_{a2}^* 4.6 ± 0.4

[a] Determined in acetonitrile. [b] Determined for air-saturated acetonitrile solutions of Ru(II) complexes.

in Table 1. As shown, besides the intense intraligand π → π* transitions at 280–330 nm, both complexes display a double humped absorption at ~387 and ~410 nm, which is typical of the dppn centered π → π* transitions, plus a broad ^{1}MLCT absorption centered at ~445 nm, in good agreement with those of dppn-containing RPCs reported in the literature.[24,54] It can also be noted that the absorptions relative to the dppn-centered transitions of **Ru1** and **Ru2** are more intense than the corresponding ones reported for the parental compound $[Ru(bpy)_2dppn]^{2+}$,[24] as expected due to the presence of two dppn units in their Ru(II) scaffolds. On the other hand, **Ru1** and **Ru2** resulted to be weakly luminescent, with the highest emission being displayed by **Ru2** in acetonitrile and ethanol (Fig. S11, ESI†).

Finally, given the presence of the ionizable dcbpy ligand in **Ru2**, the acid–base behavior of this complex in water was examined by means of spectrophotometric titrations, as described in the ESI.† Similar to what was previously reported for a parental dcbpy-containing Ru(II) complex,[55] of the two possible protonation equilibria only pK_{a2} values of 3.6 ± 0.3 and 4.6 ± 0.4, respectively, for the ground (pK_{a2}°) and the excited state (pK_{a2}^*) (Table 1) were determined by these measurements. This, along with the presence of two inflection points in the fluorescence titrations, suggested that the first

pK_a value was too low to be accurately determined. The higher value found for pK_{a2}^* relative to pK_{a2}° would be in line with the higher basicity of the complex in the excited state. It should also be noted that these data confirm that the carboxylic functions of **Ru2** are likely to be fully deprotonated at neutral pH, conferring an overall total neutral charge to the complex. Therefore, along with the different nature of their ancillary ligands, it can be envisaged that the different charges of metal complexes in physiological media (+2 for **Ru1**, 0 for **Ru2**) might have an influence on their biological behavior and interaction with cubosome nanostructures (*vide infra*).

Singlet oxygen sensitizing properties of Ru(II)-complexes and DNA interaction

A crucial requisite for a candidate PS for PDT applications relies on its ability to trigger the formation of harmful reactive species under light-irradiation, such as the highly oxidant singlet oxygen $^1O_2$, the classical warhead of PDT produced as the result of *type*-II-based pathways.[56]

The singlet oxygen sensitizing properties of Ru(II) complexes **Ru1** and **Ru2** were first assessed spectrophotometrically, by employing 1,5-dihydroxynaphtalene (DHN) as an indirect reporter for singlet oxygen. Indeed, in the presence of $^1O_2$, DHN is promptly and quantitatively oxidized to give 5-hydroxy-1,4-naphthalenedione (Juglone), thus allowing to easily follow the photoexcitation process by monitoring the decrease of the DHN absorption band, centered at 297 nm, and the simultaneous increase of the broad Juglone band at around 427 nm (see Fig. 1c for a schematic illustration of the $^1O_2$ analysis by the DHN method for **Ru1** and **Ru2** complexes).

Fig. 1b shows the absorption spectra of an acetonitrile solution containing **Ru1** and DHN subjected to increasing irradiation times (LED emitting at 434 nm, 160 mW), light-exposure determined the progressive decrease of the DHN absorption band along with the simultaneous increase of that of Juglone, thus clearly demonstrating the photosensitizing properties of **Ru1**. It should also be noted that the appearance of two clear isosbestic points in the UV-Vis titration, at ~280 and 330 nm, ruled out the formation of long-lived intermediates or byproducts. An analogous behavior was displayed by **Ru2**, as reported in Fig. S13 of the ESI.† Compared to [Ru(phen)$_3$]$^{2+}$, taken as a reference RPC for $^1O_2$ sensitization, both **Ru1** and **Ru2** exhibited remarkably higher photosensitizing features. This can be easily appreciated from the corresponding semilogaritmic plots of ln(A/A_o) over the irradiation time frame (A_0 and A are the absorbance values at 297 nm at time "*zero*" and at a generic time "*t*") reported in the inset of Fig. 1b, in which can be evidenced, for example, that a similar amount of $^1O_2$ was produced within 65–75 s by **Ru1** and **Ru2**, and in more than 200 s by [Ru(phen)$_3$]$^{2+}$. In detail, **Ru1** and **Ru2** displayed a comparable potency, as denoted by the slight differences emerging between their relative rate constants for the DHN photooxidation processes (k_{obs}), of 1.85×10^{-3} and 2.71×10^{-3}, respectively (Table 1). In addition to the indirect DHN method, the $^1O_2$ sensitizing properties of **Ru1** and **Ru2** were further probed through direct measurement of the phosphorescence signal of $^1O_2$ at 1270 nm, induced by irradiation of air-saturated acetonitrile solutions of ruthenium complexes. This allowed us to determine the relative quantum yields of $^1O_2$ generation (ϕ_Δ), which are listed, along with the one of [Ru(phen)$_3$]$^{2+}$ for comparison (ϕ_Δ = 0.38 ± 0.06), in Table 1. As shown, ϕ_Δ values of 0.54 ± 0.06 and 0.50 ± 0.07 were respectively obtained for **Ru1** and **Ru2**, thus confirming that the simultaneous presence of two dppn units into the Ru(II) scaffolds confers to these complexes a potent and comparable ability to sensitize the formation of singlet oxygen, in well agreement with the results of the UV-Vis analysis.

Since it is known that $^1O_2$ rapidly reacts with the surrounding biological substrates (estimated half-life <40 ns, range of action in the order of 20 nm),[57] leading to an extremely localized oxidative damage, the ability of a PS to effectively interact with a desired biological target may be important for its potential application in PDT, as it would ensure drug localization in close proximity to the target to be treated, strengthening the oxidative damage induced by ROS sensitization. This, along with the known DNA intercalating properties imparted by the π-expansive dppn ligands, prompted us to consider the affinity of the studied RPCs with the nucleic acid. The DNA-binding abilities of **Ru1** and **Ru2** were evaluated on *calf thymus* (*ct*-DNA) through UV-Vis analysis, by monitoring the changes in the absorption profiles of the aqueous solution of RPCs buffered at pH 7.4 induced by increasing concentrations of *ct*-DNA. As shown in Fig. 1d for a 10 μM solution of **Ru1**, the addition of *ct*-DNA resulted in a strong hypochromism in both the MLCT and $\pi \rightarrow \pi^*$ absorption bands of the metal complex, with a reduction of approximately 50 and 65% of their relative intensities in the presence of only 3 μM DNA. No blue or red shift was observed upon the addition of DNA and a very similar trend was also observed in the case of **Ru2** (see Fig. S14, ESI†). The intrinsic binding constants (K_b) of **Ru1** and **Ru2** were calculated from titration data (see the inset of Fig. 1d for a comparison between the two RPCs) as described in the ESI† and the resulting values are reported in Table 1. As shown, K_b values of 7.49×10^5 M^{-1} and 2.34×10^6 M^{-1} were respectively obtained for **Ru1** and **Ru2**, thus confirming the ability of these systems to strongly interact with DNA under abiotic conditions. It can be noted that these values are in line with the ones reported for other dppn-containing ruthenium complexes (K_b in the order of 10^6 M^{-1})[54,58,59] and though not conclusive, together with the large extent of hypochromism observed, they hint at the intercalation as the most likely binding mode for these complexes. Moreover, the possible beneficial role played by the presence of a second dppn ligand in strengthening the interaction of complexes with the biopolymer is particularly evidenced by comparing **Ru1** with its mono-dppn containing analogue, [Ru(dmbpy)(dppn)]$^{2+}$, for which a lower K_b, of almost 5.8-fold has been reported.[28]

Cytotoxicity and photoactivity of Ru(II)-complexes

To be qualified as a potential agent for photodynamic therapy, newly developed photosensitizers should be biologically inert in the dark, but highly cytotoxic when exposed to light of a

given wavelength.[60] This simple mechanism allows for selective action against the light-exposed area (*i.e.* the tumor), abolishing the systemic toxicity typically associated with traditional chemotherapeutic drugs.[46] Here, the anticancer activity of **Ru1** and **Ru2** was evaluated on A431 cells, an *in vitro* model of human epidermoid carcinoma.

As shown in Fig. 2, both compounds were found to be well tolerated by cells when no light was provided to the culture dishes. A slight difference between their *in dark* toxicities was observed, thus indicating that seemingly small modifications on the groups gathered on the bpy moieties of complexes (methyl or carboxylic functions) may influence their toxicity. In details, cell viability was reduced to 75.1 ± 4.1% and 82.4 ± 2.0% upon exposure to the highest dose of **Ru1** and **Ru2** (25 μM) in the dark, respectively. Conversely, 30-minutes of irradiation with an LED array (λ_{max} = 462 nm, 18 mW cm^{-2}) induced potent activation of the complexes, triggering complete cell death (viability < 10%) at concentrations of 0.25 μM (**Ru1**, Fig. 2a) and 5 μM (**Ru2**, Fig. 2b): Fig. 2c summarizes the IC_{50} values calculated from *in vitro* experiments. As shown, both **Ru1** and **Ru2** displayed high photo-toxic indexes (PI, defined as IC_{50} in the dark/IC_{50} upon irradiation), with values exceeding 988 and 130, respectively. From a translational point of view, higher PIs are predictive of a larger therapeutic window, with limited off-target cytotoxicity and enhanced on-target potency. Of note, notwithstanding the lack of data for the phototoxicity of dppn-containing Ru(II) complexes in A431 cells, it can be highlighted that the *in vitro* therapeutic outcomes of complexes of this study are ones of the highest among those reported in the literature for the PDT effect of dppn-containing RPCs.[23,25,61–63]

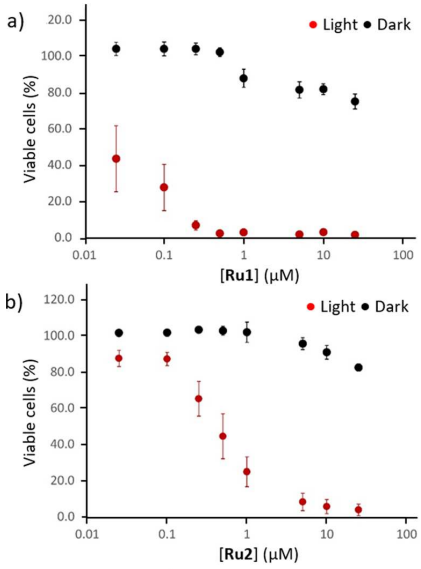

c)

	Light	Dark
IC_{50} **Ru1**	0.0253 ± 0.0107 μM	> 25 μM
IC_{50} **Ru2**	0.191 ± 0.023 μM	> 25 μM

Fig. 2 Viability of A431 epidermoid carcinoma cells assessed by MTT following treatments with **Ru1** (a) or **Ru2** (b), with or without exposure to light for 30 minutes (n = 5). Table summarizing the IC_{50} values (±SEM) for the different experimental groups (c).

Cubosome loading and characterization

The *in vitro* results highlighted the promising activity of the obtained systems in PDT. Nevertheless, their poor aqueous solubility would not be compatible with direct administration to a patient. In fact, self-aggregation phenomena might occur due to the high hydrophobicity of these systems, leading to low bioavailability, possible off-target activation and reduction of their photosensitivity and photophysical properties.[64] The encapsulation of PSs into nanocarriers is a well-known technique used to overcome these issues and to facilitate their biomedical application.[65] In this study, we prepared **Ru1** and **Ru2** cubosome-loaded formulations using monoolein (MO) as the molecular building block and PF108 as the stabilizing agent. In line with previous results,[66] the obtained samples were fluid aqueous dispersions with a milky macroscopic appearance. Cubosomes, here proposed as PS carriers, were prepared as described in paragraph 4.1 of the ESI† and characterized in terms of encapsulation efficiency and colloidal properties, namely size, size distribution and zeta potential.

Unencapsulated PSs were removed by exhaustive dialysis, then cubosomes were dissolved in methanol and the drug content was spectrophotometrically quantified. The results revealed high encapsulation values of **Ru2** (60%), whereas the amount of encapsulated **Ru1** was 9%. Besides their different structures, the two complexes also display different overall charges (at neutral pH **Ru1** features a double positive charge whereas **Ru2** is likely to be present in its neutral form) and this can be reasonably assumed to affect the encapsulation efficiency into cubosomes. Indeed, the production procedure and the excipients employed were identical for both formulations, the encapsulated PS being the sole difference.

As for the colloidal properties, DLS analysis revealed the presence of nanoparticles with an average diameter of approximately 138 and 142 nm, for **Ru1-cubo** and **Ru2-cubo** respectively (Fig. 3a). Both formulations showed a narrow size distribution with PDI values below 0.2. Concerning the nanoparticle zeta potential, we recorded a value of −9 mV for **Ru1-cubo** and −30 mV for **Ru2-cubo**, thus indicating a superior stabilization of the latter.

We monitored the average diameter, PDI and zeta potential over a period of 30 days, for a medium-term stability study of the colloidal systems (Fig. S16, ESI†). The size distribution study revealed optimal stability of **Ru2-cubo**, since the mean diameter did not vary appreciably during the 30 days on storage at 25 °C, with an average diameter of approximately 140 nm during the whole study. The PDI and zeta potential were almost constant, confirming the retention of the fairly narrow size distribution on storage. Conversely, the average

a)

	Composition (% w/w)					Characterization			
	MO	PF108	**Ru1**	**Ru2**	H_2O	D (nm)	PDI	ZP (mV)	EE %
Ru1-cubo	3.3	0.03	0.02	-	96.65	138 ± 2	0.11 ± 0.02	-13 ± 3	9 ± 3
Ru2-cubo	3.3	0.03	-	0.02	96.65	142 ± 1	0.13 ± 0.01	-30 ± 2	60 ± 5

b)

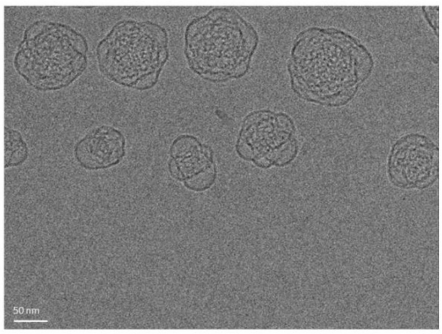

c)

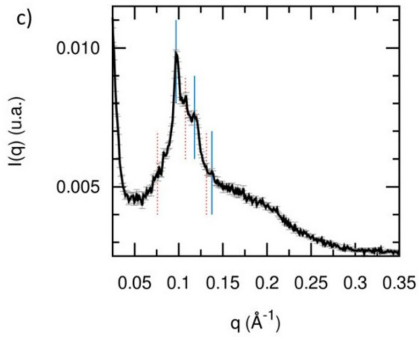

Fig. 3 **Ru1-cubo** and **Ru2-cubo** composition and characterization in terms of average diameter (*D*, nm), polydispersion index (PDI), zeta potential (ZP, mV) and encapsulation efficiency (EE%) (a). Cryo-transmission electron microscopy (b) and small angle X-ray scattering patterns of **Ru2-cubo** with indication of the Bragg peaks corresponding to the Im3 m (red dotted lines) and the Pn3 m (blue continuous lines) cubic bicontinuous phases (c).

diameter of **Ru1-cubo** increased from 138 nm (day 0) to 235 nm (day 30), the zeta potential moved to lower values, while PDI values were almost steady.

Given the obtained preliminary results of **Ru1-cubo**, namely, low encapsulation efficiency and an increase of the average diameter over 30 days of storage, we selected **Ru2-cubo** for further characterization and *in vitro* bioactivity tests. Firstly, we evaluated the nanoparticles morphology of **Ru2-cubo** by means of cryo-transmission electron microscopy (Cryo-TEM). As shown in Fig. 3b, cubosomes appear as spherical nanoparticles with an internal structure characterized by a dark matrix and bright spots, which represent the lipid phase and the water channels respectively. We then evaluated the inner nanostructure of **Ru2-cubo** through small angle X-ray scattering. Particularly, the recorded SAXS pattern shown in Fig. 3c strongly suggests the simultaneous presence of two bicontinuous cubic phases, the Pn3 m and the Im3 m, respectively characterized by lattice parameters of 92 ± 1 Å and 117 ± 1 Å and water channel radii of 38 ± 1 Å and 37 ± 1 Å. In fact, the coexistence of the two phases is often observed when MO cubosomes are stabilized with Pluronics.[66,67]

Cytotoxicity, photoactivity and ROS production of cubosomes-encapsulated Ru2

In addition to promoting solubility and stability, nanoencapsulation of photosensitizers in soft colloids has shown to improve the management of cancer in previous studies, as it allows targeted delivery and favors bio-membranes crossing.[68–71] When designing novel PS-loaded nanoparticles, it is critical to assess that the biological activity of the cargo is retained upon nano-encapsulation, and that no unspecific toxicity comes from the nanoparticle itself (*i.e.* empty vector). For such reasons, we tested the cytotoxicity (in the dark) and phototoxicity (upon LED illumination) of **Ru2-cubo** on the previously described epidermoid carcinoma model, comparing the results with the effect triggered by empty cubosomes (E-cubo, not loaded with PS). **Ru2-cubo** sensitized cancer cells to light even at a very low concentration of 0.025 μM ([**Ru2**]), with more than 50% reduction of cell viability at a dose of 0.25 μM (Fig. 4a). Calculated IC_{50} for **Ru2-cubo** was 0.268 ± 0.079 μM. The slightly higher IC_{50} of **Ru2-cubo** compared to free **Ru2** is expected for a nano-encapsulated molecule and can be partially explained by the lower intracellular localization of ruthenium, evidenced by inductively coupled plasma atomic emission spectrometry (ICP-AES), when entrapped in the soft lipid matrix (Fig. S17, ESI†). As expected, treatment with **Ru2-cubo** was efficacious only when coupled with LED irradiation, as cells incubated in the dark did not show signs of sufferance. The risk of unspecific toxicity of other components of the nanoformulation (*i.e.* monoolein and PF108) was ruled out by exposing cells to E-cubo under the same conditions (Fig. 4b).

To obtain preliminary information about the mechanism of the observed phototoxicity, we first investigated the production of intracellular ROS upon PDT using the 2′,7′-dichlorodihydro-

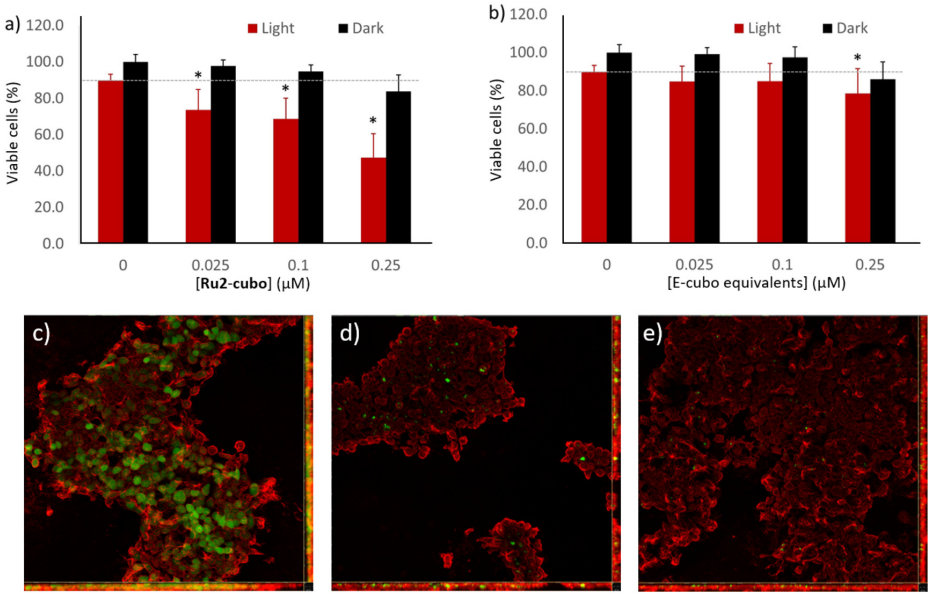

Fig. 4 Viability of A431 epidermoid carcinoma cells assessed by MTT following treatments with **Ru2-cubo** (a) or E-cubo (b), with or without exposure to light for 30 minutes. The dose is expressed as concentration of **Ru2** in the cell culture well or the corresponding volume of E-cubo. The dashed line is a guide for the eye to highlight the viability of cells exposed to light without PS. One way ANOVA with *post-hoc* Tukey HSD test was employed to substantiate differences between cells exposed only to light (no PS, 0 μM) *vs.* cells treated with **Ru2-cubo** or E-cubo and exposed to light (*$p < 0.01$) ($n = 8$). Production of ROS by A431 epidermoid carcinoma cells estimated by the oxidation of the DCF-DA sensor and visualized by confocal laser scanning microscopy (c–e). Cells treated with **Ru2-Cubo** (100 nM) and exposed to light for 10 minutes (c) or incubated in the dark (d). Untreated cells (e). The green signal corresponds to the sensor oxidized by intracellularly produced ROS to its fluorescent derivative DCF. Red signal shows the cell membranes stained with WGA. Scalebar = 50 μm.

fluorescein diacetate (DCFH-DA) assay.[72] When applied to the cell culture, the cell permeable probe DCFH-DA crosses the cell membrane and it is deacetylated by cytosolic esterases into a non-fluorescent metabolite (DCFH). In the presence of intracellular ROS, the metabolite can be oxidized to produce highly fluorescent 2′,7′-dichlorofluorescein (DCF). The amount of ROS produced by the cells in response to PDT can be estimated by measuring the green fluorescence intensity of DCF localized within the cell body.

A431 cells were treated with **Ru2-cubo**, supplied with the DCFH-DA probe and exposed to light to trigger the activation of the photosensitizer. The dose of **Ru2-cubo** (100 nM of **Ru2**) was selected to allow for the observation of ROS generation, limiting the extent of cell toxicity. Immediately after irradiation, cells were fixed, and their membranes were stained with WGA for microscopy observation. Representative images acquired by confocal laser scanning microscopy allow to observe a diffuse green fluorescence in almost 87.4% of the cells exposed **Ru2-cubo** + light (Fig. 4c). Conversely, the treatment with **Ru2-cubo** in the dark did not induce significant production of ROS, as the amount of green signal detectable (Fig. 4d) was comparable to the one observed in a well of untreated cells (control, Fig. 4e). More specifically, the percentage of ROS-producing cells calculated through image analysis was 1.3% and 0.3% for **Ru2-cubo** in the dark and for untreated cells, respectively.

We then inspected the intracellular distribution of **Ru2-cubo** into A431 cells by employing laser-scanning confocal microscopy (Fig. S18, ESI†). Despite the ability of the PS to bind DNA, our results indicated a modest localization of **Ru2-cubo** within the nuclei, at least after 1 hour of incubation of A431 cells. This was also observed for the non-encapsulated metal complex, thus suggesting that ROS oxidation of other types of macromolecules, such as proteins or membrane lipids, rather than DNA, is likely to be the cause of the observed phototoxicity under our experimental conditions. These oxidized species, in addition to losing their function, can initiate the pro-apoptotic and pro-necrotic cascade, resulting in cell damage and death.[73]

Interestingly, it can also be noted that, in contrast to the free metal complex, which, after 1 hour of incubation, evidenced a random distribution in the cellular cytosol, after the same incubation time **Ru2-cubo** was rather found to be finely localized in discrete areas.

Overall, these results confirm that the cytotoxic effect observed upon PDT with **Ru2-cubo** would be related to the capacity of this system to effectively trigger the production of intracellular ROS, as expected due to the good singlet oxygen sensitizing properties of **Ru2**.

Conclusions

In this study, we explored the potential as PSs for PDT applications of two novel Ru(II) complexes, **Ru1** and **Ru2**, characterized by two π-expansive dppn units simultaneously coordinated to their Ru(II) centers. The synthetic route followed for the preparation of these complexes may represent a valid alternative to commonly employed methods and can be potentially harnessed for the preparation of bis-heteroleptic RPCs of the general formula $[Ru(dppn)_2L]^{2+}$ (L = variously functionalized bpy ligands), whose chemical–physical and photobiological properties can be finely modulated by tuning the nature of their bidentate chelates. The simultaneous presence of two dppn ligands conferred to **Ru1** and **Ru2** optimal singlet oxygen sensitizing features and DNA-interaction capabilities, which were paralleled by a potent light-triggered toxicity exerted on squamous epithelial carcinoma cells, with PI values exceeding 988 (**Ru1**) and 130 (**Ru2**).

Given their scarce solubility in physiological media, which would preclude their direct administration for therapeutic use, **Ru1** and **Ru2** were encapsulated into cubosomes, chosen as soft nanoparticles to obtain Ru(II)-formulations with improved biopharmaceutical properties. Among the resulting hybrid systems, **Ru2-cubo** displayed superior encapsulation efficiency and stability as compared to **Ru1-cubo**, thus hinting at a subtle role played by the nature of the ancillary ligands and/or the overall charge of RPCs. For this reason, we focused our attention on the former system, which was further characterized and subjected to bioactivity investigations. Our results probed the effectiveness of **Ru2-cubo**, as denoted by the photoactivity observed even at a very low drug concentration, whereas mechanistic studies confirmed that intracellular ROS generation was likely responsible for the **Ru2-cubo**-mediated PDT efficacy.

An important aspect that deserves consideration is that soft matter nanoparticles are prone to phase transition/degradation when dispersed in fluids of biological interest.[74] However, several studies evidenced that monoolein-based cubosomes are rather stable when incubated in fetal bovine serum solution,[75,76] while when dispersed in human plasma[77] after 15 min they start to evolve towards a different kind of nanoparticle known as hexosomes, characterized by a hexagonal inner nanostructure.[78,79] Indeed, at least one investigation proved that after 10/15 min from i.v. administration in mice, cubosomes are non-altered and able to reach all the biological compartments without the release of the imaging agent they carried.

In conclusion, the results herein discussed highlight the great potential of RPCs featuring two π-expansive dppn ligands as photosensitizing agents in the blooming field of research of PDT. Going beyond providing a simple and general synthetic route for the preparation of this class of compounds, to the best of our knowledge this work also reports the first RPC to be encapsulated into cubosome nanostructures, providing fundamental knowledge about the design of pharmaceutically viable Ru(II)-cubosome formulations for PDT applications.

Author contributions

G. E. G., M. S. and L. Casula: investigation and data curation, L. G., A. D. G., C. S., G. P., F. C., S. P. and B. V.: investigation, S. M. and C. G.: supervision and project administration, L. Conti.: writing the original draft and project administration. G. E. G., M. S., L. Casula, L. Conti, C. S., B. V., C. G. and S. M. are inventors on a pending patent application pertaining to the ruthenium polypyridyl complexes described in this work. All authors have given approval to the final version of the manuscript.

Conflicts of interest

The authors declare no conflicts of interest.

Acknowledgements

The authors would like to thank Dr Annalisa Guerri, from the Department of Chemistry Ugo Schiff of the University of Florence for the Cryo-TEM measurements. UniCA-Progetti biennali di Ateneo Finanziati dalla Fondazione di Sardegna 2018 (CUP F74I19000950007) is gratefully acknowledged for (partial) financial support.

References

1 G. Gunaydin, M. E. Gedik and S. Ayan, Photodynamic Therapy for the Treatment and Diagnosis of Cancer–A Review of the Current Clinical Status, *Front. Chem.*, 2021, **9**, 686303.
2 J. H. Correia, J. A. Rodrigues, S. Pimenta, T. Dong and Z. Yang, Photodynamic Therapy Review: Principles, Photosensitizers, Applications, and Future Directions, *Pharmaceutics*, 2021, **13**, 1332.
3 L. Karner, S. Drechsler, M. Metzger, A. Hacobian, B. Schädl, P. Slezak, J. Grillari and P. Dungel, Antimicrobial Photodynamic Therapy Fighting Polymicrobial Infections-a Journey from: In Vitro to in Vivo, *Photochem. Photobiol. Sci.*, 2020, **19**, 1332–1343.
4 G. Boccalini, L. Conti, C. Montis, D. Bani, A. Bencini, D. Berti, C. Giorgi, A. Mengoni and B. Valtancoli, Methylene Blue-Containing Liposomes as New Photodynamic Anti-Bacterial Agents, *J. Mater. Chem. B*, 2017, **5**, 2788–2797.
5 L. Conti, E. Macedi, C. Giorgi, B. Valtancoli and V. Fusi, Combination of Light and Ru(II) Polypyridyl Complexes: Recent Advances in the Development of New Anticancer Drugs, *Coord. Chem. Rev.*, 2022, **469**, 214656.
6 S. Monro, K. L. Colón, H. Yin, J. Roque, P. Konda, S. Gujar, R. P. Thummel, L. Lilge, C. G. Cameron and S. A. McFarland, Transition Metal Complexes and Photodynamic Therapy from a Tumor-Centered Approach: Challenges, Opportunities, and Highlights from the Development of TLD1433, *Chem. Rev.*, 2019, **119**(2), 797–828.

7 Y. Wu, S. Li, Y. Chen, W. He and Z. Guo, Recent Advances in Noble Metal Complex Based Photodynamic Therapy, *Chem. Sci.*, 2022, **13**, 5085–5106.
8 C. Mari, V. Pierroz, S. Ferrari and G. Gasser, Combination of Ru(II) Complexes and Light: New Frontiers in Cancer Therapy, *Chem. Sci.*, 2015, **6**, 2660–2686.
9 A. Notaro and G. Gasser, Monomeric and Dimeric Coordinatively Saturated and Substitutionally Inert Ru(II) Polypyridyl Complexes as Anticancer Drug Candidates., *Chem. Soc. Rev.*, 2017, **46**, 7317–7337.
10 L. Conti, G. E. Giacomazzo, B. Valtancoli, M. Perfetti, A. Privitera, C. Giorgi, P. S. Sfragano, I. Palchetti, S. Pecchioli, P. Bruni and F. Cencetti, Highly Charged Ru(II) Polypyridyl Complexes as Photosensitizer Agents in Photodynamic Therapy of Epithelial Ovarian Cancer Cells, *Int. J. Mol. Sci.*, 2022, **23**(21), 13302.
11 L. Conti, A. Mengoni, G. E. Giacomazzo, L. Mari, M. Perfetti, C. Fagorzi, L. Sorace, B. Valtancoli and C. Giorgi, Exploring the Potential of Highly Charged Ru(II)- and Heteronuclear Ru(II)/Cu(II)-Polypyridyl Complexes as Antimicrobial Agents, *J. Inorg. Biochem.*, 2021, **220**, 111467.
12 Z. Y. Yan, J. Chen, J. Shao, Z. Q. Jiao, T. S. Tang, M. Tang, Z. G. Sheng, L. Mao, R. Huang, C. H. Huang, Z. H. Zhang, H. M. Su and B. Z. Zhu, The Cell-Impermeable Ru(II) Polypyridyl Complex as a Potent Intracellular Photosensitizer under Visible Light Irradiation via Ion-Pairing with Suitable Lipophilic Counter-Anions, *Free Radicals Biol. Med.*, 2021, **171**, 69–79.
13 S. Estalayo-Adrián, S. Blasco, S. A. Bright, G. J. McManus, G. Orellana, D. C. Williams, J. M. Kelly and T. Gunnlaugsson, Water-Soluble Amphiphilic Ruthenium (II) Polypyridyl Complexes as Potential Light-Activated Therapeutic Agents, *Chem. Commun.*, 2020, **56**, 9332–9335.
14 J. Karges, F. Heinemann, F. Maschietto, M. Patra, O. Blacque, I. Ciofini, B. Spingler and G. Gasser, A Ru(II) Polypyridyl Complex Bearing Aldehyde Functions as a Versatile Synthetic Precursor for Long-Wavelength Absorbing Photodynamic Therapy Photosensitizers, *Bioorg. Med. Chem.*, 2019, **27**(12), 2666–2675.
15 L. K. McKenzie, M. Flamme, P. S. Felder, J. Karges, F. Bonhomme, A. Gandioso, C. Malosse, G. Gasser and M. Hollenstein, A Ruthenium-Oligonucleotide Bioconjugated Photosensitizing Aptamer for Cancer Cell Specific Photodynamic Therapy, *RSC Chem. Biol.*, 2022, **3**, 85–95.
16 M. Lin, S. Zou, X. Liao, Y. Chen, D. Luo, L. Ji and H. Chao, Ruthenium(II) Complexes as Bioorthogonal Two-Photon Photosensitizers for Tumour-Specific Photodynamic Therapy against Triple-Negative Breast Cancer Cells, *Chem. Commun.*, 2021, **57**, 4408–4411.
17 A. Chettri, J. A. Roque, K. R. A. Schneider, H. D. Cole, C. G. Cameron, S. A. McFarland and B. Dietzek, It Takes Three to Tango: The Length of the Oligothiophene Chain Determines the Nature of the Long-Lived Excited State and the Resulting Photocytotoxicity of a Ruthenium(II) Photodrug, *ChemPhotoChem*, 2021, **5**(5), 421–425.
18 E. C. Glazer, Panchromatic Osmium Complexes for Photodynamic Therapy: Solutions to Existing Problems and New Questions, *Photochem. Photobiol.*, 2017, **93**(5), 1326–1328.
19 A. Zamora, E. Wachter, M. Vera, D. K. Heidary, V. Rodríguez, E. Ortega, V. Fernández-Espín, C. Janiak, E. C. Glazer, G. Barone and J. Ruiz, Organoplatinum(II) Complexes Self-Assemble and Recognize AT-Rich Duplex DNA Sequences, *Inorg. Chem.*, 2021, **60**(4), 2178–2187.
20 L. E. Joyce, J. D. Aguirre, A. M. Angeles-Boza, A. Chouai, P. K. L. Fu, K. R. Dunbar and C. Turro, Photophysical Properties, DNA Photocleavage, and Photocytotoxicity of a Series of Dppn Dirhodium(II,II) Complexes, *Inorg. Chem.*, 2010, **49**(12), 5371–5376.
21 R. N. Akhimie, J. K. White and C. Turro, Dual Photoreactivity of a New Rh2(II,II) Complex for Biological Applications, *Inorg. Chim. Acta*, 2017, **454**, 149–154.
22 S. Li, J. Zhao, X. Wang, G. Xu, S. Gou and Q. Zhao, Design of a Tris-Heteroleptic Ru(II) Complex with Red-Light Excitation and Remarkably Improved Photobiological Activity, *Inorg. Chem.*, 2020, **59**(15), 11193–11204.
23 L. Wang, H. Yin, M. A. Jabed, M. Hetu, C. Wang, S. Monro, X. Zhu, S. Kilina, S. A. McFarland and W. Sun, π-Expansive Heteroleptic Ruthenium(II) Complexes as Reverse Saturable Absorbers and Photosensitizers for Photodynamic Therapy, *Inorg. Chem.*, 2017, **56**(6), 3245–3259.
24 B. Peña, N. A. Leed, K. R. Dunbar and C. Turro, Excited State Dynamics of Two New Ru(II) Cyclometallated Dyes: Relation to Cells for Solar Energy Conversion and Comparison to Conventional Systems, *J. Phys. Chem. C*, 2012, **116**(42), 17095–17101.
25 B. A. Albani, B. Peña, N. A. Leed, N. A. B. G. De Paula, C. Pavani, M. S. Baptista, K. R. Dunbar and C. Turro, Marked Improvement in Photoinduced Cell Death by a New Tris-Heteroleptic Complex with Dual Action: Singlet Oxygen Sensitization and Ligand Dissociation, *J. Am. Chem. Soc.*, 2014, **136**(49), 17095–17101.
26 C. Reichardt, S. Monro, F. H. Sobotta, K. L. Colón, T. Sainuddin, M. Stephenson, E. Sampson, J. Roque, H. Yin, J. C. Brendel, C. G. Cameron, S. A. McFarland and B. Dietzek, Predictive Strength of Photophysical Measurements for in Vitro Photobiological Activity in a Series of Ru(II) Polypyridyl Complexes Derived from π-Extended Ligands, *Inorg. Chem.*, 2019, **58**(5), 3156–3166.
27 F. Haddache, A. Le Goff, B. Reuillard, K. Gorgy, C. Gondran, N. Spinelli, E. Defrancq and S. Cosnier, Label-Free Photoelectrochemical Detection of Double-Stranded HIV DNA by Means of a Metallointercalator-Functionalized Electrogenerated Polymer, *Chem. – Eur. J.*, 2014, **20**(47), 15555–15560.
28 S. Vidhisha, K. L. Reddy, Y. P. Kumar, M. Srijana and S. Satyanarayana, Synthesis, Characterization, Antibacterial Activity and Investigation of DNA Binding for Ru(II) Molecular "Light Switch" Complexes, *Int. J. Pharm. Sci. Rev. Res.*, 2014, **25**(1), 197–205.

29 H. Yin, M. Stephenson, J. Gibson, E. Sampson, G. Shi, T. Sainuddin, S. Monro and S. A. McFarland, In Vitro Multiwavelength PDT with 3IL States: Teaching Old Molecules New Tricks, *Inorg. Chem.*, 2014, **53**(9), 4548–4559.

30 Q. X. Zhou, W. H. Lei, J. R. Chen, C. Li, Y. J. Hou, X. S. Wang and B. W. Zhang, A New Heteroleptic Ruthenium(II) Polypyridyl Complex with Long-Wavelength Absorption and High Singlet-Oxygen Quantum Yield., *Chem. – Eur. J.*, 2010, **16**(10), 3157–3165.

31 C. W. Jiang, H. Chao, R. H. Li, H. Li and L. N. Ji, Syntheses, Characterization and Third-Order Nonlinear Optical Properties of Ruthenium(II) Complexes Containing 2-Phenylimidazo-[4,5-f][1,10]Phenanthroline and Extended Diimine Ligands, *Polyhedron*, 2001, **20**(17), 2187–2193.

32 L. N. Lameijer, T. G. Brevé, V. H. S. van Rixel, S. H. C. Askes, M. A. Siegler and S. Bonnet, Effects of the Bidentate Ligand on the Photophysical Properties, Cellular Uptake, and (Photo)Cytotoxicity of Glycoconjugates Based on the [Ru(Tpy)(NN)(L)]2 + Scaffold, *Chem. – Eur. J.*, 2018, **24**(11), 2709–2717.

33 N. Toupin, S. J. Steinke, S. Nadella, A. Li, T. N. Rohrabaugh, E. R. Samuels, C. Turro, I. F. Sevrioukova and J. J. Kodanko, Photosensitive Ru(II) Complexes as Inhibitors of the Major Human Drug Metabolizing Enzyme CYP3A4, *J. Am. Chem. Soc.*, 2021, **143**(24), 9191–9205.

34 A. C. Munteanu, A. Notaro, M. Jakubaszek, J. Cowell, M. Tharaud, B. Goud, V. Uivarosi and G. Gasser, Synthesis, Characterization, Cytotoxic Activity, and Metabolic Studies of Ruthenium(II) Polypyridyl Complexes Containing Flavonoid Ligands, *Inorg. Chem.*, 2020, **59**(7), 4424–4434.

35 G. E. Shillito, S. E. Bodman, J. I. Mapley, C. M. Fitchett and K. C. Gordon, Accessing a Long-Lived 3LC State in a Ruthenium(II) Phenanthroline Complex with Appended Aromatic Groups, *Inorg. Chem.*, 2020, **59**(23), 16967–16975.

36 K. Sztandera, M. Gorzkiewicz and B. Klajnert-Maculewicz, Nanocarriers in Photodynamic Therapy—in Vitro and in Vivo Studies, *Wiley Interdiscip. Rev.: Nanomed. Nanobiotechnol.*, 2020, **12**(3), 1509.

37 A. Q. Annu, B. Nabi, S. Kotta, J. K. Narang, S. Baboota and J. Ali, Role of Nanocarriers in Photodynamic Therapy, *Photodiagn. Photodyn. Ther.*, 2020, **30**, 101782.

38 F. Lai, M. Schlich, R. Pireddu, F. Corrias, A. Fadda and C. Sinico, Production of Nanosuspensions as a Tool to Improve Drug Bioavailability: Focus on Topical Delivery, *Curr. Pharm. Des.*, 2015, **21**(42), 6089–6103.

39 S. Murgia, S. Biffi and R. Mezzenga, Recent Advances of Non-Lamellar Lyotropic Liquid Crystalline Nanoparticles in Nanomedicine, *Curr. Opin. Colloid Interface Sci.*, 2020, **48**, 28–39.

40 J. Barauskas, C. Cervin, M. Jankunec, M. Špandyreva, K. Ribokaite, F. Tiberg and M. Johnsson, Interactions of Lipid-Based Liquid Crystalline Nanoparticles with Model and Cell Membranes, *Int. J. Pharm.*, 2010, **391**(1–2), 248–291.

41 J. C. Bode, J. Kuntsche, S. S. Funari and H. Bunjes, Interaction of Dispersed Cubic Phases with Blood Components, *Int. J. Pharm.*, 2013, **448**(1), 87–95.

42 S. Murgia, S. Bonacchi, A. M. Falchi, S. Lampis, V. Lippolis, V. Meli, M. Monduzzi, L. Prodi, J. Schmidt, Y. Talmon and C. Caltagirone, Drug-Loaded Fluorescent Cubosomes: Versatile Nanoparticles for Potential Theranostic Applications, *Langmuir*, 2013, **29**(22), 6673–6679.

43 F. D. Victorelli, L. Salvati Manni, S. Biffi, B. Bortot, H. H. Buzzá, V. Lutz-Bueno, S. Handschin, G. Calixto, S. Murgia, M. Chorilli and R. Mezzenga, Potential of Curcumin-Loaded Cubosomes for Topical Treatment of Cervical Cancer, *J. Colloid Interface Sci.*, 2022, **620**, 419–430.

44 S. Jenni, G. Picci, M. Fornasier, M. Mamusa, J. Schmidt, Y. Talmon, A. Sour, V. Heitz, S. Murgia and S. C. Caltagirone, Multifunctional Cubic Liquid Crystalline Nanoparticles for Chemo- A Nd Photodynamic Synergistic Cancer Therapy, *Photochem. Photobiol. Sci.*, 2020, **19**, 674–680.

45 U. Bazylińska, D. Wawrzyńczyk, J. Kulbacka, G. Picci, L. S. Manni, S. Handschin, M. Fornasier, C. Caltagirone, R. Mezzenga and S. Murgia, Hybrid Theranostic Cubosomes for Efficient NIR-Induced Photodynamic Therapy, *ACS Nano*, 2022, **16**(4), 5427–5438.

46 U. Bazylińska, J. Kulbacka, J. Schmidt, Y. Talmon and S. Murgia, Polymer-Free Cubosomes for Simultaneous Bioimaging and Photodynamic Action of Photosensitizers in Melanoma Skin Cancer Cells, *J. Colloid Interface Sci.*, 2018, **522**, 163–173.

47 M. C. F. Simões, J. J. S. Sousa and A. A. C. C. Pais, Skin Cancer and New Treatment Perspectives: A Review, *Cancer Lett.*, 2015, **357**(1), 8–42.

48 M. Kubeil, R. R. Vernooij, C. Kubeil, B. R. Wood, B. Graham, H. Stephan and L. Spiccia, Studies of Carbon Monoxide Release from Ruthenium(II) Bipyridine Carbonyl Complexes upon UV-Light Exposure, *Inorg. Chem.*, 2017, **56**(10), 5941–5952.

49 N. Nickita, M. J. Belousoff, A. I. Bhatt, A. M. Bond, G. B. Deacon, G. Gasser and L. Spiccia, Synthesis, Structure, Spectroscopic Properties, and Electrochemical Oxidation of Ruthenium(II) Complexes Incorporating Monocarboxylate Bipyridine Ligands, *Inorg. Chem.*, 2007, **46**(21), 8638–8651.

50 A. Notaro, M. Jakubaszek, S. Koch, R. Rubbiani, O. Dömötör, E. A. Enyedy, M. Dotou, F. Bedioui, M. Tharaud, B. Goud, S. Ferrari, E. Alessio and G. Gasser, A Maltol-Containing Ruthenium Polypyridyl Complex as a Potential Anticancer Agent, *Chem. – Eur. J.*, 2020, **26**(20), 4997–5009.

51 E. Wachter, D. K. Heidary, B. S. Howerton, S. Parkin and E. C. Glazer, Light-Activated Ruthenium Complexes Photobind DNA and Are Cytotoxic in the Photodynamic Therapy Window, *Chem. Commun.*, 2012, **48**, 9649–9651.

52 R. A. Krause, Synthesis of Mixed Complexes of Ruthenium (II) with 2,2′-Dipyridyl, *Inorg. Chim. Acta*, 1977, **22**, 209–213.

53 A. Petroni and L. D. Slep, Etchenique, R. Ruthenium(II) 2,2′-Bipyridyl Tetrakis Acetonitrile Undergoes Selective Axial Photocleavage., *Inorg. Chem.*, 2008, **47**(3), 951–956.
54 H. K. Saeed, P. J. Jarman, S. Archer, S. Sreedharan, I. Q. Saeed, L. K. Mckenzie, J. A. Weinstein, N. J. Buurma, C. G. W. Smythe and J. A. Thomas, Homo– and Heteroleptic Phototoxic Dinuclear Metallo–Intercalators Based on Ru II (Dppn) Intercalating Moieties: Synthesis, Optical, and Biological Studies, *Angew. Chem., Int. Ed.*, 2017, **56**(41), 12628–12633.
55 T. Shimidzu, T. Iyoda and K. Izaki, Photoelectrochemical Properties of Bis(2,2′-Bipyridine)(4,4′-Dicarboxy-2,2′-Bipyridine) Ruthenium(II) Chloride, *J. Phys. Chem.*, 1985, **89**(4), 642–645.
56 C. Imberti, P. Zhang, H. Huang and P. J. Sadler, New Designs for Phototherapeutic Transition Metal Complexes, *Angew. Chem., Int. Ed.*, 2020, **59**(1), 61–73.
57 A. P. Castano, T. N. Demidova and M. R. Hamblin, Mechanisms in Photodynamic Therapy: Part One - Photosensitizers, Photochemistry and Cellular Localization, *Photodiagn. Photodyn. Ther.*, 2004, **1**(4), 279–293.
58 Y. Sun, L. E. Joyce, N. M. Dickson and C. Turro, Efficient DNA Photocleavage by [Ru(Bpy)2(Dppn)]2+ with Visible Light, *Chem. Commun.*, 2010, **46**, 2426–2428.
59 S. P. Foxon, C. Metcalfe, H. Adams, M. Webb and J. A. Thomas, Electrochemical and Photophysical Properties of DNA Metallo-Intercalators Containing the Ruthenium(II) Tris(1-Pyrazolyl)Methane Unit., *Inorg. Chem.*, 2007, **46**(2), 409–416.
60 D. Van Straten, V. Mashayekhi, H. S. de Bruijn, S. Oliveira and D. J. Robinson, Oncologic Photodynamic Therapy: Basic Principles, Current Clinical Status and Future Directions, *Cancers*, 2017, **9**(2), 1–54.
61 L. M. Lifshits, J. A. Roque, P. Konda, S. Monro, H. D. Cole, D. V. Dohlen, S. Kim, G. Deep, R. P. Thummel, C. G. Cameron, S. Gujar and S. A. McFarland, Near-infrared absorbing Ru(II) complexes act as immunoprotective photodynamic therapy (PDT) agents against aggressive melanoma, *Chem. Sci.*, 2020, **11**, 11740.
62 L. N. Lameijer, S. L. Hopkins, T. G. Brevé, S. H. C. Askes and S. Bonnet, D-Versus L-Glucose Conjugation: Mitochondrial Targeting of a Light-Activated Dual-Mode-of Action Ruthenium-Based Anticancer Prodrug, *Chem. – Eur. J.*, 2016, **22**, 18484–18491.
63 S. Li, J. Zhao, X. Wang, G. Xu, S. Gou and Q. Zhao, Design of a Tris-Heteroleptic Ru(II) Complex with Red-Light Excitation and Remarkably Improved Photobiological Activity, *Inorg. Chem.*, 2020, **59**, 11193–11204.
64 S. Moghassemi, A. Dadashzadeh, R. B. Azevedo, O. Feron and C. A. Amorim, Photodynamic cancer therapy using liposomes as an advanced vesicular photosensitizer delivery system, *J. Controlled Release*, 2021, **339**(10), 75–90.
65 C. F. de Freitas, D. S. Pellosi and A. L. Tessaro, 8-Lipid-based nanoparticles in photodynamic therapy, *in Nanomaterials for Photodynamic Therapy*, 2023, 203–226.
66 M. Fornasier, S. Biffi, B. Bortot, P. Macor, A. Manhart, F. R. Wurm and S. Murgia, Cubosomes Stabilized by a Polyphosphoester-Analog of Pluronic F127 with Reduced Cytotoxicity, *J. Colloid Interface Sci.*, 2020, **580**, 286–297.
67 A. M. Falchi, A. Rosa, A. Atzeri, A. Incani, S. Lampis, V. Meli, C. Caltagirone and S. Murgia, Effects of Monoolein-Based Cubosome Formulations on Lipid Droplets and Mitochondria of HeLa Cells, *Toxicol. Res.*, 2015, **4**, 1025–1036.
68 J. Guo, M. Schlich, J. F. Cryan and C. M. O'Driscoll, Targeted Drug Delivery via Folate Receptors for the Treatment of Brain Cancer: Can the Promise Deliver?, *J. Pharm. Sci.*, 2017, **106**(12), 3413–3420.
69 Z. Zhen, W. Tang, C. Guo, H. Chen, X. Lin, G. Liu, B. Fei, X. Chen, B. Xu and J. Xie, Ferritin Nanocages to Encapsulate and Deliver Photosensitizers for Efficient Photodynamic Therapy against Cancer, *ACS Nano*, 2013, **7**(8), 6988–6996.
70 S. Demartis, G. Rassu, S. Murgia, L. Casula, P. Giunchedi and E. Gavini, Improving Dermal Delivery of Rose Bengal by Deformable Lipid Nanovesicles for Topical Treatment of Melanoma, *Mol. Pharm.*, 2021, **18**(11), 4046–4057.
71 L. Conti, S. Ciambellotti, G. E. Giacomazzo, V. Ghini, L. Cosottini, E. Puliti, M. Severi, E. Fratini, F. Cencetti, P. Bruni, B. Valtancoli, C. Giorgi and P. Turano, Ferritin Nanocomposites for the Selective Delivery of Photosensitizing Ruthenium-Polypyridyl Compounds to Cancer Cells, *Inorg. Chem. Front.*, 2022, **9**, 1070–1081.
72 S. Wang, A. Riedinger, H. Li, C. Fu, H. Liu, L. Li, T. Liu, L. Tan, M. J. Barthel, G. Pugliese, F. De Donato, M. Scotto D'Abbusco, X. Meng, L. Manna, H. Meng and T. Pellegrino, Plasmonic Copper Sulfide Nanocrystals Exhibiting Near-Infrared Photothermal and Photodynamic Therapeutic Effects, *ACS Nano*, 2015, **9**(2), 1788–1800.
73 M. Redza-Dutordoir and D. A. Averill-Bates, Activation of Apoptosis Signalling Pathways by Reactive Oxygen Species, *Biochim. Biophys. Acta*, 2016, **1863**(12), 2977–2992.
74 A. Yaghmur and H. Mu, Recent advances in drug delivery applications of cubosomes, hexosomes, and solid lipid nanoparticles, *Acta Pharm. Sin. B*, 2021, **11**(4), 871–885.
75 S. Deshpande, E. Venugopal, S. Ramagiri, J. R. Bellare, G. Kumaraswamy and N. Singh, *ACS Appl. Mater. Interfaces*, 2014, **6**(19), 17126–17133.
76 A. Gupta, T. Stait-Gardner, L. de Campo, L. J. Waddington, N. Kirby, W. S. Price and M. J. Moghaddam, *J. Mater. Chem. B*, 2014, **2**, 1225–1233.
77 J. C. Bode, J. Kuntsche, S. S. Funari and H. Bunjes, *Int. J. Pharm.*, 2013, **448**(1), 87–95.
78 C. Caltagirone, M. Arca, A. M. Falchi, V. Lippolis, V. Meli, M. Monduzzi, T. Nylander, A. Rosa, J. Schmidt, Y. Talmond and S. Murgia, *RSC Adv.*, 2015, **5**, 23443–23449.
79 V. Meli, C. Caltagirone, C. Sinico, F. Lai, A. M. Falchi, M. Monduzzi, M. Obiols-Rabasa, G. Picci, A. Rosa, J. Schmidt, Y. Talmone and S. Murgia, *New J. Chem.*, 2017, **41**, 1558–1565.

Inorganic Chemistry

pubs.acs.org/IC

Communication

Nitroimidazole-Based Ruthenium(II) Complexes: Playing with Structural Parameters to Design Photostable and Light-Responsive Antibacterial Agents

Gina Elena Giacomazzo, Luca Conti,* Annalisa Guerri, Marco Pagliai, Camilla Fagorzi, Patrick Severin Sfragano, Ilaria Palchetti, Giangaetano Pietraperzia, Alessio Mengoni, Barbara Valtancoli, and Claudia Giorgi*

Cite This: https://doi.org/10.1021/acs.inorgchem.1c03032

Read Online

ACCESS | Metrics & More | Article Recommendations | Supporting Information

ABSTRACT: 5-Nitroimidazole (5NIMH), chosen as a molecular model of nitroimidazole derivatives, which represent a broad-spectrum class of antimicrobials, was incorporated into the ruthenium complexes [Ru(tpy)(phen)(5NIM)]PF_6 (**1**) and [Ru(tpy)(dmp)(5NIM)]PF_6 (**2**) (tpy = terpyridine, phen = phenanthroline, dmp = 2,9-dimethyl-1,10-phenanthroline). Besides the uncommon metal coordination of 5-nitroimidazole in its imidazolate form (5NIM), the different architectures of the spectator ligands (phen and dmp) were exploited to tune the "mode of action" of the resulting complexes, passing from a photostable compound where the redox properties of 5NIMH are preserved (**1**) to one suitable for the nitroimidazole phototriggered release (**2**) and whose antibacterial activity against *B. subtilis*, chosen as cellular model, is effectively improved upon light exposure. This study may provide a fundamental knowledge on the use of Ru(II)−polypyridyl complexes to incorporate and/or photorelease biologically relevant nitroimidazole derivatives in the design of a novel class of antimicrobials.

Multidrug resistance of bacterial pathogens is a major health concern worldwide,[1,2] and there is an urgent need for the development of new and effective antimicrobials, which should be based on a new class of compounds, rather than on analogues of known scaffolds.

In this respect, following the encouraging results as antitumoral drugs,[3,4] an increasing interest has been devoted to Ru(II)−polypyridyl complexes, an attractive class of compounds with unique chemical-physical repertoires and whose antibacterial properties were first reported over 60 years ago.[5,6]

Among a number of Ru(II)-based antibacterial agents,[7−9] in the so-called antimicrobial photodynamic therapy (aPDT),[10−13] their light irradiation in the presence of molecular oxygen to generate reactive oxygen species (ROS), namely the potent singlet oxygen $^1O_2$, takes advantage of a complete spatial and temporal control over the drug activation.[14,15] However, despite the high efficacy of ROS even against multidrug resistance bacteria,[16,17] the need for O_2 still represents a limit in the treatment of hypoxic environments, such as anaerobic infections.[18,19] This led to the development of light-responsive complexes able to release biologically active compounds via an O_2-independent mechanism. Such processes typically require the population of ligand dissociative metal centered (^{3}MC) excited states, whose direct excitation is forbidden.[20] To overcome this issue, strain-inducing substituents are inserted in the ruthenium scaffolds, lowering the energy of the ^{3}MC states and allowing their thermal population upon excitation to the ^{3}MLCT (metal-to-ligand charge transfer) states.[21−24]

Being inspired by the versatile chemistry of Ru(II)−polypyridyl complexes and considering the renewed interest in the broad-spectrum antimicrobial activity of nitroimidazole derivatives,[25] we incorporated 5-nitroimidazole (5NIMH), the simplest molecular model of this class of compounds, into the ruthenium complexes [Ru(tpy)(phen)(5NIM)]PF_6 (**1**) and [Ru(tpy)(dmp)(5NIM)]PF_6 (**2**) (tpy = terpyridine, phen = phenanthroline, dmp = 2,9-dimethyl-1,10-phenanthroline). The different steric hindrance and electronic properties of the two ruthenium scaffolds were exploited to modulate the chemical-physical features of the resulting compounds.

Besides the successful introduction of Ru(II)−polypyridyl complexes bearing 2-nitroimidazole in the treatment and visualization of cancer,[26−28] the combination of this class of compounds with nitroimidazole derivatives to develop novel antibacterial agents still remains scarcely explored, being, to the best of our knowledge, the only exception recently reported by Sasahara and co-workers,[29] who designed two kinetically inert compounds, [$Ru(NO_2)(bpy)_2$(5NIMH)]PF_6 and *cis*-[RuCl-$(bpy)_2$(MTZ)]PF_6 (bpy = 2,2′-bipyridine, MTZ = metronidazole), effective toward metronidazole-resistant strains of *H. pylori*.

Ruthenium complexes were prepared via stepwise ligand addition, as sketched in Chart 1. Briefly, following the preparation of [Ru(tpy)(phen)Cl]PF_6 and [Ru(tpy)(dmp)Cl]-

Received: September 28, 2021

Chart 1. Synthetic Routes for Complexes 1 and 2 along with the Proton Transfer Reaction between 5NIMH and 5NIM and the Standard Numbering for the Imidazole Ring

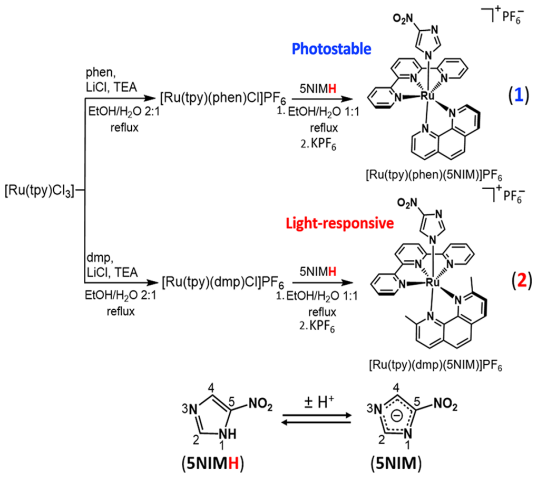

PF_6, performed accordingly to the literature,[30,31] these intermediates were allowed to react with 5-nitroimidazole in a hot ethanol−water mixture, affording the replacement of the chloro ligand with the nitroimidazole ring. Addition of aqueous KPF_6 led to the precipitation of the hexafluorophosphate salts **1** and **2**, which were obtained, after purification by flash chromatography, in 58% and 35% yields, respectively. The complexes were fully characterized by ^1H, ^{13}C NMR, HR-(ESI) MS spectrometry, X-ray, and CHN analysis (Figures S1−S13, SI).

The X-ray structures of ruthenium complexes (Figure 1a and 1b) unveil a nonstandard coordination of the nitroimidazole ligand to the ruthenium centers, involving the N3 nitrogen atom of a deprotonated imidazole moiety (5NIM in Chart 1). For the sake of completeness, the asymmetric unit (au) of **1** (Figure S12, SI) contains one metal complex with a PF_6^- as a counterion plus an acetonitrile molecule, while the one of **2** features two molecules of the metal complex (**2**A and **2**B) counterbalanced by one PF_6^- anion each, one acetonitrile and two water molecules (Figure S13, SI). Accordingly, the HR-(ESI) MS spectra of **1** and **2** (Figures S7−S9, SI) display the isotopic patterns of the mono positively charged species $[Ru(tpy)(phen)(5NIM)]^+$ and $[Ru(tpy)(dmp)(5NIM)]^+$, centered at 627.0872 and 655.1186 (m/z = 1), respectively.

Crystal structures were also optimized through DFT calculations, obtaining results in good agreement with the X-ray data (Figure S14, see the SI for further details). Moreover, the Ru-coordination by the N3 atom of 5NIM is supported by Electron Localization Function (ELF) analysis,[32,33] as shown for **2** in Figure 1c, where the hydrogen bonding between the nitroimidazole-N1 and the hydrogen atom of a water molecule can be appreciated.

Therefore, in contrast to the "classical" Ru(II)-coordination by a neutral 5NIMH unit,[34,35] also proposed by Sasahara and co-workers for *cis*-$[Ru(NO_2)(bpy)_2(5NIMH)]^+$,[29] our findings indicate that metal coordination can effectively cause the deprotonation of 5-nitroimidazole. This occurs without using strong bases to preliminarily generate the imidazolate species, as generally required to produce Ru(II)-imidazolate species.[36] In this respect, we can speculate that the marked electron-withdrawing character of the nitro group and the Ru(II)-coordination may play a synergistic role in lowering the pK_a of the imidazole ring, favoring its metal coordination as the imidazolate anion.

The structural analysis of **1** and **2** demonstrates that the insertion of two bulky methyl groups in the 2 and 9 positions of the dmp unit determines a distortion of the pseudo-octahedral geometry of **2** relative to **1**. These effects closely resemble those induced by the encumbered NN ligands in the parental compounds $[(tpy)Ru(NN)(py)]^{2+}$ (NN = 6,6′-dimethyl-2,2′-bipyridine or 2,2′-biquinoline, py = pyridine)[37] and can be summarized as follows: (1) significant lengthening of the Ru-dmp bonds; (2) displacing (tilting) of the dmp ligand, as indicated by the angles between the mean planes containing the tpy and dmp, of 62.97° (**2**A) and 67.36° (**2**B), compared to 88.78° in **1**; (3) tilting of the 5NIM toward the N(1) and N(2) atoms of tpy as denoted, for instance, by the N(1)[9]−Ru(1)[2]−N(6)[14] and N(2)[10]−Ru(1)[2]−N(6)[14] angles (numbers in square brackets refer to **2**B) which range from 82.93° to 87.51° and thus are smaller than the corresponding ones in **1**; and (4) significative rotation of 5NIM about its Ru−N bond relative to **1** (Tables S2−S4, SI). Although they stem from a solid-state analysis, these structural differences may affect, along with the different electronic properties imparted by phen or dmp, the photoinduced ligand dissociation of complexes (*vide infra*).[37,38]

Since nitroimidazoles typically trigger the generation of ROS species upon reduction of their nitro group to its radical anion,[25,39] a process that in principle requires up to six

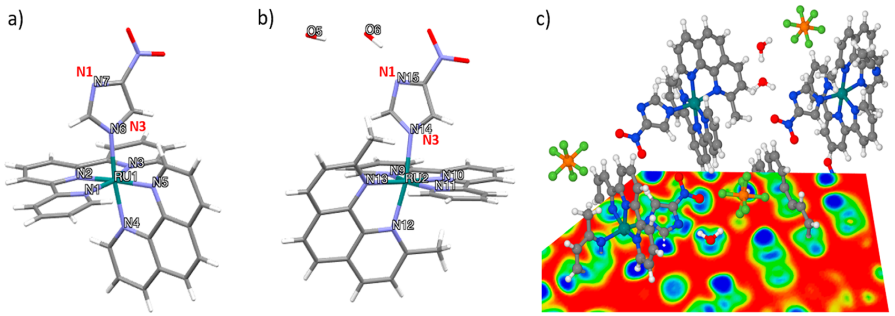

Figure 1. X-ray structures of the metal complex in **1** (a) and of **2**B in **2** (b) and ELF analysis for the au of **2** ($-CH_3CN$) (c). In red is highlighted the adopted nitrogen numbering for the imidazole ring (standard atom labels in crystal structures are in white).

https://doi.org/10.1021/acs.inorgchem.1c03032
Inorg. Chem. XXXX, XXX, XXX−XXX

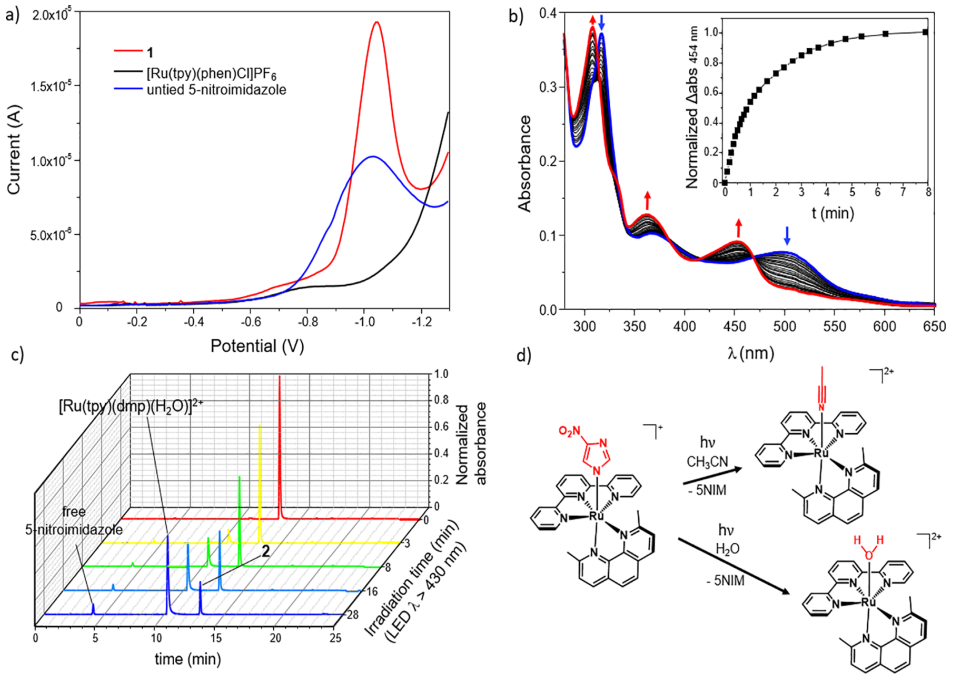

Figure 2. a) DPV analysis of **1** (1 mM), $[Ru(tpy)(phen)Cl]PF_6$ (1 mM), and 5NIMH (0.6 mM) in a methanol−water (1:5 v/v) mixture containing KCl (50 mM). b) UV−vis absorption spectra of **2** in acetonitrile at different irradiation times. c) HPLC chromatograms of **2** in water at neutral pH subjected to progressive irradiation times. d) Sketch of the ligand photoejection processes of **2**.

electrons,[40] the redox behaviors of Ru(II)-coordinated nitroimidazole rings were also investigated.

As shown in Figure 2a, where the differential pulse voltammetry (DPV) analysis of **1**, 5NIMH, and $[Ru(tpy)(phen)Cl]PF_6$ is reported, the voltammogram for the reduction of **1** displays a peak of 19.3 μA at −1.04 V, unveiling an almost unchanged reduction potential if compared to the untied 5NIMH (ca. 1.01 V vs Ag/AgCl), while no signals are observed for $[Ru(tpy)(phen)Cl]PF_6$, as expected due to the lack of electroactive moieties. An analogous behavior was found for **2** (Figure S16, SI).

The capacity of **1** and **2** to undergo photosubstitution reactions was explored by coupling UV−vis and HPLC analysis. In the dark, UV−vis measurements revealed a remarkable stability of both compounds in acetonitrile, as well as in water at pH 7.4 (Figures S17 and S18, SI), likely due to the deprotonated nature of the coordinated nitroimidazole ligand.

Conversely, light irradiation (LED emitting at 434 nm, 160 mW) of acetonitrile solutions of **2** provokes a sharp blue shift in the MLCT absorption maximum of compound, from 498 to 454 nm (Figure 2b), indicating the replacement of 5NIM by CH_3CN to form $[Ru(tpy)(phen)CH_3CN]^{2+}$.[37] No changes were instead observed for **1** under the same conditions (Figure S17c, SI), thus confirming that the different stereoelectronic characteristics imparted by phen or dmp are crucial for the photoreactivity of the resulting complexes.

A parallel HPLC experiment (Figure S20, SI) evidenced the selectivity of the photoejection process, as shown by the increase of the peaks attributed to 5NIMH and $[Ru(tpy)(phen)CH_3CN]^{2+}$ (with retention times of 4.91 and 10.91 min, respectively), while no evidence of free phen and/or tpy was observed. A similar behavior was also found for aqueous solutions of **2** at neutral pH (Figure 2c), albeit on a larger time scale, of ca. 3-fold. The quantum yields of ligand photodissociation (Φ_{434}) from the photoreactive **2** were obtained as described in the SI, following the determination of the photon flux of the light source by the procedure for potassium ferrioxalate actinometry;[41] Φ_{434} values of 0.0039(3) and 0.0011(3) resulted respectively in acetonitrile and in water, in agreement with the higher efficiency of photolysis in the former media.

Finally, *B. subtilis* strain 168 was chosen as a cellular model to preliminarily test the antibacterial activity of synthesized complexes under aerobic conditions; the obtained results are reported in Figure 3.

In the dark, **1** displays negligible toxicity, with inhibition of bacterial growth starting at 500 μM compound only (ca. 20% reduction of cell growth), while a higher effect was found for **2**. Given the comparable *in the dark* stabilities of the two complexes (Figure S18, SI), we can speculate that this finding would be rather due/partially due to distinct cellular responses imparted by their chemical structures, in analogy to other Ru compounds.[42]

Light activation does not significantly affect the antibacterial activity of the photostable **1**, as expected also due to its poor $^1O_2$ sensitizing properties (Figure S21, SI) but leads to a statistically significant enhancement of the dose-dependent activity of the photoreactive **2** (light green bars, Figure 3). For instance, a growth reduction of ca. 57% is determined by 150 μM compound, whereas a considerably lower effect (ca. 18%) is maintained in the dark. At higher doses, the "dark" toxicity of **2** becomes more relevant and lowers the photoinduced gain in the antimicrobial effect, making **2** to be optimally exploited in the 50−150 μM range of concentrations. In this respect, an

https://doi.org/10.1021/acs.inorgchem.1c03032
Inorg. Chem. XXXX, XXX, XXX−XXX

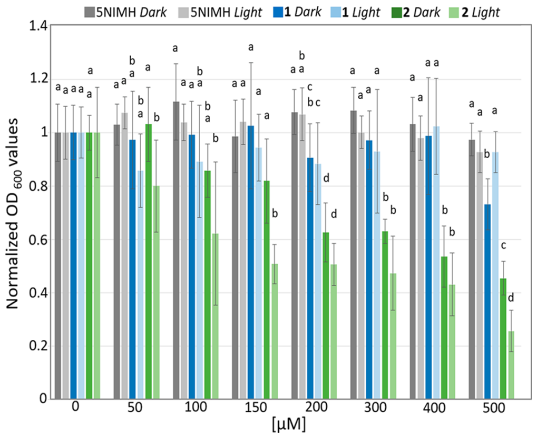

Figure 3. Antibacterial effect of 5NIMH, **1**, and **2** in the dark and upon irradiation. Significant differences were evaluated through analysis of variance (ANOVA) performed using Tukey's pairwise test. Different letters indicate significant differences ($p < 0.05$) at each concentration.

important contribution of the Ru(II)-photoproduct in the phototoxicity of **2** can be envisaged. Indeed, a parallel experiment on $[Ru(tpy)(dmp)(H_2O)]^{2+}$ (Figure S22, SI) unveiled a predominant dose-dependent activity of this scaffold relative to 5NIMH, which, similar to other tested bacterial strains (Table S6, SI), displayed a moderate activity against *B. subtilis*.[43]

In summary, we herein report on the chemical-physical characterization of two ruthenium complexes incorporating the simplest model for nitroimidazole derivatives, 5-NIMH. Besides its peculiar coordination to metal centers, this unit maintains its characteristic redox properties in both compounds, whereas the different architectures of the two ruthenium scaffolds permit switching from a photostable complex (**1**) to a suitable one for the 5NIMH photoreleasing (**2**). The relations between the properties of complexes and their biological potential were also preliminarily investigated through *in vitro* studies on *B. subtilis*, which highlighted an improved antibacterial activity of the photoreactive **2** following light irradiation.

In conclusion, these findings would provide fundamental knowledge on the use of Ru(II)−polypyridyl complexes engineered with other relevant nitroimidazole derivatives, as well as those employing 5NIMH as a "photolabile linker" between Ru(II) centers and different types of bioactive compounds. This would help in the design of a novel class of hybrid antimicrobial agents whose activity can be conveniently controlled by using light, in the fight against antimicrobial infections and resistance.

■ ASSOCIATED CONTENT

Supporting Information

The Supporting Information is available free of charge at https://pubs.acs.org/doi/10.1021/acs.inorgchem.1c03032.

Characterization, experimental and computational procedures of ruthenium complexes (PDF)

Accession Codes

CCDC 2087305−2087306 contain the supplementary crystallographic data for this paper. These data can be obtained free of charge via www.ccdc.cam.ac.uk/data_request/cif, or by emailing data_request@ccdc.cam.ac.uk, or by contacting The Cambridge Crystallographic Data Centre, 12 Union Road, Cambridge CB2 1EZ, UK; fax: +44 1223 336033.

■ AUTHOR INFORMATION

Corresponding Authors

Luca Conti − *Department of Chemistry "Ugo Schiff", University of Florence, 50019 Florence, Italy;* orcid.org/0000-0002-0402-1293; Email: luca.conti@unifi.it

Claudia Giorgi − *Department of Chemistry "Ugo Schiff", University of Florence, 50019 Florence, Italy;* Email: claudia.giorgi@unifi.it

Authors

Gina Elena Giacomazzo − *Department of Chemistry "Ugo Schiff", University of Florence, 50019 Florence, Italy*

Annalisa Guerri − *Department of Chemistry "Ugo Schiff", University of Florence, 50019 Florence, Italy;* orcid.org/0000-0001-6265-7874

Marco Pagliai − *Department of Chemistry "Ugo Schiff", University of Florence, 50019 Florence, Italy;* orcid.org/0000-0003-0240-161X

Camilla Fagorzi − *Department of Biology, University of Florence, 50019 Florence, Italy*

Patrick Severin Sfragano − *Department of Chemistry "Ugo Schiff", University of Florence, 50019 Florence, Italy*

Ilaria Palchetti − *Department of Chemistry "Ugo Schiff", University of Florence, 50019 Florence, Italy;* orcid.org/0000-0001-9366-0574

Giangaetano Pietraperzia − *Department of Chemistry "Ugo Schiff", University of Florence, 50019 Florence, Italy; European Laboratory for Non-Linear Spectroscopy (LENS), 50019 Florence, Italy*

Alessio Mengoni − *Department of Biology, University of Florence, 50019 Florence, Italy;* orcid.org/0000-0002-1265-8251

Barbara Valtancoli − *Department of Chemistry "Ugo Schiff", University of Florence, 50019 Florence, Italy*

Complete contact information is available at: https://pubs.acs.org/10.1021/acs.inorgchem.1c03032

Notes

The authors declare no competing financial interest.

■ ACKNOWLEDGMENTS

"Fondazione Cassa di Risparmio di Firenze" and MIUR, for the economic contribution within the "Progetto Dipartimenti di Eccellenza 2018-2022" allocated to the Department of Chemistry "Ugo Schiff", are gratefully acknowledged for financial support. The Mass Spectrometry Service Center (CISM) of the University of Florence is gratefully acknowledged for ESI-MS analysis.

■ REFERENCES

(1) Bhutta, Z. A.; Sommerfeld, J.; Lassi, Z. S.; Salam, R. A.; Das, J. K. Global Burden, Distribution, and Interventions for Infectious Diseases of Poverty. *Infect. Dis. Poverty* **2014**, *3*, 21.

(2) Reynoso, E. C.; Laschi, S.; Palchetti, I.; Torres, E. Advances in Antimicrobial Resistance Monitoring Using Sensors and Biosensors: A Review. *Chemosensors* **2021**, *9*, 232.

(3) Notaro, A.; Gasser, G. Monomeric and Dimeric Coordinatively Saturated and Substitutionally Inert Ru(II) Polypyridyl Complexes as Anticancer Drug Candidates. *Chem. Soc. Rev.* **2017**, *46*, 7317−7337.

(4) Monro, S.; Colón, K. L.; Yin, H.; Roque, J.; Konda, P.; Gujar, S.; Thummel, R. P.; Lilge, L.; Cameron, C. G.; McFarland, S. A. Transition Metal Complexes and Photodynamic Therapy from a Tumor-Centered Approach: Challenges, Opportunities, and Highlights from the Development of TLD1433. *Chem. Rev.* **2019**, *119*, 797−828.
(5) Dwyer, F.; Reid, I.; Shulman, A.; Laycock, G. M.; Dixson, S. The biological actions of 1,10-phenanthroline and 2,2'-bipyridine hydrochlorides, quaternary salts and metal chelates and related compounds. *Aust. J. Exp. Biol. Med. Sci.* **1969**, *47* (2), 203−218.
(6) Dwyer, F. P.; Gyarfas, E. C.; Rogers, W. P.; Koch, J. H. Biological Activity of Complex Ions. *Nature* **1952**, *170*, 190−191.
(7) Bolhuis, A.; Hand, L.; Marshall, J. E.; Richards, A. D.; Rodger, A.; Aldrich-Wright, J. Antimicrobial Activity of Ruthenium-Based Intercalators. *Eur. J. Pharm. Sci.* **2011**, *42* (4), 313−317.
(8) Li, F.; Collins, J. G.; Keene, F. R. Ruthenium Complexes as Antimicrobial Agents. *Chem. Soc. Rev.* **2015**, *44*, 2529−2542.
(9) Abreu, F. D.; Paulo, T. D. F.; Gehlen, M. H.; Ando, R. A.; Lopes, L. G. F.; Gondim, A. C. S.; Vasconcelos, M. A.; Teixeira, E. H.; Sousa, E. H. S.; De Carvalho, I. M. M. Aryl-Substituted Ruthenium(II) Complexes: A Strategy for Enhanced Photocleavage and Efficient DNA Binding. *Inorg. Chem.* **2017**, *56* (15), 9084−9096.
(10) Frei, A.; Rubbiani, R.; Tubafard, S.; Blacque, O.; Anstaett, P.; Felgenträger, A.; Maisch, T.; Spiccia, L.; Gasser, G. Synthesis, Characterization, and Biological Evaluation of New Ru(II) Polypyridyl Photosensitizers for Photodynamic Therapy. *J. Med. Chem.* **2014**, *57* (17), 7280−7292.
(11) Pierce, S.; Jennings, M. P.; Juliano, S. A.; Angeles-Boza, A. M. Peptide-Ruthenium Conjugate as an Efficient Photosensitizer for the Inactivation of Multidrug-Resistant Bacteria. *Inorg. Chem.* **2020**, *59* (20), 14866−14870.
(12) Conti, L.; Mengoni, A.; Elena, G.; Mari, L.; Perfetti, M.; Fagorzi, C.; Sorace, L.; Valtancoli, B.; Giorgi, C. Exploring the Potential of Highly Charged Ru (II) - and Heteronuclear Ru (II)/ Cu (II) -Polypyridyl Complexes as Antimicrobial Agents. *J. Inorg. Biochem.* **2021**, *220*, 111467.
(13) Boccalini, G.; Conti, L.; Montis, C.; Bani, D.; Bencini, A.; Berti, D.; Giorgi, C.; Mengoni, A.; Valtancoli, B. Methylene Blue-Containing Liposomes as New Photodynamic Anti-Bacterial Agents. *J. Mater. Chem. B* **2017**, *5*, 2788−2797.
(14) Ali, H.; Van Lier, J. E. Metal Complexes as Photo- and Radiosensitizers. *Chem. Rev.* **1999**, *99* (9), 2379−450.
(15) Conti, L.; Bencini, A.; Ferrante, C.; Gellini, C.; Paoli, P.; Parri, M.; Pietraperzia, G.; Valtancoli, B.; Giorgi, C. Highly Charged Ruthenium(II) Polypyridyl Complexes as Effective Photosensitizer in Photodynamic Therapy. *Chem. - Eur. J.* **2019**, *25* (45), 10606−10615.
(16) Le Gall, T.; Lemercier, G.; Chevreux, S.; Tücking, K. S.; Ravel, J.; Thétiot, F.; Jonas, U.; Schönherr, H.; Montier, T. Ruthenium(II) Polypyridyl Complexes as Photosensitizers for Antibacterial Photodynamic Therapy: A Structure−Activity Study on Clinical Bacterial Strains. *ChemMedChem* **2018**, *13* (20), 2229−2239.
(17) Feng, Y.; Sun, W. Z.; Wang, X. S.; Zhou, Q. X. Selective Photoinactivation of Methicillin-Resistant Staphylococcus Aureus by Highly Positively Charged RuII Complexes. *Chem. - Eur. J.* **2019**, *25* (61), 13879−13884.
(18) Bonnet, S. Why Develop Photoactivated Chemotherapy? *Dalt. Trans.* **2018**, *47*, 10330−10343.
(19) Havrylyuk, D.; Stevens, K.; Parkin, S.; Glazer, E. C. Toward Optimal Ru(II) Photocages: Balancing Photochemistry, Stability, and Biocompatibility through Fine Tuning of Steric, Electronic, and Physiochemical Features. *Inorg. Chem.* **2020**, *59* (2), 1006−1013.
(20) Wagenknecht, P. S.; Ford, P. C. Metal Centered Ligand Field Excited States: Their Roles in the Design and Performance of Transition Metal Based Photochemical Molecular Devices. *Coord. Chem. Rev.* **2011**, *255* (5), 591−616.
(21) Knoll, J. D.; Albani, B. A.; Turro, C. New Ru(II) Complexes for Dual Photoreactivity: Ligand Exchange and $^1O_2$ Generation. *Acc. Chem. Res.* **2015**, *48* (8), 2280−2287.
(22) Wachter, E.; Howerton, B. S.; Hall, E. C.; Parkin, S.; Glazer, E. C. A New Type of DNA "Light-Switch": A Dual Photochemical Sensor and Metalating Agent for Duplex and G-Quadruplex DNA. *Chem. Commun.* **2014**, *50*, 311−313.
(23) Baranoff, E.; Collin, J. P.; Furusho, J.; Furusho, Y.; Laemmel, A. C.; Sauvage, J. P. Photochemical or Thermal Chelate Exchange in the Ruthenium Coordination Sphere of Complexes of the $Ru(Phen)_2L$ Family (L = Diimine or Dinitrile Ligands). *Inorg. Chem.* **2002**, *41* (5), 1215−1222.
(24) Hecker, C. R.; Fanwick, P. E.; McMillin, D. R. Evidence for dissociative photosubstitution reactions of $[Ru(Trpy)(Bpy)(NCCH_3)]^{2+}$. Crystal and molecular structure of $[Ru(Trpy)(Bpy)(Py)](PF_6)_2 \bullet (CH_3)_2CO$. *Inorg. Chem.* **1991**, *30*, 659−666.
(25) Ang, C. W.; Jarrad, A. M.; Cooper, M. A.; Blaskovich, M. A. T. Nitroimidazoles: Molecular Fireworks That Combat a Broad Spectrum of Infectious Diseases. *J. Med. Chem.* **2017**, *60* (18), 7636−7657.
(26) Mazuryk, O.; Suzenet, F.; Kieda, C.; Brindell, M. The biological effect of the nitroimidazole derivative of a polypyridyl ruthenium complex on cancer and endothelial cells. *Metallomics* **2015**, *7*, 553.
(27) Mazuryk, O.; Foria, K. O.; Żak, A.; Suzenet, F.; Belowska, P. A.; Brzozowski, T.; Stochel, G.; Brindell, M. Nitroimidazole derivatives of polypyridyl ruthenium complexes: Towards understanding their anticancer activity and mode of action. *Eur. J. Pharm. Sci.* **2017**, *101*, 43−55.
(28) Son, A.; Kawasaki, A.; Hara, D.; Ito, T.; Tanabe, K. Phosphorescent Ruthenium Complexes with a Nitroimidazole Unit that Image Oxygen Fluctuation in Tumor Tissue. *Chem. - Eur. J.* **2015**, *21*, 2527−2536.
(29) Sasahara, G. L.; Gouveia Júnior, F. S.; Rodrigues, R. de O.; Zampieri, D. S.; Fonseca, S. G. da C.; Gonçalves, R. de C. R.; Athaydes, B. R.; Kitagawa, R. R.; Santos, F. A.; Sousa, E. H. S.; Nagao-Dias, A. T.; Lopes, L. G. de F. Nitro-Imidazole-Based Ruthenium Complexes with Antioxidant and Anti-Inflammatory Activities. *J. Inorg. Biochem.* **2020**, *206*, 111048.
(30) Bai, L.; Li, F.; Wang, Y.; Li, H.; Jiang, X.; Sun, L. Visible-Light-Driven Selective Oxidation of Benzyl Alcohol and Thioanisole by Molecular Ruthenium Catalyst Modified Hematite. *Chem. Commun.* **2016**, *52*, 9711−9714.
(31) Bonnet, S.; Collin, J. P.; Gruber, N.; Sauvage, J. P.; Schofield, E. R. Photochemical and Thermal Synthesis and Characterization of Polypyridine Ruthenium(II) Complexes Containing Different Monodentate Ligands. *Dalton Trans* **2003**, 4654−4662.
(32) Becke, A. D.; Edgecombe, K. E. A Simple Measure of Electron Localization in Atomic and Molecular Systems. *J. Chem. Phys.* **1990**, *92*, 5397.
(33) Silvi, B.; Savin, A. Classification of Chemical Bonds Based on Topological Analysis of Electron Localization Functions. *Nature* **1994**, *371*, 683−686.
(34) Reddy, K. B.; Cho, M. O. P.; Wishart, J. F.; Emge, T. J.; Isied, S. S. Cis-Bis(Bipyridine)Ruthenium Imidazole Derivatives: A Spectroscopic, Kinetic, and Structural Study. *Inorg. Chem.* **1996**, *35* (25), 7241−7245.
(35) Yang, X. J.; Drepper, F.; Wu, B.; Sun, W. H.; Haehnel, W.; Janiak, C. From Model Compounds to Protein Binding: Syntheses, Characterizations and Fluorescence Studies of [RuII(Bipy)(Terpy)L]2+ Complexes (Bipy = 2,2′-Bipyridine; Terpy = 2,2′:6′, 2″-Terpyridine; L = Imidazole, Pyrazole and Derivatives, Cytochrome C). *Dalt. Trans.* **2005**, *21* (2), 256−67.
(36) Wu, A.; Masland, J.; Swartz, R. D.; Kaminsky, W.; Mayer, J. M. Synthesis and Characterization of Ruthenium Bis(β-Diketonato) Pyridine-Imidazole Complexes for Hydrogen Atom Transfer. *Inorg. Chem.* **2007**, *46* (26), 11190−11201.
(37) Knoll, J. D.; Albani, B. A.; Durr, C. B.; Turro, C. Unusually Efficient Pyridine Photodissociation from Ru(II) Complexes with Sterically Bulky Bidentate Ancillary Ligands. *J. Phys. Chem. A* **2014**, *118* (45), 10603−10610.
(38) Albani, A. B.; Whittemore, T.; Durr, B. C.; Turro, C. Steric and Electronic Factors Associated with the Photoinduced Ligand Exchange of Bidentate Ligands Coordinated to Ru(II). *Photochem. Photobiol.* **2015**, *91*, 616−623.

https://doi.org/10.1021/acs.inorgchem.1c03032
Inorg. Chem. XXXX, XXX, XXX−XXX

(39) Azam, A.; Peerzada, M. N.; Ahmad, K. Parasitic Diarrheal Disease: Drug Development and Targets. *Front. Microbiol.* **2015**, *6*, 1183.
(40) Brett, A. M. O.; Serrano, S. H. P.; Gutz, I.; La-Scalea, M. A.; Cruz, M. L. Voltammetric Behavior of Nitroimidazoles at a DNA-Biosensor. *Electroanalysis* **1997**, *9* (14), 1132−1137.
(41) Havrylyuk, D.; Deshpande, M.; Parkin, S.; Glazer, E. C. Ru(Ii) Complexes with Diazine Ligands: Electronic Modulation of the Coordinating Group Is Key to the Design of "Dual Action" Photoactivated Agents. *Chem. Commun.* **2018**, *54*, 12487−12490.
(42) Mari, C.; Pierroz, V.; Ferrari, S.; Gasser, G. Combination of Ru(II) complexes and light: new frontiers in cancer therapy. *Chem. Sci.* **2015**, *6*, 2660−2686.
(43) Thomas, C.; Gwenin, C. D. The Role of Nitroreductases in Resistance to Nitroimidazoles. *Biology (Basel, Switz.)* **2021**, *10* (5), 388.

https://doi.org/10.1021/acs.inorgchem.1c03032
Inorg. Chem. XXXX, XXX, XXX−XXX

Inorganic Chemistry

pubs.acs.org/IC

Article

Ruthenium(II) Polypyridyl Complexes and Metronidazole Derivatives: A Powerful Combination in the Design of Photoresponsive Antibacterial Agents Effective under Hypoxic Conditions

Gina Elena Giacomazzo, Luca Conti,* Camilla Fagorzi, Marco Pagliai, Claudia Andreini, Annalisa Guerri, Brunella Perito, Alessio Mengoni, Barbara Valtancoli, and Claudia Giorgi*

Cite This: https://doi.org/10.1021/acs.inorgchem.3c00214

Read Online

ACCESS | Metrics & More | Article Recommendations | Supporting Information

ABSTRACT: Ruthenium(II) polypyridyl complexes (RPCs) are gaining momentum in photoactivated chemotherapy (PACT), thanks to the possibility of overcoming the classical reliance on molecular oxygen of photodynamic therapy while preserving the selective drug activation by using light. However, notwithstanding the intriguing perspectives, the translation of such an approach in the development of new antimicrobials has been only barely considered. Herein, MTZH-1 and MTZH-2, two novel analogues of metronidazole (MTZ), a mainstay drug in the treatment of anaerobic bacterial infections, were designed and inserted in the strained ruthenium complexes $[Ru(tpy)(dmp)(MTZ\text{-}1)]PF_6$ (**Ru2**) and $[Ru(tpy)(dmp)(MTZ\text{-}2)]PF_6$ (**Ru3**) (tpy = terpyridine, dmp = 2,9-dimethyl-1,10-phenanthroline) (Chart 1). Analogously to the parental compound $[Ru(tpy)(dmp)(5NIM)]PF_6$ (**Ru1**) (5-nitroimidazolate), the Ru(II)-imidazolate coordination of MTZ derivatives resulted in promising Ru(II) photocages, capable to easily unleash the bioactive ligands upon light irradiation and increase the antibacterial activity against *Bacillus subtilis*, which was chosen as a model of Gram-positive bacteria. The photoreleased 5-nitroimidazole-based ligands led to remarkable phototoxicities under hypoxic conditions (<1% O_2), with the lead compound **Ru3** that exhibited the highest potency across the series, being comparable to the one of the clinical drug MTZ. Besides, the chemical architectures of MTZ derivatives made their interaction with NimAunfavorable, being NimA a model of reductases responsible for bacterial resistance against 5-nitroimidazole-based antibiotics, thus hinting at their possible use to combat antimicrobial resistance. This work may therefore provide fundamental knowledge in the design of novel photoresponsive tools to be used in the fight against infectious diseases. For the first time, the effectiveness of the "*photorelease antimicrobial therapy*" under therapeutically relevant hypoxic conditions was demonstrated.

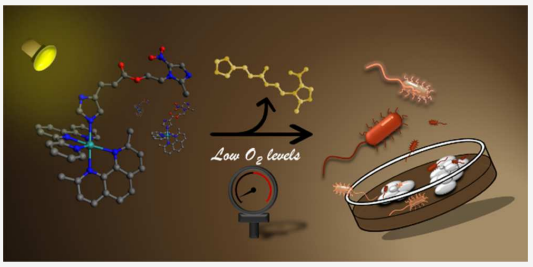

INTRODUCTION

Antimicrobial resistance (AMR) is now a leading cause of death worldwide.[1] Notwithstanding the attention on this global health threat has increased in recent years, the widespread use of antibiotics has dramatically facilitated the emergence of drug-resistant populations of microorganisms, with the result that many hundreds of thousands of deaths are currently due to common, previously treatable, infections. The fight against AMR can no longer wait, and, alongside a more conscious use of antibiotics, there is an urgent need for the development of effective antimicrobials, which should be based on a new class of compounds, rather than on analogues of known scaffolds.

In this respect, transition metal complexes are promising sources for new antimicrobials as they offer augmented electronic properties and a rich variety of three-dimensional structures if compared to their organic counterparts.[2−4] According to the literature, a number of complexes of transition metals (including Mn, Cu, Zn, Ru, Rh, Pd, Ag, Ir, Pt, Au, *etc.*) were shown to possess antibacterial properties,[5−11] with few of them that reached the clinical use.[12−14] However, many opportunities offered by the application of inorganic chemistry to this field of research remain unexplored.

Recently, the encouraging results obtained in the design of antitumoral agents[15−20] have renewed the interest in Ru(II)-polypyridyl complexes (RPCs), a versatile class of compounds whose antibacterial potential was first reported over 70 years ago.[21,22] Their rich chemical−physical repertoire, which

Received: January 18, 2023

Chart 1. Chemical Structures of Nitroimidazole-Containing Ligands 5NIMH, MTZ, MTZH-1, and MTZH-2 and of the Ruthenium Complexes Ru1, Ru2, and Ru3

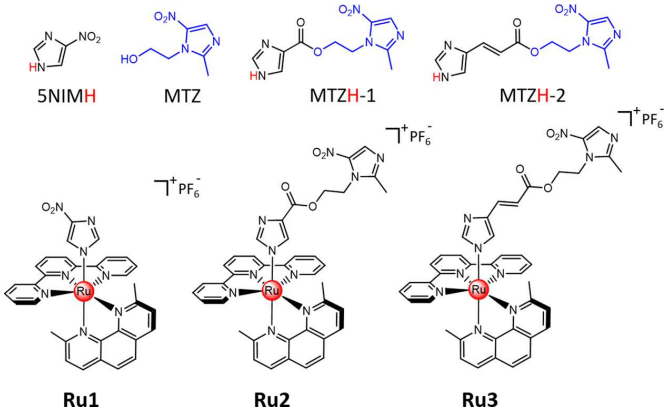

includes versatile optical and luminescent properties, capacity to interact with key biological targets, and amenability to synthetic tailoring (just to name a few), has been indeed exploited to develop new classes of antibacterial agents.[23−28] Of particular relevance is the combination of RPCs with light in the so-called antimicrobial photodynamic therapy (aPDT),[29−32] a technique that relies on the irradiation of a photosensitizer (RPCs) to promote the generation of highly cytotoxic reactive oxygen species (ROS).[33−36] Besides ROS sensitization, whose effectiveness against both sensitive and multidrug-resistant bacteria has been reported,[37,38] the main advantage of aPDT consists in the complete spatiotemporal control over the drug activation, which offers the important chance to overcome overdose and side effect issues normally associated with the systemic administration of antimicrobials. However, the reliance of aPDT on molecular oxygen still threatens its application to hypoxic environments, such as anaerobic infections.[39] This has led to the birth of photoresponsive RPCs able to exert cytotoxic effects *via* O_2-independent mechanisms, through, for instance, the photorelease of biologically active compounds. Since these processes usually require the population of ligand dissociative metal-centered (^{3}MC) states, whose direct excitation is forbidden, strain-inducing substituents are commonly inserted into Ru(II) scaffolds to lower the energy of ^{3}MC states and permit their thermal population.[40,41] In spite of the attractive perspectives, and in net contrast to photoactivated chemotherapy (PACT), where this strategy is gaining momentum,[42−44] the translation of such an approach in the research of new antimicrobials has been only sparingly investigated. In fact, very few examples[45−47] followed the pioneering work by Sadler and coworkers on the use of Ru(II) photocages to control the liberation of the antituberculosis drug isoniazid (INH)[48] and, importantly, none of them inspected the antibacterial potential under the more therapeutically relevant, hypoxic conditions.

With this regard, we recently reported on the combination between RPCs and 5-nitroimidazole (5NIMH), taken as the simplest molecular model of 5-nitroimidazoles,[49] an intriguing class of broad-spectrum antimicrobial agents, whose peculiar mode of action, based on intracellular bioactivation of the nitro group to toxic radical species, makes them effective even under low-oxygen conditions.[50,51] We showed that the $[Ru(tpy)(dmp)]^{2+}$ scaffold could be successfully employed to control the photoinduced liberation of 5NIMH from $[Ru(tpy)(dmp)(5NIM)]PF_6$ (**Ru1**) (tpy = terpyridine, dmp = 2,9-dimethyl-1,10-phenanthroline) (Chart 1). Indeed, the presence of two bulky methyl groups in the 2 and 9 positions of dmp favored the selective photoejection of the monodentate ligand, enhancing the antibacterial activity against *Bacillus subtilis*, even though only moderate phototoxicities were observed due to the low efficacy of 5NIMH. This prompted us to further explore the use of the $[Ru(tpy)(dmp)]^{2+}$ scaffold to cage more potent nitroimidazole-based antimicrobials.

Herein, MTZH-1 and MTZH-2, two novel derivatives of metronidazole (2-(2-methyl-5-nitro-1*H*-imidazol-1-yl)-ethanol), namely, one of the mainstay drugs for the treatment of anaerobic bacterial infections, were synthesized and inserted into the corresponding ruthenium complexes $[Ru(tpy)(dmp)(MTZ\text{-}1)]PF_6$ (**Ru2**) and $[Ru(tpy)(dmp)(MTZ\text{-}2)]PF_6$ (**Ru3**) (Chart 1). Besides the characterization of the obtained compounds, their capacity to effectively release the MTZ derivatives upon LED illumination was investigated, whereas their biological activities were inspected against *B. subtilis*, which was chosen as a model of Gram-positive bacteria, *in the dark* and following light exposure, both in normoxic (21% O_2) and hypoxic (<1% O_2) conditions. Moreover, the abilities of MTZH-1 and MTZH-2 to interact with NimA, taken as a target protein responsible for metronidazole resistance, were evaluated.

The aim of this study is to demonstrate that RPCs and MTZ derivatives can be combined together to realize promising antibacterial agents, effective under low-oxygen conditions, and whose activation can be conveniently controlled in a spatiotemporal manner by using light. To the best of our knowledge, this study also probes for the first time the effectiveness of the "*photorelease antimicrobial therapy*" approach under hypoxia.

EXPERIMENTAL SECTION

Materials. All materials were of reagent grade and used without further purification. The DMF used for the preparation of the MTZ derivatives was obtained through distillation under a vacuum after using barium oxide as a dehydrating agent.

Synthesis of MTZH-1. To a solution of 1*H*-imidazole-5-carboxylic acid (300 mg, 2.68 mmol) in 4 mL of anhydrous DMF, *N*,*N*′-

https://doi.org/10.1021/acs.inorgchem.3c00214
Inorg. Chem. XXXX, XXX, XXX−XXX

dicycloexylcarbodiimide (DCC, 458 mg, 2.95 mmol) and 4-dimethylaminopyridine (DMAP, 66 mg, 0.54 mmol) were added. After stirring for 20 min at 45 °C, MTZ (493 mg, 2.68 mmol) was added to the reaction mixture, which was left stirring at 45 °C for 2 days. The evaporation under the vacuum of the solvent led to an oil that was dissolved in 200 mL of CH_2Cl_2, washed twice with 30 mL of H_2O, and once with 20 mL of a NaCl-saturated solution. The organic phase was dried over Na_2SO_4 and evaporated under reduced pressure. The crude product was purified on silica gel using a DCM/MeOH mixture from 15:1 to 10:1 v/v as an eluent.

Yield 18%. ^{1}H NMR (CD_3OD, 400 MHz): δ 7.95 (s, 1H, H_m), 7.80 (s, 1H, H_i) 7.73 (s, 1H, H_j), 4.78 (t, 2H, J = 5.2 Hz, $-CH_2$), 4.71 (t, 2H, J = 4.8 Hz, $-CH_2$), 2.51 (s, 3H, CH_3) ppm. ^{13}C NMR (CD_3OD, 100 MHz): 151.8, 139.5, 137.9, 131.9, 62.3, 45.8, 13.2 ppm. ESI MS m/z: calcd for $C_{10}H_{11}N_5O_4$ $[MTZH\text{-}1]^+$ (m/z = 1) 265.08, found 288.08 $[MTZH\text{-}1 + Na^+]$ and 552.83 $[2MTZH\text{-}1 + Na^+]$ (m/z = 1).

Synthesis of MTZH-2. Analogously to the preparation of the metronidazole ester MTZH-1, DCC (370 mg, 2.39 mmol) and DMAP (54 mg, 0.44 mmol) were added to a solution of urocanic acid (300 mg, 2.17 mmol), previously dissolved in 5 mL of anhydrous DMF. The resulting mixture was stirred for 15 min at r.t and, after the addition of MTZ (399 mg, 2.17 mmol), the reaction mixture was left stirring at 45 °C for 4 days. The solvent was then removed in a vacuum, and the resulting oily residue was dissolved in 200 mL of CH_2Cl_2, washed twice with 30 mL of H_2O, and once with 20 mL of a NaCl-saturated solution. The organic phase was dried over Na_2SO_4 and evaporated under reduced pressure, affording a crude product that was further purified on silica gel (DCM/MeOH from 20:1 to 10:1 v/v).

Yield 26%. ^{1}H NMR ($(CD_3)_2SO$, 400 MHz): δ 8.05 (s, 1H, H_m), 7.80 (s, 1H, H_i), 7.56 (s, 1H, H_j) 7.49 (d, J = 15.6 Hz, 1H, $-CH$), 6.27 (d, J = 15.6, 1H, $-CH$), 4.65 (t, J = 4.8 Hz, 2H, $-CH_2$), 4.49 (t, J = 4.8 Hz, 2H, $-CH_2$), 2.48 (s, 3H, $-CH_3$). ^{13}C NMR ($(CD_3)_2SO$, 100 MHz): 167.2, 152.5, 139.6, 139.0, 134.1, 113.4, 62.9, 46.0, 15.0 ppm. ESI MS m/z: calcd for $C_{12}H_{13}N_5O_4$ $[MTZH\text{-}2]^+$ (m/z = 1) 291.09, found 314.17 $[MTZH\text{-}2 + Na^+]$ (m/z = 1).

*Synthesis of [Ru(tpy)(dmp)(MTZ-1)]PF_6 (**Ru2**).* MTZH-1 (80 mg, 0.30 mmol) was added to a solution of the ruthenium intermediate [Ru(dmp)(tpy)Cl]PF_6 (180 mg, 0.25 mmol) in 60 mL of degassed H_2O-EtOH (50:50% v/v). The reaction mixture was stirred at reflux for 6 h under a N_2 atmosphere while being protected from light exposure. After cooling at r.t., the addition of a KPF_6-saturated aqueous solution afforded the precipitation of the ruthenium compound, which was collected by filtration under reduced pressure and washed with water. The crude product was purified by flash chromatography on silica gel (DCM/MeOH 20:1 v/v with 10% of acetone) to obtain complex **Ru2** as a red solid.

Yield 130 mg, 64%.^{1}H NMR ($(CD_3)_2CO$, 400 MHz): δ 8.90 (d, J = 8.4 Hz, 1H, H_d or H_e), 8.86–8.70 (m, 4H, H_3, and H_3), 8.43 (d, J = 8.0 Hz, 1H, H_f or H_g), 8.40 (d, J = 8.8 Hz, 1H, H_b or H_c), 8.30 (t, J = 8.0 Hz, 1H, $H_{4'}$), 8.26–8.04 (m, 6H, H_d or H_e, H_b or H_c, H_6, H_5), 7.90 (s, 1H, H_m), 7.56 (br, 2H, H_4), 7.44 (d, J = 8.0 Hz, 1H, H_f or H_g), 7.24 (s, 1H, H_i), 6.51 (s, 1H, H_j), 4.68 (t, J = 5.2 Hz, 2H, $-CH_2$ MTZ-1), 4.51 (t, J = 5.2 Hz, 2H, $-CH_2$ MTZ-1), 2.45 (s, 3H, $-CH_3$ MTZ-1), 2.32 (s, 3H, CH_3 dmp), 1.94 (s, 3H, CH_3 dmp) ppm. ^{13}C NMR ($(CD_3)_2CO$, 100 MHz): δ 167.5, 166.9, 159.7, 159.6, 159.0, 154.3, 151.8, 149.1, 148.7, 142.6, 139.2, 137.7, 137.6, 136.2, 133.3, 132.6, 130.1, 129.7, 129.3, 128.3, 127.7, 127.5, 127.1, 126.6, 125.3, 124.4, 63.2, 55.1, 45.2, 25.5, 23.9, 14.1 ppm. HR-ESI MS m/z: calcd for $C_{39}H_{33}N_{10}O_4Ru$ [**Ru2** − PF_6^-]$^+$ (m/z = 1) 807.17243, found 807.17124 [**Ru2** − KPF_6^-]$^+$ (m/z = 1) and 404.09067 [**Ru2** + H^+-PF_6^-]$^{2+}$ (m/z = 2).

*Synthesis of [Ru(tpy)(dmp)(MTZ-2)]PF_6 (**Ru3**).* In analogy to the preparation of **Ru2**, MTZH-2 (73 mg, 0.25 mmol) was added to a solution of [Ru(dmp)(tpy)Cl]PF_6 (150 mg, 0.21 mmol) in 60 mL of degassed H_2O−EtOH (50:50% v/v). The reaction mixture was stirred at 70 °C for 7 h under a N_2 atmosphere while being protected from light exposure and then cooled at r.t. The addition of a saturated KPF_6 aqueous solution afforded the precipitation of the ruthenium complex, which was collected by filtration under reduced pressure and washed with water. The product was purified by flash chromatography on silica gel (DCM/MeOH 15:1 v/v with 10% of acetone) to obtain complex **Ru3** as a red solid.

Yield 112 mg, 62%. ^{1}H NMR ($(CD_3)_2CO$, 400 MHz): δ 8.90 (d, J = 8.8 Hz, 1H, H_d or H_e), 8.81 (d, J = 8.8 Hz, 2H, $H_{3'}$),8.75 (d, J = 7.2 Hz, 2H, H_3), 8.43 (d, J = 8.8 Hz, 1H, H_f or H_g), 8.38 (d, J = 8.8 Hz, 1H, H_b or H_c), 8.32 (t, J = 8.4 Hz, 1H, $H_{4'}$), 8.25–8.03 (m, 6H, H_d or H_e, H_b or H_c, H_4, H_6), 7.88 (s, 1H, H_m), 7.54 (br, 2H, H5), 7.45 (d, J = 8.4 Hz, 1H, H_f or H_g), 7.39 (s, 1H, H_i), 7.23 (d, J = 17.2 Hz, 1H, $-CH$ MTZ-2), 6.73 (s, 1H, H_j), 6.15 (d, J = 16.4 Hz, 1H, $-CH$ MTZ-2), 4.71 (t, J = 5.2, 2H, -CH_2 MTZ-2), 4.52 (t, J = 4.8 Hz, 2H, $-CH_2$ MTZ-2), 2.56 (s, 3H, $-CH_3$ MTZ-2), 2.44 (s, 3H, $-CH_3$ dmp), 1.95 (s, 3H, $-CH_3$ dmp) ppm. ^{13}C ($(CD_3)_2CO$, 100 MHz): δ 167.4, 167.0, 165.7, 159.7, 154.4, 151.8, 149.1, 148.7, 139.2, 137.7, 137.6, 136.4, 129.2, 128.3, 127.6, 127.5, 127.1, 125.3, 124.4, 117.3, 63.0, 45.5, 25.6, 24.0, 14.0 ppm. HR-ESI MS m/z: calcd for $C_{41}H_{35}N_{10}O_4Ru$ [**Ru3** − PF_6^-]$^+$ (m/z = 1) 833.18808, found 833.18796 [**Ru3** − PF_6^-]$^+$ (m/z = 1) and 417.09812 [**Ru3** + H^+ − PF_6^-]$^{2+}$ (m/z = 2).

Methods. During the synthesis of ruthenium compounds, low-light conditions were maintained to avoid any photodecomposition issues. The [Ru(dmp)(tpy)Cl]PF_6 intermediate was prepared according to methods reported in the literature.[52]

Irradiation of ruthenium complexes was performed by employing a low-energy blue light-emitting diode as a light source (LED, λ_{max} = 434 nm, 160 mW). Photolysis experiments were performed in acetonitrile and in an aqueous solution (PBS buffer, pH 7.4) and were followed by ultraviolet−visible (UV−vis) spectroscopy and high-performance liquid chromatography (HPLC) analyses. In the UV−vis measurements, solutions of **Ru2** and **Ru3** (10 μM) in acetonitrile or aqueous media (total volume of 2 mL) were subjected to increasing irradiation times, and the resulting absorption spectra were collected. In the HPLC measurements, solutions of ruthenium complexes ([Ru] = 100 μM) in aqueous media (total volume of 1 mL) were irradiated for increasing time frames and, at each irradiation point, a 10 μL aliquot of the irradiated solution was injected in the HPLC system. Chromatographic conditions were optimized by using as a gradient mixture of H_2O/CH_3CN acidified with 0.1% of formic acid as an eluent, as specified in Table S4 of Supporting Information (SI). The quantum yields for the photodissociation of MTZ derivatives from **Ru2** and **Ru3** (Φ_{434} values) in acetonitrile and water were, respectively, determined through UV−vis spectroscopy and HPLC analysis. Indeed, in water, the close proximity between the ^{1}MLCT absorption maximum values corresponding to the starting ruthenium compounds and to the aqua-photoproduct $[Ru(tpy)(dmp)(H_2O)]^{2+}$ (centered at around 480−490 nm),[53] along with the broader absorption displayed by **Ru2** and **Ru3** in this solvent, made difficult an equally accurate determination of the Φ_{434} values in water by means of UV−vis measurements. Φ_{434} values were determined by the slope of the linear regression of the moles of the reactant plotted as a function of the moles of the absorbed photons, as previously described.[49] The photon flux of the light source was obtained by the potassium ferrioxalate actinometry procedure according to methods reported in the literature,[54] and resulted in being 5.76 × 10^{-7} E/s.

The singlet oxygen-sensitizing properties of ruthenium compounds were investigated through UV−vis analysis by using 1,5-dihydroxynaphthalene (DHN) as an indirect reporter for $^1O_2$ and according to methods reported in the literature. To this aim, solutions of metal complexes ([Ru] = 10 μM) in aqueous media (PBS buffer, pH 7.4) containing DHN at a concentration of 3.3 × 10^{-4} M were irradiated for progressive time frames for a total period of 10 min. Spectra were acquired by using a solution containing only the ruthenium compound as a blank reference at the same pH and concentration of the measuring cuvette.

The determination of inhibitory concentrations was performed as previously reported.[49] Briefly, overnight grown liquid cultures of the facultative anaerobic bacterium *B. subtilis* 168 were prepared in 10 mL of an LB medium from single colonies freshly grown on LB agar Petri plates. Cultures were incubated at 37 °C in a rotatory shaker at 225

https://doi.org/10.1021/acs.inorgchem.3c00214
Inorg. Chem. XXXX, XXX, XXX−XXX

Scheme 1. Synthetic Routes Followed for the Synthesis of the Ester Derivatives of Metronidazole MTZH-1 and MTZH-2 and Their Corresponding Ruthenium Complexes Ru2 and Ru3

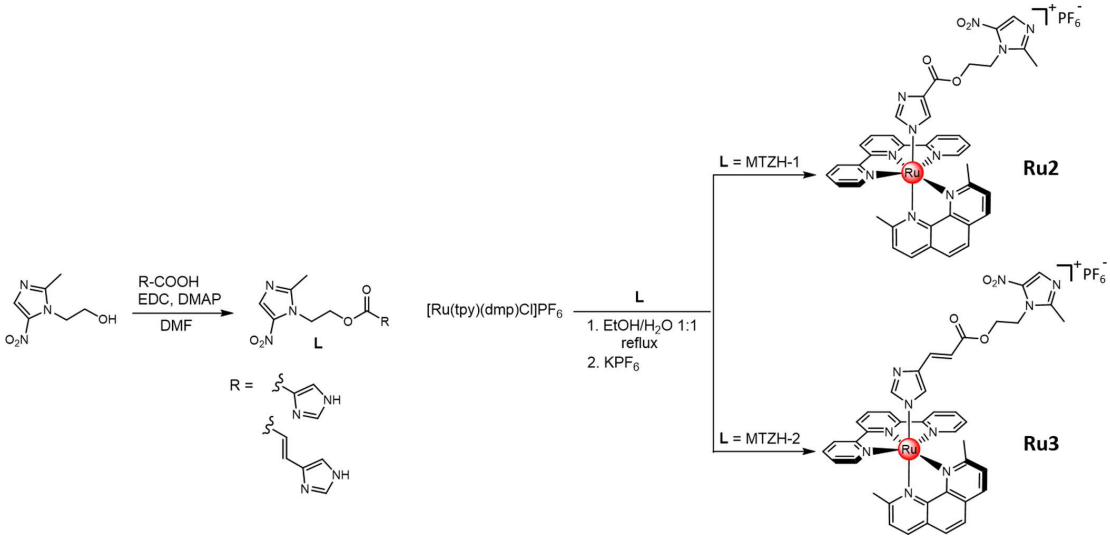

rpm for 24 h and diluted cultures of *B. subtilis* (OD_{600} = 0.05) were dosed with different concentrations of nitroimidazole-based compounds and ruthenium complexes. The activity of each compound was tested under the dark and following light irradiation, both in normoxia (21% O_2) and under hypoxic conditions (<1% O_2). In the photoirradiation experiments, cells were exposed to irradiation (LED emitting light at 434 nm, 1.25 mW) for 40 min; under these conditions, no statistical differences in the blank absorbance between the light- and dark-treated groups of cells were observed. The photon flux in each plate resulted in being 4.72×10^{-9} E/s, as determined by the ferrioxalate actinometer method.[54] Cell growth was carried out statically, by incubating microtiter plates at 37 °C, and it was evaluated by registering the OD_{600} values after 24 h for aerobiosis cultures and after 7 days for the anaerobiosis test. Each test was performed in triplicate, using LB with 0.25% glucose and 0.1% potassium nitrate as culture media to sustain the growth of *B. subtilis* both in aerobiotic and anaerobiotic conditions.[55] In Figure 3, where the observed antibacterial activities displayed by the tested compounds are reported, the OD_{600} values are normalized and indicate the ratio of cell growth compared to the (untreated) control cells. Differences in the growth were statistically evaluated by the one-way analysis of variance (ANOVA) test and the Tukey post-hoc test (Table S5, SI). The cell growth ratios between different conditions are shown in Figure S35 of SI: lower values indicate lower growth in the first condition tested compared to the second one. Heatmaps were drawn in an R environment, with the package *pheatmap* 1.0.12.

Density functional theory calculations have been carried out with the Gaussian 09 suite of programs[56] at the B3LYP/6-31+G(d) level of theory. The molecular structure of all studied molecules has been optimized with a very tight criterium, and it has been verified that a minimum has been located by computing the vibrational frequencies, which are all real. Mulliken, Lowdin, and natural population analysis have been performed to determine the atomic charges and to provide further insights into the ligand/ruthenium complex interactions.

Instrumentation. The ^1H, ^{13}C NMR, COSY, and HSQC spectra were collected with a Bruker 400 MHz spectrometer. Electronic absorption spectroscopy was performed by using a PerkinElmer Lambda 6 spectrophotometer in a 1 × 1 cm^2 quart cuvette. Fourier transform infrared (FTIR) spectra of compounds were obtained between 500 and 4000 cm^{-1} by a Nicolet iS5 Spectrometer equipped with an iD7 ATR accessory (Thermo Fischer Scientific Inc). HPLC analysis was performed on a Water Alliance 2690 HPLC equipped with a Waters 2487 Abs UV−vis detector set at 270 nm and a KROMASIL 100 Å C−18 150 × 4.6 column. In the determination of inhibitory concentration, the OD 600 values were registered by using an Infinite Pro 200 plate reader (Tecan, Switzerland); the experiments performed under anaerobic conditions were conducted in an anaerobiosis jar (Oxoid jar with Anaerogen 2.5 L), with the system described in paragraph 4 of SI.

RESULTS AND DISCUSSION

Synthesis and Characterization of Ruthenium Complexes. Metronidazole stands for a reference drug for the treatment of anaerobic infections. However, several anaerobic bacteria and protozoa were shown to develop resistance to MTZ, making it important to research suitable alternatives.[57] Herein, we designed two analogues of MTZ, in which the clinical drug was coupled with 1*H*-imidazole-5-carboxylic acid (MTZH-1) or urocanic acid (MTZH-2), two imidazole-containing ligands of biological interest and whose imidazole moieties can be exploited as linking units to the Ru(II) centers (*vide infra*). The synthetic routes followed for the synthesis of the metronidazole derivatives MTZH-1 and MTZH-2, as well as for their corresponding ruthenium complexes **Ru2** and **Ru3**, are reported in Scheme 1.

As shown, the MTZ derivatives were synthesized *via* Steglich esterification: MTZ was allowed to react with 1*H*-imidazole-5-carboxylic acid (MTZH-1) or urocanic acid (MTZH-2) in the presence of *N*,*N*′-dicycloexylcarbodiimide (EDC) as a coupling reagent and 4-dimethylaminopyridine (DMAP) as a catalyst. This led to the formation of MTZH-1 and MTZH-2, which were obtained, after purification on silica gel, in 18 and 26% yields, respectively. Their insertion into ruthenium complexes **Ru2** and **Ru3** was accomplished *via* stepwise ligand addition (Scheme 1), in analogy to the synthetic process previously reported for **Ru1**.[49] Briefly, following the preparation of $[Ru(dmp)(tpy)Cl]PF_6$, performed according to the literature,[52,58] this intermediate was allowed to react with MTZH-1 and MTZH-2 in a hot ethanol−water mixture for 6−

https://doi.org/10.1021/acs.inorgchem.3c00214
Inorg. Chem. XXXX, XXX, XXX−XXX

7 h under an inert atmosphere, affording the replacement of the chloro ligand with the imidazole rings. Then, the addition of aqueous KPF_6 led to the precipitation of the hexafluorophosphate salts **Ru2** and **Ru3**, which were obtained, after purification by flash chromatography, in 64 and 62% yields, respectively. The identity of compounds was confirmed through ^{1}H, ^{13}C, COSY, and HSQC NMR spectroscopy, high-resolution mass spectrometry (HRMS), electron absorption (UV−vis), and attenuated total reflectance (ATR)-FTIR analysis (see SI, Figures S1−S27).

The crystal structure of MTZH-2 was also determined through X-ray single-crystal analysis, as reported in the SI, Figure S12. As shown, the asymmetric unit (a.u.) of MTZH-2 contains two distinct molecules that form intermolecular "*nitrogen*" hydrogen bonds, involving the NH group and the acceptor aza-nitrogen atom, respectively, of their imidazole and nitroimidazole moieties. The occurrence of intramolecular interactions between the $-NO_2$ group and the nearest aliphatic H atom, which confer to the molecule a bent conformation, can be also highlighted. Quite interestingly, the whole crystal displayed a singular "*wall−hole*" disposition, where the wall was identified by several molecules of ligands, stabilized by intermolecular bonds and stacking interactions between their imidazole/nitroimidazole rings; these molecules surrounded the resulting channel (hole), which was, in turn, occupied by the solvent molecules identified in the crystal (Figure S12b).

Useful insights into the mode of coordination of MTZ derivatives into ruthenium complexes **Ru2** and **Ru3** came from their HR-ESI MS spectra, which were characterized by the presence of the isotopic patterns relative to the mono positively charged species $[Ru(tpy)(dmp)(MTZ\text{-}1)]^+$ and $[Ru(tpy)(dmp)(MTZ\text{-}2)]^+$, respectively, centered at 807.17124 and 833.18795 (m/z = 1) (Figures S17, S18, S24 and S25 of SI). These data indicated the preferential Ru(II) coordination of MTZH-1 and MTZH-2 by the deprotonated amine nitrogen atom of the imidazolate MTZ-1 and MTZ-2 forms, rather than through their neutral aza-nitrogen atoms (Chart 1), in strict analogy to what was previously found for **Ru1**.[49] Density functional theory (DFT) calculations performed on MTZ derivatives further corroborated this coordination mode, as denoted by the higher atomic charges determined on the amine nitrogens of the imidazole rings relative to those on the aza-nitrogens gathered on the nitroimidazole moieties of ligands (Table S3). Therefore, in contrast to the "*classical*" Ru(II) coordination by neutral imidazole-based ligands reported for analogue RPCs,[59−62] these findings suggest that the variable protonation state of the imidazole units,[63] alongside with metal coordination, would afford Ru(II)-imidazolate species, without the need of strong bases as generally required to preliminary obtain the imidazolate forms of ligands.[64] Such an unusual coordination mode can be of use to modulate the properties of the resulting metal complexes as photocages, as stronger Ru−N^- bonds would ensure higher thermal stabilities while maintaining sufficient ligand photoejection quantum yields (Φ_{PS}) (*vide infra*).

The absorption properties of ruthenium complexes were also considered. Figure 1 reports the electronic absorption spectra of **Ru2** and **Ru3** in acetonitrile and in an aqueous solution (PBS buffer, pH 7.4), along with the one of **Ru1** for comparison. As generally found for RPCs,[59] these compounds display the typical $^{1}\pi\pi^*$ transitions relative to tpy and dmp ligands in the UV region along with a broad, unresolved metal-to-ligand Ru(dπ) → tpy/dmp(π^*) charge transfer (^{1}MLCT) band in the visible range. In acetonitrile, the lowest energy absorption bands of **Ru2** and **Ru3** are slightly blue-shifted compared to **Ru1**, with maximum values centered at 482 nm (ε = 7124 M^{-1} cm^{-1}), 492 nm (ε = 6167 M^{-1} cm^{-1}), and 500 nm (ε = 7344 M^{-1} cm^{-1}) for **Ru2**, **Ru3**, and **Ru1**, respectively (also see Table 1). Smaller variations between the wavelengths corresponding to the maxima of ^{1}MLCT transitions were displayed in aqueous media. A residual absorption tail within the 550−650 nm range of the spectra can be also evidenced for all of the complexes, thus providing a promising feature for their activation by using low-energy light, with enhanced depth penetration into tissues. On the other side, these complexes emerged to be weakly emissive, likely due to nonradiative decay pathways promoted by the competitive population of ^{3}MC states.[65]

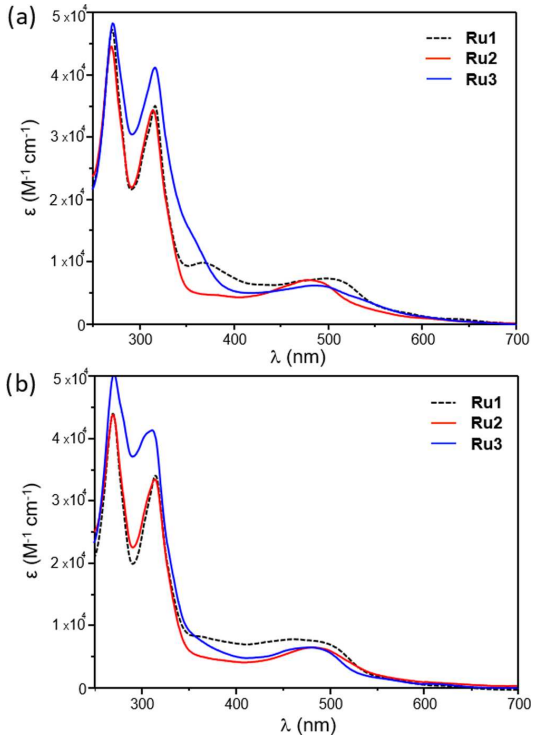

Figure 1. Electronic absorption spectra of **Ru1**, **Ru2**, and **Ru3** in acetonitrile (a) and in a PBS buffer solution, pH 7.4 (b).

Photoreactivity of Ruthenium Complexes. The ability of **Ru2** and **Ru3** to release the MTZ derivatives upon light irradiation was explored in acetonitrile and in an aqueous solution (PBS buffer, pH 7.4) by coupling UV−vis and HPLC analyses. The obtained results for **Ru2** and **Ru3** are, respectively, reported in Figures 2 and S30 and S31 of SI.

Contrary to dark conditions, in which, analogously to **Ru1**, these systems displayed remarkable stability (Figures S28 and S29, SI), visible-light exposure (LED emitting at 434 nm, 160 mW) determined clear changes in the electronic absorption spectra of both compounds, indicating the occurrence of photoejection processes. For instance, as shown in Figure 2a for acetonitrile solutions of **Ru2**, light exposure promoted a

https://doi.org/10.1021/acs.inorgchem.3c00214
Inorg. Chem. XXXX, XXX, XXX−XXX

Table 1. Absorption Maxima and Photoinduced Ligand Substitution Quantum Yields (Φ_{434}) for Ru1, Ru2, and Ru3

complex	λ_{max}/nm (ε/M^{-1} cm^{-1}) in CH_3CN	λ_{max}/nm (ε/M^{-1} cm^{-1}) in H_2O	Φ_{434} in CH_3CN[a]	Φ_{434} in H_2O[b]
Ru1	498 (7349)	462/490 (7831/7438)	0.0039 (3)[c]	0.0011 (3)[c]
Ru2	480 (7006)	485 (6475)	0.0079 (9)	0.00027 (2)
Ru3	488 (6200)	480 (6442)	0.0059 (4)	0.0015 (2)

[a]Determined through UV−vis measurements. [b]obtained by HPLC analysis. [c]Ref 49.

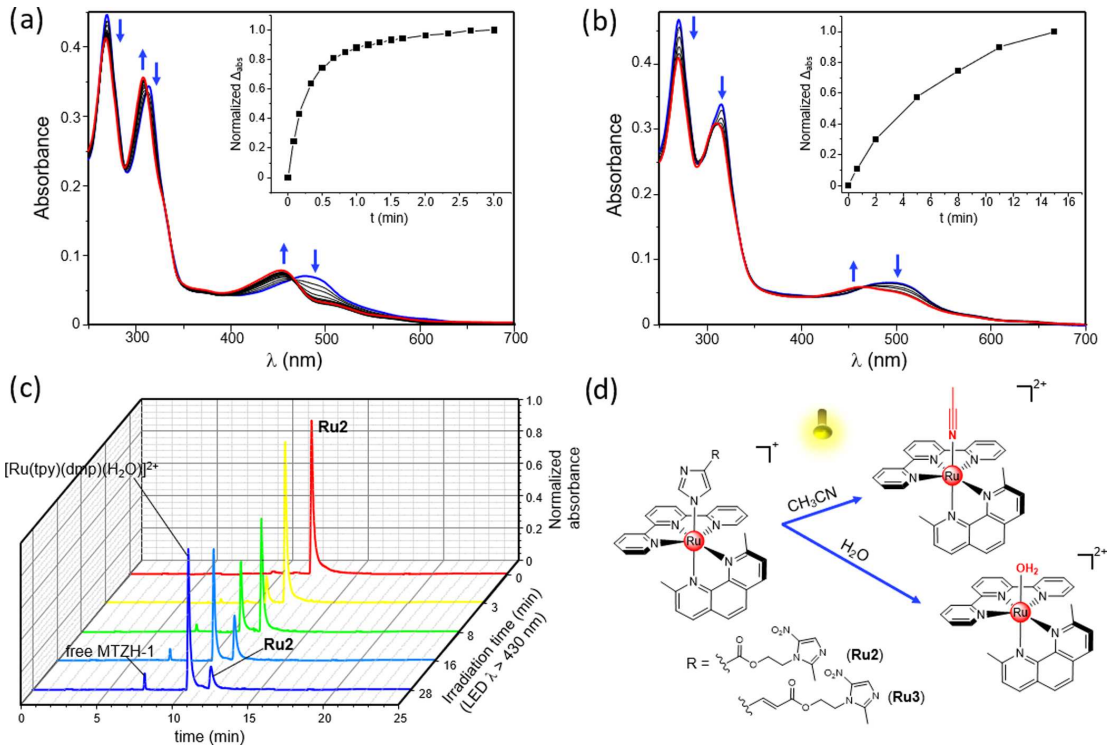

Figure 2. UV−vis absorption spectra of **Ru2** in acetonitrile (a) and in water at neutral pH (b) registered at different irradiation times. Photolysis of **Ru2** in an aqueous solution monitored by means of HPLC analysis (c). Proposed ligand photoejection processes underwent by **Ru2** and **Ru3** (d).

sharp blue shift in the ^{1}MLCT absorption maximum of the metal complex, from 480 to 454 nm, indicating the substitution of MTZH-1 with a solvent molecule to give $[Ru(tpy)(dmp)(CH_3CN)]^{2+}$.[66−68] Photolysis of **Ru2** also took place in aqueous media, albeit on a larger time scale (Figure 2b), thus providing a key prerequisite for biological applications. Importantly, the presence in the UV−vis titrations of multiple isosbestic points indicated the direct conversion to single photoproducts. Parallel HPLC experiments provided further evidence of the selectivity of the photoejection processes. Indeed, as shown in Figure 2c, where the chromatograms of aqueous solutions of **Ru2** exposed to increasing irradiation times are reported, light irradiation promoted the progressive decrease of the peak associated with the starting metal complex (retention time t_r of 11.77 min), accompanied by the appearance of two new peaks at 7.42 and 10.35 min, which can be, respectively, attributable to the liberated MTZH-1 and the resulting Ru(II) aquocomplex. The lack of evidence of free tpy or dmp confirmed the selective photorelease of the monodentate imidazole ligand. Analogue results were also obtained for **Ru3**, as shown by photolysis experiments reported in Figures S30 and S31 of SI.

The quantum yields for the ligand photodissociation from **Ru2** and **Ru3** (Φ_{434} values) were determined through the UV−vis and HPLC analyses as previously described and following the determination of the LED photon flux by the potassium ferrioxalate actinometry procedure.[49,54] The obtained results are summarized, along with the ones previously determined for **Ru1**, as shown in Table 1. As shown, the light-induced detachment of nitroimidazole-containing ligands in water occurred with Φ_{434} values ranging from 0.00027(2) to 0.0015(2), with **Ru3** being the most efficient. Higher values, of 0.0079 (9) (**Ru2**) and 0.0059 (4) (**Ru3**), were found in acetonitrile, indicating a higher efficiency of photolysis in organic media. Overall, it can be noted that the results determined for **Ru1**, **Ru2**, and **Ru3** turned out to be at least one order of magnitude lower if compared to the parental compound $[Ru(tpy)(dmp)(py)]^{2+}$ (py = pyridine), for whom, for example, the photorelease of a py unit in acetonitrile was reported to take place with a quantum yield of 0.058.[53] On the other hand, the lower photoreactivities of **Ru1**, **Ru2**, and **Ru3**

https://doi.org/10.1021/acs.inorgchem.3c00214
Inorg. Chem. XXXX, XXX, XXX−XXX

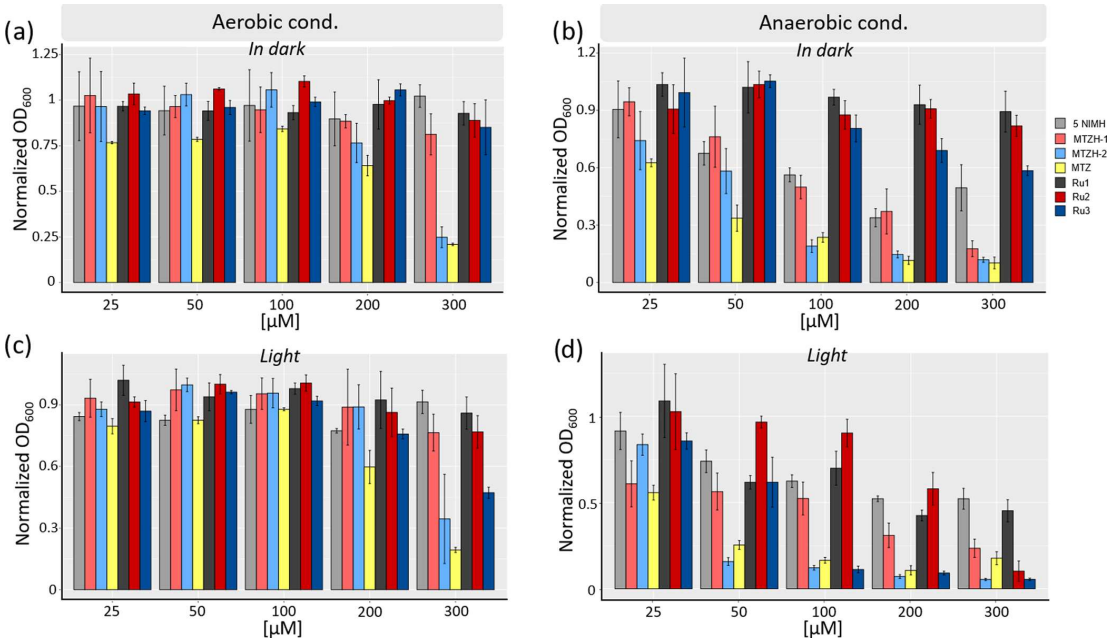

Figure 3. Antibacterial effect of ruthenium photocages **Ru1**, **Ru2**, and **Ru3**, their corresponding imidazole-based ligands 5NIMH, MTZH-1, and MTZH-2, and MTZ evaluated in the dark and following light activation under both aerobic (a, c) and anaerobic (b, d) conditions. Ratios of the normalized OD_{600} values are reported with respect to the blank control (*Y*-axis) as a function of different drug concentrations ([μM], *X*-axis).

were counterbalanced by remarkable stabilities displayed in dark conditions (Figures S28 and 29, SI). Therefore, apart from the different stereoelectronic features of ruthenium complexes, we can speculate that the peculiar Ru(II)−N^- coordination of nitroimidazole-containing ligands may affect both their thermal stability and photoreactivity, tuning the properties of the resulting complexes as photocages. Accordingly, this class of monodentate ligands would represent a suitable alternative to more extensively explored leaving groups, such as pyridines,[69] pyrazines,[54] amines,[70] thioethers,[71] and nitriles,[72] in an effort to answer the increasing demand for the development of new Ru(II)-based photocages, with sufficient ligand photoejection quantum yields without a concomitant loss in thermal stability.[53]

Lastly, since various pathways are, in principle, made accessible by irradiation, the capacity of ruthenium complexes to sensitize the production of singlet oxygen ($^1O_2$) was also evaluated. To this aim, aqueous solutions of metal compounds, in the presence of 1,5-dihydroxynaphtalene (DHN) as an indirect probe for $^1O_2$, were exposed to progressive irradiation times, and the resulting UV−vis spectra were collected. As shown in Figure S32 (SI), no evidence of the formation of Juglone, namely the photo-oxidation product of DHN, was observed during the overall time frame investigated. This confirms, in analogy to **Ru1**, the scarce sensitizing properties of **Ru2** and **Ru3** and further supports the population of dissociative ^{3}MC states, which can be harnessed to exert cytotoxic effects in low-oxygen conditions.[73]

***In Vitro* Antibacterial Activity and Interaction with NimA.** Preliminary to the evaluation of the antibacterial properties of Ru(II) compounds, their capacity to be effectively internalized by *B. subtilis* strain 168, which was selected as a model of Gram-positive bacteria, was investigated through inductively coupled plasma atomic emission spectroscopy (ICP-AES), as described in the SI (paragraph 3). As shown in Figure S33, all three complexes were found to be successfully internalized by bacterial cells, with the cell uptake following the order **Ru3** > **Ru1** > **Ru2**, thus suggesting a subtle influence of the different nitroimidazole derivatives on the permeation abilities of their resulting Ru(II) complexes.

We then inspected the antibacterial activities of **Ru1**, **Ru2**, and **Ru3**, along with the ones of their corresponding nitroimidazole-based ligands 5NIMH, MTZH-1, and MTZH-2; the effect of MTZ was also analyzed for comparison. Experiments were performed in the *dark* and following blue-light irradiation (LED emitting at 434 nm, t = 40 min) both in normoxia (21% O_2) and in hypoxia (<1% O_2), by using the experimental setup described in the SI (paragraph 4). The obtained results, expressed as normalized OD_{600} values indicating the ratio of cell growth compared to the control (untreated) cells, are reported in Figure 3.

As shown in Figure 3a, *in* the *dark* and under aerobic conditions, all of the tested compounds generally displayed negligible toxicity, except for MTZ and MTZH-2, which led to a remarkable effect starting at relatively high drug doses (>200 μM), with a *ca.* 75% reduction of cell growth at a higher concentration tested (300 μM). Irradiation under these conditions slightly affected the activities of the investigated compounds (Figure 3c). Indeed, only modest phototoxicities were observed for high doses of ruthenium complexes, with **Ru3** being the most effective compound across the series, featuring a *ca.* 40% reduction of cell growth at 300 μM.

A completely different scenario was observed under anaerobiosis. As it can be noted from Figure 3b, in the dark,

https://doi.org/10.1021/acs.inorgchem.3c00214
Inorg. Chem. XXXX, XXX, XXX−XXX

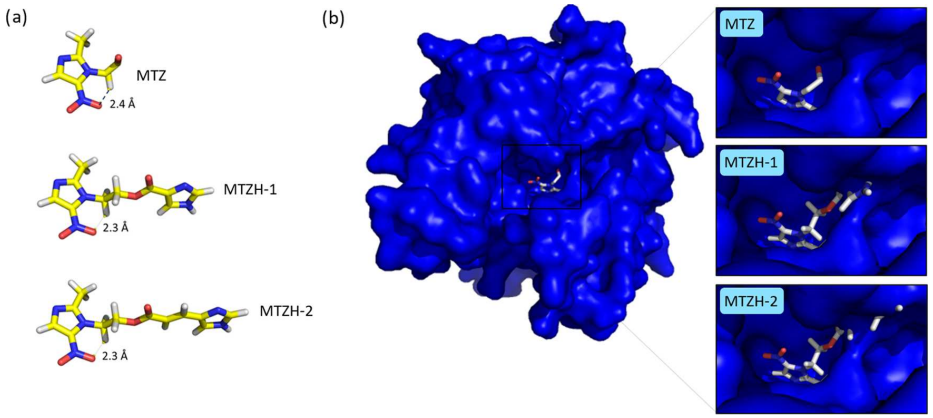

Figure 4. Experimental MTZ structure in the 1W3R PDB file and optimized MTZH-1 and MTZH-2 structures computed through DFT calculations (a) and MTZ, MTZH-1, and MTZH-2 ligands interacting with NimA protein (the surface of the protein is marked in in blue) (b).

all of the MTZ-containing compounds exhibited a sharp dose-dependent activity, with MTZH-2 and MTZ that displayed the highest, and comparable, effects. For instance, at a concentration of 100 μM, MTZH-2 and MTZ induced a reduction of cell growth around 75%, whereas a lower, though remarkable, effect (*ca.* 50%) was found for MTZH-1 at the same dose. Interestingly enough, even the less potent 5NIMH was found to induce a net dose-dependent effect under these conditions, in contrast to the scarce efficacy displayed in the aerobic tests of the present and previous reports.[49,74] The superior effectiveness of nitroimidazole-based compounds observed under anaerobic compared to aerobic conditions can be rationalized by considering the generally accepted mode of action of nitroimidazoles.[50] Indeed, this class of antimicrobials typically relies on the preliminary bioactivation of the nitro group, which occurs through its intracellular reduction to a radical anion to result in harmful ROS species, capable of interacting with a variety of cellular targets. However, high oxygen levels cause the rapid reoxidation of the radical anion, resulting in a futile cycle that impairs the bactericidal potential under aerobic conditions.

From Figure 3b, it also emerges that the antibacterial effects of "*Ru-free*" nitroimidazole-based ligands are effectively masked by their inclusion into ruthenium complexes, as indicated by the good tolerability demonstrated by cells toward **Ru1**, **Ru2**, and **Ru3** in the dark. Among these complexes, it can be highlighted the highest toxicity of **Ru3**, which, however, did not exceed a *ca.* 48% reduction of cell growth at the maximum dose tested.

Instead, the bioactivities of these ligands were partially or almost fully recovered upon irradiation under anaerobiosis, pointing at a different behavior to what is commonly observed in PACT, where the light-mediated effects are severely jeopardized when switching from aerobic to anaerobic conditions.[73,75] In fact, as shown in Figure 3d, the three ruthenium complexes displayed a sharp dose-dependent effect, with **Ru3** being the lead compound across the series. For instance, light irradiation of this complex at a concentration of 100 μM unleashed a *ca.* 9-fold enhancement of activity compared to dark conditions and induced, yet for drug doses above 50 μM, a comparable potency to the one of MTZ. In other words, the adoption of the photocaging strategy to control the liberation of this MTZ derivative would allow reproducing the high effectiveness of MTZ under hypoxic conditions but with the key advantage arising from the spatiotemporal control over the drug activation ensured by the use of light. It can be also noted that the phototoxicity of this complex nicely paralleled the effect of the *Ru-free* MTZH-2 derivative, thus making the liberation of this potent bioactive compound likely to be the cause of the observed photoactivity.

Lower, though remarkable, phototoxicities were induced by **Ru1** and **Ru2**, with **Ru2** that was the least effective in the 0–200 μM range. Its relatively low efficacy can be tentatively rationalized by considering that, besides the higher antibacterial activity of MTZH-1 relative to 5NIMH, the latter ligand was more efficiently photoreleased in aqueous media than MTZH-1 (Table 1). A rough correlation between the observed antibacterial activities of Ru(II) complexes and their cellular uptake should be also pointed out. This would suggest that an optimal balance between the biological activity of "*caged*" ligands, their capacity to be easily released from Ru(II)-photocages and the permeation abilities of the intact Ru(II) complexes, is crucial for the phototoxicity of the resulting Ru(II)-based antimicrobials.

Furthermore, the following remarks can be highlighted from the cell growth ratios registered between the different conditions tested, reported in Figure S35 of the SI: (i) the efficacy of nitroimidazole-based compounds is clearly enhanced in anaerobic compared to aerobic conditions and (ii) in neither aerobic nor anaerobic conditions, their antibacterial activity is markedly affected by light activation. Instead, irradiation in hypoxia strongly improved the dose-dependent activities of the photolabile complexes **Ru1**, **Ru2**, and **Ru3**, with **Ru3** featuring the highest phototoxicity across the series. Such results were also confirmed by measuring the cell viability after exposure to anaerobic conditions; as shown in Table S5 of SI, the effect of the photoactivated complexes under hypoxia not only reduced cell growth but also cell viability (*i.e.*, photoactivated complexes showed a bactericidal activity), with a complete killing of bacterial cells at 200 μM photoactivated **Ru2** and **Ru3** complexes. We also specify that effects on growth kinetics, and not only on overall growth and viability, can be present. However, the experimental setting of anaerobic conditions strongly limited the possibility of

https://doi.org/10.1021/acs.inorgchem.3c00214
Inorg. Chem. XXXX, XXX, XXX−XXX

measuring continuous growth kinetic data, which were then not included in the present study.

Lastly, bacterial resistance toward 5-nitroimidazole-based antibiotics is generally believed to be associated with decreased drug uptake and/or altered/deficient reduction efficiency. Concerning the latter point, several classes of resistant bacterial strains have been shown to possess *Nim* genes, which encode for reductase enzymes capable of converting the nitro group of the drug into a nonbactericidal amine and thus preventing the accumulation of the toxic nitro radical. More in detail, a previous study reporting on the crystal structure of NimA from *Deinococcus radiodurans* (drNimA) complexed with MTZ[76] proposed that the inactivation of this antibiotic would be the result of a two-electron reduction process taking place in the active site of the protein and mediated by the covalent binding of the cofactor pyruvate with His-71. Therefore, being inspired by these findings, we further considered the interaction of MTZ derivatives with the active site of NimA, which was selected as a representative model for this family of reductases.

To this aim, the molecular structures of MTZ, MTZH-1, and MTZH-2 ligands were optimized with DFT calculations at the B3LYP/6-31+G(d) level of theory. The obtained results, shown in Figure 4a, evidenced that these ligands are characterized by an intramolecular hydrogen bond between the $-NO_2$ group of the nitroimidazole residue and the nearest hydrogen atom of a $-CH_2$ residue, in good agreement with the X-ray data above discussed for MTZH-2 (also see SI, paragraph 1.2). It can be noted that such a hydrogen bond reduces the mobility of the ring moiety with respect to the substituents, and a similar intramolecular bond can be also observed in the experimental MTZ structure present in the PDB file 1W3R, thus confirming the agreement between experimental and our computed ligands. Then, the ring of each compound was superposed onto MTZ in 1W3R in NimA obtaining the results reported in Figure 4b. As shown, the rigidity imparted by the intramolecular interactions combined with the more extended chains gathered on the ester functions of MTZH-1 and MTZH-2 made these compounds clash with the NimA protein structure, whereas MTZ is nicely accommodated within the active site of the protein. Therefore, these preliminary data suggest that the different chemical structures of the two MTZ derivatives would impact their susceptibility to drug inactivation by NimA and hint at their possible use as potential options for clinicians to manage resistance to nitroimidazole-based antibiotics.

CONCLUSIONS

The net disparity between the countless examples of PACT agents and those studied for the photorelease of bioactive ligands in the design of new antimicrobials prompted us to design two novel derivatives of the antibiotics MTZ, MTZH-1, and MTZH-2, which were inserted in the corresponding strained ruthenium complexes **Ru2** and **Ru3**. The two MTZ derivatives were synthesized by Steglich esterification, by coupling MTZ with different imidazole-containing ligands of biological interest and whose imidazole moieties were exploited as linking units to Ru(II) centers. Analogously to the parental compound **Ru1**, the unusual Ru(II) coordination of MTZ derivatives in their imidazolate forms conferred the resulting Ru(II) complexes promising features as photocages, as denoted by the good stability shown in the *dark* and by the possibility to easily cause the detachment of MTZ-based ligands from ruthenium scaffolds upon exposure to visible light. The biological potential of metal-free ligands and metal complexes was tested on *B. subtilis*, which was chosen as a model of Gram-positive bacteria, and experiments were conducted both under normoxic (21% O_2) and hypoxic (<1% O_2) conditions. Our results highlighted two main findings: (i) the activity of metronidazole-containing ligands was remarkably enhanced by switching from aerobic to anaerobic conditions, as expected in consideration of the peculiar mode of action of the class of nitroimidazole-based antimicrobials. (ii) The insertion of ligands into ruthenium complexes masked their activity when kept in the *dark*, whereas light irradiation under hypoxia provoked a strong dose-dependent activity, with the lead compound **Ru3** that unleashed a comparable effect to one of the MTZ. These findings, therefore, probed that the photocaging strategy can be successfully exploited to control the activity of optimally designed MTZ derivatives, affording remarkable antibacterial activities under low-oxygen conditions upon light activation of the prodrugs.

Lastly, preliminary studies on the interaction of the MTZ derivatives with NimA, chosen as a model of reductases responsible for bacterial resistance against 5-nitroimidazole-based antibiotics, unveiled that the different chemical architectures of these bioactive ligands made their protein sequestration unfavorable if compared to MTZ, thus hinting at their possible use in the treatment of bacteria resistant to nitroimidazole-based antimicrobials.

In conclusion, the results of this work may provide fundamental knowledge for the development of suitable alternatives to be used in the struggle against infectious diseases, effective under hypoxic conditions and whose activation could be selectively controlled by using light. Moreover, for the first time, the effectiveness of the "*photorelease antimicrobial therapy*" approach under hypoxia was demonstrated.

ASSOCIATED CONTENT

Supporting Information

The Supporting Information is available free of charge at https://pubs.acs.org/doi/10.1021/acs.inorgchem.3c00214.

NMR, MS, ATR-FTIR, UV−vis, and fluorescence spectra of compounds; X-ray and DFT analysis; ICP-AES analysis; materials and methods; and experimental details, including photographs of the experimental setup for the antibacterial tests (PDF)

Accession Codes

CCDC 2231746 contains the supplementary crystallographic data for this paper. These data can be obtained free of charge via www.ccdc.cam.ac.uk/data_request/cif, or by emailing data_request@ccdc.cam.ac.uk, or by contacting The Cambridge Crystallographic Data Centre, 12 Union Road, Cambridge CB2 1EZ, UK; fax: +44 1223 336033.

AUTHOR INFORMATION

Corresponding Authors

Luca Conti − *Department of Chemistry "Ugo Schiff", University of Florence, 50019 Firenze, Italy*; orcid.org/0000-0002-0402-1293; Email: luca.conti@unifi.it

Claudia Giorgi − *Department of Chemistry "Ugo Schiff", University of Florence, 50019 Firenze, Italy*; Email: claudia.giorgi@unifi.it

https://doi.org/10.1021/acs.inorgchem.3c00214
Inorg. Chem. XXXX, XXX, XXX−XXX

Authors

Gina Elena Giacomazzo − *Department of Chemistry "Ugo Schiff", University of Florence, 50019 Firenze, Italy*

Camilla Fagorzi − *Department of Biology, University of Florence, 50019 Firenze, Italy*

Marco Pagliai − *Department of Chemistry "Ugo Schiff", University of Florence, 50019 Firenze, Italy;* orcid.org/0000-0003-0240-161X

Claudia Andreini − *Department of Chemistry "Ugo Schiff", University of Florence, 50019 Firenze, Italy; Magnetic Resonance Center (CERM), University of Florence, 50019 Firenze, Italy*

Annalisa Guerri − *Department of Chemistry "Ugo Schiff", University of Florence, 50019 Firenze, Italy;* orcid.org/0000-0001-6265-7874

Brunella Perito − *Department of Biology, University of Florence, 50019 Firenze, Italy*

Alessio Mengoni − *Department of Biology, University of Florence, 50019 Firenze, Italy;* orcid.org/0000-0002-1265-8251

Barbara Valtancoli − *Department of Chemistry "Ugo Schiff", University of Florence, 50019 Firenze, Italy*

Complete contact information is available at: https://pubs.acs.org/10.1021/acs.inorgchem.3c00214

Author Contributions

This manuscript was written through the contributions of all authors. All authors have given approval to the final version of this manuscript.

Notes

The authors declare no competing financial interest.

■ ACKNOWLEDGMENTS

The authors would like to thank Ing. Matteo Giacomazzo for the experimental setup employed for the biological tests and Prof. Mirko Severi of the Department of Chemistry "Ugo Schiff" for the ICP-AES analysis. The Mass Spectrometry Center of the University of Florence is also gratefully acknowledged for mass spectrometry analysis.

■ REFERENCES

(1) Thompson, T. The Staggering Death Toll of Drug-Resistant Bacteria. *Nature* **2022**, DOI: 10.1038/d41586-022-00228-x.

(2) Frei, A.; Zuegg, J.; Elliott, A. G.; Baker, M.; Braese, S.; Brown, C.; Chen, F.; G Dowson, C.; Dujardin, G.; Jung, N.; King, A. P.; Mansour, A. M.; Massi, M.; Moat, J.; Mohamed, H. A.; Renfrew, A. K.; Rutledge, P. J.; Sadler, P. J.; Todd, M. H.; Willans, C. E.; Wilson, J. J.; Cooper, M. A.; Blaskovich, M. A. T. Metal Complexes as a Promising Source for New Antibiotics. *Chem. Sci.* **2020**, *11*, 2627−2639.

(3) Pandey, A.; Boros, E. Coordination Complexes to Combat Bacterial Infections: Recent Developments, Current Directions and Future Opportunities. *Chem. - Eur. J.* **2021**, *27*, 7340−7350.

(4) Morrison, C. N.; Prosser, K. E.; Stokes, R. W.; Cordes, A.; Metzler-Nolte, N.; Cohen, S. M. Expanding Medicinal Chemistry into 3D Space: Metallofragments as 3D Scaffolds for Fragment-Based Drug Discovery. *Chem. Sci.* **2020**, *11*, 1216−1225.

(5) Kottelat, E.; Chabert, V.; Crochet, A.; Fromm, K. M.; Zobi, F. Towards Cardiolite-Inspired Carbon Monoxide Releasing Molecules − Reactivity of d 4, d 5 Rhenium and d 6 Manganese Carbonyl Complexes with Isocyanide Ligands. *Eur. J. Inorg. Chem.* **2015**, *2015*, 5628−5638.

(6) Rajalakshmi, S.; Fathima, A.; Rao, J. R.; Nair, B. U. Antibacterial Activity of Copper(<scp>ii</Scp>) Complexes against Staphylococcus Aureus. *RSC Adv.* **2014**, *4*, 32004−32012.

(7) Chowdhury, T.; Dasgupta, S.; Khatua, S.; Acharya, K.; Das, D. Executing a Series of Zinc(II) Complexes of Homologous Schiff Base Ligands for a Comparative Analysis on Hydrolytic, Antioxidant, and Antibacterial Activities. *ACS Appl. Bio Mater.* **2020**, *3*, 4348−4357.

(8) Bernier, C. M.; DuChane, C. M.; Martinez, J. S.; Falkinham, J. O.; Merola, J. S. Synthesis, Characterization, and Antimicrobial Activity of Rh III and Ir III N-Heterocyclic Carbene Piano-Stool Complexes. *Organometallics* **2021**, *40*, 1670−1681.

(9) Amoah, C.; Obuah, C.; Ainooson, M. K.; Adokoh, C. K.; Muller, A. Synthesis, Characterization and Antibacterial Applications of Pyrazolyl-Sulfonamides and Their Palladium Complexes. *New J. Chem.* **2021**, *45*, 3716−3726.

(10) Frei, A.; Ramu, S.; Lowe, G. J.; Dinh, H.; Semenec, L.; Elliott, A. G.; Zuegg, J.; Deckers, A.; Jung, N.; Bräse, S.; Cain, A. K.; Blaskovich, M. A. T. Platinum Cyclooctadiene Complexes with Activity against Gram-positive Bacteria. *ChemMedChem* **2021**, *16*, 3165−3171.

(11) Glišić, B. Đ.; Djuran, M. I. Gold Complexes as Antimicrobial Agents: An Overview of Different Biological Activities in Relation to the Oxidation State of the Gold Ion and the Ligand Structure. *Dalton Trans.* **2014**, *43*, 5950−5969.

(12) Nyssen, O. P.; Perez-Aisa, A.; Castro-Fernandez, M.; Pellicano, R.; Huguet, J. M.; Rodrigo, L.; Ortuñ, J.; Gomez-Rodriguez, B. J.; Pinto, R. M.; Areia, M.; Perona, M.; Nuñez, O.; Romano, M.; Gravina, A. G.; Pozzati, L.; Fernandez-Bermejo, M.; Venerito, M.; Malfertheiner, P.; Fernanadez-Salazar, L.; Gasbarrini, A.; Vaira, D.; Puig, I.; Megraud, F.; O'Morain, C.; Gisbert, J. P. European Registry on Helicobacter Pylori Management: Single-capsule Bismuth Quadruple Therapy Is Effective in Real-world Clinical Practice. *United Eur. Gastroenterol. J.* **2021**, *9*, 38−46.

(13) Barillo, D. J.; Barillo, A. R.; Korn, S.; Lam, K.; Attar, P. S. The Antimicrobial Spectrum of Xeroform. *Burns* **2017**, *43*, 1189−1194.

(14) Mjos, K. D.; Orvig, C. Metallodrugs in Medicinal Inorganic Chemistry. *Chem. Rev.* **2014**, *114*, 4540−4563.

(15) Monro, S.; Colón, K. L.; Yin, H.; Roque, J.; Konda, P.; Gujar, S.; Thummel, R. P.; Lilge, L.; Cameron, C. G.; McFarland, S. A. Transition Metal Complexes and Photodynamic Therapy from a Tumor-Centered Approach: Challenges, Opportunities, and Highlights from the Development of TLD1433. *Chem. Rev.* **2019**, *119*, 797−828.

(16) Conti, L.; Macedi, E.; Giorgi, C.; Valtancoli, B.; Fusi, V. Combination of Light and Ru(II) Polypyridyl Complexes: Recent Advances in the Development of New Anticancer Drugs. *Coord. Chem. Rev.* **2022**, *469*, No. 214656.

(17) Mari, C.; Pierroz, V.; Ferrari, S.; Gasser, G. Combination of Ru(<scp>ii</Scp>) Complexes and Light: New Frontiers in Cancer Therapy. *Chem. Sci.* **2015**, *6*, 2660−2686.

(18) Conti, L.; Ciambellotti, S.; Giacomazzo, G. E.; Ghini, V.; Cosottini, L.; Puliti, E.; Severi, M.; Fratini, E.; Cencetti, F.; Bruni, P.; Valtancoli, B.; Giorgi, C.; Turano, P. Ferritin Nanocomposites for the Selective Delivery of Photosensitizing Ruthenium-Polypyridyl Compounds to Cancer Cells†. *Inorg. Chem. Front.* **2022**, *9*, 1070−1081.

(19) Liu, J.; Zhang, C.; Rees, T. W.; Ke, L.; Ji, L.; Chao, H. Harnessing Ruthenium(II) as Photodynamic Agents: Encouraging Advances in Cancer Therapy. *Coord. Chem. Rev.* **2018**, *363*, 17−28.

(20) Conti, L.; Giacomazzo, G. E.; Valtancoli, B.; Perfetti, M.; Privitera, A.; Giorgi, C.; Sfragano, P. S.; Palchetti, I.; Pecchioli, S.; Bruni, P.; Cencetti, F. Highly Charged Ru(II) Polypyridyl Complexes as Photosensitizer Agents in Photodynamic Therapy of Epithelial Ovarian Cancer Cells. *Int. J. Mol. Sci.* **2022**, *23*, No. 13302.

(21) Dwyer, F. P.; Gyarfas, E. C.; Rogers, W. P.; Koch, J. H. Biological Activity of Complex Ions. *Nature* **1952**, *170*, 190−191.

(22) Dwyer, F. P.; Reid, I. K.; Shulman, A.; Laycock, G. M.; Dixson, S. The Biological Actions of 1,10-Phenanthroline and 2,2′-Bipyridine Hydrochlorides, Quaternary Salts and Metal Chelates and Related Compounds. *Aust. J. Exp. Biol. Med. Sci.* **1969**, *47*, 203−218.

(23) Li, F.; Collins, J. G.; Keene, F. R. Ruthenium Complexes as Antimicrobial Agents. *Chem. Soc. Rev.* **2015**, *44*, 2529−2542.
(24) Smitten, K. L.; Fairbanks, S. D.; Robertson, C. C.; de la Serna, J. B.; Foster, S. J.; Thomas, J. A. Ruthenium Based Antimicrobial Theranostics − Using Nanoscopy to Identify Therapeutic Targets and Resistance Mechanisms in *Staphylococcus Aureus*. *Chem. Sci.* **2020**, *11*, 70−79.
(25) ChunYan, Z.; RuJian, Y.; LiQiang, W.; HaiYan, H.; JinTao, W.; XiangWen, L.; XueMin, D.; YanShi, X. Design, Synthesis, and Evaluation of Aryl-Thioether Ruthenium Polypyridine Complexes: A Multi-Target Antimicrobial Agents against Gram-Positive Bacteria. *Eur. J. Med. Chem.* **2022**, *240*, No. 114562.
(26) Chen, Y.; Liu, L.; Wang, X.; Liao, Z.; Wang, R.; Xiong, Y.; Cheng, J.; Jiang, G.; Wang, J.; Liao, X. The Synthesis and Antibacterial Activity Study of Ruthenium-Based Metallodrugs with a Membrane-Disruptive Mechanism against Staphylococcus Aureus. *Dalton Trans.* **2022**, *51*, 14980−14992.
(27) Wang, R.; Wei, M.; Wang, X.; Chen, Y.; Xiong, Y.; Cheng, J.; Tan, Y.; Liao, X.; Wang, J. Synthesis of Ruthenium Polypyridine Complexes with Benzyloxyl Groups and Their Antibacterial Activities against Staphylococcus Aureus. *J. Inorg. Biochem.* **2022**, *236*, No. 111954.
(28) Heinemann, F.; Karges, J.; Gasser, G. Critical Overview of the Use of Ru(II) Polypyridyl Complexes as Photosensitizers in One-Photon and Two-Photon Photodynamic Therapy. *Acc. Chem. Res.* **2017**, *50*, 2727−2736.
(29) Le Gall, T.; Lemercier, G.; Chevreux, S.; Tücking, K. S.; Ravel, J.; Thétiot, F.; Jonas, U.; Schönherr, H.; Montier, T. Ruthenium(II) Polypyridyl Complexes as Photosensitizers for Antibacterial Photodynamic Therapy: A Structure−Activity Study on Clinical Bacterial Strains. *ChemMedChem* **2018**, *13*, 2229−2239.
(30) Munteanu, A.-C.; Uivarosi, V. Ruthenium Complexes in the Fight against Pathogenic Microorganisms. An Extensive Review. *Pharmaceutics* **2021**, *13*, No. 874.
(31) Arenas, Y.; Monro, S.; Shi, G.; Mandel, A.; McFarland, S.; Lilge, L. Photodynamic Inactivation of Staphylococcus Aureus and Methicillin-Resistant Staphylococcus Aureus with Ru(II)-Based Type I/Type II Photosensitizers. *Photodiagn. Photodyn. Ther.* **2013**, *10*, 615−625.
(32) Youf, R.; Müller, M.; Balasini, A.; Thétiot, F.; Müller, M.; Hascoët, A.; Jonas, U.; Schönherr, H.; Lemercier, G.; Montier, T.; Le Gall, T. Antimicrobial Photodynamic Therapy: Latest Developments with a Focus on Combinatory Strategies. *Pharmaceutics* **2021**, *13*, No. 1995.
(33) Jain, A.; Garrett, N. T.; Malone, Z. P. Ruthenium-based Photoactive Metalloantibiotics †. *Photochem. Photobiol.* **2022**, *98*, 6−16.
(34) Boccalini, G.; Conti, L.; Montis, C.; Bani, D.; Bencini, A.; Berti, D.; Giorgi, C.; Mengoni, A.; Valtancoli, B. Methylene Blue-Containing Liposomes as New Photodynamic Anti-Bacterial Agents. *J. Mater. Chem. B* **2017**, *5*, 2788−2797.
(35) Feng, Y.; Sun, W.; Wang, X.; Zhou, Q. Selective Photoinactivation of Methicillin-Resistant Staphylococcus Aureus by Highly Positively Charged Ru II Complexes. *Chem. - Eur. J.* **2019**, *25*, 13879−13884.
(36) Conti, L.; Mengoni, A.; Giacomazzo, G. E.; Mari, L.; Perfetti, M.; Fagorzi, C.; Sorace, L.; Valtancoli, B.; Giorgi, C. Exploring the Potential of Highly Charged Ru(II)- and Heteronuclear Ru(II)/Cu(II)-Polypyridyl Complexes as Antimicrobial Agents. *J. Inorg. Biochem.* **2021**, *220*, No. 111467.
(37) Maisch, T. Resistance in Antimicrobial Photodynamic Inactivation of Bacteria. *Photochem. Photobiol. Sci.* **2015**, *14*, 1518−1526.
(38) Pierce, S.; Jennings, M. P.; Juliano, S. A.; Angeles-Boza, A. M. Peptide−Ruthenium Conjugate as an Efficient Photosensitizer for the Inactivation of Multidrug-Resistant Bacteria. *Inorg. Chem.* **2020**, *59*, 14866−14870.
(39) Bonnet, S. Why Develop Photoactivated Chemotherapy? *Dalton Trans.* **2018**, *47*, 10330−10343.
(40) Knoll, J. D.; Turro, C. Control and Utilization of Ruthenium and Rhodium Metal Complex Excited States for Photoactivated Cancer Therapy. *Coord. Chem. Rev.* **2015**, *282*−*283*, 110−126.
(41) Knoll, J. D.; Albani, B. A.; Turro, C. Excited State Investigation of a New Ru(Ii) Complex for Dual Reactivity with Low Energy Light. *Chem. Commun.* **2015**, *51*, 8777−8780.
(42) van Rixel, V. H. S.; Ramu, V.; Auyeung, A. B.; Beztsinna, N.; Leger, D. Y.; Lameijer, L. N.; Hilt, S. T.; Le Dévédec, S. E.; Yildiz, T.; Betancourt, T.; Gildner, M. B.; Hudnall, T. W.; Sol, V.; Liagre, B.; Kornienko, A.; Bonnet, S. Photo-Uncaging of a Microtubule-Targeted Rigidin Analogue in Hypoxic Cancer Cells and in a Xenograft Mouse Model. *J. Am. Chem. Soc.* **2019**, *141*, 18444−18454.
(43) Imberti, C.; Zhang, P.; Huang, H.; Sadler, P. J. New Designs for Phototherapeutic Transition Metal Complexes. *Angew. Chem., Int. Ed.* **2020**, *59*, 61−73.
(44) Cole, H. D.; Roque, J. A.; Shi, G.; Lifshits, L. M.; Ramasamy, E.; Barrett, P. C.; Hodges, R. O.; Cameron, C. G.; McFarland, S. A. Anticancer Agent with Inexplicable Potency in Extreme Hypoxia: Characterizing a Light-Triggered Ruthenium Ubertoxin. *J. Am. Chem. Soc.* **2022**, *144*, 9543−9547.
(45) Garner, R. N.; Pierce, C. G.; Reed, C. R.; Brennessel, W. W. Photoinitiated Treatment of Mycobacterium Using Ru(II) Isoniazid Complexes. *Inorg. Chim. Acta* **2017**, *461*, 261−266.
(46) de Sousa, A. P.; Gondim, A. C. S.; Sousa, E. H. S.; de Vasconcelos, M. A.; Teixeira, E. H.; Bezerra, B. P.; Ayala, A. P.; Martins, P. H. R.; de França Lopes, L. G.; Holanda, A. K. M. An Unusual Bidentate Methionine Ruthenium(II) Complex: Photo-Uncaging and Antimicrobial Activity. *JBIC J. Biol. Inorg. Chem.* **2020**, *25*, 419−428.
(47) Nunes, E. D.; Villela, A. D.; Basso, L. A.; Teixeira, E. H.; Andrade, A. L.; Vasconcelos, M. A.; Do Nascimento Neto, L. G.; Gondim, A. C. S.; Diógenes, I. C. N.; Romo, A. I. B.; Nascimento, O. R.; Zampieri, D.; Paulo, T. F.; De Carvalho, I. M. M.; De França Lopes, L. G.; Sousa, E. H. S. Light-Induced Disruption of an Acyl Hydrazone Link as a Novel Strategy for Drug Release and Activation: Isoniazid as a Proof-of-Concept Case. *Inorg. Chem. Front.* **2020**, *7*, 859−870.
(48) Smith, N. A.; Zhang, P.; Greenough, S. E.; Horbury, M. D.; Clarkson, G. J.; McFeely, D.; Habtemariam, A.; Salassa, L.; Stavros, V. G.; Dowson, C. G.; Sadler, P. J. Combatting AMR: Photoactivatable Ruthenium(<scp>ii</Scp>)-Isoniazid Complex Exhibits Rapid Selective Antimycobacterial Activity. *Chem. Sci.* **2017**, *8*, 395−404.
(49) Giacomazzo, G. E.; Conti, L.; Guerri, A.; Pagliai, M.; Fagorzi, C.; Sfragano, P. S.; Palchetti, I.; Pietraperzia, G.; Mengoni, A.; Valtancoli, B.; Giorgi, C. Nitroimidazole-Based Ruthenium(II) Complexes: Playing with Structural Parameters to Design Photostable and Light-Responsive Antibacterial Agents. *Inorg. Chem.* **2022**, *61*, 6689−6694.
(50) Ang, C. W.; Jarrad, A. M.; Cooper, M. A.; Blaskovich, M. A. T. Nitroimidazoles: Molecular Fireworks That Combat a Broad Spectrum of Infectious Diseases. *J. Med. Chem.* **2017**, *60*, 7636−7657.
(51) Kim, P.; Zhang, L.; Manjunatha, U. H.; Singh, R.; Patel, S.; Jiricek, J.; Keller, T. H.; Boshoff, H. I.; Barry, C. E.; Dowd, C. S. Structure−Activity Relationships of Antitubercular Nitroimidazoles. 1. Structural Features Associated with Aerobic and Anaerobic Activities of 4- and 5-Nitroimidazoles. *J. Med. Chem.* **2009**, *52*, 1317−1328.
(52) Kaveevivitchai, N.; Zong, R.; Tseng, H.-W.; Chitta, R.; Thummel, R. P. Further Observations on Water Oxidation Catalyzed by Mononuclear Ru(II) Complexes. *Inorg. Chem.* **2012**, *51*, 2930−2939.
(53) Havrylyuk, D.; Stevens, K.; Parkin, S.; Glazer, E. C. Toward Optimal Ru(II) Photocages: Balancing Photochemistry, Stability, and Biocompatibility Through Fine Tuning of Steric, Electronic, and Physiochemical Features. *Inorg. Chem.* **2020**, *59*, 1006−1013.
(54) Havrylyuk, D.; Deshpande, M.; Parkin, S.; Glazer, E. C. Ru(<scp>ii</Scp>) Complexes with Diazine Ligands: Electronic Modulation of the Coordinating Group Is Key to the Design of "Dual Action" Photoactivated Agents. *Chem. Commun.* **2018**, *54*, 12487−12490.

https://doi.org/10.1021/acs.inorgchem.3c00214
Inorg. Chem. XXXX, XXX, XXX−XXX

(55) Nicholson, W. L.; Park, R. Anaerobic Growth of *Bacillus subtilis Alters* the Spectrum of Spontaneous Mutations in the RpoB Gene Leading to Rifampicin Resistance. *FEMS Microbiol. Lett.* **2015**, *362*, No. fnv213.
(56) Frisch, M. J.; Trucks, G. W.; Schlegel, H. B.; Scuseria, G. E.; Robb, M. A.; Cheeseman, J. R.; Scalmani, G.; Barone, V.; Mennucci, B.; Petersson, G. A.; Nakatsuji, H.; Caricato, M.; Li, X.; Hratchian, H. P.; Izmaylov, A. F.; Bloino, J.; Zheng, G.; Sonnenberg, J. L.; Hada, M.; Ehara, M.; Toyota, K.; Fukuda, R.; Hasegawa, J.; Ishida, M.; Nakajima, T.; Honda, Y.; Kitao, O.; Nakai, H.; Vreven, T.; Montgomery, J. A., Jr.; Peralta, J. E.; Ogliaro, F.; Bearpark, M.; Heyd, J. J.; Brothers, E.; Kudin, K. N.; Staroverov, V. N.; Kobayashi, R.; Normand, J.; Raghavachari, K.; Rendell, A.; Burant, J. C.; Iyengar, S. S.; Tomasi, J.; Cossi, M.; Rega, N.; Millam, J. M.; Klene, M.; Knox, J. E.; Cross, J. B.; Bakken, V.; Adamo, C.; Jaramillo, J.; Gomperts, R.; Stratmann, R. E.; Yazyev, O.; Austin, A. J.; Cammi, R.; Pomelli, C.; Ochterski, J. W.; Martin, R. L.; Morokuma, K.; Zakrzewski, V. G.; Voth, G. A.; Salvador, P.; Dannenberg, J. J.; Dapprich, S.; Daniels, A. D.; Farkas, Ö.; Foresman, J. B.; Ortiz, J. V.; Cioslowski, J.; Fox, D. J. *Gaussian 09*; Gaussian, Inc: Wallingford CT, 2009.
(57) Dingsdag, S. A.; Hunter, N. Metronidazole: An Update on Metabolism, Structure−Cytotoxicity and Resistance Mechanisms. *J. Antimicrob. Chemother.* **2018**, *73*, 265−279.
(58) Das, B.; Jia, C.; Ching, K.; Bhadbhade, M.; Chen, X.; Ball, G. E.; Colbran, S. B.; Zhao, C. Ruthenium Complexes in Homogeneous and Heterogeneous Catalysis for Electroreduction of CO 2. *ChemCatChem* **2020**, *12*, 1292−1296.
(59) Yang, X.-J.; Drepper, F.; Wu, B.; Sun, W.-H.; Haehnel, W.; Janiak, C. From Model Compounds to Protein Binding: Syntheses, Characterizations and Fluorescence Studies of [Ru II (Bipy)(Terpy)-L] 2+ Complexes (Bipy = 2,2′-Bipyridine; Terpy = 2,2′:6′,2″-Terpyridine; L = Imidazole, Pyrazole and Derivatives, Cytochrome C). *Dalton Trans.* **2005**, 256−267.
(60) Reddy, K. B.; Cho, M. P.; Wishart, J. F.; Emge, T. J.; Isied, S. S. Cis -Bis(Bipyridine)Ruthenium Imidazole Derivatives: A Spectroscopic, Kinetic, and Structural Study. *Inorg. Chem.* **1996**, *35*, 7241−7245.
(61) Heijden, M.; Van Vliet, P. M.; Haasnoot, J. G.; Reedijk, J. Synthesis and Characterization of Cis-(2,2′-Bipyridine)(2,2′-Biquinoline) Dichlororuthenium(<scp>II</Scp>) and Its Co-Ordination Chemistry with Imidazole Derivatives. *J. Chem. Soc., Dalton Trans.* **1993**, 3675−3679.
(62) Sasahara, G. L.; Gouveia, F. S., Jr; de Oliveira Rodrigues, R.; Zampieri, D. S.; da Cruz Fonseca, S. G.; de Cássia Ribeiro Gonçalves, R.; Athaydes, B. R.; Kitagawa, R. R.; Santos, F. A.; Sousa, E. H. S.; Nagao-Dias, A. T.; de França Lopes, L. G. Nitro-Imidazole-Based Ruthenium Complexes with Antioxidant and Anti-Inflammatory Activities. *J. Inorg. Biochem.* **2020**, *206*, No. 111048.
(63) Hasegawa, K.; Ono, T.; Noguchi, T. Ab Initio Density Functional Theory Calculations and Vibrational Analysis of Zinc-Bound 4-Methylimidazole as a Model of a Histidine Ligand in Metalloenzymes. *J. Phys. Chem. A* **2002**, *106*, 3377−3390.
(64) Wu, A.; Masland, J.; Swartz, R. D.; Kaminsky, W.; Mayer, J. M. Synthesis and Characterization of Ruthenium Bis(*β*-Diketonato) Pyridine-Imidazole Complexes for Hydrogen Atom Transfer. *Inorg. Chem.* **2007**, *46*, 11190−11201.
(65) Siewert, B.; Langerman, M.; Hontani, Y.; Kennis, J. T. M.; van Rixel, V. H. S.; Limburg, B.; Siegler, M. A.; Talens Saez, V.; Kieltyka, R. E.; Bonnet, S. Turning on the Red Phosphorescence of a [Ru(Tpy)(Bpy)(Cl)]Cl Complex by Amide Substitution: Self-Aggregation, Toxicity, and Cellular Localization of an Emissive Ruthenium-Based Amphiphile. *Chem. Commun.* **2017**, *53*, 11126−11129.
(66) Knoll, J. D.; Albani, B. A.; Durr, C. B.; Turro, C. Unusually Efficient Pyridine Photodissociation from Ru(II) Complexes with Sterically Bulky Bidentate Ancillary Ligands. *J. Phys. Chem. A* **2014**, *118*, 10603−10610.
(67) Hecker, C. R.; Fanwick, P. E.; McMillin, D. R. Evidence for Dissociative Photosubstitution Reactions of (Acetonitrile)-(Bipyridine)(Terpyridine)Ruthenium(2+). Crystal and Molecular Structure of [Ru(Trpy)(Bpy)(Py)](PF6)2.Cntdot.(CH3)2CO. *Inorg. Chem.* **1991**, *30*, 659−666.
(68) Yoshikawa, N.; Yamabe, S.; Kanehisa, N.; Kai, Y.; Takashima, H.; Tsukahara, K. Syntheses, Characterization, and DFT Investigation of New Mononuclear Acetonitrile- and Chloro-Ruthenium(II) Terpyridine Complexes. *Inorg. Chim. Acta* **2006**, *359*, 4585−4593.
(69) Havrylyuk, D.; Hachey, A. C.; Fenton, A.; Heidary, D. K.; Glazer, E. C. Ru(II) Photocages Enable Precise Control over Enzyme Activity with Red Light. *Nat. Commun.* **2022**, *13*, No. 3636.
(70) Zayat, L.; Salierno, M.; Etchenique, R. Ruthenium(II) Bipyridyl Complexes as Photolabile Caging Groups for Amines. *Inorg. Chem.* **2006**, *45*, 1728−1731.
(71) Chen, Q.; Cuello-Garibo, J. A.; Bretin, L.; Zhang, L.; Ramu, V.; Aydar, Y.; Batsiun, Y.; Bronkhorst, S.; Husiev, Y.; Beztsinna, N.; Chen, L.; Zhou, X. Q.; Schmidt, C.; Ott, I.; Jager, M. J.; Brouwer, A. M.; Snaar-Jagalska, B. E.; Bonnet, S. Photosubstitution in a Trisheteroleptic Ruthenium Complex Inhibits Conjunctival Melanoma Growth in a Zebrafish Orthotopic Xenograft Model. *Chem. Sci.* **2022**, *13*, 6899−6919.
(72) Li, A.; Turro, C.; Kodanko, J. J. Ru(II) Polypyridyl Complexes as Photocages for Bioactive Compounds Containing Nitriles and Aromatic Heterocycles. *Chem. Commun.* **2018**, *54*, 1280−1290.
(73) Roque, J.; Havrylyuk, D.; Barrett, P. C.; Sainuddin, T.; McCain, J.; Colón, K.; Sparks, W. T.; Bradner, E.; Monro, S.; Heidary, D.; Cameron, C. G.; Glazer, E. C.; McFarland, S. A. Strained, Photoejecting Ru(II) Complexes That Are Cytotoxic Under Hypoxic Conditions. *Photochem. Photobiol.* **2020**, *96*, 327−339.
(74) Thomas, C.; Gwenin, C. D. The Role of Nitroreductases in Resistance to Nitroimidazoles. *Biology* **2021**, *10*, No. 388.
(75) Zhang, C.; Guo, X.; Da, X.; Wang, Z.; Wang, X.; Zhou, Q. A Ru-Anthraquinone Dyad with Triple Functions of PACT, Photoredox Catalysis and PDT upon Red Light Irradiation. *Dalton Trans.* **2021**, *50*, 10845−10852.
(76) Leiros, H.-K. S.; Kozielski-Stuhrmann, S.; Kapp, U.; Terradot, L.; Leonard, G. A.; McSweeney, S. M. Structural Basis of 5-Nitroimidazole Antibiotic Resistance. *J. Biol. Chem.* **2004**, *279*, 55840−55849.

https://doi.org/10.1021/acs.inorgchem.3c00214
Inorg. Chem. XXXX, XXX, XXX−XXX